ICP/EXT-05-01016

Subsurface Flow and Transport Model Development for the Operable Unit 7-13/14 Remedial Investigation and Feasibility Study

Swen O. Magnuson
A. Jeffrey Sondrup

March 2006

Idaho Cleanup Project

The Idaho Cleanup Project is operated for the
U.S. Department of Energy by CH2M◆WG Idaho, LLC

ICP/EXT-05-01016
Revision 0
Project No. 23378

Subsurface Flow and Transport Model Development for the Operable Unit 7-13/14 Remedial Investigation and Feasibility Study

Swen O. Magnuson
A. Jeffrey Sondrup

Edited by LauraLee Gourley

March 2006

Idaho Cleanup Project
Idaho Falls, Idaho 83415

Prepared for the
U.S. Department of Energy
Assistant Secretary for Environmental Management
Under DOE Idaho Operations Office
Contract DE-AC07-05ID14516

ABSTRACT

In support of the remedial investigation and baseline risk assessment and feasibility study for Operable Unit 7-13/14, a numerical model has been developed to simulate subsurface transport of contaminants released from buried waste at the Subsurface Disposal Area at the Idaho National Laboratory Site. The model, referred to as the remedial investigation and feasibility study model, is the latest and most comprehensive in a series of Subsurface Disposal Area subsurface contaminant transport models, and features significant improvements over the most recent predecessor model presented in the *Ancillary Basis for Risk Analysis*. The model incorporates and uses the latest characterization and monitoring data and represents the current best interpretation of water movement and contaminant transport in the Subsurface Disposal Area subsurface.

This document contains a summary of the conceptual model and how it was implemented into a numerical model, not only for purposes of assessing risk, but also for purposes of evaluating remedial alternatives as part of the feasibility study. The report contains all relevant model assumptions, and the basis for selection of model parameter values. In addition, it describes all modifications and improvements made to the Ancillary Basis for Risk Analysis model, and summarizes specific modeling studies supporting the revisions. Simulation results, in terms of moisture distributions and resulting contaminant concentrations, are presented for the remedial investigation and baseline risk assessment base case and different sensitivity cases. Finally, a discussion of the model's applicability, strengths, limitations, and general uncertainty is included.

CONTENTS

ABSTRACT iii

ACRONYMS xvii

1. INTRODUCTION 1-1

1.1 Modeling Background 1-1

1.2 Subsurface Disposal Area Background 1-2

1.3 Objectives 1-4

1.4 Scope 1-4

1.5 Report Organization 1-4

2. PREVIOUS OPERABLE UNIT 7-13/14 COMPREHENSIVE MODELS AND IMPROVEMENTS FOR THE REMEDIAL INVESTIGATION AND FEASIBILITY STUDY MODEL 2-1

2.1 Predecessor Models 2-1

2.1.1 Interim Risk Assessment Model 2-1
2.1.2 Ancillary Basis for Risk Analysis Model 2-2

2.2 Corrections to the Ancillary Basis for Risk Analysis Model 2-2

2.2.1 Vadose Zone Vertical Grid Extension 2-2
2.2.2 Spatially Variable Interbed Porosity and Permeability 2-3
2.2.3 Interface Between Source-Release and Vadose Zone Models 2-3

2.3 Aquifer Domain Extension 2-3

2.4 Lithology Database Quality Assessment 2-3

2.5 No Spreading Area Influence in the Vadose Zone 2-4

2.6 Reduction of Infiltration Rate Assigned Inside the Subsurface Disposal Area 2-4

2.7 Facilitated Transport of Plutonium-239 and Plutonium-240 2-4

2.8 Revision of Sediment Distribution Coefficients 2-4

2.9 Gaseous-phase Simulation of Carbon-14 and Volatile Organic Compounds 2-5

2.10 Increased Number of Waste Streams 2-5

3. TETRAD SIMULATION CODE 3-1

3.1 Description 3-1

3.2 Modifications to Version 12.7 Resulting in Version 12.7ms 3-3

3.3 Quality Control 3-3

4. OPERABLE UNIT 7-13/14 FLOW AND TRANSPORT MODEL DESCRIPTION 4-1

4.1 Conceptual Model 4-1

4.2 Assumptions 4-3

4.2.1 Flow 4-3
4.2.2 Transport 4-4

4.3 Vadose Zone Model 4-5

4.3.1 Domain and Horizontal Discretization 4-5
4.3.2 Lithology 4-5
4.3.3 Vertical Discretization 4-12
4.3.4 Hydrologic Properties 4-12
4.3.5 Boundary Conditions 4-21
4.3.6 Initial Conditions 4-25
4.3.7 Contaminant Transport 4-26

4.4 Aquifer Model 4-34

4.4.1 Transport Properties 4-35
4.4.2 Aquifer Permeability Comparison 4-35
4.4.3 Comparison to Estimated Aquifer Flow Directions 4-35
4.4.4 Link to Operable Unit 10-08 for Future Aquifer Model Development 4-38

5. SIMULATIONS SUPPORTING PARAMETERIZATION OF THE OPERABLE UNIT 7-13/14 MODEL 5-1

5.1 Measured Interbed Moisture Comparisons 5-1

5.1.1 Advanced Tensiometer Monitoring Network 5-1
5.1.2 Remedial Investigation and Feasibility Study Base Model Comparison to Deep Tensiometer Monitoring Network Matric Potentials 5-1
5.1.3 Remedial Investigation and Feasibility Study Base Model Comparison to Interbed Saturation 5-5
5.1.4 Remedial Investigation and Feasibility Study Base Model Comparison to Interbed Vertical Water Fluxes 5-5

5.2 Fractured Basalt Hydrologic Property 5-6

5.3 Magnesium Chloride Dust Suppressant Transport 5-6

5.4 Development and Calibration of the Volatile Organic Compound Transport Model 5-23

5.4.1 Objectives 5-23
5.4.2 Volatile Organic Compound Model Description 5-23

5.4.3 Volatile Organic Compound Model Calibration Methodology 5-35
5.4.4 Volatile Organic Compound Transport Model Calibration 5-36
5.4.5 Final Calibration Results 5-42
5.4.6 Volatile Organic Compound Transport Model Calibration Summary 5-51
5.4.7 Impact of Fluctuating Barometric Pressure Boundary Condition 5-51

5.5 Dual-Phase Carbon-14 Simulations 5-52

5.5.1 Carbon-14 Partitioning from Column Experiment 5-52
5.5.2 Carbon-14 Beryllium Block Near-Field Simulation 5-53
5.5.3 Operable Unit 7-13/14 Model Carbon-14 Implementation 5-53
5.5.4 Summary 5-56

6. OPERABLE UNIT 7-13/14 FATE AND TRANSPORT MODEL RESULTS 6-1

6.1 Baseline Risk Assessment Base-Case Simulation with Comparison to Monitoring Results 6-1

6.1.1 Vadose Zone: 0 to 10.7 m (0 to 35 ft) 6-1
6.1.2 Vadose Zone: 10.7 to 76.2 m (35 to 250 ft) 6-8
6.1.3 Aquifer 6-13

6.2 Receptor Locations and Extraction of Simulated Aquifer Concentrations for Risk Evaluation 6-42

6.3 Risk and Hazard Index Isopleth Methodology 6-44

6.4 Base-Case Sensitivity Simulations 6-45

6.4.1 Upper-bound Inventories 6-45
6.4.2 No B-C Interbed 6-45
6.4.3 High Infiltration Inside the Subsurface Disposal Area 6-48
6.4.4 Pit 4 Inventory Not Removed and No Beryllium Block Grouting 6-48
6.4.5 Low Background Infiltration 6-51
6.4.6 No Low-Permeability Region in Aquifer 6-52
6.4.7 Fractured Basalt Anisotropy 6-52
6.4.8 No Sorption in Vadose Zone Interbeds 6-56

6.5 Feasibility Study Simulations 6-57

6.5.1 Modified Resource Conservation and Recovery Act Type C Surface Barrier 6-57
6.5.2 Evapotranspiration Surface Barrier 6-57
6.5.3 In Situ Grouting 6-59
6.5.4 Partial Retrieval, Treatment, and Disposal 6-60
6.5.5 Full Retrieval, Treatment, and Disposal 6-60
6.5.6 Full Retrieval, Treatment, and Disposal with No Infiltration-reducing Cap 6-60
6.5.7 Evapotranspiration Surface Barrier with 1.0-cm/year Infiltration 6-60
6.5.8 Modified Resource Conservation and Recovery Act Type C Surface Barrier with Low Background Infiltration 6-60

6.6 Radiological Low-Level Waste Performance Assessment Simulations 6-61

7. SUMMARY 7-1

7.1 Limitations 7-2

7.2 Uncertainty/Sensitivity 7-3

7.3 Areas for Improvement of the Remedial Investigation and Baseline Risk Assessment Model 7-4

8. REFERENCES 8-1

Appendix A—Comparison of Simulation Results with TETRAD 12.7 and TETRAD 12.7ms A-1

Appendix B—Description of the Electronic Archive of Simulation Code, Input Files, Simulation Results, Software Management Agreement, and Listing of PV-Wave Processing Codes B-1

Appendix C—Aquifer Model Domain Extension C-1

Appendix D—Analysis of Aquifer Hydraulic Gradient in the Radioactive Waste Management Complex Vicinity D-1

Appendix E—Comparison of Additional Interbed Hydrologic Properties to Estimated Values E-1

Appendix F—Reanalysis of B-C Interbed Porosity Spatial Variability F-1

Appendix G—Complete Carbon Tetrachloride Vapor-Phase Model Calibration Results G-1

Appendix H—Operable Unit 7-13/14 Numerical Dispersion Evaluation H-1

FIGURES

1-1. Map of the Radioactive Waste Management Complex showing pits, trenches, and soil vault rows within the Subsurface Disposal Area 1-3

4-1. Horizontal domain for the remedial investigation and feasibility study vadose zone flow and transport 4-6

4-2. Horizontal discretization for the vadose zone model domain 4-7

4-3. Kriged ground surface elevation (feet above mean sea level) for the second-level refined grid 4-8

4-4. Kriged thickness (feet) of the surficial sediment for the second-level refined grid 4-8

4-5. Kriged surface (feet above mean sea level) of the A-B interbed for the second-level refined grid 4-9

4-6. Kriged thickness (feet) of the A-B interbed for the second-level refined grid 4-9

4-7. Kriged surface (feet above mean sea level) of the B-C interbed for the first-level refined grid 4-10

4-8. Kriged thickness (feet) of the B-C interbed for the first-level refined grid 4-10

4-9. Kriged surface (feet above mean sea level) of the C-D interbed for the base grid 4-11

4-10. Kriged thickness (feet) of the C-D interbed for the base grid 4-11

4-11. Southwest and northeast views of the base grid beneath the Subsurface Disposal Area showing vertical conformable gridding 4-13

4-12. Southwest and northeast views of the first-level refined grid showing vertical conformable gridding 4-13

4-13. Southwest view of the second-level refined grid showing vertical conformable gridding 4-14

4-14. Kriged permeability (mD) for the B-C and C-D interbeds 4-17

4-15. Kriged porosity for the B-C and C-D interbeds 4-18

4-16. Maximum simulated porosity for the B-C interbed 4-20

4-17. Spatially variable infiltration assignment for model domain inside the Subsurface Disposal Area 4-22

4-18. Locations of additional water applied during the 1962, 1969, and 1982 flooding events in the Subsurface Disposal Area in the second-level refined grid 4-23

4-19. Initial condition simulation showing the time history of water saturation in the C-D interbed beneath the Subsurface Disposal Area 4-25

4-20. Initial condition simulation showing time history of water saturation in the basalt matrix beneath the C-D interbed 4-26

4-21. Subsurface Disposal Area infiltration rates with averages by source area for dissolved-phase contaminants 4-32

4-22. Subsurface Disposal Area infiltration rates with averages by source area for carbon-14 4-33

4-23. Subsurface Disposal Area infiltration rates with averages by source area for volatile organic compound contaminants 4-33

4-24. Transmissivity (feet^2/day) from pump tests in the Subsurface Disposal Area vicinity 4-36

4-25. Simulated groundwater average horizontal linear velocities (meter/year) for the first-level refined grid in the aquifer domain compared to interpreted aquifer flow directions as a function of time 4-37

4-26. Simulated vertical average linear velocities (m/year) for the uppermost layer in the first-level refined grid in the aquifer domain 4-38

5-1. Location of advanced tensiometers in the Subsurface Disposal Area. 5-2

5-2. Simulated water potential (cm H_20) for the base case with comparison to averaged measured water potentials from McElroy and Hubbell (2003) 5-3

5-3. Maximum interbed water saturations with an interbed van Genuchten N parameter set to 1.323 5-7

5-4. Maximum interbed water saturations with an interbed van Genuchten N parameter set to 1.523 5-8

5-5. Maximum interbed water saturations with an interbed van Genuchten N parameter set to 2.423 5-9

5-6. Maximum interbed vertical water flux (cm/year) for the base-case model and estimated vertical flux from McElroy and Hubbell (2003) 5-10

5-7. Simulated vertical average linear velocity in fractured basalt beneath the B-C interbed for A) B_w =2.0, B) B_w =1.5, and C) B_w =1.001 5-11

5-8. Estimated locations of magnesium chloride application in 1984, 1985, and 1992 through 1993 5-13

5-9. Simulated magnesium chloride application rates and locations in 1984 5-14

5-10. Simulated cumulative magnesium chloride application rates and locations from 1984 through 1993 5-15

5-11. Locations for cross section (yellow shaded) and time history (orange shaded) comparisons for chloride simulations 5-16

5-12. Simulated chloride concentrations with 100% annual release of applied chloride brine 5-16

5-13. Simulated (red line) and observed (blue diamonds) chloride concentrations at the D06-DL02 lysimeter location 5-17

5-14. Simulated (red line) and observed (blue diamonds) chloride concentrations at the I-4S-DL15 and I-4D-DL14 lysimeter locations 5-18

5-15. Locations receiving additional water to emulate infiltration in ditches along the primary east-west access road across the Subsurface Disposal Area 5-19

5-16. Simulated chloride concentrations with an additional 10 cm infiltrating along the east-west access road each year in April 5-20

5-17. Simulated (red line) and observed (blue diamonds) chloride concentrations at the D06-DL02 lysimeter location with an additional 10 cm infiltrating along the east-west access road each year in April 5-20

5-18. Simulated (red line) and observed (blue diamonds) chloride concentrations at the I-4S-DL15 location with an additional 10 cm infiltrating along the east-west access road each year in April 5-21

5-19. Simulated chloride concentrations with additional 30 cm infiltrating along the east-west access road each year in April 5-21

5-20. Simulated (red line) and observed (blue diamonds) chloride concentrations at the D06-DL02 lysimeter location with additional 30 cm infiltrating along the east-west access road each year in April 5-22

5-21. Simulated (red stars) and observed (blue diamonds) chloride concentrations at the I-4S-DL15 location with an additional 30 cm infiltrating along the east-west access road each year in April 5-22

5-22. Simulated chloride concentrations at a series of increasing depths for the base (chlor1) and for the additional 10 cm (chlor4) and 30 cm (chlor5) of water infiltrating in April along the east-west access road 5-24

5-23. Barometric pressure data with square-wave approximation as implemented in the carbon tetrachloride calibration simulation 5-28

5-24. Locations of air-drilled wells (excluding reverse-air-rotary) in the vicinity of the Subsurface Disposal Area with a depth of greater than 18 m (60-ft) 5-29

5-25. Operable Unit 7-08 vapor extraction and vapor monitoring well locations 5-32

5-26. Depth of vapor ports and extraction intervals in Operable Unit 7-08 wells 5-33

5-27. Operable Unit 7-08 vapor vacuum extraction with treatment unit operation history 5-34

5-28. Results of carbon tetrachloride source-release parameter variations showing combinations that result in 50% of the original mass remaining in the year 2000 5-38

5-29. Carbon tetrachloride vapor concentration contours on a west-east cross section of the base model grid through the center of the Subsurface Disposal Area 5-40

5-30. Comparison of simulated vapor concentration results using assigned tortuosity values (Table 5-6) and tortuosity values calculated by the model for each gridblock using the Millington formulation 5-41

5-31. Comparison of simulated and measured carbon tetrachloride vapor concentration vertical profiles for select vapor-monitoring wells in the vicinity of the Subsurface Disposal Area 5-44

5-32. Comparison of simulated (stars) and measured (diamonds) carbon tetrachloride vapor concentration time histories for select vapor-monitoring ports in the vicinity of the Subsurface Disposal Area through the year 1995 5-45

5-33. Screen intervals for aquifer monitoring wells in relation to vertical aquifer model grid discretization 5-47

5-34. Time-history comparison of simulated (stars) and measured (diamonds) carbon tetrachloride concentrations in the aquifer at wells in and around the Subsurface Disposal Area through the year 2005 5-48

5-35. Time history of measured and simulated carbon tetrachloride concentrations in aquifer at wells in and around the Subsurface Disposal Area 5-50

5-36. Time-history comparison of simulated carbon tetrachloride mass flux to the aquifer, with and without surface barometric pressure fluctuations 5-52

5-37. Maximum simulated aquifer carbon-14 concentration, anywhere in the simulation domain, at a depth of 12 m (39.3 ft), with and without surface barometric pressure fluctuations 5-54

5-38. Maximum simulated concentration anywhere in the aquifer, with and without aseous-phase partitioning in the vadose zone transport model 5-55

5-39. Time history of simulated (red line) and observed (blue diamonds) carbon-14 aqueous-phase concentrations at Well USGS-92 5-56

5-40. Comparison of time histories for simulated carbon-14 concentrations (red line) to observed monitoring results (blue diamonds) for aquifer monitoring wells in the vicinity of the Subsurface Disposal Area 5-57

5-41. Simulated aquifer carbon-14 concentrations (pCi/L) at the 12-m (39.3-ft) depth for the year 2004 5-59

6-1. Time-history comparison of simulated (red line) and observed (blue diamonds) concentrations for uranium-238 in the lysimeters at Wells PA01, PA02, and W08 6-2

6-2. Time-history comparison of simulated (red line) and observed (blue diamonds) concentrations for uranium-238 in the lysimeters at Well W23 6-4

6-3. Cross sections in the second-level refined grid vadose zone domain 6-5

6-4. Cross sections showing simulated uranium-238 aqueous concentrations in Calendar Year 2004 6-6

6-5. Time-history comparison of simulated (red line) and observed (blue diamonds) concentrations for technetium-99 in the lysimeters at Well W23 6-7

6-6. Cross section showing simulated technetium-99 aqueous concentrations in Calendar Year 2004 6-8

6-7. Time-history comparison of simulated (red line) and observed (blue diamonds) concentrations for nitrate in Lysimeters PA02-L16 and W25-L08 6-9

6-8. Time history-comparison of simulated (red line) and observed (blue diamonds) concentrations for uranium-238 in the lysimeters in the 10.7- to 76.2-m (35- to 250-ft) depth interval 6-10

6-9. Time-history comparison of simulated (red line) and observed (blue diamonds) concentrations for technetium-99 in the lysimeters in the 10.7- to 76.2-m (35- to 250-ft) depth interval 6-11

6-10. Time-history comparison of simulated (red line) and observed (blue diamonds) concentrations for nitrate in the lysimeters in the 10.7- to 76.2-m (35-to 250-ft) depth interval 6-12

6-11. Comparison of simulated (red line) and observed (blue diamonds) nitrate (as N) concentration time histories for aquifer-monitoring wells in the vicinity of the Subsurface Disposal Area 6-14

6-12. Simulated aquifer nitrate concentrations (mg/L) for the year 2004 for the refined aquifer domain 6-16

6-13. Simulated aquifer nitrate concentrations (mg/L) for the year 2004 for the base aquifer domain 6-17

6-14. Simulated and observed nitrate concentrations superimposed onto monitoring locations in the vicinity of the Radioactive Waste Management Complex 6-18

6-15. Simulated aquifer nitrate concentration profiles beneath the Subsurface Disposal Area 6-20

6-16. Simulated aquifer nitrate concentrations (mg/L) for north-south cross sections through the location of maximum simulated concentration at times corresponding to profiles shown in Figure 6-15 6-21

6-17. Time history of the simulated nitrate flux from the vadose zone simulation at the grid location profiled in Figure 6-15 6-22

6-18. Comparison of simulated (red line) and observed (blue diamonds) chromium concentration time histories for aquifer-monitoring wells in the vicinity of the Subsurface Disposal Area 6-23

6-19. Simulated aquifer chromium concentrations (ug/L) for Calendar Year 2004 for the refined aquifer domain. Background concentrations are not added to simulation results 6-25

6-20. Comparison of simulated (red line) and observed (blue diamonds) iodine-129 concentration time histories for aquifer-monitoring wells in the vicinity of the Subsurface Disposal Area 6-27

6-21. Comparison of simulated (red line) and observed (blue diamonds) technetium-99 concentration time histories for aquifer-monitoring wells in the vicinity of the Subsurface Disposal Area 6-29

6-22. Comparison of simulated (red line) and observed (blue diamonds) americium-241 concentration time histories for aquifer-monitoring wells in the vicinity of the Subsurface Disposal Area 6-31

6-23. Comparison of simulated (red line) and observed (blue diamonds) neptunium-237 concentration time histories for aquifer-monitoring wells in the vicinity of the Subsurface Disposal Area 6-33

6-24. Comparison of simulated (red line) and observed (blue diamonds) plutonium-238 concentration time histories for aquifer-monitoring wells in the vicinity of the Subsurface Disposal Area 6-35

6-25. Comparison of simulated (red line) and observed (blue diamonds) plutonium-239 concentration time histories for aquifer-monitoring wells in the vicinity of the Subsurface Disposal Area 6-37

6-26. Simulated aquifer carbon-14 concentration profiles beneath the Subsurface Disposal Area 6-41

6-27. Simulated aquifer uranium-238 concentration profiles beneath the Subsurface Disposal Area 6-42

6-28. Subsurface Disposal Area fence superimposed on the first-level refined grid of the aquifer simulation for purpose of defining hypothetical receptor locations for the draft remedial investigation and baseline risk assessment 6-43

6-29. Subsurface Disposal Area fence plus a 100-m buffer superimposed on the first-level refined grid of the aquifer simulation for the purpose of defining hypothetical receptor locations for the low-level waste performance assessment and composite analysis 6-44

6-30. Comparison of the base (B) and the upper-bound inventory (Bu) maximum simulated concentration anywhere in the aquifer for uranium-238, carbon-14, and nitrate 6-46

6-31. Comparison of the base (B) and the no B-C interbed (Bnbc) maximum simulated concentration anywhere in the aquifer for uranium-238, carbon-14, and nitrate 6-47

6-32. Comparison of the base (B) and high infiltration inside the Subsurface Disposal Area (Bhi) maximum simulated concentration anywhere in the aquifer for uranium-238, carbon-14, and nitrate 6-49

6-33. Maximum simulated water saturation in the B-C and C-D interbeds for the high-infiltration rate of 23 cm/year (9 in./year) everywhere inside the Subsurface Disposal Area 6-50

6-34. Comparison of the base (B) and Pit 4 inventory not removed and no beryllium block grouting (B4ng) maximum simulated concentration anywhere in the aquifer for uranium-238 and carbon-14 6-51

6-35. Comparison of the base (B) and low background infiltration (Bloi) maximum simulated concentration anywhere in the aquifer for uranium-238, carbon-14, and nitrate 6-53

6-36. Comparison of the base (B) and no low-permeability region in aquifer (Bnlk) maximum simulated concentration anywhere in the aquifer for uranium-238, carbon-14, and nitrate 6-54

6-37. Time history of maximum simulated aquifer concentrations for a range of fractured basalt anisotropy ratios for B_g6, FmR_g6, and FmRpa_g6 simulations 6-58

6-38. Comparison of the base (B) and the no sorption in the interbeds (BcP) maximum simulated concentration anywhere in the aquifer along the INL Site boundary and at the extreme southern extent of the model domain for plutonium-239 and plutonium-240 6-59

TABLES

4-1. Parameterization of hydrologic properties and source of parameters for surficial sediment, A-B interbed, and fractured basalt 4-14

4-2. Parameterization of hydrologic properties and source of parameters for the basalt matrix for dual-continua simulations 4-20

4-3. Historical flooding volumes and application rates at the Subsurface Disposal Area 4-23

4-4. Sediment distribution coefficients for Operable Unit 7-13/14 remedial investigation and feasibility study simulations 4-27

4-5. Aqueous-phase tortuosity values for the remedial investigation and feasibility study model 4-29

4-6. Half-lives for radioactive contaminants of potential concern used in the remedial investigation and feasibility study groundwater-pathway simulations 4-30

4-7. Contaminant groups for Operable Unit 7-13/14 simulations 4-31

5-1. Simulated water potential statistics (cm H_20) for a range of van Genuchten N values for the B-C and C-D interbeds 5-4

5-2. Volatile organic compound chemical and transport properties 5-27

5-3. Information on air-drilled wells at the Subsurface Disposal Area with a depth greater than 18 m (60 ft), excluding wells drilled using reverse-air circulation 5-29

5-4. Best available data for volatile organic compound source-release model inputs 5-36

5-5. Ranges of volatile organic compound source-release model inputs examined 5-37

5-6. Initial tortuosity values for the different material types used in the model 5-39

6-1. Comparison of aquifer model concentrations and observed concentrations with no adjustments for background concentrations 6-39

ACRONYMS

ABRA	Ancillary Basis for Risk Analysis
COPC	contaminant of potential concern
INL	Idaho National Laboratory
IRA	Interim Risk Assessment
RI/BRA	remedial investigation and baseline risk assessment
RI/FS	remedial investigation and feasibility study
RWMC	Radioactive Waste Management Complex
SDA	Subsurface Disposal Area
USGS	United States Geological Survey
VOC	volatile organic compound
VVET	vapor vacuum extraction with treatment

Subsurface Flow and Transport Model Development for the Operable Unit 7-13/14 Remedial Investigation and Feasibility Study

1. INTRODUCTION

This document presents development of the predictive flow and transport model used to evaluate the fate of contaminants from waste buried in the Subsurface Disposal Area (SDA) for the ongoing Operable Unit 7-13/14 remedial investigation and baseline risk assessment (RI/BRA) and feasibility study. This document is a companion to the draft RI/BRA and relies on discussions of geology, hydrology, and contaminant monitoring presented in the draft RI/BRA. A separate companion document describes the source-release model that addresses inventory and release mechanisms (Anderson and Becker 2006). An assumption is made that review of the draft RI/BRA will not produce substantive comments that would warrant changes to this modeling report.

1.1 Modeling Background

A series of numerical simulators have been developed by the Operable Unit 7-13/14 Project to represent water movement and contaminant transport beneath the SDA. Before this current model, the most recent model was the flow and transport simulation model developed for the Ancillary Basis for Risk Analysis (ABRA) (Holdren et al. 2002). That model will be referred to as the ABRA model in this report. An earlier model that preceded the ABRA model was presented in Magnuson and Sondrup (1998) and was used for the Interim Risk Assessment (IRA) (Becker et al. 1998). That model is referred to as the IRA model. Each of these previous models represented best available knowledge of subsurface information at the time they were developed to assess risks from transport of contaminants along the groundwater pathway. This information has evolved over time, along with understanding of the impacts of some of the assumptions included in the earlier modeling and the belated discovery of some minor errors in the implementation of the ABRA model, necessitating the development of a new model to support the Operable Unit 7-13/14 remedial investigation and feasibility study (RI/FS).

In this sequence of models developed for the Operable Unit 7-13/14 Project, the aquifer portion of subsurface pathway modeling has always been treated conservatively with simplistic assumptions that result in three-dimensional, advective-dispersive transport. Emphasis has been on developing the vadose zone model to relax conservative assumptions used in screening-level models.

The model developed for this report, called the RI/FS model, represents the most current and comprehensive interpretation of water and contaminant movement in the subsurface and was derived from the model presented in the ABRA. The improved information, minor errors in the ABRA model, and revised assumptions are summarized in Section 2. For the benefit of readers familiar with the ABRA model, detailed comparisons of assumptions and parameterization between the ABRA model and the RI/FS model are presented throughout this report.

The RI/FS model represents water movement and contaminant transport in the subsurface after contaminants are released from their disposal locations. This representation mimics flow and transport, where possible, and makes conservative assumptions otherwise. Simulations were also completed to support the Operable Unit 7-13/14 feasibility study, using this updated model with reduced infiltration and various treatments on waste inventory beginning in Calendar Year 2010. These same feasibility study simulations also support the radiological low-level waste performance assessment and composite analysis required to meet Department of Energy Order 435.1 requirements.

1.2 Subsurface Disposal Area Background

Originally established in 1949 as the National Reactor Testing Station, the Idaho National Laboratory (INL) Site is a Department of Energy-managed reservation, occupying 2,305 km^2 (890 mi^2) in the northeastern region of the Snake River Plain. The INL Site extends nearly 63 km (39 mi) from north to south, is about 58 km (36 mi) wide in its broadest southern portion, and occupies parts of five southeastern Idaho counties (Holdren et al. 2002).

Located in the southwestern quadrant of the INL Site, the Radioactive Waste Management Complex (RWMC) encompasses a total of 72 ha (177 acres) and is divided into three separate areas by function: the SDA, the Transuranic Storage Area, and the administration and operations area. The current size of the SDA is 39 ha (97 acres)—approximately 35 of the 97 acres contains waste. Located adjacent to the east side of the SDA, the Transuranic Storage Area was added to RWMC in 1970, encompasses 23 ha (58 acres), and is used to store, prepare, and ship stored transuranic waste to the Waste Isolation Pilot Plant. The 9-ha (22-acre) administration and operations area at RWMC includes administrative offices, maintenance buildings, equipment storage, and miscellaneous support facilities (Holdren et al. 2002).

The SDA is a radioactive waste landfill with shallow subsurface disposal units consisting of pits, trenches, and soil vaults (see Figure 1-1). Constituents in the landfill include hazardous chemicals, remote-handled fission and activation products, and transuranic radionuclides. Waste acceptance criteria and record-keeping protocols for the facility have changed over time in keeping with waste management technology and legal requirements. Today's requirements are much more stringent as a result of knowledge developed over the past several decades about potential environmental effects of waste management techniques. Previously, however, shallow landfill disposal of radioactive and hazardous waste was the conventional disposal technology.

Construction, operation, and decommissioning of INL Site nuclear reactor testing programs have resulted in large volumes of waste. Various containers were used in shipping and disposing of waste, including steel drums, casks, cardboard cartons, and wooden boxes. Larger individual items—such as tanks, furniture, process and laboratory equipment, engines, and vehicles—were placed separately as loose trash. Additionally, liquid waste was buried in the SDA, including direct disposal of free liquids to pits and trenches and disposal of solidified liquids in containers (Holdren et al. 2002).

Radioactive waste from off-INL Site sources originated from a variety of facilities, including military and other defense agencies, universities, commercial operations, and the U.S. Atomic Energy Commission. The primary off-INL Site contributor was the Rocky Flats Plant. Shipping of waste to the INL Site from the Rocky Flats Plant began in April 1954 and continued into late 1989. Waste from the Rocky Flats Plant was deposited underground in a series of pits and trenches until 1970, when the U.S. Atomic Energy Commission policy was implemented requiring segregation and retrievable storage of all solid transuranic waste. After 1970, transuranic waste received from the Rocky Flats Plant was placed in aboveground, earthen-covered retrievable storage at the Transuranic Storage Area. Aboveground stored waste was designated as transuranic retrievable waste (Vejvoda 2005). Initially, waste was stacked in pits and trenches. However, beginning in 1963, some waste was dumped to reduce labor costs and minimize radiation exposure of personnel. Current disposal operations stack contact-handled waste to maximize disposal capacity of the landfill. Remote-handled waste is placed in either concrete vaults or the bulk storage area.

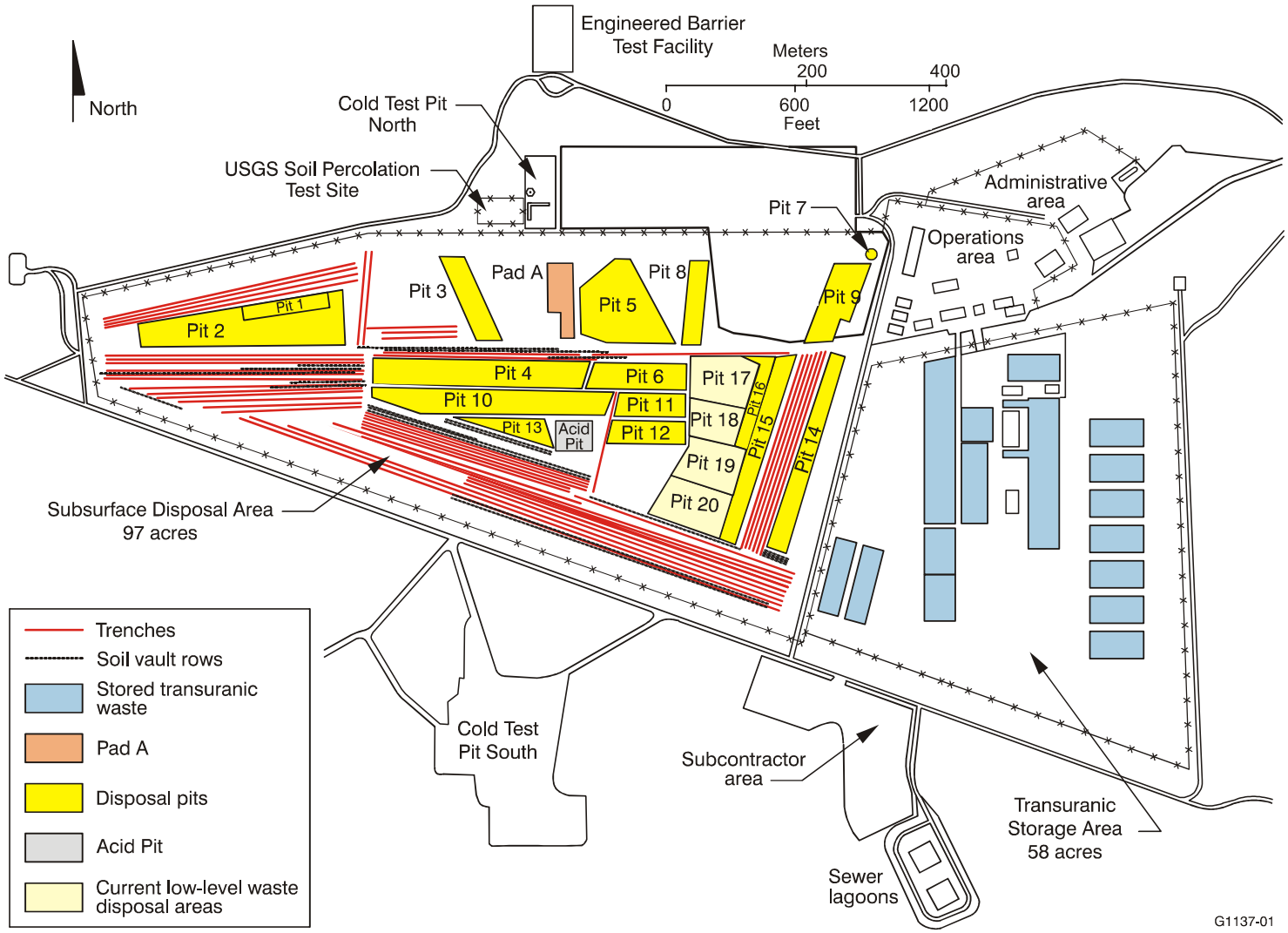

Figure 1-1. Map of the Radioactive Waste Management Complex showing pits, trenches, and soil vault rows within the Subsurface Disposal Area.

1.3 Objectives

The overall objective in developing the RI/FS model was to create a simulator that would be sufficiently representative of water movement and contaminant transport so that predictive simulations would be suitable to support decisions that will be made during the Operable Unit 7-13/14 RI/FS process. In this instance, sufficiently representative means the model generally represents observed transport or can be demonstrated to be conservative with respect to maximizing groundwater-pathway concentrations. For clarity, the latter would result in overpredicting concentrations in the aquifer.

This document has the following specific objectives:

- Summarize modifications and improvements to the ABRA model and parameters
- Summarize specific modeling studies that support revisions to the ABRA model
- Document base-case model simulations used for the Operable Unit 7-13/14 RI/BRA
- Document base-case sensitivity simulations for the Operable Unit 7-13/14 RI/BRA
- Document feasibility study simulations for Operable Unit 7-13/14
- Document simulations for the Department of Energy Order 435.1 performance assessment and composite analysis
- Summarize limitations of the resulting model in terms of calibration and processes included and excluded.

1.4 Scope

This document provides a complete description of the Operable Unit 7-13/14 flow and transport model used for the RI/FS. Also presented are modeling studies conducted since the ABRA model was developed to support revision of the ABRA model and determination of parameters in the Operable Unit 7-13/14 RI/FS flow and transport model.

1.5 Report Organization

Previous IRA and ABRA modeling efforts for Operable Unit 7-13/14 are summarized and corrections and refinements to the ABRA model are discussed in Section 2.

The TETRAD numerical simulator is described in Section 3, along with modifications to the TETRAD simulator to facilitate use for Operable Unit 7-13/14 RI/FS modeling.

The conceptual model, underlying assumptions, and complete description of the Operable Unit 7-13/14 flow and transport model are provided in Section 4.

Section 5 presents simulations that were performed as part of parameterizing the RI/FS model. Section 5 also includes comparisons to measured matric potentials from the advanced tensiometer network, comparisons of simulated velocities in the fractured basalt, a simulation study on chloride brine transport beneath the SDA, CCl_4 calibration, and the implementation process for simulating C-14 with partitioning into the gaseous phase.

A comparison of simulated concentrations from the RI/FS model in the surficial sediment, deeper vadose zone, and aquifer are discussed in Section 6, along with a description of the RI/BRA sensitivity

simulations, simulations to be performed for the feasibility study, and simulations performed for the performance assessment and composite analysis.

Appendixes A through H contain complete details of supplemental modeling studies that support the Operable Unit 7-13/14 RI/FS model.

2. PREVIOUS OPERABLE UNIT 7-13/14 COMPREHENSIVE MODELS AND IMPROVEMENTS FOR THE REMEDIAL INVESTIGATION AND FEASIBILITY STUDY MODEL

This section describes previous models developed for Operable Unit 7-13/14 to represent comprehensive evaluations of subsurface water and contaminant movement for the purpose of risk analysis. It then summarizes improvements implemented in the RI/FS model.

2.1 Predecessor Models

The RI/FS model represents culmination of a sequence of iterative modeling. The two previous iterations of three-dimensional modeling are the IRA model and the ABRA model. Both are described briefly to provide context for the RI/FS model.

2.1.1 Interim Risk Assessment Model

The IRA model represented the first attempt to simulate flow and transport through the entire vadose zone and aquifer domains for an extensive suite of contaminants of potential concern (COPCs). Calibration of vadose zone perched water behavior and an interpreted contribution to nitrate concentrations in the aquifer were attempted for the IRA model. Results were termed limited in their degree of success in emulating observed behavior. Attempts to improve calibration were hindered by lack of a widespread, well-behaved, identifiable plume in the vadose zone attributed strictly to dissolved-phase transport. Typically, contaminants in the vadose zone beneath the SDA (see Section 4 of the draft RI/BRA) are either not detected or are detected at very low concentrations with no stable temporal trends; therefore, monitoring data that could be used to demonstrate transport of a dissolved-phase nonsorbing contaminant were extremely sparse. The IRA model was used to make a series of 10,000-year predictive aquifer simulations for 52 contaminants. Results of that modeling formed the basis for risk estimates in the IRA (Becker et al. 1998) and were used to screen contaminants for the ABRA.

Waste management personnel at the INL Site also used the IRA model to update both the performance assessment (Case et al. 2000) and the composite analysis (McCarthy et al. 2000). The IRA model development, implementation, and results have undergone extensive review by Fabryka-Martin, Gee, and Flint (1999) and the U.S. Geological Survey (USGS) (Rousseau et al. 2005). Though reviews of the IRA model were generally complimentary, none concluded that the IRA model was satisfactory for developing conclusive predictions of the fate and transport of contaminants in the subsurface. The USGS review was by far the most extensive. The main comments from Rousseau et al. (2005) about modeling flow and transport of radionuclides at RWMC follow:

- Modeling performed for the IRA cannot necessarily be shown to be conservative.
- Spatial variability of hydrologic and transport properties of the sedimentary interbeds should be evaluated, and the impact of including this spatial variability into the IRA model should be assessed.
- Impacts of additional sources of vadose zone water from the Big Lost River system on predicted contaminant concentrations should be evaluated.

- Selected distribution coefficient (K_d) values used in the IRA cannot be shown to be conservative because they do not account for (1) colloidal transport, (2) the enhanced actinide mobility fraction observed in column studies, (3) variations in mineralogy, (4) nonlinearity of isotherms, and (5) fluctuations in pore-water chemistry. Furthermore, K_d values taken from the literature cannot be shown to be representative of the SDA.

2.1.2 Ancillary Basis for Risk Analysis Model

The ABRA model was developed to respond to each of the USGS review observations, particularly the second and third bullets (Rousseau et al. 2005). The vadose zone and aquifer portions of the simulation domain were separated, allowing increased discretization in the vadose zone model. This improved discretization included a gridding method that used variable gridblock thicknesses to better conform to the topography of the interbeds. The lithologic selections included interpretations from 22 additional wells drilled in 1999. Sediment cores were collected from the B-C and C-D interbeds and analyzed for hydrologic and transport properties. These analyses allowed a spatial description of the hydrologic properties to be implemented in the ABRA model. The aquifer model was further calibrated to take advantage of seven new wells completed since publication of the IRA model.

Additional refinement in the vadose zone model allowed an improved resolution of waste streams in the source-release model, with a closer match between infiltration rates assigned in the vadose zone model and those assigned in the source-release model. Twenty-four contaminants, which were all radionuclides with the exception of nitrate, were simulated with the ABRA model. Volatile organic compounds (VOCs) were not simulated with the ABRA model.

This ABRA model was used to make estimates of possible effects on groundwater-pathway risks from implementation of a preliminary set of remedial alternatives. Results of this modeling were documented in the Preliminary Evaluation of Remedial Alternatives (Zitnik et al. 2002). Alternatives that were evaluated singly and in combinations included an infiltration-reducing cap, in situ grouting, in situ vitrification, and waste removal.

2.2 Corrections to the Ancillary Basis for Risk Analysis Model

Three errors in the ABRA model were discovered since publication of the ABRA report. These errors have been corrected in the RI/FS model and are discussed individually.

2.2.1 Vadose Zone Vertical Grid Extension

The bottom 27.4 m (90 ft) of the vadose zone simulation domain were inadvertently omitted from the ABRA. This 27.4-m (90–ft) portion represents fractured basalt and would, therefore, have had minimal impact on the simulation results because fractured basalt hydrologic-property parameterization ensures rapid water movement. Because only dissolved-phase transport was simulated in the ABRA, this rapid water movement also ensured rapid dissolved-phase transport. There would not have been any noticeable increase in contaminant travel times through the vadose zone if the 27.4 m (90 ft) had been included.

Because the RI/FS model includes vapor-phase transport, the missing 27.4 m (90 ft) would be potentially more important; therefore, the RI/FS model domain now correctly extends down to the bottom of the vadose zone, requiring additional gridblocks in the base vadose zone domain, and slightly adds to the computational requirements for the RI/FS model.

2.2.2 Spatially Variable Interbed Porosity and Permeability

Kriged B-C and C-D interbed porosities and permeabilities were used in the ABRA. A row versus column indexing inconsistency in the assignment of permeabilities resulted in an incorrect permeability field for both the B-C and C-D interbeds. The kriged permeability fields from Leecaster (2002) are now correctly implemented in the RI/FS model. In addition, an error occurred in selecting minimum versus averaged porosities from the core–sample-characterization results for the B-C interbed. This error was also corrected. Additionally, Leecaster (2002) used the minimum instead of average porosities from each location where core samples were evaluated for the B-C interbed evaluation. The spatial variability analysis and kriging of porosities onto the vadose zone-model domains for the B-C and C-D interbed was reanalyzed for the RI/FS model with slightly higher averaged B-C interbed porosities. The reanalysis is contained in Appendix F. Neither of these errors was substantive in affecting simulation results presented in the ABRA.

2.2.3 Interface Between Source-Release and Vadose Zone Models

The source-release model requires a count of the number of gridblocks into which contaminant mass was loaded. In conducting the ABRA, this number of gridblocks was slightly increased, but the information provided to the source-release model was not updated. The result was to slightly increase the mass input to the vadose zone model above what should have been applied.

An additional check was added to the software interface between the source-release and vadose zone models. This interface program processes source-release results into the format necessary for input to the vadose zone flow and transport model. The additional check ensures consistency between the numbers of gridblocks in both models and thereby verifies that mass out of the source model equals mass into the vadose zone model.

2.3 Aquifer Domain Extension

The 1E-05 risk isopleth at the time of maximum overall risk for a spatially-consistent receptor was not closed in the ABRA aquifer model domain (see Figure 6-31 in Holdren et al. [2002]). Instead, this risk isopleth extended south of the INL Site boundary. For the RI/FS model, the aquifer domain was extended southward and westward to ensure the 1E-05 risk isopleth would be closed. This task required adopting permeabilities from the Operable Unit 10-08 aquifer model[a] (McCarthy et al. 1995) for extended portions of the domain, and interpolating new boundary conditions from Calendar Year 2000 water level data (i.e., the same that were used for the ABRA aquifer model calibration). Extension of the aquifer model domain is explained in detail in Appendix C.

2.4 Lithology Database Quality Assessment

An extensive effort to document selected lithologic contacts between sediment and basalt in the vadose zone and the thickness of the surficial sediment and sedimentary interbeds was conducted in support of RI/FS modeling. Results of this effort are documented in the *Updated Stratigraphic Selections for Wells in the Vicinity of the Subsurface Disposal Area* (Ansley, Helm-Clark, and Magnuson 2004). During this effort, previous stratigraphic selections by Anderson et al. (1996) were verified to be correctly entered into the data files used for the RI/FS spatial variability and kriging analysis. The primary effort, however, was in reevaluating lithologic selections for each well drilled since 1995, and in making new

[a] The updated INL Site-wide aquifer model, in preparation for Operable Unit 10-08, will maintain consistency with simulated SDA-vicinity water velocities from the Operable Unit 7-13/14 RI/FS model in accordance with the *Idaho National Engineering and Environmental Laboratory Operable Unit 10-08 Sitewide Groundwater Model Work Plan* (DOE-ID 2004).

selections for wells drilled since publication of the ABRA report through March 2003. The basis for lithologic selection for each well was reviewed and reinterpreted, as necessary, using suites of geophysical logs as the primary basis and driller lithologic logs as a last resort. This prioritization method resulted in several occurrences where the nonzero thickness locations used for the ABRA became zero-thickness locations in the draft RI/BRA and vice versa. These occurrences are highlighted in Table A-1 of Ansley, Helm-Clark, and Magnuson (2004). After lithologic selections were finalized, the spatial variability analysis and kriged surfaces and thicknesses of sedimentary features were updated (Leecaster 2004) for the vadose zone RI/FS model.

2.5 No Spreading Area Influence in the Vadose Zone

The ABRA model included a steady-state influence of additional water above the C-D interbed to emulate the effect of the spreading areas. Sensitivity simulations, without this additional water, presented in the ABRA showed that the effect of the additional water was to dilute the resulting aquifer concentrations for contaminants that underwent dissolved-phase transport. This finding was most applicable for contaminants with long half-lives that do not undergo substantial decay during transit of the vadose zone. Since short-lived contaminants, such as Sr-90 and Cs-139, are not evaluated for groundwater pathway in the RI/FS, it is appropriate that the RI/FS model does not include this additional spreading area water above the C-D interbed.

2.6 Reduction of Infiltration Rate Assigned Inside the Subsurface Disposal Area

Three infiltration rates were assigned to different regions inside the SDA in the ABRA model. These rates represented low-, medium-, and high-infiltration rates and were based on inverse modeling to neutron probe access tube measurements documented in the UNSAT-H infiltration model calibration report (Martian 1995). The high-infiltration rate of 24.1 cm/year (9.5 in./year) was based on results from three locations that had extremely high-infiltration rates due to the neutron probe access tubes being located in areas of low topography (e.g., near ditches). Excluding these three infiltration rates from the Martian (1995) estimates resulted in an upper-bound or high-infiltration rate of 10.0 cm/year (3.9 in./year), which was judged more appropriate for an upper-bound on infiltration through the waste.

2.7 Facilitated Transport of Plutonium-239 and Plutonium-240

Facilitated transport mechanisms (e.g., colloidal transport) may affect contaminant migration in the SDA subsurface. In the ABRA, facilitated transport was considered only as a sensitivity case. As recommended by Batcheller and Redden (2004), facilitated transport for a portion of the Pu-239 and Pu-240 inventory in the buried waste was adopted in the base-case model by assigning a K_d of 0 mL/g for the source zone, surficial sediment, and the A-B interbed. Batcheller and Redden (2004) further concluded that plutonium would sorb to the deeper B-C and C-D interbeds, inhibiting continued downward transport through the vadose zone.

2.8 Revision of Sediment Distribution Coefficients

Distribution coefficient values used in the RI/FS model were reassessed. In the methodology used for the batch tests (Fjeld, Coates, and Elzerman 2000), on which several of the values in the ABRA were based, the fraction of soil samples that were above 250 µm was removed before testing. Using only finer sediment particles in the batch tests introduced a bias to the results that overestimated the distribution coefficients. Using a weight ratio of the sieved fraction to the estimated total sample weight, an Environmental Protection Agency recommended method (EPA 1999) was used to adjust distribution

coefficients downward for actinium, americium, plutonium, and thorium. Distribution coefficients for uranium and neptunium were revised upward, based on results of batch tests measured on soil cores from wells drilled in Fiscal Year 2003 (Leecaster and Hull 2004). The complete list of final distribution coefficients for the RI/FS modeling appears in Table 4-4.

2.9 Gaseous-phase Simulation of Carbon-14 and Volatile Organic Compounds

Carbon-14 was simulated as a purely dissolved-phase contaminant in the ABRA, resulting in overestimated groundwater-pathway transport because two processes were neglected that allowed C-14 to escape the vadose zone through land surface. These processes were (1) partitioning of C-14 into the gaseous phase, which allows part of the C-14 mass to diffuse through the upper land surface boundary, and (2) gaseous-phase advection through that same boundary in response to changes in barometric pressure. In addition to simulating dissolved-phase movement of C-14, the RI/FS model also includes partitioning of C-14 into the gaseous phase, which accounts for losses to the atmosphere.

Volatile organic compounds were not simulated for the ABRA. Instead, VOCs were estimated by scaling the IRA (Becker et al. 1998) model results by the ratio of an updated inventory to the previous inventory. Current inventories were used for the RI/FS model, and the updated RI/FS model was used to simulate VOC transport. Calibration was performed using CCl_4 measurements from the extensive vadose zone gas-port-monitoring network and data from the groundwater-monitoring network. The calibration was performed primarily by adjusting tortuosity values, but much of the information gained from calibrating the IRA model was used in the RI/FS model. Another calibration parameter was the fractured basalt permeability horizontal-to-vertical anisotropy ratio. The ratio was changed from 30:1 used in the ABRA model to 300:1. This change helped to match the observed spreading of CCl_4 in the vadose zone, and demonstrated linkage between the flow model and the transport model for CCl_4. The VOC transport model also included the effects of air drilling and vapor vacuum extraction.

2.10 Increased Number of Waste Streams

In the ABRA model, the SDA was divided into 13 source areas for modeling contaminant release. For the RI/FS model, improvements in knowledge of contaminant inventories were used to refine the assignment into 18 source areas for modeling contaminant release and subsequent transport. A slight variation on the locations of the 18 waste streams was used when simulating VOCs (where the areas for Pits 4, 5, and 10 were slightly reduced in extent). This reduction is based on the Waste Information and Location Database tool and confirmation through soil-gas surveys (Housley, Sondrup, and Varvel 2002). Because of the influence of C-14 release from beryllium blocks on the C-14 risk, a third and different grouping was used to represent the blocks for the C-14 modeling.

3. TETRAD SIMULATION CODE

3.1 Description

The TETRAD computer code (Vinsome and Shook 1993), Version 12.7ms, was used for the RI/FS to simulate flow and transport. The TETRAD code has complete multiphase, multicomponent simulation capabilities and can mimic the behavior of any number of components in aqueous, gaseous, oleic, and solid phases. The TETRAD code has dual-permeability capabilities, which allow movement of components in a coupled fracture-matrix system. When dual permeability is invoked, water and contaminants move in both the aqueous and gaseous phases in both the fracture network and the basalt matrix. This dual-permeability feature was used in the RI/FS model to simulate movement of VOCs and C-14.

The general conservation equation solved by the TETRAD simulator for accumulation, flux, decay or degradation, and sources for any component *i* can be written as:

$$\frac{\partial W_i}{\partial t} + \vec{\nabla} \cdot \vec{N}_i - R_i + q_i = 0 \tag{3-1}$$

where:

$\frac{\partial W_i}{\partial t}$ is the accumulation term that consists of net changes in concentration of the component *i* in any phase, including the adsorbed phase

$\vec{\nabla} \cdot \vec{N}_i$ is the divergence of the flux of component *i*

R_i is the change in concentration arising from decay of component *i*

q_i represents sources or sinks of component *i*.

The accumulation term can be written as:

$$W_i = \varphi\left(S_w \rho_w w_i + S_g \rho_g y_i + S_o \rho_o x_i\right) + \left((1-\varphi)\rho_s V_i\right) / M_i \tag{3-2}$$

where:

φ is the porosity

S_j are the phase saturations (*w* aqueous, *g* gaseous, *o* oleic) of component *i*

ρ_j are the phase molar densities (*w* aqueous, *g* gaseous, *o* oleic) of component *i*

w_i y_i, and x_i are the mole fractions of component *i* in the aqueous, gaseous, and oleic phases, respectively

ρ_s is the solid phase density

V_i is the mole fraction of component *i* adsorbed on the solid phase

M_i is the molecular weight of component *i*.

A generalized sorption relationship is available in TETRAD that allows for sorption onto the solid phase from any of the other three phases.

The flux term in Equation (3-1) is comprised of an advection and dispersion term for each phase given by:

$$\vec{N}_i = \left[\rho_w \vec{u}_w w_i - \vec{D}_{iw} \cdot \vec{\nabla}(\rho_w w_i)\right] + \left[\rho_g \vec{u}_g y_i - \vec{D}_{ig} \cdot \vec{\nabla}(\rho_g y_i)\right] + \left[\rho_o \vec{u}_o x_i - \vec{D}_{io} \cdot \vec{\nabla}(\rho_o x_i)\right] \quad . \tag{3-3}$$

In Equation (3-3), the $\vec{u}_j$ are the phase advective fluxes given by the multiphase version of Darcy's law:

$$\vec{u}_j = \frac{-kk_{rj}}{\mu_j}\left(\vec{\nabla} P_j - \rho_j \vec{g}\right) \tag{3-4}$$

where:

k is the intrinsic permeability

k_{rj} is the relative phase permeability

μ_j is the phase viscosity

P_j is the phase pressure

$\vec{g}$ is gravitational constant in vector form.

$\vec{D}_{ij}$ is the phase-dependant dispersion tensor comprised of molecular diffusion modified by porosity, phase saturation, tortuosity, and mechanical dispersion, consisting of phase dispersivities modified by directional components of advective phase fluxes (Bear 1972). The gravitational energy term is negative given that the positive z-direction is oriented downward in the TETRAD code.

The reaction term in Equation (3-1) accounts for decay or degradation of component *i* and is written as:

$$R_i = -A_{i\mathrm{K}}\left(m_i + V_i(1-\varphi)\rho_r\right) + A_{\omega i}\left(m_\omega + V_\omega(1-\varphi)\rho_r\right); \mathrm{K} \neq \omega \tag{3-5}$$

where m_i is the total aqueous mass of i. The first term on the right hand side of Equation (3-5) accounts for component *i* decaying with a rate constant $A_{i\mathrm{K}}$ into component K; whereas the second term on the right-hand side is the formation of *i* from destruction of component ω with a rate constant $A_{\omega i}$.

The final term on the right-hand side of Equation (3-1) is the source/sink term, q_i. This term accounts for addition or extraction of component *i* through wells or boundary conditions.

The TETRAD Version 12.7 code previously was used for the IRA and ABRA models. Before conducting modeling for the RI/FS, an evaluation exercise was performed to determine whether TETRAD was still the most appropriate code to use. This exercise resulted in a recommendation to continue using TETRAD for groundwater-pathway simulations for the RI/FS (Appendix C of Holdren and Broomfield 2004).

3.2 Modifications to Version 12.7 Resulting in Version 12.7ms

Modifications to improve computational efficiency for environmental modeling applications with the TETRAD simulator, Version 12.7, were described in Shook et al. (2003). The modified code resulting from this effort is called TETRAD, Version 12.7ms. Modifications were performed as part of an INL Laboratory-Directed Research and Development Project and consisted of allowing component-specific convergence criteria to be specified. This allowed tighter convergence criteria on those components representing contaminants, and looser criteria for those components representing pure water, air, and a required nonaqueous phase liquid. Appendix A describes simulation problems used to establish comparability of results between TETRAD Version 12.7 and Version 12.7ms. Two problems were simulated and results between the two versions were considered to be adequately consistent.

Two additional changes were implemented in the TETRAD simulator during transition from Version 12.7 to 12.7ms: (1) implementation of a Millington formulation (see Section 5.4.4.2) for calculating tortuosity during the simulation, based on total porosity and gaseous-phase saturation; and (2) modifications to limit repetitive time-step output for problems with frequent surface or internal boundary condition changes (e.g., emulating barometric pressure fluctuations or positive pressures imposed downhole during drilling of wells). These two changes only affected input and output from the TETRAD simulator and did not affect the solution method used internally.

3.3 Quality Control

The TETRAD 12.7ms simulator is a proprietary code, and its use constitutes an off-the-shelf application by modeling staff from the INL Site. Quality control for these types of simulations consists of ensuring that results are reproducible. This requires archiving a version of the simulator, model inputs, model outputs, and processing codes used to create inputs and outputs. An extensive searchable electronic archive is maintained by the Operable Unit 7-13/14 Project for this purpose. A description of this archive is contained in Appendix B. Appendix B also contains a copy of the software management agreement between the Idaho Cleanup Project and the Operable Unit 7-13/14 Project for this purpose.

4. OPERABLE UNIT 7-13/14 FLOW AND TRANSPORT MODEL DESCRIPTION

4.1 Conceptual Model

The general conceptual flow model treated water movement as though subsurface sediment were a heterogeneous, isotropic, porous medium. Net infiltration of meteoric water into the subsurface was described in the model by three constant rates representing areas of low, medium, and high infiltration (Martian 1995). Surficial sediment and sedimentary interbeds were simulated with varying thicknesses and upper-surface elevations (Leecaster 2004). Only the three uppermost interbeds were considered in the conceptual model. These were the A-B, B-C, and C-D interbeds. Interbeds deeper than the C-D interbed, though present in reality, were not included in the simulations. These deeper interbeds are also discontinuous, based on the fewer number of wells to this depth, and it is conservative to neglect them.

For strictly dissolved-phase contaminant transport, flow in the fractured basalt portion of the subsurface was considered as occurring only in the fracture network to emulate an anisotropic medium with a low effective porosity and a high permeability. For contaminants that also partition into the gaseous phase, both the exchange of water between the fracture network and the basalt matrix, and flow within the basalt matrix were assumed to affect flow and transport.

Sources of water were considered to be constant, allowing steady-state assignment of boundary conditions. The exception was including three transient events to represent historical flooding of the SDA. Transient infiltration events in response to changes in daily and seasonal meteorological conditions were evaluated in the IRA model and, as long as an assumption of equilibrium reversible sorption was included, these transient simulations showed no difference from the steady-state simulation at depth in the vadose zone.

Water that infiltrates the subsurface but does not contact buried waste serves primarily to dilute groundwater-pathway concentrations. Therefore, the effect of water migrating laterally at depth in the vadose zone from either Spreading Area A or B, or from the Big Lost River, was not included in the conceptual model. These additional sources of water were evaluated in the ABRA model and were found, primarily, to result in additional dilution for strictly dissolved-phase contaminants.

Movement of water in the aquifer was considered controlled by regional flow in the aquifer. Permeabilities were considered to be uniform vertically and pressures in the aquifer were considered to be in hydrostatic equilibrium, implying predominantly horizontal flow in the aquifer. Because of the long simulation time durations of hundreds to thousands of years, movement of water within the Snake River Plain aquifer was considered steady state. Neglecting transient influences in the aquifer, such as those that might occur from the spreading areas, is conservative because temporary changes in the direction of water velocity would result in additional dilution.

The effective depth of the Snake River Plain aquifer was assumed to be 76 m (250 ft). Robertson, Schoen, and Barraclough (1974) derived this estimate from the depth where tritium was observed in wells downgradient of the injection well at the Idaho Nuclear Technology and Engineering Center facility. More recent evaluations of temperature profiles indicate that the effective thickness is greater (Smith 2002). With predominantly horizontal flow, using a thinner aquifer thickness is conservative because less dilution occurs.

Locally, groundwater flow was affected by a region of low permeability in the aquifer (Wylie and Hubbell 1994). This region has been identified in wells immediately south of the SDA. This low-permeability region may extend underneath the SDA, as evidenced by the estimated transmissivity from a recent pumping test in Well M17S located centrally inside the SDA. Low velocities in the aquifer, as a result of including this low-permeability region, have an impact on model results. As contaminants enter the aquifer from the vadose zone, less dilution occurs in gridblocks with low aquifer velocities, and simulated contaminant concentrations are higher than they would be if the aquifer velocity were greater.

The general conceptual transport model for dissolved-phase transport considered advection, dispersion, diffusion, radioactive chain decay and ingrowth, and sorption in the sediment portions of the simulation domain.

In the fracture network within the basalt and basalt-matrix portions of the simulations, no sorption was assumed. Sorption in surficial and interbed sediment was assumed to follow linear reversible isotherms that could be described by use of K_ds. Sediment K_ds were assigned based on best-estimate values rather than conservative screening values. A set of best-estimate K_ds from Holdren and Broomfield (2004) was used in this application.

Facilitated transport mechanisms (e.g., colloidal transport) may affect contaminant migration in the SDA subsurface. Studies conducted with SDA interbed sediments have shown that very small fractions of plutonium and americium may move in a facilitated manner in the SDA. Grossman et al. (2001) showed that a very low mobile fraction forming from natural colloids in the soil (i.e., much less than 1%) was possible. Batcheller and Redden (2004) considered colloid formation from high-temperature processes and estimated that 3.7% of the waste stream could form colloids. This higher fraction is used for transport of Pu-239 and Pu-240 in the RI/BRA base case. Facilitated transport for Pu-239 and Pu-240 was considered to occur in the source zone and through the surficial sediment and A-B interbeds. The deeper B-C and C-D interbeds were considered as not allowing this facilitated transport to continue downward through the vadose zone because the B-C and C-D interbeds were treated as continuous in the model. This resulted in mechanical filtration for these two isotopes at this depth (Batcheller and Redden 2004) because water velocities are slowed at the interbeds. There are several locations where there are gaps in the B-C interbed inside the SDA (see Figure 4-8), but the interpolation process (Leecaster 2004) results in a nonzero thickness given the 76.2- × 76.2-m (250- × 250-ft) dimension of the gridblocks for the B-C interbed. There is a sensitivity case evaluated in Section 6.4.2 where the entire B-C interbed is neglected to examine the potential effects of gaps in the B-C interbed.

Single isolated detections of contaminants in the aquifer have occurred in the SDA during monitoring of subsurface contaminants. Though these isolated detections may be indicative of contaminant transport, it is not feasible with the current modeling approach to try to emulate each one. Instead, the subsurface-transport model attempts to mimic large-scale overall behavior of contaminants in the subsurface. This approach directs the model to emulate contaminants that are consistently present in a distributed manner in the subsurface. Contaminant monitoring in some locations in the vadose zone has identified likely trends in uranium, Tc-99, and nitrate. While not distributed adequately to be useful for calibration, these trends are compared against simulation results in Section 6.

Evaluation of aquifer contamination from upgradient sources in Section 2.3.4 of the draft RI/BRA concluded that there may be an influence from upgradient facilities on contaminant concentrations in the aquifer. The aquifer model ignores this possible influence and only considers regional background concentrations when making comparisons between simulated and observed results. Potential impacts from commingling plumes are the scope of the Operable Unit 10-08 Groundwater Modeling Project (DOE-ID 2004).

4.2 Assumptions

This section lists all assumptions that resulted from the conceptual model (discussed previously) or that were necessary to develop the subsurface model. Assumptions are divided into flow and transport categories. Most of these assumptions were the same as those used in developing the ABRA model. Assumptions that were modified for the RI/FS are italicized. These assumptions were applied only to the single-continua, dissolved-phase, subsurface flow and transport modeling. Assumptions relative to dual-continua modeling are included in Section 5.4.

4.2.1 Flow

- Infiltration is spatially variable inside the SDA and is greater than infiltration that occurs outside the SDA because of disturbed soil profiles with reduced vegetation inside the SDA.

- The spatially variable infiltration description of Martian (1995), adapted for the ABRA model, is adequate for base-case modeling.

- The higher infiltration rates, beginning in 1952, are implemented as though they were effective across the SDA.

- The background infiltration rate outside the SDA, through undisturbed vegetated sediment, is 1 cm/year (0.4 in./year).

- Initial conditions obtained from simulating a background infiltration rate of 1 cm/year (0.4 in./year) for 300,000 days (approximately 820 years) are adequate for representing the vadose zone beneath the SDA.

- The amount of water entering the SDA from the three historical floods is adequately estimated by Vigil (1988).

- Duration of infiltration from each of the historical flooding events is 10 days.

- Infiltration patterns in the SDA will remain the same indefinitely into the future for the base-case simulations and will be revised for feasibility study cases to reflect impact of an infiltration-reducing cover.

- The high-infiltration rate assigned over parts of the SDA by Martian (1995) is sufficient to account for occasional flooding of the SDA that may occur in the future for the base-case simulations.

- The surficial sediment and sedimentary interbeds have spatially variable lithologic surfaces and thicknesses that influence water and contaminant movement.

- Interbeds below the C-D interbed are thin and discontinuous and do not significantly affect flow and transport near the SDA. Neglecting the interbeds is conservative with respect to maximizing the groundwater-pathway concentrations.

- Hydrologic properties in the surficial sediment and A-B interbed are homogeneous. Hydrologic properties in the B-C and C-D interbeds are heterogeneous and varied spatially.

- The B-C and C-D interbeds have a low-porosity, low-permeability feature at their upper surface, which indicates either sediment within the interbed or the effect of fracture infilling by fine-grained sediment in the low-permeability basalt immediately above the interbed. (Though this feature was included in the subsurface model and discussed in detail in the IRA and ABRA modeling text, it was not specifically identified as an assumption.)

- Waste has the same hydrologic properties as surficial sediment.

- Flow in fractured porous basalt is controlled by the fracture network and is adequately represented as an anisotropic high-permeability, low-porosity, equivalent-porous continuum using a Darcian description.

- The field-scale hydraulic properties for fractured basalt were adequately described through inverse modeling by Magnuson (1995) for the large-scale infiltration test.

- *Any effect of water, from the Big Lost River discharged to the spreading areas, on water movement in the vadose zone beneath the SDA is neglected*. (In the ABRA, the effect of this influence was shown to primarily dilute concentrations for contaminants with long half-lives in the vadose zone and the aquifer. Not including the spreading-area influence is conservative with respect to maximizing the groundwater-pathway concentrations.)

- Water movement in the aquifer is treated as steady state. Possible influences of discharges from the Big Lost River to the spreading areas do not influence flow in the aquifer in the immediate vicinity of the SDA.

- Water levels corrected for borehole deviations from Fiscal Year 2003 are adequate for calibrating the Snake River Plain aquifer model and are representative of long-term, steady-state conditions.

- Within the aquifer, pressure is assumed to be in hydrostatic equilibrium and water movement is predominantly horizontal.

- A continuous region of low permeability exists locally in the aquifer, south and southwest of the SDA, that affects local flow directions.

- The effective depth of the Snake River Plain aquifer is 76 m (250 ft) (Robertson, Schoen, and Barraclough 1974).

4.2.2 Transport

- Field-measured concentrations of contaminants are generally representative and valid, based on data quality requirements associated with sampling activities. Single, isolated detections of contaminants are anomalous and not representative because contaminants are not consistently present.

- Advection, dispersion, diffusion, sorption, and radioactive decay are the only processes that influence dissolved-phase contaminant movement in the subsurface beneath the SDA.

- A linear equilibrium reversible distribution coefficient is representative of all geochemical processes that occur between contaminants dissolved in water and sediment. All available site-specific information will be used to determine appropriate contaminant distribution coefficients.

- Distribution coefficients are homogeneous in the interbeds.
- Sorption does not occur in fractured basalt portions of the vadose zone and aquifer.
- *Facilitated transport occurs in the vadose zone above the B-C interbed for Pu-239 and Pu-240. These isotopes undergo sorption within the B-C and C-D interbeds (Batcheller and Redden 2004).*
- No upgradient INL Site facilities influence aquifer-contaminant concentrations near the SDA, with the exception of nitrate, which has an estimated local background concentration of 1.4 mg/L.
- Feasibility study remedial alternatives will address (1) all estimated contamination retained in waste at the time of treatment, and (2) all contamination previously released that is still within the surficial sediment portion of the vadose zone model.

4.3 Vadose Zone Model

4.3.1 Domain and Horizontal Discretization

The same vadose zone horizontal domain and discretization was used in the RI/FS model as was used in the ABRA model. The extent of the vadose zone domain is shown in Figure 4-1. This horizontal extent was judged adequate to simulate flow and transport without undue influence from horizontal no-flux boundaries.

Horizontal gridding for the final vadose zone domain is shown in Figure 4-2. Two concentric levels of refinement are used to obtain adequate grid resolution in the SDA. The largest horizontal grids are 152.4 m (500 ft) on a side and the smallest gridblocks are 38.1 m (125 ft) on a side. Selection of the grid domain required a balance between the objectives of maximizing the extent of the domain so that outlying wells (e.g., Wells M7S, M15S, and M16S) could be included, while still obtaining sufficient resolution in the SDA for representing disposal locations and geologic and hydrologic features. Some outlying wells were not encompassed in the vadose zone simulation domain. The final domain extent was adequate to simulate transport without undue influence from the horizontal no-flux boundaries, which would otherwise truncate further horizontal spreading of water and contaminants in the vadose zone.

4.3.2 Lithology

An extensive effort to document selected lithologic contacts between sediment and basalt in the vadose zone and the thickness of the surficial sediment and sedimentary interbeds was conducted in support of the RI/FS model. The results of this effort are documented in Ansley, Helm-Clark, and Magnuson (2004). During this effort, previous interpretations by Anderson et al. (1996) were verified to be correctly entered into the data files used for the spatial variability and kriging analysis. The primary effort, however, was in reevaluating lithologic selections for each well drilled since 1995 and in making new selections for wells drilled since publication of the ABRA through March 2003. The basis for lithologic selection at each well was reviewed and reinterpreted as necessary using suites of geophysical logs as the primary basis and driller lithologic logs as a last resort. Table B-1 in Ansley, Helm-Clark, and Magnuson (2004) is the stratigraphic database for 134 wells deeper than the surficial sediment; this database is the foundation from which the RI/FS vadose zone model lithology is derived.

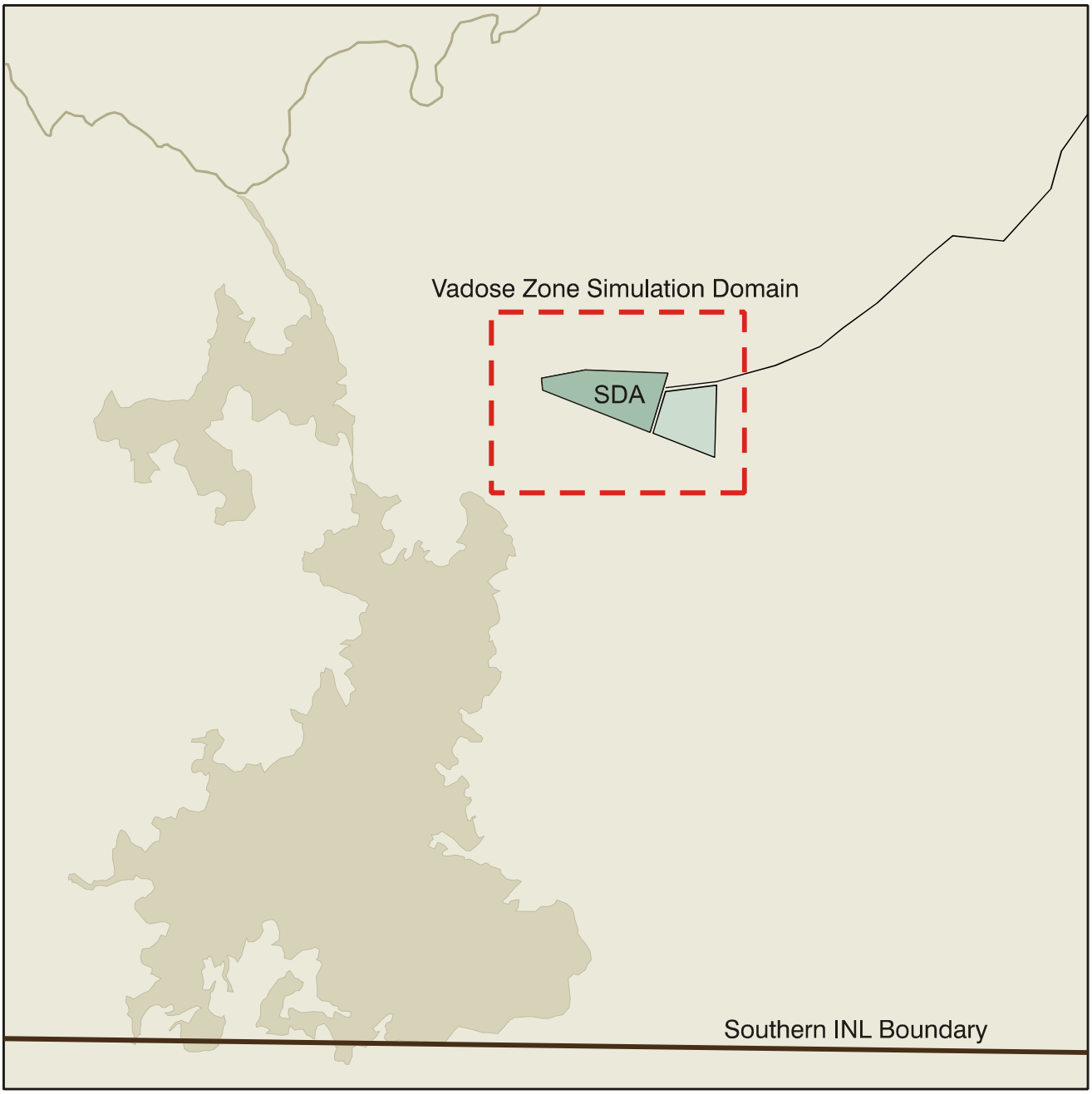

G1569-01

Figure 4-1. Horizontal domain for the remedial investigation and feasibility study vadose zone flow and transport.

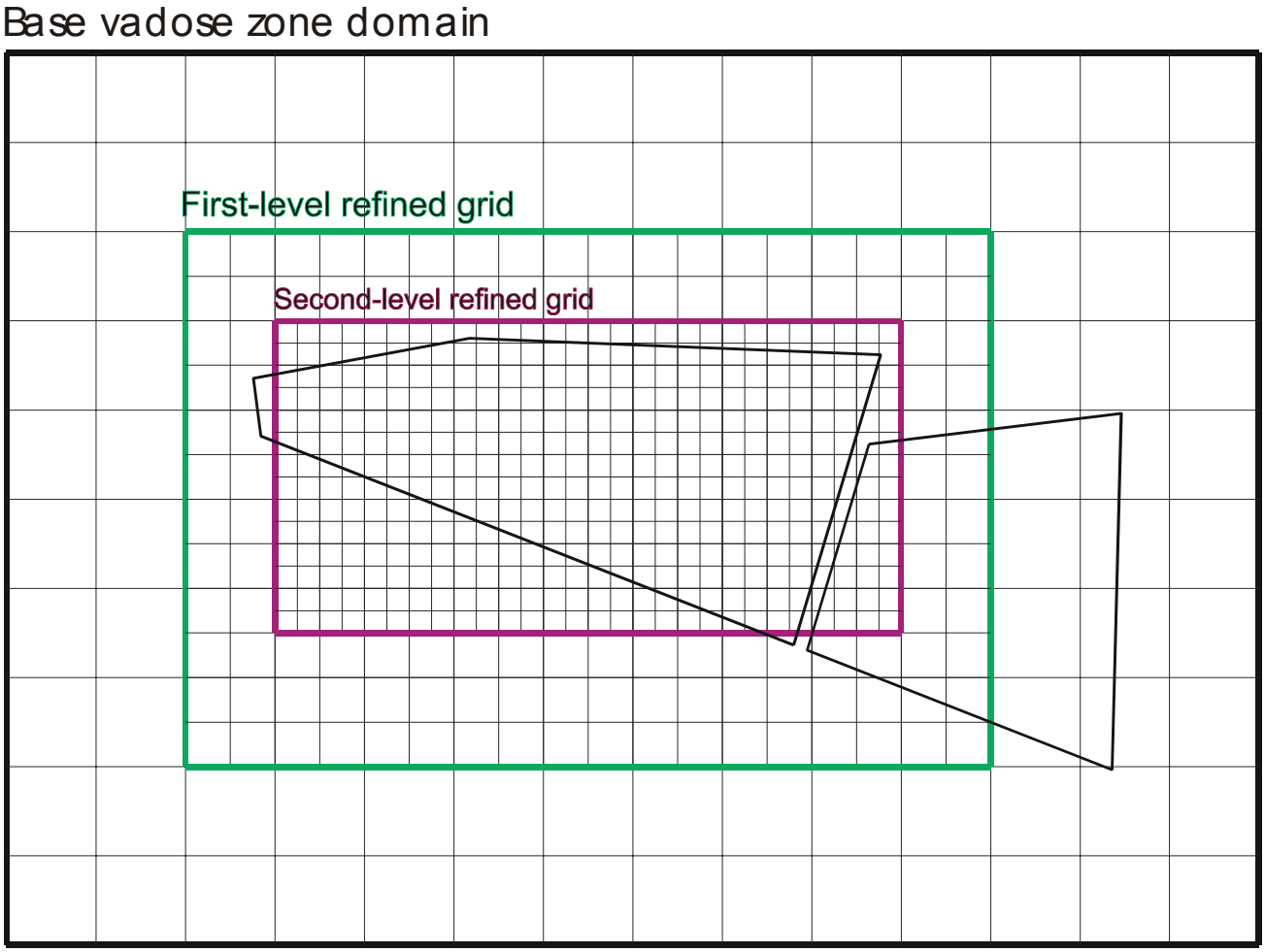

Figure 4-2. Horizontal discretization for the vadose zone model domain.

After lithologic selections were finalized, the spatial variability analysis and the kriged surfaces and thicknesses of the sedimentary features were updated for the Operable Unit 7-13/14 vadose zone model (Leecaster 2004). Surfaces and thicknesses, along with standard deviations for the surficial sediment and the A-B, B-C, and C-D interbeds were kriged for the base and refined grids and are contained in Leecaster (2004). The kriged surfaces and thicknesses are shown in Figures 4-3 through 4-10. The kriged results generally honor the data, with limited exceptions where both zero and nonzero thickness observations exist within a single grid. This is a result of single values being estimated for each grid and the smoothing that results from kriging. All lithologic selections were used in the kriging process without introducing bias by selectively removing locations with nonzero thickness when there were zero thickness locations nearby. The A-B interbed has two continguous regions of gridblocks where the kriged thickness was zero, and is indicated by the zero contour line in Figure 4-6. These regions persist through the kriging because of the large number of wells with strictly zero thickness. Although it may be confusing to see an interpreted upper surface of the A-B interbed when that interbed is interpreted to be absent (compare Figure 4-5 to Figure 4-6), there was no A-B interbed in the model gridblocks inside the zero contour line indicated in Figure 4-6. The upper surface appears contiguous and nonzero everywhere in Figure 4-5 because the lithologic database (Ansley, Helm-Clark, and Magnuson 2004) contains information on the contact between the A and B basalt flows and treats the contact as the upper surface of the A-B interbed where it is not present.

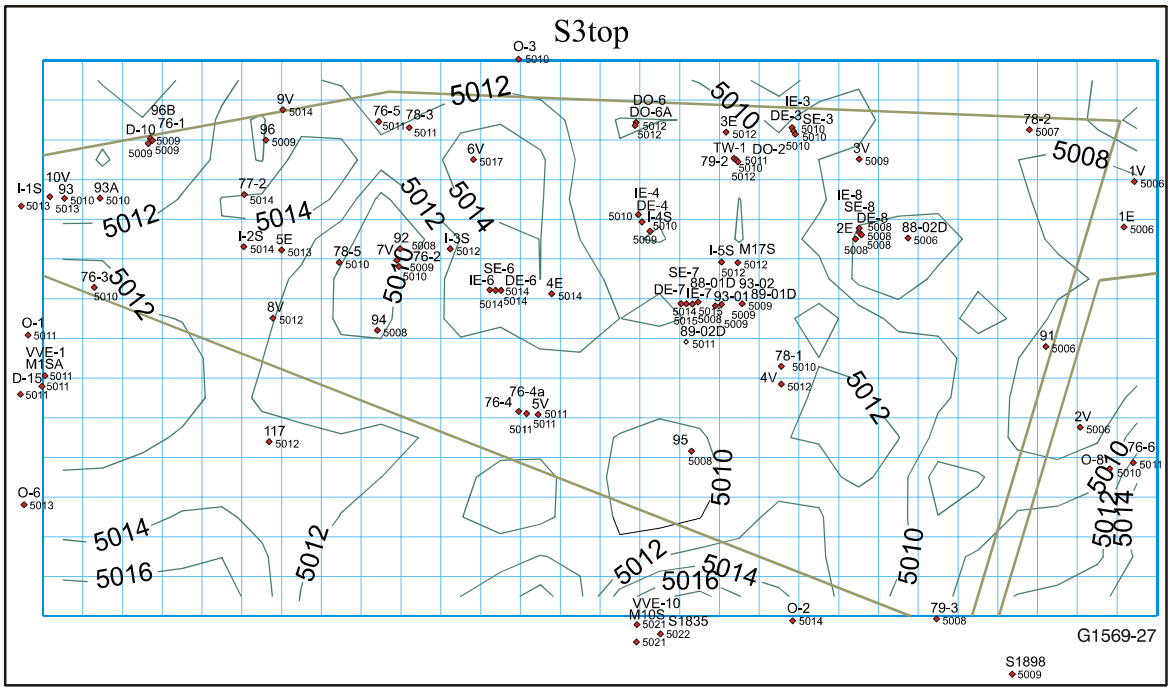

Figure 4-3. Kriged ground surface elevation (feet above mean sea level) for the second-level refined grid.

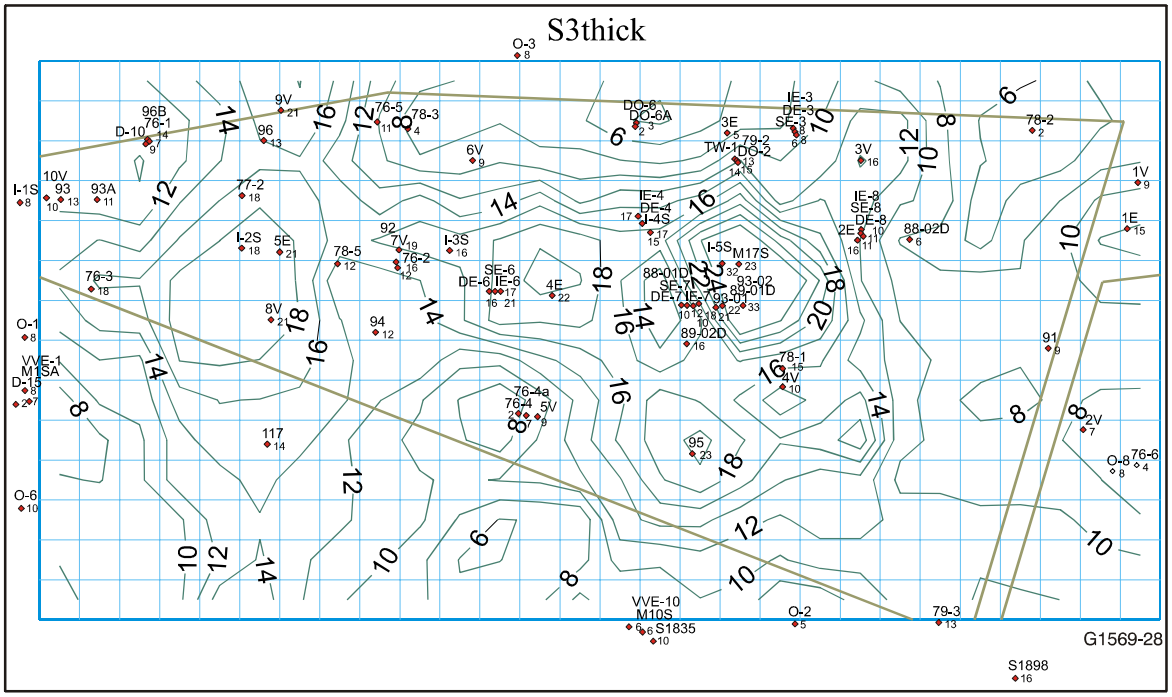

Figure 4-4. Kriged thickness (feet) of the surficial sediment for the second-level refined grid.

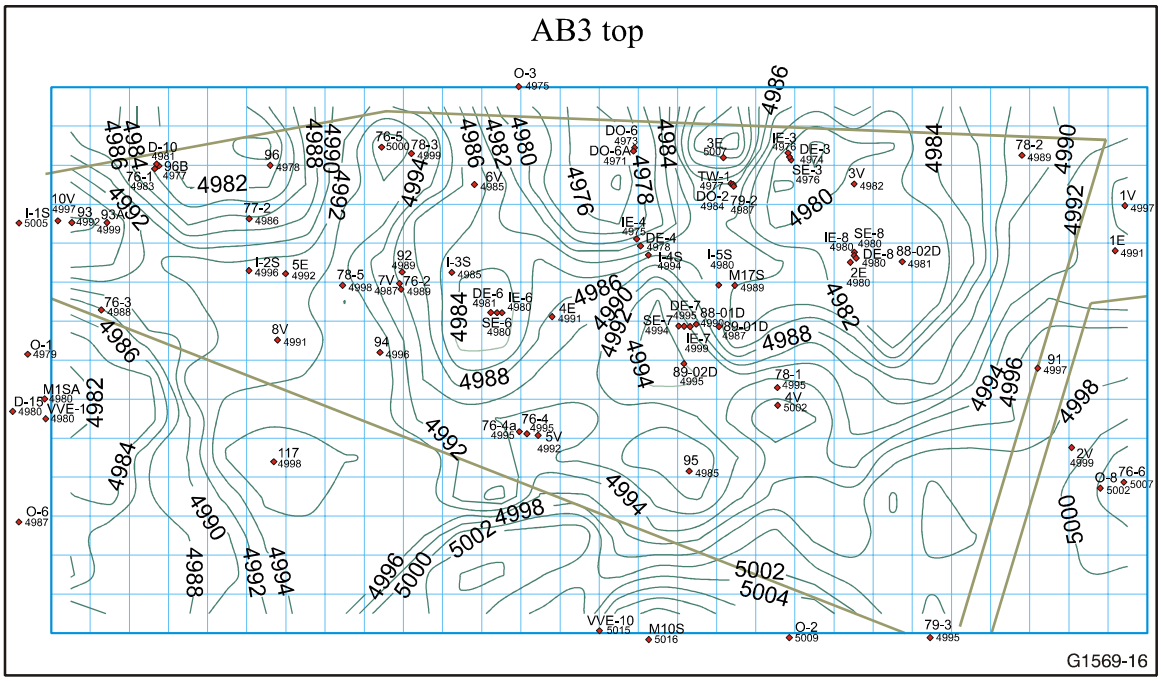

Figure 4-5. Kriged surface (feet above mean sea level) of the A-B interbed for the second-level refined grid.

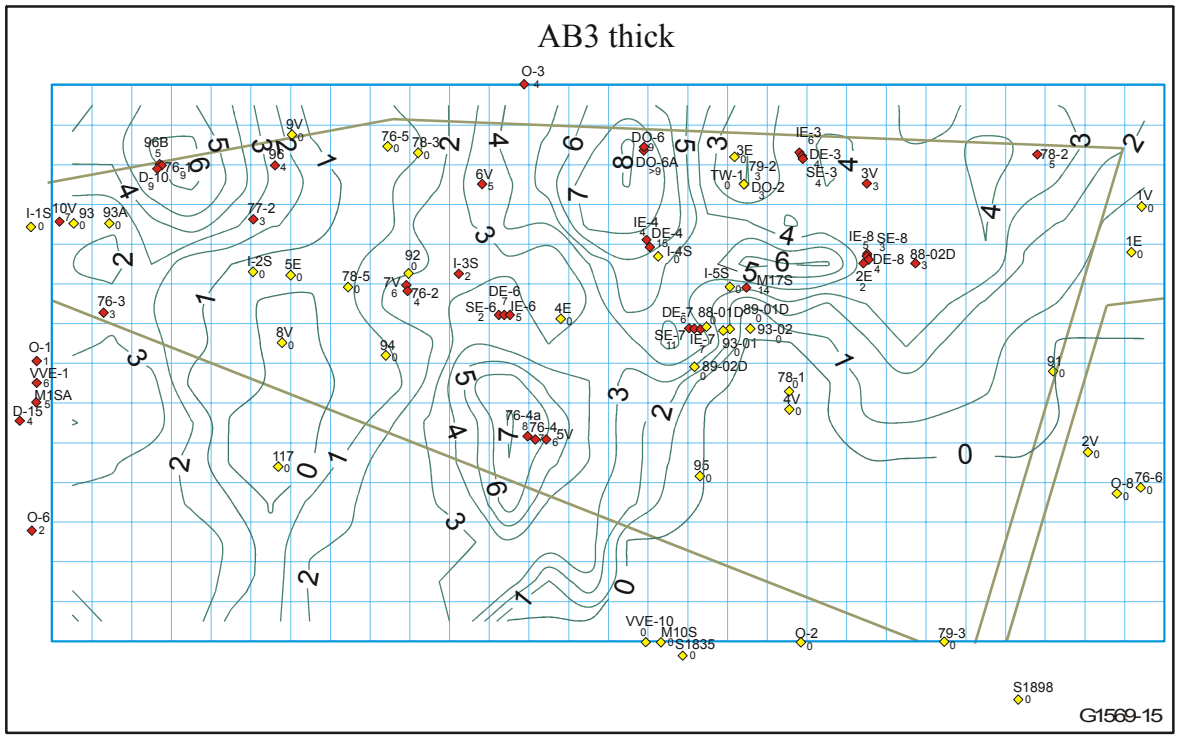

Figure 4-6. Kriged thickness (feet) of the A-B interbed for the second-level refined grid. Yellow symbols mark the locations where the A-B interbed is absent.

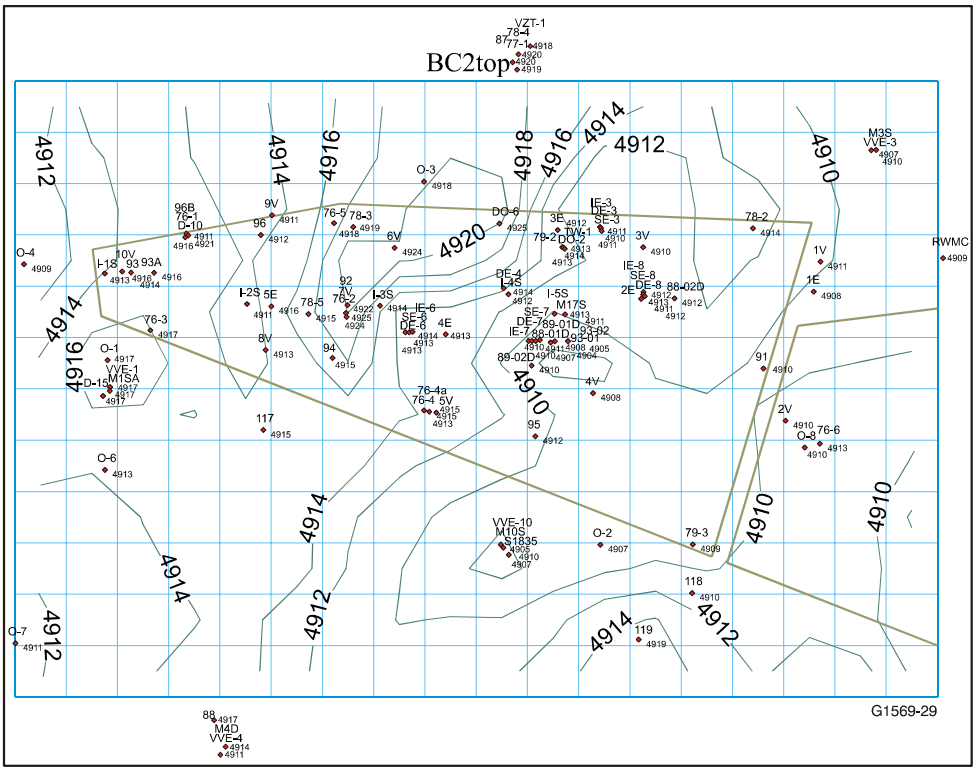

Figure 4-7. Kriged surface (feet above mean sea level) of the B-C interbed for the first-level refined grid.

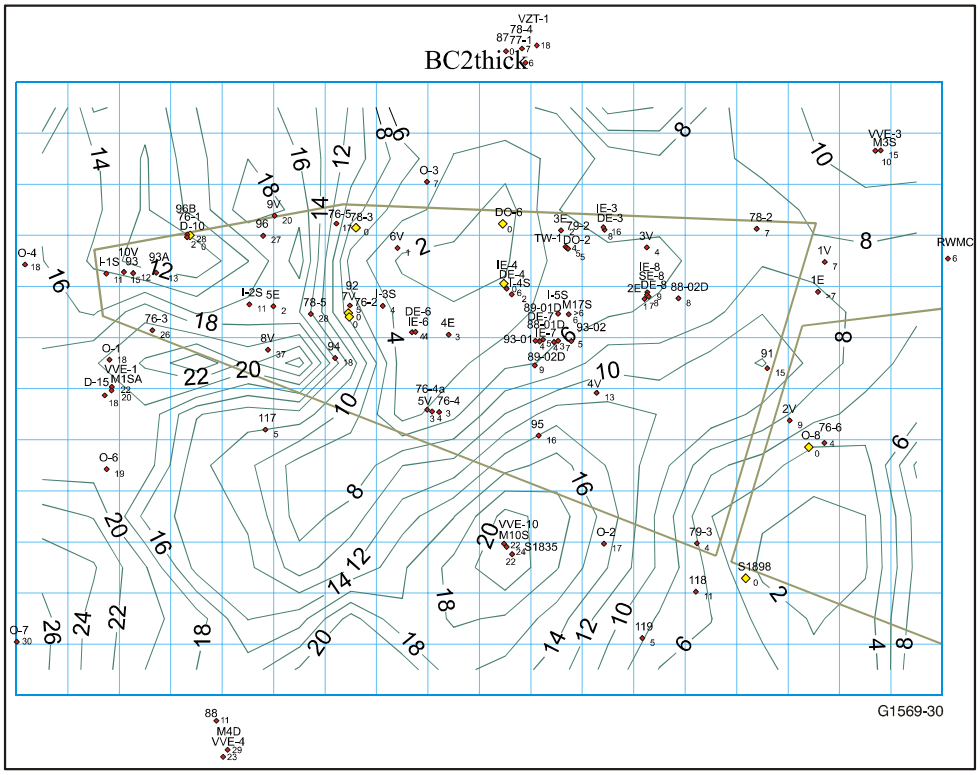

Figure 4-8. Kriged thickness (feet) of the B-C interbed for the first-level refined grid. Yellow symbols mark the locations where the B-C interbed is absent

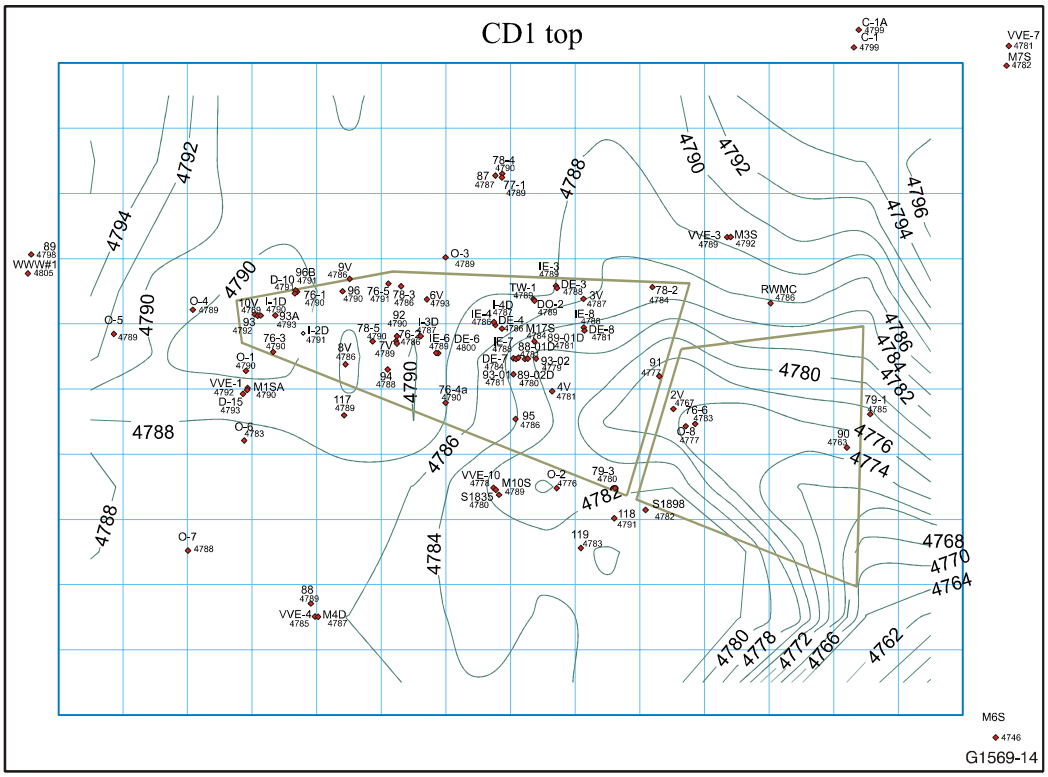

Figure 4-9. Kriged surface (feet above mean sea level) of the C-D interbed for the base grid. Note the trough leading southeasterly from the Subsurface Disposal Area toward Well M6S.

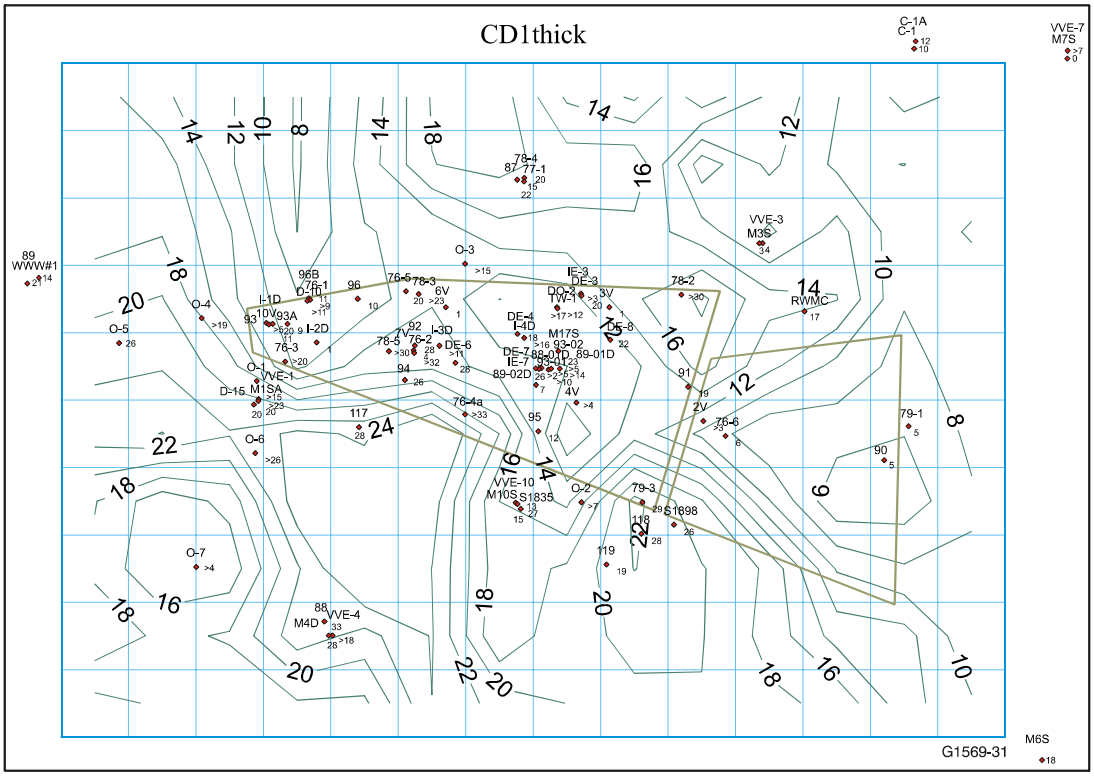

Figure 4-10. Kriged thickness (feet) of the C-D interbed for the base grid.

Both surface shape and thickness of each of the sedimentary features impact movement of water and contaminants through the subsurface. In particular, an interpreted trough or channel in the upper surface of the C-D interbed—that develops in the eastern half of the SDA and extends to the southeastern corner of the domain—influences water and contaminant movement above and through the C-D interbed.

4.3.3 Vertical Discretization

The next step in development of the RI/FS vadose zone model was vertical discretization of the base simulation domain. The kriged lithologic surfaces from Leecaster (2004) were used in conjunction with the horizontally discretized domains to create a conformable vertical grid. A minimum vertical grid size, maximum vertical grid size, and a geometric factor for increasing vertically adjacent gridblocks were assigned for each lithologic unit in the base vadose zone domain. Minimum grid size was 0.5 m (1.6 ft) for each of the sediment and basalt units, except for the A-B interbed, where a minimum grid size of 0.4 m (1 ft) was assigned. The geometric factor for the ratio between successive vertical gridblocks was a maximum of 1.5, which is a commonly used ratio to ensure numerical accuracy. Maximum vertical gridblock size was 3 m (9.8 ft) in the sediment units and 10 m (33 ft) in the basalt. Logic for adjusting vertical gridblock sizes was applied vertically at each horizontal gridblock location to allow for an optimum match of the gridblock interfaces to the kriged surface elevations. By having the same minimum gridblock size specified for both the sediment and basalt features, uniformity of gridblock sizes was ensured across lithologic interfaces. The total number of vertical gridblocks determined through this process was 80 at each horizontal location for the base vadose zone simulation domain. The upper surface of the vadose zone simulation domain was variable and was determined from the kriged elevation for the surficial sediment. The lower surface of the vadose zone simulation domain was assigned as a flat plane at the water table. As discussed previously, this assignment was correctly implemented for the RI/FS model as opposed to the ABRA model, where the plane was assigned at an elevation 27.5 m (90 ft) above the aquifer.

The logic for vertical grid discretization was different for the refined areas. Vertical discretization for the base domain was not adjusted further, based on the kriged elevations in the refined grids. Rather, the kriged elevations for the refined grids were compared to the conformable vertical discretization determined from the base grid, and then, as necessary, the material properties assigned in the refined domains were adjusted. This process resulted in smooth grid interfaces in the base domain and some degree of stair stepping in the refined grids. This can be seen in Figures 4-11 through 4-13, which show three-dimensional views of resulting grids, starting with the base grid and ending with the second-level grid refinement. These three-dimensional views are distorted both horizontally and vertically because the software (Visual Numerics 2001) that produces the views projects them onto a cube. The outline of the SDA is shown in each case projected just above the cube.

One special-case modification was made to lithologic assignments once the conformable grid was built. At a subset of grid locations in the second-level refined grid that represented the Low-Level Waste Pits (i.e., contiguous Pits 17 through 20), the region assigned as surficial sediment was extended downward 9.1 m (30 ft) from the top of the model to represent the approximate depth of these pits.

4.3.4 Hydrologic Properties

This section describes the assignment of hydrologic properties for the RI/FS model. Properties for the single-continua model are described first, with a comparison to measurements from core samples collected from wells installed after the assignments were made. Then additional properties necessary for the dual-continua simulations are described.

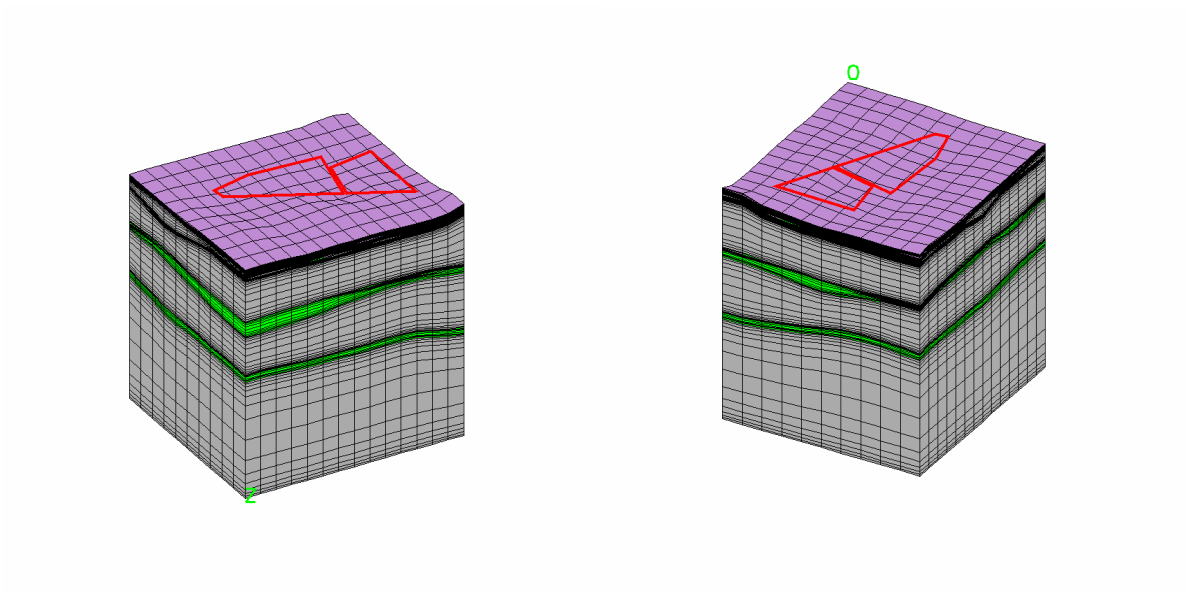

Figure 4-11. Southwest and northeast views of the base grid beneath the Subsurface Disposal Area showing vertical conformable gridding. The vertical extent shows the entire vadose zone simulation domain. Interbed grids are shaded green and fractured basalt grids are shaded gray (vertical exaggeration about a factor of 12). The A-B interbed appears black as a result of fine vertical discretization in these views.

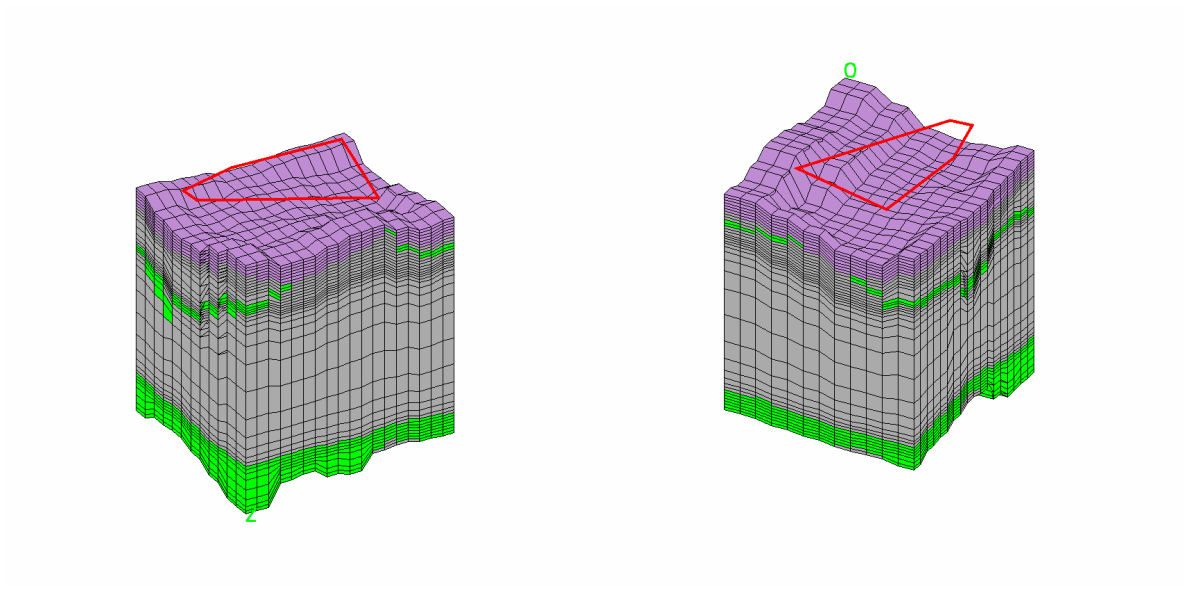

Figure 4-12. Southwest and northeast views of the first-level refined grid showing vertical conformable gridding. The first level of grid refinement extended to the base of the B-C interbed beneath the Subsurface Disposal Area (vertical exaggeration about a factor of 45).

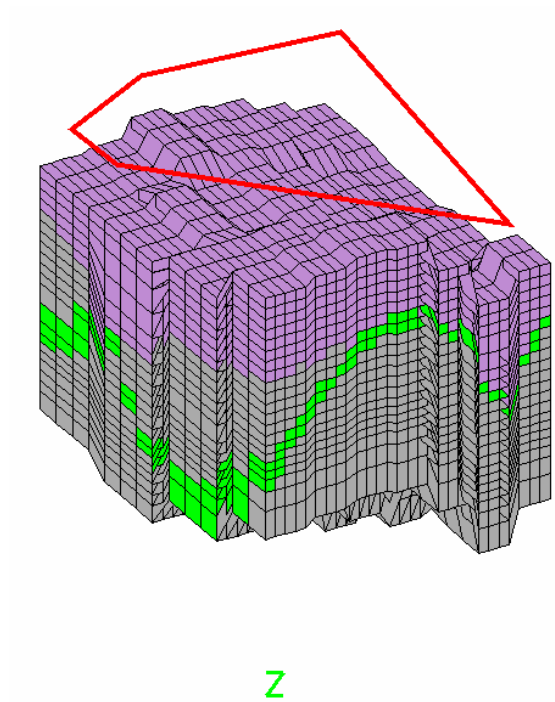

Figure 4-13. Southwest view of the second-level refined grid showing vertical conformable gridding. The second level of grid refinement extended to the base of the A-B interbed beneath the Subsurface Disposal Area. Note the A-B interbed merging with the surficial sediment (vertical exaggeration about a factor of 120).

4.3.4.1 Single Continua. Hydrologic properties for porosity and permeability of the surficial sediment and the A-B interbed were assigned the same properties as the ABRA model (see Table 4-1) because no new information was available for these units. The fractured basalt porosity and vertical permeability were the same as the ABRA. The fractured basalt horizontal permeability was increased one order of magnitude from the value used in the ABRA and is now assigned a value of 90,000 mD. This increase was identified as part of the CCl_4 transport calibration (see Section 5.4).

Table 4-1. Parameterization of hydrologic properties and source of parameters for surficial sediment, A-B interbed, and fractured basalt.

Parameter	Permeability	Porosity	Source of Parameter
Surficial sediment	680 mD, isotropic	0.50 cm^3/cm^3 (Martian 1995)	Average of calibrated properties in Martian (1995)
A-B interbed	4 mD	0.57 cm^3/cm^3 (Magnuson and McElroy 1993)	Waste Area Group 3 modeling in Rodriguez et al. (1997)
Fractured basalt	300 mD vertical and 90,000 mD horizontal	0.05 cm^3/cm^3 (Magnuson 1995)	Magnuson (1995)

For all sediment in the simulation domain, van Genuchten (1980) equations were used to describe the relationship between water potential and moisture content. The Mualem (1976) equation was used to describe the relationship between saturation and relative permeability. The three-phase van Genuchten

constitutive equations, as adapted by Parker, Lenhard, Kuppusamy (1987) with slight modifications to the normalized saturation terms, implemented in TETRAD are

$$P_{c_ow} = \frac{\sigma_{ow}\rho_w g}{\sigma_{gw}\alpha}\left[\left(\bar{S}_w\right)^{-1/\gamma} - 1\right]^{1/\beta} \tag{4-1}$$

and

$$P_{c_go} = \frac{\sigma_{go}\rho_w g}{\sigma_{gw}\alpha}\left[\left(1-\bar{S}_g\right)^{-1/\gamma} - 1\right]^{1/\beta} \tag{4-2}$$

where:

P_{c_ow} and P_{c_go} are the interphase capillary pressure between the oleic-aqueous and gaseous-oleic phases, respectively

σ_{ij} is the surface tension between phases *i* and *j*

ρ_w is the density of water

α is the van Genuchten fitting parameter related to the inverse air-entry pressure

β is the van Genuchten fitting parameter related to the pore size distribution

$\gamma = 1 - 1/\beta$.

The normalized saturation terms in Equations (4-1) and (4-2) are given by the following equations:

$$\bar{S}_w = \frac{S_w - S_{wr}}{1 - S_{wr}} \qquad \bar{S}_g = \frac{S_g}{1 - S_{wr}} \tag{4-3}$$

where S_{wr} is the irreducible aqueous-phase saturation. In this simulation study, there was never any oleic phase present; therefore, σ_{go} was set to zero and σ_{ow} and σ_{gw} were set to one. The effect was to make Equation (4-1) represent the capillary pressure between the aqueous and gaseous phases. This capillary pressure is the same as water potential in the absence of osmotic pressure. The term water potential expressed as centimeters of water will be used for the remainder of this report.

The relative permeability terms for the aqueous and gaseous phases implemented in TETRAD are

$$k_{rw} = \left(\bar{S}_w\right)^{1/2}\left[1 - \left[1 - \left(\bar{S}_w\right)^{1/\gamma}\right]^{\gamma}\right]^2 \tag{4-4}$$

and

$$k_{rg} = \left(\frac{S_g - S_{gr}}{1 - S_{wr} - S_{gr}} \right)^{1/2} \left[1 - \left[1 - \left(\frac{S_g - S_{gr}}{1 - S_{wr} - S_{gr}} \right)^{1/\gamma} \right] \right]^{2\gamma} \tag{4-5}$$

where S_{gr} .is the irreducible gaseous-phase saturation.

Parameters assigned for the van Genuchten moisture characteristic curve were taken from GWSCREEN (Rood 1999) default values that were based on the average of four SDA surficial sediment samples that were hydraulically characterized and reported in Baca et al. (1992). The values for residual moisture content, van Genuchten α , and van Genuchten β were 0.142 cm^3/cm^3, 1.066 m^{-1}, and 1.523 (dimensionless), respectively. These values were the same as those used in the ABRA model. In the TETRAD model, the residual water saturation is entered rather than the residual water content. The S_{wr} calculated from the GWSCREEN defaults is 0.292. This value was used in the RI/FS model for all sediment features.

A Corey-type analytical equation was used to describe the constitutive relationships for basalt fractures. The equations implemented in TETRAD are

$$P_{c_gw} = A_{gw} \left(1 - S_w\right)^{B_{gw}} \tag{4-6}$$

and

$$k_{ri} = A_i \left[S_w - S_{wr} \big/ 1 - S_{sr} \right]^{B_i} \tag{4-7}$$

where A_{gw}, B_{gw}, A_i, and B_i are fitting parameters for phase *i* (*w* aqueous, *g* gaseous, *o* oleic).

The moisture characteristic curve parameters for fractured basalt in the RI/FS model were slightly different from those used for the IRA and ABRA models. Two parameters in the analytic expression used for relative permeability of the fractured basalt portions of the simulation domain are the residual water saturation and a parameter that controls the amount of curvature. For the ABRA, the values for residual water saturation and the amount of curvature were 0.0 and 1.001, respectively. In the RI/FS model, these two parameters are assigned values of 0.01 and 2.0, respectively. The reason for the change was to take advantage of faster simulations that resulted from different parameters. Either parameterization results in rapid movement of water down through the fractured basalt, as discussed in Section 5.2. The simulation speedup from this change, approximately a factor of 2, resulted from less numerical overshoot and undershoot behavior for gridblocks near saturation in the iterative solution. The nearly linear slope of the water saturation relative-permeability curve—with the amount-of-curvature parameter set to 1.001—resulted in the iterative solution overshooting and then undershooting the correct solution when water saturation approached unity. These overshoots resulted in additional iterations to obtain a mass-convergent solution.

Kriged permeability fields for the B-C and C-D interbeds are shown in Figure 4-14. The kriged porosity fields for the B-C and C-D interbeds are shown in Figure 4-15. Only the most refined grid for each interbed is shown, although kriging results were provided in Leecaster (2002) for all base and refined grids. For these grids, the average of the kriged porosities for the B-C and C-D interbeds was 0.354 and 0.428, respectively.

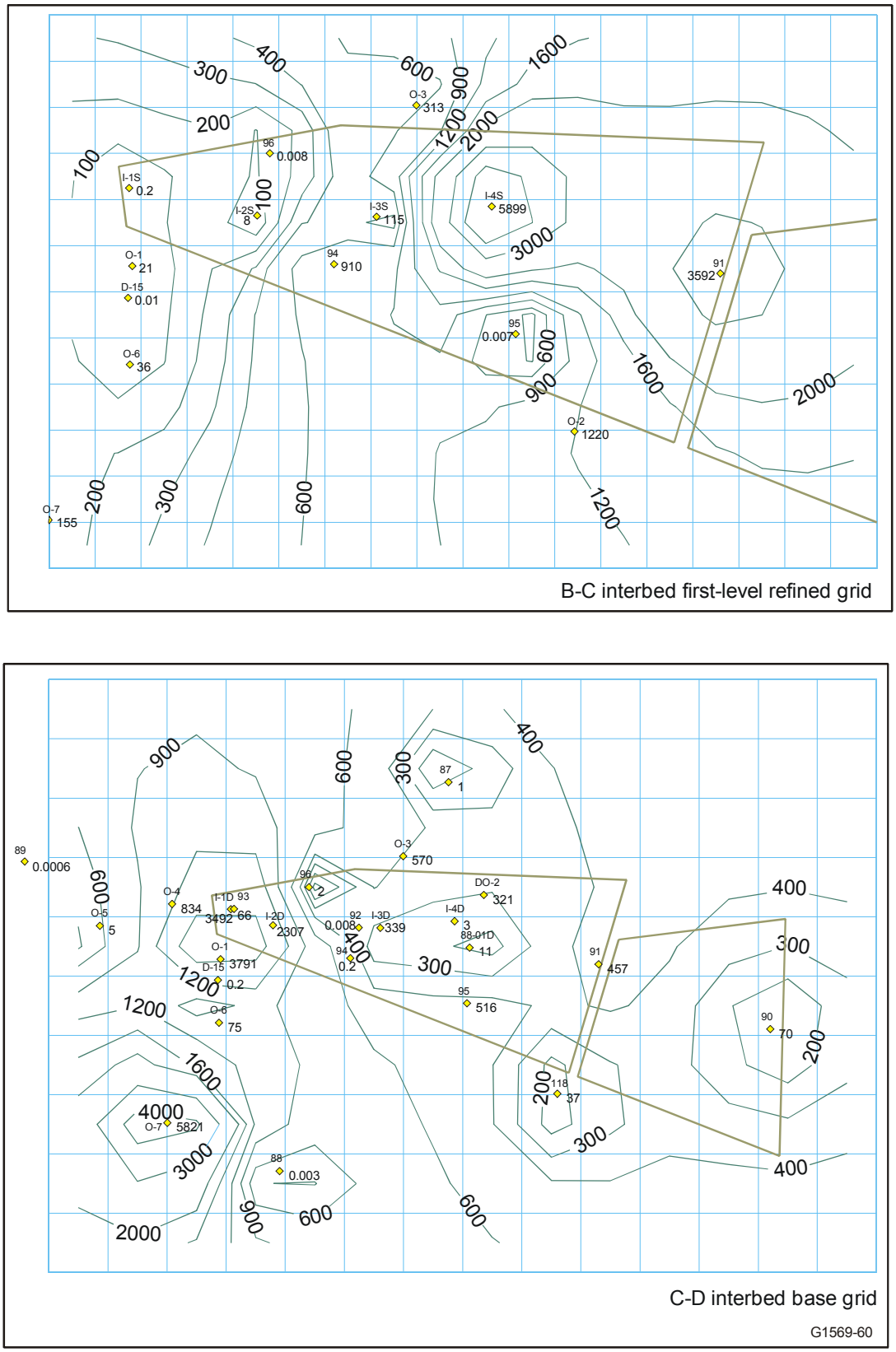

Figure 4-14. Kriged permeability (mD) for the B-C and C-D interbeds. Measured values from core samples are indicated at their respective locations.

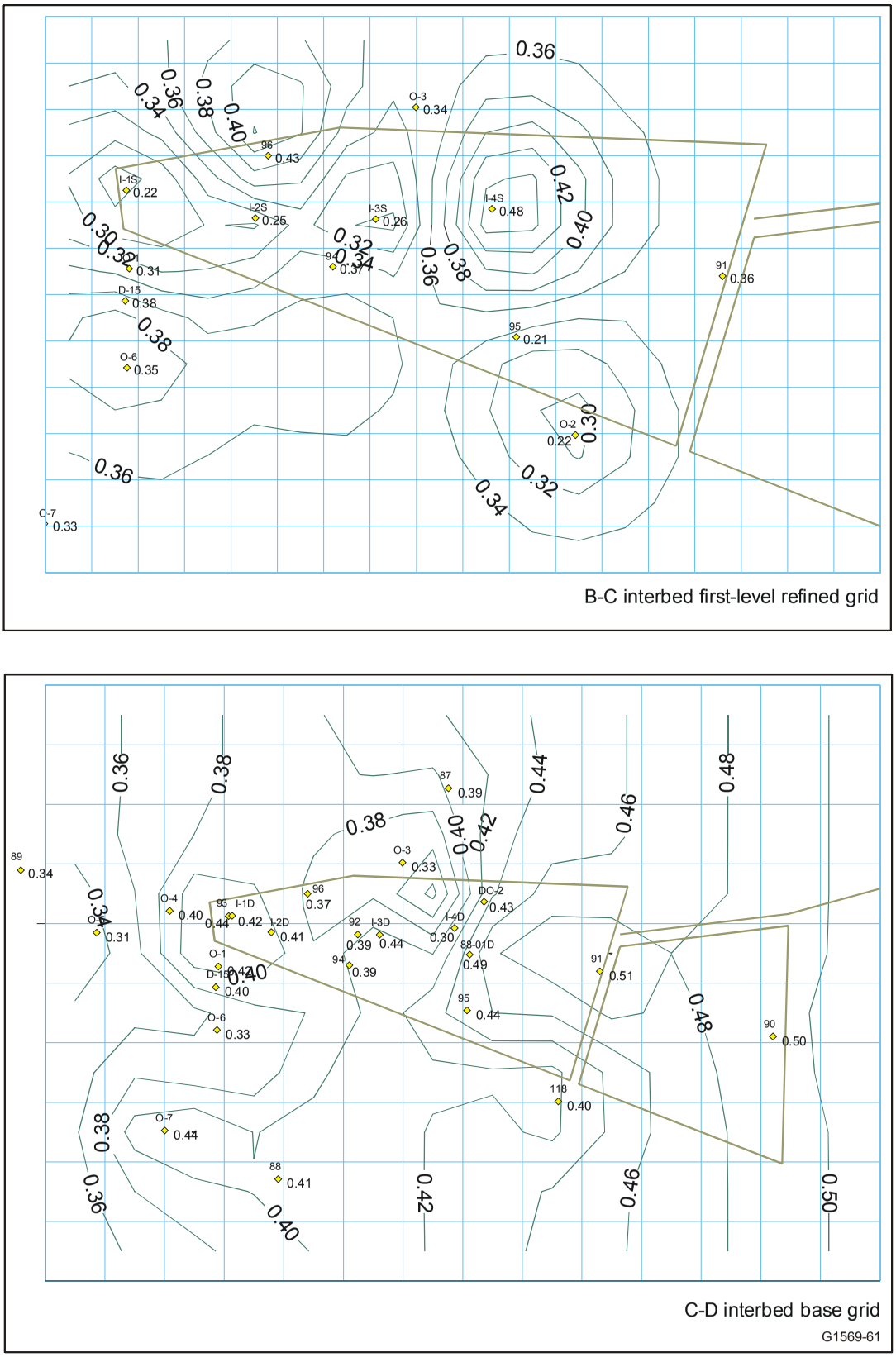

Figure 4-15. Kriged porosity for the B-C and C-D interbeds. Measured values from core samples are indicated at their respective locations.

Similar to the ABRA and IRA models, a low permeability value of 1 mD and a low porosity value of 0.05 were assigned to the top gridblocks representing both the B-C and C-D interbeds. This was accomplished by identifying the uppermost gridblock representing these interbeds in the grid with the greatest level of refinement, and then assigning the low-porosity and low-permeability value to that gridblock and the next two interbed gridblocks beneath it for a total of three low-permeability, low-porosity gridblocks. The three low-permeability, low-porosity gridblocks were used to emulate the thicker, single low-permeability, low-porosity gridblock used in the IRA model, and was necessary for the RI/FS model CCl_4 calibration (see Section 5.4). This low-permeability feature represents either a low-permeability sedimentary feature at the top of the interbeds or, more likely, a low-permeability feature caused by fine sediment infilling of fractures in the basalt immediately above the interbed. The latter occurs from deposition of entrained sediment fines as infiltration continues to occur through overlying basalt emplaced after formation of the interbeds. Inclusion of this low-permeability, low-porosity feature was necessary to achieve simulated conditions close to saturation at locations within the interbeds and to facilitate spreading of CCl_4 in the vadose zone as part of transport calibration.

An artifact of this assignment of low-permeability, low-porosity gridblocks is shown in Figure 4-16, which portrays the maximum simulated porosity for the first level of grid refinement for the B-C interbed. A variable number of vertical gridblocks represent the B-C interbed at each location. In Figure 4-16, the actual maximum simulated porosity, after the low-permeability, low-porosity gridblocks were implemented, was queried at each horizontal location. These values are posted in Figure 4-16 within each gridblock. Then these maximum values are contoured using the same intervals as in Figure 4-15. Two thinner regions of the B-C interbed show up in this plot. These are regions where the maximum porosity is 0.05 and occurs because the number of vertical gridblocks in these regions was three or less and, therefore, the entire interbed thickness was assigned the low-permeability, low-porosity value. Also posted in Figure 4-16 are the average value of the maximums (i.e., 0.316) and the overall average of all the B-C interbed (i.e., 0.206). These values show the effect of the assigned low-permeability, low-porosity gridblocks in lowering porosity. For clarification, although hydrologic properties were assigned differently in the low-permeability, low-porosity portions of the interbeds, distribution coefficients were assigned to these portions consistently with the rest of the interbeds.

4.3.4.1.1 Comparison to Subsequent Measured Interbed Properties—Core samples collected during drilling in Fiscal Year 2003 by the Operable Unit 7-08 Project were analyzed for hydrologic properties. These measured properties were compared to estimates for those locations based on kriging results from Leecaster (2002) and against sample results from nearby wells. These comparisons are included in Appendix E of this report. In general, measured porosities were lower than predicted porosities or the closest observed porosity from nearby wells. Agreement in permeability values was better, with the majority of observed values within the prediction interval from Leecaster (2002). The new results were closer to the kriged predictions than to the overall median, leading to a conclusion that modeling the spatial distribution of permeability was an improvement over predicting a single overall mean for the interbeds. Overall, the new measurements were within the range exhibited in previous hydrologic properties sampling. Statistical analysis of new permeability and porosity values are either within or below the kriged predictions for these properties in 60% of the samples. Small sample size makes analysis of results more uncertain, but, given that condition, the data do not suggest significant bias in the kriging results. Therefore, the kriging analysis in Leecaseter (2002) was supported by the new data.

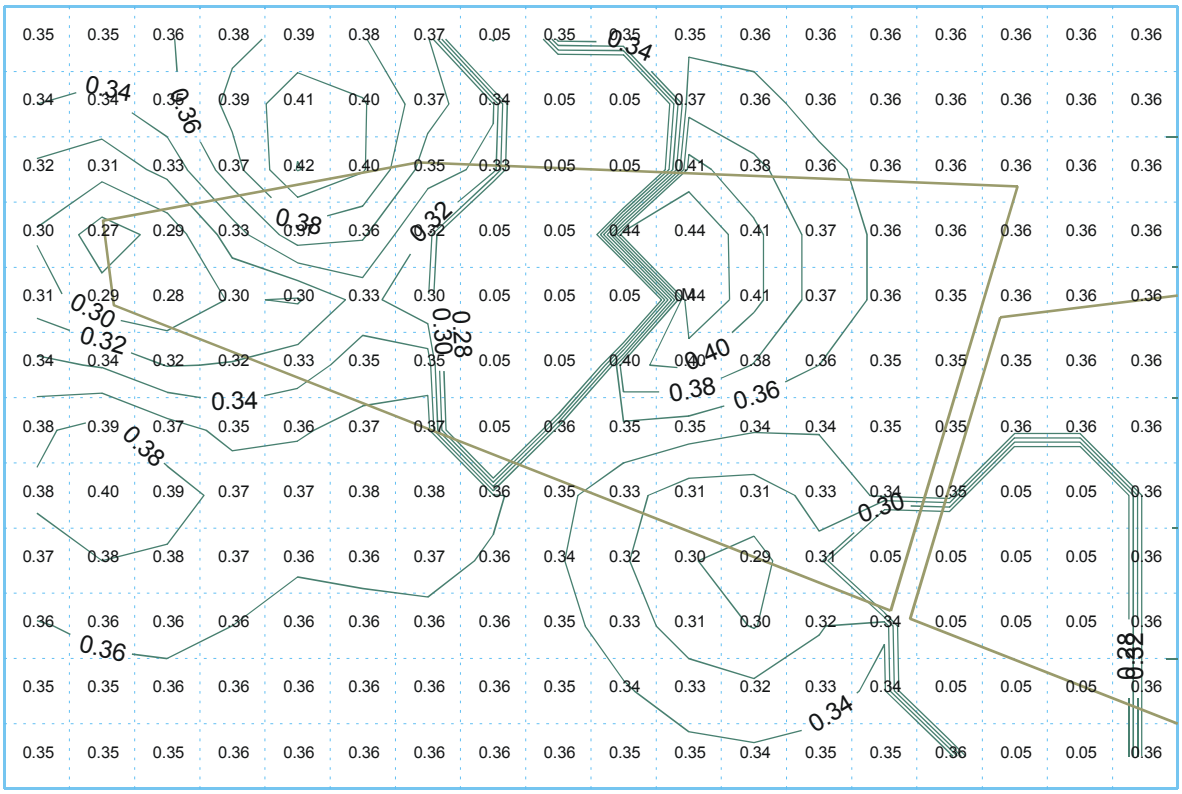

Figure 4-16. Maximum simulated porosity for the B-C interbed.

4.3.4.2 Dual Continua. Additional properties necessary to simulate water movement in dual-continua media (sometimes referred to as dual-permeability media) are described in this section. The second continuum in this case is the basalt matrix. This continuum becomes necessary in RI/FS modeling when there is substantial movement of water or contaminants from the basalt fractures into the basalt matrix. For contaminants that partition into the gaseous phase and undergo the more rapid process of diffusion, such as VOCs or C-14, simulating the second continuum of the basalt matrix becomes necessary. The hydrologic property values used for the basalt matrix are shown in Table 4-2.

Table 4-2. Parameterization of hydrologic properties and source of parameters for the basalt matrix for dual-continua simulations.

Parameter	Value	Source
Permeability	0.05 mD, isotropic	Magnuson (1995)
Porosity	0.10 cm^3/cm^3	Sondrup (1998)
van Genuchen alpha	3.840 m^{-1}	Bishop (1991)
van Genuchten N	1.474	Bishop (1991)
Residual water saturation	0.066	Bishop (1991)

A dual-continua simulation (Warren and Root 1963) consists of two separate continuums that are mathematically interconnected. In the dual-continua approach, there is a fracture domain overlapping with a matrix domain; therefore, there are twice as many gridblocks as in the single-continuum simulation. Because fractures run through the entire domain, it is necessary to assign sediment properties to those portions of the fracture domain that correspond to either surficial sediment or interbeds. A parameter called the characteristic matrix block length had to be increased in these same sediment blocks to ensure the flux of water was correctly represented through the combined sediment for both continua. For the basalt fractures, the characteristic matrix block length was set to 20 m (65.6 ft), which was an increase from the previously used value of 2 m (6.6 ft) in the IRA modeling. This increase was a result of calibration for the VOC model. In the interbeds, this characteristic matrix block length value was increased to 1,000 m (3,280.8 ft). The other dual-continua parameters remained the same as those for the ABRA. The transmissibility multiplier for fracture-matrix connections was left at 6.0 to result in three orthogonal sets of fractures with a connectivity factor of 0.5 in each of these three directions to allow partial contact between matrix blocks across the fractures.

4.3.5 Boundary Conditions

Boundary conditions are discussed first for the aqueous-phase portion of the model and then for additional gaseous-phase boundary conditions that were necessary for dual-continua simulations. Boundary conditions are generally discussed in terms of top surface, lateral sides, and bottom surface of the simulation domain.

4.3.5.1 Aqueous Phase

***4.3.5.1.1 Surface*—**Aqueous-phase surface boundary conditions for the vadose zone model primarily consist of assigning water fluxes. Two types of water fluxes were imposed on the simulation domain, representing steady-state conditions and historical flooding conditions. Gaseous-phase boundary conditions of atmospheric pressure were also applied across the upper surface of the domain to prevent pressure building up in the subsurface during infiltration events.

As with the ABRA model, three infiltration rates were assigned to different regions inside the SDA for the RI/FS model. These rates represented a low-, medium-, and high-infiltration rate and were based on inverse modeling to neutron probe access tube measurements from Martian (1995). The spatial assignment was modified slightly, based on preliminary inverse modeling of moisture contents from Type B probes within the waste. The modeling is termed preliminary because it was determined the moisture content results were impacted by thermal influences and were not finalized. Despite the preliminary and qualitative nature of the inverse-modeling-infiltration estimates, the infiltration values for gridblocks containing Type B soil moisture and resistivity Probes Pit 5-TW1, MM2-3, and 741-08 were changed to the high-infiltration rate. Figure 4-17 shows the resulting distribution of the three assigned infiltration rates across the SDA.

In the RI/FS model, the value assigned for the high-infiltration rate was changed to 10.0 cm/year (3.9 in./year), rather than the 24.1 cm/year (9.4 in./year) value used in the ABRA model. The high ABRA infiltration rate of 24.1 cm/year (9.5 in./year) included the effect of three locations that had extremely high-infiltration rates due to neutron probe access tubes being located in areas of low topography (e.g., ditches) (Martian 1995). Excluding these elevated infiltration rates resulted in a high-infiltration rate of 10.0 cm/year (3.9 in./year), which was judged more representative of upper-bound water infiltration through waste in the SDA. The change in the high-infiltration rate from 24.1 to 10.0 cm/year (9.4 to 3.9 in./year) resulted in a reduction in the overall average assigned infiltration across the SDA from 8.5 cm/year (3.3 in./year) in the ABRA model to 5.0 cm/year (1.9 in./year) in the RI/FS model.

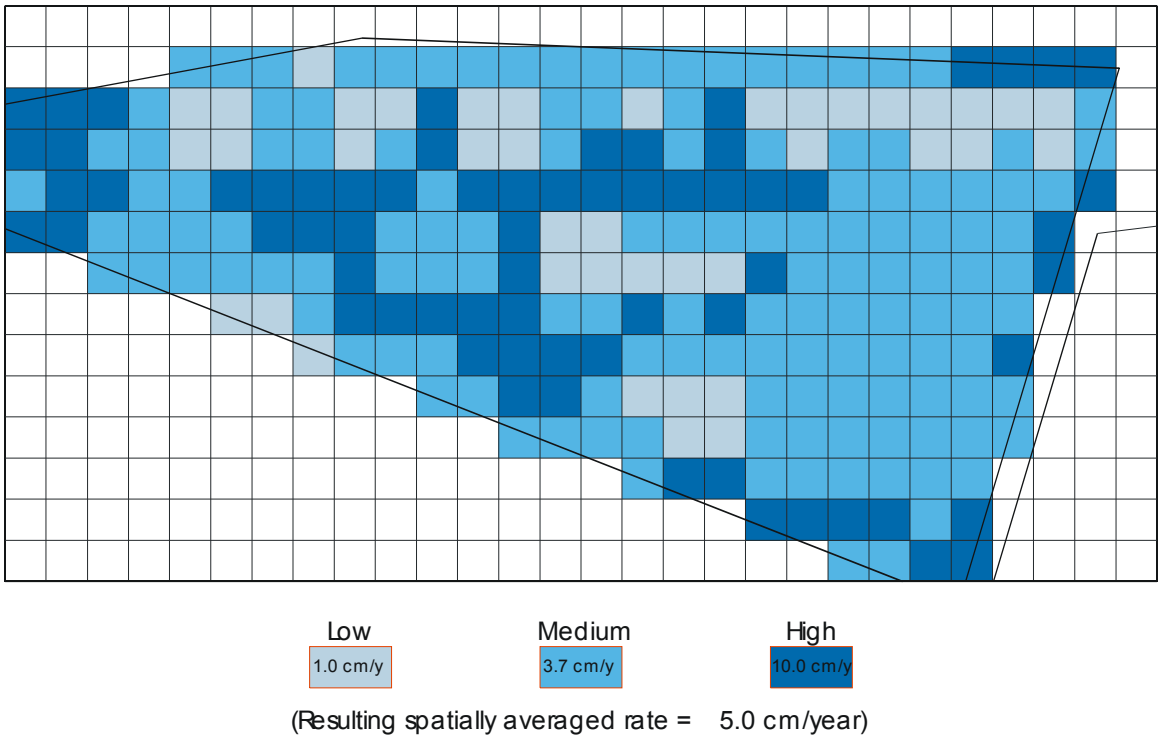

Figure 4-17. Spatially variable infiltration assignment for model domain inside the Subsurface Disposal Area.

The horizontal discretization of the SDA in the RI/FS model limits the extent that infiltration can be assigned on a site-specific basis. High infiltration through ditches or temporary collapse features that focus infiltration are beyond the scope of modeling. When considering transport from buried waste, infiltration rates need to be assigned based on what infiltration is likely to be through the waste, rather than infiltration through ditches near roads.

Outside the SDA, surface infiltration was assigned the same rate of 1 cm/year (0.4 in./year) that was used in ABRA modeling, based on Cecil et al. (1992).[b]

Three historical flooding events have occurred in the SDA and were included in the RI/FS model, essentially using the same method as the IRA model, but with slight differences caused by differences in gridding. Figure 4-18 shows locations where additional water was imposed at the surface for the 1962, 1969, and 1982 floods, respectively. Estimates of the amount of water that entered the SDA for each of the floods were taken from Vigil (1988) and are shown in Table 4-3. Each flood was assumed to last 10 days. The locations selected for the 1962 flood exclude gridblocks representing Pit 3, which was open and flooded in 1962. However, because the source-release model does not include the effect of the floods, this omission has no substantial effect.

b. This surface infiltration rate estimate is expected to decrease, based on an ongoing reevaluation by INL Site scientists.

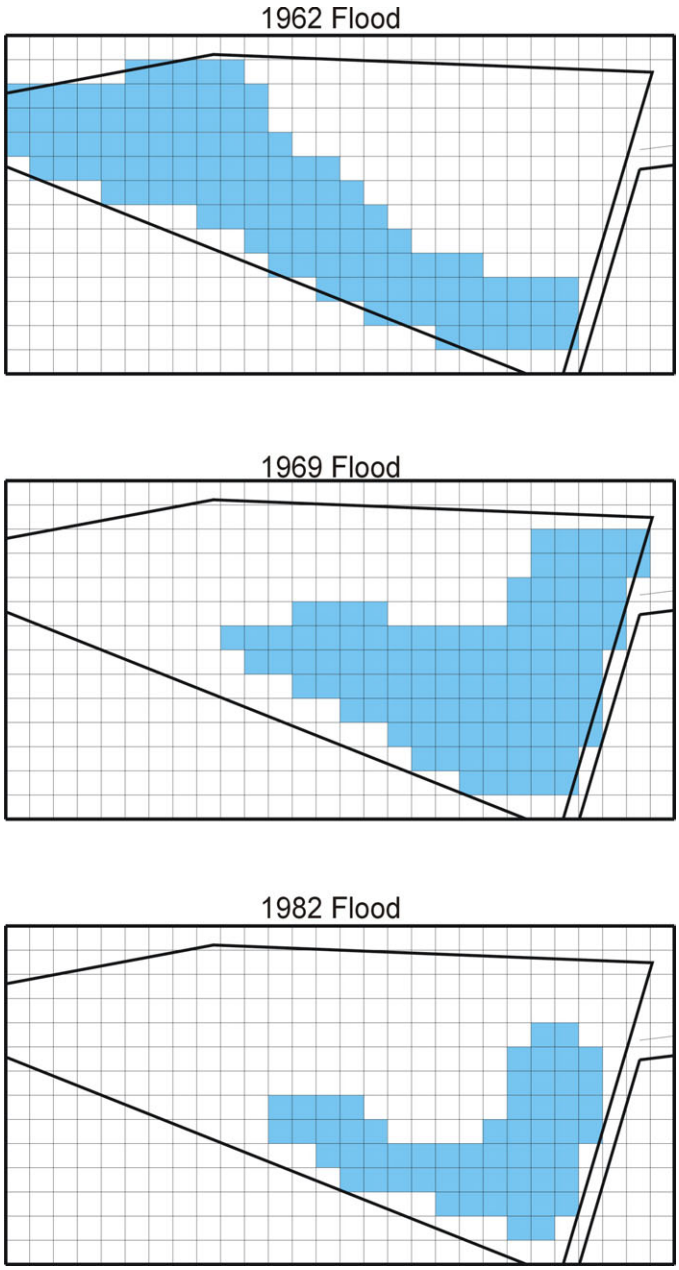

Figure 4-18. Locations of additional water applied during the 1962, 1969, and 1982 flooding events in the Subsurface Disposal Area in the second-level refined grid.

Table 4-3. Historical flooding volumes and application rates at the Subsurface Disposal Area.

Year	Estimated Volume (acre-ft)	Infiltration Rate (m/day)
1962	30	2.26×10^{-2}
1969	20	1.68×10^{-2}
1982	8.3	1.24×10^{-2}

4.3.5.1.2 Bottom—The lower boundary of the vadose zone domain was assigned a vapor-static atmospheric pressure to emulate a water table condition. Water and tracer components (i.e., contaminants) in the water could freely advect out through the bottom boundary of the simulation domain.

4.3.5.1.3 Horizontal—Default no-flux boundaries were allowed for all horizontal or lateral sides of the simulation domain. This was different from the ABRA, because there was no influence from the spreading areas included at the western boundary above the C-D interbed. Although the USGS tracer test (Nimmo et al. 2001) showed that there can be an influence above the C-D interbed, when that influence was included in the ABRA model, it only served to dilute simulated groundwater-pathway concentrations for long half-life radioactive contaminants that migrated strictly as dissolved in the aqueous phase. Therefore, the influence of the spreading areas was not included in the RI/FS modeling.

4.3.5.2 Vapor Phase

4.3.5.2.1 Surface—Surface boundary conditions for the VOC transport model consisted of 1) a diffusion boundary condition, and 2) a fluctuating surface pressure to mimic changes in barometric pressure. The diffusion boundary condition, as implemented in TETRAD, allows molecular diffusion across grid boundaries. The diffusion occurs as if there was an extra external gridblock with fixed saturations and mole fractions. In this case, the external gridblock at land surface represents the atmosphere and was assumed to be completely saturated with air. This implies a zero concentration boundary for VOC vapor diffusion. The width of the external gridblock, which determines the diffusion length, is equal to the thickness of the uppermost gridblock in the model.

Barometric pressure fluctuations at land surface were included in the VOC model calibration, but were not included in the base-case simulations for the draft RI/BRA due to extremely long simulation times. In lieu of a fluctuating pressure, a constant pressure equal to atmospheric pressure was assigned at the upper surface of the domain. As discussed below in Sections 5.4.7 and 5.5.3, not including barometric pumping in the base-case simulations was conservative for the groundwater pathway as less mass escaped through the upper surface of the model domain. Implementation of the fluctuating atmospheric pressure boundary condition is described in Section 5.4.2.3.2.

4.3.5.2.2 Horizontal—Diffusion boundaries similar to those assigned at land surface were also assigned to the lateral boundaries and were necessary because of the relatively small domain size compared to the size of the plume. First-type aerostatic pressure boundary conditions were also assigned to the lateral boundaries, based on a gradient of 0.012 kPa/m.

4.3.5.2.3 Bottom—The bottom of the vadose zone model domain was prescribed the same water-table type boundary condition for the vapor-phase model as was prescribed for the dissolved-phase model (see Section 4.3.5.1.2). However, for the vapor-phase model, this condition was imposed on both the fracture and matrix domain, although the majority of the contaminant flux occurred in the fracture domain. This approach to assigning the bottom boundary conservatively lets contaminant mass advect out the bottom of the model domain without being influenced by contaminant mass already present in the aquifer.

4.3.5.2.4 Internal—Both air injection during well drilling and gas removal due to vapor vacuum extraction operations were included in the dual-phase transport model. More than 40 wells have been drilled in the vicinity of the SDA using air as the fluid; this does not include reverse-air-circulation drilled wells, which typically recover most of the injected air. In wells drilled with air before 1994, air was injected at approximately 1,000 cfm and 250 psi to bring drill cuttings to the surface. A survey of SDA drill logs indicates that for most of the wells, circulation was partially or totally

lost below about 18.3 m (60 ft), which meant a large volume of air has been pumped into the subsurface of the SDA. Implementation of air-drilling in the model is described in Section 5.4.2.3.2.

Vapor vacuum extraction was also included in the model in much the same way air injection is handled. One difference with extraction is that phases are extracted rather than components. In this case, the gaseous phase is extracted, which is mostly air but can also include any water vapor or VOC vapor. Also, extraction is simpler because the extraction interval does not change the way an injection interval changes when a well is drilled. Three historic vapor extraction tests were included in the calibration and base-case simulations. They include the 1989 2-week test, the 1990 4-month test, and the 1993 Organic Contamination in the Vadose Zone Treatability Study. All of these tests pumped from Well 8901. In the base-case simulations, actual Operable Unit 7-08 operations from January 1996 through January 2005 were included, involving extraction from multiple wells. Base-case simulations also included future vapor extraction activities to the year 2010, assuming extraction from six wells for 10 months a year. Vapor extraction implementation in the model is described in Section 5.4.2.3.2.

4.3.6 Initial Conditions

Initial conditions for all simulations were obtained by assigning an initial water saturation of 50% to the entire simulation domain in both the single- and dual-continua domains. Then the simulation was run for 300,000 days (approximately 820 years) to let the system come into equilibrium. Water saturation in the C-D interbed was monitored to determine whether equilibrium had been obtained. Figure 4-19 shows the simulated time history of water saturation at a location at the top of the C-D interbed, located centrally beneath the SDA for a single-continuum domain. Initially, this gridblock wets up as excess water in the fractured basalt from above the interbed moves into and through the interbed. After the first approximate 50 years, change in saturation was negligible, indicating that steady-state conditions had been achieved.

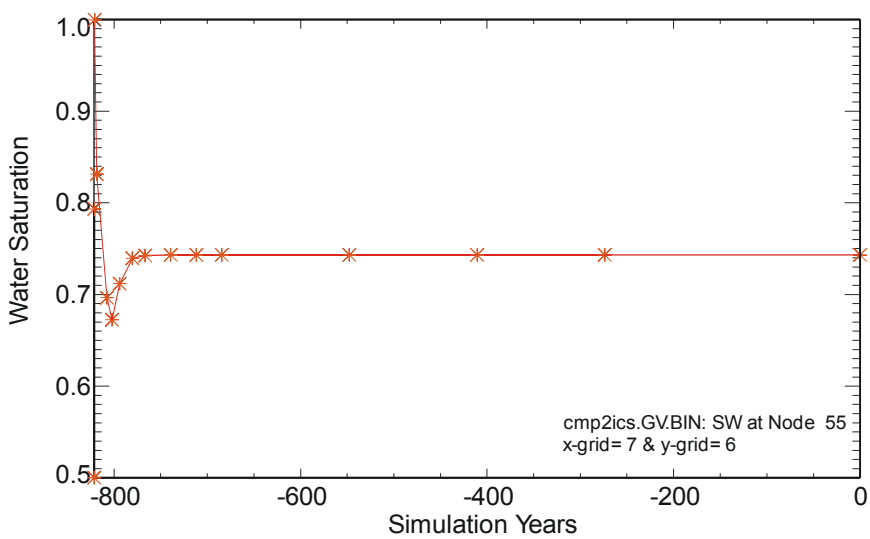

Figure 4-19. Initial condition simulation showing the time history of water saturation in the C-D interbed beneath the Subsurface Disposal Area.

For the dual-continua initial conditions simulation, results for the fracture domain are virtually identical to those in Figure 4-19. Water saturation in the matrix domain for the same horizontal location, but beneath the C-D interbed in the basalt, is shown in Figure 4-20. Water saturation in the basalt beneath the interbed takes considerably longer to stabilize. Even after the approximate 820-year simulation, there

is still a slight amount of drainage occurring, but, with the vast majority of the flow occurring in the fracture domain, this small residual change has a negligible effect on the simulation.

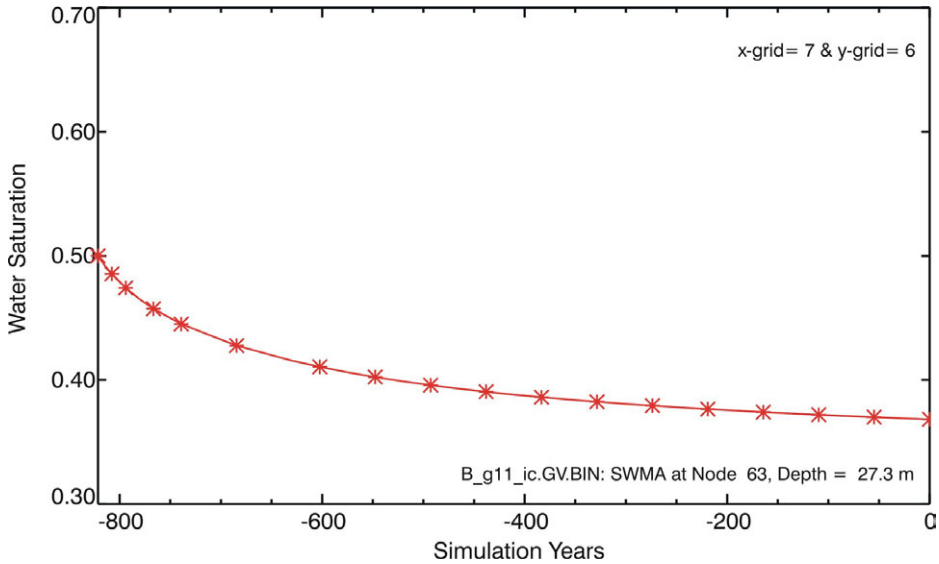

Figure 4-20. Initial condition simulation showing time history of water saturation in the basalt matrix beneath the C-D interbed.

4.3.7 Contaminant Transport

This section discusses transport in the vadose zone model. Topics addressed are transport mechanisms and their parameterization, contaminants that were simulated and how they were grouped, how these contaminants were introduced into the vadose zone model from the source-release model, and how contaminants were transferred out of the vadose zone model.

4.3.7.1 Transport Mechanisms. General mechanisms included in the transport model were advection, mechanical dispersion, diffusion, sorption, radioactive decay, buoyancy, and facilitated transport. Each is discussed in the following subsections.

***4.3.7.1.1 Distribution Coefficients*—**Sorption was considered to follow linear, reversible isotherms that could be described using distribution coefficients, or K_ds. A K_d lumps all possible geochemical interactions into a single parameter. Because sorption was assumed not to occur within the fractured basalt portions of either the vadose zone or the aquifer, only sediment K_d values were necessary in the RI/FS model.

Table 4-4 provides K_ds used in the RI/FS model that were defined for use in Holdren and Broomfield (2004). Values for Ac-227, Am-241, Am-243, Pu-238, Pu-239, and Pu-240 were decreased from those used in the IRA and ABRA models to account for sieving of interbed material (Hull 2003). Values for Np-237 and uranium isotopes were increased based on additional batch equilibrium measurements from interbed cores (Leecaster and Hull 2004). The value for C-14 is different than the value in Holdren and Broomfield (2004) because the ABRA and RI/FS values were transposed in Holdren and Broomfield (2004). The C-14 value of 0.4 mL/g was selected from the conservative end of the range presented in Plummer, Hull, and Fox (2004). The value for chromium also is incorrect in Holdren and Broomfield (2004). Chromium was simulated in both the IRA and ABRA models with a K_d of 0.1 mL/g. This same value is used in the RI/FS model. Distribution coefficients for VOCs are discussed in Section 5.4.

Table 4-4. Sediment distribution coefficients for Operable Unit 7-13/14 remedial investigation and feasibility study simulations.

Contaminant	Distribution Coefficient (mL/g)
Ac-227	2.25E+02
Am-241	2.25E+02
Am-243	2.25E+02
C-14	4.00E-01
Cl-36	0.00E+00
I-129	0.00E+00
Nb-94	5.00E+02
Np-237	2.30E+01
Pa-231	8.00E+00
Pb-210	2.70E+02
Pu-238	2.50E+03
Pu-239	0.00E+00[a] and 2.50E+03[b,c]
Pu-240	0.00E+00[a] and 2.50E+03[b,c]
Ra-226	5.75E+02
Sr-90	6.00E+01
Tc-99	0.00E+00
Th-229	5.00E+02
Th-230	5.00E+02
Th-232	5.00E+02
U-233	1.54E+01
U-234	1.54E+01
U-235	1.54E+01
U-236	1.54E+01
U-238	1.54E+01
Chromium	1.00E-01
Nitrate	0.00E+00
Carbon tetrachloride	1.00E-03[d] and 2.20E-01[e]
Methylene chloride	1.00E-03[d] and 4.40E-03[e]
Tetrachloroethylene	1.00E-03[d] and 1.82E-01[e]

a. Mobile fraction source release, surficial sediment, and A-B interbed.
b. Mobile fraction in B-C and C-D interbeds.
c. Nonmobile fraction source release, surface sediment, and interbeds.
d. Volatile organic compounds in basalt.
e. Volatile organic compounds in surface sediment and interbeds.

4.3.7.1.2 Facilitated Transport—Plutonium mobility in the RI/FS model was based on research by Batcheller and Redden (2004). The source-term model accounts for the mobile fraction leaving the waste form. In the vadose zone model, this released mobile fraction of plutonium is then allowed to migrate with a 0 K_d through the surficial sediment and A-B interbed. The B-C and C-D interbeds are assigned the sediment K_d value of 2,500 mL/g from Table 4-4. Facilitated transport is considered for Pu-239 and Pu-240, but not for Pu-238. As discussed in Section 5.1.3 of the draft RI/BRA, Pu-238 is not simulated with a colloidal fraction based on the work of Batcheller and Redden (2004), which showed that certain processes at Rocky Flats Plant could produce colloids. The fraction of Rocky Flats Plant plutonium that is mobile is 3.7% for the RI/FS model. Pu-238 was not simulated with a colloidal fraction because it would have been separated as an impurity and would not have gone through the high-temperature processes that generate colloids.

4.3.7.1.3 Other Transport Parameters—A variety of additional parameters were required to implement the vadose zone transport model. These additional parameters were particle density, diffusion coefficients, tortuosity, and decay half-lives. Particle density was assigned the typical value of 2,700 kg/m^3 for sediment (Freeze and Cherry 1979). This was the same value assigned in the ABRA model. Because sorption was assumed not to occur in fractured basalt, the grain density assigned for that portion of the simulation domain did not matter.

Diffusion of contaminants within the aqueous phase was assigned the common literature value of 1×10^{-5} cm^2/second (Freeze and Cherry 1979). This was the same value assigned in the ABRA model. The restriction of diffusion caused by tortuosity also was included, based on a relationship from Lerman (1988) that was used to describe diffusion, as shown in Equation (4-8):

$$D = D_o \theta_w^2 \tag{4-8}$$

where:

D = diffusion in the porous medium (length^2/time)

D_o = free-water diffusion coefficient (length^2/time)

θ_w = volumetric moisture content (unitless).

Various formulations of diffusion and tortuosity are implemented in different simulators. In the TETRAD simulator, diffusion within the aqueous phase is treated, as shown in Equation (4-9):

$$D_{eff} = \frac{\theta_w D_o}{\tau_w} \tag{4-9}$$

where:

D_{eff} = effective diffusion coefficient (length^2/time)

τ_w = aqueous-phase tortuosity.

The aqueous-phase tortuosity term for TETRAD was then calculated, as shown in Equation (4-10):

$$\tau_w = \frac{1}{\theta_w} \quad . \tag{4-10}$$

The end result of this application is to have greater tortuosity values assigned for drier conditions. Single tortuosity values were assigned for each sedimentary feature and for fractured basalt. Tortuosity values were determined using Equation (4-10) and are given in Table 4-5. Tortuosity values were based on the average simulated water content for each sedimentary feature from the base RI/FS model (shown in the second column of Table 4-5), and either the assigned porosity for surficial sediment and the A-B interbed or the average of the kriged values for the B-C and C-D interbeds (shown in the third column of Table 4-5). Fractured basalt has low-simulated moisture content, approximately the same as the assigned residual water saturation; therefore, fractured basalt was arbitrarily assigned a high aqueous-phase tortuosity.

Table 4-5. Aqueous-phase tortuosity values for the remedial investigation and feasibility study model.

Material	Average Simulated Water Saturation (cm^3/cm^3)	Assigned or Average Porosity (cm^3/cm^3)	TETRAD Tortuosity (dimensionless)
Surficial sediment	0.59	0.50	3.4
A-B interbed	0.70	0.57	2.5
B-C interbed	0.68	0.354	4.2
C-D interbed	0.63	0.428	3.7
Fractured basalt	—	—	100

Vapor-phase tortuosity values were used as a calibration parameter. Initially, tortuosity values were calculated from an empirical expression derived by Millington (1959) and later modified to improve agreement between model results and observed data. Later, the Millington formulation was directly implemented in the TETRAD code so the tortuosity values could vary spatially and temporally. This, however, was unsuccessful in improving agreement between model results and observed data, and ultimately the tortuosity values were assigned constant values for each material type. This is discussed in detail in Section 5.4.

Longitudinal and transverse dispersivity values of 5.0 and 0.5 m (16.4 and 1.6 ft), respectively, were assigned in the vadose zone transport model. The longitudinal value is the same as was used in the IRA and ABRA models and was originally based on inverse modeling from the large-scale infiltration test (Magnuson 1995). The transverse dispersivity value of 0.5 m (1.6 ft) is the same as was used in the ABRA model and was assigned by using the modeling rule-of-thumb that the transverse dispersion is one-tenth the longitudinal dispersion (Freeze and Cherry 1979). The 5.0-m (16.4-ft) longitudinal value is smaller than would be assigned using the general rule-of-thumb that the dispersivity should be approximately one-tenth of the domain size (Gelhar 1986). In the absence of calibration data (e.g., breakthrough of a nonsorbing contaminant), no basis is available to substantially adjust the dispersivity values from those used in the ABRA model. Ideally, higher concentrations would result for pulses of mobile contaminants because the lower dispersivity would produce a sharper simulated front. For a long, slow release (e.g., a solubility-limited release of a lower-mobility contaminant), the lower dispersivity ideally would result in a slightly later first arrival. However, because dispersion control consisting of higher order solutions that limit numerical dispersion was not used in the TETRAD

simulation, the relative contribution of numerical dispersion compared to simulated dispersion in the vadose zone model is unknown. No dispersivities were assigned for vapor-phase transport because diffusion would dominate the dispersive fluxes.

Half-lives for each radioactive COPC were assigned based on literature values (GE 1989) and are given in Table 4-6.

Table 4-6. Half-lives for radioactive contaminants of potential concern used in the remedial investigation and feasibility study groundwater-pathway simulations.

Contaminant	Half-life (years)
Ac-227	2.18E+01
Am-241	4.32E+02
Am-243	7.38E+03
C-14	5.73E+03
Cl-36	3.01E+05
I-129	1.57E+07
Np-237	2.14E+06
Pa-231	3.28E+04
Pb-210	2.23E+01
Pu-238	8.78E+01
Pu-239	2.41E+04
Pu-240	6.57E+03
Ra-226	1.60E+03
Tc-99	2.13E+05
Th-229	7.34E+03
Th-230	7.70E+04
Th-232	1.41E+10
U-233	1.59E+05
U-234	2.45E+05
U-235	7.04E+08
U-236	2.34E+07
U-238	4.47E+09

4.3.7.2 Contaminant Groupings. Contaminant release and subsurface transport were simulated for 31 contaminants, which were grouped into 11 groups of contaminants for fate and transport simulation. This same grouping was used in source-term simulations (Anderson and Becker 2006). Members of a decay chain are assigned to the same group. Isotopes in the chain with a half life of more than 1 year were included explicitly in simulations, while contaminants with shorter half-lives were assumed to be in equilibrium with long-lived parents. Grouping for COPCs and long-lived decay-chain members is defined in Table 4-7 as Groups 1 through 5. Some of the long-lived daughter products were not identified as COPCs in the ABRA (Holdren et al. 2002), but were included to confirm that they pose no unacceptable risk and to assess sensitivity and uncertainty. Some RI/FS sensitivity cases reduce release of the parent nuclide and thus increase ingrowth of the daughter in the waste zone.

Table 4-7. Contaminant groups for Operable Unit 7-13/14 simulations.

Simulation Group	Group Name	Contaminants in Group[a]	Description	Basis for Group
Group 1	Am-241	Am-241, Np-237, U-233, and Th-229	Pu-241 decay chain	Neptunium series beginning at Am-241, created by weapons' production.
Group 2	Am-243	Am-243, Pu-239, U-235, Pa-231, and Ac-227	Am-243/Pu-239 decay chain	Am-243 to Pu-239 (both created primarily by weapons' production) to actinium series initiated by U-235.
Group 3	Pu-240	Pu-240, U-236, Th-232, and Ra-228	Pu-240 decay chain	Pu-240 to U-236 (created primarily by weapons' production) to thorium series initiated by Th-232.
Group 4[b]	Pu-238	Pu-238, U-234, Th-230, Ra-226, and Pb-210	Pu-238 decay chain	Pu-238 (created primarily by reactor operations) to U-234 to mid-uranium series.
Group 5[b]	U-238	U-238, U-234, Th-230, Ra-226, and Pb-210	Uranium decay chain	Uranium series initiated by U-238 (primarily from weapons' production).
Group 6	Tc-99	Tc-99, I-129, and Cl-36	Mobile activation products	Created by reactor operations.
Group 8[c]	C-14	C-14	Mobile activation product	Requires dual-phase simulation. Created by reactor operations.
Group 9	Nb-94	Nb-94 and Sr-90	Fission and activation products	Surface pathways only. Created by reactor operations.
Group 10	Nitrate	Nitrate (as nitrogen) and chromium	Toxic chemicals	Nonvolatile (single-phase), nonradioactive chemicals. Nitrate is contained primarily in Series-745 sludge from Rocky Flats Plant. Mobile with no decay. Chromium is a possible model performance indicator.
Group 11	Volatile organic compound	Carbon tetrachloride, Methylene chloride, Tetrachloroethylene, and 1,4-dioxane	Toxic chemicals in organic sludge	Volatile (dual-phase) nonradioactive chemicals. Scaled in the Ancillary Basis for Risk Analysis.

a. Simulations include contaminants that are not contaminants of concern. The additional contaminants are decay-chain products or are useful for other reasons (e.g., comparison to performance assessment modeling and interpreting model performance and uncertainty).
b. Groups 4 and 5 both contain U-234, Th-230, Ra-226, and Pb-210.
c. Group 7 contained tritium, which was dropped as a model performance indicator.

4.3.7.3 Source Release Implementation in Vadose Zone Model. The vadose zone model implements the temporal source-term release (Anderson and Becker 2006) spatially in an automated fashion, using a PV-Wave program. PV-Wave is a commercial visual data analysis software program that was used for pre and post-processing model results (see Appendix B). In addition to being spatially distributed, the source release is also distributed vertically at each assigned location based on the number of gridblocks within the surficial sediment at that location. Once released, the contaminants are allowed to migrate with the simulated water movement. Anderson and Becker (2006) divided the SDA into 18 source areas for modeling contaminant release and transport of radionuclides and chemicals, except for C-14, which used nine source areas. The source-release model was linked with the vadose zone model through assigned infiltrations that resulted from assigned spatially variable surface water fluxes. Individual assigned water fluxes for each gridblock within the 18 source areas were averaged for use in the source-release modeling. Figures 4-21 through 4-23 show the resulting average infiltration for each source area. Figure 4-23 is necessary because areas representing Pits 4, 5, and 10 were reduced for VOC simulations, based on disposal location knowledge.

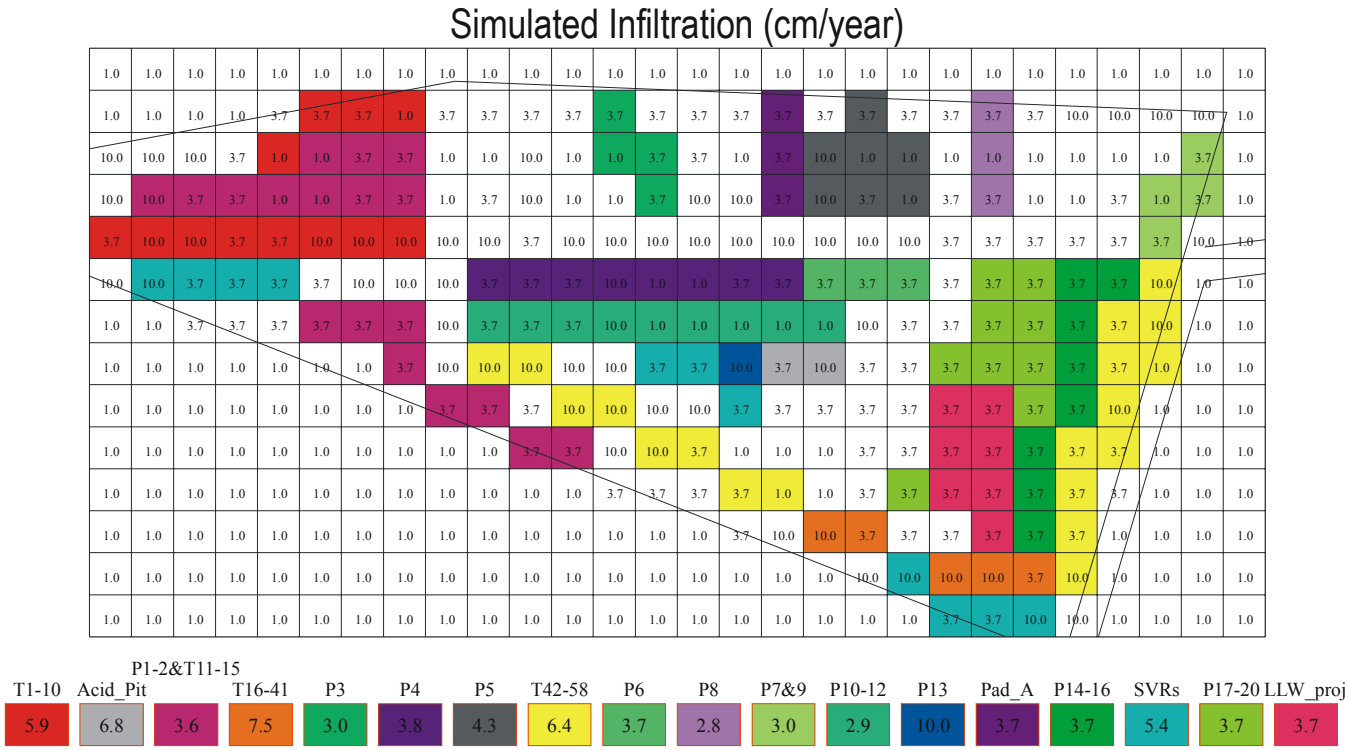

Figure 4-21. Subsurface Disposal Area infiltration rates with averages by source area for dissolved-phase contaminants.

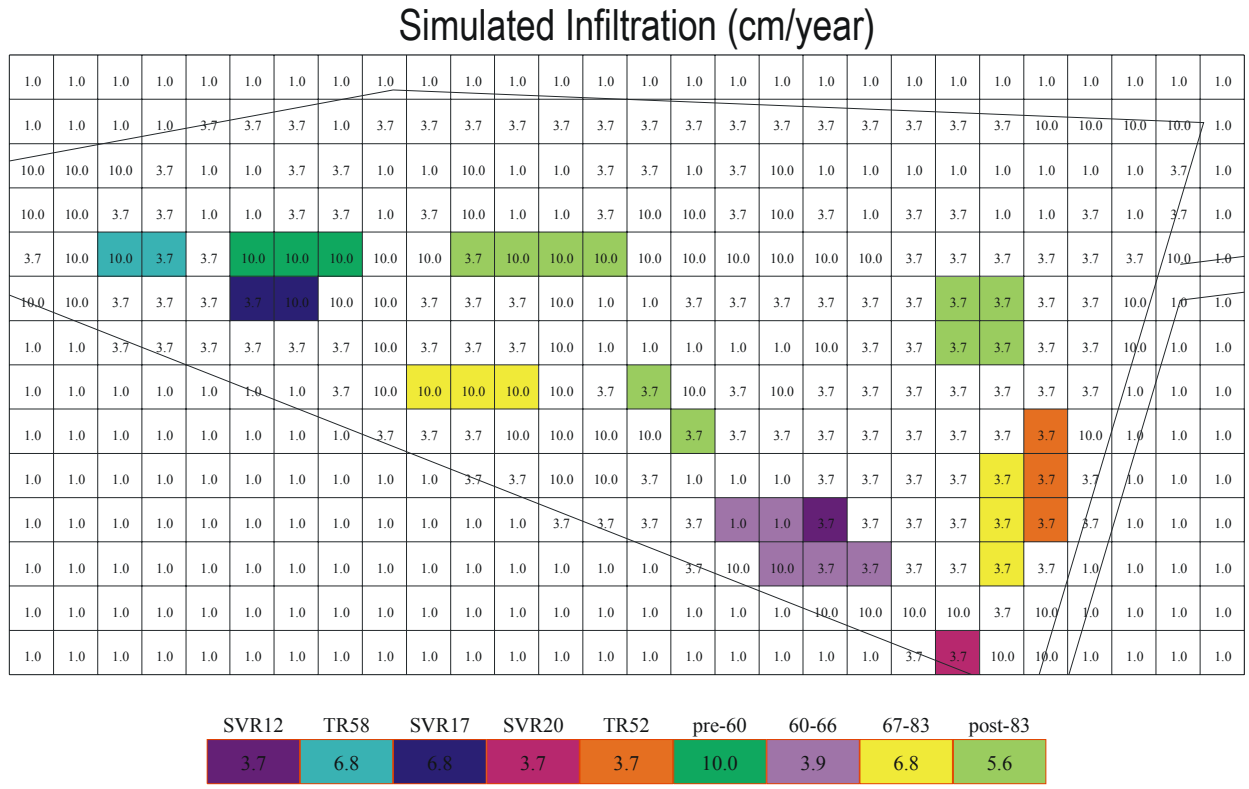

Figure 4-22. Subsurface Disposal Area infiltration rates with averages by source area for carbon-14.

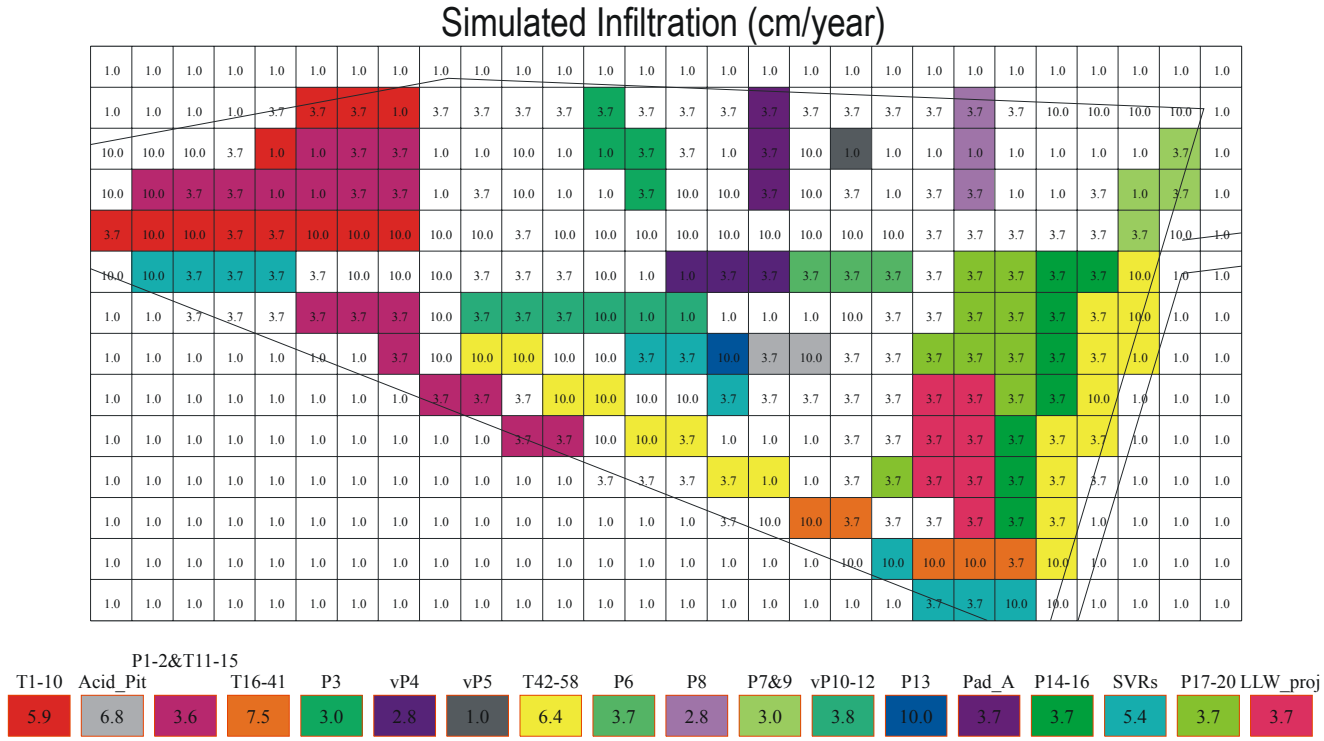

Figure 4-23. Subsurface Disposal Area infiltration rates with averages by source area for volatile organic compound contaminants.

The general methodology for distributing contaminant release vertically at each location was to

1. Start release in the first gridblock that was at a depth of greater than 1.5 m (4.9 ft) below the top surface. This was equivalent to maintaining a clean overburden thickness of 1.5 m (4.9 ft).

2. End release one gridblock above the bottommost surficial sediment gridblock. This maintained a clean underburden thickness of at least 0.5 m (1.6 ft).

Two exceptions were implemented to these general rules. First, Pad A releases were assigned to the second gridblock beneath the surface for the three gridblock locations representing Pad A. The reason for this assignment is that Pad A waste is actually buried above grade, and the second gridblock down was the closest approximation that could be made in the model; the uppermost gridblock was being used to assign infiltration rates. Second, Acid Pit sources were assigned at the bottommost gridblock to approximate burial at the bottom of an open pit. The Low-Level Waste Pit is not listed as an exception for waste zone thickness assignments. As discussed previously, the surficial sediment at the grid locations representing the low-level waste disposal pits were deepened to 9.1 m (30 ft) when the lithologic assignments for the gridblocks were made. With this approach, the general methodology correctly assigned waste for low-level waste streams that went into the active pit.

4.3.7.4 Interface from Vadose Zone Model to Aquifer Model. The primary result used in the aquifer model is the flux of water and contaminants from the bottom of the vadose zone simulation domain. These time-varying fluxes were extracted, using a PV-Wave program, from each gridblock in the base vadose zone domain to build a table of flux values that was used as input into the aquifer model.

4.4 Aquifer Model

The objective in the aquifer simulation was to evaluate three-dimensional advective-dispersive transport in a predominantly horizontal flow regime. The aquifer flow model had been updated in the ABRA to take advantage of additional water level data (Whitmire 2001). For the RI/FS model, the aquifer domain was again revised to extend the domain farther to the south and west. This extension ensured that risk isopleths at the 1.E-05 level were closed within the simulation domain. Permeability values were not adjusted to improve agreement between simulated and observed water levels for this extension to the ABRA domain. Appendix C contains complete details of this aquifer domain extension. A summary of the domain extension is included here.

The domain was extended westward so that it was twice the width of the ABRA aquifer model domain. The domain was extended southward so that it was three times the height (in a north-south sense) of the ABRA aquifer model domain. Hydrologic properties in the extended domain were taken from McCarthy et al. (1995). The low-permeability region immediately south and southwest of the SDA was retained. Prescribed head boundary conditions were based on interpolated water levels measured in 2003 and were applied with an assumption of hydrostatic conditions. Porosity was assigned uniformly for the entire model domain and had the same value as in the ABRA model, 0.06. Simulated velocities in the new extended domain are compared to the old domain in Appendix C. With the larger domain, monitoring wells with considerably lower water levels got included in interpolating boundaries, and the head gradient imposed across the domain was greater, leading to increased velocities away from the SDA. However, with retention of the low-permeability region in the SDA vicinity, the velocities remain slow, keeping aquifer simulation results essentially consistent with the ABRA.

4.4.1 Transport Properties

Simulating transport in the aquifer model was straightforward compared to the vadose zone. The flux of water and contaminants from the vadose zone model were applied as an upper-boundary condition in the refined portion of the model. The remainder of the upper surface of the model and the bottom surface of the model were treated as no-flux areas. Contaminants could advect through external boundaries.

Because it was assumed that sorption did not occur within fractured basalt, and only fractured basalt was simulated in the aquifer portion of the model, no K_d values were necessary in the aquifer portion of the model. Diffusion was included and was parameterized the same as in the vadose zone model. Tortuosity was assigned using the same approach as in the vadose zone model (i.e., following the approach in Lerman [1988]), with a resulting value of 16.7 (dimensionless). Dispersion was parameterized differently in the aquifer model than in the vadose zone model. Longitudinal and transverse dispersivity values of 9 and 4 m (30 and 13 ft) were assigned, respectively. These values were the same as those used in the ABRA model. Similar to the vadose zone model, assigned dispersivity values are small relative to the one-tenth domain size general rule of thumb.

4.4.2 Aquifer Permeability Comparison

Six single well pump tests were conducted in Fiscal Year 2003 (Jolley 2003) on aquifer monitoring wells that previously did not have transmissivity estimates. These additional transmissivity tests serve as a check on the assigned permeability values. The additional tests were for Wells M11S, M13S, M14S, M15S, M16S, and M17S. Figure 4-24 shows results of the additional tests posted at the well locations, along with previous estimates. Only Well M17S comes close to the region assigned in the aquifer model as a low-permeability zone, and it has an estimated transmissivity of 500 ft^2/day. This transmissivity is lower than that of many of the upgradient wells, but is not in the range of the assigned value for the low-permeability region south and southwest of the SDA. The additional well tests do show that assigned permeability for the region upgradient of the SDA is reasonable.

4.4.3 Comparison to Estimated Aquifer Flow Directions

An evaluation of flow directions in the aquifer in the local vicinity of the SDA was conducted for the Operable Unit 7-13/14 Project (see Appendix D for complete evaluation). In this evaluation, water levels were evaluated over time using three-point solutions with groupings of three wells to determine flow directions as a function of time. The flow directions are plotted using a rose diagram, similar to that normally used to plot wind velocities. Figure 4-25 shows the comparison of simulated and interpreted flow directions. Wells used for the comparison that are within the refined domain are labeled with blue text, and well triplets used to determine direction over time are labeled with purple text. The rose diagrams are plotted at the approximate centroid of each triplet. The larger the rose diagram in the figure, the larger the separation between wells and the less likelihood of errors due to very low gradients, which increase likelihood of measurement error influencing results. The interpreted flow directions often show a slight southeastward component beneath the eastern half of the SDA and beneath the Transuranic Storage Area, indicating some agreement with flow directions from the RI/FS aquifer model.

Regarding the RI/FS aquifer flow model, general flatness of the water table in the immediate SDA vicinity, coupled with an apparent low-permeability region to the south-southwest of the SDA, precludes completely accurate determination of groundwater flow directions. The presence of a low-permeability region is hypothesized on an increasingly compelling body of supporting evidence and evaluations. This hypothesis also is consistent with the interpretation by Roback et al. (2001) that RWMC is in a low-permeability region extending southerly from the Lost River Range onto the INL Site.

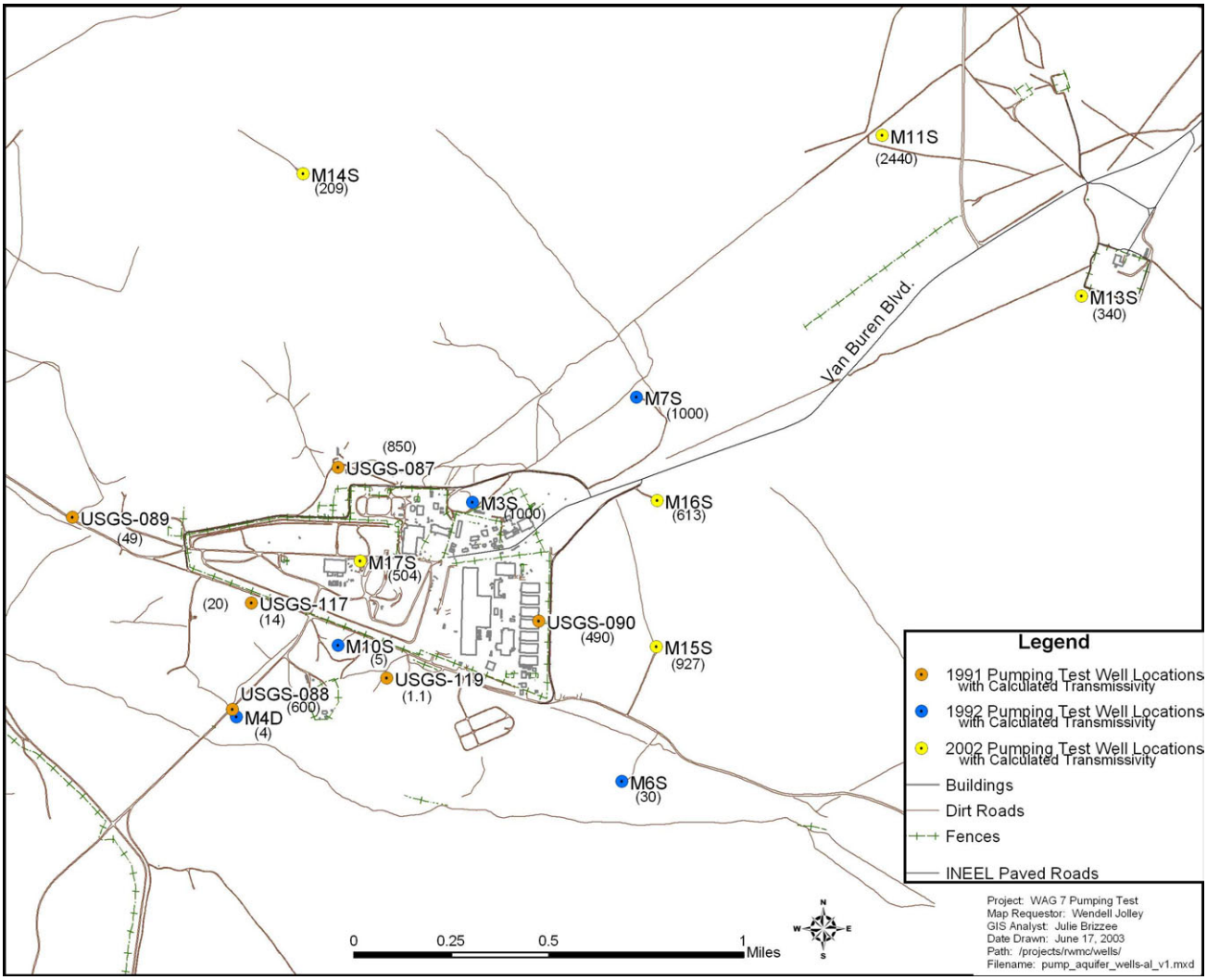

Figure 4-24. Transmissivity (feet^2/day) from pump tests in the Subsurface Disposal Area vicinity (from Jolley [2003]).

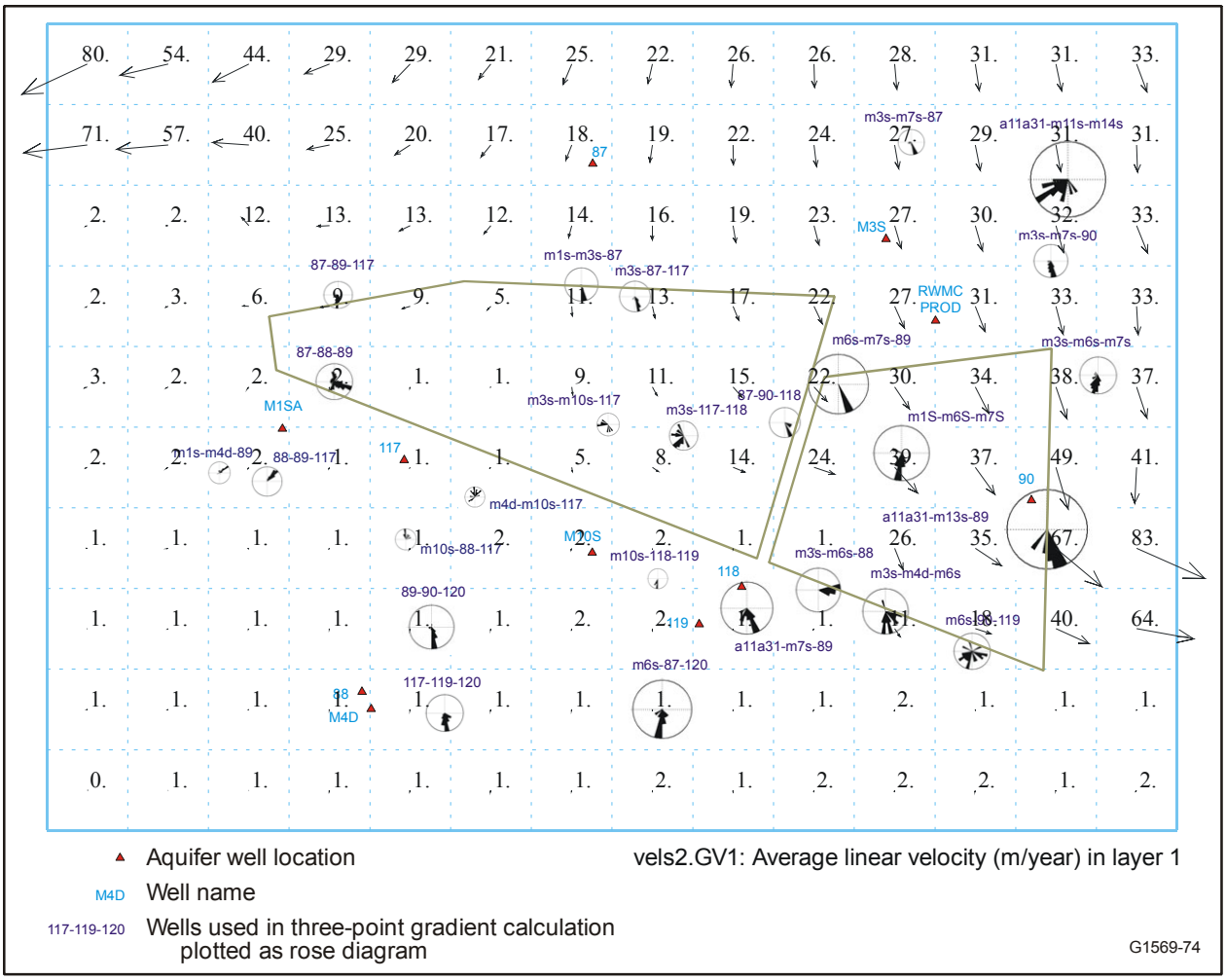

Figure 4-25. Simulated groundwater average horizontal linear velocities (meter/year) for the first-level refined grid in the aquifer domain compared to interpreted aquifer flow directions as a function of time.

An assumption in the aquifer model was that flow was predominantly horizontal. This assumption was implemented by assigning permeability as uniform in the vertical direction at each location in the model and by assuming that pressure within the aquifer was in hydrostatic equilibrium with the water table at each location, including the assigned boundary pressures. The only location where slight vertical velocities resulted was within the refined area of the aquifer domain where additional water is applied from the vadose zone model. Figure 4-26 shows the simulated vertical average linear velocity at each gridblock in the upper layer of the aquifer model for just the refined area. Comparing velocities in the vertical direction to those in the horizontal direction (Figure 4-25) shows that velocities were predominantly horizontal, even in this refined area, which received some additional water flux from the vadose zone model. The effect of increasing the fractured-basalt anisotropy ratio to 300:1 can be seen where vertical velocities at the top of the aquifer were larger in the southeastern corner due to water getting concentrated during transit of the vadose zone by the topography of the C-D interbed channeling water to the southeast. This does not substantially impact simulation results as discussed in Section 6.4.7.

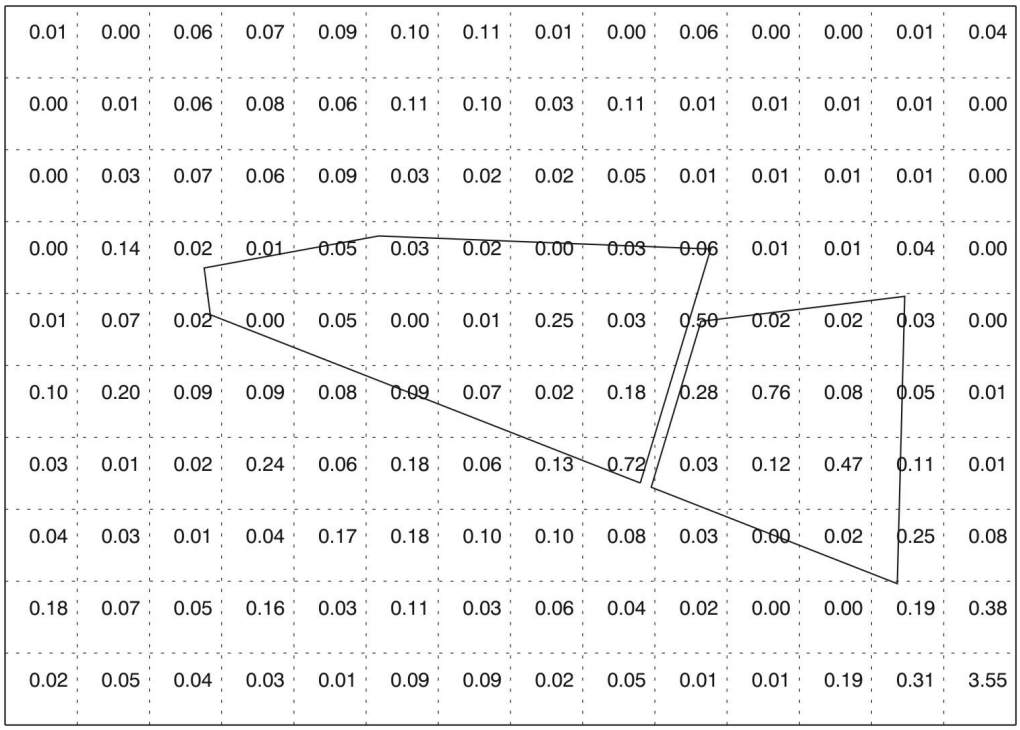

Figure 4-26. Simulated vertical average linear velocities (m/year) for the uppermost layer in the first-level refined grid in the aquifer domain.

4.4.4 Link to Operable Unit 10-08 for Future Aquifer Model Development

The impact of increased velocities, from extending the aquifer simulation domain and reinterpolating head boundaries, demonstrates uncertainty in the aquifer simulation. Overall, treatment of water movement in the aquifer is simplistic with water movement being primarily two-dimensional with limited three-dimensional contaminant movement. Improving representation of the movement of water and contaminants within the aquifer is the scope of the Operable Unit 10-08 Groundwater Modeling Project (DOE-ID 2004). The Operable Unit 10-08 groundwater model is currently under development to represent INL-scale transport, considering contaminant loading from all facilities concurrently. The potential effect of commingled plumes from INL Site facilities is one primary reason this model is being developed. This Site-wide model is being developed using information from the disciplines of geology, hydrology, contaminant chemistry, isotope chemistry, and thermal transport. This Site-wide model will use contaminant loading to the aquifer from individual waste area group facility models and has the stated goal of being consistent with local velocities from waste area group models if they are based on local information (e.g., the Operable Unit 7-13/14 model's representation of the low-permeability zone).

5. SIMULATIONS SUPPORTING PARAMETERIZATION OF THE OPERABLE UNIT 7-13/14 MODEL

This section describes simulations that were performed during development of the updated Operable Unit 7-13/14 model. These simulations augment and support selection of parameters in the model. In some cases, this is simply a comparison of simulated to observed concentrations for noncontaminant of concern constituents. In other cases, such as CCl_4, there was a substantial effort devoted to calibrating the model to mimic observed distributions of contaminants.

5.1 Measured Interbed Moisture Comparisons

This section presents a comparison of measured and simulated interbed water potentials. A summary of the deep tensiometer monitoring network is provided, followed by a description of the calibration process where the van Genuchten parameters of the interbeds were slightly modified from those in the ABRA model. Lastly, the final RI/FS model results are compared in terms of simulated fluxes through the interbed and fluxes estimated from measured water potentials and measured soil hydrologic properties.

5.1.1 Advanced Tensiometer Monitoring Network

Advanced tensiometers were developed for use in the deep vadose zone to monitor infiltration, distribution, and drainage of water under unsaturated conditions. A network of these instruments was installed in the vadose zone beneath and adjacent to the SDA at depths ranging from 2.7 to 117 m (9 to 385 ft) below land surface. Locations of 26 wells that comprise the advanced tensiometer network are shown in Figure 5-1. Installation of the deep tensiometer network and monitoring results are summarized in the draft RI/BRA report (Section 2).

Overall, the monitoring network has been active primarily through a series of drier than average years with no large transient events and a general drying trend. Even so, there have been transient events recorded as a result of infiltration inside the SDA. Averaged water potentials indicate wetter conditions inside the SDA compared to outside, especially for the B-C interbed. The influence of higher surface infiltration inside the SDA is dampened at the depth of the C-D interbed. These observations are used in the next section where model results are compared to observations.

5.1.2 Remedial Investigation and Feasibility Study Base Model Comparison to Deep Tensiometer Monitoring Network Matric Potentials

To compare TETRAD-simulated results with measured water potentials, the TETRAD-simulated results have to be converted to comparable units. The TETRAD simulator internally tracks water pressure in absolute pressure (kPa) and outputs pressure in the same unit. The field-measured water potentials are customarily measured and reported in pressure units of centimeters of water of tension. To convert from absolute pressure units to water potential units also requires outputting the TETRAD-simulated absolute air pressure (kPa). Using the relationship that capillary pressure is equal to pressure of the wetting fluid minus pressure of the nonwetting fluid, and conversions between pressure units of kPa and centimeters of water, the conversion is

$$P_c\,(cm\ H_2 0) = \left[P_w - P_g\ (kPa) \right] \left[10.1678 \frac{cm\ H_2 0}{kPa} \right] \tag{5-1}$$

where:

P_c = capillary pressure or water potential (cm H_20)

P_w = simulated pressure of wetting fluid, water in this case (kPa)

P_g = simulated pressure of nonwetting fluid, gas in this case (kPa).

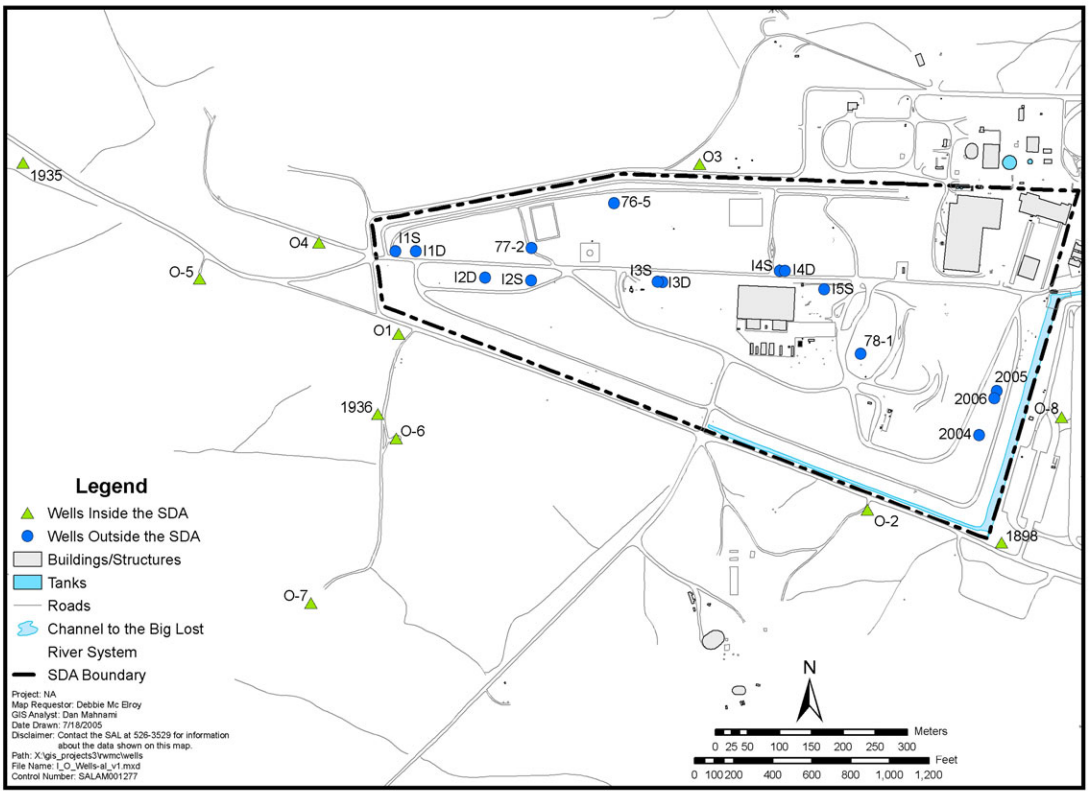

Figure 5-1. Location of advanced tensiometers in the Subsurface Disposal Area.

The final base-case model results for simulated water potentials in the B-C and C-D interbeds are shown in Figure 5-2. The 4/2001 simulation time shown was chosen because it was sufficiently after the 1982 flood for simulated water potentials to be constant and also adequately close to the comparison period from where potentials were averaged in McElroy and Hubbell (2003). Contour lines in the figure were generated with a PV-Wave processing routine and represent the maximum water potential at any location vertically across the identified interbed, with maximum in this case meaning the wettest condition. For comparison, averaged water potentials from McElroy and Hubbell (2003) are shown in Figure 5-2 at their respective locations. The principal observation that can be drawn from the simulated results is that they show good agreement to the observed trend of wetter conditions inside the SDA compared to outside. The simulated results also show a slight easterly shifting of the simulated wettest area in the C-D interbed, which is likely due to the general slope of this interbed. Lastly, there is a water collection point in the extreme southeastern corner of the C-D interbed, where saturated conditions developed, as can be seen by the water potential of zero at this location. This water collection point is caused by further horizontal movement of water above the interbed being constrained by the boundaries of the simulation domain, but is shown elsewhere in this report to not significantly influence transport results (see Section 6.4.7).

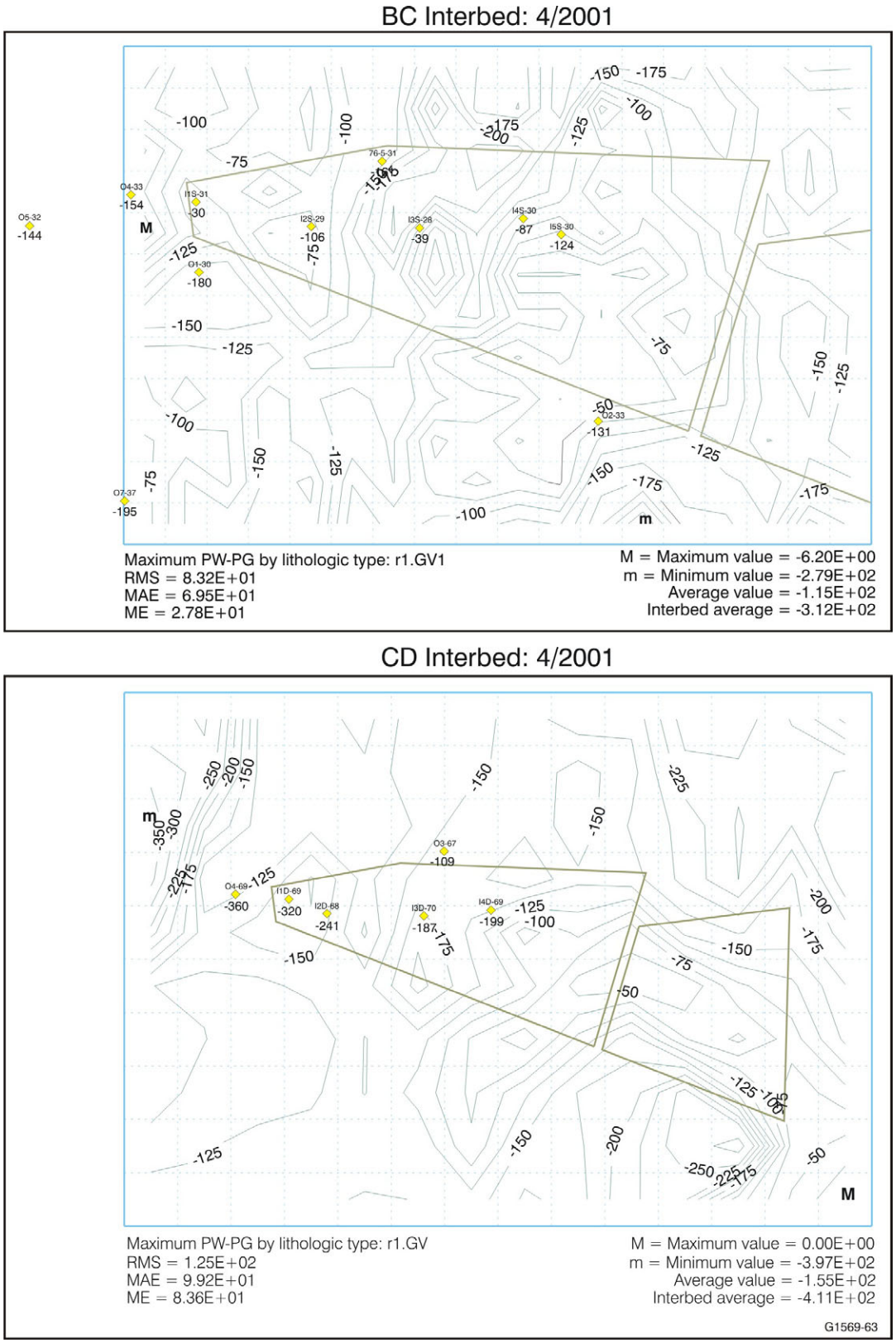

Figure 5-2. Simulated water potential (cm H_20) for the base case with comparison to averaged measured water potentials from McElroy and Hubbell (2003).

Preliminary to obtaining the final base-case model results, a set of simulations were conducted to try to improve agreement between simulated and observed water potentials from the advanced tensiometer monitoring network. In these simulations, the van Genuchten sorting parameter N, used for sediment portions of the vadose zone model, was varied from 1.323 to 2.423. These simulations also required simulating 300,000 days for obtaining steady-state initial conditions. Simulated matric potentials were extracted at locations that correspond to the deep tensiometer monitoring network and were compared statistically to averaged water potentials from McElroy and Hubbell (2003). This comparison included calculating root mean squared error, mean average error, and mean error relative to measured values and tabulating the lowest, highest, and average water potential from the maximum water potential extracted vertically through simulated interbed gridblocks at each horizontal location for both the B-C and C-D interbeds and the overall average for all interbed gridblocks. Ideally, the lowest and highest simulated interbed water potential would mimic the range of the observed water potential range, which was about -320 and -30 cm, respectively, from McElroy and Hubbell (2003). Table 5-1 shows a comparison of simulated water potentials and calculated comparison statistics for a range of values for the different values of the van Genuchten N parameter.

Table 5-1. Simulated water potential statistics (cm H_20) for a range of van Genuchten N values for the B-C and C-D interbeds.

Name	van Genuchten N	Low	High	Average of Maximums	Overall Interbed Average	Root Mean Squared Error	Mean Average Error	Mean Error
B-C Interbed								
observed		-320	-30					
r3	1.323	-259	0	-98	-309	92	77	45
r1 (base)	1.523	-279	-6	-115	-312	83	70	28
r5	1.723	-279	-16	-124	-305	79	65	19
r7	2.023	-268	-25	-128	-288	76	62	13
r9	2.423	-253	-32	-129	-262	73	60	11
C-D Interbed								
observed		-360	-109					
r3	1.323	-407	0	-141	-413	134	107	95
r1 (base)	1.523	-397	0	-155	-412	125	99	84
r5	1.723	-375	0	-159	-402	123	97	81
r7	2.023	-347	0	-159	-379	124	98	82
r9	2.423	-322	-1	-155	-343	127	101	86

Increasing the van Genuchten N parameter results in an improvement in the root mean squared error, mean average error, and mean error for the B-C interbed, and slightly worsens agreement between simulated and observed water potentials in the C-D interbed. Agreement between simulated low and high maximum values and the observed range in the deep tensiometers mostly improves in both the B-C and C-D interbeds with increasing values of the N parameters. The general effect of increasing the N parameter can be seen in the Average of the Maximums and Overall Interbed Average columns, where the values show that both interbeds get wetter overall.

5.1.3 Remedial Investigation and Feasibility Study Base Model Comparison to Interbed Saturation

Rather than simply picking the van Genuchten N parameter from the simulation with the best statistical fit to the observed averaged water potentials presented in the previous section, consideration was also given to how wetter conditions within the interbeds affect CCl_4 transport. Figures 5-3, 5-4, and 5-5 show the maximum simulated water saturation at each horizontal gridblock location for both the B-C and C-D interbeds. In these three figures, the simulated water saturation above 0.9 is shaded to indicate the wettest regions. Also shown in red are the locations where perched water has been observed or immediately above the interbeds. At the lowest van Genuchten N value of 1.323 (Figure 5-3), the extent of the wettest region is largest for both the B-C and C-D interbeds. As the value of N increases (Figures 5-4 and 5-5), the zones with elevated saturations decrease in size. With calibration to CCl_4 as one of the objectives in developing this model, the simulations with extensive wet regions in the interbed better served to spread out simulated CCl_4 concentrations horizontally in the vadose zone and better mimicked observed CCl_4 behavior. As discussed in the section on modeling of CCl_4, the wetter interbeds best served to reduce downward vapor-phase diffusion. Choosing a simulation as the base case was a matter of balancing the improvement in observed fit to the water potentials against a decrease in agreement for the CCl_4 transport modeling. With these competing interests, the status quo value of N equal to 1.523 that was used in the ABRA was selected for continued use in the RI/FS model.

5.1.4 Remedial Investigation and Feasibility Study Base Model Comparison to Interbed Vertical Water Fluxes

In addition to comparisons of simulated and observed matric potentials, comparisons were also made between estimated water fluxes from those matric potentials and simulated water fluxes from the model. The simulated maximum vertical Darcy velocities across the B-C and C-D interbeds are shown in Figure 5-6. Irregular contour intervals set at 0.5, 1, 3, 5, 7, 10, 15, 20, and 25 cm/year are used to show adequate detail. These results illustrate spatial distribution of simulated water fluxes.

The degree of focusing of water movement by simulated variable topography and the presence and absence of the A-B interbed is notable. The spatial average of the assigned infiltration rate inside the SDA is 5 cm/year (1.9 in./year). By the depth of the B-C interbed, a large portion of the western half of the SDA is at a deficit relative to this value. West of the SDA boundary, there is zone of increased vertical water flux primarily due to depressions in the upper surface of both the A-B and B-C interbeds. In the eastern half of the SDA, there is a large area of increased water flux that extends southward past the southern SDA boundary. By the depth of the C-D interbed, there is no zone of increased water flux west of the SDA boundary. The zone of increased flux through the B-C interbed has dissipated. The zone of elevated water flux in the eastern half of the SDA persists through the C-D interbed, although it has shifted toward the east-southeast due to the topography of the top of the C-D interbed. The interpolated channel in the upper surface of the C-D interbed, leading east-southeast beneath the Transuranic Storage Area, does capture some water and directs it all the way to the southeastern corner of the model domain, where it is forced to go through the C-D interbed due to the horizontal no-flux boundaries.

These zones of increased water flux exert an influence on where simulated contaminants migrate through the vadose zone. For comparison purposes, estimated steady-state vertical Darcian fluxes at the deep tensiometer monitoring locations from Hubbell et al. (2004) are shown in Figure 5-6. These estimated values are based on the averaged matric potentials from McElroy and Hubbell (2003), the use of a unit-gradient assumption, and hydraulic characterization of saturated and unsaturated properties of collocated core samples. Comparability of the simulated and estimated fluxes varies. In the B-C interbed, the simulated high-infiltration region west of the SDA is partially supported by estimated values for Wells O4 and I4. The low value at Well O1, south of the western SDA boundary, agrees with the simulated flux through this region. The two extremely high-infiltration estimates at Wells I-2S and I-4S are so far out of range that there is no comparison in the simulated results. The low estimated flux at

Well O3, closer to the center of the SDA, agrees well. Elevated values at Wells I-5S and O2 show relatively good agreement with the simulated region of elevated flux in the eastern half of the SDA. In the C-D interbed, there is less agreement, partly caused by coarser discretization. The simulated water flux across the western part of the SDA does not vary much from 1 cm/year (0.4 in./year), while the estimated values range from 7.8 to 213 cm/year (3 to 83.8 in./year). Note that if the spreading-area water source were still included in these simulations, the simulated flux would show better agreement.

5.2 Fractured Basalt Hydrologic Property

The TETRAD parameter, B_w (see Equation [4-7]), controls the degree of curvature in the relative permeability for the fractured basalt for the aqueous phase. This parameter was changed from 1.001 in the ABRA model to 2.0 in the RI/FS model. A set of simulations was conducted with assigned values of 2.0, 1.5, and 1.001 for the B_w parameter. Figure 5-7 shows the simulated vertical average linear velocity through the fractured basalt for a horizontal slice through the simulation domain beneath the B-C interbed with these B_w parameters. The contour intervals within each of the plots in Figure 5-7 are equal, but are different between plots. An approximate one order of magnitude reduction in the simulated vertical velocity in changing the B_w parameter from 1.001 to 2.0 exists. Also, less focusing of vertical water movement with the higher B_w parameter occurs. Overall, however, the velocities remain large and maintain rapid transport down through the fractured basalt portions of the vadose zone domain with any of the B_w parameter values. Given this rapid transport through fractured basalt for any of the B_w parameters from this range and a computational speedup factor of about 20X with the B_w parameter value of 2.0 compared to 1.001 (10.2 central processing unit hours versus 217.2 central processing unit hours for these comparison simulations), the B_w value of 2.0 was selected for use in the RI/FS model.

5.3 Magnesium Chloride Dust Suppressant Transport

Magnesium chloride brine was applied as a dust suppressant on SDA roads between 1984 and 1993. Subsequent arrival of this magnesium chloride at lysimeter monitoring locations in the vadose zone was first noted by Hubbell (1993). Monitoring subsequent movement of the chloride from this application in the vadose zone and aquifer gives insight into movement of water and dissolved-phase transport in general. Although the RI/FS vadose zone model was not strictly calibrated against this chloride transport, an effort was made to simulate application and transport of chloride to see if the RI/FS model emulated the observed transport.

Hull and Bishop (2003) present a detailed description of the reasons for the magnesium chloride application, the possible effects on transport, the most probable mass of magnesium chloride applied to the roads, the location of the applications, and the monitoring results that imply quick movement through the vadose zone. These monitoring observations were updated with more recent monitoring results in Koeppen et al. (2005). Results from both reports are compared against simulation results in this section.

One caution must be given before making any comparisons between simulated and observed results. A limitation is inherent in the source-release and vadose zone transport models related to discretization. The gridblocks in the most refined portion of the model are 38.1 m (125 ft) on a side. Infiltration rates through these gridblocks are constant and have to best approximate an average for each gridblock. Undoubtedly infiltration varies across an area 38.1 m (125 ft) on a side within the SDA, especially around roadways.

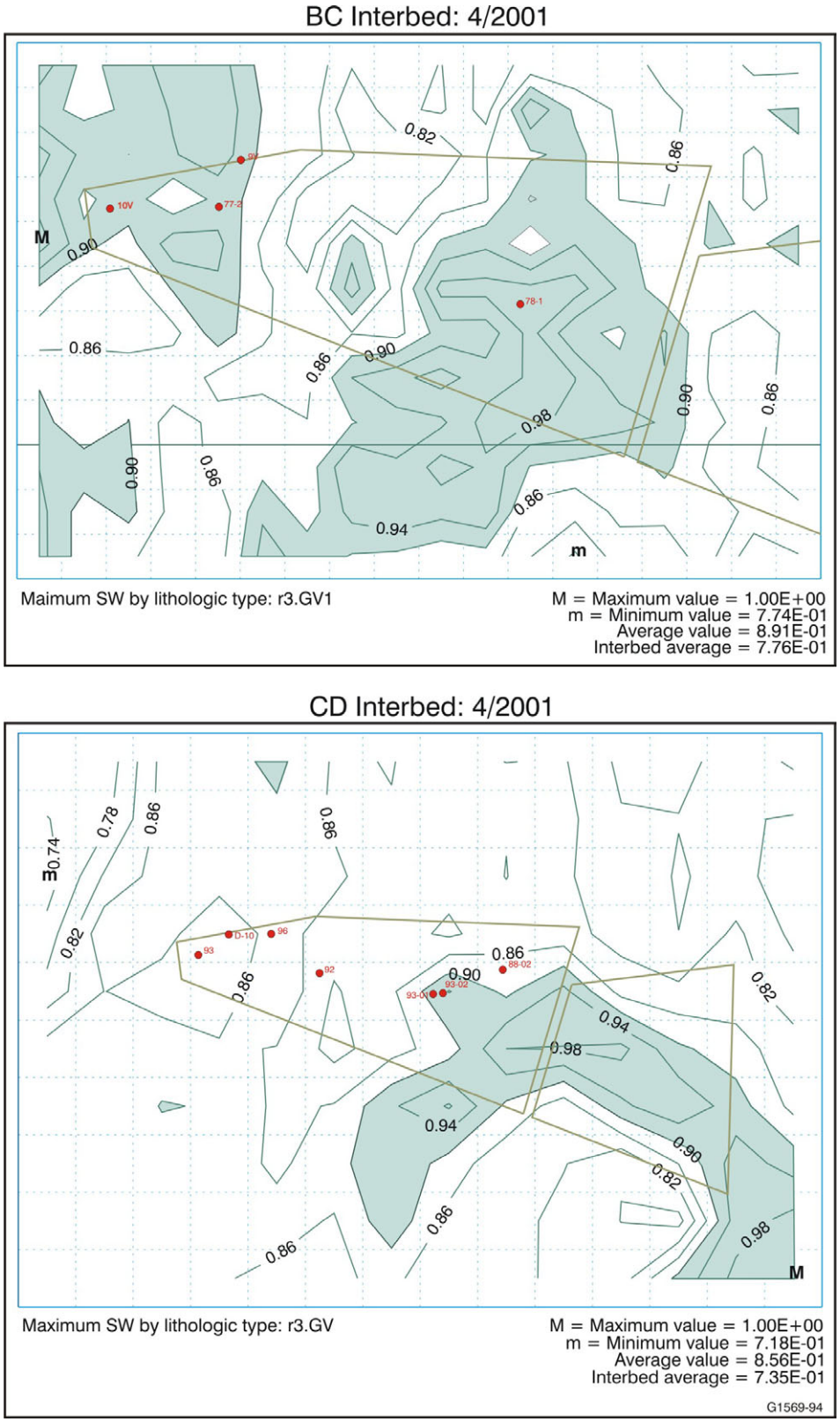

Figure 5-3. Maximum interbed water saturations with an interbed van Genuchten N parameter set to 1.323. Red symbols indicate well locations where perched water was observed at least once.

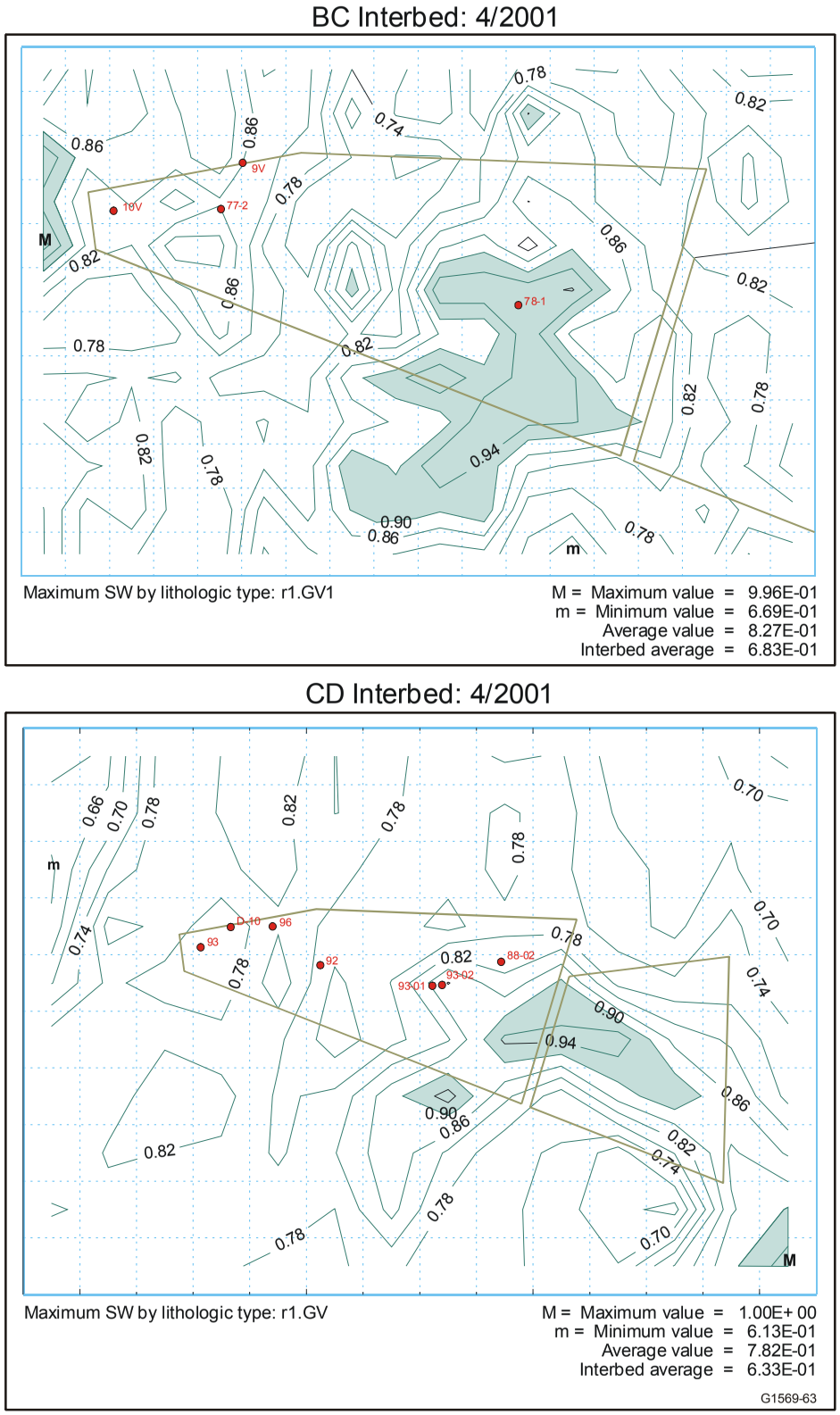

Figure 5-4. Maximum interbed water saturations with an interbed van Genuchten N parameter set to 1.523 (base case). Red symbols indicate well locations where perched water was observed at least once.

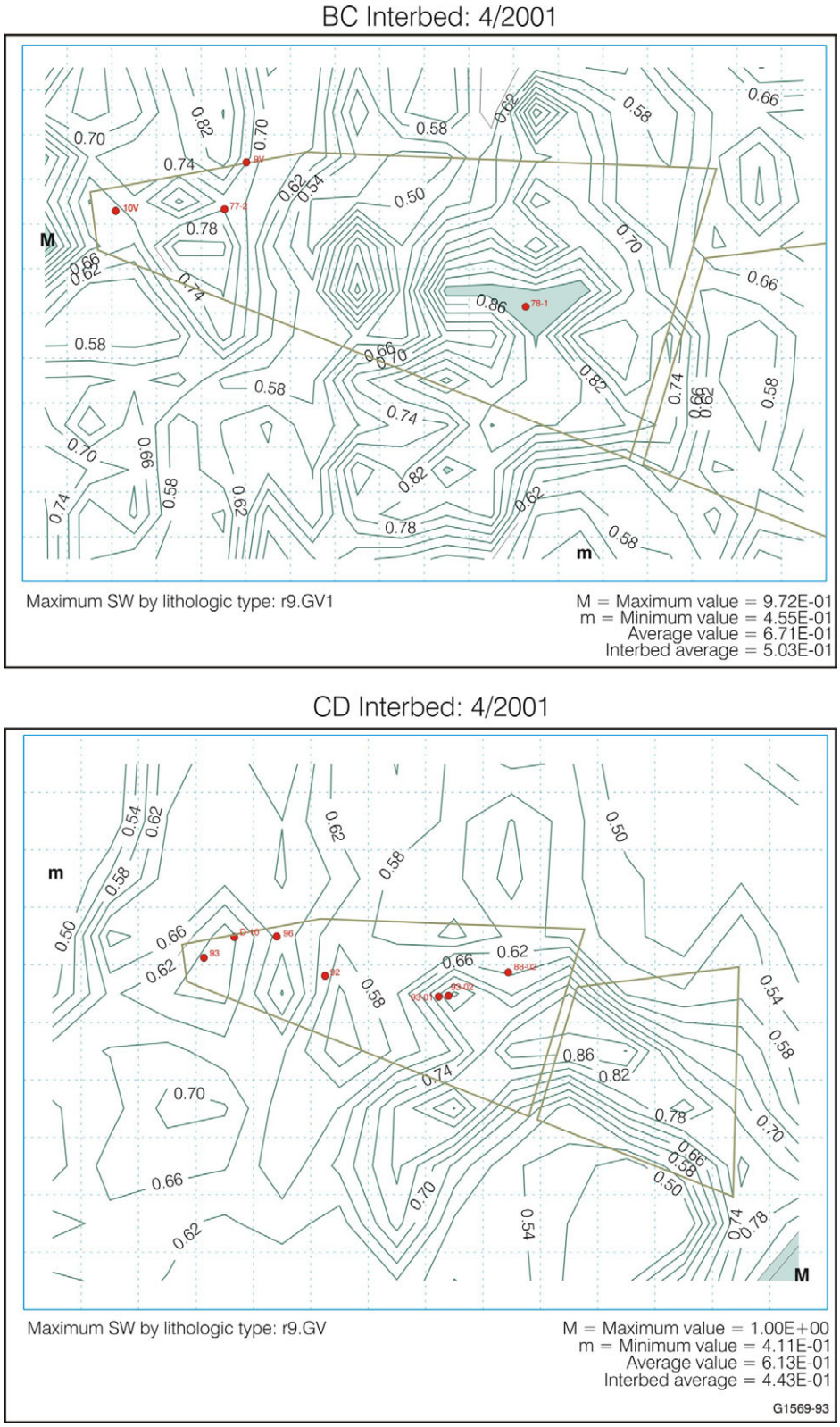

Figure 5-5. Maximum interbed water saturations with an interbed van Genuchten N parameter set to 2.423. Red symbols indicate well locations where perched water was observed at least once.

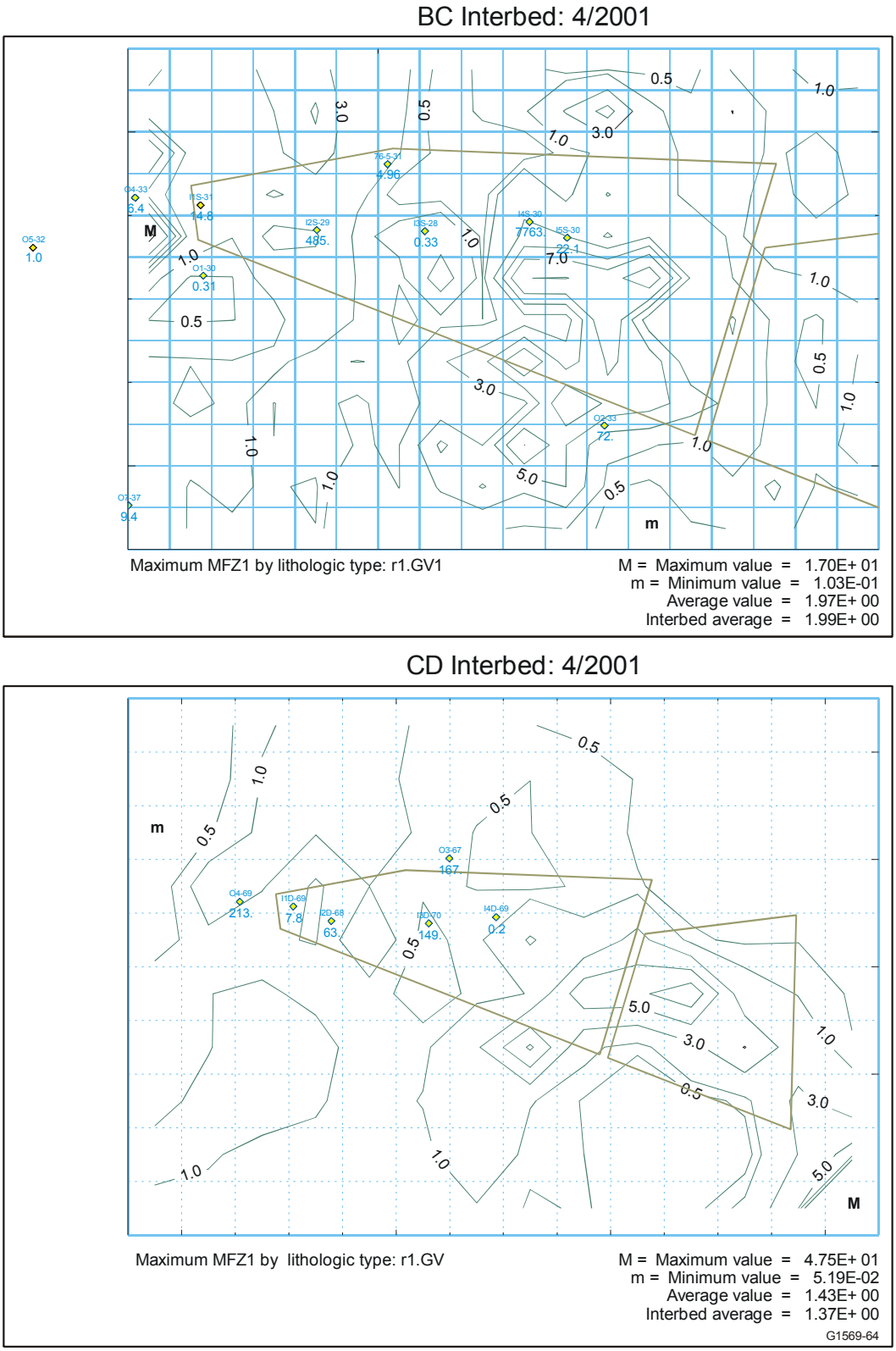

Figure 5-6. Maximum interbed vertical water flux (cm/year) for the base-case model and estimated vertical flux from McElroy and Hubbell (2003).

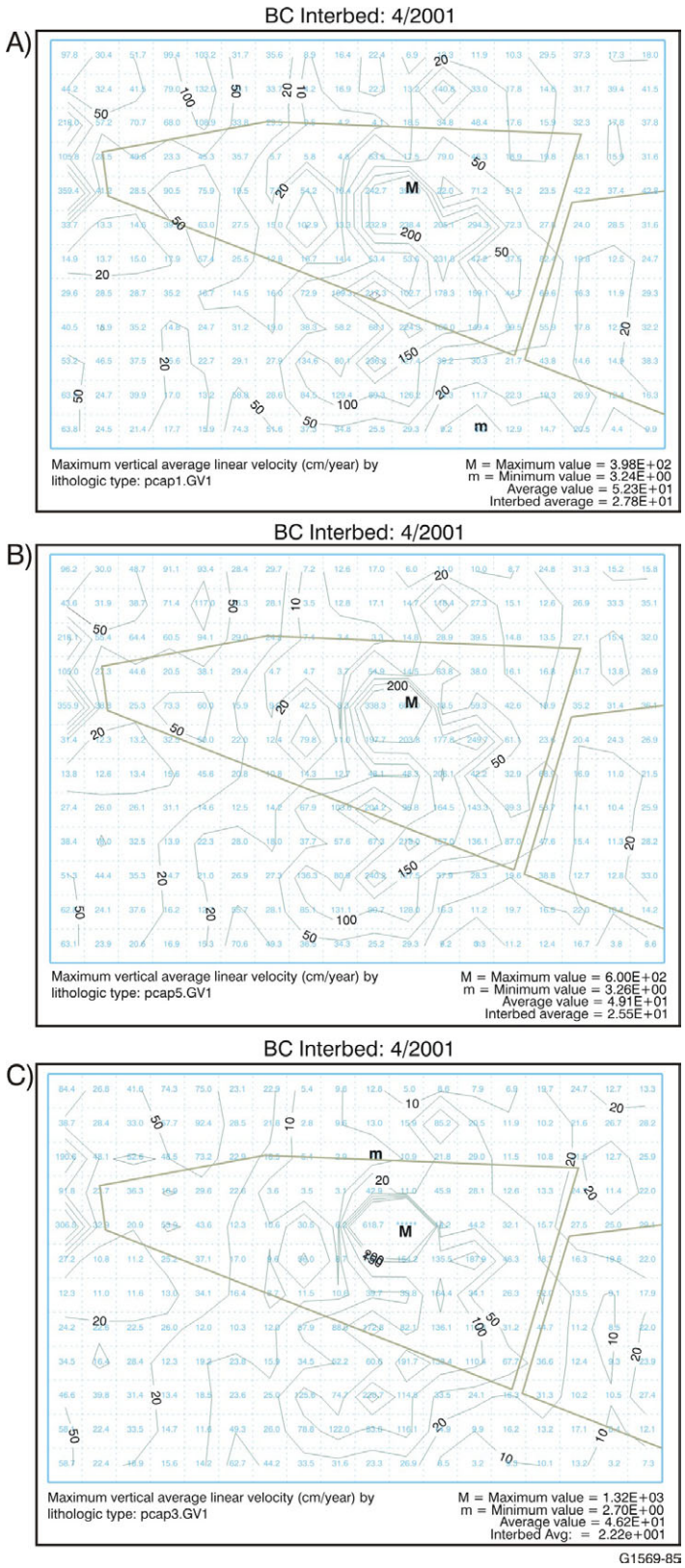

Figure 5-7. Simulated vertical average linear velocity in fractured basalt beneath the B-C interbed for A) B_w =2.0, B) B_w =1.5, and C) B_w =1.001.

Figure 5-8 shows the locations where magnesium chloride brine was determined to have been applied in the SDA (Hull and Bishop 2003) with the RI/FS model's first- and second-level refined grids superimposed. Figure 5-8 shows information for all years brine was applied. The brine application for each year was averaged for those gridblocks contacting an application zone in Figure 5-8. These averaged mass amounts were released in the model in the second gridblock below land surface at a depth of 0.75 m (2.5 ft) so they did not interfere with application of the surface boundary water fluxes in the uppermost gridblock. Figure 5-9 shows the volume in gallons of brine for Calendar Year 1984 applied to the gridblocks in the model. Rather than showing similar figures for 1985 and 1992 through 1993, Figure 5-10 shows the cumulative application for the entire application period of 1984 through 1993.

Two chloride brine release scenarios were initially evaluated using the ABRA model, a gradual release scenario and a 100% annual release scenario. In the 100% annual release scenario, releases of the chloride mass into the model occurred at a constant rate for a 1-year period, beginning at the midpoint of the application year. In the gradual release scenario, a fraction equivalent to 0.1632 of the estimated total mass applied was released each year until the total mass was released. Because the simulation results underestimated the observed chloride concentrations, only the 100% release scenario was used when updating the chloride brine simulations in the RI/FS model. This update used the base RI/FS model, including assigned surface infiltration fluxes (excluding the three historical flooding events) to simulate chloride brine transport, resulting from application of brine to the surface of the SDA. The three flooding events were not included because they all occurred before the first brine application.

Results for these chloride brine simulations were evaluated using cross sections and time histories. The locations for both are shown in Figure 5-11. The cross section was selected because it contains the D06-DL02 lysimeter, which shows the best breakthrough of the chloride brine. Because there can be multiple lysimeters at different elevations for an individual well location, lysimeters are referred to in this section using the combined well name-lysimeter number identifier. The northern time-history location was likewise selected for the same reason. The southern time-history location was selected to show results from a location where brine was applied at the surface.

Simulation results with the 100% annual release are shown in Figure 5-12. The simulation time of May 2003 was chosen because it corresponded to a year with a sampling event where chloride was elevated to the highest priority for analyses in one round; therefore, it has the most chloride analyses from the vadose zone monitoring system. Monitoring results from lysimeters within this cross section are superimposed at their respective locations. These results used the same time window of plus or minus 1 year and were averaged when more than one sample was available. Although the simulation results underpredict the monitoring results, the northward slope of the A-B interbed can be seen to slightly impact the simulation results. This northward spread at depth partially could explain why lysimeter DO6-DL02 shows such high concentrations when there are no records of brine being applied in the northern half of the SDA.

The simulated chloride concentration time history for the 100% annual release at the D06-DL02 location and depth is shown in Figure 5-13, along with observed monitoring results. The top plot shows both simulated and observed results with a consistent vertical axis, and illustrates the extent of the underprediction of the simulated results compared to the observed. The bottom plot uses a secondary axis for the field-monitoring results to allow the magnitude of the simulation results to be seen. There are at least two causes for underprediction. First, large gridblock sizes in the RI/FS model result in averaging the chloride mass over large volumes and thereby reducing the simulated concentration. In reality, chloride brine predominantly infiltrates into the subsurface over a small area defined by ditches along the roads. Second, in the simulation there was no chloride brine released above this location.

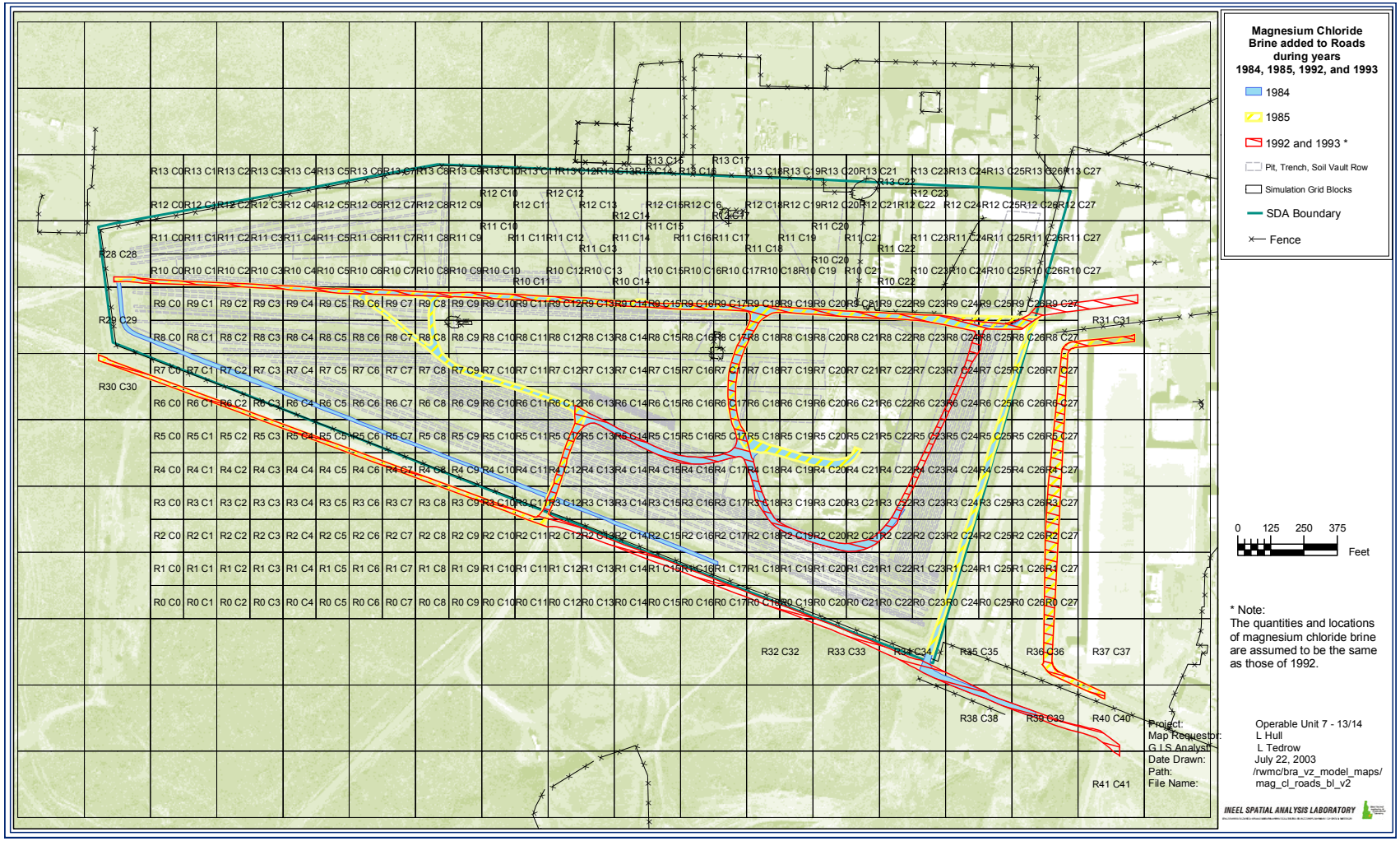

Figure 5-8. Estimated locations of magnesium chloride application in 1984, 1985, and 1992 through 1993 (after Hull and Bishop 2003).

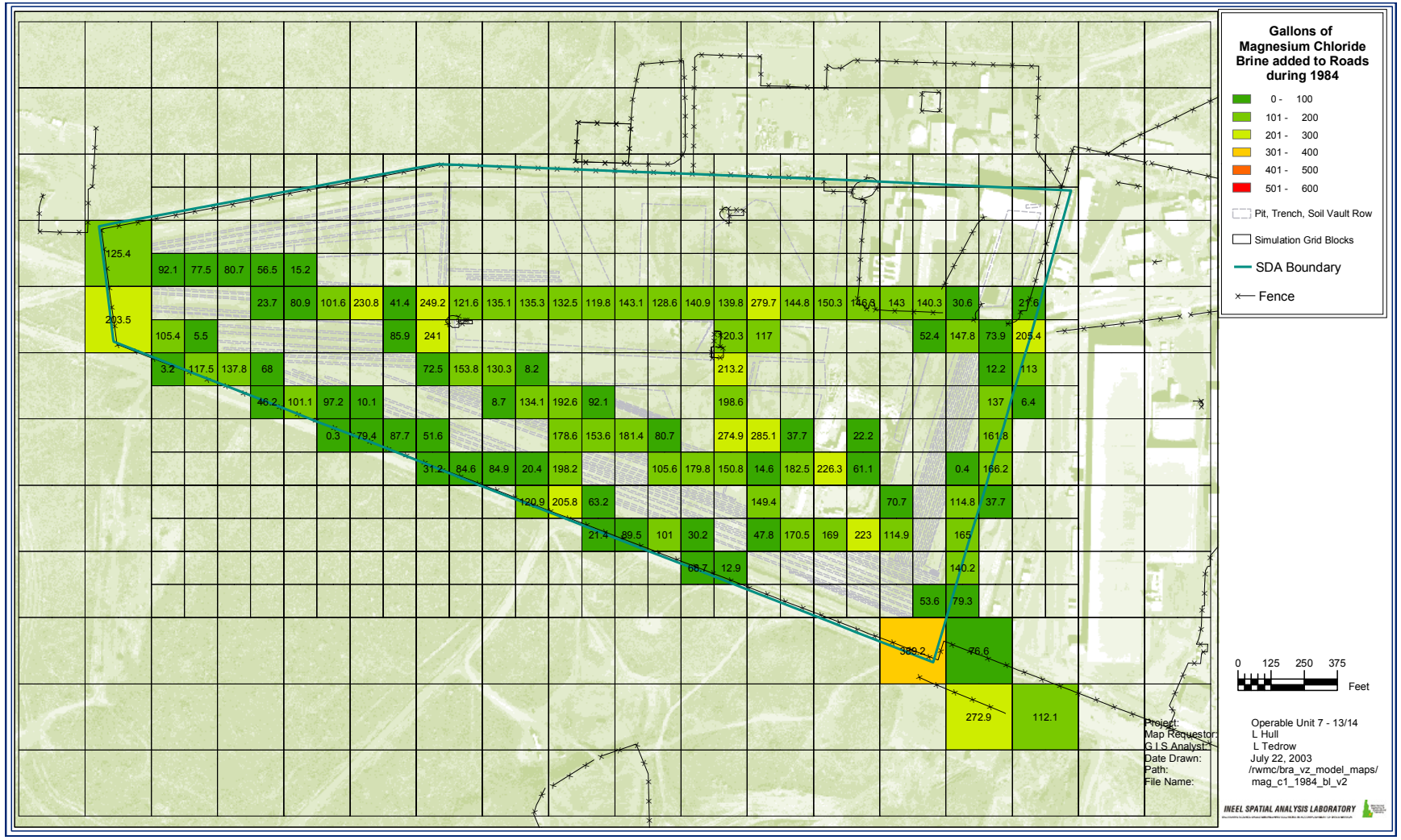

Figure 5-9. Simulated magnesium chloride application rates and locations in 1984.

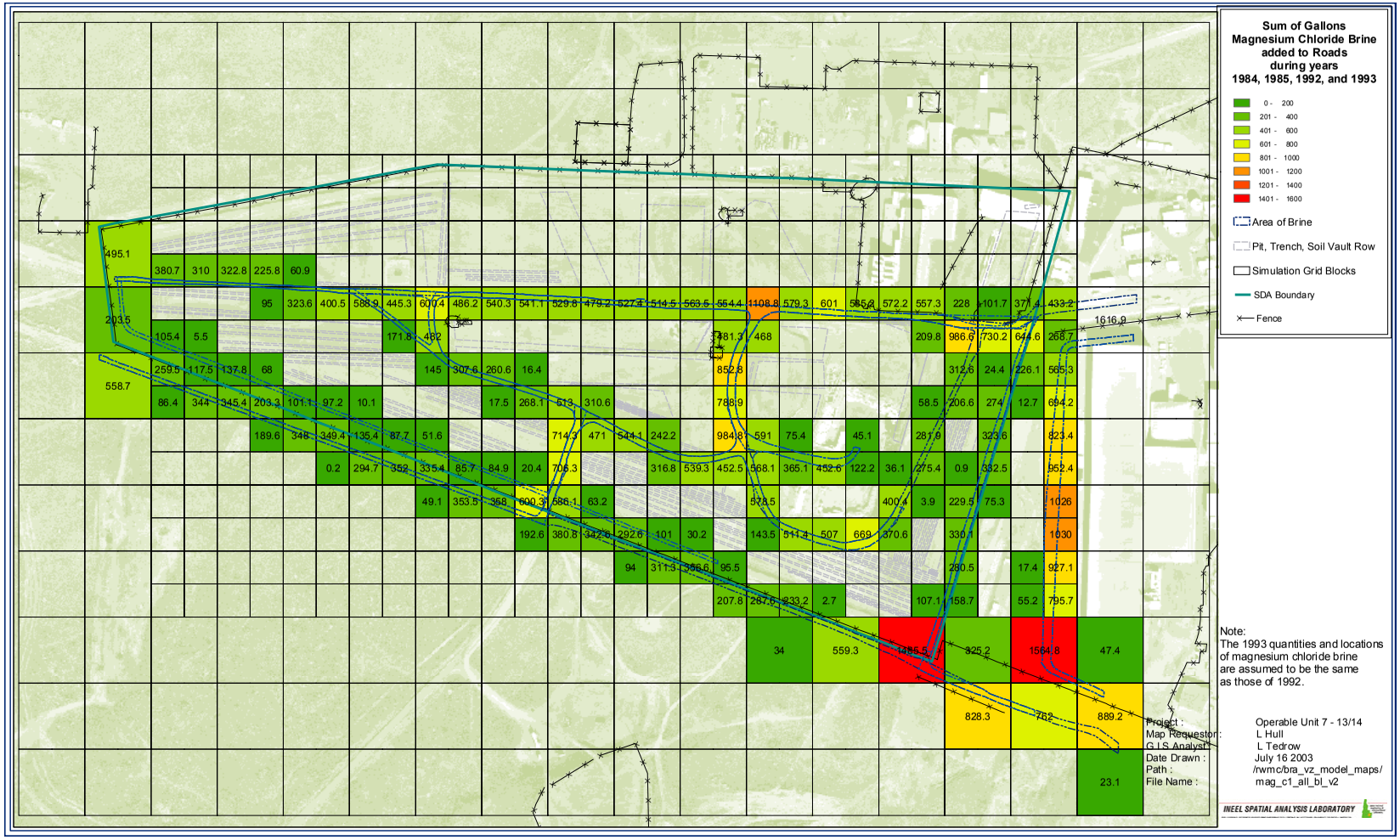

Figure 5-10. Simulated cumulative magnesium chloride application rates and locations from 1984 through 1993.

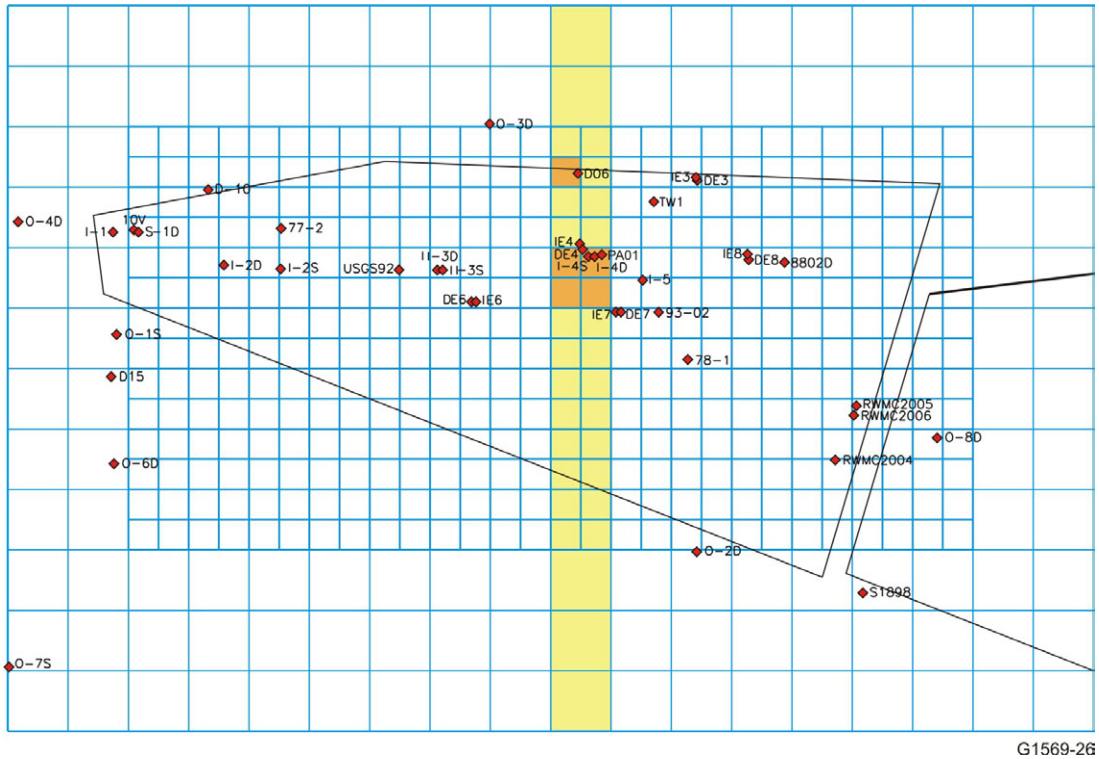

Figure 5-11. Locations for cross section (yellow shaded) and time history (orange shaded) comparisons for chloride simulations. Well locations are indicated by red diamonds.

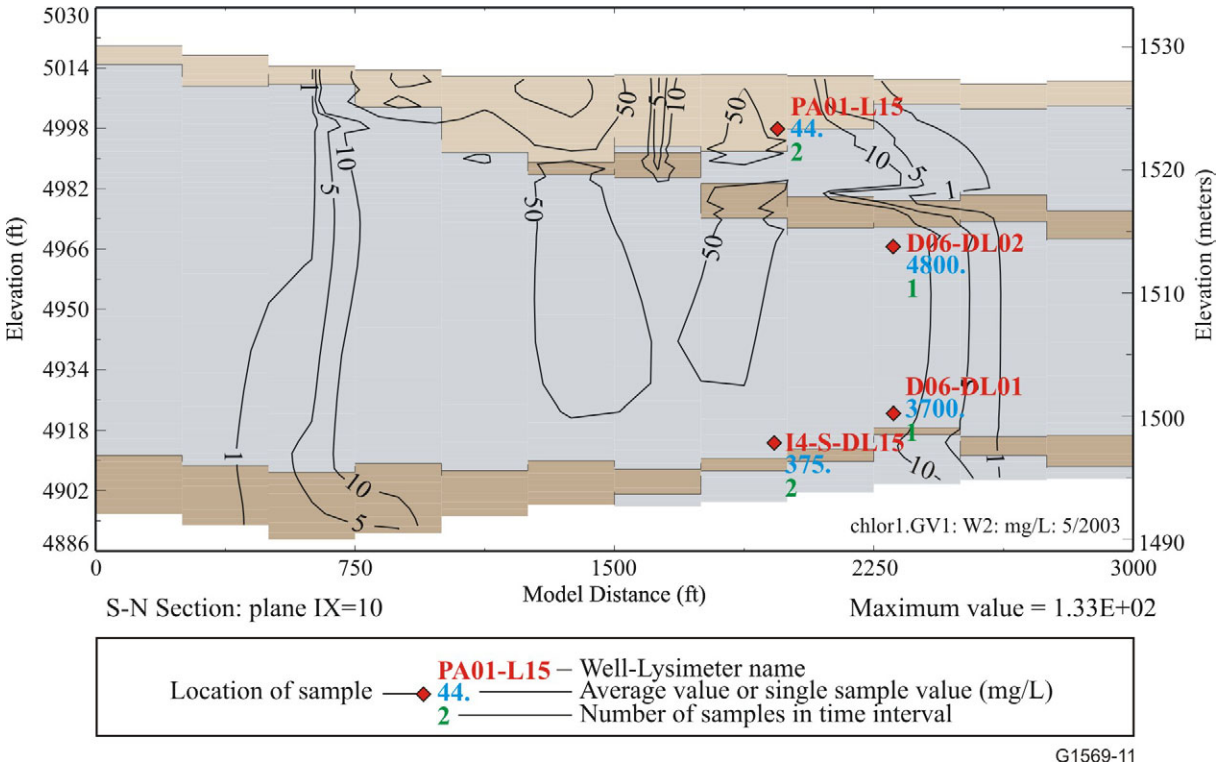

Figure 5-12. Simulated chloride concentrations with 100% annual release of applied chloride brine. See Figure 5-11 for location of cross section.

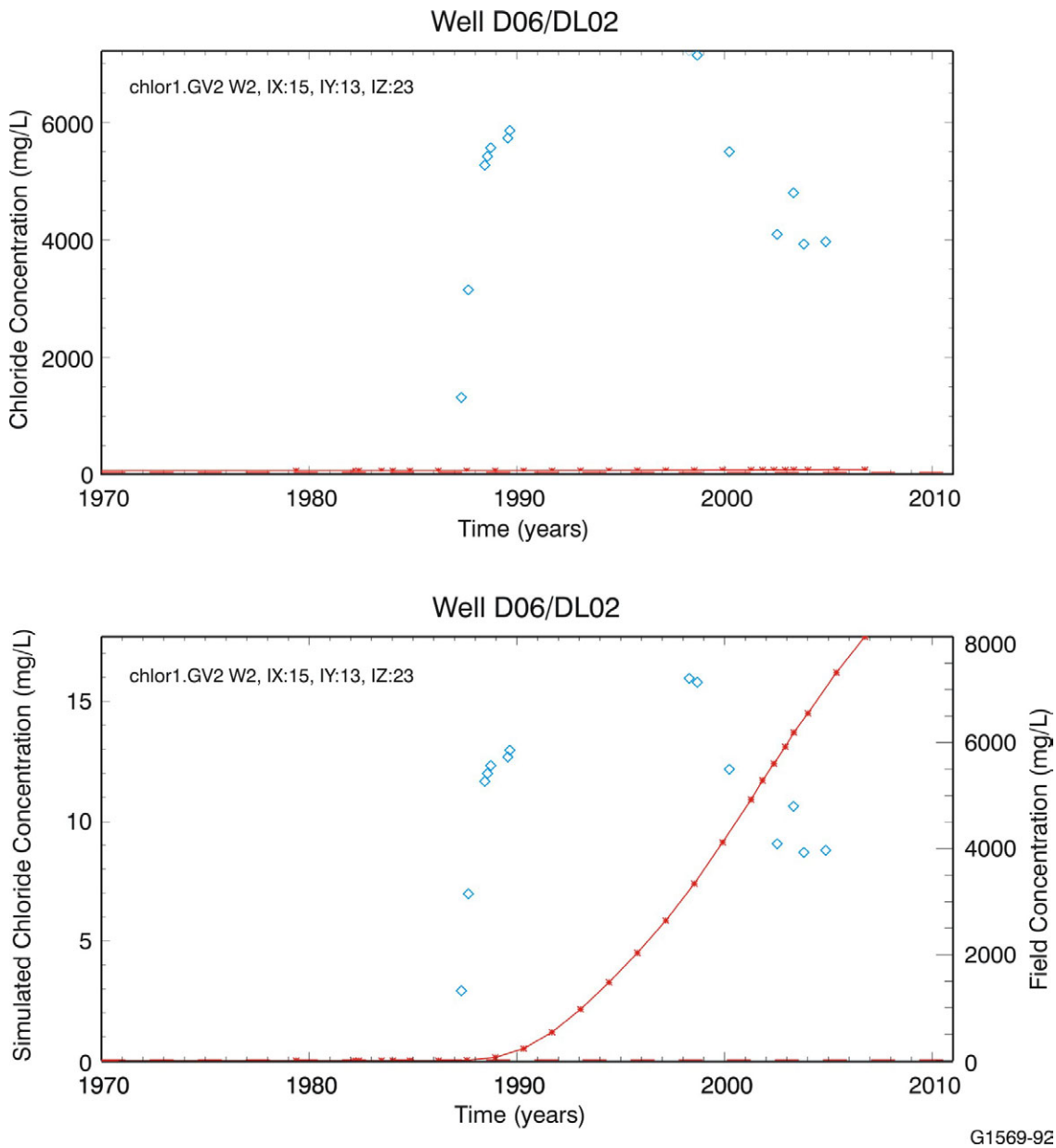

Figure 5-13. Simulated (red line) and observed (blue diamonds) chloride concentrations at the D06-DL02 lysimeter location. The bottom plot has observed concentrations plotted on the right axis. See Figure 5-11 for lysimeter location.

Figure 5-14 shows simulated chloride concentrations for locations I-4S-DL15 and I-4D-DL14, which do have chloride brine applied above them in the simulation. Although the simulation results underpredict the observed concentrations, there is at least an observable breakthrough using the same vertical scale.

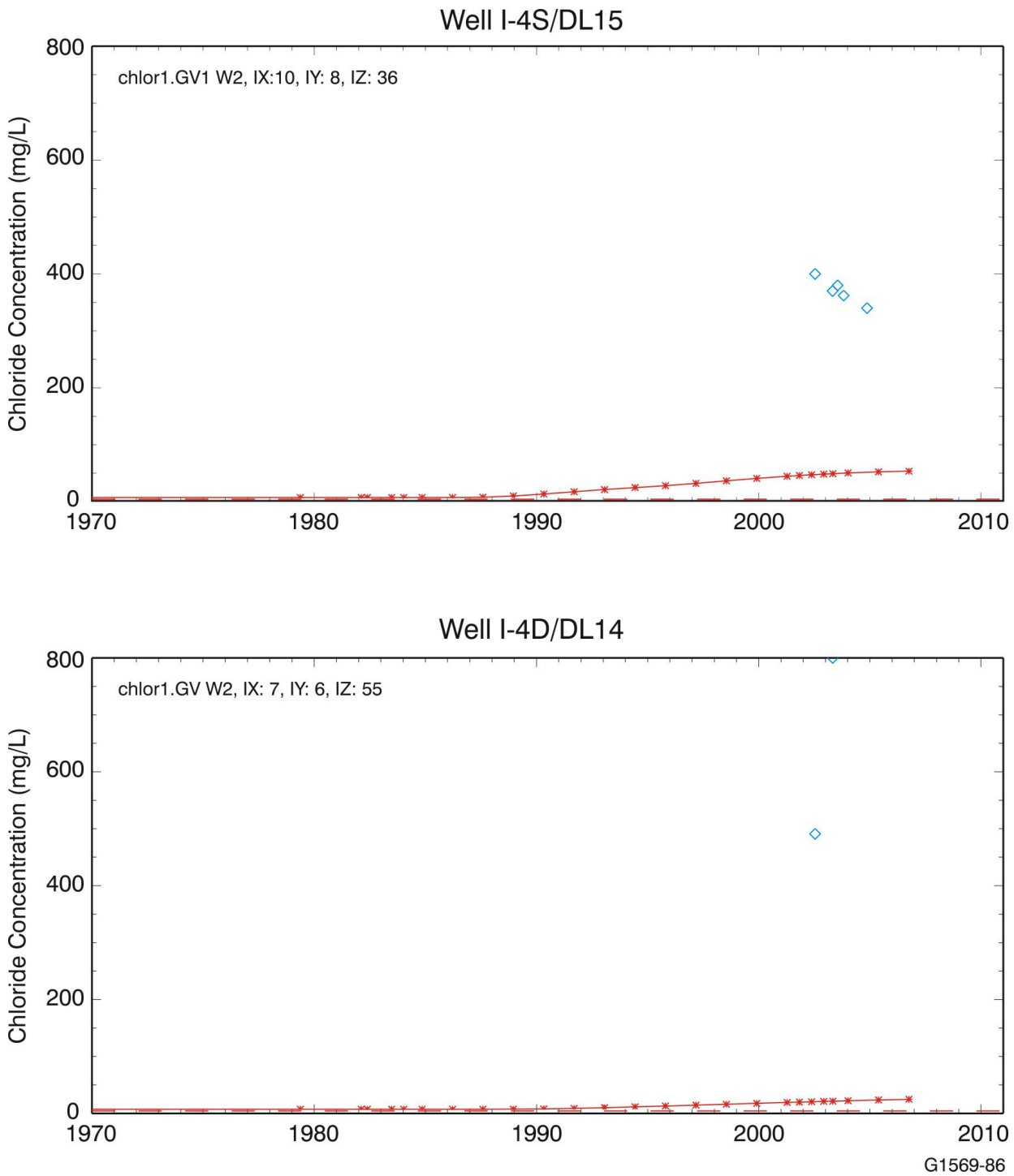

Figure 5-14. Simulated (red line) and observed (blue diamonds) chloride concentrations at the I-4S-DL15 and I-4D-DL14 lysimeter locations. See Figure 5-11 for lysimeter locations.

Both simulated chloride time histories in Figures 5-13 and 5-14 show monotonically increasing concentrations that do not mimic the transient double-pulse character in the monitoring results at D06-DL02. This may be due to use of constant infiltration rates from the RI/FS model that were developed with a primary focus on infiltration through waste zones.

The question about the impact of constant infiltration rates led to the next two simulations where a spring infiltration event occurred at the locations shown in Figure 5-15. The locations were chosen to emulate additional infiltration occurring in ditches bordering the main east-west access road across the SDA. In these simulations, 10 and 30 cm of water were applied to the ditch area during a 30-day period, beginning April 1 of each year for years that had greater than 10 in. of precipitation since Calendar Year 1975. This resulted in increased infiltration in 19 out of 30 years from 1975 through 2004. Figures 5-16 through 5-18 show simulation results for the case of an additional 10 cm of water each year in April. Figures 5-19 through 5-21 show simulation results for the case of an additional 30 cm of water each year in April. The additional water accelerates transport, as can be seen in the time-history figures. Simulated concentrations at depth increase with the additional water applied along the ditches, but observed concentrations are still underpredicted. For the 30-cm simulation, concentrations have peaked by Calendar Year 2004 and then decrease, indicating the simulated front has passed this depth.

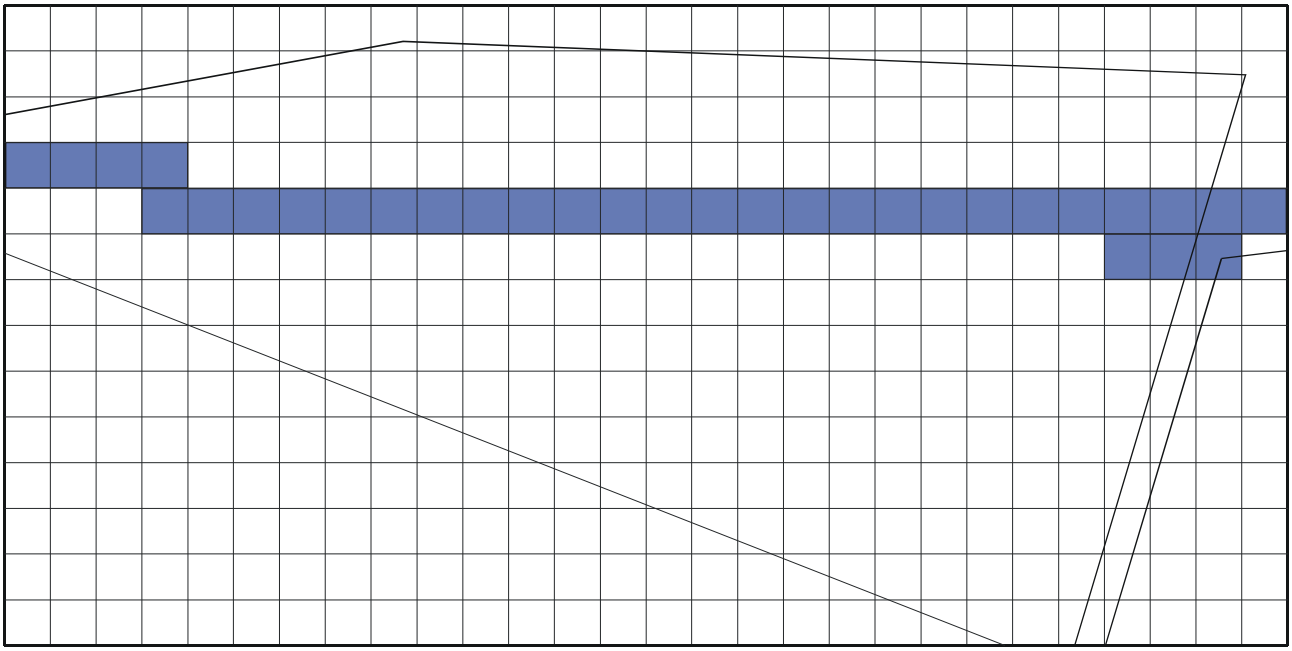

Figure 5-15. Locations receiving additional water to emulate infiltration in ditches along the primary east-west access road across the Subsurface Disposal Area.

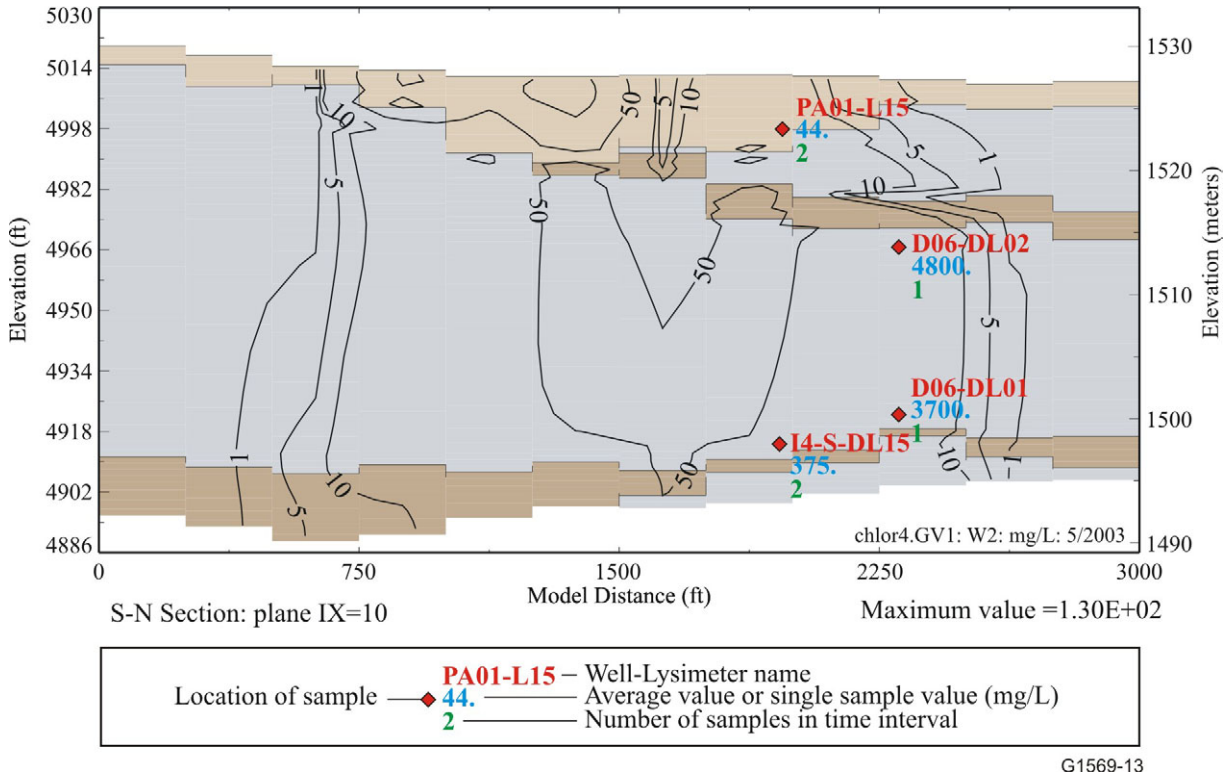

Figure 5-16. Simulated chloride concentrations with an additional 10 cm infiltrating along the east-west access road each year in April. See Figure 5-11 for location of cross section.

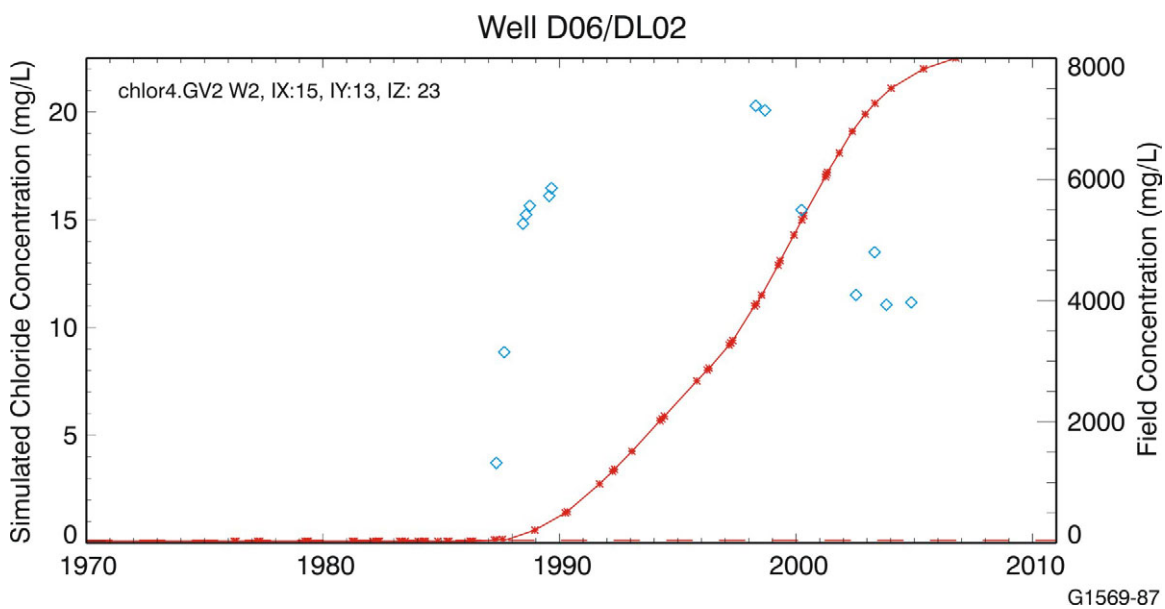

Figure 5-17. Simulated (red line) and observed (blue diamonds) chloride concentrations at the D06-DL02 lysimeter location with an additional 10 cm infiltrating along the east-west access road each year in April. Note that the plot has observed concentrations plotted on the right axis. See Figure 5-11 for lysimeter location.

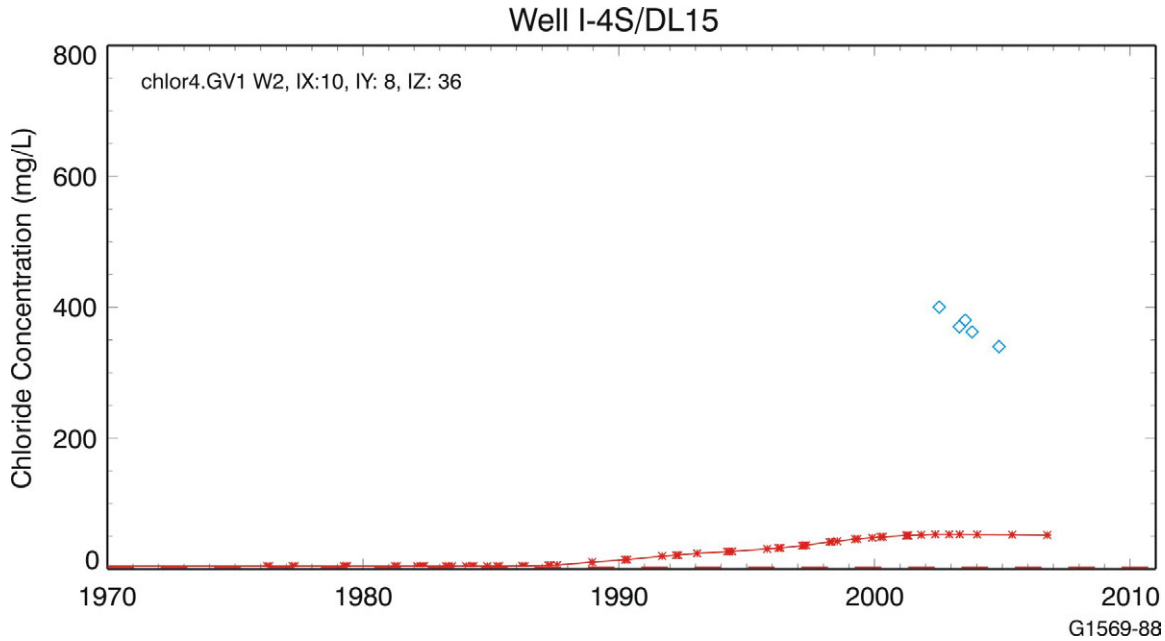

Figure 5-18. Simulated (red line) and observed (blue diamonds) chloride concentrations at the I-4S-DL15 location with an additional 10 cm infiltrating along the east-west access road each year in April. See Figure 5-11 for lysimeters location.

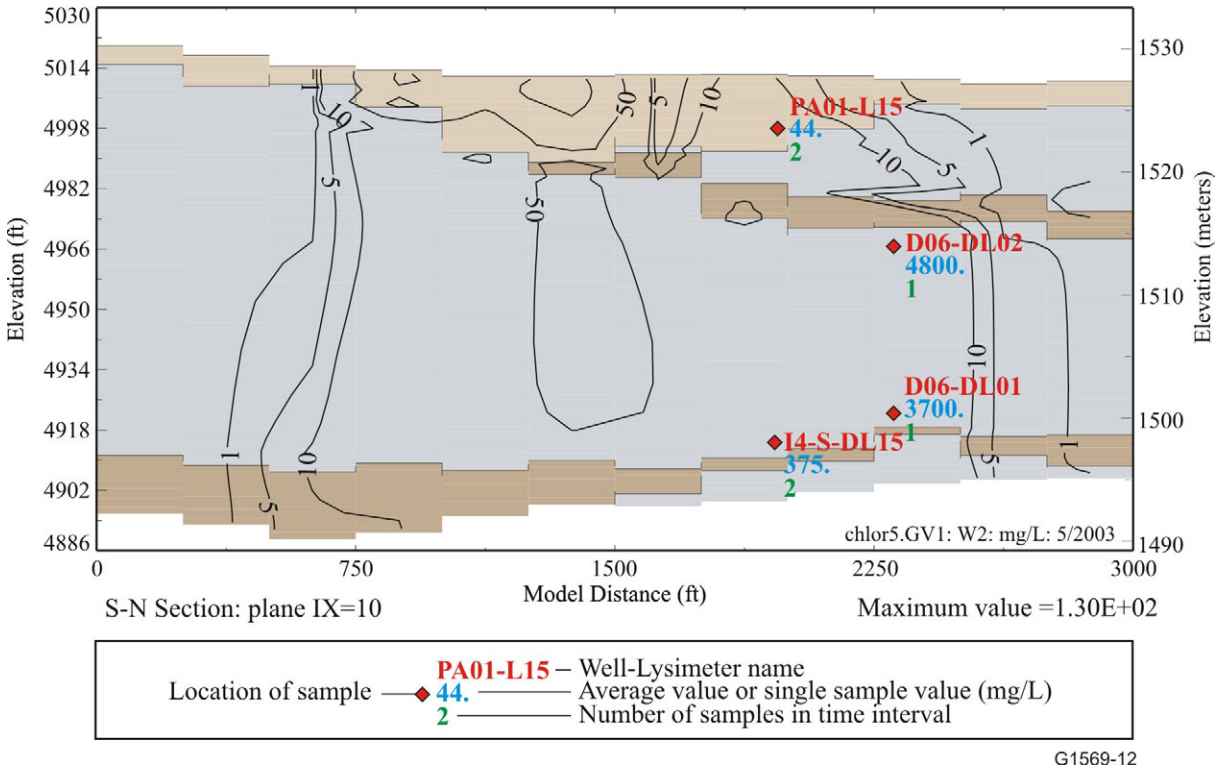

Figure 5-19. Simulated chloride concentrations with additional 30 cm infiltrating along the east-west access road each year in April. See Figure 5-11 for location of cross section.

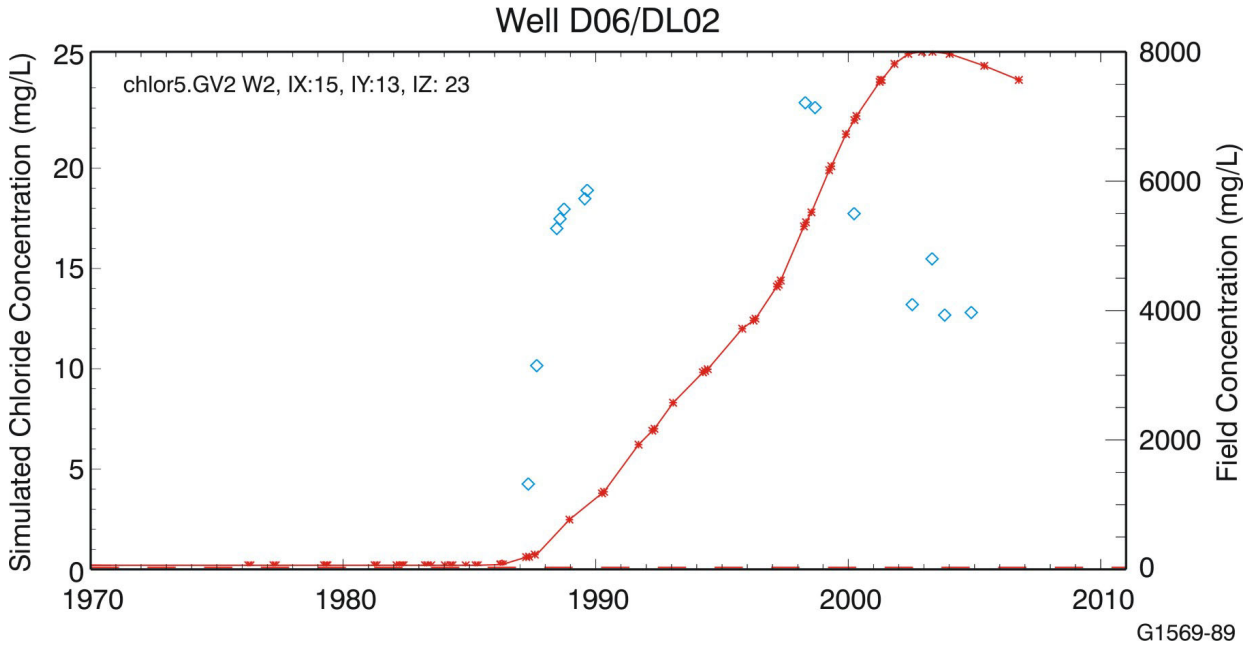

Figure 5-20. Simulated (red line) and observed (blue diamonds) chloride concentrations at the D06-DL02 lysimeter location with additional 30 cm infiltrating along the east-west access road each year in April. Note that the plot has observed concentrations plotted on the right axis. See Figure 5-11 for lysimeter location.

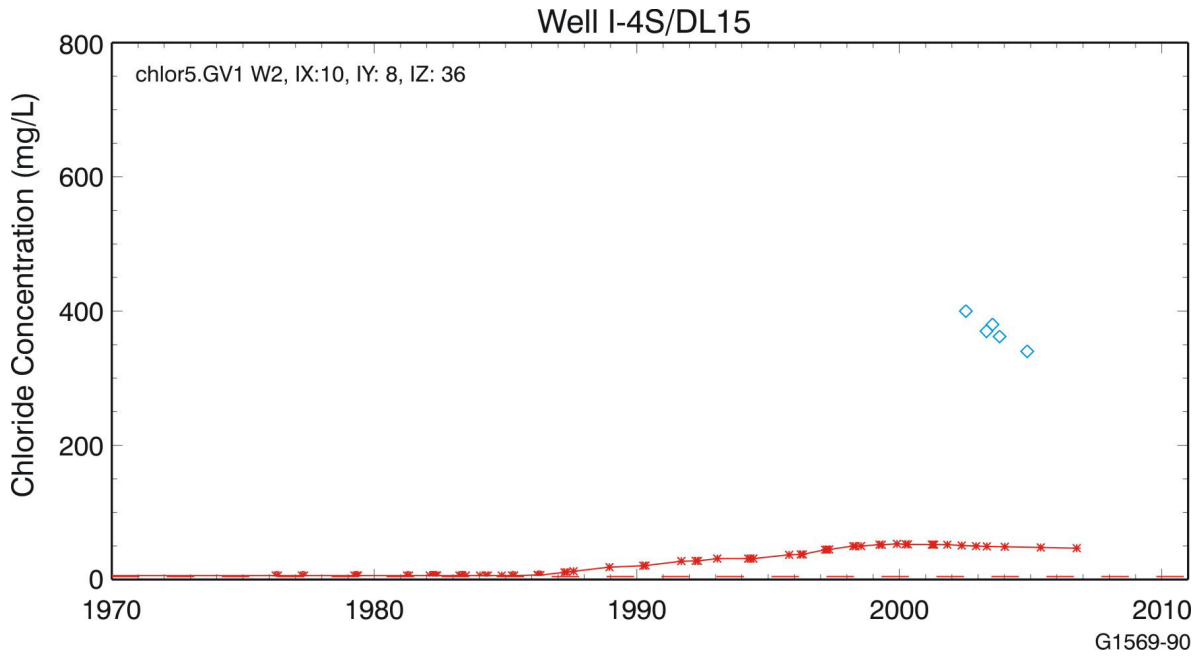

Figure 5-21. Simulated (red stars) and observed (blue diamonds) chloride concentrations at the I-4S-DL15 location with an additional 30 cm infiltrating along the east-west access road each year in April. See Figure 5-11 for lysimeter location.

To compare transient behavior between the base case and additional water simulations, a profile with chloride concentration time histories from increasing depths for one location is shown in Figure 5 22. The location shown is for a gridblock in the second-level refined grid that corresponds to the I-4S-DL15 lysimeter. The depths portrayed are shallower than those shown previously for this lysimeter. The transient source that shows the characteristic double hump is evident at the shallow depth, which is only one gridblock lower than the gridblock where the chloride is released in the model. At this shallow depth, additional water serves primarily to dilute concentrations. However, at subsequently greater depths, the simulations with additional water result in higher simulated chloride concentrations. They also retain the transient character of the chloride release better than the base model.

In summary, relative to the chloride simulations, the RI/FS model has difficulty mimicking these very specific concentration time histories, even with additional water applied in an attempt to flush the chloride downward. This difficulty is primarily attributed to averaging induced by large gridblock sizes. The model with additional water applied along ditches does mimic the advance to depth in the B-C interbed, albeit at lower concentrations. The preferential nature of flow and transport is obvious in the chloride brine monitoring results when compared to this attempt to simulate brine advance. Any future efforts to simulate magnesium chloride brine movement in the subsurface should probably be performed within a more limited two-dimensional, cross-sectional model that would allow for greater discretization and improved representation of lithology.

5.4 Development and Calibration of the Volatile Organic Compound Transport Model

When the Operable Unit 7-13/14 ABRA was published, Operable Unit 7-08 in conjunction with Operable Unit 7-13/14 was in the process of updating and recalibrating the VOC transport model due to significant revisions in the CCl_4 inventory estimates. As a result, VOCs were not simulated in the ABRA transport model; rather, results from the IRA were scaled, based on the most current VOC inventory estimates. This was deemed appropriate from the standpoint that modeling with different inventory estimates would not change the risk estimates considerably. However, since the ABRA, the VOC transport model has been updated with all the corrections to the ABRA model described in this document, and has undergone additional calibration. The model also has been updated to simulate vapor vacuum extraction and includes actual operations data. This section describes VOC modeling objectives, methodology, and results of calibration.

5.4.1 Objectives

Objectives of CCl_4 calibration were to construct a model that could adequately reproduce the observed migration of CCl_4 from the SDA, and predict with a relatively high degree of confidence future concentrations of COPCs that migrate as a vapor (Group 11, VOCs and Group 8, C-14).

5.4.2 Volatile Organic Compound Model Description

The VOC transport model uses the same basic model that was developed for transport of dissolved-phase contaminants. All aspects of the dissolved-phased model for simulating water movement in the vadose zone and aquifer are the same for the VOC transport model. However, because VOCs are transported in the subsurface in multiple phases and by a number of complex, interrelated processes, additional capabilities were necessary for the VOC transport model that were not required for the flow or dissolved-phase transport model. Additional relevant transport processes and geologic features were

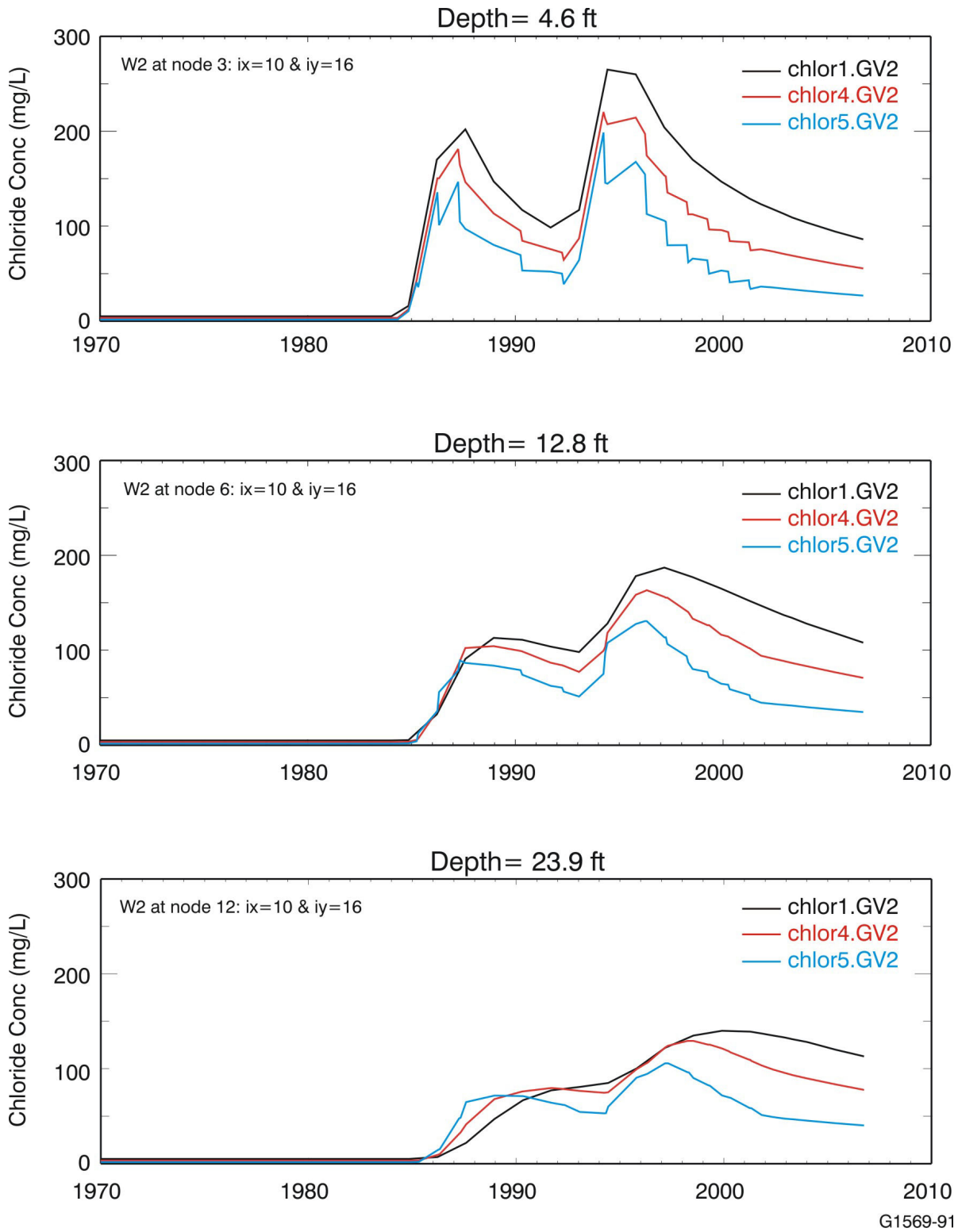

Figure 5-22. Simulated chloride concentrations at a series of increasing depths for the base (chlor1) and for the additional 10 cm (chlor4) and 30 cm (chlor5) of water infiltrating in April along the east-west access road.

included in the model only if they could be represented with reasonable accuracy, and if they produced a measurable effect on the results. Additional processes and features of the VOC transport model include the following:

- Dual-permeability, dual-porosity representation of the subsurface basalt
- Phase partitioning
- Vapor advection due to density, barometric pressure fluctuations, air injection during drilling, and vapor vacuum extraction phase partitioning
- Vapor diffusion with diffusion boundary conditions.

These additional processes and features are discussed in more detail in the following subsections.

5.4.2.1 Conceptual Model of Volatile Organic Compound Transport. Volatile organic compounds are transported through the subsurface by two primary mechanisms: advection and diffusion. Advection refers to passive transport of contaminants with the bulk movement of a mobile phase (i.e., gaseous, aqueous, or oleic). Diffusion is a spreading process that moves contaminants from areas of high concentration to areas of low concentration by intermolecular collisions. Partitioning occurs between all phases and is assumed to be an equilibrium process.

In the SDA, significant movement of a liquid oleic phase is unlikely because of the high viscosity of the treated waste. Even if liquid VOCs were present, the relatively small amount that might separate from the treated waste would likely residualize near the source. The high volatility of the VOCs and the relatively dry nature of the INL Site suggest that vapor transport is an important transport mechanism, especially in the basalt portions of the vadose zone. Gaseous movement of VOCs occurs primarily through diffusion and advection. Gaseous advection occurs primarily in the fractured basalt. Aqueous-phase VOCs migrate with infiltrating water, following established flow paths primarily in the sediment and fractured basalt. The basalt matrix acts primarily as a storage site for both gaseous- and aqueous-phase VOCs. The following subsections discuss VOC transport mechanisms in more detail.

5.4.2.2 Volatile Organic Compound Transport Model Assumptions. This section lists assumptions unique to the VOC transport model that are not listed in Section 4.2:

- All VOC COPCs were assumed to be contained in sludge. This is true for all of the tetrachloroethylene and 1,4-dioxane and 99.5% of the CCl_4, but only 51% of the methylene chloride was buried sludge. The other 49% of methylene chloride was contained in paper, rags, trash, dirt, and concrete.
- The VOC release rate (i.e., source term) was controlled by drum failure and diffusion through sludge, except for the methylene chloride that was not sludge; this portion was released by diffusion and no credit was taken for drum containment.
- In the year 2000, 50% of the original VOC mass had been released, and 50% remained in the pits (Sondrup et al. 2004).
- The vadose zone basalt is represented as a dual-continua (i.e., dual porosity and permeability) media to account for transport and storage in both the fractures and the matrix (see Section 4.3.4.2).
- Interphase mass transfer is linear and reversible.

- Partitioning between aqueous and gaseous phases is adequately described using Henry's Law.[c]

- Distribution coefficients are homogeneous in the interbeds, and sorption is negligible in basalt.

- Aqueous-phase VOCs migrate with infiltrating water, following established flow paths.

- Gaseous movement of VOCs occurs through diffusion and advection.

- Gaseous diffusion can be represented by Fickian diffusion, using an effective diffusion coefficient that includes a tortuosity factor.

- Gaseous advection is the result of density gradients and pressure gradients. Pressure gradients are caused by barometric pressure fluctuations, positive-pressure air drilling, and vapor vacuum extraction operations. Gaseous advection due to thermal gradients is negligible.

- Barometric pressure fluctuations can be adequately represented using a square-wave approximation. Fluctuations caused by passage of pressure fronts are important, while higher frequency variations due to wind gusts or diurnal temperature changes can be neglected.

- All air-drilled wells were drilled at the same speed and with the same air injection rate. Air recovery during drilling was 100% above the depth of 40 m (131 ft) below land surface, and 0% below 40 m (131 ft).

- Base-case simulations assume the Operable Unit 7-08 vapor vacuum extraction with treatment (VVET) system will operate 10 months (i.e., January through October) of each year, from 2005 through 2009, and will extract from wells in use at the end of 2004. Actual data from all other vapor vacuum extraction activities (i.e., 2-week test [1989], 4-month test [1990], treatability study [1993], and Operable Unit 7-08 operations from January 1996 through January 2005) are included.

- Eighty percent of VOC waste in the Accelerated Retrieval Project retrieval area was removed in January 2004, and containment of the remaining 20% failed in January 2004 (see Section 5.1.1 of the draft RI/BRA for an explanation).

- Injection and extraction wells are located in the center of the gridblock they occupy.

- Contaminant degradation was not included in the model.

- Calibration of the VOC transport model was performed using only CCl_4. Effects from the presence of other VOCs on partitioning and transport of CCl_4 were inconsequential for calibration.

5.4.2.3 Volatile Organic Compound Fate and Transport Mechanisms and Parameters.

This section contains a description of the following transport processes and parameters and how they were implemented in the VOC transport model:

- Phase partitioning, including sorption
- Gaseous diffusion and advection
- Aqueous diffusion, advection, and dispersion.

---

[c] Henry's Law: a fact in physical chemistry: the weight of a gas dissolved by a liquid is proportional to the pressure of the gas.

5.4.2.3.1 Phase Partitioning—Typically, VOCs in the vadose zone will partition into all phases, seeking an equilibrium condition. The relative amount of chemical in two neighboring phases in equilibrium is described by partition coefficients. Partitioning between vapor and aqueous phases is described by Henry's law. Henry's Law coefficients, shown in Table 5-2, are simply the vapor pressure of pure compound divided by the aqueous solubility.

Partitioning of VOCs between the aqueous and solid phases often is described using a distribution coefficient, which assumes sorption is linear and reversible. The distribution coefficient for VOCs is simply the product of the organic carbon partition coefficients (mL/g) and the fraction of organic carbon in the soil (dimensionless). The amount of sorption, therefore, depends strongly on the type of geologic material (especially the amount of organic carbon), and the type of chemical constituents dissolved in water. In the model, sorption was assumed to occur in sediment, based on an organic carbon content value of 0.05% reported by Colwell (1988). Sorption in basalt was considered negligible. Organic carbon partition coefficients are shown in Table 5-2.

5.4.2.3.2 Gaseous Transport—Gaseous- or vapor-phase migration in the vadose zone is typically much more rapid than aqueous transport. The rate of vapor transport strongly depends on soil-moisture content. Soil moisture will retard vapor migration by reducing the pore space available for vapor movement and through partitioning of the vapor phase into the aqueous phase. The relatively dry nature of the SDA suggests that vapor transport is an important transport mechanism.

Vapor diffusion in porous media is described by Fick's first law, which states that the contaminant flux is proportional to the concentration gradient. The proportionality constant is called the effective diffusion coefficient. In a porous medium, contaminant molecules must travel longer diffusion paths because of the structure of the medium and moisture in the pore space. To account for the longer diffusion paths, the effective diffusion coefficient is the product of the free-air diffusion coefficient and the gas- or air-filled porosity, divided by a parameter of the medium called the tortuosity. Free-air diffusion coefficients are presented in Table 5-2. Gaseous-phase tortuosity values were an important calibration parameter. Initial estimates of tortuosity were calculated using an expression derived by Millington (1959). These values were adjusted as part of the model calibration process and are discussed in Section 5.4.4.2.

Table 5-2. Volatile organic compound chemical and transport properties.

Property	Carbon Tetrachloride	Tetrachloroethylene	Methylene Chloride	1,4-Dioxane
Molecular weight (g/mole)	154	166	85	88
Density (kg/m^3)	1,584	1,631	1,335	1,033
Henry's constant (nondim)	0.75	0.442	0.058	0.00021
Organic carbon partition coefficient, K_{oc} (mL/g)	439	364	8.8	1.23
Free Air diffusion coefficient (m^2/day)	0.72	0.69	0.87	1.98

Vapor-phase advection can result from pressure, density, and thermal gradients in the subsurface. Pressure gradients can be caused by barometric pressure fluctuations, positive-pressure air drilling, and vapor extraction operations. To implement barometric pressure fluctuations in TETRAD, only low-frequency variations associated with passage of pressure fronts were considered. According to Auer et al. (1996), these low-frequency variations have a much larger impact on subsurface gas transport than the high-frequency variations caused by diurnal temperature fluctuations and local wind gusts. Another approximation consisted of representing actual pressure variations that are somewhat sinusoidal with a square wave. This was done for convenience and to preclude extremely long run times due to time-step limitations. An examination of barometric pressure at the SDA over several months showed a period for low-frequency perturbations of approximately 10 days. The average pressure during this period was 845 mb (84.5 kPa) with an average deviation (amplitude) of approximately ±7 mb (0.7 kPa). Figure 5-23 illustrates the square-wave fit to the barometric pressure data for a 2-month interval from the examination period. In TETRAD, the air pressure at land surface was alternately increased 14 mb for 10 days and then decreased 14 mb for 10 days for the entire simulation. Although barometric pressure fluctuations were included in the calibration, they could not be included in the base-case simulations due to extremely long simulation times caused by the short time step limitation. The effects of not including barometric pressure are discussed in Section 5.4.7.

Pressure gradients resulting from air injection during well drilling have the potential to move vapor-phase VOCs because of the high pressures involved and the permeable basalt subsurface. Many wells in the vicinity of the SDA have been drilled with air to bring drill cuttings to the surface. Since 1994, reverse-air circulation, which uses a dual-wall drill stem, has been used because it recovers most of the injected air. Before 1994, more than 40 wells were drilled without reverse-air circulation. A survey of SDA drill logs indicates that, for most of these wells, circulation (i.e., air recovery) was partially or totally lost below about 18 m (60 ft). This meant that a large volume of air had been pumped into the subsurface at high pressures.

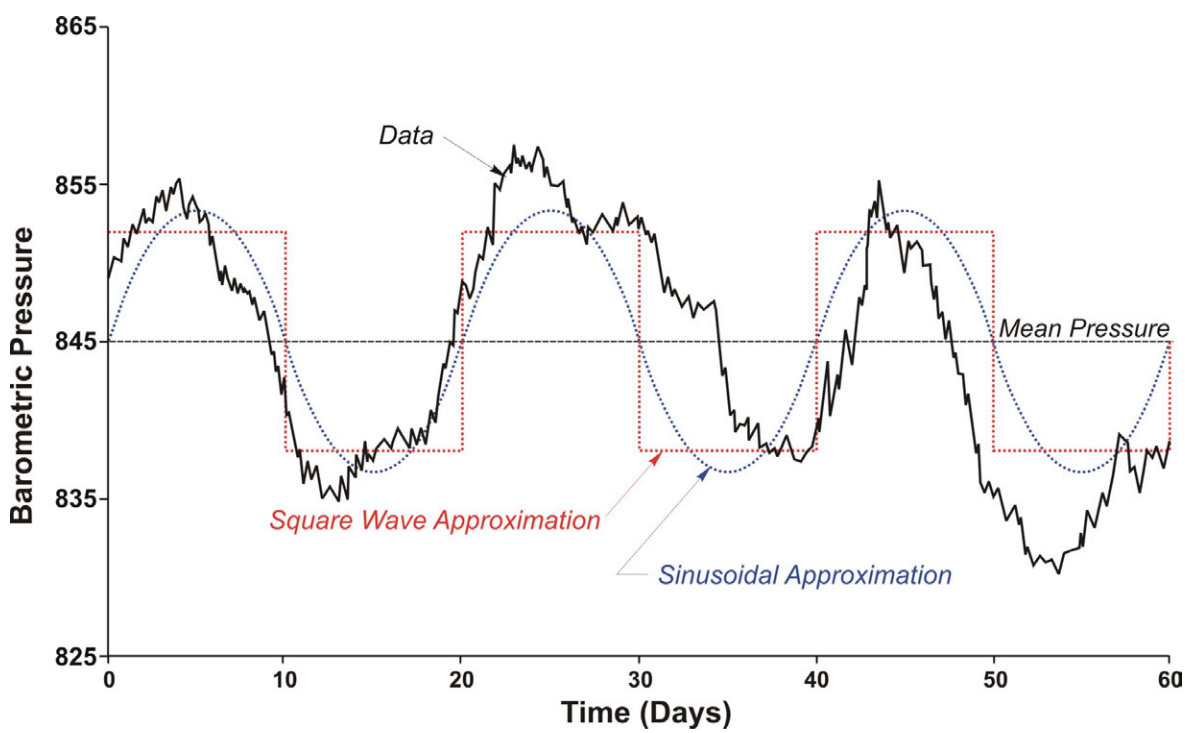

Figure 5-23. Barometric pressure data with square-wave approximation as implemented in the carbon tetrachloride calibration simulation.

Figure 5-24 shows the location of air-drilled wells with a depth greater than 18 m (60 ft) that did not use reverse-air circulation. Drill dates, depths, and drill methods for these wells are listed in Table 5-3. An examination of the drilling logbooks shows that the wells in Table 5-3 were typically drilled at speeds of about 9 m (30 ft) per day at air pressures of 125 to 250 psi and injection rates of 750 to 1,100 cfm. In TETRAD, either the pressure or the injection rate may be specified with a limit put on the one that is not specified. The air injection rate was set to 1,000 cfm with no limit on the pressure. The length of the injection interval was increased in steps of approximately 9 m (30 ft) each day until the terminal depth was reached and air was injected over the entire length of the interval each day.

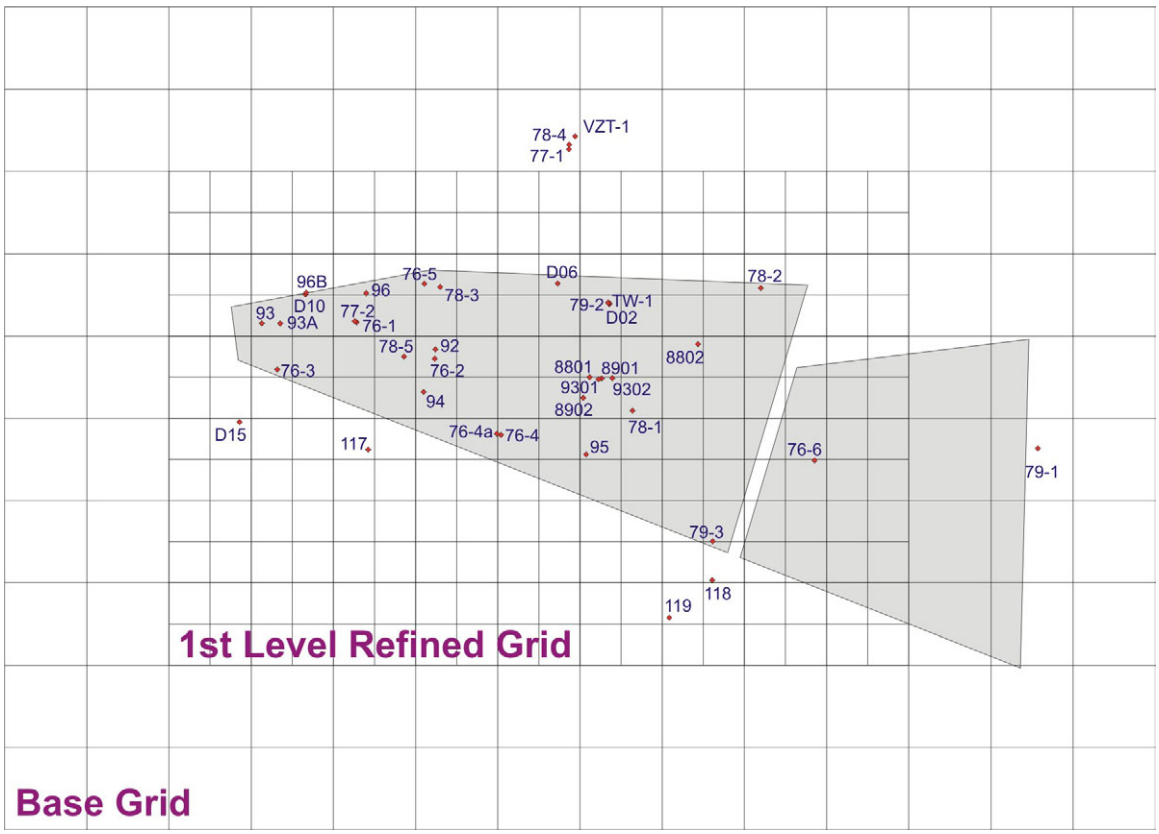

Figure 5-24. Locations of air-drilled wells (excluding reverse-air-rotary) in the vicinity of the Subsurface Disposal Area with a depth of greater than 18 m (60-ft).

Table 5-3. Information on air-drilled wells at the Subsurface Disposal Area with a depth greater than 18 m (60 ft), excluding wells drilled using reverse-air circulation.

Well	Year	Depth (ft)	Drill Method
USGS-92	1972	247	Air rotary/core
USGS-93	1972	246	Air rotary/core
USGS-93A	1972	233	Air rotary/core
USGS-94	1972	302	Air rotary/core
USGS-95	1972	246	Air rotary/core
USGS-96	1972	236	Air rotary/core

Table 5-3. (continued).

Well	Year	Depth (ft)	Drill Method
USGS-96B	1975	229	Air rotary/core
76-1	1976	228	Air rotary/tricone/core
76-2	1976	253	Air rotary/core
76-3	1976	240	Air rotary/core
76-4	1976	215	Air rotary/tricone/core
76-4A	1976	254	Air rotary/tricone/core
76-5	1976	245	Air rotary/core
76-6	1976	244	Air rotary/core
77-1	1977	600[a]	Air rotary/core/water
77-2	1977	87	Air rotary/core
78-1	1978	82	Air rotary/core
78-2	1978	253	Air rotary/core
78-3	1978	248	Air rotary/core
78-4	1978	350	Air rotary/tricone
78-5	1978	250	Air rotary/core
79-1	1979	244	Air rotary/core
79-2	1979	223	Air rotary/core
79-3	1979	262	Air rotary/tricone/core
D02	1986	243	Air rotary/tricone/core
D06	1986	126	Air rotary/tricone/core
D10	1987	239	Air rotary/core
D15	1987	252	Air rotary/tricone/core
TW-1	1987	238	Air rotary/tricone/core
USGS-117	1987	655	Tricone/air
USGS-118	1987	622	Air rotary/core
USGS-119	1987	705	Tricone/air
USGS-120	1987	705	Tricone/air
8801	1988	245	Air rotary/core
8802	1988	221	Air rotary/core
VZT-1	1988	132	Air rotary
8901	1989	249	Air rotary/tricone/core
8902	1990	245	Tricone/air

Table 5-3. (continued).

Well	Year	Depth (ft)	Drill Method
9301	1993	238	Air rotary
9302	1993	238	Air rotary

a. Drilled to 272 ft with air, drilled to 600 ft with water.

Vapor vacuum extraction is simulated in the model similar to the way air injection is handled. One difference with extraction is that phases are extracted rather than components. In this case, the gaseous phase is extracted, which is mostly air but can also include any water vapor or VOC vapor. Also, extraction is simpler because extraction intervals do not change the way injection intervals changes when the well is drilled. Three historic vapor extraction tests were included in the calibration and base-case simulations, including the 1989 2-week test, the 1990 4-month test, and the 1993 Organic Contamination in the Vadose Zone Project treatability study. All of these tests pumped from Well 8901.

In 1996, Operable Unit 7-08 began operation of a large-scale VVET system to remove vapor-phase VOCs from the vadose zone. The system consisted of three thermal oxidizer (i.e., treatment) units (i.e., Units A, B, and C) and multiple extraction wells with different length extraction intervals at different depths. Since beginning operations, the units have essentially been shutdown only for maintenance or when breakdowns occur. The original units have been upgraded with more efficient and reliable treatment units (i.e., Units D, E, and F) and additional extraction wells have been drilled. Actual VVET operations from January 1996 through January 2005 were included for base-case simulations. Base-case simulations also included future vapor extraction activities through the year 2010 and assumed extraction from six wells (two per treatment unit) for 10 months a year.

To implement vapor extraction in the model, a volumetric removal rate of gas and vapor was assigned to the extraction interval for each well that was connected to a VVET unit. The original VVET units (i.e., A, B, and C) only monitored total flow into the unit; therefore, if extraction was from multiple wells, assumptions had to be made regarding the division of flow between each well. Fortunately, however, the number of viable extraction wells were limited and most of the time the units were only connected to one well. In 2002 to 2003, several new extraction wells were drilled and flow meters have been installed at each wellhead. Since that time, the recorded flow rates for each well have been used in the model. For future operations from 2005 to 2010, the VVET system was assumed to operate in the same configuration as was being used at the beginning of 2005. In that configuration, Unit D was removing 160 scfm from Well SE6, and 240 scfm from Well IE6; Unit E was removing 200 scfm each from Wells SE7 and 8901; and Unit F was removing 200 scfm each from Wells SE8 and 7E. Figure 5-25 shows the locations of current vapor extraction wells that may be used by Operable Unit 7-08. Figure 5-26 shows the depth of the extraction intervals. Extraction in the model took place from gridblocks that corresponded to the location and depth of the extraction interval. The operating time for each of the extraction units is shown graphically in Figure 5-27. Not shown in Figure 5-27 are the wells that were connected to the units while they were operating.

Vapor density gradients caused when high molecular weight compounds, such as CCl_4, are vaporized into the surrounding air, also cause vapor advection. Falta et al. (1989) and Mendoza and Frind (1990a, 1990b) suggest that density driven gas flow will be significant where total gas density exceeds ambient gas density by more than 10% and the gas-phase permeability is greater than 1×10^{-7} cm^2, which is within the range of fractured basalt permeability. Density driven flow is likely to be important immediately below the source where concentrations are highest. Table 5-2 contains molecular weights of the VOCs.

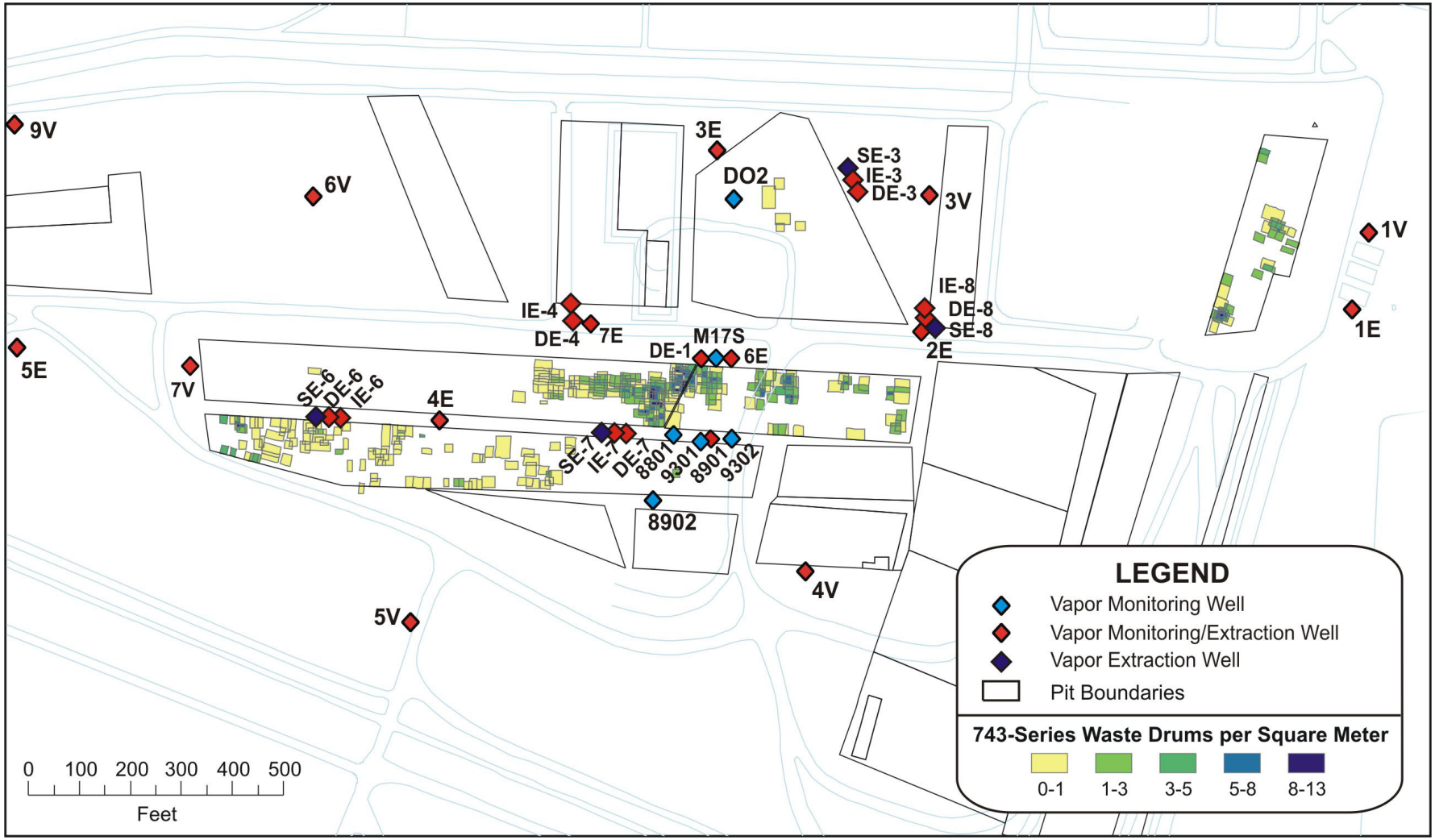

Figure 5-25. Operable Unit 7-08 vapor extraction and vapor monitoring well locations.

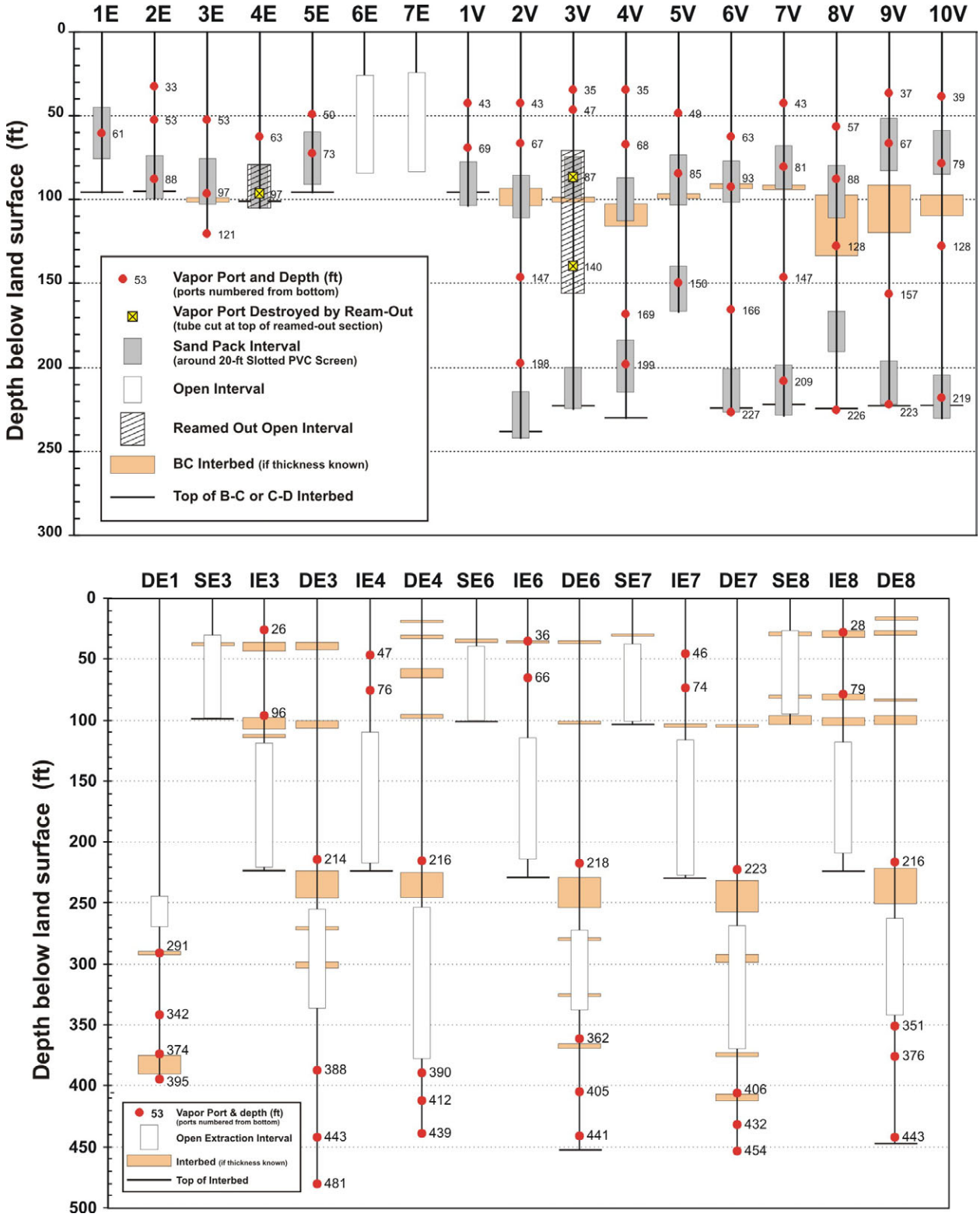

Figure 5-26. Depth of vapor ports and extraction intervals in Operable Unit 7-08 wells.

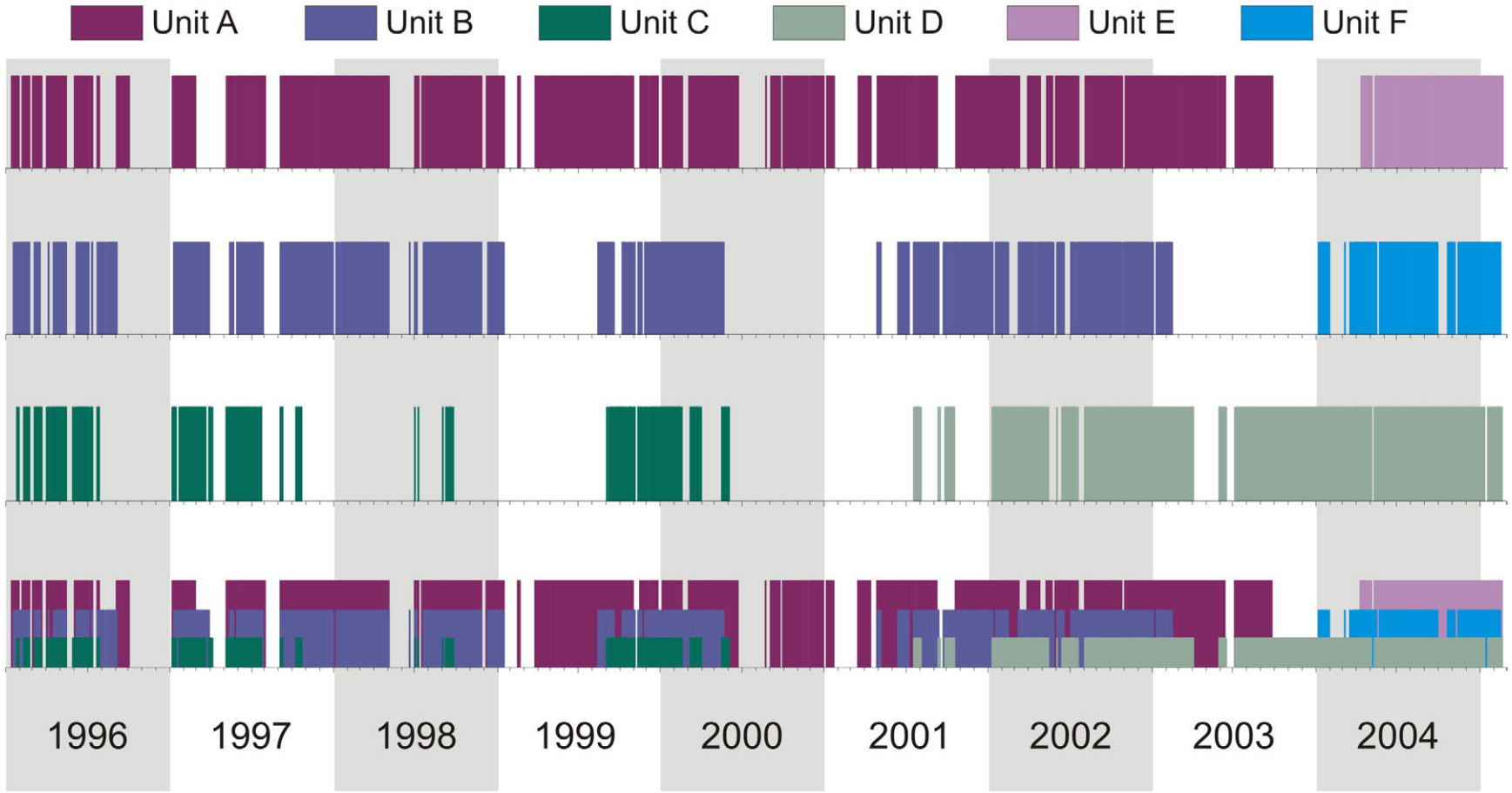

Figure 5-27. Operable Unit 7-08 vapor vacuum extraction with treatment unit operation history.

Vapor advection caused by thermal gradients is not likely to be significant and was not included in the simulation study. The subsurface was assumed to be isothermal.

5.4.2.3.3 Aqueous Transport—Aqueous transport of VOCs can take place as a result of advection and diffusion, even though advection is typically much more rapid. Dissolved VOCs are transported by aqueous advection whenever water moves in the subsurface. Section 4 contains an extensive discussion of water movement in the vadose zone and aquifer. Aqueous diffusion acts the same as vapor diffusion, but aqueous-diffusion coefficients are usually four to five orders of magnitude less than vapor-diffusion coefficients. Aqueous-diffusion coefficients used in the RI/FS model were assigned a value four orders of magnitude less than the free-air-diffusion coefficients (Table 5-2).

5.4.2.3.4 Degradation—Although degradation of CCl_4 has probably occurred in the SDA subsurface, it was not included in simulations because of uncertainty regarding the rate and mechanism. In the environment, CCl_4 is degraded more readily under anaerobic conditions. In the SDA subsurface, aerobic conditions likely dominate; however, anaerobic conditions may occur in isolated locations, allowing for CCl_4 degradation.

The presence of chloroform, a transformation product of CCl_4, is evidence that reductive dechlorination has occurred in the SDA subsurface. Historical records do not indicate chloroform disposal in the SDA, but chloroform has been detected in the groundwater and soil gas beneath the SDA. Neglecting degradation is conservative because byproducts of CCl_4 degradation (i.e., chloroform, methylene chloride, and chloromethane) have transport properties similar to CCl_4, yet they are less toxic (i.e., have higher risk-based concentrations).

5.4.2.4 Interface from the Vadose Zone Model to Aquifer Model. Section 4.3.7.4 describes the process for transferring dissolved-phase simulation results from the vadose zone model to the aquifer model. In that case, the flux of water and the aqueous flux of contaminants from the fractured basalt were transferred from the vadose zone to the aquifer on a grid-by-grid basis. Because the VOC model has the added complexities of being dual continua, it was necessary to capture the flux of contaminant within the matrix domain. No gaseous-phase flux of contaminants is present in either the fracture or matrix domain because vapor-phase contaminants partition into the aqueous phase as water saturations increase near the water table and then advect out the bottom of the model domain. Direct partitioning from the vapor phase into the aquifer across the water table is not considered. Since contaminant mass advects out the bottom of the model domain without being influenced by contaminant mass already present in the aquifer, this approach is conservative because it maximizes aquifer concentrations. Direct partitioning would decrease overall as concentrations increased in the aquifer.

5.4.3 Volatile Organic Compound Model Calibration Methodology

Calibration was achieved through a trial-and-error process of adjusting particular parameters within reasonable uncertainty ranges until model results adequately agreed with observations of CCl_4 in vadose zone soil-gas and aqueous concentrations in the aquifer. Carbon tetrachloride was chosen because it has the largest inventory and available data set for comparison, and documentation of its disposal history and origin is better when compared to other VOCs. Given the high degree of subsurface heterogeneity, the goal of calibration was to match observed general trends and not be overly concerned with matching values at specific points. Comparison of model results to observed data was both qualitative and subjective, relying primarily on visual observations of plots that compare model results to data.

Calibration focused primarily on data collected through 1995, before the start of full-scale VVET operations by Operable Unit 7-08. By doing this, calibration focused on matching data and trends that resulted from natural, ambient processes and not on artificial processes (e.g., vapor extraction).

Comparisons were made of actual VOC mass removed to simulated mass removed, but parameter adjustments were not warranted based on the level of agreement.

5.4.4 Volatile Organic Compound Transport Model Calibration

As part of the IRA model calibration (Magnuson and Sondrup 1998), several model inputs were modified to improve calibration. Some modifications were small deviations from the original value and others were significant. Parameter values that were modified only slightly were kept the same for model calibration. These include the fraction of organic carbon (f_{oc}), which affects sorption, the basalt matrix porosity, the duration of air drilling, and barometric pressure amplitude and wavelength.

For the VOC model calibration, source-release and tortuosity values were the only inputs initially intended to be used as part of calibration. However, in an effort to improve the match between simulated and observed data, other parameters or features of the model were modified. Each of these calibration steps are discussed in the following subsections.

5.4.4.1 Source Release. Source releases are calculated external to the VOC transport model, using the computer code DUST-MS (Anderson and Becker 2006). Inputs to the source model include source inventory, drum-failure rates, and diffusivity of VOCs in sludge. Table 5-4 lists the best available data for the source model inputs.

Table 5-4. Best available data for volatile organic compound source-release model inputs.

Model Input	Value	Source
Carbon tetrachloride inventory	7.9E+05 kg	Miller and Varvel (2005)
Dumped drum corrosion-failure rate	11.7 years[a]	Anderson and Becker (2006)
Stacked drum corrosion-failure rate[b]	22.6 years[a]	Anderson and Becker (2006)
Initial drum-failure rate	28.5%	Anderson and Becker (2006)
Carbon tetrachloride diffusivity in sludge	2.5E-06 cm^2/s	Lowe et al. (2003)

a. Expressed as a mean-time-to-failure, using a normal distribution with a standard deviation of one-half the mean time to failure.
b. Very small percentage of the Series-743 sludge drums was stacked.

To help constrain the source model, Sondrup et al. (2004) attempted to estimate the amount of CCl_4 remaining in the pits by using chlorine data obtained from neutron-gamma logging of waste. Vapor sampling of Type B vapor probes and nuclear logging of Type A probe holes suggest a substantial amount of VOCs remain in the pits even after 40 years of burial. Although a defensible quantitative estimate could not be obtained, Sondrup et al. (2004) used other information and recommended that 50% of VOCs remaining in year 2000 be used for modeling purposes as a target for the source-release model.

In order to determine feasible combinations of source model inputs that could produce a release where 50% of the source remained in the pits in the year 2000, three cases of source-model simulations were run by varying the three parameters that control release: (1) initial drum-failure rate, (2) corrosion-failure rate for dumped drums, and (3) diffusivity of VOCs in sludge. In each case, two of the three values were held fixed, and the other value was varied over a predetermined range. The corrosion-failure rate for stacked drums was not examined because nearly all of the Series-743 drums were dumped. Table 5-5 shows the range of values examined for each of the three parameters. Figure 5-28 shows graphical results for the three cases in terms of percent of original mass remaining in the year 2000.

Table 5-5. Ranges of volatile organic compound source-release model inputs examined.

Case	Model Input	Best Available Value	Range of Values Examined
1	Dumped drum corrosion mean-time-to-failure	11.7 years[a]	10 to 60 years[a]
2	Initial drum-failure rate	28.5%	0 to 50%
3	Carbon tetrachloride diffusivity in sludge	2.5E-06 cm^2/s	2.5E-10 to 2.5E-05

a. Standard deviation was half the mean-time-to-failure.

In Case 1, a value of 50% mass remaining was achieved with a drum mean-time-to-failure of approximately 45 years. In Case 2, with the mean-time-to-failure fixed at 11.7 years and the diffusivity fixed at 2.5E-06 cm^2/s, there were no values of initial failure rate that would keep 50% mass remaining in the year 2000. Even the extreme case of an initial failure rate of 0% (i.e., corrosion-failure only) resulted in only 6% of the original mass remaining in the year 2000. This is because the other two parameters (i.e., mean-time-to-failure = 11.7 years, diffusivity = 2.5E-06 cm^2/s) allow the mass to be released much too rapidly. Therefore, to test the source-release dependence on initial drum-failure rate, a mean-time-to-failure value of 45 years was used. Forty-five years was the value from Case 1 that resulted in 50% of the mass remaining in the source. Using this value, an initial drum-failure rate of 0% resulted in 70% of the mass remaining in the year 2000 and a value of 50% resulted in half of that (35%). The results are linear.

For Case 3, the mean-time-to-failure was fixed at 11.7 years as recommended by Anderson and Becker (2006), and the initial-failure rate at 28.5%. In order to achieve 50% mass remaining in the year 2000 for Case 3, the sludge diffusivity must be approximately 3E-10 cm^2/s. This is more than four orders of magnitude greater than the value suggested by Lowe et al. (2003). The exercise of varying source parameters to achieve a remaining mass of 50% suggests that (1) the mean-time-to-failure of 11.7 years as proposed by Anderson and Becker (2006) is too short for Series-743 sludge drums, or (2) the sludge diffusivity determined by Lowe et al. (2003) is too large (i.e., diffusion too rapid), or (3) some combination of 1 or 2 is correct. The answer is more likely that the mean-time-to-failure for the drums is too large, or more likely that bagging is preventing release of VOCs and no credit is being taken for bagging. Visual observations of waste during the Glovebox Excavator Method Project retrieval (Olson 2004) indicated that while many of the drums had corroded, many of the polyethylene bags within the drums appeared to be intact and acted as a barrier to VOC release. Therefore, a longer mean-time-to-failure for the drums would be more representative of an effective container-failure rate that includes influence of the bags. Thus, the mean-time-to-failure for the VOC source-release model was chosen to be 45 years, while the other parameters were assigned the best available values shown in Table 5-5.

5.4.4.2 Tortuosity Values. Before calibration, initial tortuosity values were estimated from an empirical formula determined by Millington (1959). The Millington formulation relates tortuosity (τ), to porosity (θ) and water saturation (S_w) as shown below:

$$\tau = \frac{\theta_T^{\,2}}{\left[\theta_T\left(1 - S_w\right)\right]^{7/3}} \quad . \tag{5-2}$$

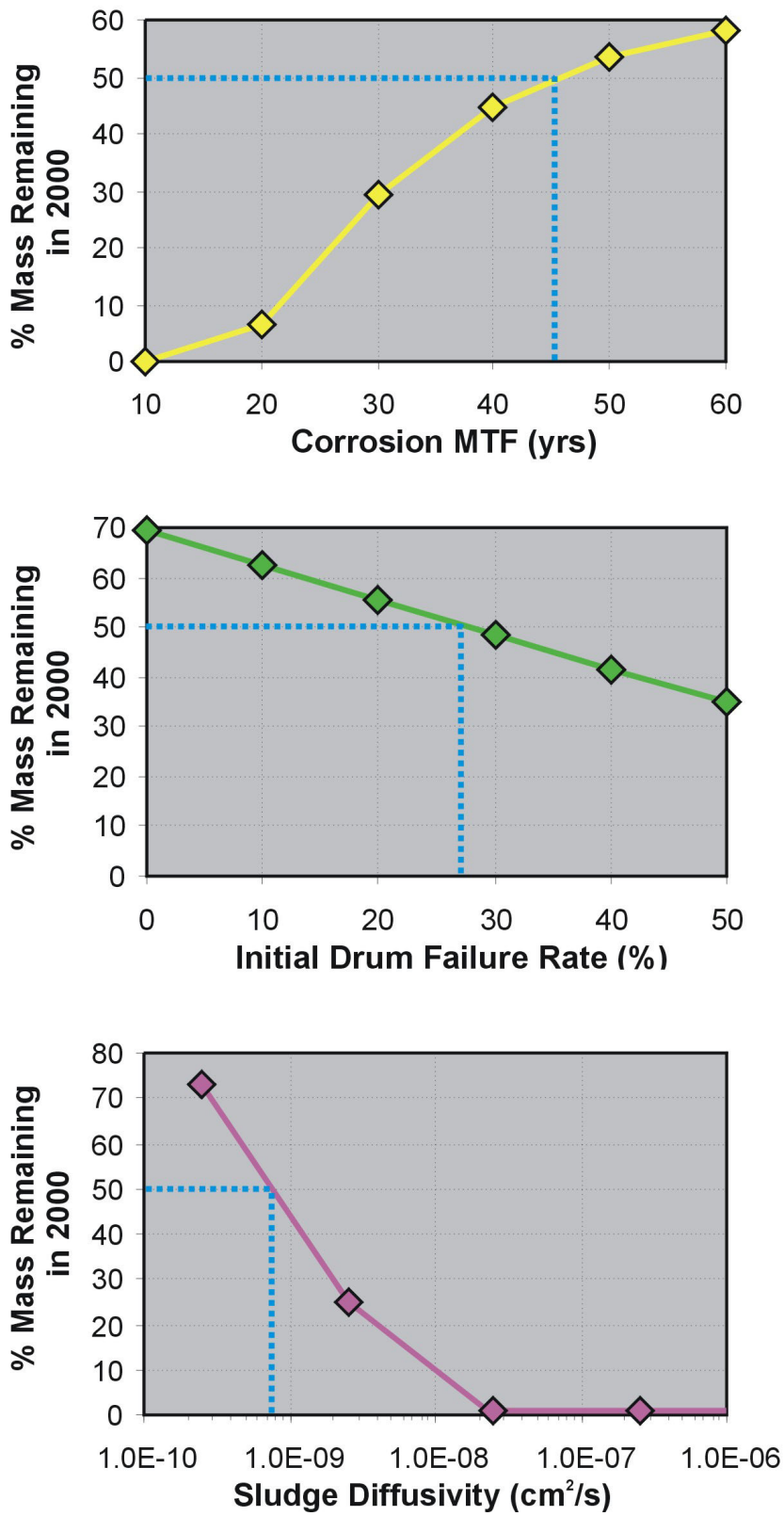

Figure 5-28. Results of carbon tetrachloride source-release parameter variations showing combinations that result in 50% of the original mass remaining in the year 2000.

Table 5-6 lists initial tortuosity values used in the VOC model calibration, using average saturation and porosity values from the ABRA model.

Table 5-6. Initial tortuosity values for the different material types used in the model.

Material Type	Tortuosity
Surficial sediment	6
A-B interbed	10
B-C interbed	7
C-D interbed	7
Fractured basalt	3[a]
Matrix basalt	9

a. Final value changed to 1 as a result of the calibration.

During the calibration process, numerous simulations with different tortuosity values were performed in an attempt to improve the match to observed data. The values investigated for each material type ranged from 1 up to as high as 30. In the end, however, the original values shown in Table 5-6 produced the best overall results with one exception. Early during the calibration process, it was clear that a tortuosity value of 3 for fractured basalt was too high and that a value of 1 produced the best overall match to vadose zone vapor and groundwater concentrations. Except for that change, the other values remained the same. Figure 5-29 shows a cross section of results for CCl_4 vadose zone vapor concentrations using the final tortuosity values.

Larger interbed tortuosity values were investigated in an attempt to cause more spreading of the vadose zone plume. The tortuosity values in Table 5-6 resulted in a general underestimation of the vadose zone vapor concentrations and aquifer concentrations at some of the outlying wells (e.g., M6S and M7S). Although the larger tortuosity values created the favorable effect of a broader vadose zone plume, they overly restricted the downward movement of VOCs near the SDA and caused an underestimation of the groundwater concentrations close to the SDA.

Other variations of tortuosity were attempted to improve calibration. The first variation was a direct implementation of the Millington formulation in the model. Equation (5-2) was programmed into the TETRAD model and the tortuosity values for each gridblock were calculated at each time step, based on the porosity and phase saturations. However, the simulation with the Millington formulation within TETRAD was not successful in terms of computational feasibility and desired effect. At many locations, water saturations approached saturated conditions (S_w=1) and the Millington tortuosity values approached infinity. This creates a computational burden, but one that is not overwhelming. The larger problem is that the tortuosity values are so large that transport is overly retarded and the match of simulated to observed data, especially in the aquifer, is very poor. Figure 5-30 compares simulation results using tortuosity values calculated by the model according to the Millington formulation against those using the final calibration tortuosity values shown in Table 5-6.

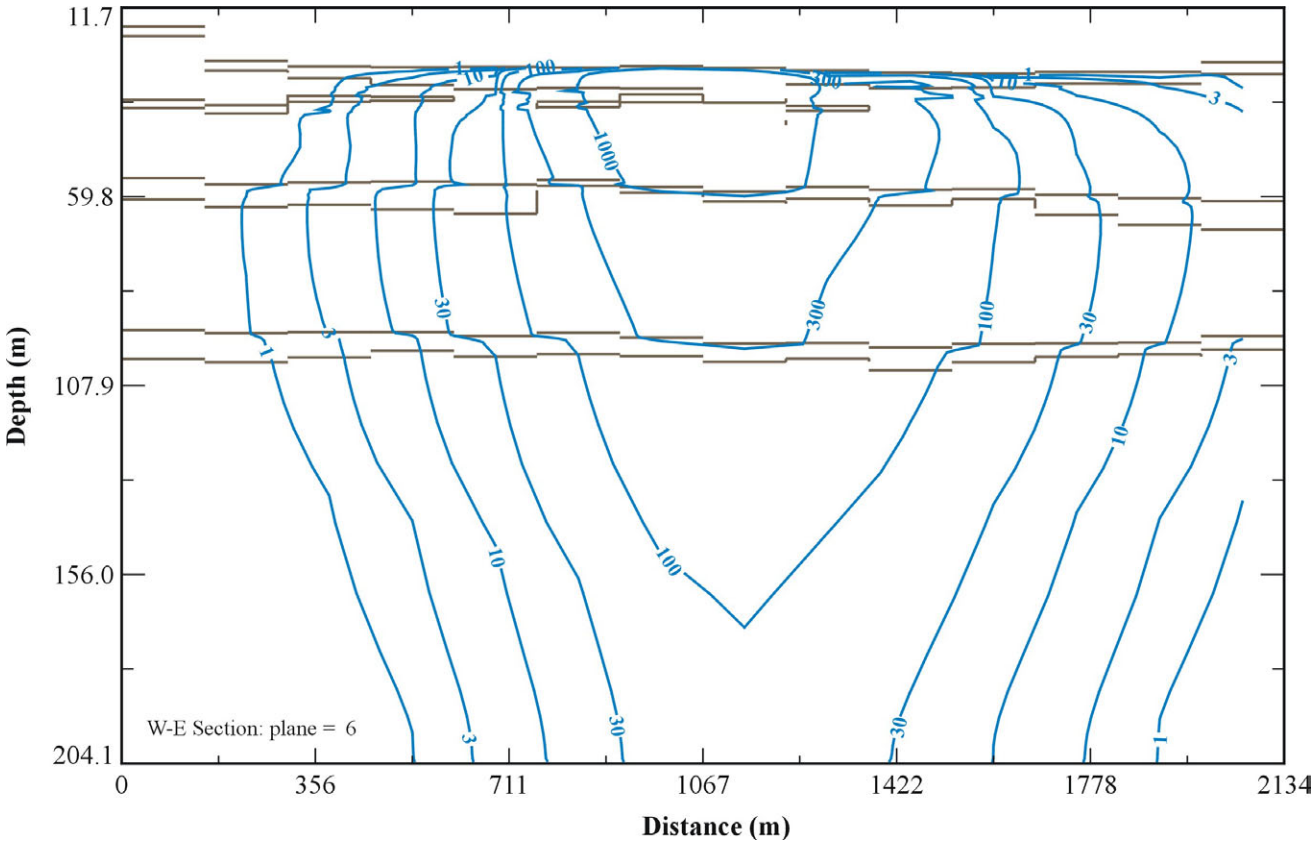

Figure 5-29. Carbon tetrachloride vapor concentration contours on a west-east cross section of the base model grid through the center of the Subsurface Disposal Area. Surface sediment and A-B, B-C, and C-D interbed locations are shown with horizontal lines.

The other tortuosity variation was a compromise between simulations that used single tortuosity values for the different material types and simulations that used the built-in Millington formulation. These additional simulations were performed with the values shown in Table 5-6, but with the added complication that smaller zones within some of the sediment layers were assigned slightly larger tortuosity values to account for the higher moisture contents. The higher moisture contents are the result of higher infiltration rates within the SDA. Results of these simulations were not significantly better than simulations with homogeneous values for the sediment layers.

5.4.4.3 Other Calibration Modifications. One limitation of the model is that it does not produce the amount of lateral spreading indicated by monitoring data. During the calibration process, three other model parameters were modified in an attempt to increase spreading of the VOC plume in the vadose zone and aquifer. The first change was to increase the fractured basalt permeability horizontal to vertical anisotropy ratio from the value of 30:1 used in the IRA and ABRA models to a value of 300:1. This change produced a better match of the observed spreading of CCl_4 in the vadose zone. Section 6.4.7 contains additional details on this parameter modification.

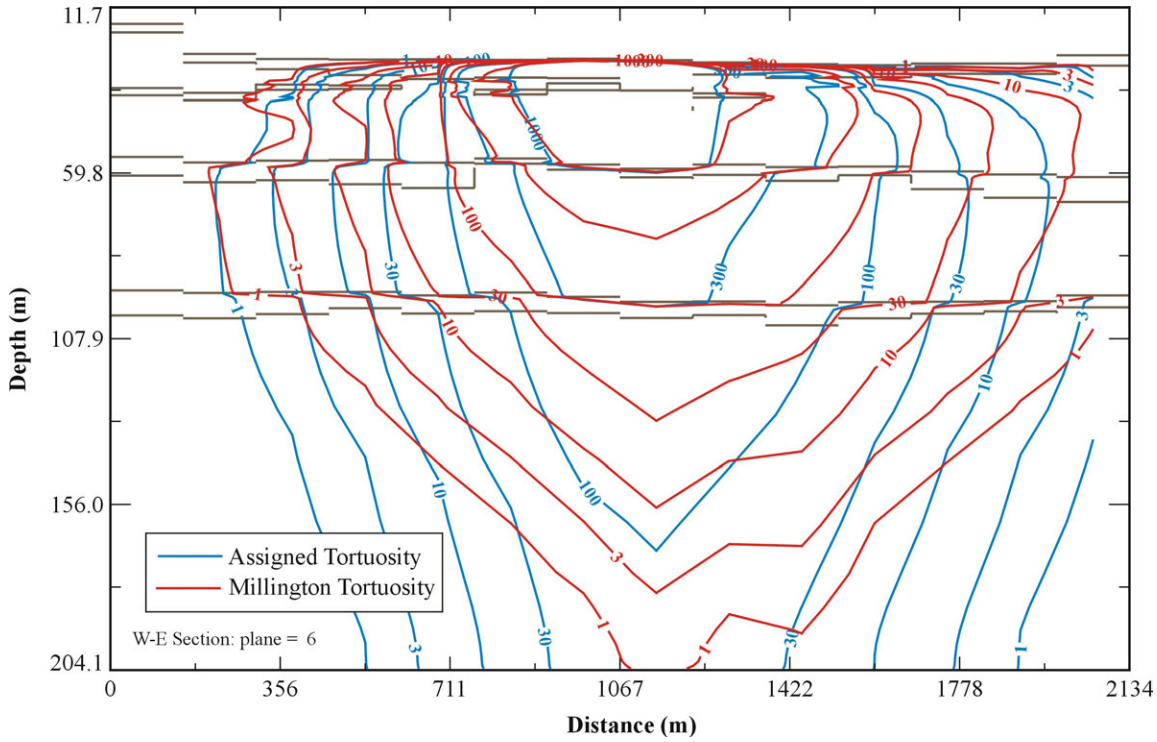

Figure 5-30. Comparison of simulated vapor concentration results using assigned tortuosity values (Table 5-6) and tortuosity values calculated by the model for each gridblock using the Millington formulation. Results are shown on a west-east cross section of the base model grid through the center of the Subsurface Disposal Area. Surface sediment and A-B, B-C, and C-D interbed locations are shown with horizontal lines.

The second parameter modification that helped increase lateral spreading of the plume was to increase the basalt matrix characteristic block length from the value of 2 m (6.6 ft) used in the IRA and ABRA models to a value of 20 m (65.6 ft). The larger matrix block length forces more of the flow and contaminant to be moved through the high-permeability fractures.

The third modification implemented to increase lateral movement of VOCs was to increase the number of low-permeability, low-porosity layers on the interbeds from 1 to 3. The rationale for this is discussed in Section 4.3.4.1. In the IRA and ABRA models, the top gridblock of each of the interbeds was assigned low-permeability, low-porosity properties. When the RI/FS model was created, it was noticed that the finer discretization around the basalt-interbed interfaces resulted in low-permeability, low-porosity gridblocks that were approximately one-third the thickness of those used in the IRA and ABRA model. Simulations were performed where the number of low-permeability, low-porosity gridblocks was increased to 2 and 3. The simulation using three gridblocks produced the best match to observed data. It also made the RI/FS model similar to the IRA and ABRA models in terms of the thickness of the low-permeability, low-porosity layer.

Each of these modifications by themselves helped to improve lateral spreading, but the model still could not match the overall breadth of the vadose zone plume. The inability of the model to reproduce this condition is more likely a result of neglecting historical impacts on water flow in the vadose zone and aquifer flow due to infiltration into the spreading areas, and the inability to characterize and incorporate heterogeneity into the model on an appropriate scale. However, this should not be viewed as a fundamental deficiency. The amount of VOCs in the outer fringes of the plume is a very small percentage

of the total mass. Matching the concentrations in this region was secondary to obtaining a good match to concentration trends in the interior of the plume. The calibration produced a good match to vadose zone concentrations near to and below the burial pits where the majority of the mass exists and enters the aquifer.

5.4.5 Final Calibration Results

At each step of the calibration process, simulated results were compared to (1) time-averaged, vapor concentration, vertical profiles at each vapor monitoring well, (2) vapor concentration time histories at each vapor port, and (3) aquifer concentration time histories at each aquifer well. This section contains selected vapor concentration comparisons at different locations and depths to represent the entire vadose zone plume. The full set of results is contained in Appendix G. All aquifer results are shown in this section.

In this section, vapor- or gas-phase concentrations are given in ppm (i.e., parts per million), which is a volume/volume ratio and is the same as ppmv. Aquifer or aqueous concentrations are given in μg/L (i.e., mass of contaminant/volume of aqueous solution). For low concentrations, μg/L is the same as ppb (parts per billion), which is a mass/mass (e.g., μg/kg) ratio.

5.4.5.1 Carbon Tetrachloride Vapor Concentration Vertical Profiles. Figure 5-31 shows a comparison of simulated concentrations at the simulation time of January 1, 1994 to time-averaged vertical profiles of the CCl_4 concentration at selected wells. The measured data are the average of data collected over a 4-year period from January 1, 1992 to January 1, 1996. An average was taken because the concentration at a single point can vary considerably with time. Horizontal bars through each averaged data point indicate plus or minus 1 standard deviation for data at that port over the 4-year period. The 4-year averaging period was somewhat arbitrary, but was made large to represent as much data as possible, and remove influence of short-term events like vapor extraction during the 1993 treatability study. Also, many monitoring wells were being drilled over this period, which can cause short-term variations in the data.

Data from wells near the center of the SDA were deemed to be more important for calibration, and more effort was focused on matching the profile of these wells. The model results compared well with measured concentrations in these wells below the B-C interbed. However, above the B-C interbed, specifically toward land surface, the concentrations predicted by the model are greater than the measured data in many cases. This deviation is primarily due to discretization around the source areas (i.e., pits). In the model grid, monitoring wells are located in the same gridblocks that are designated as source gridblocks (i.e., pits). Because wells in the model were located as if they were drilled through the center of source pits, they showed a high concentration near land surface where the pits are located, especially because the source is still active (i.e., releasing mass). In reality, monitoring wells are located next to or between pits and concentrations near the surface would be lower than if the monitoring wells were drilled in the pits. At depth, differences in port locations and pit locations become less important because of the vertical distance from the source location.

Again, the simulation results and data compare quite well at locations inside and near the SDA. However, at wells such as Well M7S (approximately 914 m [3,000 ft] from the northeastern corner of the SDA), the simulation results are much lower than the data. In general, lateral spreading was less in the simulation results than is apparent in the data. This is one of the reasons that the larger basalt permeability anisotropy ratio of 300:1 was investigated and selected over the previously used 30:1. The larger horizontal-to-vertical permeability ratio was helpful in causing more lateral spreading in the model, but it was still not enough to produce the degree of spreading apparent in the data. However, as previously stated, matching concentrations in this region was secondary to obtaining a good match to concentration

trends at the interior of the plume. Calibration produced a good match to vadose zone concentrations near to and below the burial pits where the majority of the mass exists and enters the aquifer.

5.4.5.2 Carbon Tetrachloride Vapor Concentration Time Histories. Figure 5-32 shows time-history comparisons for CCl_4 vapor concentrations at several selected vapor ports in and around the SDA. Simulated data are plotted in the most refined grid that contains the monitoring port. In general, simulation results are in good agreement with measured data. The best agreement was obtained for ports closer to the source areas.

Perturbations in the modeled concentrations are due to air injection during well drilling and VVET operations. In the model, data were saved roughly every 500 days (i.e., 1.4 years), except during some well-drilling events and VVET events. In these cases, data were saved more often in an attempt to capture the higher frequency changes that occur as a result of the event. Variation in measured data is due to VVET operations, well drilling, and barometric pressure fluctuations. Because it is not feasible to include actual barometric data in the simulation, changes in measured concentrations caused by these data cannot be matched. Therefore, the purpose was to match the magnitude of the measured data.

5.4.5.3 Carbon Tetrachloride Aquifer Concentration Time Histories. Simulation results used for comparison to measured aquifer data were taken from the second gridblock down in the aquifer model. The second gridblock extends from 8 to 16 m (26 to 52 ft) from the top of the model, which represents the water table. This depth interval corresponds to the depth of the screened interval in most of the monitoring wells near the SDA. The only exception is Well M4D, which is open from approximately 61 to 70 m (200 to 230 ft) below the water table. For this well, simulation results from a corresponding gridblock deeper in the model are used for comparison.

Figure 5-33 shows how the screened interval of several monitoring wells near the SDA corresponds to the vertical grid in the aquifer model. The elevation of the pumps is within the second gridblock from the top of model for most of the wells. In Figure 5-33, the top of the model grid was placed at the average elevation of the water table based on measurements from 2005. If the top of the model grid were placed 3 m (10 ft) higher, reflective of the water table elevation 10 years ago, nearly all of the pumps would fall within the second or third gridblock from the top.

Figure 5-34 compares the time history of measured CCl_4 concentrations to simulation results for aquifer wells in the vicinity of the SDA. The same data and well locations are shown on Figure 5-35. Model results and measured data are shown through the year 2005. Although the calibration focused on data collected before 1996, it is doubtful whether VVET operations have impacted aquifer results significantly by 2005. In addition, some wells were drilled or began being monitored after 1995 (i.e., Wells M14S, M15S, M16S, M17S, and OW2); therefore, no data for these wells exist from before 1995 to use for comparison.

Model results are a mixture of underpredictions, overpredictions, and good matches of the measured data. Only in a few cases do the model results and measured data compare well in magnitude and trend. This is not surprising because of the highly irregular and unpredictable distribution of CCl_4 in the aquifer. The model underpredicts concentrations at Wells M3S, M6S, M7S, M16S, A11A31, USGS-88, USGS-120, and the RWMC Production Well. However, the model matches the magnitude and trend of measured data quite well at Wells M1S, M4D, USGS-87, USGS-89, and USGS-90. The match is reasonable, but not quite as good, at Wells M14S, M15S and OW2. The model overpredicts concentrations at Wells USGS-117 and USGS-119, and considerably overpredicts concentrations at Well M17S, which is the only aquifer well inside the SDA boundary. However, the measured concentrations at Well M17S seem unreasonably low given the close proximity of the well to the VOC sources.

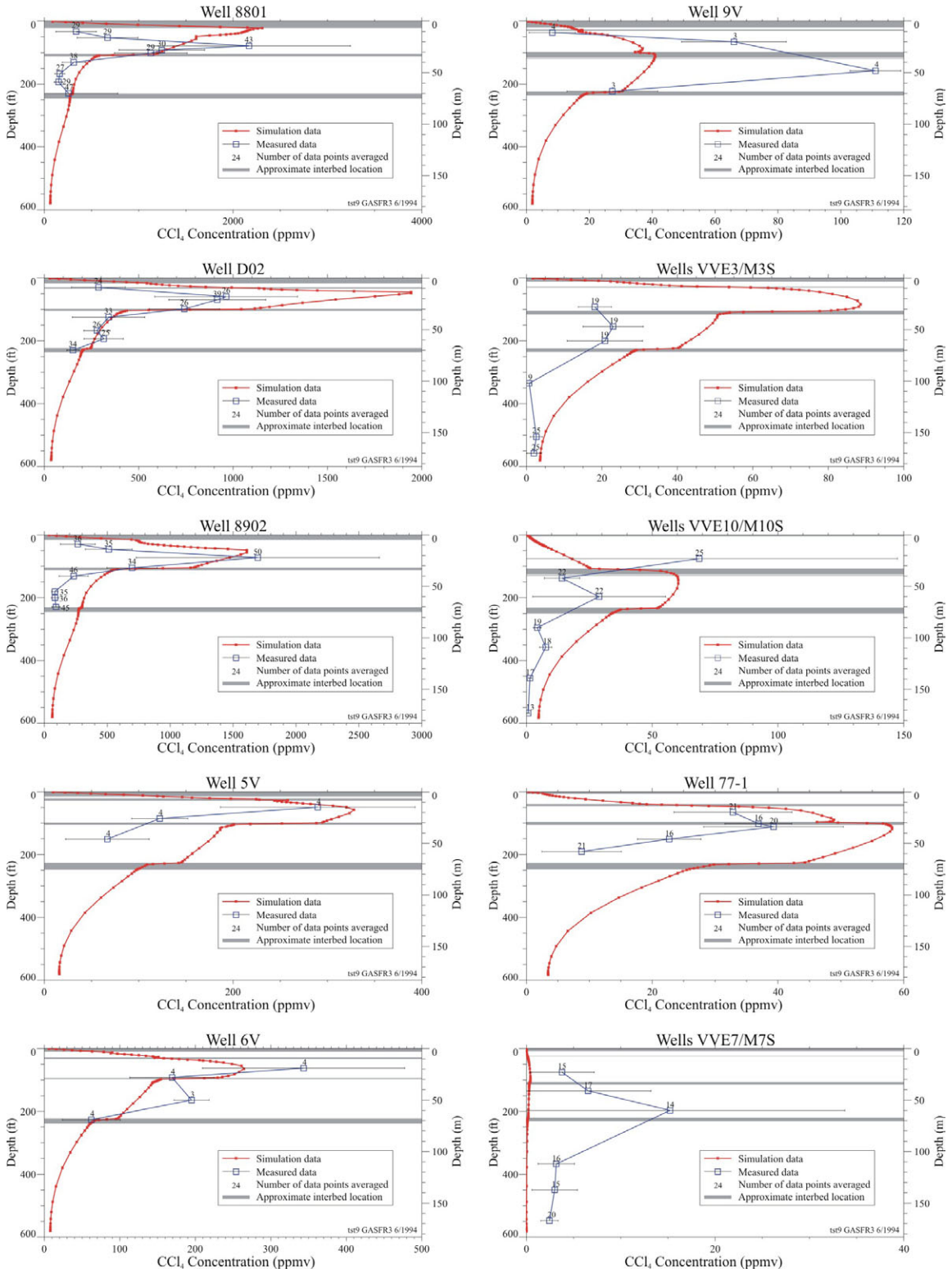

Figure 5-31. Comparison of simulated and measured carbon tetrachloride vapor concentration vertical profiles for select vapor-monitoring wells in the vicinity of the Subsurface Disposal Area. The simulated data are from June 1994. The measured data were averaged over a 4-year period from January 1, 1992 to January 1, 1996. Error bars on the measured data represent plus or minus 1 standard deviation.

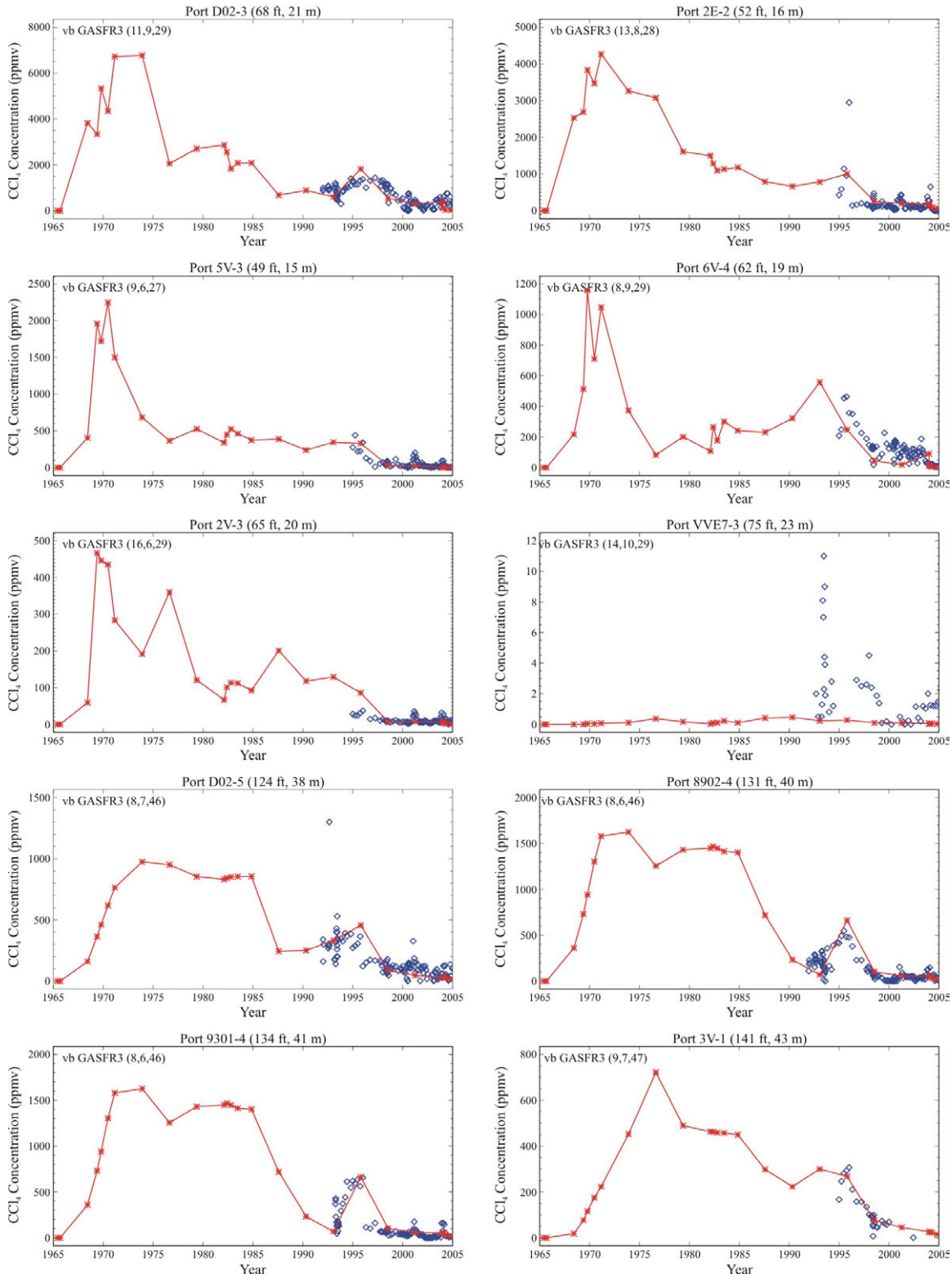

Figure 5-32. Comparison of simulated (stars) and measured (diamonds) carbon tetrachloride vapor concentration time histories for select vapor-monitoring ports in the vicinity of the Subsurface Disposal Area through the year 1995. The port name and depth below land surface is indicated above each graph.

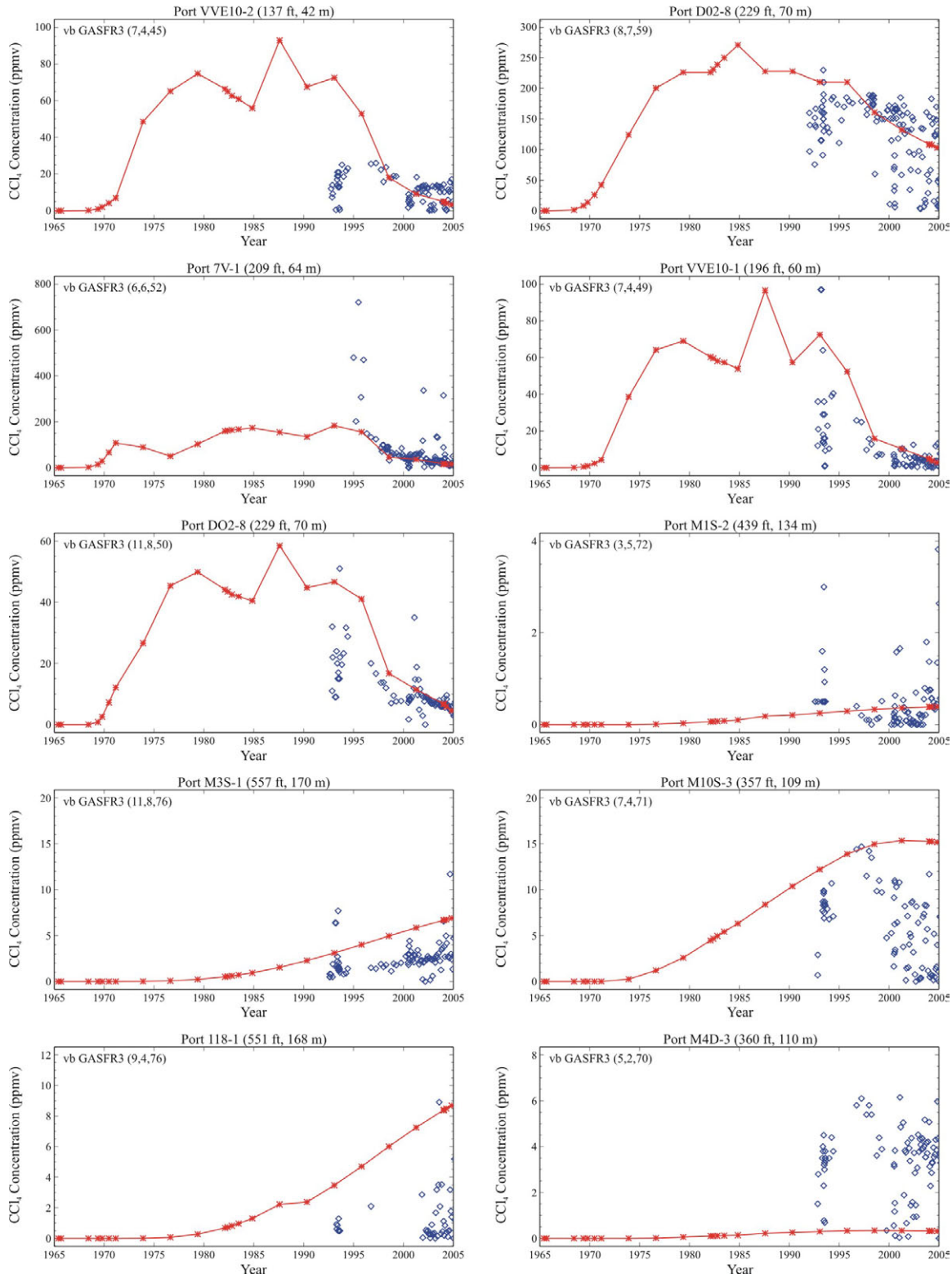

Figure 5-32. (continued).

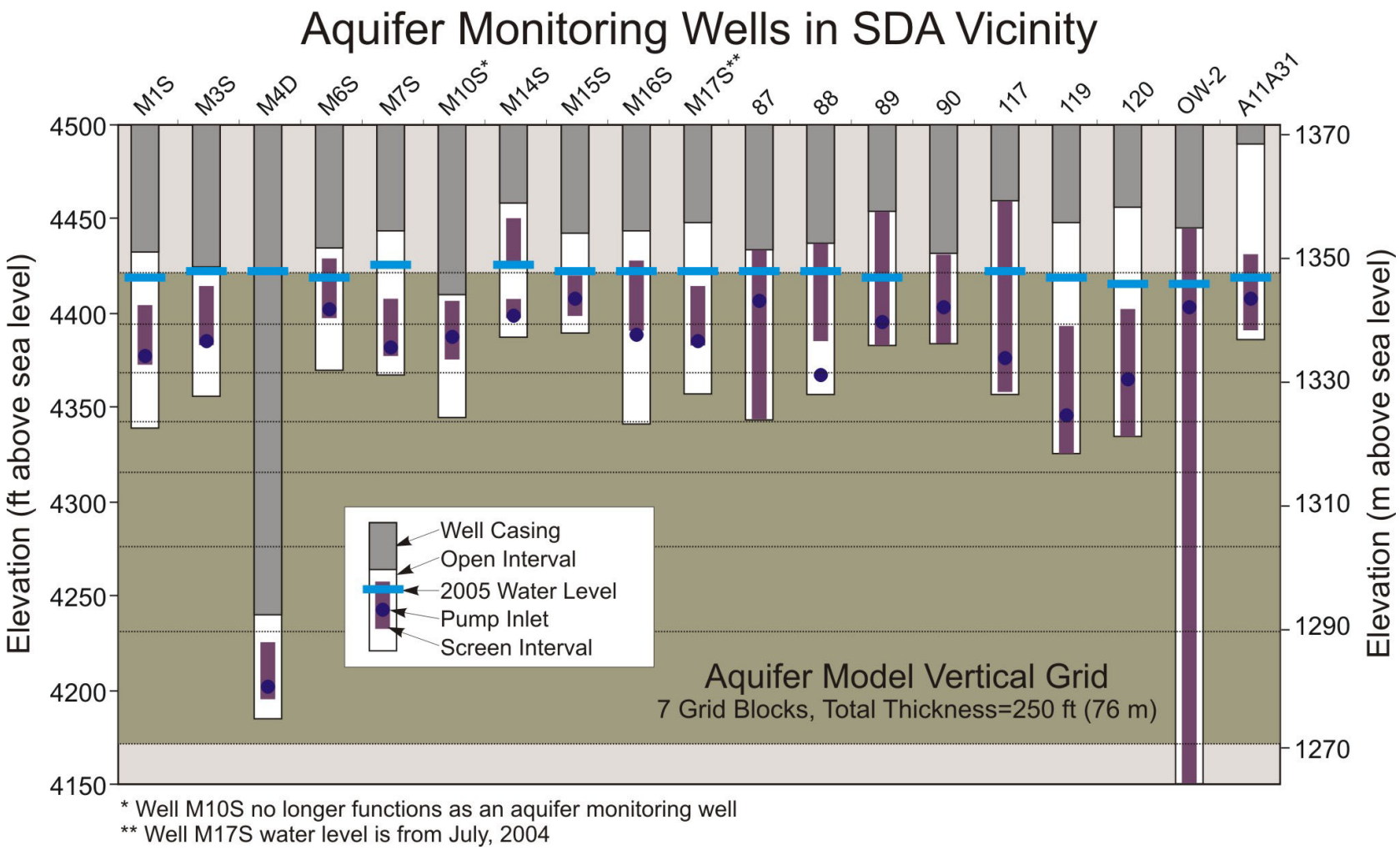

Figure 5-33. Screen intervals for aquifer monitoring wells in relation to vertical aquifer model grid discretization. The top of the model grid is placed at the average 2005 water table elevation of the wells shown.

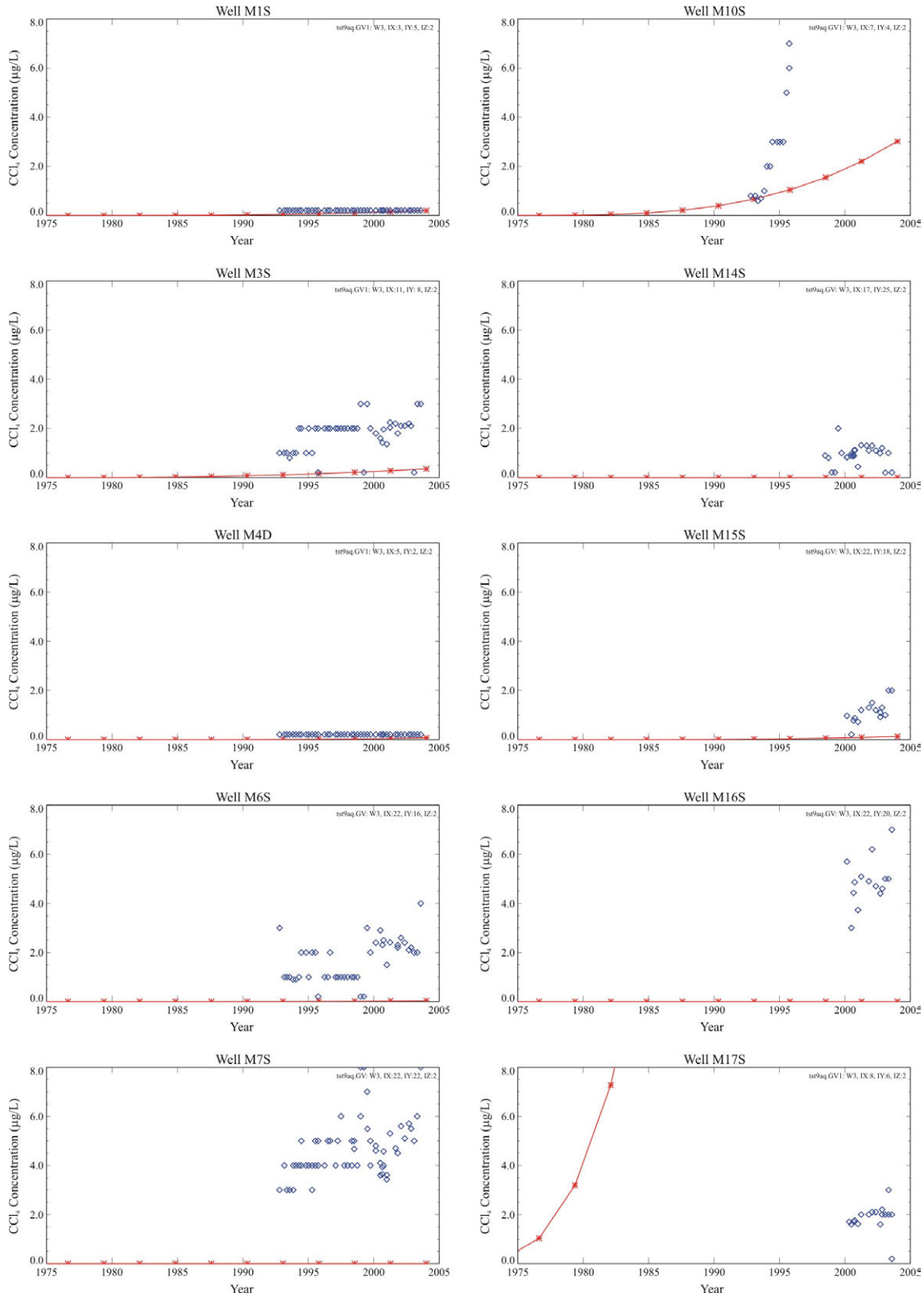

Figure 5-34. Time-history comparison of simulated (stars) and measured (diamonds) carbon tetrachloride concentrations in the aquifer at wells in and around the Subsurface Disposal Area through the year 2005.

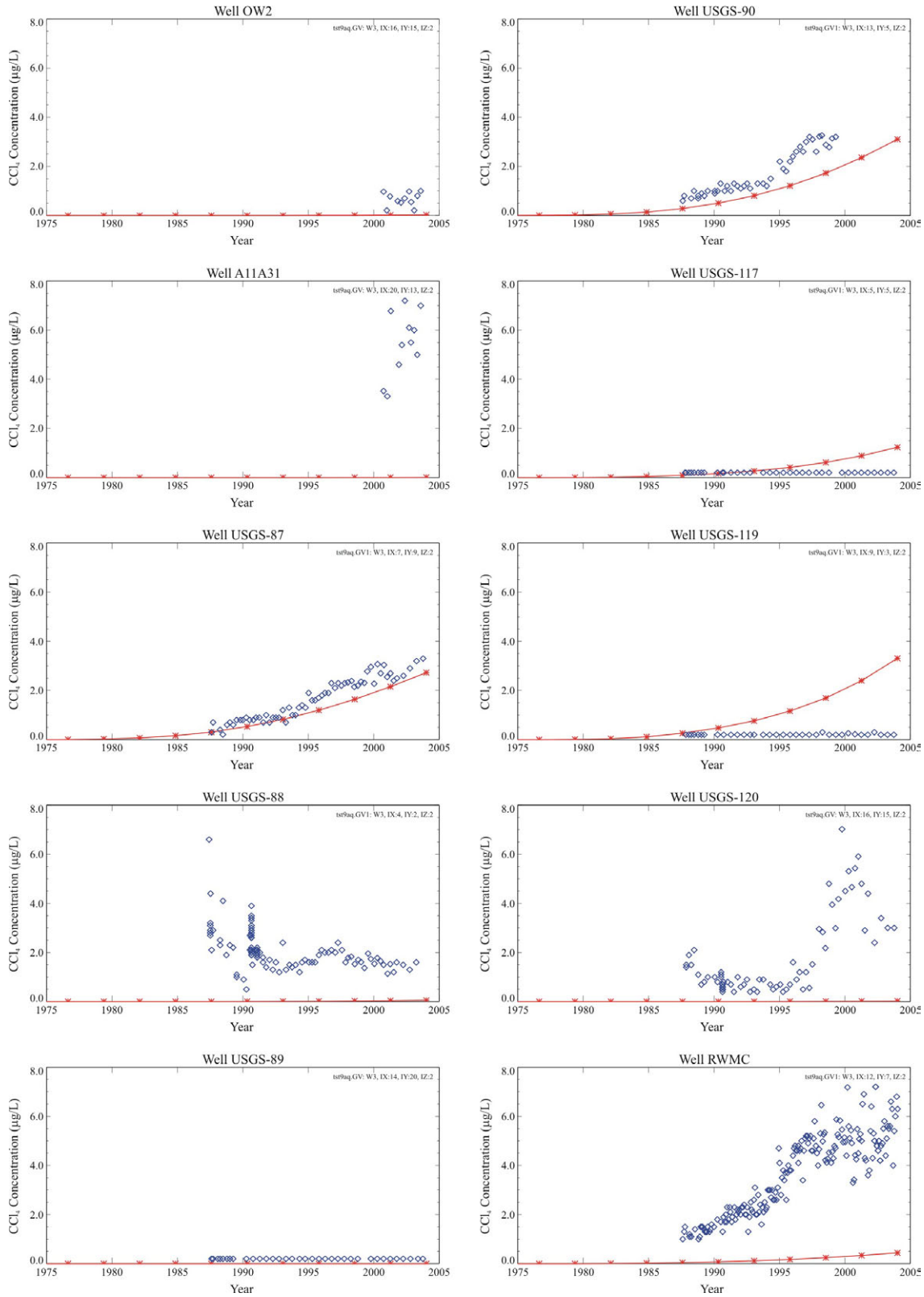

Figure 5-34. (continued).

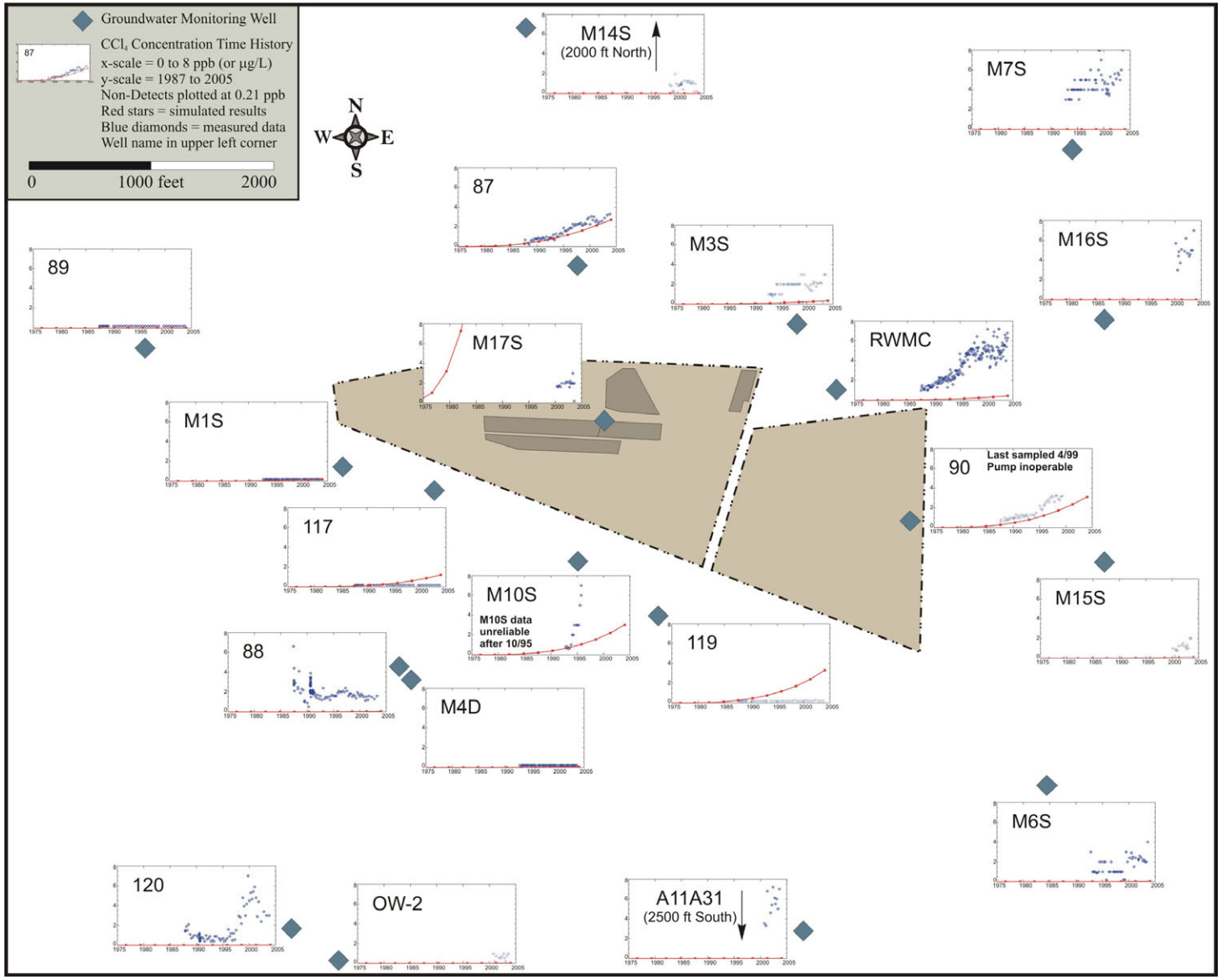

Figure 5-35. Time history of measured and simulated carbon tetrachloride concentrations in aquifer at wells in and around the Subsurface Disposal Area. The source pits shaded in the Subsurface Disposal Area are the primary carbon tetrachloride source pits.

In general, the RI/FS model results are similar to the IRA model results for the aquifer. Interim Risk Assessment model results at the RWMC Production Well agreed better because more VOCs in the IRA model were assigned to Pit 9, which is closer to the RWMC Production Well. However, knowledge of VOC waste burial locations has vastly improved since the IRA model, and it is likely that if the current distribution of VOC waste were used in the IRA model, the results would be similar to the results obtained for the RI/FS model.

5.4.6 Volatile Organic Compound Transport Model Calibration Summary

Numerous source and transport model simulations were performed in order to create a model that would adequately reproduce the observed migration of CCl_4 from the SDA, and predict, with a relatively high degree of confidence, future concentrations of VOCs and other contaminants that are transported in a vapor phase. The effort was aided considerably by modeling work performed for the IRA and other modeling efforts (e.g., Sondrup 1998).

The first step of calibration was to establish an appropriate source-release model that was compatible with the estimate of CCl_4 mass remaining in the pits. This involved investigation of several source-release parameter combinations. In the end, only one of the combinations that produced the desired result seemed reasonable. The next step was to calibrate the transport model by adjusting tortuosity values of the different material types in the model. Although numerous combinations of tortuosity values were investigated, the final tortuosity values were the same as the initial estimated values, except for a change in the fracture basalt tortuosity.

In general, the simulated results matched the observed data quite well close to the SDA, with one prominent exception—the model greatly overpredicted the aquifer concentrations at Well M17S. However, low concentrations in this well do not seem representative, given its proximity to the source. Also, the model did not do a very good job of matching the spread of contamination in the vadose zone. Other parameters of the model (e.g., fracture basalt anisotropy ratio, matrix basalt characteristic block length, and thickness of the low-permeability, low-porosity layer) were modified to increase spreading, and, although each by themselves improved the result, the model still could not match the overall breadth of the vadose zone plume. However, since the amount of CCl_4 on the outer fringes of the plume is a very small percentage of the total mass entering the aquifer, matching concentrations away from the SDA was a less critical part of calibration. Because of good agreement of simulated data to measured data within and near the SDA in both the vadose zone and the aquifer, the calibration was deemed successful.

5.4.7 Impact of Fluctuating Barometric Pressure Boundary Condition

Simulations were performed to quantify the impact of a fluctuating barometric pressure boundary condition. Figure 5-36 shows the mass flux of CCl_4 to the aquifer both with and without a fluctuating barometric pressure boundary condition. The results show that when barometric pumping is not included in the simulation, the flux to the aquifer increases. The increase is approximately 40% in the year 2000 and 30% in the year 2125, when the flux to the aquifer peaks. The results for flux to the atmosphere are similar, but in this case the flux decreases when barometric pumping is not included. Therefore, not including barometric pumping is conservative for the groundwater pathway, but is not conservative for the air pathway.

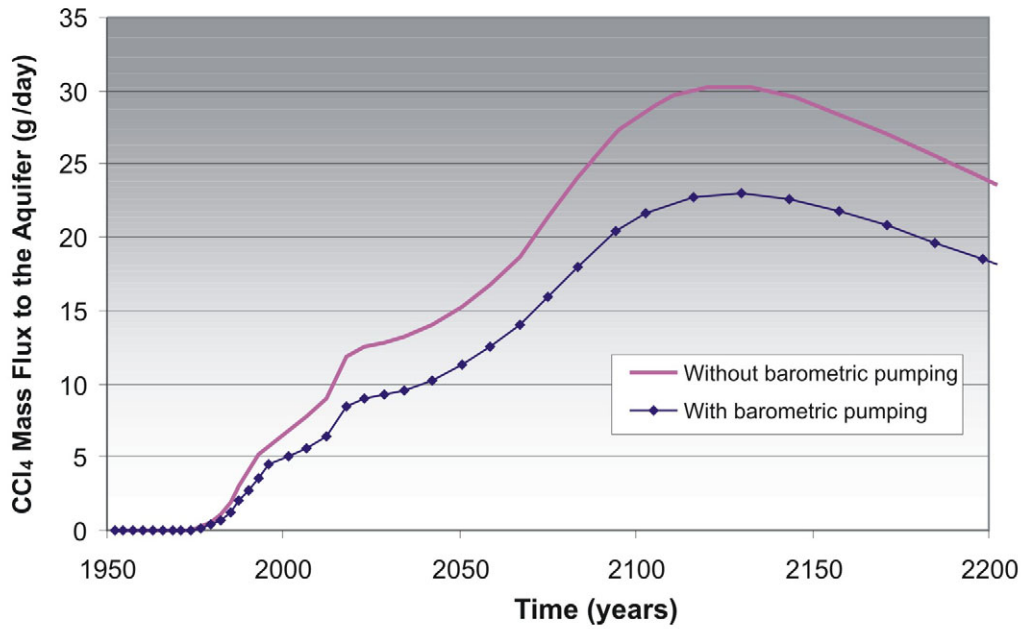

Figure 5-36. Time-history comparison of simulated carbon tetrachloride mass flux to the aquifer, with and without surface barometric pressure fluctuations.

5.5 Dual-Phase Carbon-14 Simulations

In the ABRA, C-14 was simulated as a strictly dissolved-phase contaminant. This meant that C-14 could not partition into the gaseous phase and undergo additional transport processes (e.g., diffusion in the gaseous phase). Therefore, C-14 could not diffuse out through the upper surface of the simulation domain (land surface). This was a conservative approach that maximized C-14 concentrations in the groundwater pathway. However, in the ABRA, the C-14 concentrations in the groundwater pathway were overpredicted by two to three orders of magnitude due to this conservatism when compared to currently observed concentrations from contaminant monitoring.

For the RI/FS model, the simulation of C-14 was modified to allow C-14 to partition into the gaseous phase. This means that C-14 existed in both the aqueous and gaseous phase and underwent transport in both phases simultaneously. This approach to simulating C-14 was most easily accommodated by adopting the dual-continua model implemented for the VOC modeling previously described. Before simulating C-14 with the full-scale dual-continua vadose zone model, two interim simulation efforts were conducted to determine the appropriate partitioning parameters and the possible effect of increased diffusion to land surface in the immediate vicinity of the beryllium blocks, which contain a large fraction of the C-14 inventory. These two interim studies are briefly described first, followed by the implementation of C-14 in the dual-continua vadose zone model developed for VOCs.

5.5.1 Carbon-14 Partitioning from Column Experiment

A simulation study was conducted to determine the correct partitioning for C-14 in a combined aqueous- and gaseous-phase system. This simulation study used experimental data from a 3-m (9.8-ft) high × 0.9-m (3-ft)-diameter mesoscale column where an aqueous-phase tracer (i.e., bromide), a gaseous-phase tracer (i.e., SF_6), and C-14, which partitioned into both phases, was monitored. The column experiment was designed to mimic conditions in the waste zone at the SDA and had a constant

low flux of water applied at the surface. The column experiment also allowed gaseous-phase diffusion out the surface. Inverse modeling was applied to this set of column data to match both the aqueous- and gaseous-phase transport. This inverse modeling study is documented in Martian (2003).

Parameters describing partitioning of C-14 comprise the primary output from the inverse study used in RI/FS modeling. In Martian (2003), C-14 was treated as if it were carbon dioxide, with the partitioning estimated from Henry's Law. The resulting TETRAD input parameter A was 2.9×10^4 kPa and is essentially the inverse of the effective Henry's Law constant, assuming constant temperature and pressure.

The inverse modeling application resulted in excellent matches to observed water flux, breakthrough of the bromide and SF_6 tracers, and breakthrough of C-14 from the column in both the aqueous and gaseous phases. Because of this good agreement, a conclusion was made that effective Henry's Law partitioning adequately described the partitioning of C-14 in the column and could be used, with the normal cautions on upscaling, for the RI/FS vadose zone modeling.

5.5.2 Carbon-14 Beryllium Block Near-Field Simulation

A significant portion of C-14 buried in the SDA is in beryllium reflector blocks. As beryllium corrodes, C-14 and tritium are released and partition into the aqueous and gaseous phases. With contaminant release concentrated in a small area within the surficial sediment, higher gaseous-phase concentration gradients would be established between release sites and the short distance to land surface, where movement of air maintains a gaseous-phase concentration of essentially zero. A hypothesis that this increased concentration gradient could result in additional release of C-14 from the subsurface was tested in a study documented in Nalla (2004). Subsurface and atmospheric sampling from an instrumented location in the SDA was used in an inverse modeling study.

Even with the less-than-desired match to observed C-14 and tritium migration behavior, it was concluded that a substantial fraction, on the order of 80% of the C-14 mass, is released to land surface through diffusion. This indicated that it was indeed important to include diffusional loss through land surface in the RI/FS model. The Nalla (2004) recommendation to reduce C-14 release from beryllium reflector blocks by 80% for use in the subsurface model was not implemented; that implementation would have resulted in accounting doubly for the release to the atmosphere because surface diffusional losses also were included in the RI/FS model.

5.5.3 Operable Unit 7-13/14 Model Carbon-14 Implementation

The VOC dual-continua model described in Section 5.4 was used to simulate transport of C-14. Use of this dual-continua model takes advantage of additional calibration achieved in VOC modeling. The assigned contaminant mass locations for C-14 were different from locations for the strictly aqueous-phase contaminants, as discussed in Section 4.3.7.3.

5.5.3.1 Carbon-14 Model Boundary Conditions. The aqueous-phase boundary conditions were kept the same as the RI/FS VOC dual-continua model. Two changes were made to the gaseous-phase boundary conditions. First, the lateral zero-concentration boundaries were omitted because they were unnecessary for simulation of C-14. They were unnecessary because the C-14 contaminant mass did not reach the boundaries in appreciable quantities, as it did for VOC contaminants. Second, similar to VOC modeling, barometric-pressure fluctuations at land surface were eventually neglected in C-14 modeling. They were neglected primarily for computational expediency, because including barometric fluctuations required using a minimum 10-day time step, which resulted in long run times—on the order of 2 months of computer processing time—to achieve approximately 700 years of simulation time (the radionuclide

simulations for the base case and sensitivity simulations were all planned to be simulated to 1,000 years into the future, and out to peak concentrations within 10,000 years). This was not feasible within even the most generous time constraints. Fortunately, the effect of neglecting barometric fluctuations was conservative, because more C-14 mass was retained in the simulation domain and migrated through the groundwater pathway.

The effect of not including barometric fluctuations was tested by making comparative simulations, with and without barometric pumping. These comparisons used the sensitivity simulation of the comparative base case (i.e., B4ng_g8), which comprised no removal of Pit 4 inventory and no grouting of beryllium blocks. Figure 5-37 shows a comparison of the maximum simulated aquifer concentration as a function of time at a depth of 12 m (39.3 ft) anywhere in the simulation domain, with and without barometric pumping. Concentrations for each simulation are extracted for both anywhere in the model domain and anywhere in the domain outside the SDA fence. The effect of not including barometric-pressure fluctuations for locations outside the SDA fence was to increase the simulated aquifer concentration by approximately 20%. It was slightly larger inside the SDA, with an approximate 25% increase. Implementing C-14 simulations without barometric-pressure fluctuations brought back some of the conservatism that had been reduced by simulating gaseous-phase partitioning.

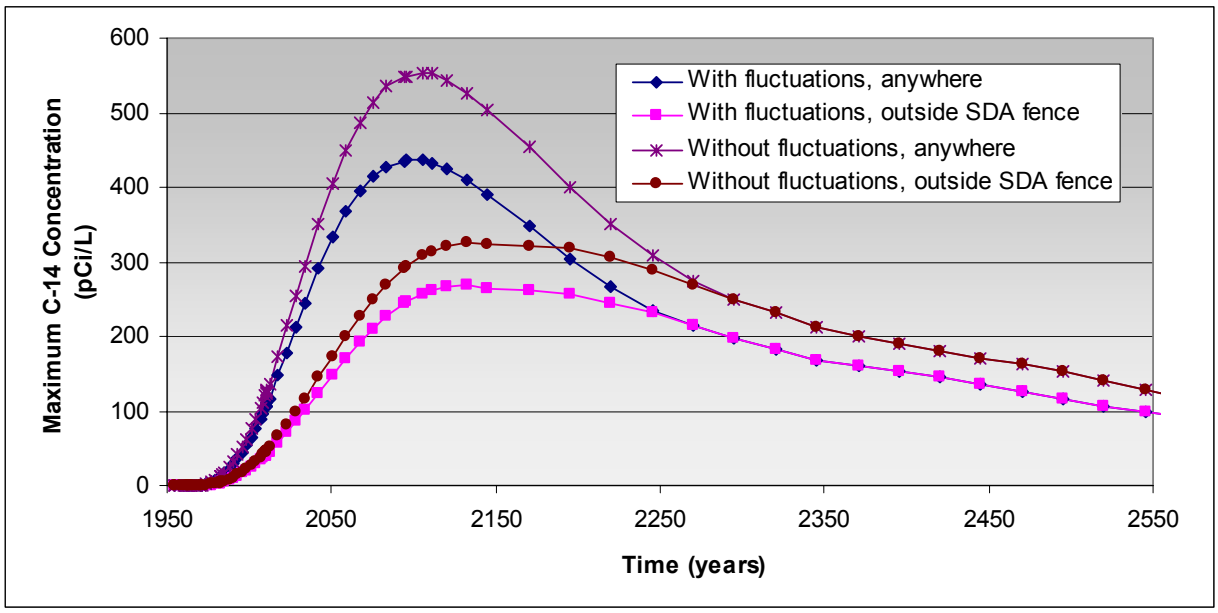

Figure 5-37. Maximum simulated aquifer carbon-14 concentration, anywhere in the simulation domain, at a depth of 12 m (39.3 ft), with and without surface barometric pressure fluctuations.

5.5.3.2 Carbon-14 Comparison without Gaseous-Phase Partitioning. To demonstrate the effect of including gaseous-phase partitioning in the RI/FS model, an additional simulation was performed where C-14 source release was imposed on the single-continua model used for contaminants that migrated strictly in the aqueous phase, essentially reverting to the method used in the ABRA for simulating C-14 migration. Figure 5-38 shows a comparison of the maximum simulated concentration anywhere in the aquifer for case B4ng_g8 with gaseous partitioning in the vadose zone model and diffusion at land surface to the same simulation where gaseous-phase partitioning is not included. In the case where gaseous partitioning is not allowed, no diffusive loss to land surface occurs. The results are presented with both a linear and logarithmic scale concentration axis because the difference is so large (i.e., approximately two orders of magnitude).

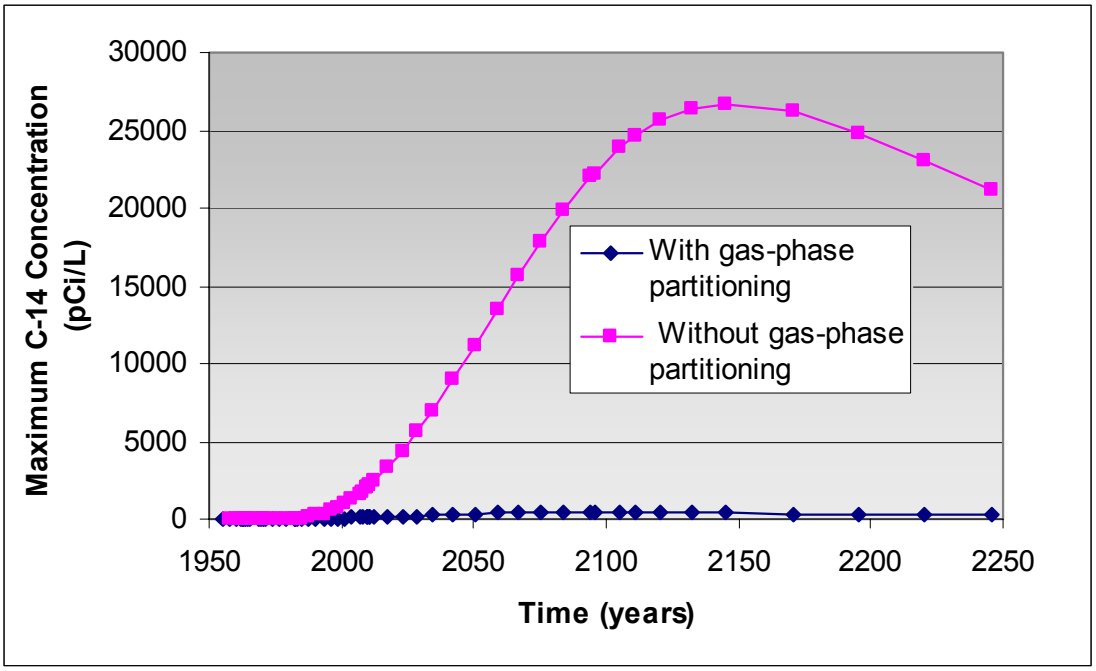

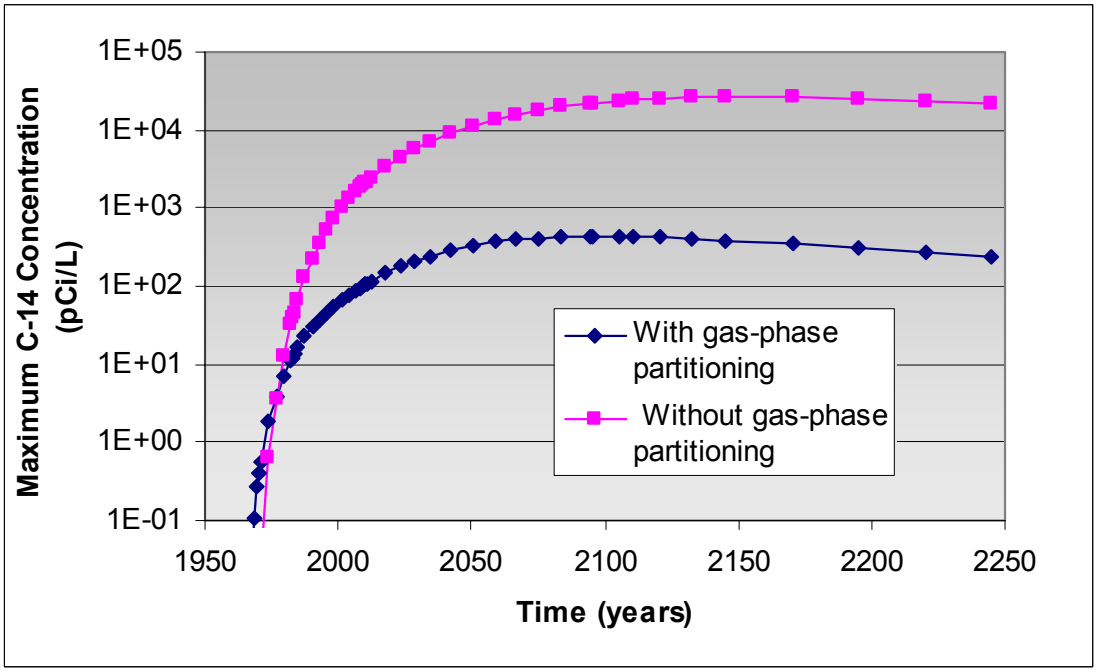

Figure 5-38. Maximum simulated concentration anywhere in the aquifer, with and without gaseous-phase partitioning in the vadose zone transport model.

5.5.3.3 Carbon-14 Model Remedial Investigation and Baseline Risk Assessment Base-Case Simulation Results. The base-case final simulation for C-14 did not include barometric-pressure fluctuations. No consistently elevated concentrations or trends have been in evidence for C-14 monitoring in the vadose zone. One location that has shown detections is the perched water in Well USGS-92 above the C-D interbed. Figure 5-39 shows a comparison of the simulated C-14 aqueous-phase concentration at the gridblock representing this location to the monitoring results. No

background concentration is added to the simulation results. Even with inclusion of gaseous-phase partitioning and diffusional losses to land surface, the simulated concentrations still overpredict the sporadic observed values, indicating the simulation result is still conservative.

The simulated aquifer concentration time histories for C-14 at locations containing aquifer-monitoring wells are shown in Figure 5-40. Monitoring results for C-14 that represent 3σ detections, or greater, are included as blue diamonds on the time-history plots along with a whisker-style indication of their associated 1σ uncertainties. Results show the sporadic nature of detections and demonstrate that simulation results are conservative because they overpredict measured groundwater concentrations in Wells M17S and USGS-119, though not nearly to the degree recorded in the ABRA. The overprediction at Well M17S is consistent with CCl_4 results in that the model overpredicts measured data. Figure 5-41 shows simulated aquifer C-14 concentrations in the first-level refined grid for the aquifer domain. The simulated elevated concentrations are more centrally located beneath the southeastern corner of the SDA when compared to other contaminants (e.g., nitrate).

5.5.4 Summary

There is a substantial reduction in simulated concentration results when gaseous-phase partitioning of C-14 is included in the RI/FS model. Excluding barometric pressure fluctuations at land surface was conservative since the simulated groundwater concentrations were higher than they would have been had barometric pressure fluctuations been included. However, conservatism is slight and does not negate the reason for including gaseous-phase partitioning in the first place.

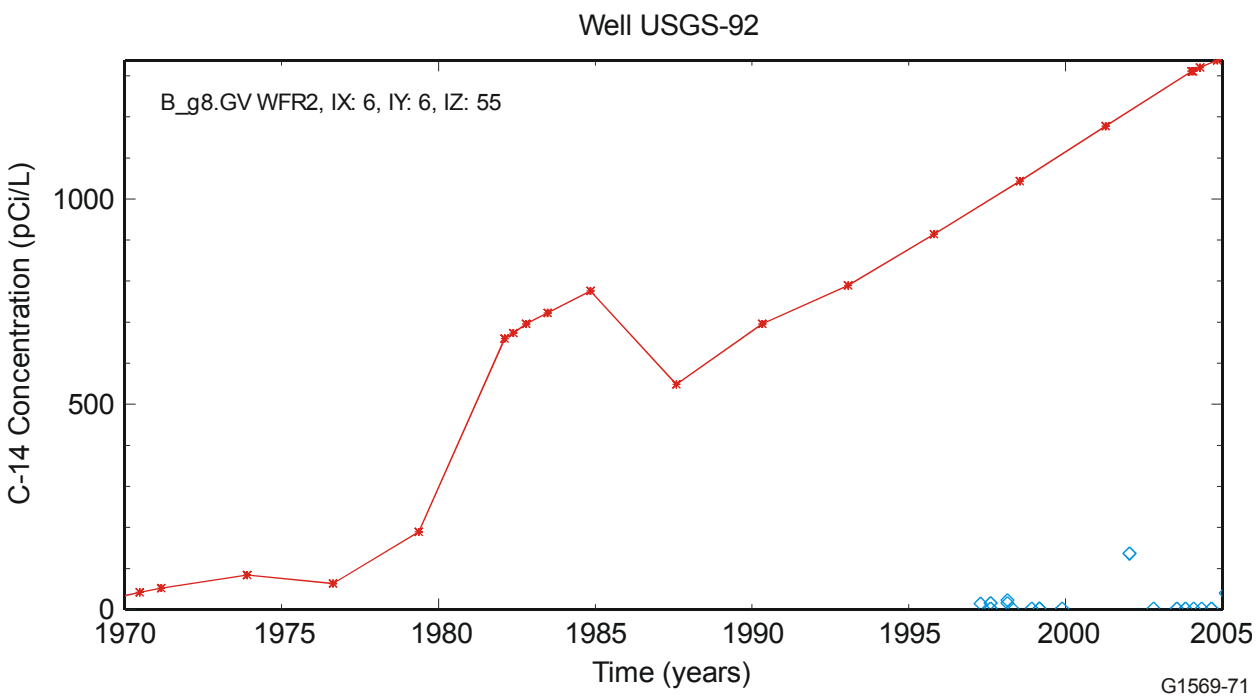

Figure 5-39. Time history of simulated (red line) and observed (blue diamonds) carbon-14 aqueous-phase concentrations at Well USGS-92.

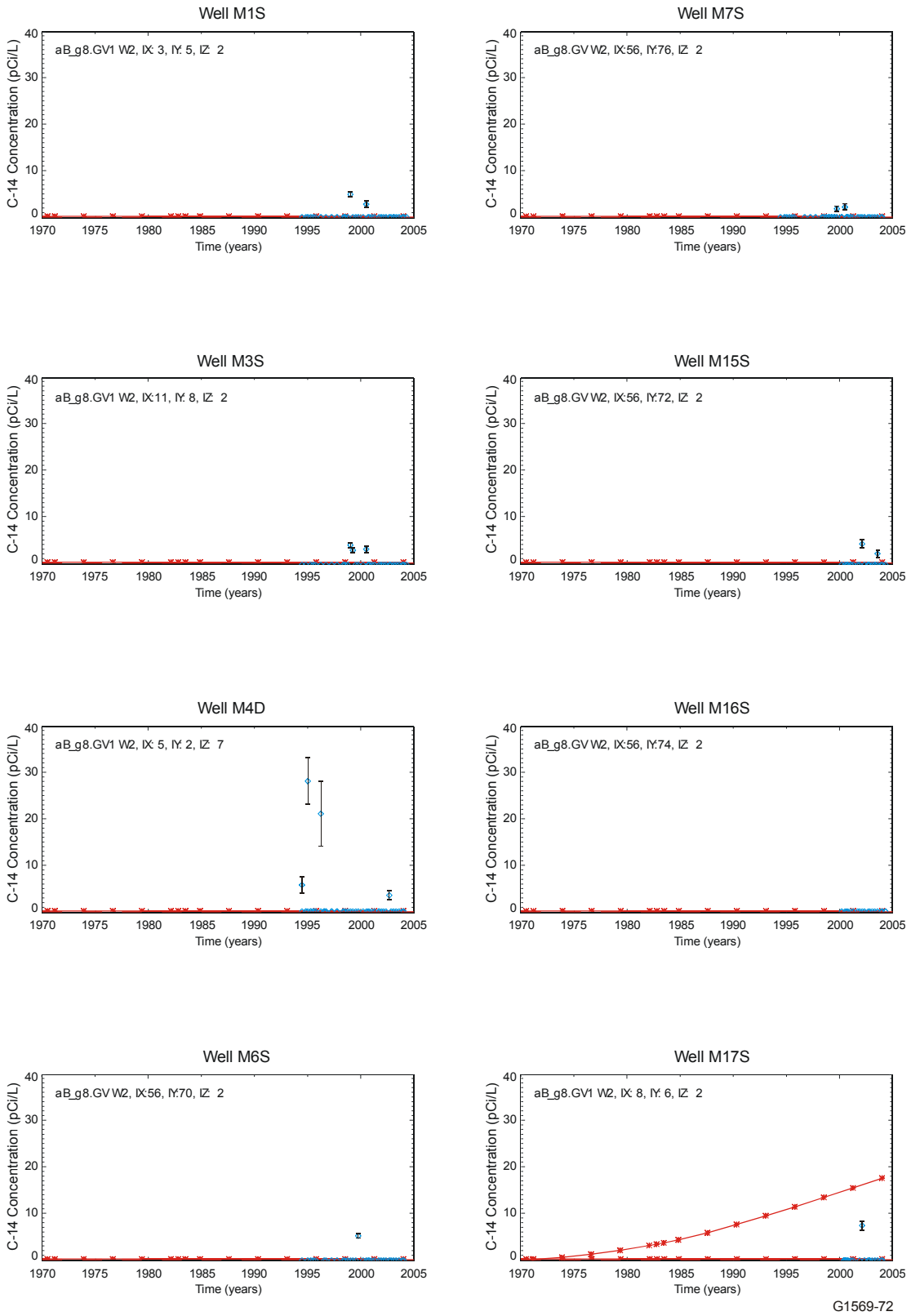

Figure 5-40. Comparison of time histories for simulated carbon-14 concentrations (red line) to observed monitoring results (blue diamonds) for aquifer monitoring wells in the vicinity of the Subsurface Disposal Area.

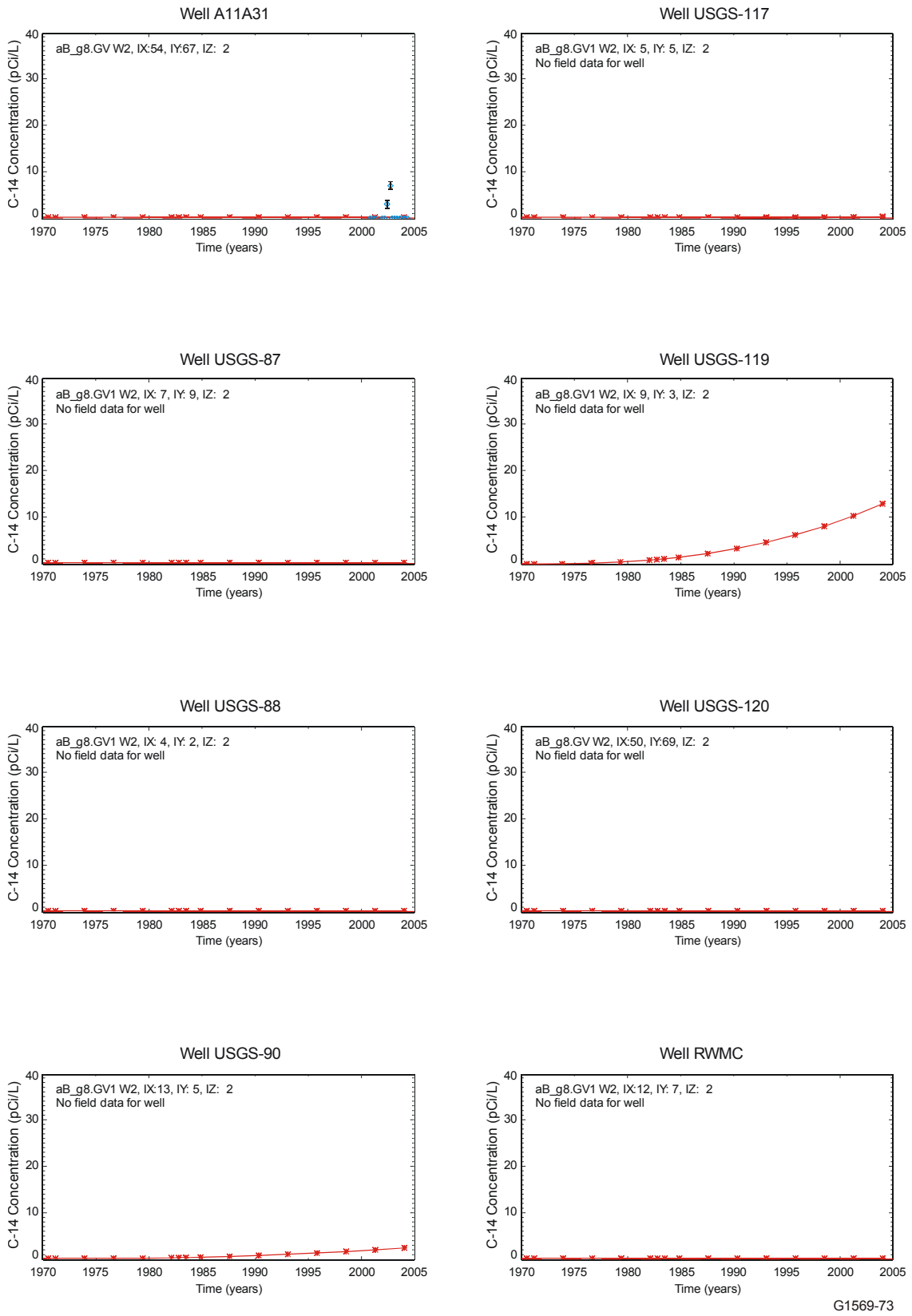

Figure 5-40. (continued).

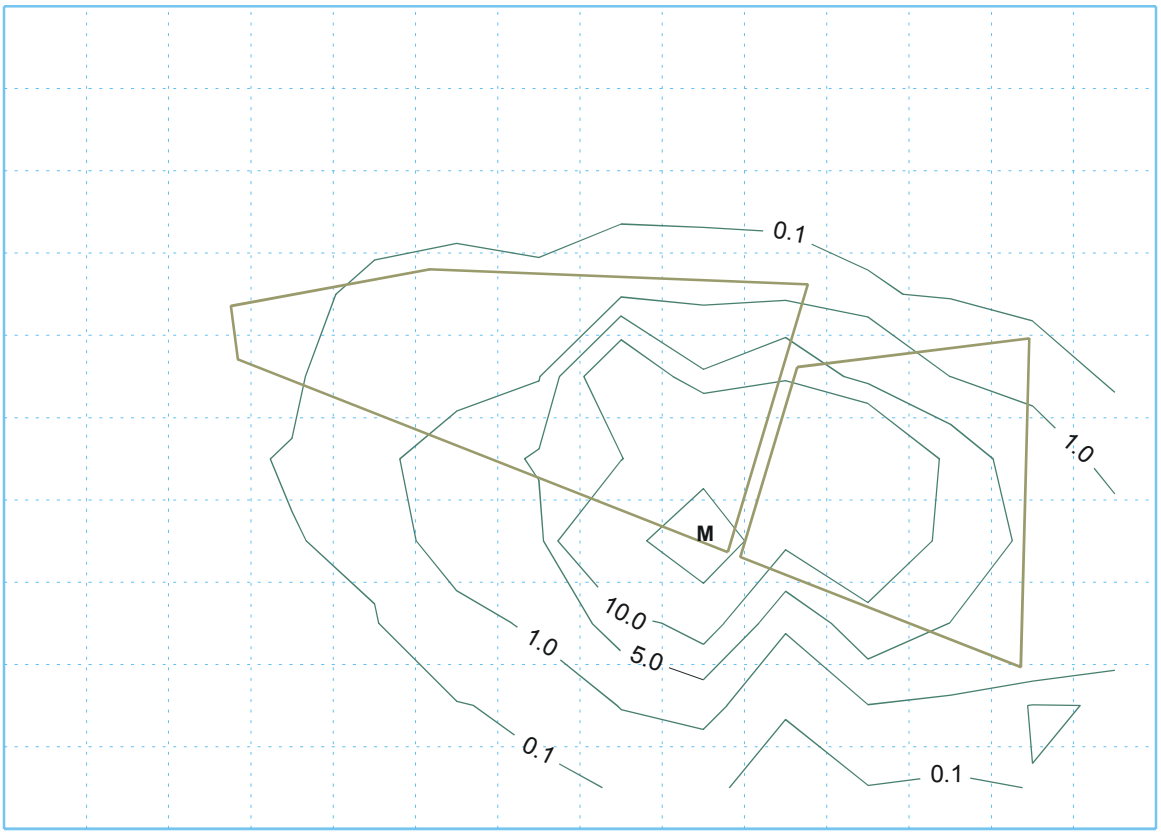

aB_g8.GV1: W2: IZ= 2: 1/2004

M = Maximum value = 8.92E+ 01

G1569-79

Figure 5-41. Simulated aquifer carbon-14 concentrations (pCi/L) at the 12-m (39.3-ft) depth for the year 2004.

6. OPERABLE UNIT 7-13/14 FATE AND TRANSPORT MODEL RESULTS

This section presents comparisons of the base-case model to contaminant monitoring results, describes sensitivity simulations performed for the draft RI/BRA, and describes simulations performed for the feasibility study.

6.1 Baseline Risk Assessment Base-Case Simulation with Comparison to Monitoring Results

The numerical model, implemented as discussed in Sections 4 and 5, was used to simulate each COPC for the RI/BRA base case. The source-release model provided contaminant inputs to the vadose zone model. This section presents comparisons of simulated results with observed concentrations for selected contaminants to illustrate transport model performance. These comparisons are presented in sequence for the vadose zone from 0 to 10.7 m (0 to 35 ft), the deeper vadose zone from 10.7 to 76.2 m (35 to 250 ft) that contains the B-C and C-D interbeds, and the aquifer. The comparisons are primarily time histories and aquifer concentration contours at points in time. The contaminants, for which simulation results are presented in the vadose zone, are U-238, Tc-99, and nitrate. These contaminants were identified in Section 4 of the draft RI/BRA as showing either elevated concentrations relative to background or significant increasing trends. In the aquifer, the presentation focuses on simulation results for nitrate and chromium, because those contaminants can be discerned above background aquifer concentrations. Additionally, time histories are presented for all radionuclide contaminants with any detections. Simulation time histories for CCl_4 were presented previously in Section 5.4.5. The full set of CCl_4 results is contained in Appendix G.

6.1.1 Vadose Zone: 0 to 10.7 m (0 to 35 ft)

This section focuses on the U-238, Tc-99, and nitrate simulation results for those locations showing elevated concentrations or trends in the vadose zone at depths less than 10.7 m (35 ft). In general, this region encompasses the waste zone and surficial sediment down to the first basalt interface. Because there can be multiple lysimeters at different elevations for an individual well location, lysimeters are referred to in this section using a combined well name-lysimeter number identifier.

6.1.1.1 Uranium-238. From Section 4 of the draft RI/BRA, lysimeters at Wells PA01, PA02, W08, and W23 show substantially elevated concentrations relative to an estimated background concentration of 1.1 pCi/L for the vadose zone. This background concentration is added onto simulation results in the following time histories. The first set of time histories shown in Figure 6-1 is for lysimeters at Wells PA01, PA02, W08, 98-4, and W25; all five wells are located in the east-central portion of the SDA. At first impression, the simulation results show almost no agreement; however, this difference is explained by the relationship of the gridblocks containing the lysimeters to the locations where U-238 is released from the source model into the vadose zone model. The locations of the lysimeters can be seen in Figure 6-3. For example, Figure 6-1 also shows a simulated concentration time history for U-238 for a gridblock that is one gridblock north of the location containing Well PA02-L16. This latter gridblock location is assigned the Pad A waste stream. The time history at this location shows better agreement with observed monitoring results. The concentrations are slightly underpredicted, but are well within the same order of magnitude. Lysimeters in Wells PA01 and W08 also are not in gridblock locations that have a U-238 source release superimposed on them; for similar reasons, these wells show poor agreement with observed concentrations. Lysimeters in Wells 98-4 and W25 show similar behavior, with location relative

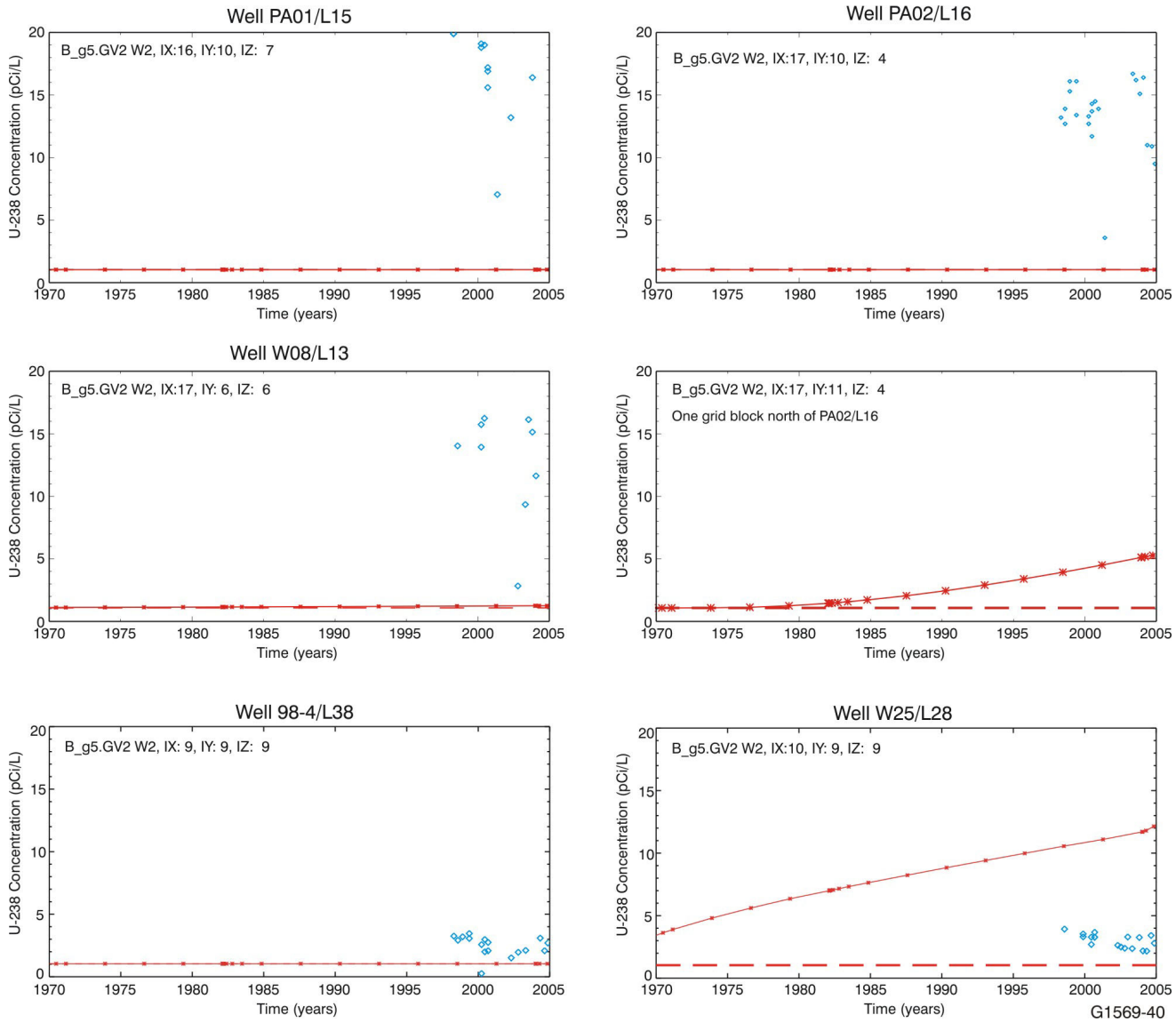

Figure 6-1. Time-history comparison of simulated (red line) and observed (blue diamonds) concentrations for uranium-238 in the lysimeters at Wells PA01, PA02, and W08. Background concentration is indicated by the dashed line.

to gridblocks where waste streams are applied as being important. The lysimeter in Well 98-4 corresponds to the gridblock one cell west of the Pit 4 waste stream and shows reasonable agreement with monitoring data, which is similar to the estimated background. The lysimeter in Well W25, however, just barely corresponds to the westernmost gridblock receiving the Pit 4 waste stream, and the simulated results overpredict monitoring results, which again are similar to the estimated background concentration. With a model as coarsely discretized as the RI/FS model, some locations will show good agreement and some locations will not, depending on where mass is loaded into the vadose zone model from the source model. Also, simulated concentrations represent an average for the entire gridblock, whereas monitoring results represent point data that will vary spatially.

The simulated concentration time history shown in Figure 6-2 is for the three lysimeters in Well W23, located in the western portion of the SDA. This gridblock corresponds to the source-release area of Trenches 1 through 10, which does have U-238 mass imposed on it. As a result, simulated concentrations are nonzero for this location and, although low compared to the observed concentrations, are within an order of magnitude of the monitoring results.

To avoid giving the erroneous impression that U-238 is underpredicted everywhere, vertical cross sections, which include source-release locations in the second-level refined grid, are presented in Figure 6-3. Figure 6-3 shows the locations of the cross sections—two west-east and one south-north. The additional blue shading on the locations of the cross sections indicates source-release gridblocks, with the darker shading showing those locations with higher source-release fluxes and the lighter shading showing those locations with lower source-release fluxes. Figure 6-4 shows cross sections from the indicated locations for a simulation time corresponding to Calendar Year 2004. Monitoring results from this time period are posted on the plot at their approximate location. Also posted beneath these two values is the number of monitoring results that were available from this lysimeter from an arbitrary 2-year period before and after the indicated time. Only samples with detections are posted. Lithologic divisions can be discerned in the cross sections. Land surface is the uppermost solid line and shows slight variations in surface elevation. Solid lines also indicate the bottom of the surficial sediment and the A-B interbed.

The effects of discretization and where U-238 mass is assigned in the model can be clearly seen in the cross sections shown in Figure 6-4. The effect of the U-238 mass assignment, relative to the location of Well PA02, also can be seen in the cross sections. The southernmost Pad A waste stream gridblock shows up in cross sections of both the W-E Section: Plane 11, and in the S-N Section: Plane 17. Well PA02 is in the gridblock just to the south, and it shows very little simulated U-238 mass in contrast to monitoring results for Well PA02, which show U-238 is elevated. In addition, simulation results in the cross sections show that the majority of the U-238 remains within the lower part of the surficial sediment and selectively migrates downward, with some influence from gaps in the A-B interbed.

6.1.1.2 Technetium-99. Only one vadose zone location in the 0- to 10.7-m (0- to 35–ft) depth zone shows an increasing trend for Tc-99. This location is Well W23 and Figure 6-5 shows the simulated results compared to monitoring results for this location. The estimated background concentration for Tc-99 in the vadose zone is 0 pCi/L; therefore, it is not added to the time-history simulation results. Time histories in Figure 6-5 are presented using a logarithmic scale for concentration due to Tc-99 being substantially overpredicted at this location, as well as almost everywhere else in the simulations. Figure 6-6 shows a west-east cross section from the second-level refined grid for simulated Tc-99 concentrations in Calendar Year 2004. The Tc-99 overprediction in the vadose zone model is probably caused by the source-release model overpredicting the release of Tc-99.[d]

---

d. A task to improve the source-release and fate and transport modeling for Tc-99 is ongoing for incorporation into the Operable Unit 7-13/14 feasibility study to provide a better basis for remedial decisions.

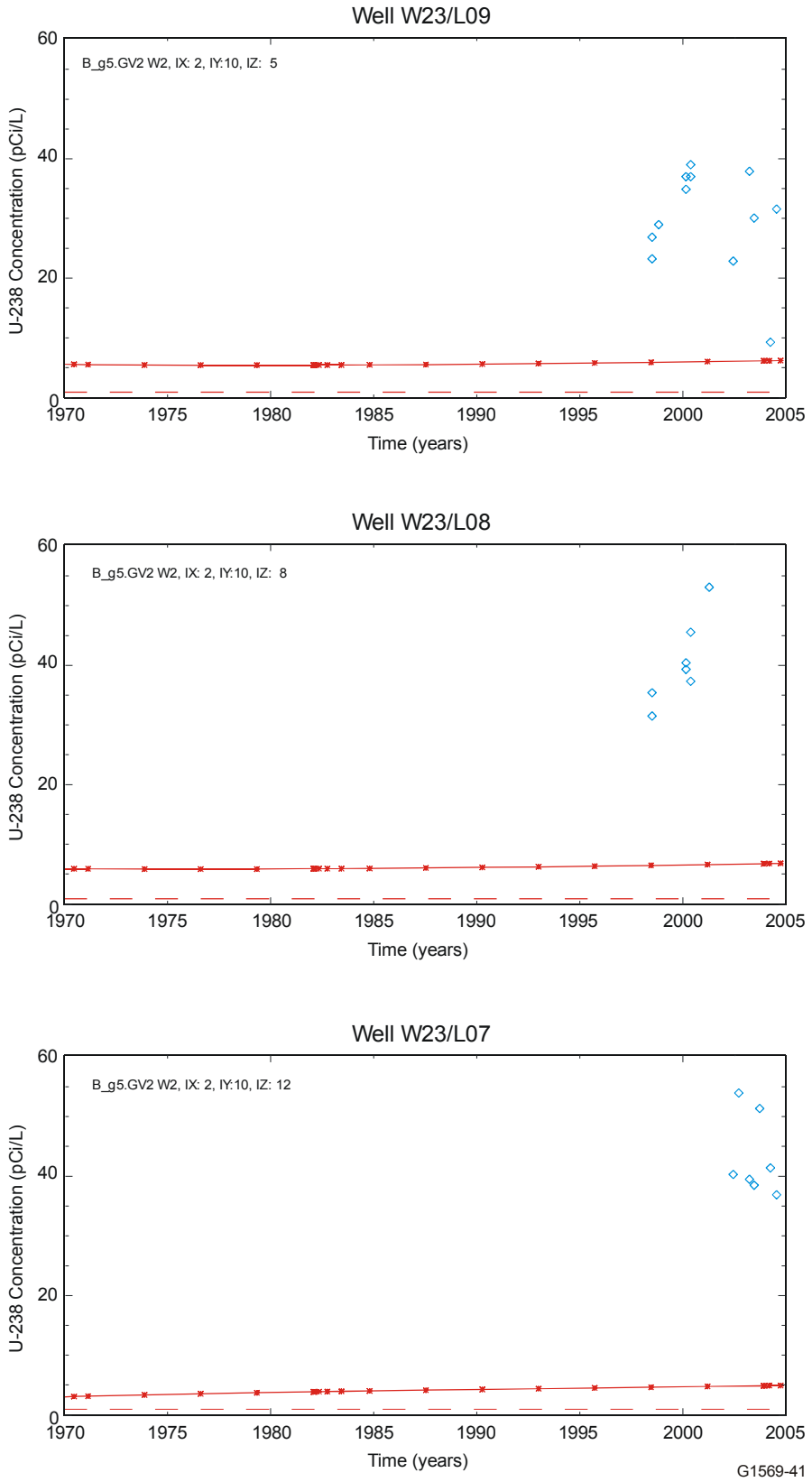

Figure 6-2. Time-history comparison of simulated (red line) and observed (blue diamonds) concentrations for uranium-238 in the lysimeters at Well W23. Background concentration is indicated by the dashed line.

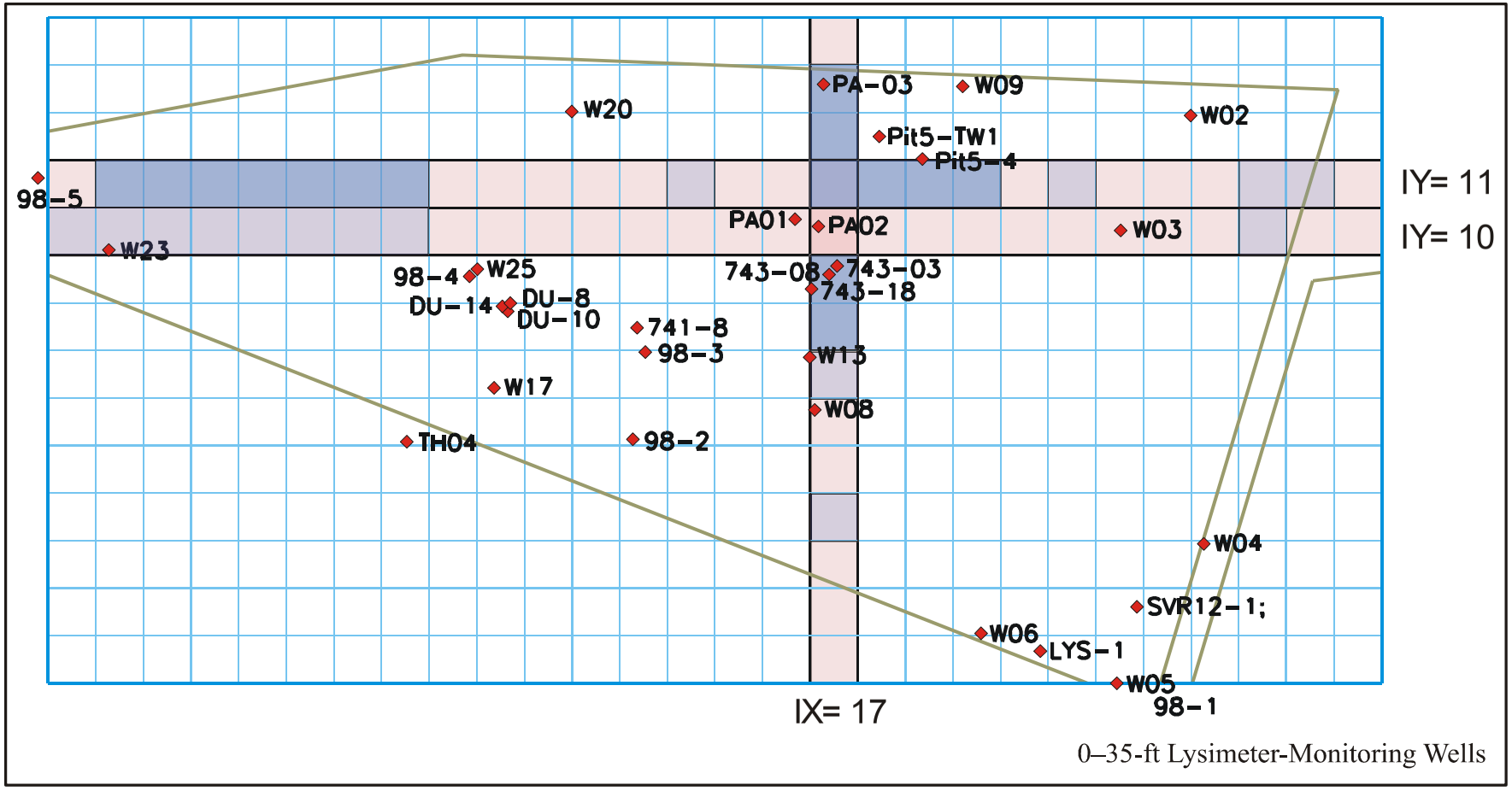

G1569-17

Figure 6-3. Cross sections in the second-level refined grid vadose zone domain. Darker blue shaded gridblocks indicate locations of primary uranium-238 mass loading from the source-release model.

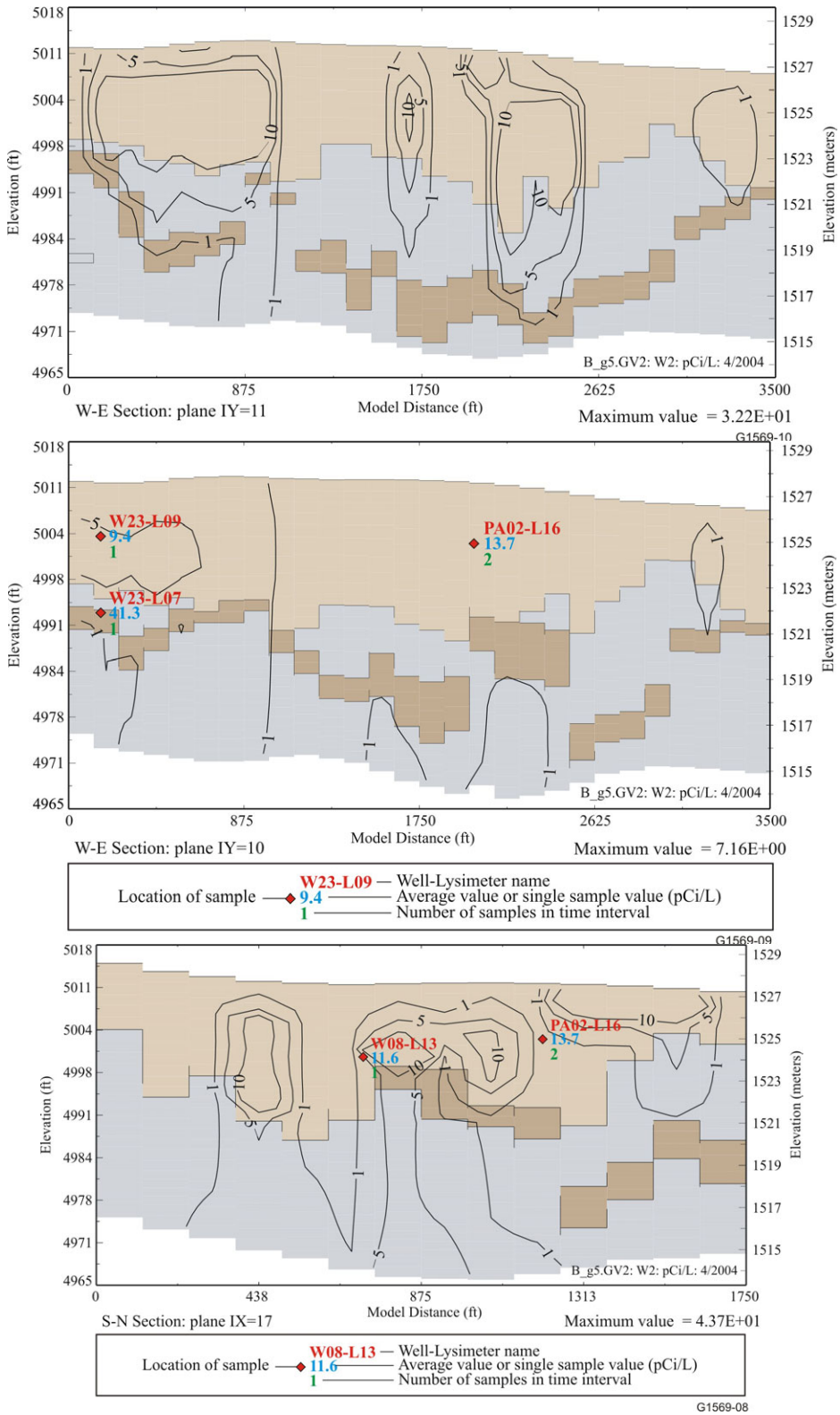

Figure 6-4. Cross sections showing simulated uranium-238 aqueous concentrations in Calendar Year 2004 (see Figure 6-3 for the location of the cross section).

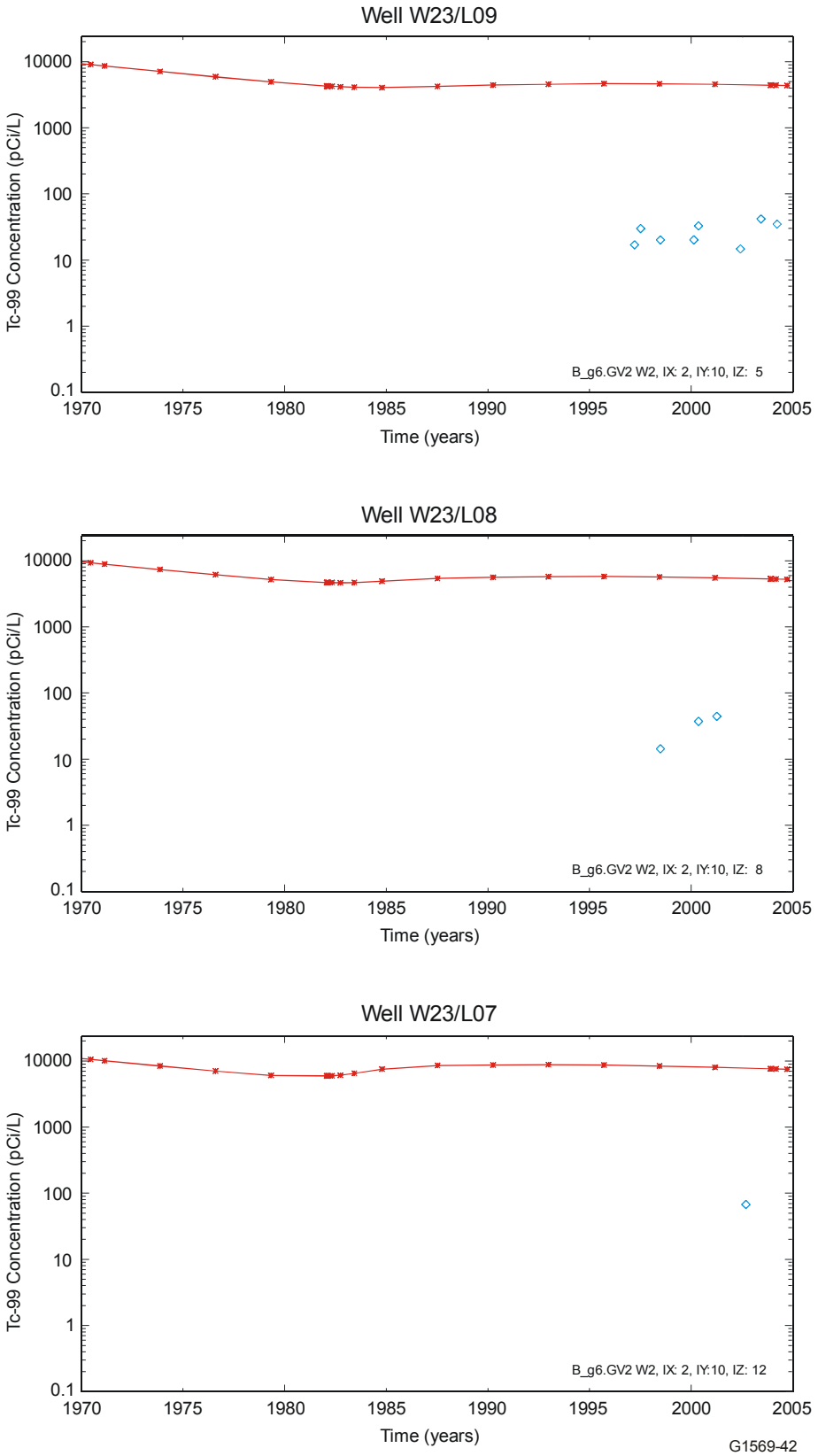

Figure 6-5. Time-history comparison of simulated (red line) and observed (blue diamonds) concentrations for technetium-99 in the lysimeters at Well W23.

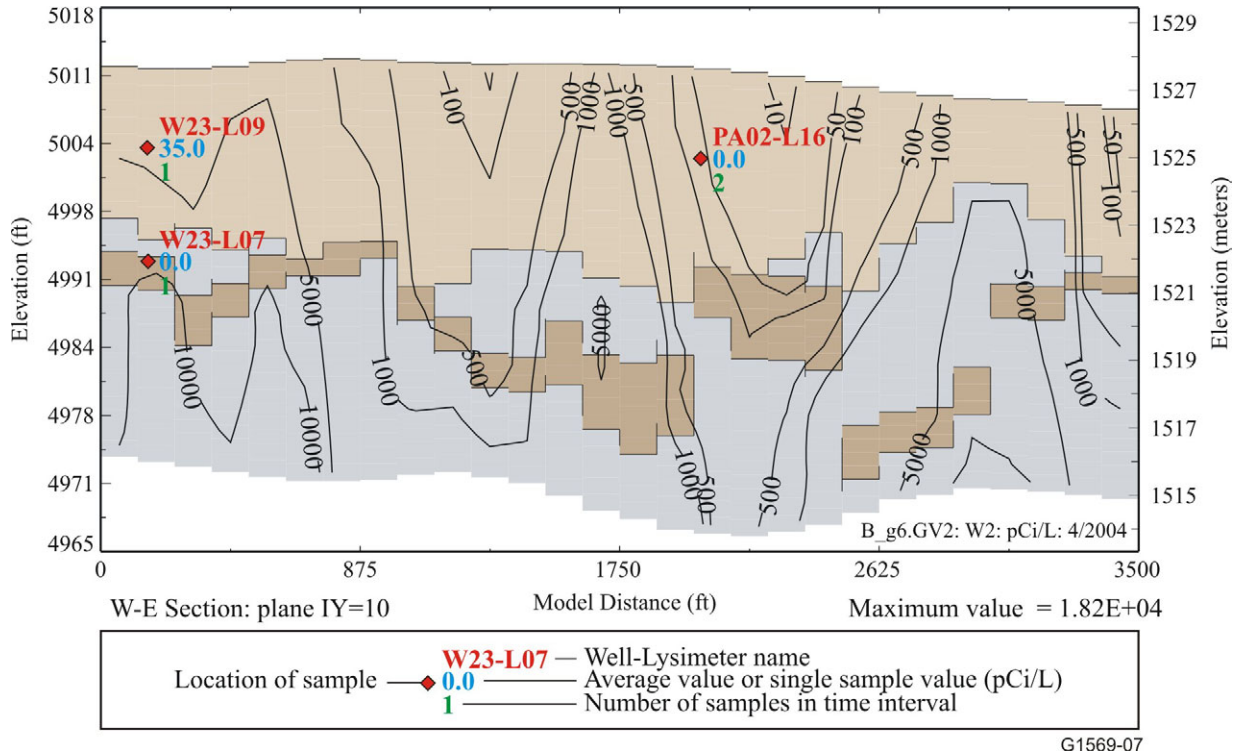

Figure 6-6. Cross section showing simulated technetium-99 aqueous concentrations in Calendar Year 2004 (see Figure 6-3 for the location of the cross section).

6.1.1.3 Nitrate—Elevated nitrate concentrations were seen at two locations, Wells PA02 and W25, in the 0- to 10.7-m (0- to 35-ft) zone (see Figure 6-7). The vertical concentration scale is different for the two locations in order to show detail, although both show the simulated concentration to be higher than the observed concentration. In contrast to the U-238 simulation results, even though the gridblock containing Well PA02 does not receive contaminant mass from the source-release model assigned to it, sufficient mass is assigned to the nearby Pad A waste stream blocks to result in appreciable nitrate appearing in the simulation results at this location. These locations were chosen because they show elevated nitrate concentrations; therefore, the model results at all other locations would also show overprediction, leading toward the conclusion that nitrate simulation results are conservative with respect to maximizing groundwater-pathway concentrations.

6.1.2 Vadose Zone: 10.7 to 76.2 m (35 to 250 ft)

Similar to the shallow vadose zone in the 0- to 10.7-m (0- to 35-ft) interval, simulated time histories are compared in this section for those monitoring locations from the 10.7- to 76.2-m (35- to 250-ft) interval that have elevated—even if only slightly—U-238, Tc-99, and nitrate concentrations.

6.1.2.1 Uranium-238. Lysimeters showing slightly elevated U-238 concentrations above background are I1S-DL09, I4S-DL15, D06-DL01, DO6-DL02 and TW1-DL04. For the Well D06 location, only the uppermost lysimeter (i.e., Lysimeter DL02) is shown in Figure 6-8. Intervals of 10.7 to 42.7 m (35 to 140 ft) and 42.7 to 76.2 m (140 to 250 ft) are combined for this discussion because so few locations are showing elevated concentrations in the deeper interval.

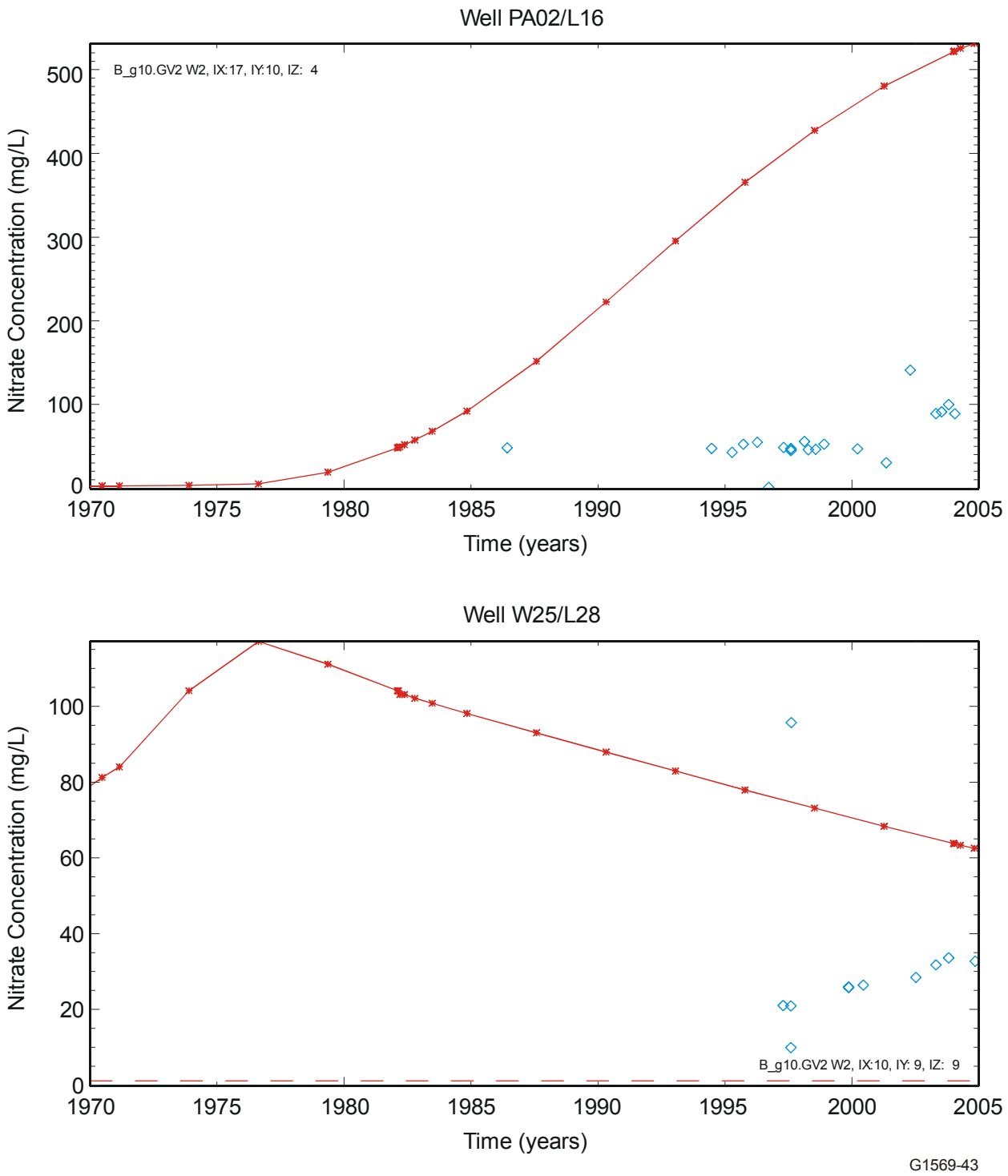

Figure 6-7. Time-history comparison of simulated (red line) and observed (blue diamonds) concentrations for nitrate in Lysimeters PA02-L16 and W25-L08. Background concentration is indicated by the dashed line.

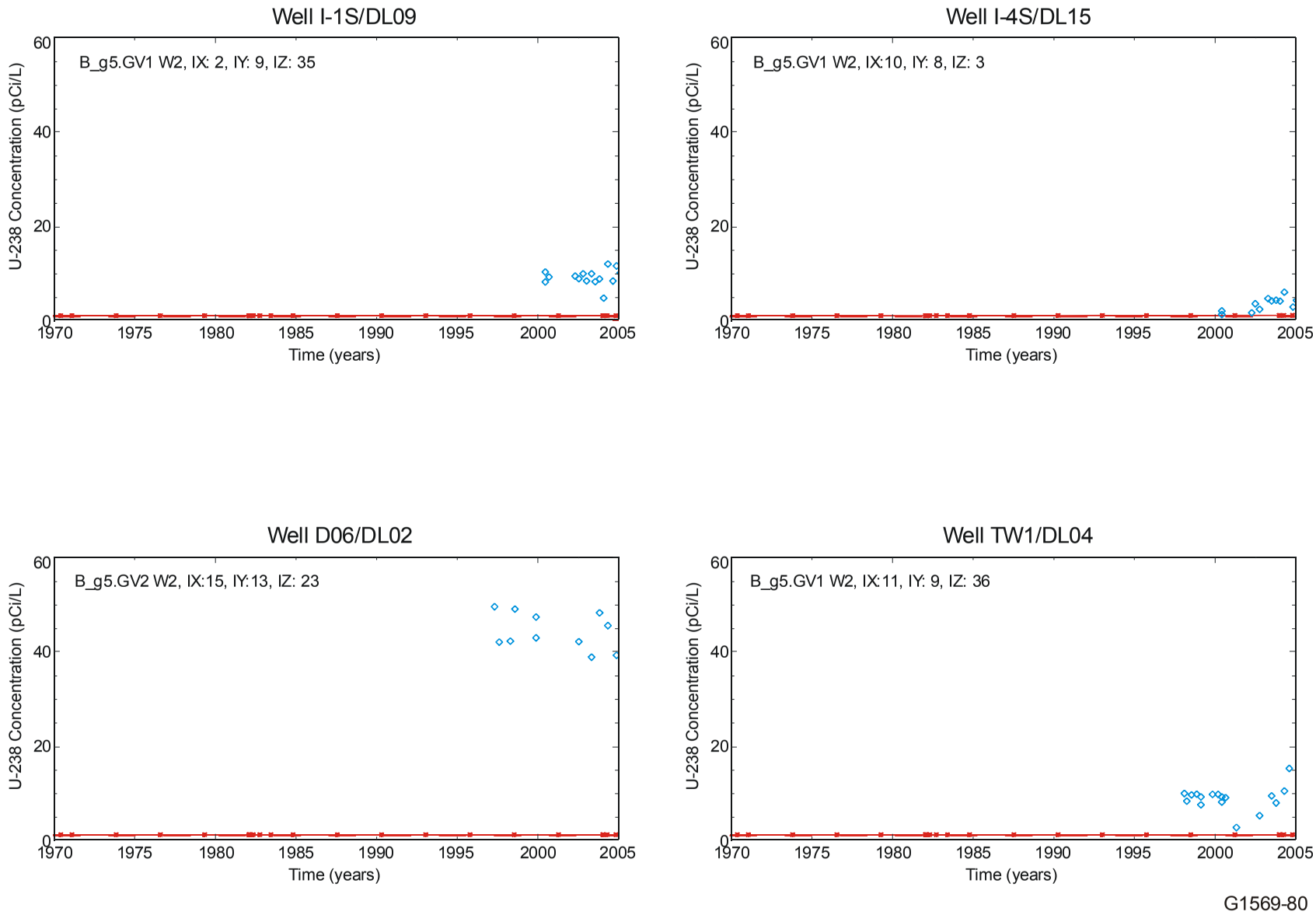

Figure 6-8. Time history-comparison of simulated (red line) and observed (blue diamonds) concentrations for uranium-238 in the lysimeters in the 10.7- to 76.2-m (35- to 250-ft) depth interval. Background concentration is indicated by the dashed line.

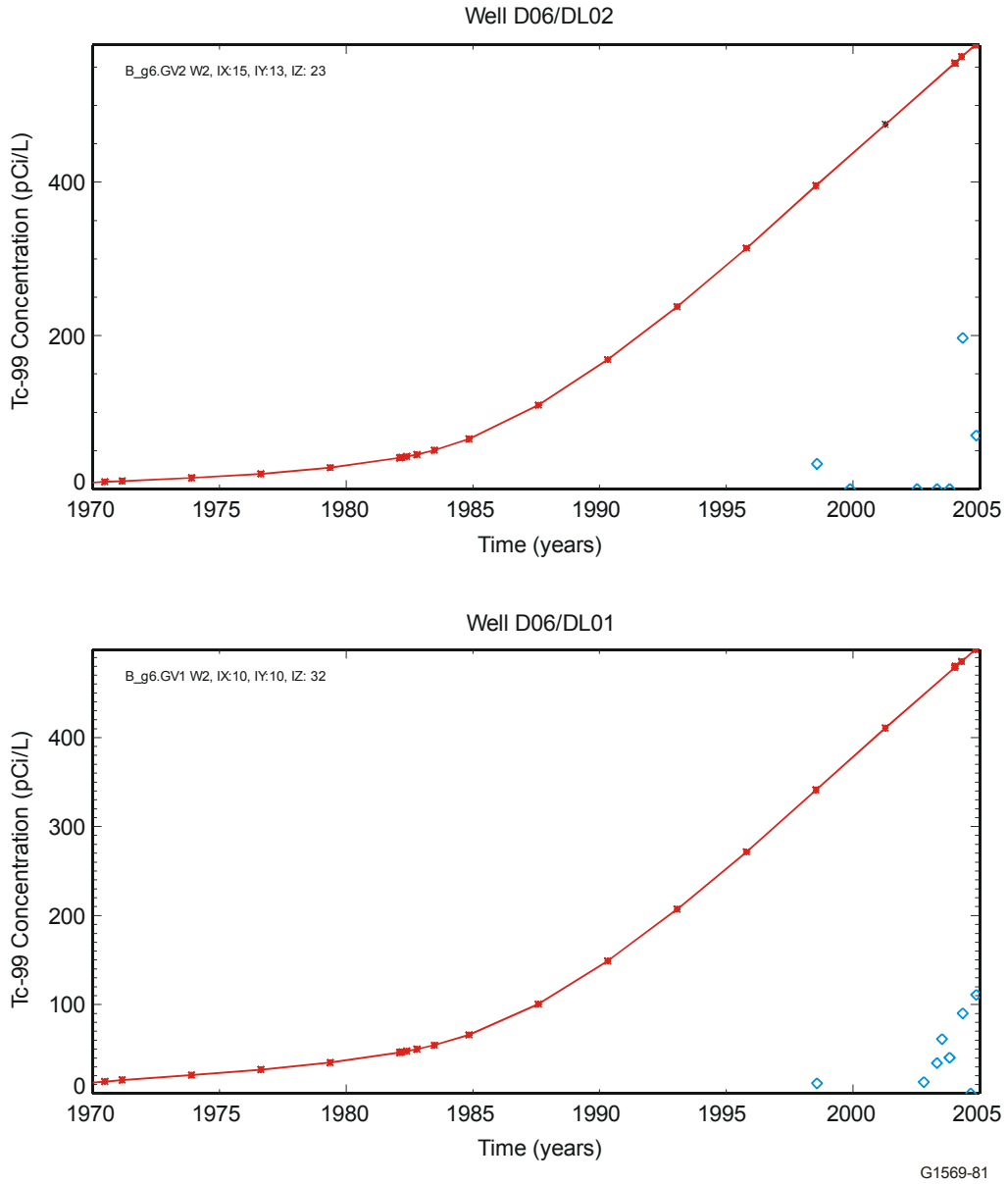

Figure 6-9. Time-history comparison of simulated (red line) and observed (blue diamonds) concentrations for technetium-99 in the lysimeters in the 10.7- to 76.2-m (35- to 250-ft) depth interval.

Although simulated concentrations are nonzero, they are very low and essentially plot just at background. Simulations represent averaged concentrations over larger gridblock volumes at this depth—76.2 m (250 ft) on a side—and again cannot be expected to exactly mimic observations at a specific point. Also note that the plots show only locations with elevated concentrations. The other monitoring locations (i.e., the majority) all show nondetects.

6.1.2.2 Tc-99. Elevated concentrations of Tc-99 in the 10.7- to 76.2-m (35- to 250-ft) interval were observed at Wells D06 in Lysimeters DL01 and DL02. Simulated Tc-99 concentrations for gridblocks containing these lysimeters are shown in Figure 6-9. These results are plotted with a linear vertical axis because the concentrations are not as overpredicted at this location as they were for the shallower Well W23 location shown previously.

6.1.2.3 Nitrate. Elevated concentrations of nitrate in the 10.7- to 76.2-m (35- to 250-ft) interval were observed at Wells I-2S and I-4S. These simulation results are shown in Figure 6-10. Lysimeter I-2S-DL11 shows very high monitoring results for nitrate; therefore, it is not surprising that the model underpredicts in comparison. Lysimeter I-4S-DL15 has lower monitoring results; the model results overpredict for this location.

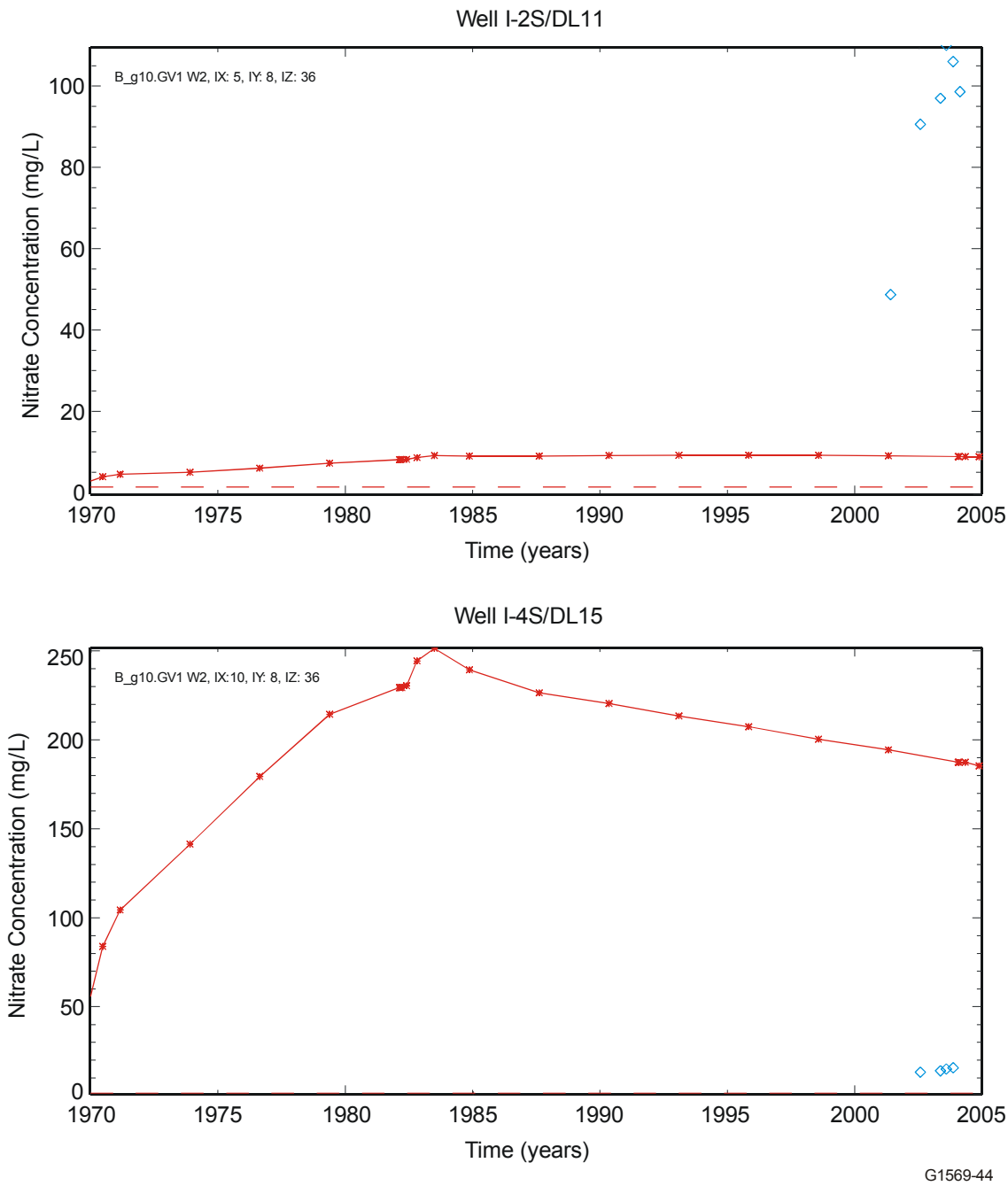

Figure 6-10. Time-history comparison of simulated (red line) and observed (blue diamonds) concentrations for nitrate in the lysimeters in the 10.7- to 76.2-m (35-to 250-ft) depth interval. Background concentration is indicated by the dashed line.

6.1.3 Aquifer

This subsection first compares simulated and observed nitrate and chromium concentrations. These two contaminants are chosen for consistency to allow comparison to ABRA modeling results and because they offer insight into how the model results compare to monitoring data. Both contaminants are conservative in that they do not sorb, and thus, avoid the complication of assigning a K_d. Lastly, time histories for simulated aquifer concentrations for all contaminants in the RI/FS model that have detections from aquifer monitoring are compared to the observations.

6.1.3.1 Comparison of Simulated and Observed Nitrate Concentrations. This subsection shows comparisons of simulated results and monitoring results for nitrate as elemental nitrogen. Time histories, contour plots, and vertical profiles through the aquifer domain are presented to show spatial resolution.

Calibration to the observed aquifer nitrate concentrations was not attempted for these simulations. Rather, simulations for both the vadose zone and the aquifer were developed based on best-available information. Then simulations were run once in a forward mode.

Nitrate is a ubiquitous chemical in groundwater. Background concentrations must be considered when making comparisons, even though it is assumed for RI/FS modeling that contaminant concentrations in the vicinity of the SDA are not influenced by upgradient sources. A background concentration of 1.0 mg/L was added to simulated values in the time-history plots shown in Figure 6-11. This background concentration appears appropriate for the local RWMC area and is within the range of background concentrations typical for the INL Site (i.e., 0.4 to 5.0 mg/L) as presented in Section 4 of the draft RI/BRA document. The time-history plots are all shown with a consistent time axis and a consistent concentration axis, except for Well M17S, which has one-order-of-magnitude-larger concentration axis to show the simulated results. Simulation results representing all wells, except Well M4D, are taken from the second gridblock down in the aquifer model. Well M4D is unique in that it is screened much deeper; therefore, simulated concentrations from deeper in the model are used. The second gridblock extends from 8 to 16 m (26 to 52 ft) in the aquifer domain and is similar to most of the screened intervals in the monitoring wells (see Figure 5-33). As such, simulated concentrations represent concentrations at a depth of 12 m (39 ft) below the water table. In general, the simulation results show slightly lower predicted concentrations in the aquifer than those in the ABRA model due to a combination of reduced inventory and changes in transport through the vadose zone. Figure 6-11 illustrates that nitrate is sometimes overpredicted and sometimes shows no contribution from SDA sources when compared to monitoring data. Also evident in the monitoring data is that the mean local background estimate has some degree of variability around it.

A contour plot of the simulated nitrate concentrations in Calendar Year 2004 is shown in Figures 6-12 and 6-13 for the refined and base aquifer-simulation domains, respectively. Again, concentrations are taken from the second gridblock down from the aquifer model. The estimated local background of 1.0 mg/L is not added to the simulation results in Figures 6-12 and 6-13. Simulated results show that nitrate is predicted to move east-southeast within the area of the refined domain due to topography influences in the vadose zone and slightly south-southeastern water velocities under the eastern portion of the SDA and the Transuranic Storage Area. In the larger base domain, control of the regional gradient is exerted and the simulated plume moves south-southwest.

The predicted movement of nitrate east-southeast within the aquifer model-refined domain can be seen more easily in Figure 6-14, where time histories from Figure 6-11 are portrayed in spatial relation to their well locations. Elevated nitrate concentrations are predicted by current time for Wells M17S, USGS-119, USGS-90, and M15S, which are all beneath the SDA or south-southeast. Well M6S would

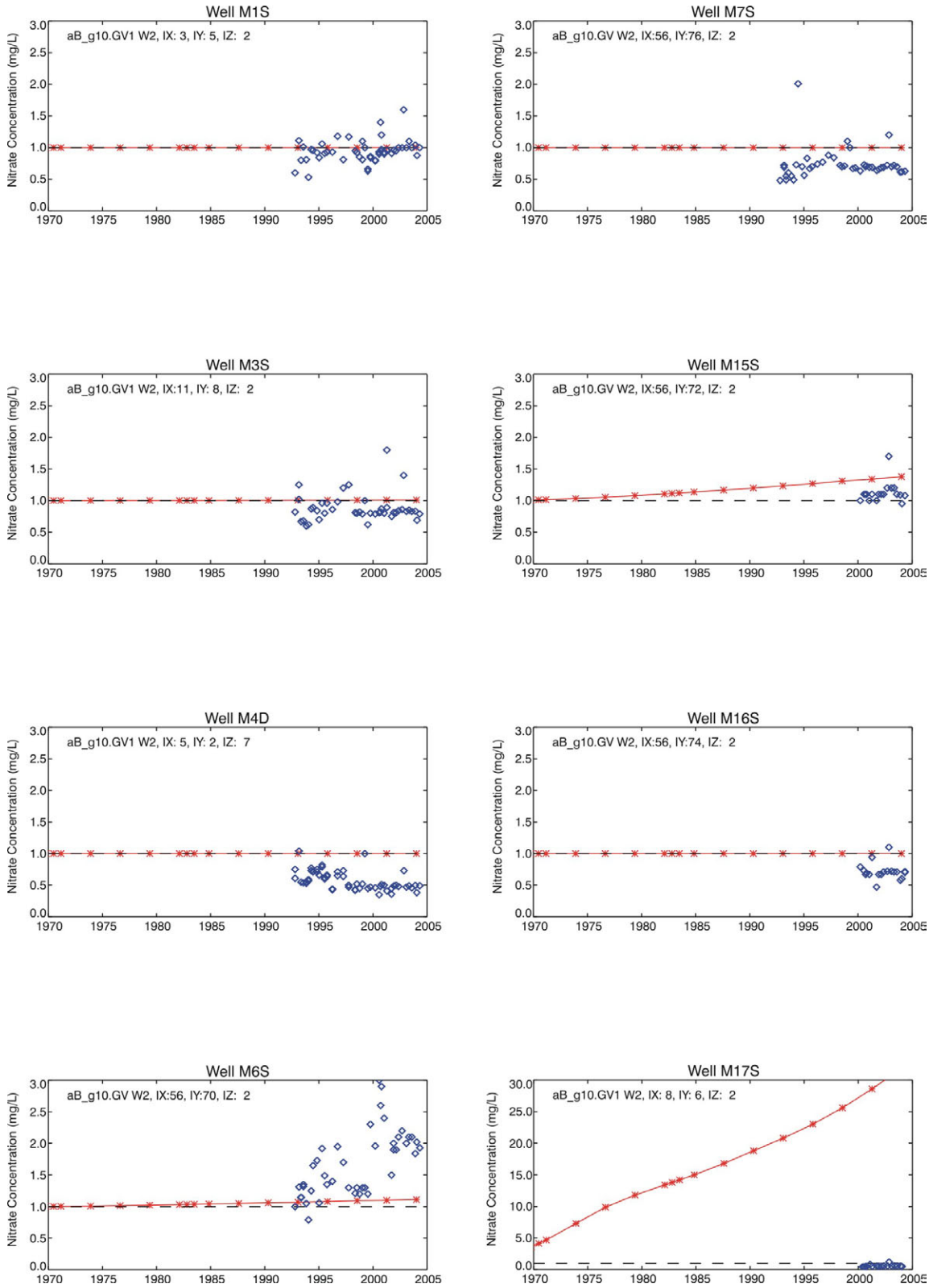

Figure 6-11. Comparison of simulated (red line) and observed (blue diamonds) nitrate (as N) concentration time histories for aquifer-monitoring wells in the vicinity of the Subsurface Disposal Area. Background concentration is indicated by the dashed line.

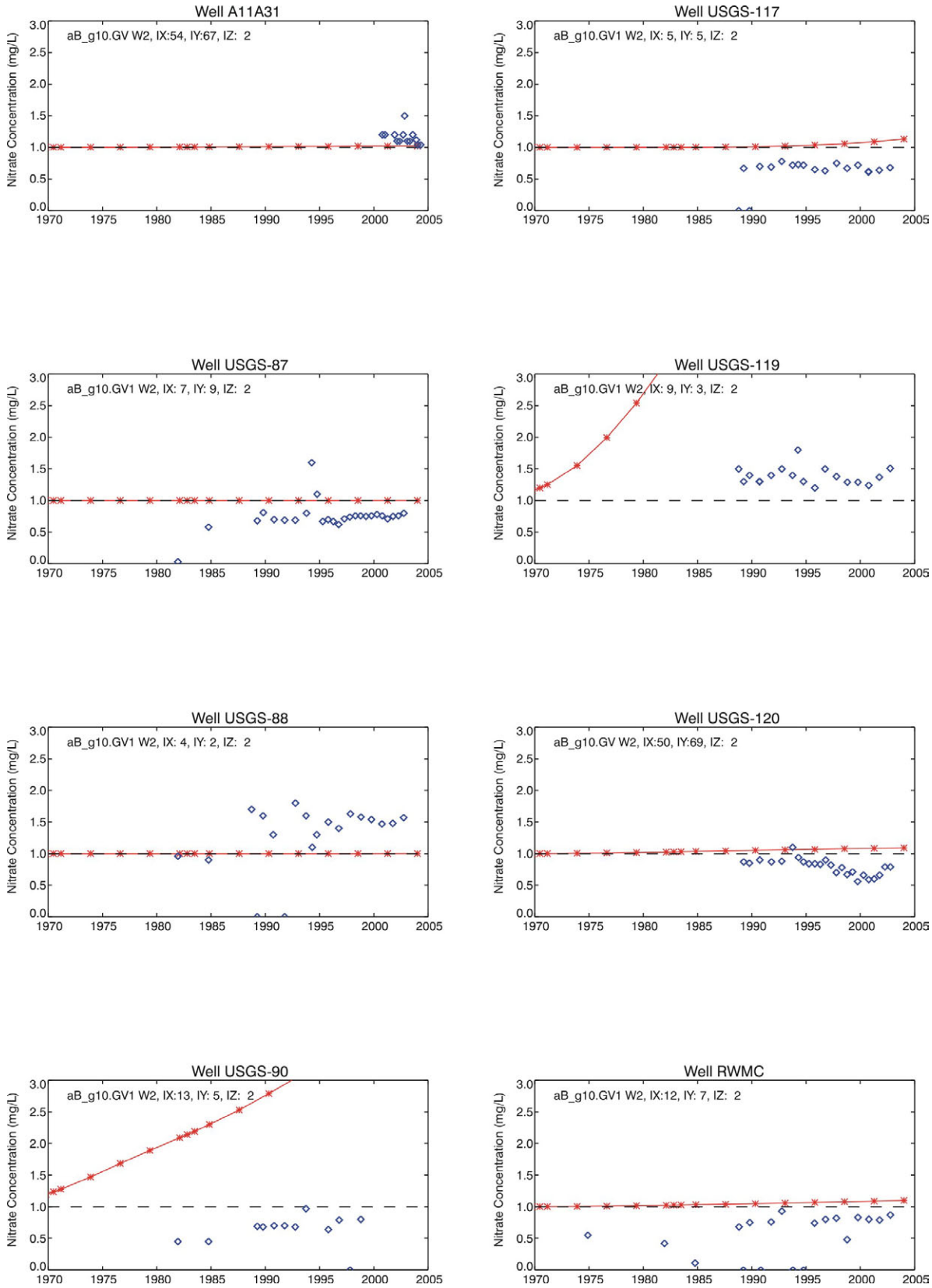

Figure 6-11. (continued).

have a higher predicted concentration, but it is outside the refined area; therefore, the predicted concentration is subject to averaging over a much larger gridblock volume, which dilutes the simulated concentration. In terms of monitoring data, some patterns can be interpreted when compared to the local background estimate of 1.0 mg/L. For purposes of comparison, monitoring results are grouped into four classes with an indication found in the upper right corner of each time-history plot. An "L" indicates the monitoring data were mostly below the background, an "M" indicates the monitoring data mostly match the background, and an "H" indicates the monitoring data are mostly higher than the background. Following this categorization, Wells USGS-87, M3S, M7S, M16S, USGS-90, M17S, USGS-117, M4D, and USGS-120 all show concentrations mostly below background. Wells M1S and M15S match the local background. Wells USGS-119 and USGS-88 are elevated compared to the local background and Well M6S has the highest concentrations above the local background estimate. Grouped in this fashion, monitoring data also show a tendency for nitrate concentrations to be elevated in several wells south of the SDA, with one group including Wells USGS-119, M15S, and M6S, which are in the direction of predicted local transport to the southeast.

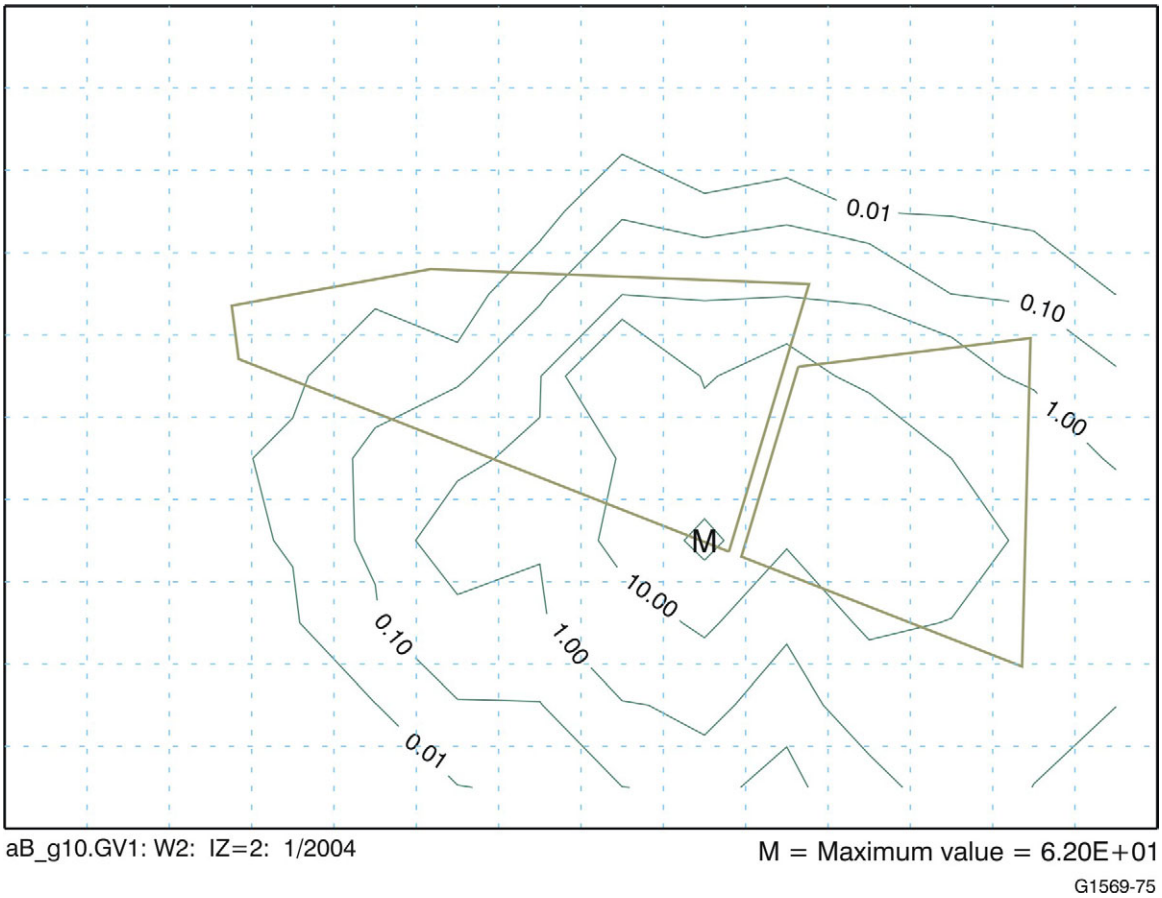

Figure 6-12. Simulated aquifer nitrate concentrations (mg/L) for the year 2004 for the refined aquifer domain. The results do not include any additional contribution from local background concentrations.

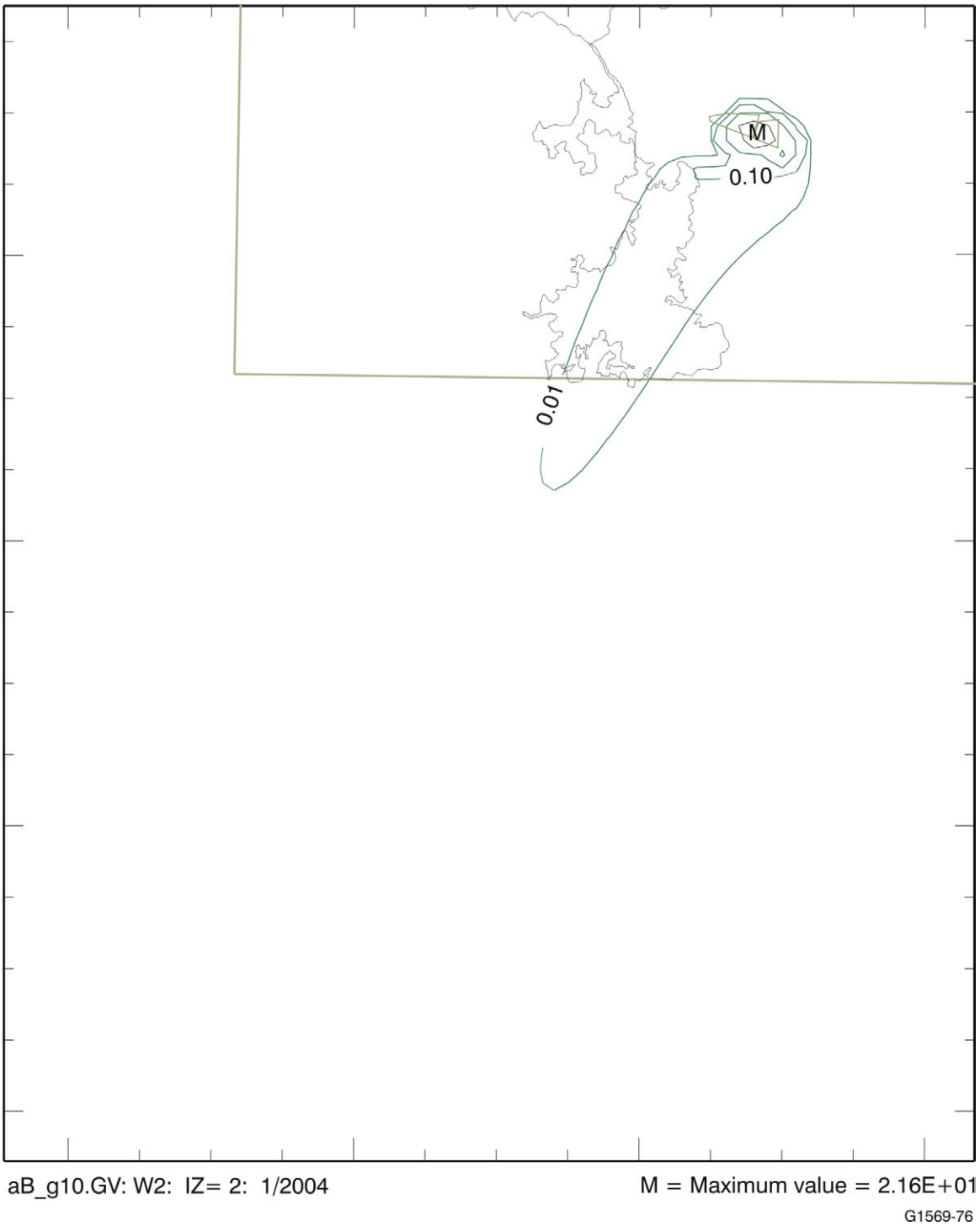

Figure 6-13. Simulated aquifer nitrate concentrations (mg/L) for the year 2004 for the base aquifer domain. The results do not include any additional contribution from local background concentrations.

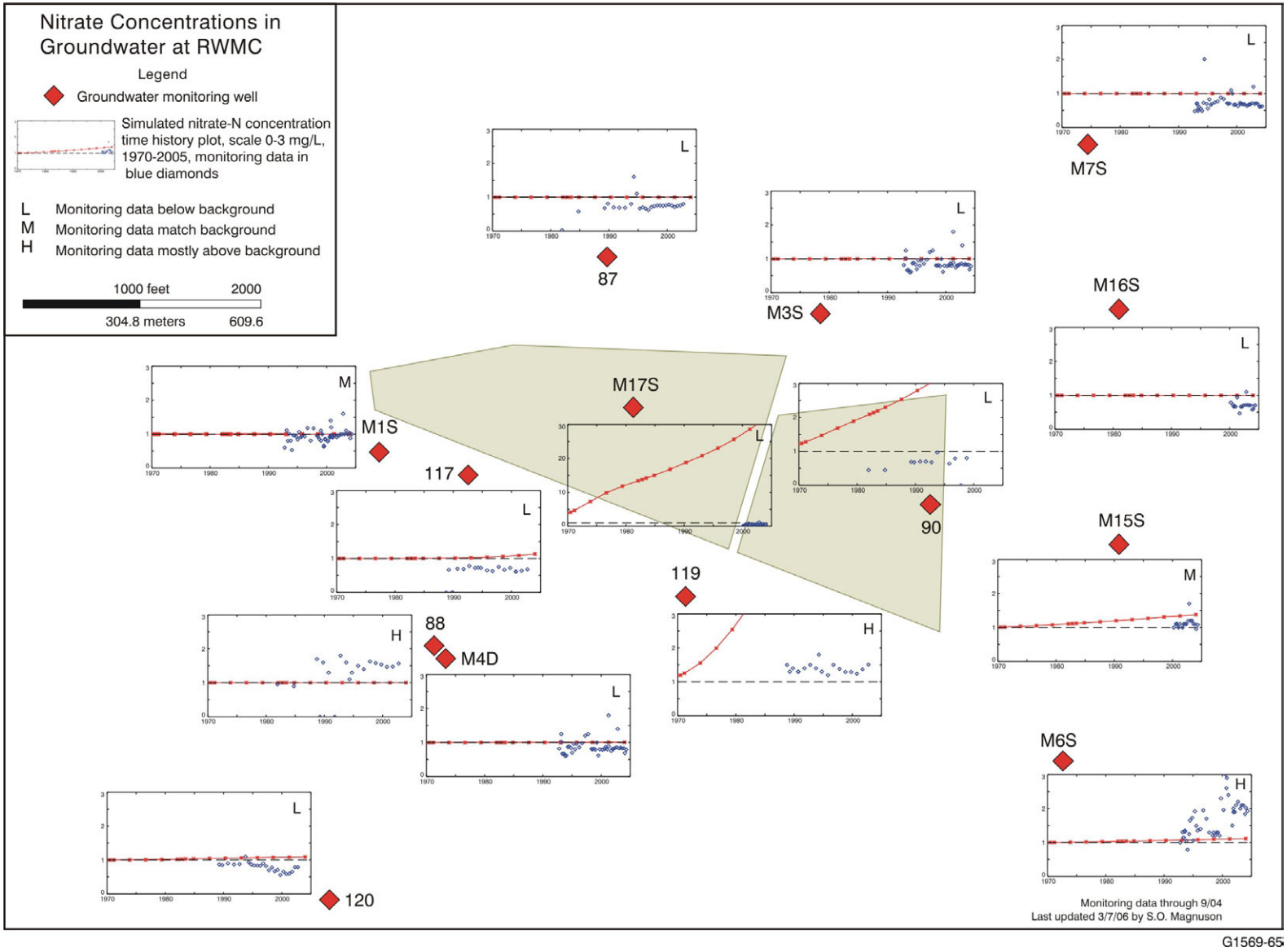

Figure 6-14. Simulated and observed nitrate concentrations superimposed onto monitoring locations in the vicinity of the Radioactive Waste Management Complex. Background concentration is indicated by dashed line.

Most of the monitoring data are consistent with the conceptual model and numerical implementation. The aquifer flow system is dominated by a low-permeability region south and southwest of the SDA that directs flow eastward around the low-permeability system. In comparing simulation results to monitoring results, concentrations are overpredicted in Well M17S (inside the SDA), Well USGS-119 (immediately south of the SDA), and Well USGS-90 (east of the SDA). Predicted concentrations slightly overpredict observed concentrations at Well M15S (east of the Transuranic Storage Area).

Concentrations are underpredicted at Well M6S (southeast of the SDA). The simulation results at the grid location corresponding to Well M6S are subject to additional dilution due to being outside the refined area. Without this dilution, the agreement would be better. The majority of other locations outside this predicted contaminant plume essentially shows no simulated impact above local background concentration. Obviously, the system is more complex than has been represented in the model. However, the model does provide a foundation for explaining most of the observed behavior and, thus, meets a goal of general representativeness.

Vertical profiles of simulated nitrate concentrations at the gridblock location with the maximum simulated concentration in Calendar Year 2004 (Figure 6-12) are shown in Figure 6-15 for four different dates. These plots do not have the background concentration added to the simulation results. This same location remains the location of maximum concentration until Calendar Year 2120, when it shifts southward with the center of mass. Note that the horizontal-concentration scale changes in the profile for Calendar Year 2997. Contours of the simulated concentration for the same times from the corresponding north-south cross section in the refined aquifer domain are shown in Figure 6-16. Only Calendar Years 2004, 2066, and 2110 are shown, because the simulated concentration for Calendar Year 2997 is below 1 mg/L.

Understanding the dynamic behavior of simulated profiles requires knowing (1) the contaminant-loading history from the vadose zone simulation at this location, (2) that water flux from the vadose zone is relatively constant, and (3) that the low-permeability region in the aquifer results in slow horizontal velocities, which increases the effect of contaminant flux coming into the model from the vadose zone. A one-to-one correspondence from the bottom of the vadose zone to the top of the refined domain in the aquifer and nitrate loading from the vadose zone model for the gridblock location profiled in Figure 6-15 is shown in Figure 6-17. During the period up to approximately Calendar Year 2050, contaminant flux to the aquifer is increasing. A profile from this period (i.e., Calendar Year 2004) shows consistently decreasing simulated concentrations with depth in the aquifer. Shortly after this period, nitrate flux from the vadose zone begins to decrease while water flux stays the same. This begins to result in lower concentrations at the surface (Calendar Year 2066), possibly indicating that a slight downward gradient has developed in the aquifer simulation within the low-permeability region. By Calendar Year 2110, this reversal in the concentration gradient has almost penetrated to the bottom of the simulation domain. At a much later time (i.e., Calendar Year 2997), the concentration gradient is reversed, with the highest concentration at the bottom of the domain, although concentrations at this later time are much lower.

This simulation behavior of the concentration not always being greatest at the uppermost gridblock has implications when extracting concentrations from the model for risk assessment. It would not necessarily always be conservative to use concentrations from the uppermost gridblock in the aquifer domain. In this baseline risk assessment, concentrations are taken from the second gridblock down, as discussed in Section 6.2. Section 6.1.1.3.3 shows similar vertical profiles for other contaminants to further illustrate this point.

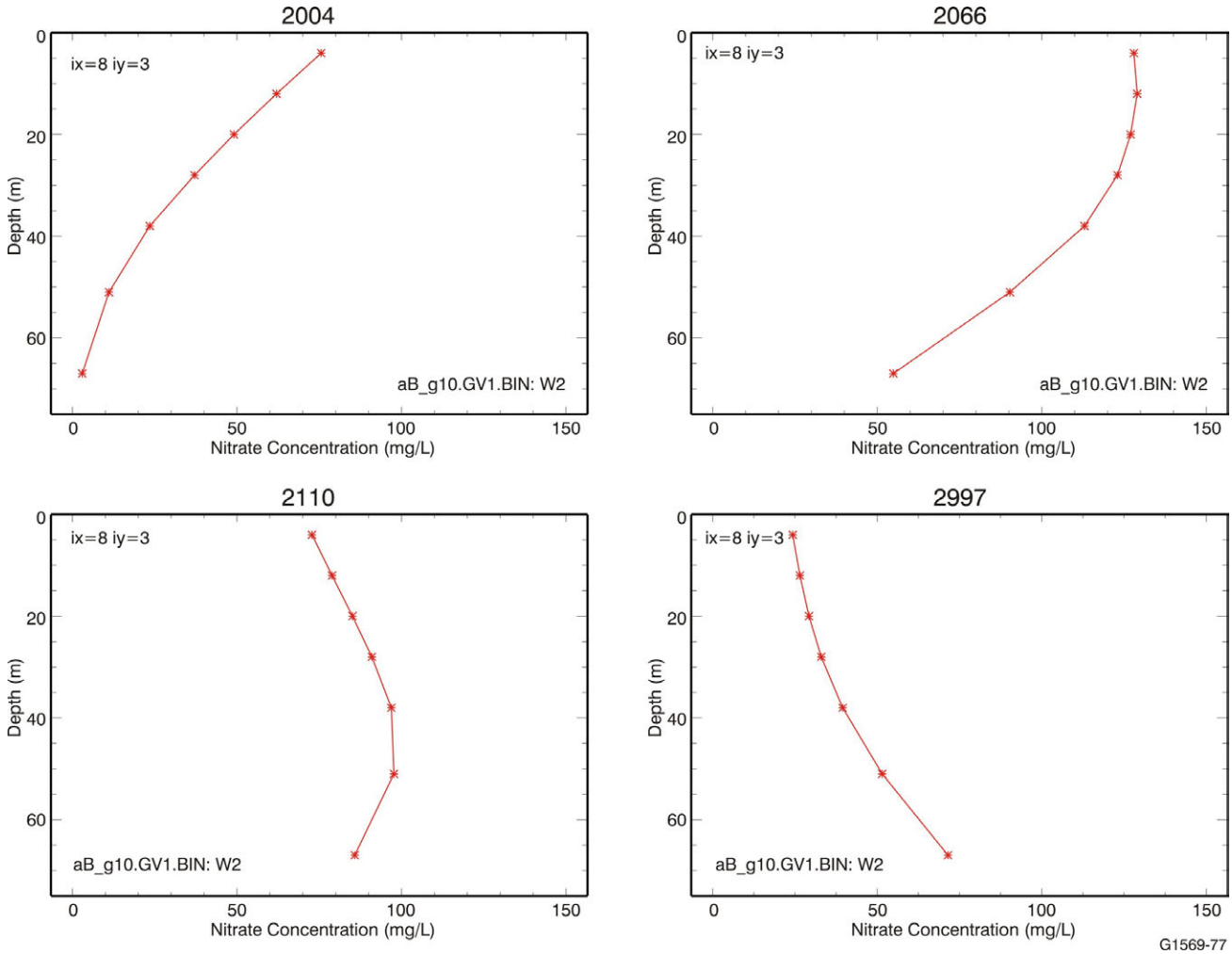

Figure 6-15. Simulated aquifer nitrate concentration profiles beneath the Subsurface Disposal Area. The year is shown at the top of each plot.

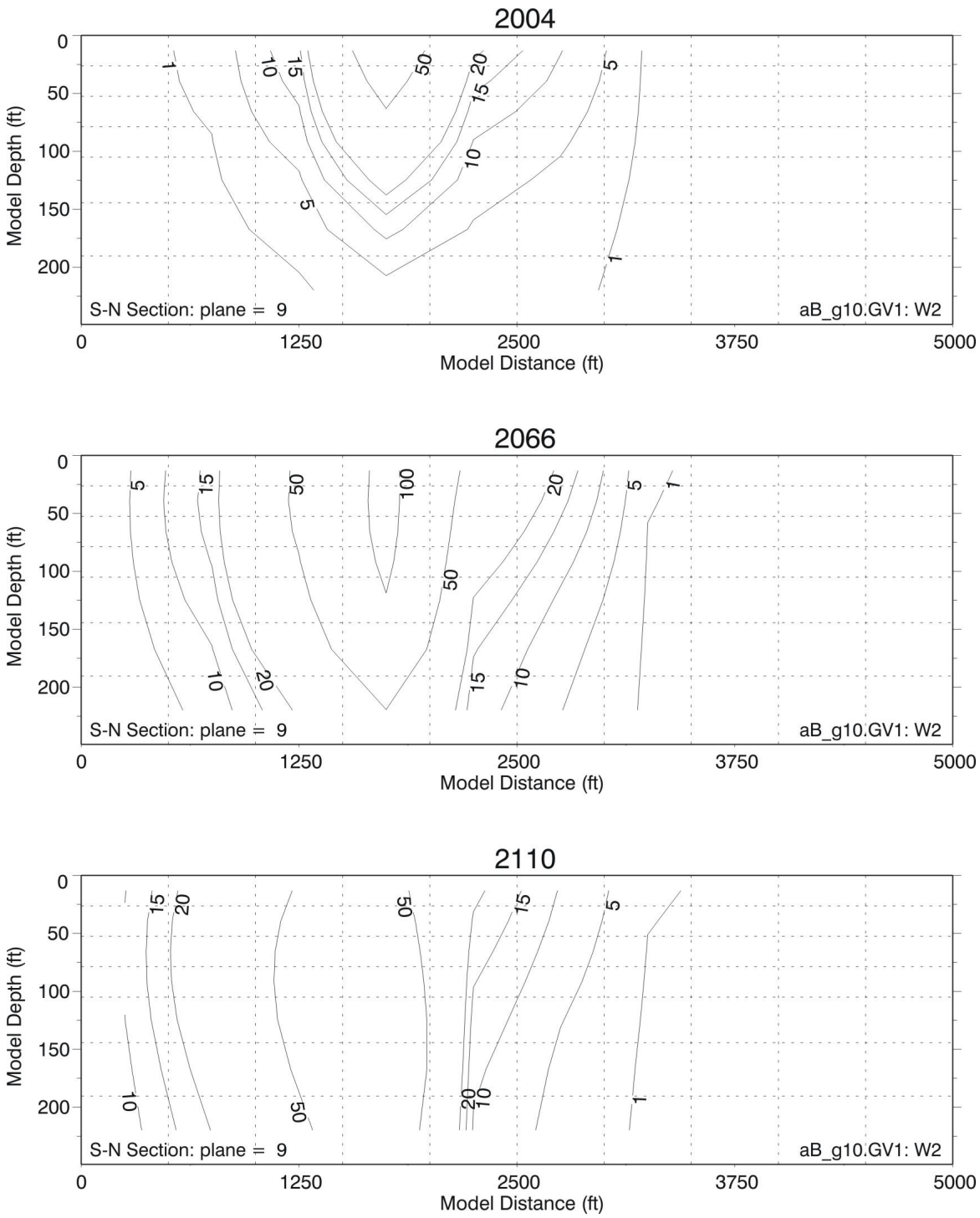

Figure 6-16. Simulated aquifer nitrate concentrations (mg/L) for north-south cross sections through the location of maximum simulated concentration at times corresponding to profiles shown in Figure 6-15.

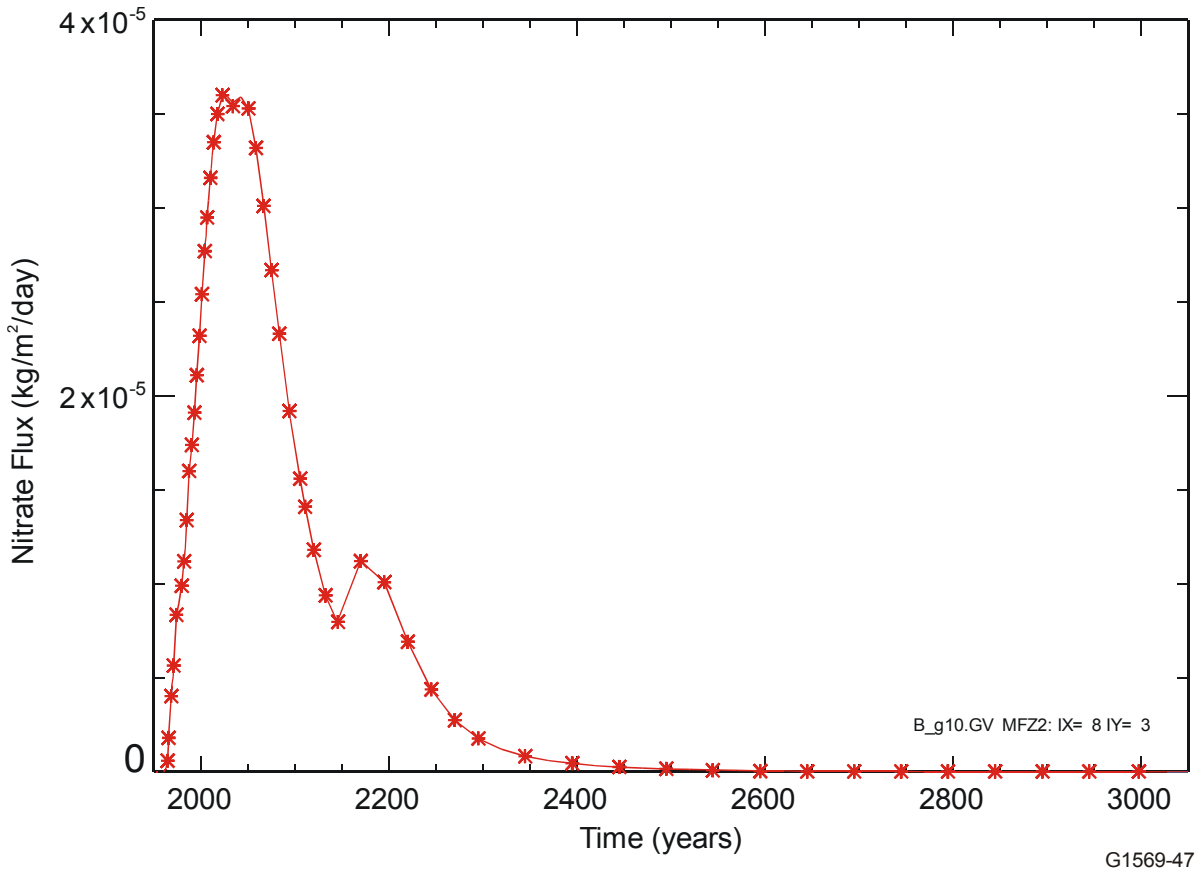

Figure 6-17. Time history of the simulated nitrate flux from the vadose zone simulation at the grid location profiled in Figure 6-15.

6.1.3.2 Comparison of Simulated and Observed Chromium Concentrations. Chromium is another contaminant buried in the SDA for which transport was simulated. In these transport simulations, chromium was assumed to remain in the mobile hexavalent state. Though chromium is not considered a COPC in the draft RI/BRA, subsurface model predictions for chromium are compared to measured values because sufficient monitoring data are available to support the comparison. Figure 6-18 illustrates time histories of simulated chromium concentrations compared to observed aquifer concentrations. The monitored concentrations are inferred to represent hexavalent chromium also. Similar to the time-history plots for nitrate concentrations, the simulated chromium concentrations are added onto the upper end of the aquifer background concentration range of 1-22 µg/L for the Snake River Plain aquifer (see Section 4 of the draft RI/BRA). Only simulated chromium concentrations for Wells M17S and USGS-119 begin to be discernable above background for the 1970 through Fiscal Year 2004 timeframe presented in Figure 6-18. The maximum simulated chromium concentration anywhere in the aquifer through Fiscal Year 2004 is 30 µg/L. This concentration is approximately an order of magnitude greater than the maximum simulated chromium concentration through the same period for the ABRA model. Both the ABRA and RI/FS models underpredict observed values.

Field data for chromium show considerable variability, similar to nitrate. Locations showing the most consistent elevated concentrations are Wells M1S, M15S, and M6S. Two of these are in the direction of interpreted and simulated flow to the east-southeast in the locally refined portion of the aquifer domain.

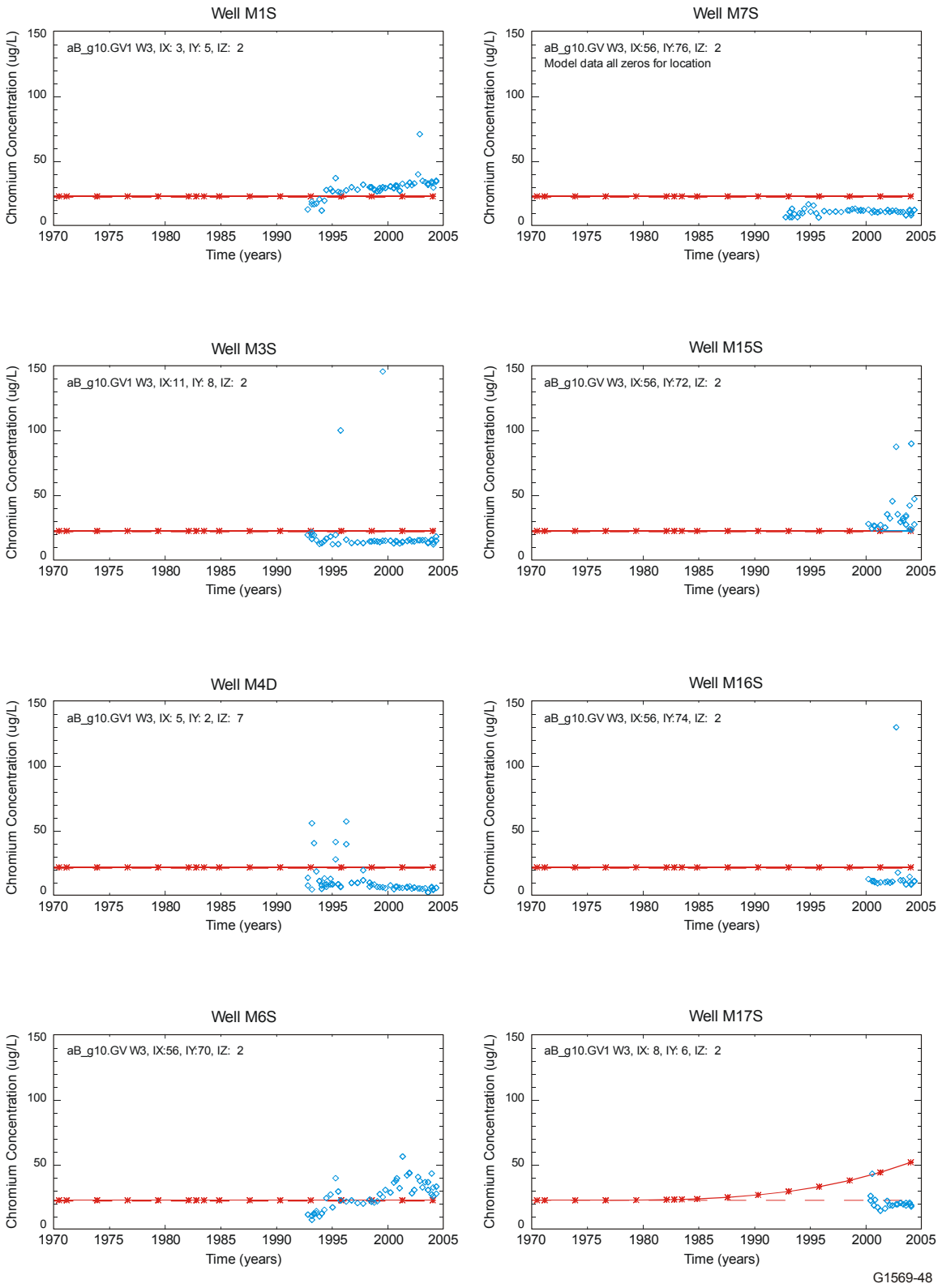

Figure 6-18. Comparison of simulated (red line) and observed (blue diamonds) chromium concentration time histories for aquifer-monitoring wells in the vicinity of the Subsurface Disposal Area. Background concentration is indicated by the dashed line.

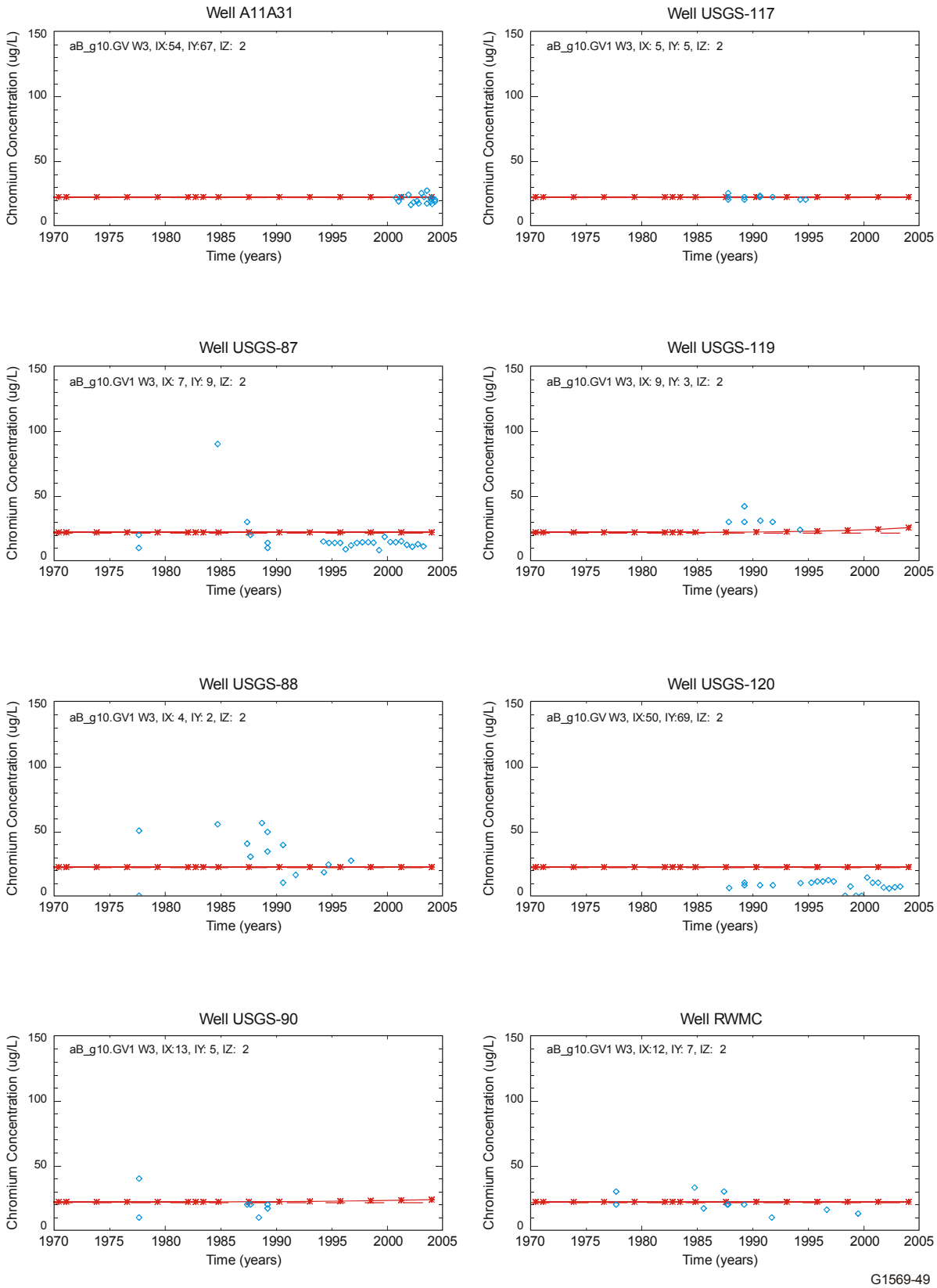

Figure 6-18. (continued).

The maximum simulated chromium concentration anywhere in the aquifer through Fiscal Year 2004 is 34 µg/L (see Figure 6-19). This is approximately an order of magnitude greater than the maximum simulated chromium concentration through the same period for the ABRA model and reflects an improvement when compared to field monitoring results (see Section 4 of the draft RI/BRA). Simulated chromium concentrations, although slightly underpredicted, are approaching the same order of magnitude as the observed chromium concentrations in the aquifer just south of the SDA. Note that it is uncertain to what extent impacts from SDA waste or from upgradient facilities have on these observed concentrations.

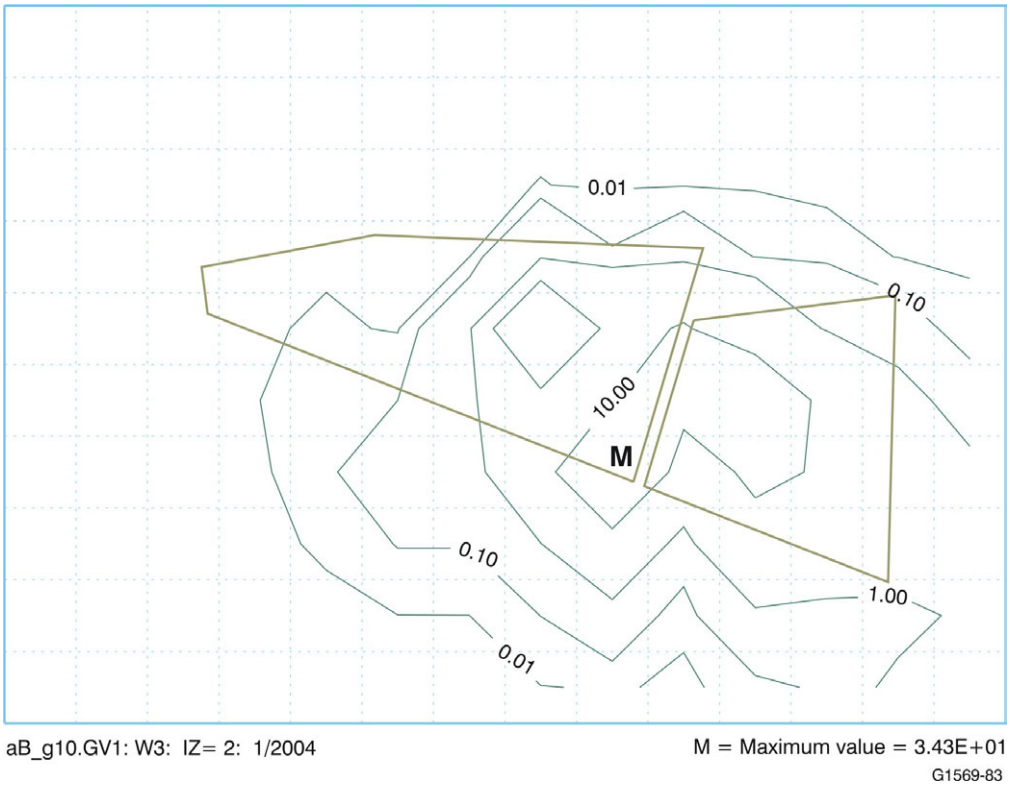

Figure 6-19. Simulated aquifer chromium concentrations (ug/L) for Calendar Year 2004 for the refined aquifer domain. Background concentrations are not added to simulation results.

6.1.3.3 Comparisons of Simulated and Observed Concentrations for Dissolved-Phase Radionuclide Constituents. This subsection presents comparisons of time histories of simulated results from the base-case simulation for those dissolved-phase radionuclides that have detections in the aquifer from monitoring. These contaminants are I-129, Tc-99, Am-241, Np-237, Pu-238, and Pu-239. Results are presented graphically as time-history comparisons to field-monitoring results at grid locations representing SDA aquifer-monitoring wells (Figures 6-20 through 6-25). In contrast to results presented previously for nitrate and chromium, contaminants in these figures are anthropogenic and have no background concentrations to add to simulation results, except for I-129 with a local background of 0.05 pCi/L. This latter background is indistinguishable in Figure 6-20. Monitoring results for radionuclide COPCs that represent 3σ detections, or greater, are included as blue diamonds on the time-history plots along with a whisker-style indication of their associated 1σ uncertainties. In cases where analyses were performed but no COPCs were detected, nondetects are plotted in green at the extreme lower-bound inventory of the plot. Simulation results are portrayed as a continuous line with black asterisks. Simulation results representing all wells, except Well M4D, are taken from the second gridblock down in the aquifer model. Well M4D is unique because it is screened much deeper; therefore, simulated

concentrations from deeper in the model are used. The second gridblock extends from 8 to 16 m (26 to 52 ft) in the aquifer domain and is similar to most of the screened intervals in the monitoring wells. As such, simulated concentrations represent concentrations at a depth of 12 m (39 ft) below the water table.

Results in Figures 6-20 through 6-25 highlight the erratic nature of detections compared to the majority of nondetect results, and those results lend credence to the assumption that these detections are not representative of transport and simulation results need not mimic them. These sporadic detections include low-level actinide concentrations that are just at instrument detection limits and may be false-positives.

Table 6-1 lists the maximum simulated concentrations from anywhere in the aquifer through Calendar Year 2004 for all human health COPCs, their long-lived decay-chain progeny, and chromium. No background concentrations are added to any of the simulated results. All simulated peak values listed in Table 6-1 occur during Calendar Year 2004, indicating that concentrations were still increasing at that time. For comparison, corresponding maximum simulated concentrations through 2001 for the ABRA model and through 1995 from the IRA model are given in the third and fourth columns of Table 6-1. Aquifer background concentrations from Section 4 of the draft RI/BRA are shown in the fifth column of Table 6-1 for comparison to simulation results. The last two columns present the range of observed values taken from the nature and extent discussion in Section 4 of the draft RI/BRA, along with comments concerning some of those values. Observed values from earlier than 1987 are not presented in Table 6-1. Numerous COPCs do not have corresponding analyses, as indicated in Table 6-1.

Changes in simulated values between the RI/FS model and the ABRA model result from numerous causes. The simulated C-14 concentration drops two orders of magnitude primarily due to allowing C-14 to partition into the gaseous phase and diffuse to the atmosphere. This vapor-phase simulation is discussed in Section 5.5. Simulated concentrations for Np-237 and the uranium isotopes have decreased due to an increase in their assigned distribution coefficients. Simulated concentrations for Pu-239 and Pu-240 increased due to increased mobility above the B-C interbed. Plutonium-238 was not treated this way, but shows a slightly increased concentration nonetheless, most likely due to either changes in inventory, changes in water travel time resulting from the topography, or both. Simulated concentrations for the fission products (i.e., Tc-99 and I-129) and activation products (i.e., C-14 and Cl-36) all decreased due to changes in inventory and source-release parameters. All other COPCs have slight changes that are most likely due to inventory changes or changes in assigned parameters for release mechanisms.

In comparing simulated results from the RI/FS model to the range of observed 3σ detections or the background concentrations, several patterns emerge. Simulated aquifer concentrations for fission and activation products are still overpredicted to varying degrees compared to observed monitoring results, but not as much as they were for the ABRA. This overprediction is thought to be more likely caused by inadequacies in the source-release model than in the subsurface flow and transport model. Monitoring results for U-234, U-235, and U-238 are similar to reported background values. Simulated uranium isotope values are much less than observed values or background values, consistent with the conclusion of no observable impact in aquifer monitoring to date. All other contaminants are predicted to be either not in the aquifer yet or to be present at concentrations below detectable levels. If it is assumed that background concentrations for anthropogenic radioisotopes are zero for those contaminants not explicitly identified in Knobel, Orr, and Cecil (1992), then model results are in agreement with nondetections for this last group of contaminants. This statement disregards sporadic detections of plutonium isotopes and Am-241 as anomalies. At a minimum, for this latter set of contaminants, model results are not in conflict with observed results. Inorganic contaminants (i.e., nitrate and chromium) are both overpredicted when compared to the majority of observed values.

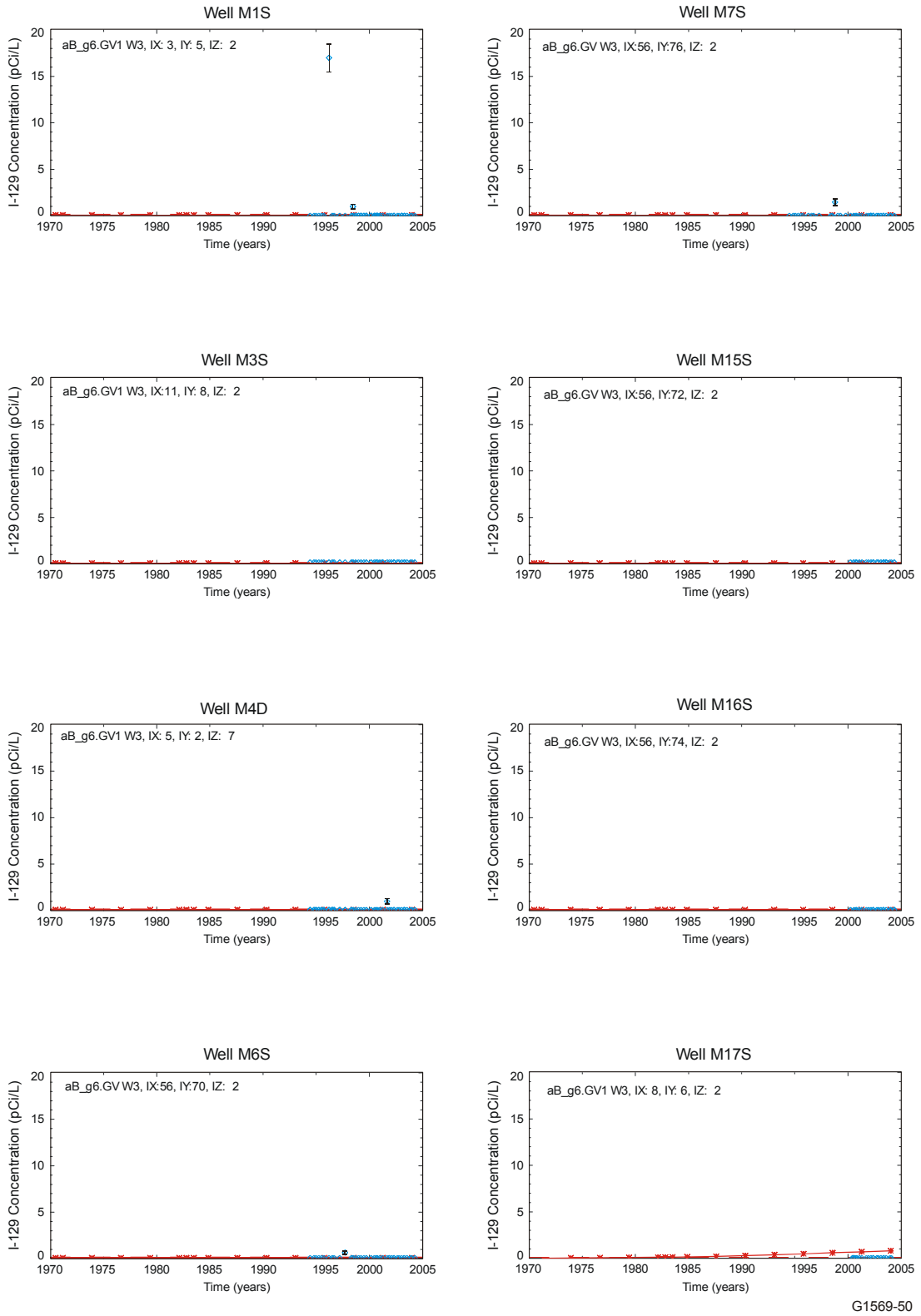

Figure 6-20. Comparison of simulated (red line) and observed (blue diamonds) iodine-129 concentration time histories for aquifer-monitoring wells in the vicinity of the Subsurface Disposal Area. Background concentration is indicated by the dashed line.

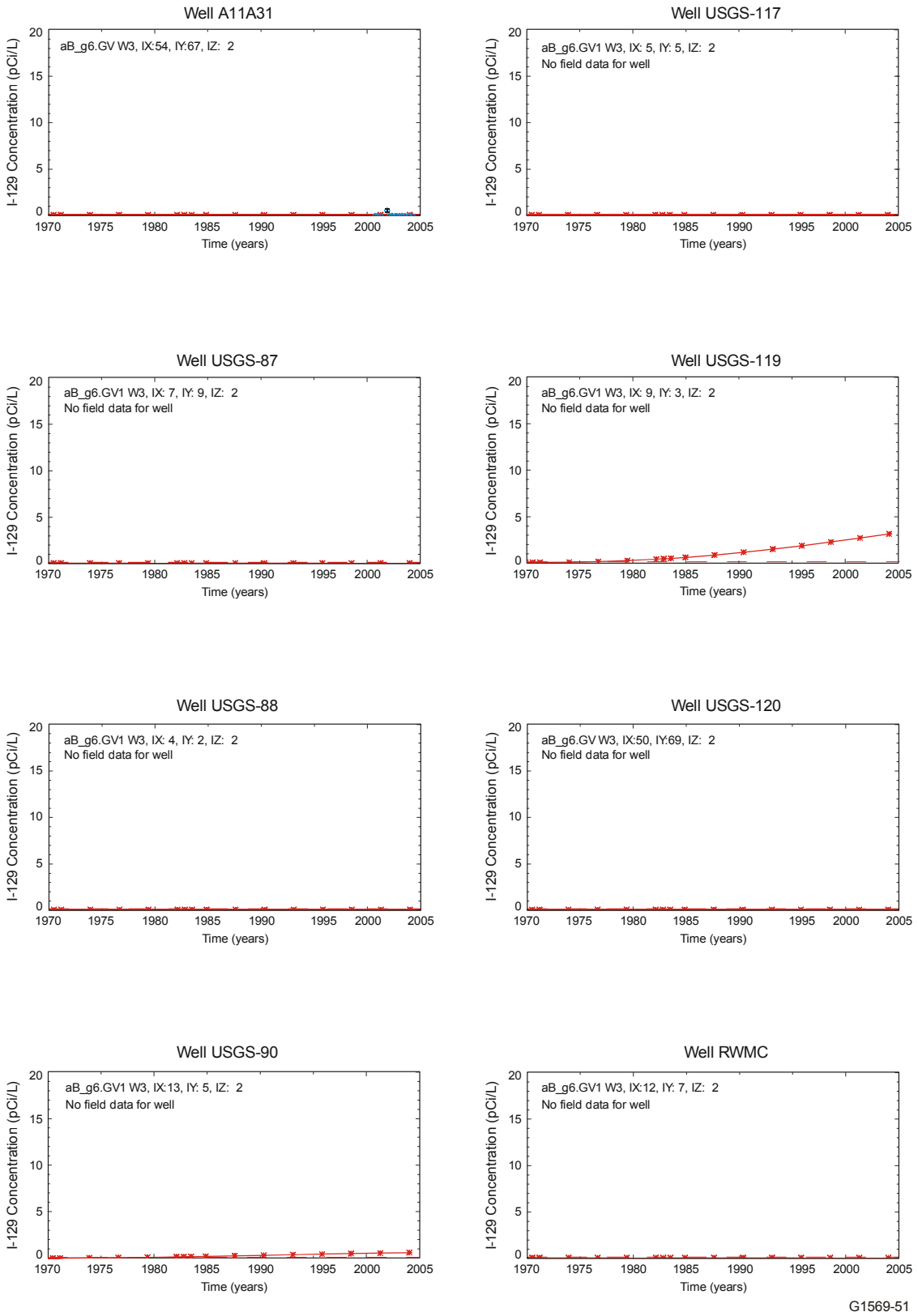

Figure 6-20. (continued).

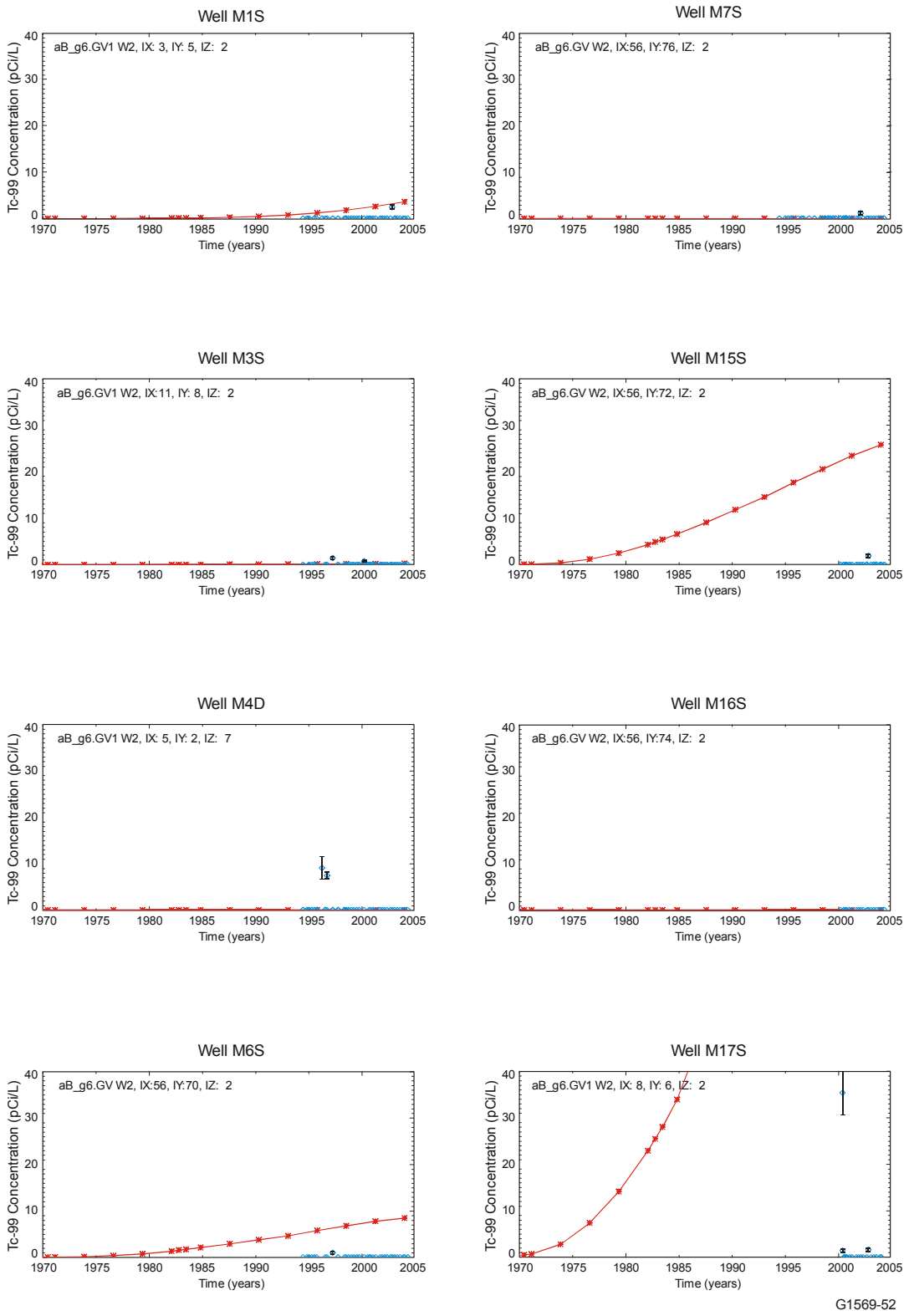

Figure 6-21. Comparison of simulated (red line) and observed (blue diamonds) technetium-99 concentration time histories for aquifer-monitoring wells in the vicinity of the Subsurface Disposal Area.

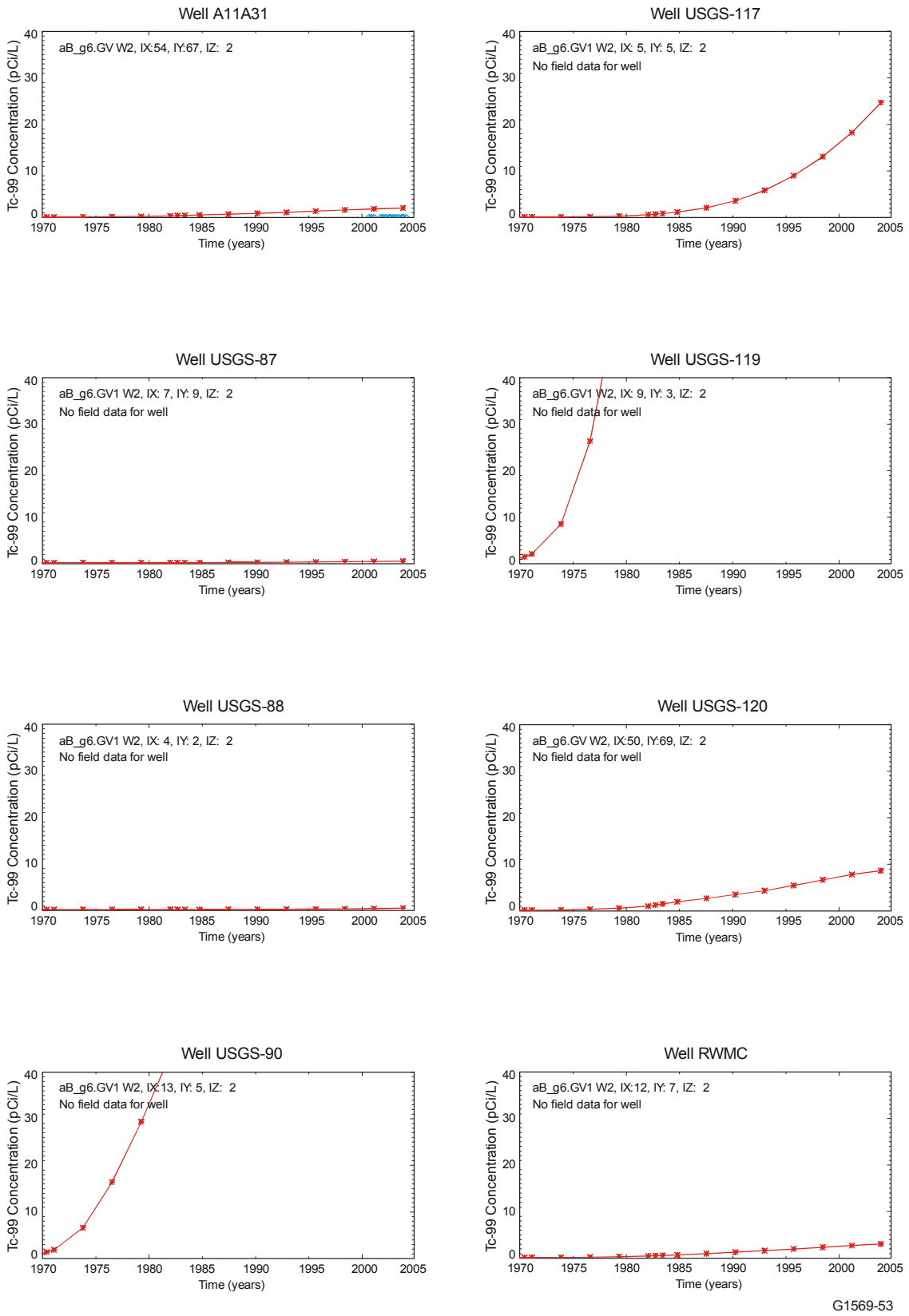

Figure 6-21. (continued).

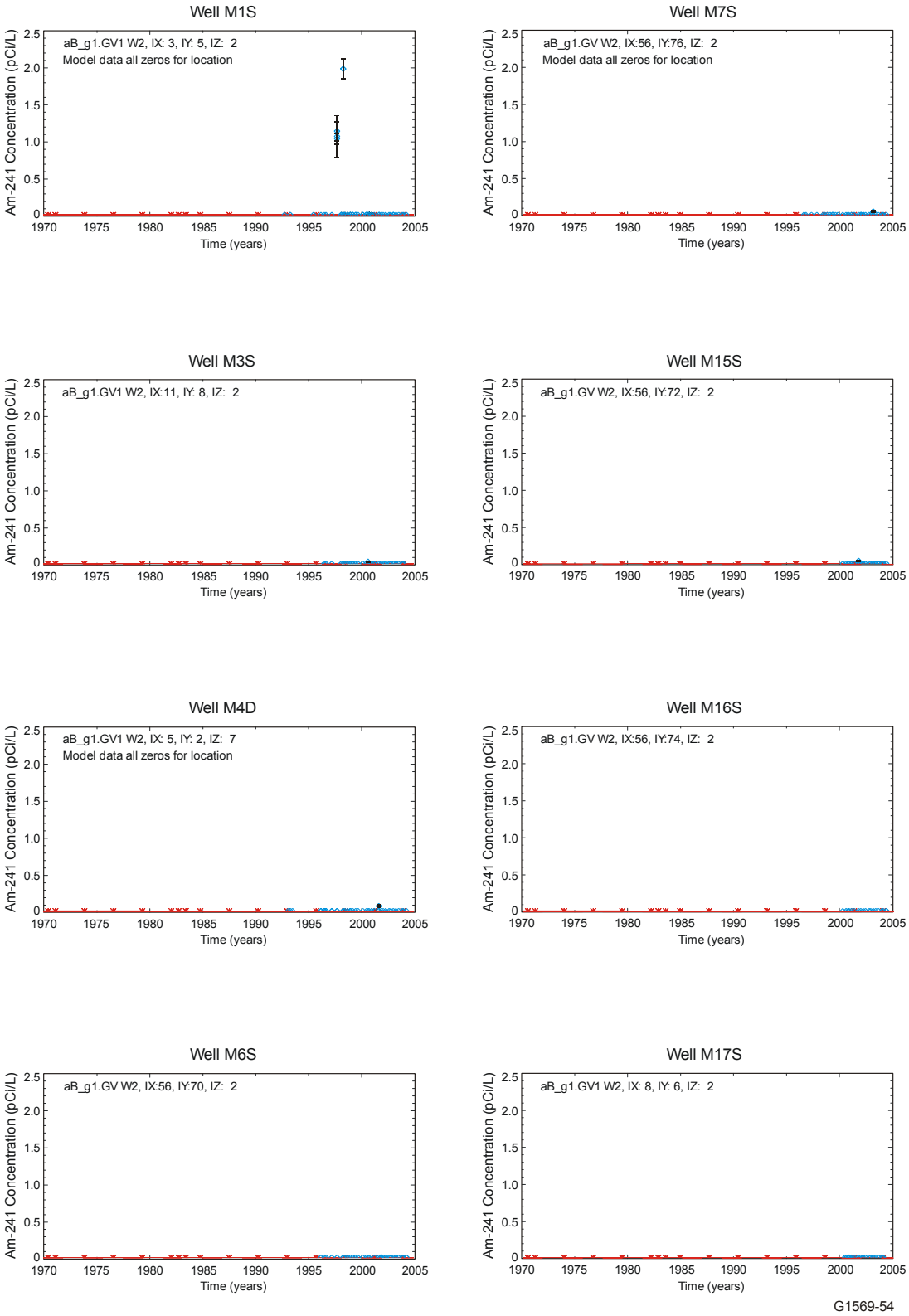

Figure 6-22. Comparison of simulated (red line) and observed (blue diamonds) americium-241 concentration time histories for aquifer-monitoring wells in the vicinity of the Subsurface Disposal Area.

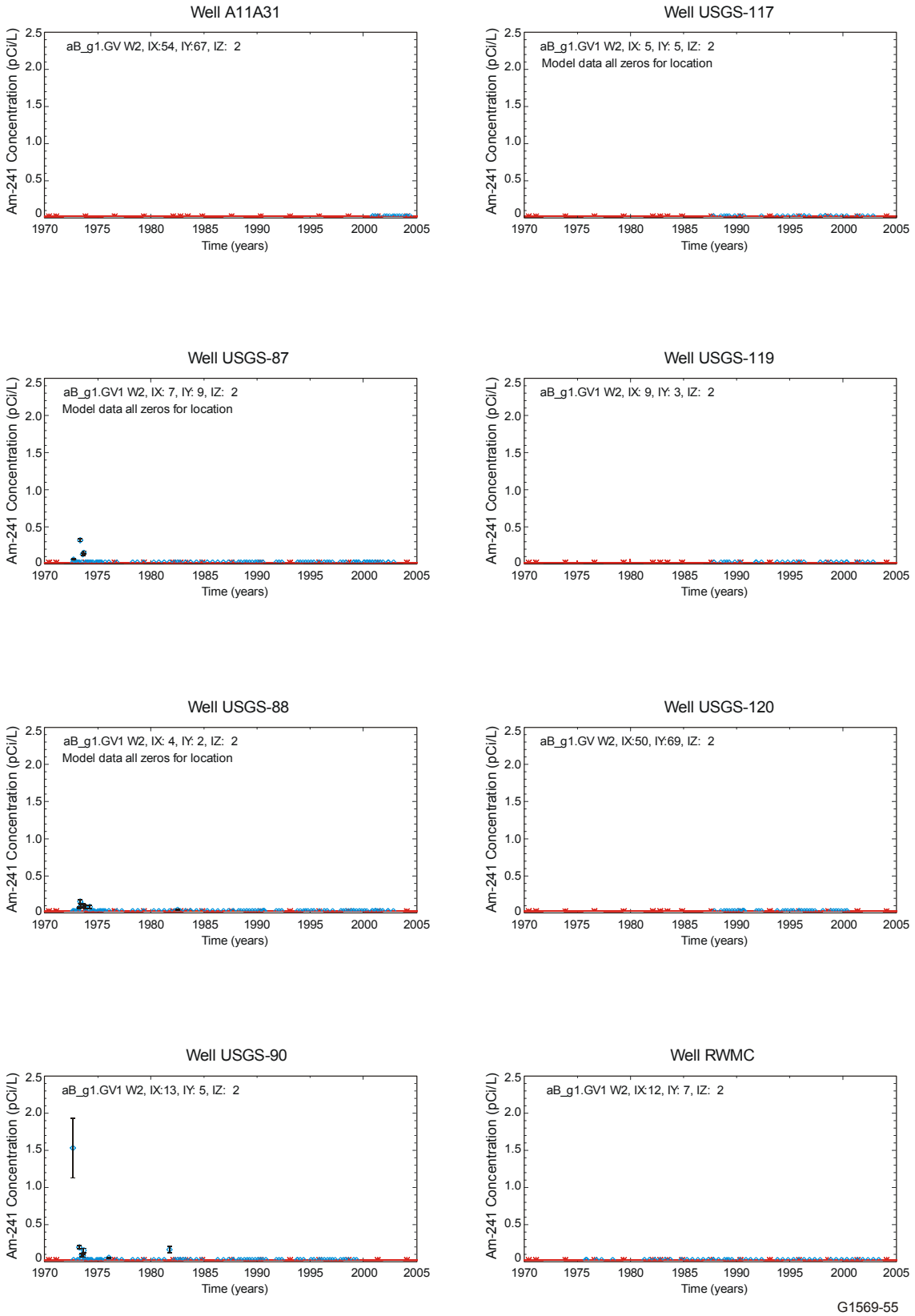

Figure 6-22. (continued).

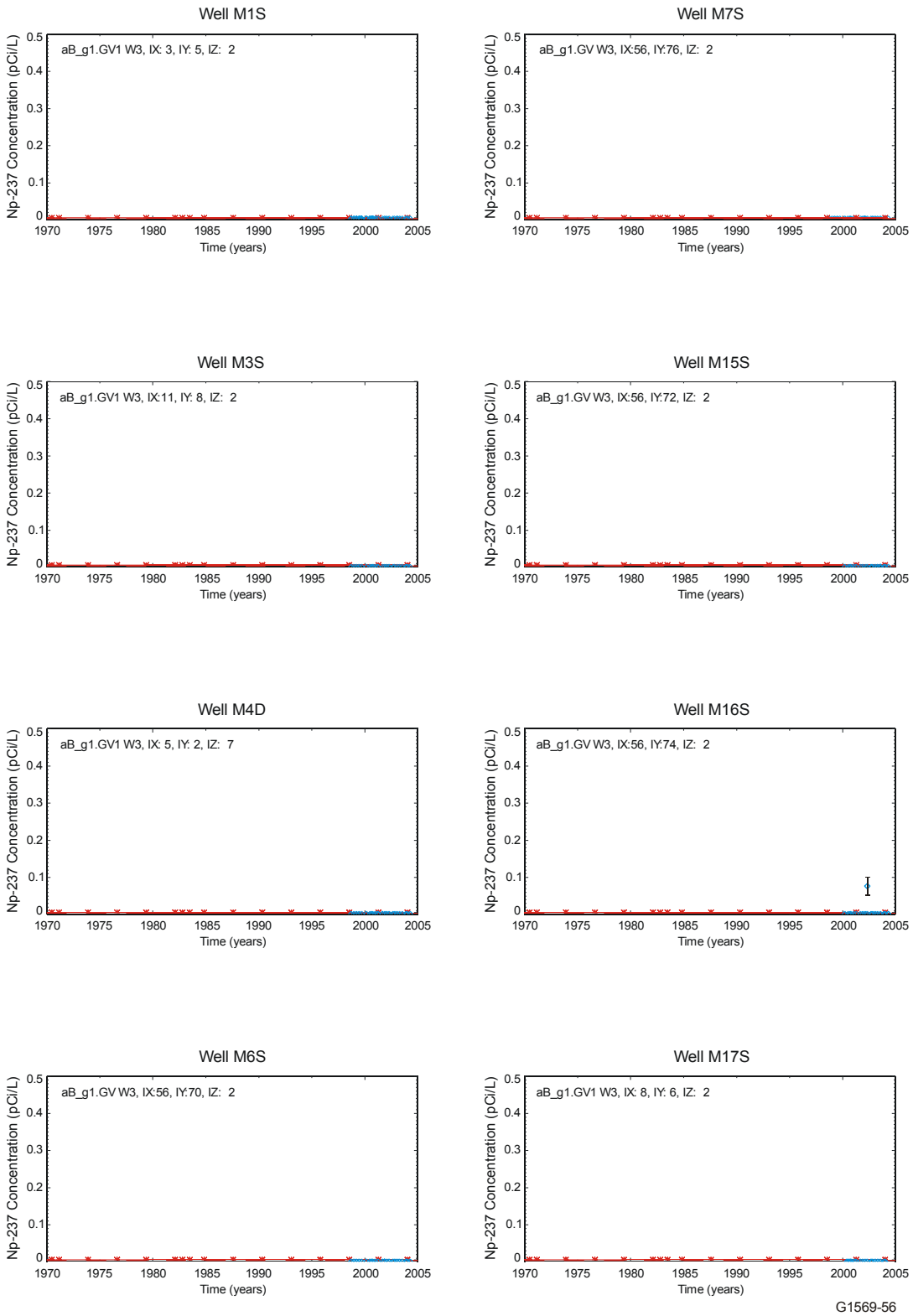

Figure 6-23. Comparison of simulated (red line) and observed (blue diamonds) neptunium-237 concentration time histories for aquifer-monitoring wells in the vicinity of the Subsurface Disposal Area.

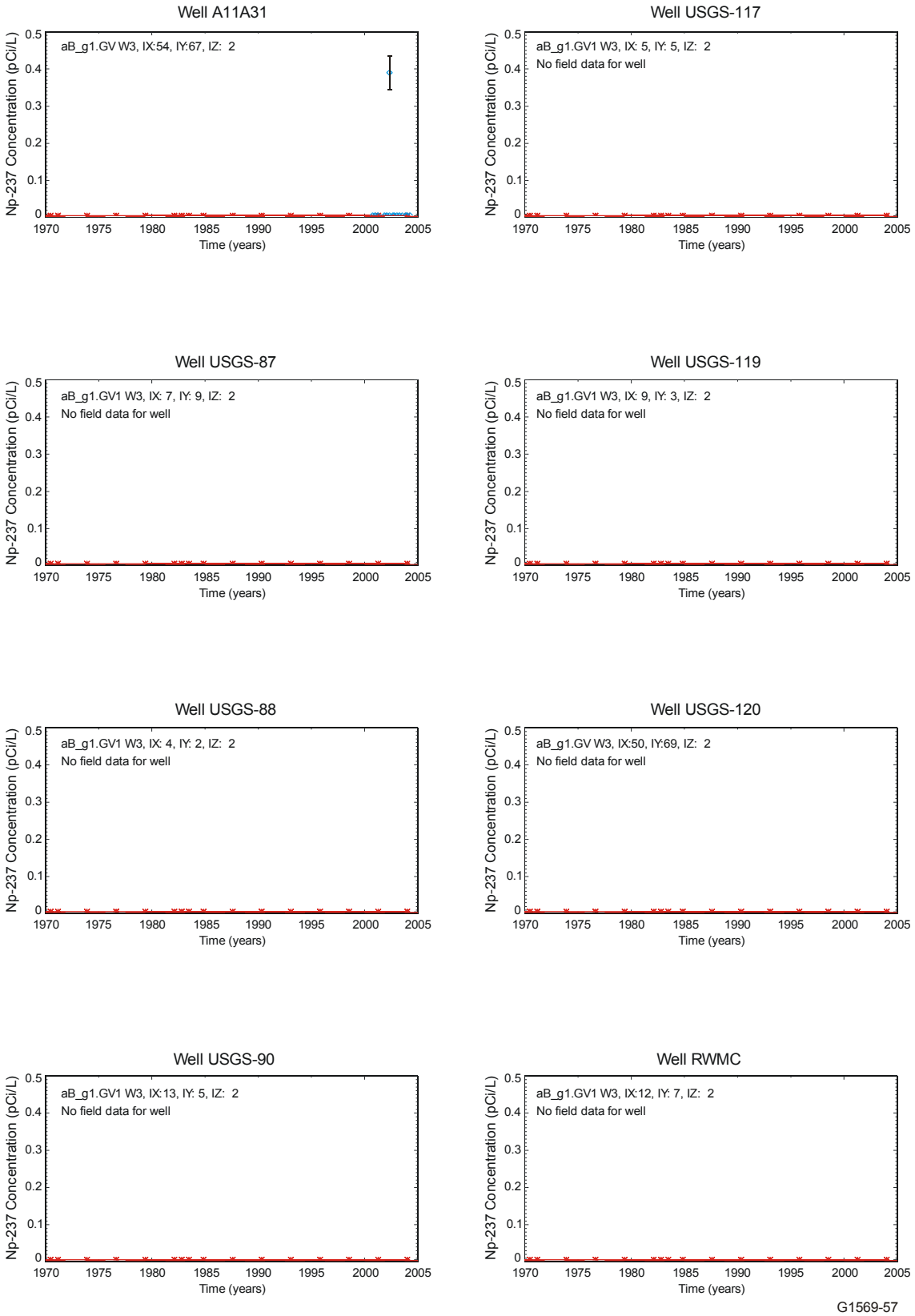

Figure 6-23. (continued).

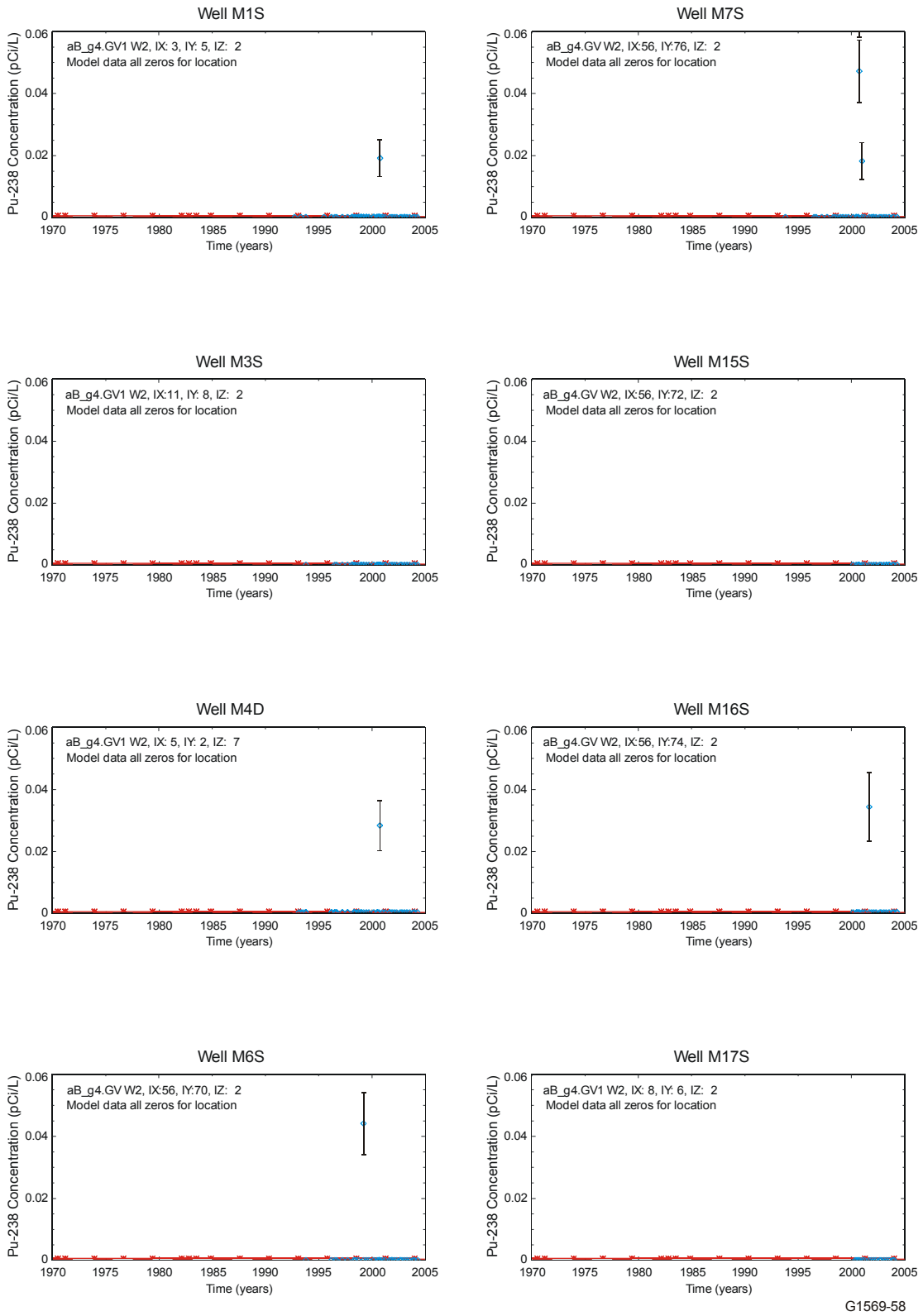

Figure 6-24. Comparison of simulated (red line) and observed (blue diamonds) plutonium-238 concentration time histories for aquifer-monitoring wells in the vicinity of the Subsurface Disposal Area.

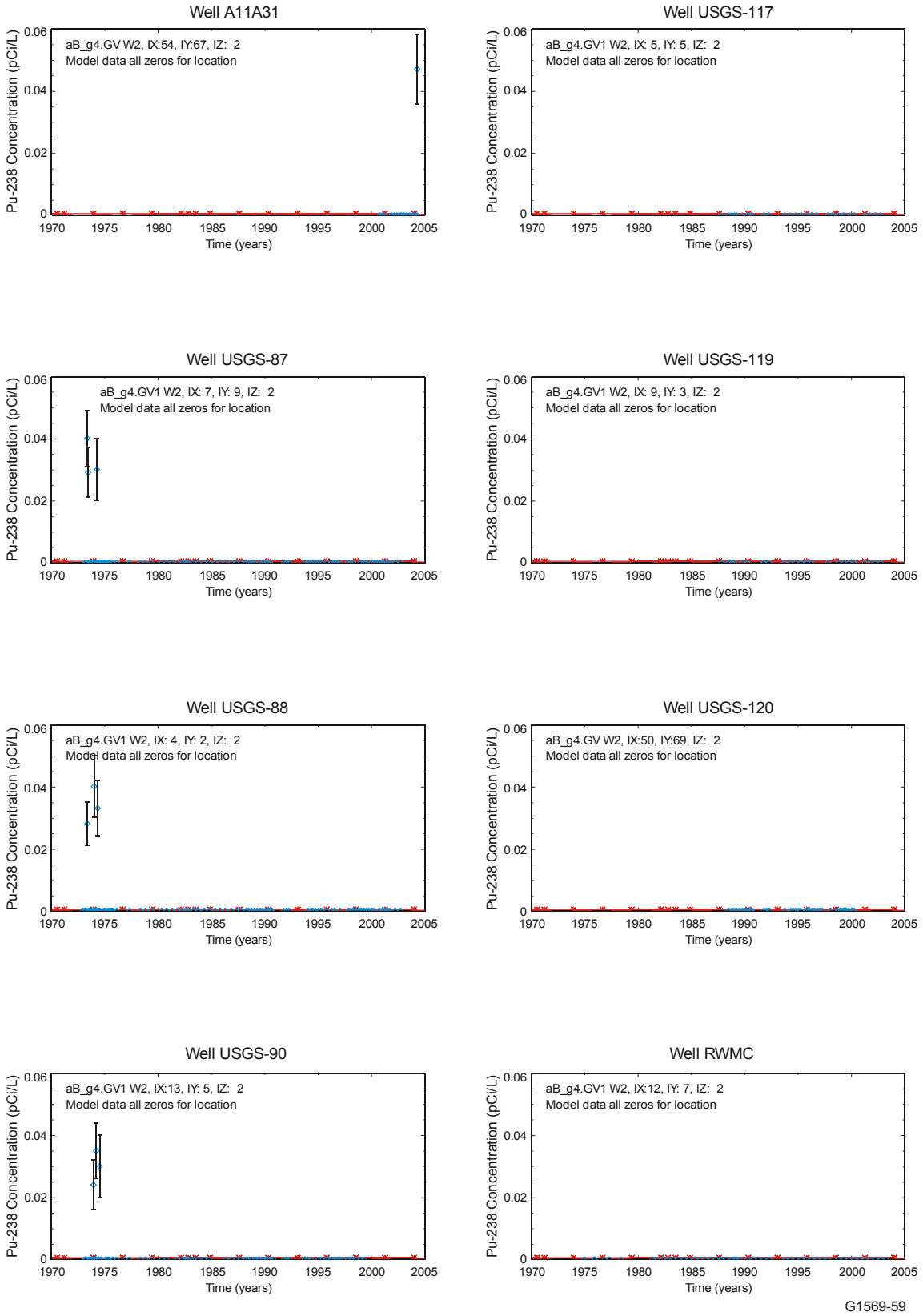

Figure 6-24. (continued).

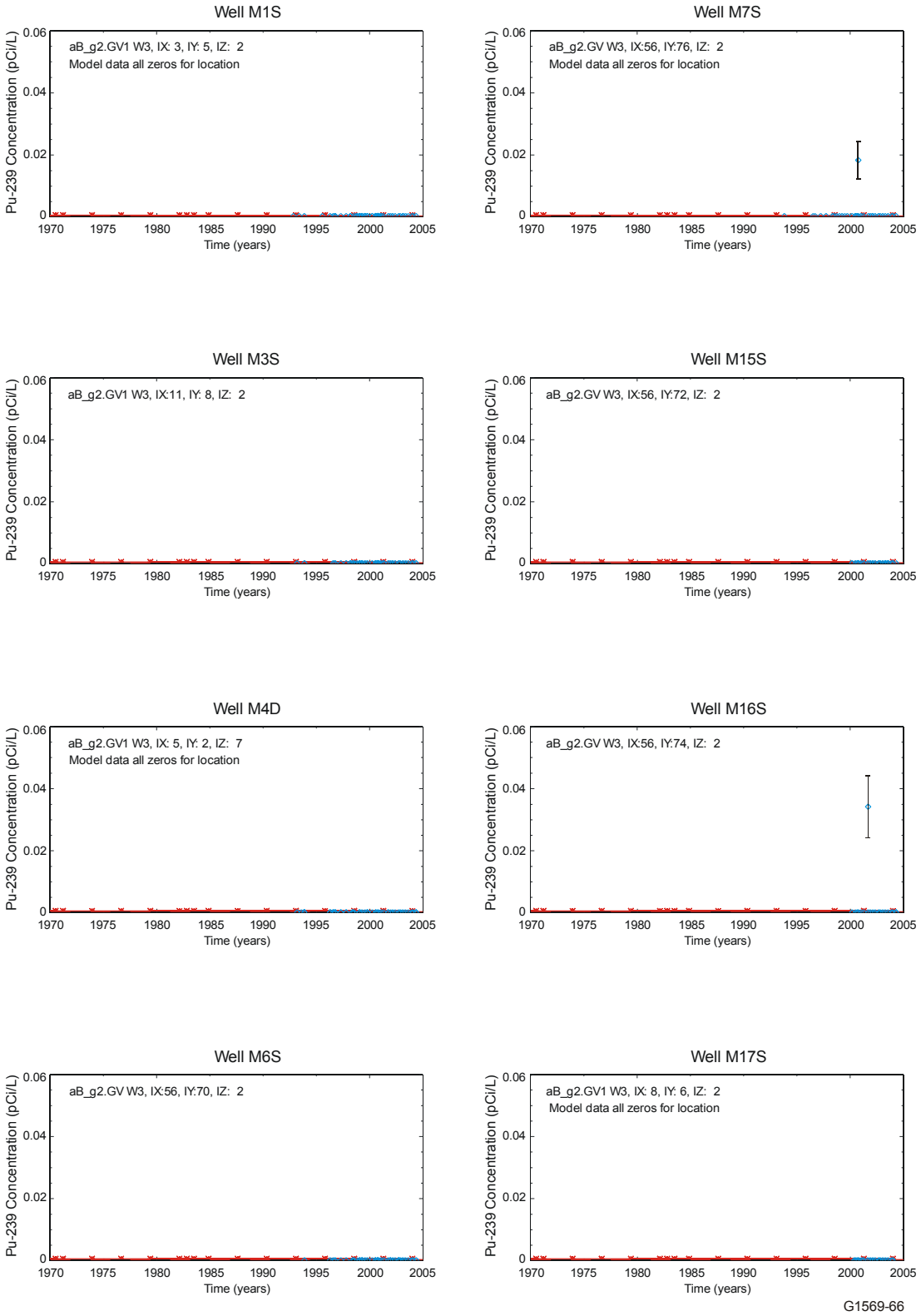

Figure 6-25. Comparison of simulated (red line) and observed (blue diamonds) plutonium-239 concentration time histories for aquifer-monitoring wells in the vicinity of the Subsurface Disposal Area.

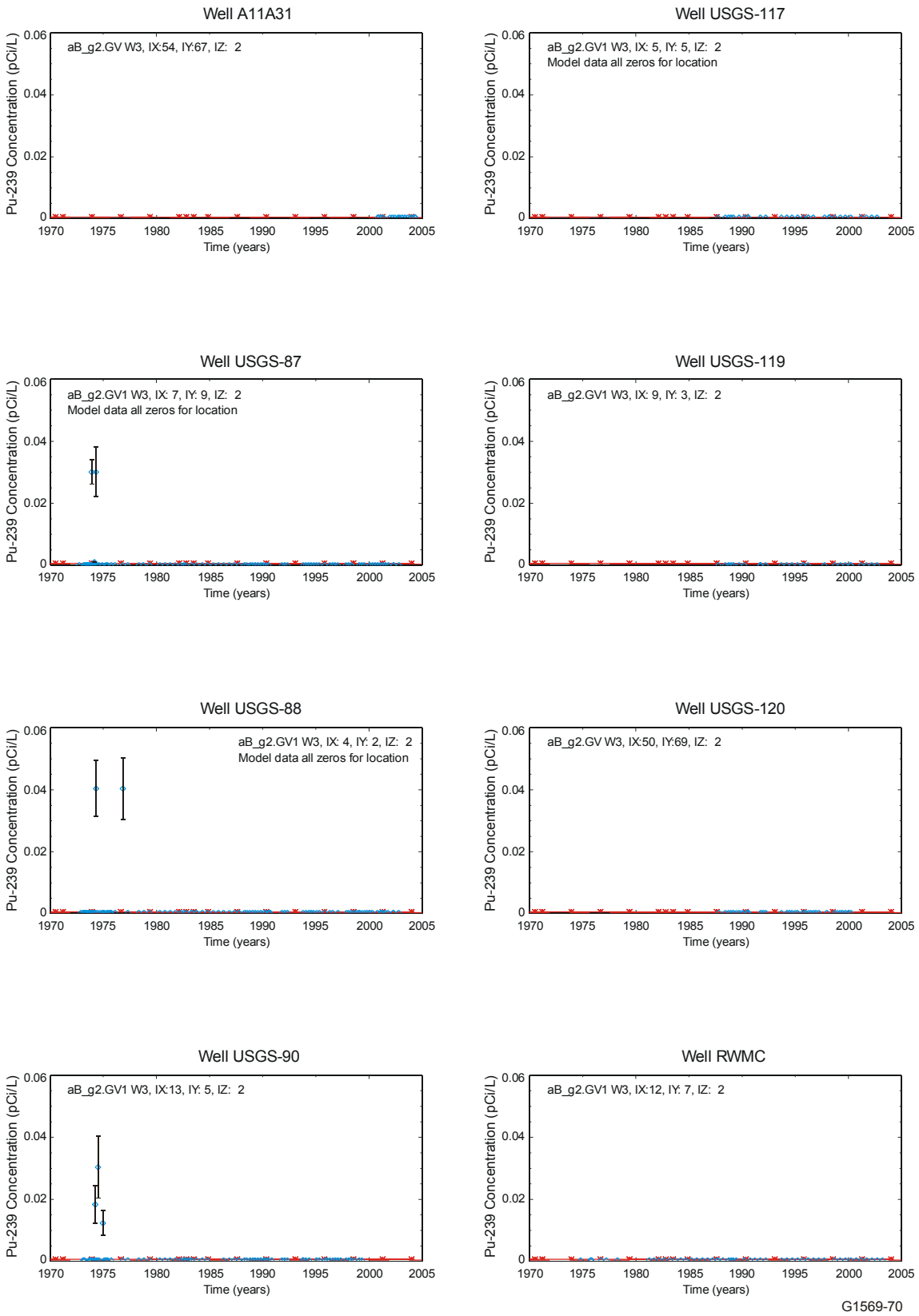

Figure 6-25. (continued).

Table 6-1. Comparison of aquifer model concentrations and observed concentrations with no adjustments for background concentrations.

Contaminant[a]	RI/FS Model Concentration[b] (pCi/L)	ABRA Model Concentration[c] (pCi/L)	IRA Model Concentration[d] (pCi/L)	Aquifer Background Concentration[e] (pCi/L)	Range of Detections[f] (pCi/L)[g]	Comments on Detections[g]
Ac-227	2E-11	5E-07	6E-08	NE	No analyses[h]	None
Am-241	7E-17	9E-17	1E-06	0	0.026–1.97	None
Am-243	3E-19	7E-24	2E-11	NE	No analyses	None
C-14	8E+01	3E+03	5 E+00	NE	1.8–42.1	Analysis began in 1994
Cl-l36	4E+00	3E+02	1E+00	NE	All nondetects	Analyses for Cl-36 began in the year 2001; Cl-36 analyses are done semiannually
I-129	1E+01	5E+01	4E+00	0	0.59–17.0	None
Nb-94	—	1E-23	1E-14	NE	No analyses	None
Np-237	1E-10	4E-04	8E-04	NE	0.08–0.38	None
Pa-231	1E-10	7E-06	1E-06	NE	No analyses	None
Pb-210	1E-17	3E-10	4E-08	NE	No analyses	None
Pu-238	4E-26	0	1E-12	0	0.018–0.37	NA
Pu-239	3E-17	5E-28	2E-11	0	0.034–4.3	None
Pu-240	3E-17	3E-30	7E-12	0	0.034–4.3	None
Ra-226	3E-17	4E-09	1E-08	0.01–0.37	4.0–12.7	Reported through gamma analysis when detected above laboratory instrument and sample matrix background
Ra-228	7E-19	—[i]	8E-12	0–2.7	No analyses	Reported through gamma analysis when daughter products are detected above laboratory instrument and sample matrix background
Tc-99	5E+03	4E+04	5E+01	NE	0.97–35.4	None
Th-229	4E-11	1E-06	4E-08	NE	No analyses	None
Th-230	2E-14	3E-06	8E-7	NE	No analyses	None
Th-232	2E-18	6E-13	1E-11	NE	No analyses	None
U-233	8E-08	4E-03	3E-04	NA	No analyses	NA
U-234	4E-10	1E-01	5E-02	1.92	2.0–4.3	None
U-235	2E-10	2E-02	3E-03	0.15	0.18–3.0	None
U-236	9E-09	4E-03	2E-03	NA	No analyses	None
U-238	9E-10	3E-01	4E-02	0.90	1.7–2.1	None

Table 6-1. (continued).

Contaminant[a]	RI/FS Model Concentration[b] (pCi/L)	ABRA Model Concentration[c] (pCi/L)	IRA Model Concentration[d] (pCi/L)	Aquifer Background Concentration[e] (pCi/L)	Range of Detections[f] (pCi/L)[g]	Comments on Detections[g]
Nitrate (as nitrogen-N)	6E+01 mg/L	1E+02 mg/L	1.4E+01 mg/L	0.4–5.0 mg/L	0.28–3.4 mg/L	None
Chromium (total)	3E+01 µg/L	1E+00 µg/L	1E-01µg/L	1–22 µg/L	4.6–99.6 µg/L	Most other high chromium values were approximately 40 to 60 pCi/L
Carbon tetrachloride	1E+02 µg/L	—[i]	8E+00 µg/L	0 µg/L	0–8 µg/L[f]	None
Methylene chloride	1E+01 µg/L	—[i]	1E-01 µg/L	0 µg/L	0–6 µg/L	Single detection of 6 µg/L was not believed to be a valid result
Tetrachloroethylene	1E+01 µg/L	—[i]	6E-01 µg/L	0 µg/L	0–0.4 µg/L[f]	None
1,4-dioxane	1E+02 µg/L	—[i]	—[i]	0 µg/L	No analyses	1,4-dioxane was only recently added to the analyte list

a. Observed values from earlier than 1987 are not presented in this table.
b. Maximum simulated concentration at 12-m depth through Fiscal Year 2004.
c. Maximum simulated concentration at 12-m depth through Fiscal Year 2001.
d. Maximum simulated concentration at 12-m depth through Fiscal Year 1995.
e. Aquifer background concentrations are from Table 4-1 in the draft remedial investigation and baseline risk assessment.
f. In the Subsurface Disposal Area-vicinity wells since 1987.
g. The range of observed values is taken from the nature and extent discussion in Section 4 of the draft remedial investigation and baseline risk assessment.
h. See the respective contaminant discussions in Section 4 of the draft remedial investigation and baseline risk assessment regarding lack of analysis.
i. Not reported in the IRA or ABRA.

ABRA = Ancillary Basis for Risk Analysis (Holdren et al. 2002)
IRA = Interim Risk Assessment (Becker et al. 1998)
NA = information not available on background concentrations
NE = not established
RI/FS = remedial investigation and feasibility study

Note: 0.0 pCi/L for radionuclides signifies a nondetectable result (i.e., result is <3σ and <maximum detectable concentration) using traditional radiochemical analyses methods.

Simulated vertical profiles of C-14 and U-238 concentrations within the aquifer are shown in Figures 6-26 and 6-27 to illustrate behavior for selected contaminants. These vertical profiles are at the same horizontal location as that shown previously in Figure 6-15 for nitrate, which generally contained the maximum concentration for most times. Similar to profiles for nitrate, there are times when the maximum concentration does not occur at the uppermost gridblock for C-14. This is because contaminant flux from the vadose zone model behaved similarly for nitrate and C-14 with a pulse of contaminant followed by clean water. The simulated profile for U-238 shows that the maximum concentration always occurs in the uppermost gridblock, reflecting the long-duration, delayed contaminant flux from the vadose zone model. The overall implication for the baseline risk assessment remains the same, that it is not necessarily conservative to extract concentrations from the uppermost gridblock.

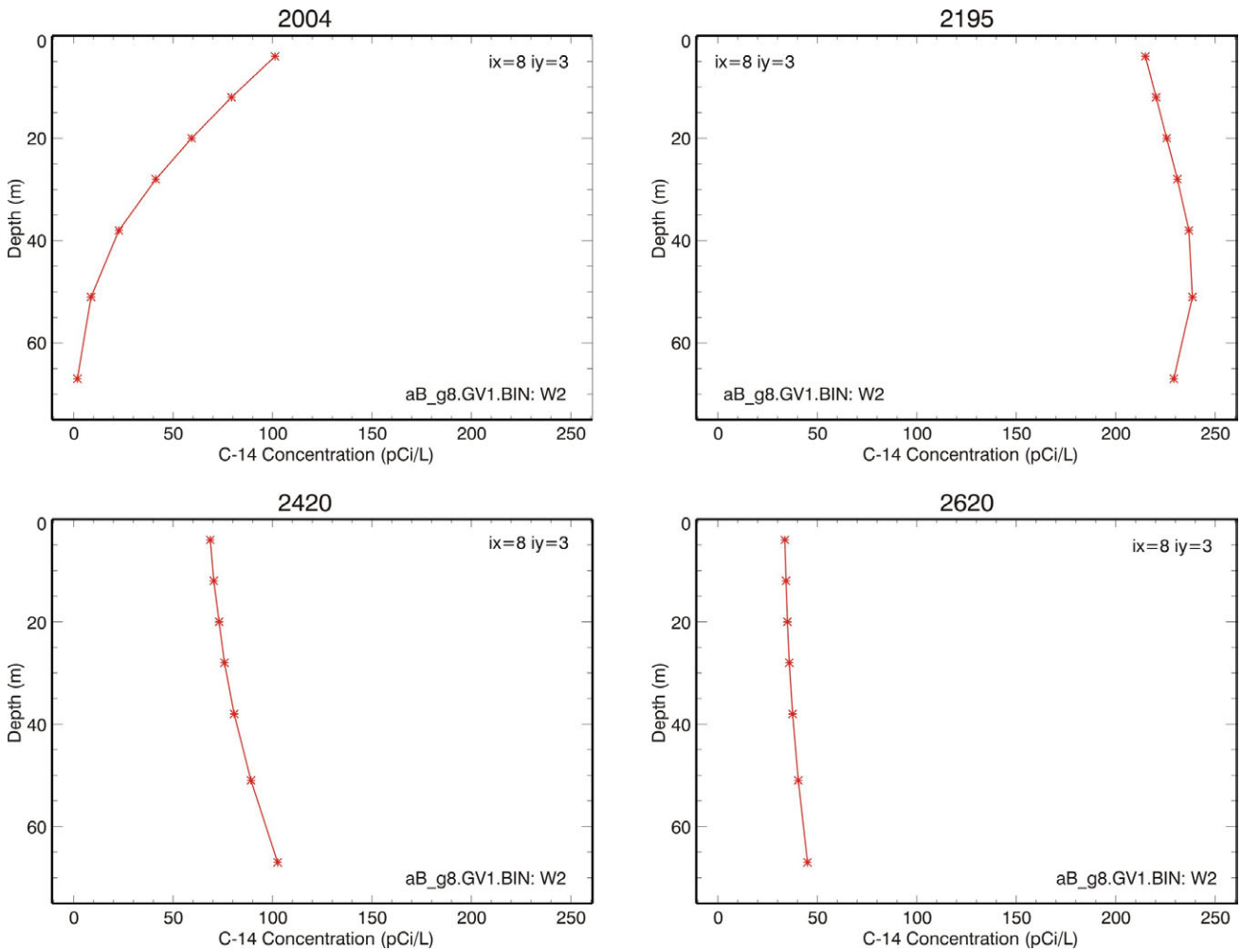

Figure 6-26. Simulated aquifer carbon-14 concentration profiles beneath the Subsurface Disposal Area. The year is shown at the top of each plot.

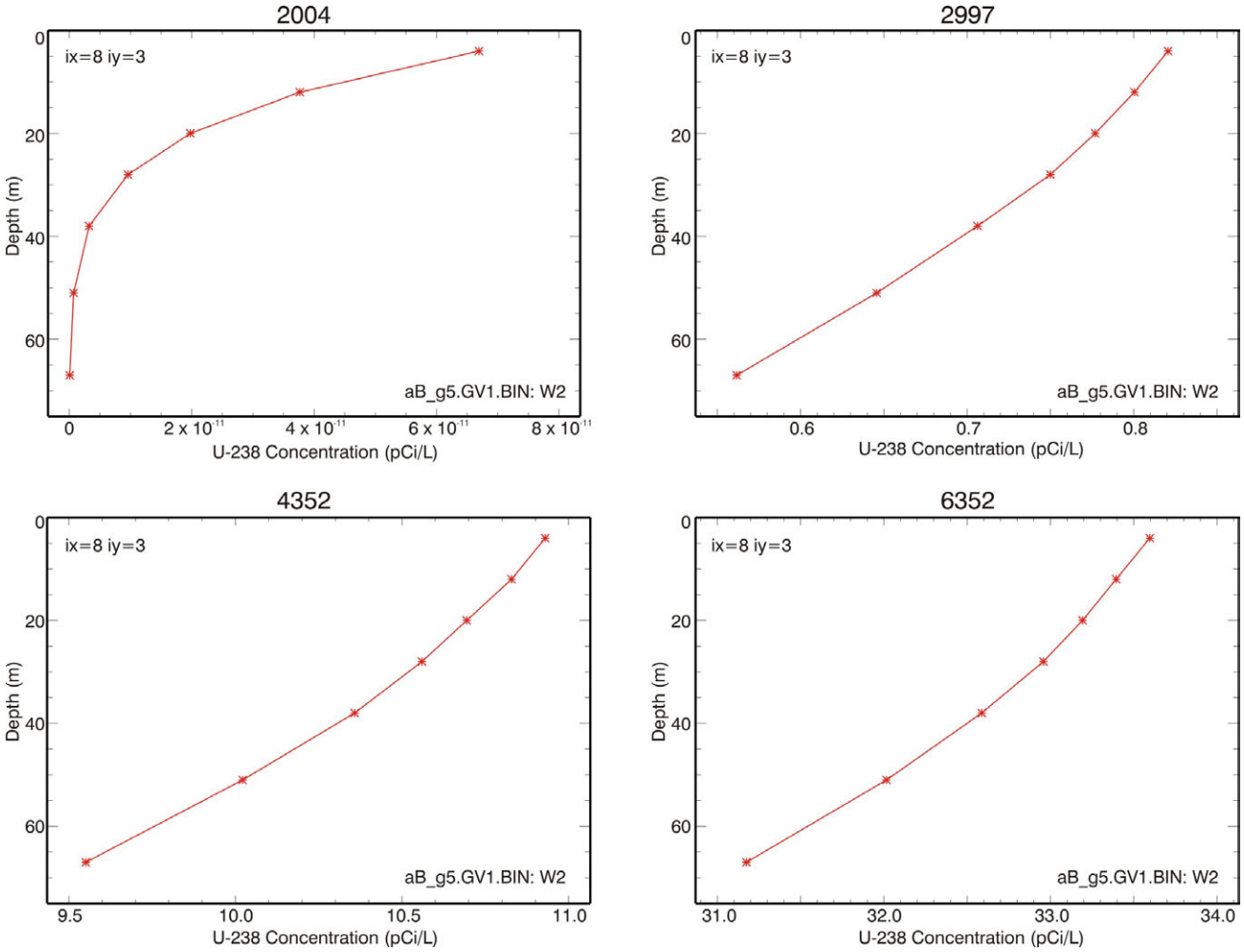

Figure 6-27. Simulated aquifer uranium-238 concentration profiles beneath the Subsurface Disposal Area. The year is shown at the top of each plot.

6.2 Receptor Locations and Extraction of Simulated Aquifer Concentrations for Risk Evaluation

Simulated aquifer COPC concentrations and hypothetical receptors are used for the risk evaluation. These simulated concentrations are taken from the results from a variety of locations. For the draft RI/BRA, the locations where receptors are allowed are defined in Holdren and Broomfield (2004) as being at the INL Site boundary during the period of institutional control, which lasts until Calendar Year 2110, and up to the RWMC fence boundary after institutional control ends. This receptor definition was implemented for purposes of extracting simulated concentrations from the TETRAD model results at the current SDA fence boundary as shown in Figure 6-28. Maximum simulated aquifer concentrations, as a function of time from those gridblocks with a centroid located outside the SDA fence, were used in calculations. Shaded blocks in the Figure 6-28 represent locations that were excluded from the risk evaluation.

The location of the gridblock with the maximum concentration changed during every simulation. Generally, but not always, the location of maximum simulated aquifer concentration occurred either within the SDA or at one of the gridblocks in immediate proximity to the SDA. For some mobile

contaminants, such as Tc-99, the maximum simulated concentration occurred in gridblocks away from the SDA to the southeast. These occurrences most likely resulted because of lateral movement of water and contaminants away from the SDA that was caused by the general slope of the B-C and C-D interbeds to the east-southeast. This lateral movement demonstrates the importance of including variable interbed topography in simulating water and contaminant transport through the vadose zone.

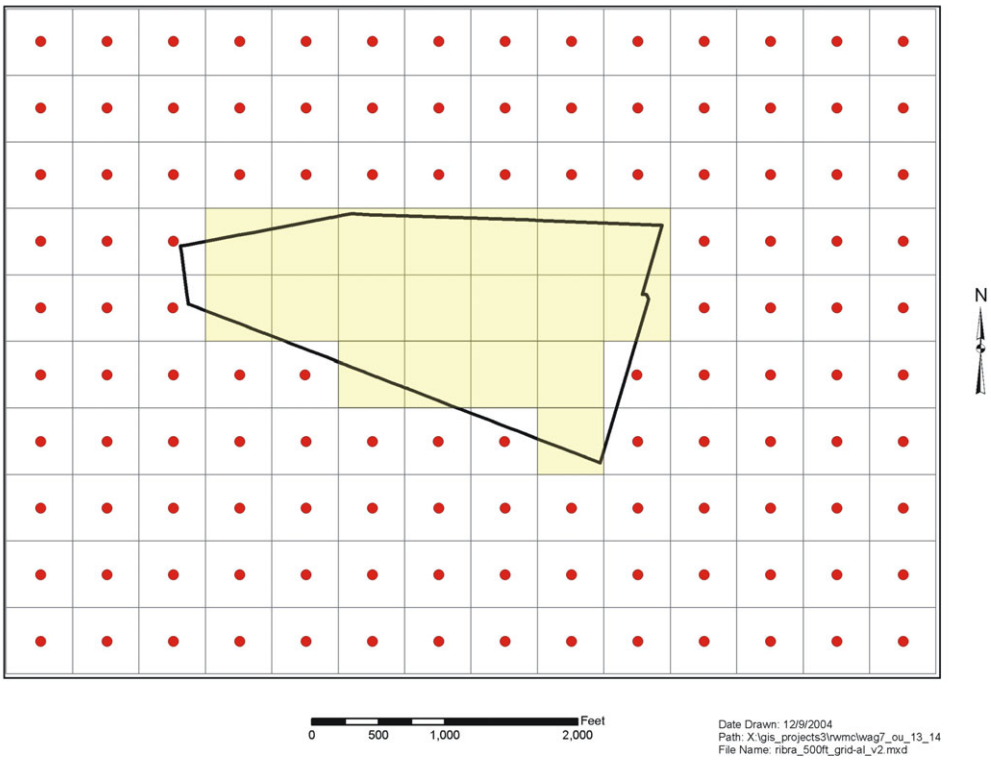

Figure 6-28. Subsurface Disposal Area fence superimposed on the first-level refined grid of the aquifer simulation for purpose of defining hypothetical receptor locations for the draft remedial investigation and baseline risk assessment. Gridblocks whose centroid (indicated by a dot) is outside the fence boundary are potential receptor locations.

Extraction of maximum simulated concentrations as a function of time from the TETRAD results was automated via a PV-Wave post-processing routine. In addition to determining maximum concentrations along the INL Site boundary and for locations outside the SDA fence, there were two other methods implemented. To provide results for comparisons to simulated concentrations and risks from the ABRA model, the maximum simulated concentration anywhere, including the excluded gridblocks inside the SDA fence boundary, were extracted. And lastly, for the low-level waste performance assessment and composite analysis, simulation results were extracted slightly differently because a 100-m buffer zone outside the SDA facility fence is defined in Department of Energy Order 435.1, resulting in a slightly different set of allowed receptor locations with more gridblocks proscribed as receptor locations.
The potential receptor locations for the low-level waste performance assessment and composite analysis are indicated in Figure 6-29 with the proscribed gridblocks shaded. Maximum concentration as a function of time was saved in files, along with gridblock locations of the maximums.

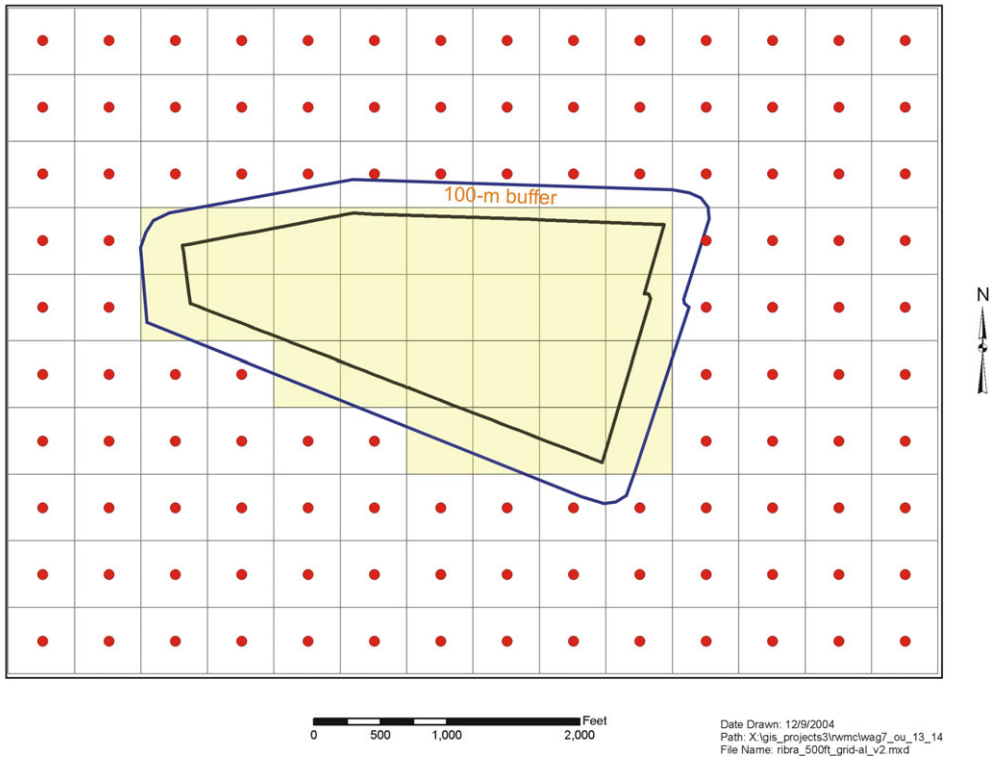

Figure 6-29. Subsurface Disposal Area fence plus a 100-m buffer superimposed on the first-level refined grid of the aquifer simulation for the purpose of defining hypothetical receptor locations for the low-level waste performance assessment and composite analysis. Gridblocks whose centroid (indicated by a dot) is outside the 100-m buffer are potential receptor locations.

In all cases, simulated concentrations are extracted from the second gridblock down from the top of the aquifer. This gridblock extends from the 8- to 16-m (26.2- to 52.5-ft) depth with a midpoint of 12 m (39.4 ft). This second gridblock approximates a well that is screened from 8 to 16 m (26.2 to 52.5 ft). As shown previously in Section 6.1, concentration profiles are not always automatically highest at the uppermost gridblock, depending on the contaminant mass loading history. Therefore, it is not automatically conservative to extract concentrations from the uppermost gridblock.

6.3 Risk and Hazard Index Isopleth Methodology

As indicated in the previous simulation, the location of maximum concentration shifted spatially over time. Risk determined from these location-varying concentrations is conservative because it is not realistic to require a receptor to get water from a well at one location during one time period, and then switch to getting water from a different well at another location for another time period. To evaluate the amount of conservatism, a different approach was used to evaluate risk for a receptor that got water from a well at one location consistently. This approach used a spatially-consistent receptor. In this method, simulated concentrations for all COPCs at each gridblock (second gridblock down again) at each time were converted to their equivalent risks and summed to get the cumulative risk. These spatially-consistent receptor risks could then either be contoured to show the horizontal extent of risk, or further interrogated to determine the maximum spatially-consistent receptor risk as a function of time. These extensive calculations were automated in a PV-Wave post-processing routine. The results of these analyses are presented in Section 6 of the draft RI/BRA.

6.4 Base-Case Sensitivity Simulations

This section discusses implementation of simulations for the RI/BRA sensitivity analyses, which were defined in Holdren and Broomfield (2004). Results, when presented, are in terms of water saturations or simulated concentrations. Results are presented for U-238, C-14, and nitrate simulations to demonstrate the impact from a variety of contaminants with sorbing and nonsorbing behavior for most of the sensitivity cases. Exceptions are presentation of Pu-239 and Pu-240 for a case with no sorption in the interbeds and Tc-99 for evaluation of impacts from increasing the fractured-basalt permeability anisotropy ratio. Technetium-99 and I-129 are not shown for most of the sensitivity cases because those results are being revised for the feasibility study. The C-14 results presented in these sensitivity simulations use the model that includes both gaseous-phase and dissolved-phase transport and the effect of vapor vacuum extraction described above in Sections 5.4 and 5.5. Both the time and concentration axes vary on the sensitivity results plots to show adequate detail in the results to discern behavior. The sensitivity results also are presented in terms of impacts to groundwater-pathway risks in Section 6 of the draft RI/BRA. These sensitivity simulations test assumptions used in the model, and as such, the simulations represent an assessment of conceptual uncertainty.

6.4.1 Upper-bound Inventories

A simulation suite was performed where upper-bound inventories were used instead of best estimates. The only difference in the subsurface flow and transport models was that a different source term was supplied. The entire suite of potential contaminants was simulated. Figure 6-30 shows a comparison of the concentration of U-238, C-14, and nitrate between the base case and the upper-bound inventory simulation. In each case, simulated concentrations are larger, although it takes longer for this to be evident for U-238, which undergoes sorption, thus, the longer time portrayed on the horizontal axis. Note that the concentrations shown in this sensitivity section are for the maximum simulated concentration anywhere in the aquifer, including beneath the SDA, for all simulated times. This is in contrast to risks presented in Section 6 of the draft RI/BRA, which are based on maximum simulated concentration anywhere outside the SDA fence after institutional control ends in Calendar Year 2110.

6.4.2 No B-C Interbed

The method used to define interbed upper surfaces and interbed thicknesses resulted from a consistent statistical approach that was based on all lithologic data available. To incorporate spatial variability, geostatistical analysis and interpolation methods were implemented and robustly tested by Leecaster (2002) and updated in Leecaster (2004). As with the ABRA model, the RI/FS model used kriging results without imposing any bias into them. In the IRA model, kriging results were modified to enforce gaps in the interbeds in gridblock locations containing wells that showed an interbed was missing at that location.

To bound the effect of including gaps, a simulation suite was performed where the entire B-C interbed was treated as though it were missing. The gridblocks that were assigned B-C interbed properties for the RI/FS model were assigned properties of fractured basalt instead. This allowed the mobile fraction of Pu-239 and Pu-240 to continue migrating down to the C-D interbed before being affected by the higher distribution coefficient. Upper-boundary conditions for water infiltration rates and contaminant source-term results were unchanged from the RI/FS model. The entire suite of potential contaminants was simulated, except for VOCs (Group 11). As a result of not simulating VOCs, C-14 simulation results for this case do not include the effect of VVET operation. Figure 6-31 shows a comparison of concentration of U-238, C-14, and nitrate between the RI/FS model and the sensitivity simulation without the B-C interbed. As expected, in each case, the simulated concentrations for the sensitivity case show an earlier breakthrough due to absence of the B-C interbed, with the largest

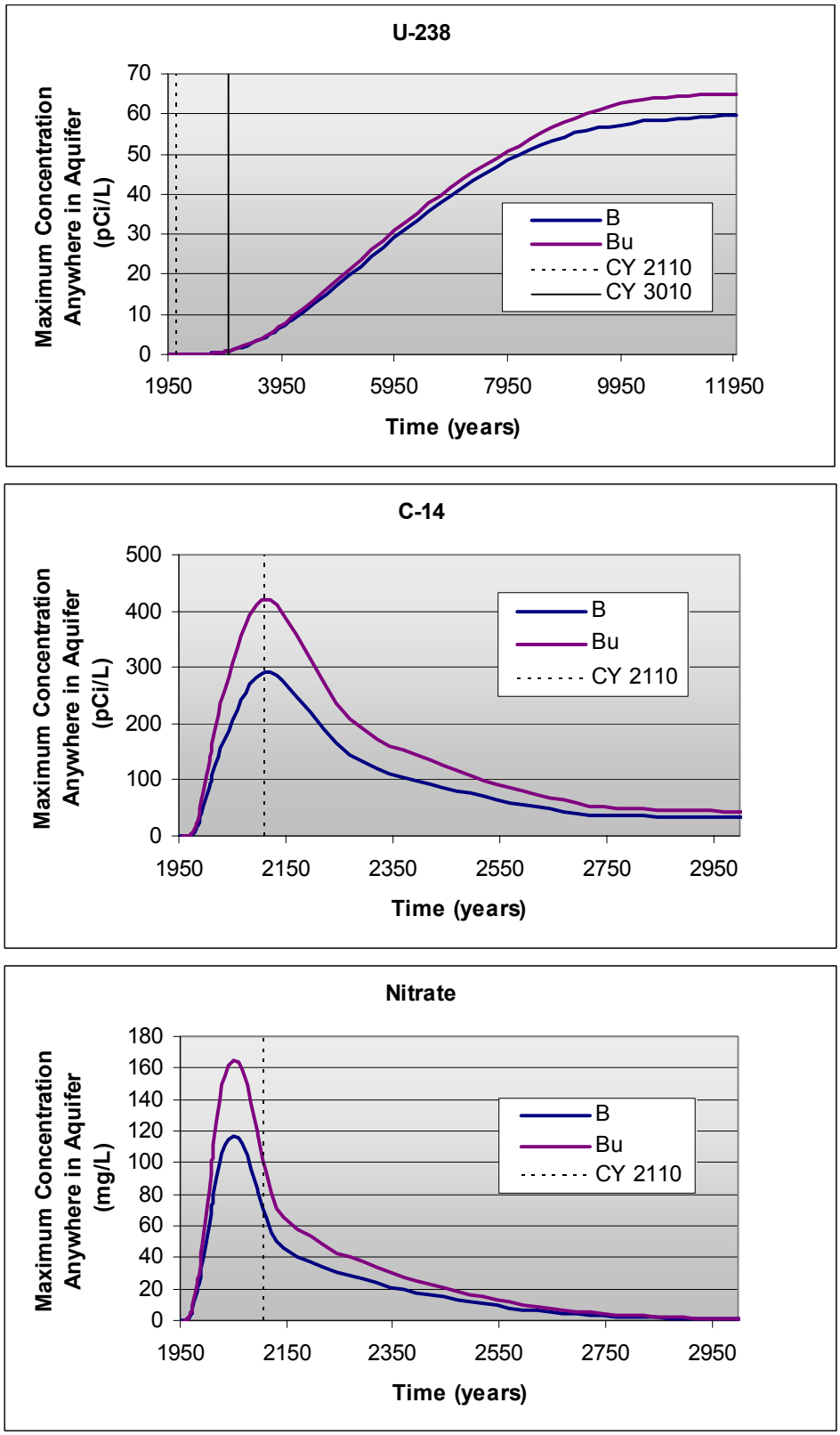

Figure 6-30. Comparison of the base (B) and the upper-bound inventory (Bu) maximum simulated concentration anywhere in the aquifer for uranium-238, carbon-14, and nitrate.

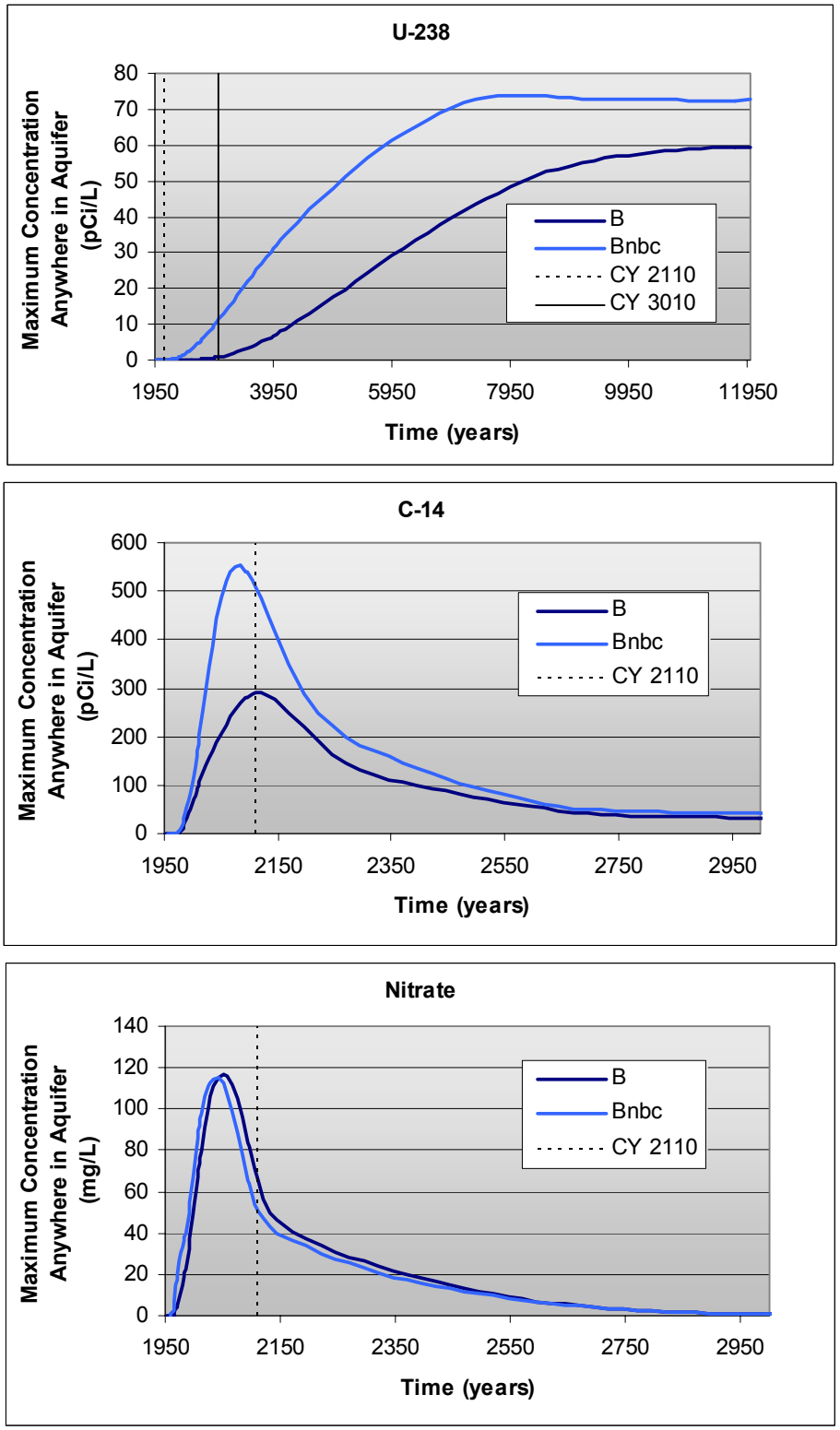

Figure 6-31. Comparison of the base (B) and the no B-C interbed (Bnbc) maximum simulated concentration anywhere in the aquifer for uranium-238, carbon-14, and nitrate. The carbon-14 results do not include the effect of vapor vacuum extraction operations.

change in results for U-238, where lack of sorption in the B-C interbed exaggerates impact. Magnitudes of peaks do not change substantially with U-238 and C-14 both increasing. The nitrate peak concentration decreases slightly, possibly due to interactions between where nitrate is released into the vadose zone model and the locations where nitrate would otherwise have been redirected when transiting the B-C interbed.

6.4.3 High Infiltration Inside the Subsurface Disposal Area

Water infiltration rates are assigned at the upper boundary of the vadose zone simulation domain. These amounts of water also are input into the source-term model and impact contaminant release. Uncertainty in assigned infiltration rates is acknowledged. To bound the effect of the infiltration rate being greater than was assigned, a sensitivity simulation was performed whereby the infiltration rate everywhere inside the SDA boundary was assigned a value of 23 cm/year (9 in./year), both in the source-release model and in the vadose zone flow and transport model, beginning in 1952. The water infiltration rate outside the SDA boundary remained at the background estimate of 1.0 cm/year (0.4 in./year). The 23-cm/year (9-in./year) infiltration rate is the same as the total annual average precipitation on the INL Site and represents a conservative upper-bound inventory on the possible net infiltration into the subsurface. The entire suite of potential contaminants was simulated.

Figure 6-32 shows a comparison of U-238, C-14, and nitrate concentrations between the base case and the sensitivity simulation with a high-infiltration rate inside the SDA. As expected, in each case, the simulated concentrations for the sensitivity case show higher concentrations and reach peak values sooner than the base-case simulated concentrations. Conceptually, water that contacts waste results in higher concentrations uniformly in the groundwater pathway. Results of this sensitivity case demonstrate this aspect of the conceptual model.

In addition to the effect on groundwater-pathway concentration results, this sensitivity simulation lends itself to assessing the impacts on simulated interbed saturations. Figure 6-33 illustrates the resulting maximum simulated water saturations in the B-C and C-D interbeds for the high-infiltration case. Water saturations in Figure 6-33 can be compared to those for the base case, which are shown previously in Section 5.1, Figure 5-4. The extent of high saturation areas above 0.9 is considerably larger, especially in the B-C interbed. Better agreement with locations that had shown perched water in the western half of the SDA is shown. These locations are shown in the base-case results presented in Section 6.1.

6.4.4 Pit 4 Inventory Not Removed and No Beryllium Block Grouting

The base-case model included removal of a portion of the Pit 4 inventory, based on the assumption that the Accelerated Retrieval Project was completed. Likewise, grouting of beryllium blocks also was included. This sensitivity study considered a case where neither of these actions occurred. The entire suite of potential contaminants was simulated.

Figure 6-34 shows a comparison of U-238 and C-14 concentrations between the base case and sensitivity simulation with the Pit 4 inventory not reduced and without beryllium block grouting. Nitrate is not shown because there was no change to the source-release modeling for this sensitivity case. Simulated U-238 concentrations for the sensitivity case are essentially the same because, although there is a larger inventory available for release in the sensitivity case, the solubility limit for U-238 keeps the source-release term almost equivalent between the two cases. The simulated C-14 concentration is slightly higher for the sensitivity case because there is a greater release from the source model due to a larger inventory.

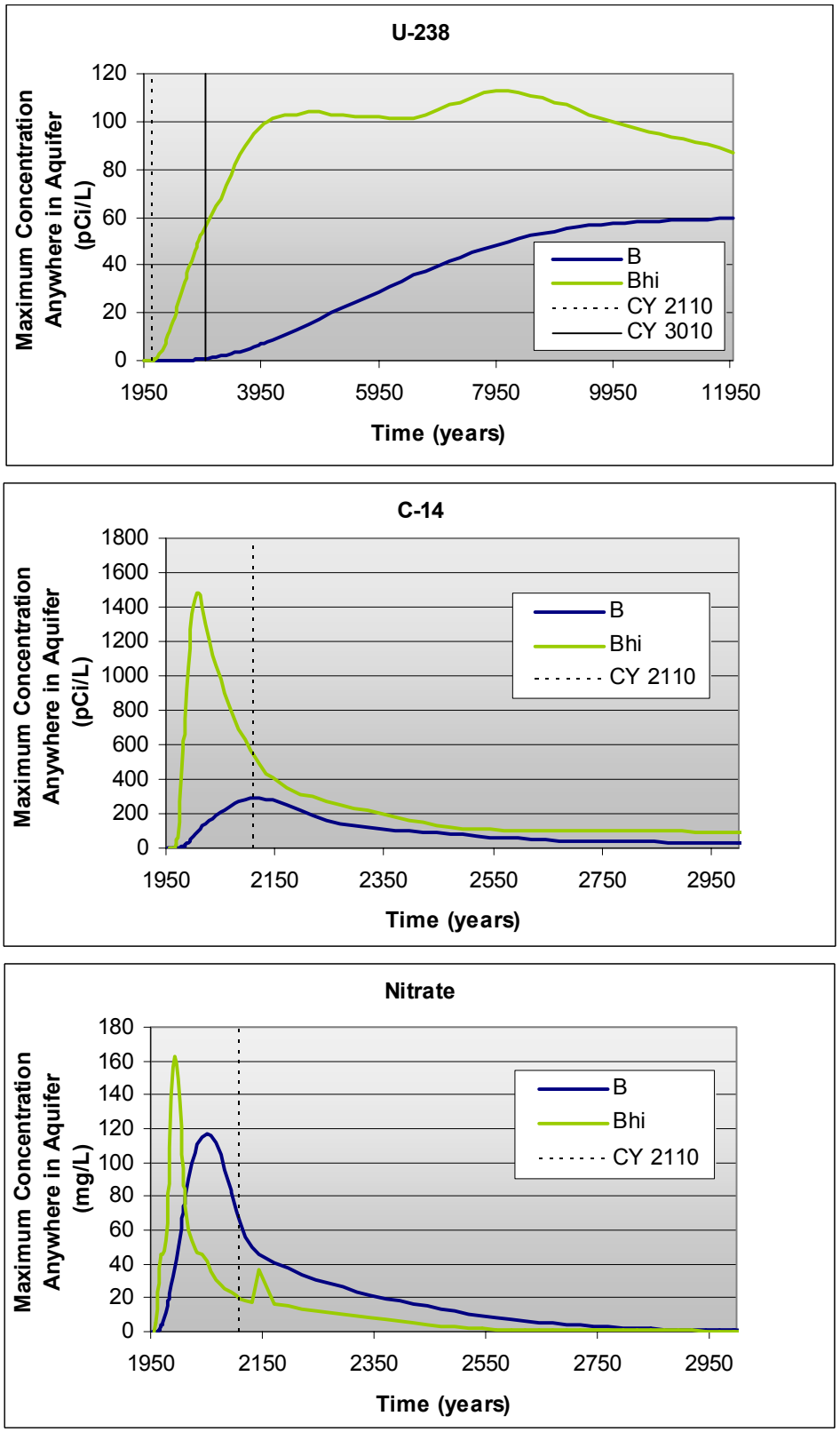

Figure 6-32. Comparison of the base (B) and high infiltration inside the Subsurface Disposal Area (Bhi) maximum simulated concentration anywhere in the aquifer for uranium-238, carbon-14, and nitrate.

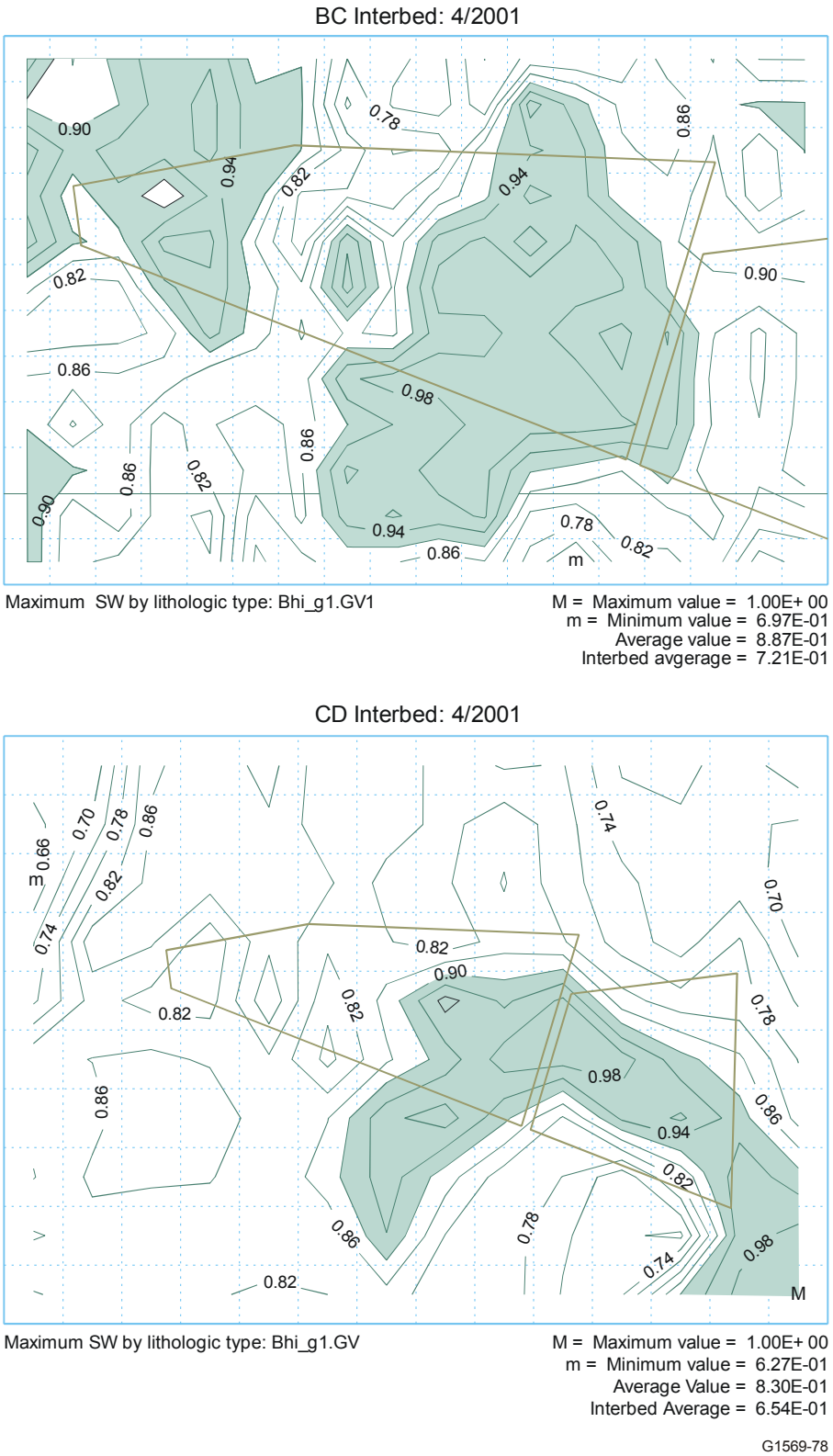

Figure 6-33. Maximum simulated water saturation in the B-C and C-D interbeds for the high-infiltration rate of 23 cm/year (9 in./year) everywhere inside the Subsurface Disposal Area.

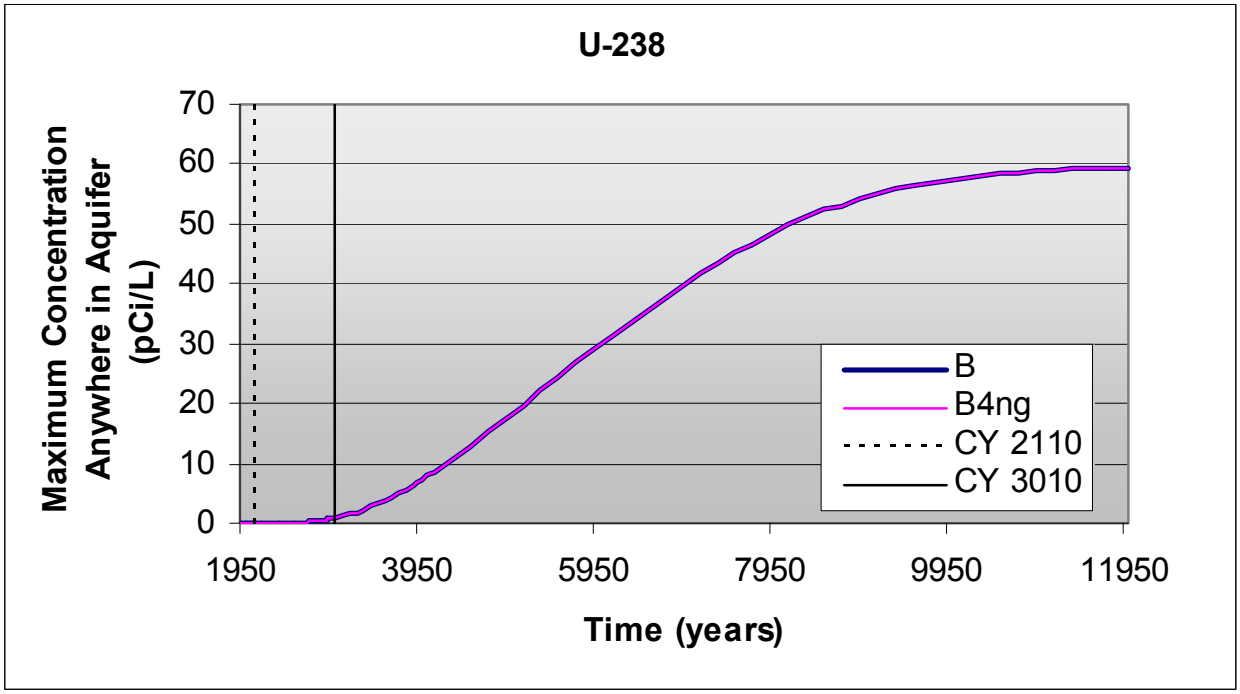

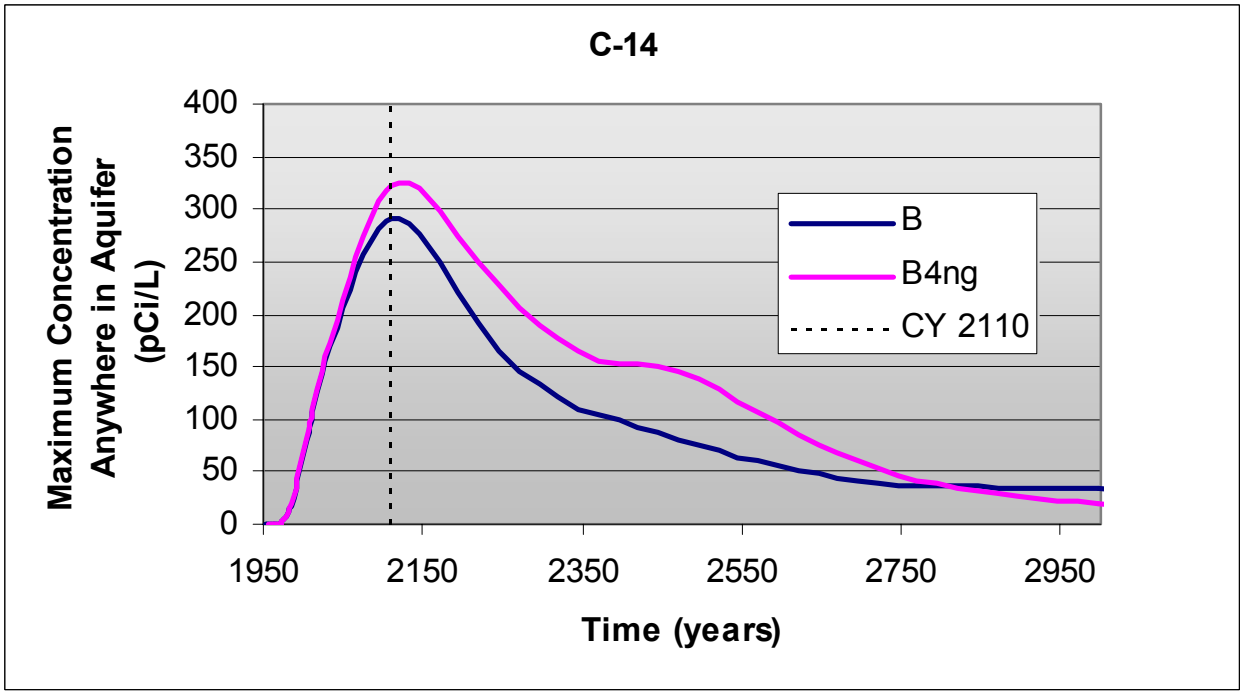

Figure 6-34. Comparison of the base (B) and Pit 4 inventory not removed and no beryllium block grouting (B4ng) maximum simulated concentration anywhere in the aquifer for uranium-238 and carbon-14. Nitrate is not shown because there was no change to the source-release modeling for this case.

6.4.5 Low Background Infiltration

The infiltration rate outside the SDA was assigned a value of 1.0 cm/year (0.4 in./year) for the RI/FS model. In this sensitivity case, a background infiltration rate that is an order of magnitude lower

was assigned to test the impact on simulated groundwater-pathway concentrations. This lower rate was assigned because ongoing investigations may lead to the conclusion that the 1.0 cm/year (0.4 in./year) background infiltration rate is too high. The lower background infiltration rate was used for initial conditions for this sensitivity simulation and was continued for infiltration outside the SDA beginning in 1952. The entire suite of potential contaminants was simulated.

Figure 6-35 shows a comparison of U-238, C-14, and nitrate concentrations between the base case and the sensitivity simulation with a lower background infiltration rate outside the SDA. For each of these three contaminants, simulated concentrations arrived slower in the sensitivity case, showing the effect of slower velocities in the vadose zone that result from less water overall in simulations. Peak concentrations for U-238 and nitrate increased, likely due to less dilution with less water overall coming into the aquifer from the vadose zone domain. However, the C-14 concentrations decreased, with the decrease likely due to specific interactions between where it is released into the vadose zone model and reductions in velocity.

6.4.6 No Low-Permeability Region in Aquifer

This case was not specified in Holdren and Broomfield (2004), and updates results of a similar assessment done after IRA modeling (Magnuson 1998), where the effect of not including the low-permeability zone in the aquifer was simulated. In the RI/FS model, the low-permeability region in the aquifer is assumed to be continuous and have substantially slow movement of water within the aquifer beneath the SDA. This slower movement results in less dilution of influxing vadose zone contaminants than would otherwise occur. Simulating only the aquifer portion of the groundwater pathway for this sensitivity simulation was necessary because the vadose zone simulation was unaffected.

Figure 6-36 shows a comparison of U-238, C-14, and nitrate concentrations between the base case and the sensitivity simulation without the low-permeability region in the aquifer. Simulated concentrations, without the low-permeability region in the aquifer, are markedly reduced. This reduction in concentration when the low-permeability region is absent demonstrates a conservative aspect of the RI/FS model.

6.4.7 Fractured Basalt Anisotropy

This case also was not specified in Holdren and Broomfield (2004). The need for this case arose when it was discovered that by using a fractured basalt anisotropy ratio of 300:1 for the horizontal-to-vertical permeability, some additional lateral water movement above the C-D interbed occurred that resulted in some water and contaminants contacting the horizontal no-flux boundary in the southeastern corner of the vadose zone simulation domain. For some short-duration periods before the end of institutional control in 2110, this lateral movement results in the peak concentration in the aquifer occurring beneath this extreme southeastern gridblock location in the vadose zone model domain.

A series of simulations were made to evaluate the effect of the selected anisotropy ratio in the fractured basalt. The RI/FS model uses an anisotropy ratio of 300:1, with horizontal permeability being 300 times greater than vertical permeability. This anisotropy ratio allows some of the water moving down through the vadose zone to migrate laterally to the extreme southeastern corner of the simulation domain, where it cannot spread further due to the lateral no-flow constraint imposed by the domain boundary.

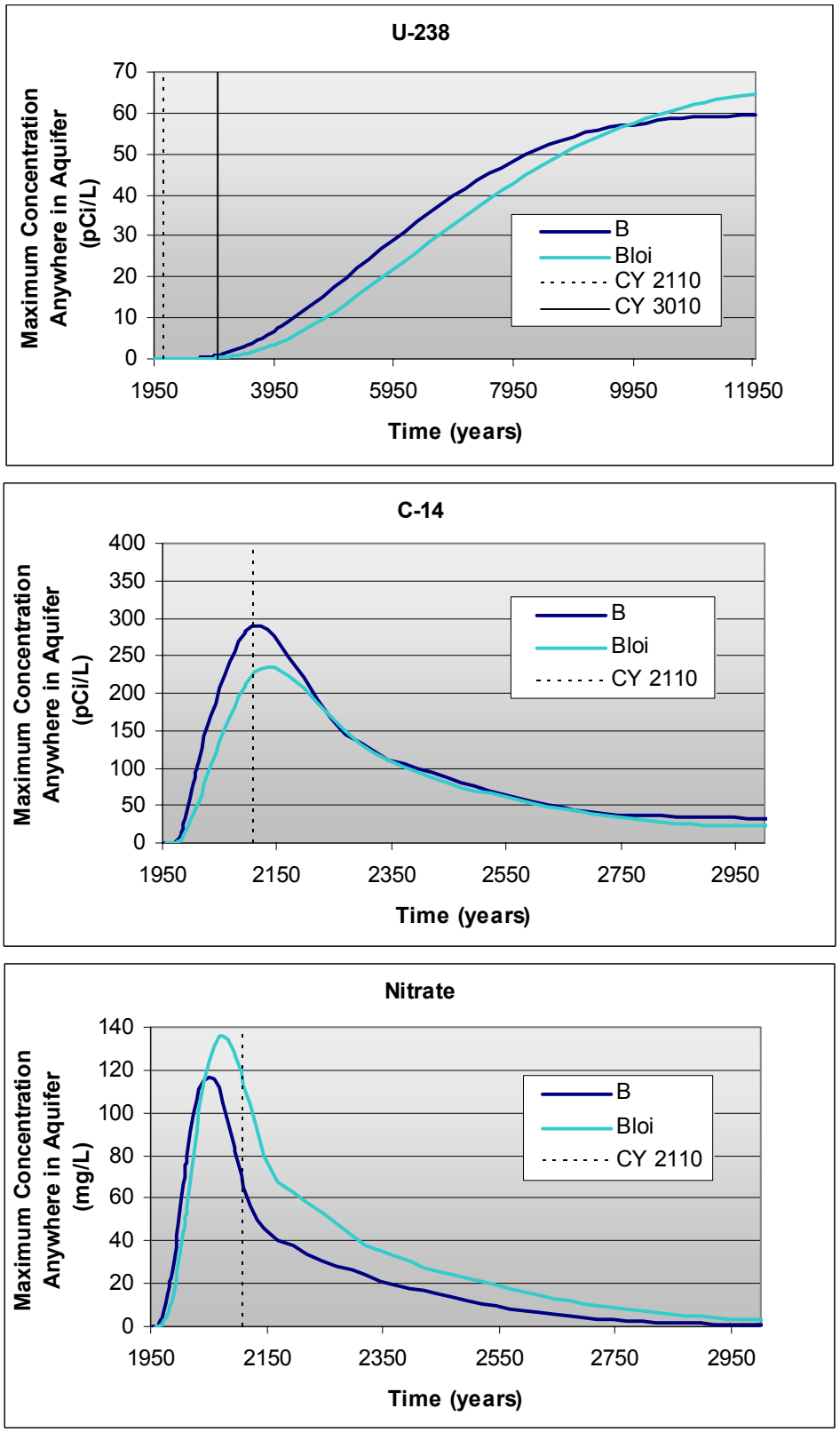

Figure 6-35. Comparison of the base (B) and low background infiltration (Bloi) maximum simulated concentration anywhere in the aquifer for uranium-238, carbon-14, and nitrate.

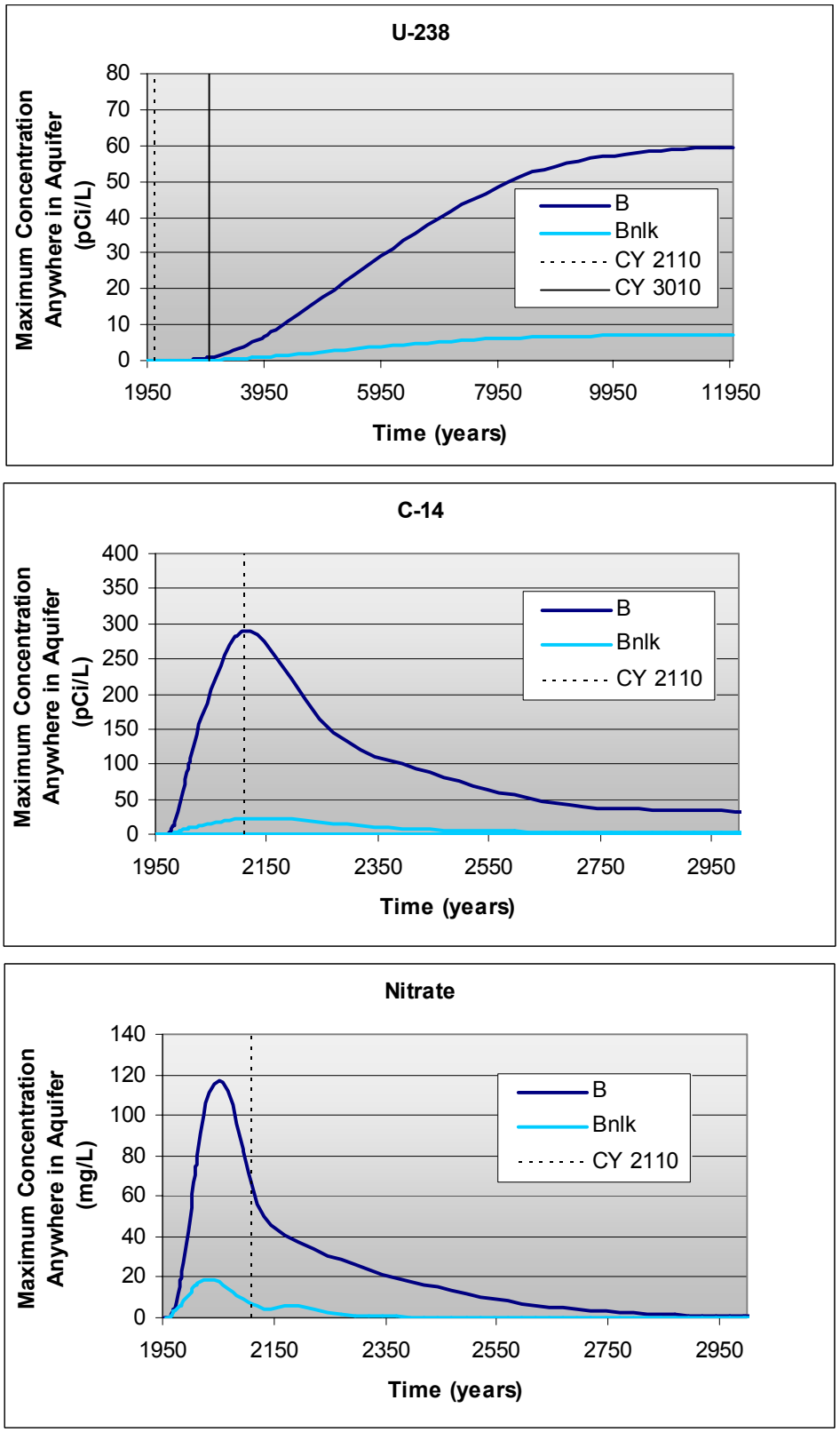

Figure 6-36. Comparison of the base (B) and no low-permeability region in aquifer (Bnlk) maximum simulated concentration anywhere in the aquifer for uranium-238, carbon-14, and nitrate.

The 300:1 ratio was a change from the 30:1 ratio that was used in the ABRA model, but was the same as the ratio that was used for the IRA model. The increase from the ABRA anisotropy value resulted from calibrating simulation results to observed CCl_4 concentrations in the vadose zone and in the aquifer, which required spreading the observed contaminant further laterally within the vadose zone domain to show better agreement between model results and monitoring results.

A possible concern with water and contaminants contacting the lateral vadose zone boundary is that resulting simulated aquifer results are inordinately affected by the boundary. In other words, if the domain extended further laterally, water and contaminants would not "pile up" at this corner of the model and potentially be forced through the interbed, thereby resulting in higher simulated aquifer concentrations than would otherwise occur.

Extending the vadose zone domain laterally, while technically feasible, could not easily be accomplished. Instead the effect of lateral movement of water and contaminants was investigated by making a series of sensitivity simulations where the anisotropy ratio was reduced. In these sensitivity simulations, water does not spread as far and behaves increasingly more like a one-dimensional simulation as the anisotropy ratio decreases and water and contaminant movement is more confined to the vertical direction.

Three different fractured-basalt anisotropy ratios were simulated in addition to the 300:1 ratio used in the RI/FS model. The ratios were 30:1, 3:1, and 1:1 with the latter case representing an isotropic condition. Cases that were simulated were the base case (B), which has no infiltration reducing cap; the modified Resource Conservation and Recovery Act Type-C barrier (FmR), with an infiltration reducing cap imposed at Calendar Year 2010; and the low-level waste performance assessment variant of the FmR run where only low-level waste contaminants were simulated (FmRpa). The contaminant group that was simulated, Group 6 (g6), included Tc-99, I-129, and Cl-36.

Comparisons of the effect of anisotropy ratios using the maximum simulated Tc-99 aquifer concentrations extracted from the second gridblock down in the aquifer are shown in Figure 6-37. For the B_g6 simulation anisotropy comparisons, the maximum concentrations are taken anywhere in the aquifer, including directly beneath the SDA, which is in contrast to locations for evaluating risk in the draft RI/BRA where the receptor location is considered to be outside the SDA fence (see Section 6.2). For the FmR_g6 and FmRpa_g6 simulations, concentration results are extracted from the same depth in the aquifer, but the area representing the SDA plus 100-m outside the SDA fence are excluded, consistent with receptor locations for the low-level waste performance assessment (see Section 6.2). For the B_g6 simulations, maximum concentrations always occur in the aquifer below the SDA or south of the SDA. Locations of the simulated maximum concentration are captured in the processing of simulation results, but are not indicated on Figure 6-37. For comparing the FmR_g6 and FmRpa_g6 simulations, maximum concentrations, for the most part, are also either beneath the SDA or south of the SDA. However, at some times up to Calendar Year 2060 in the 300:1 (base-case) simulation, the maximum concentration occurs in the extreme southeastern gridblock of the refined portion of the aquifer domain.

These results give some validity to the concern of the lateral boundary influencing the results, since there is a slight increase in the FmR and FmRpa simulated aquifer concentrations for the 300:1 anisotropy case during simulated time periods of Calendar Year 2000 to Calendar Year 2050, which is when the peak occurs in the extreme southeastern corner of the refined domain. This slight increase shows up as a "bump" in the 300:1 results. For the FmR_g6 simulation, this bump contains the overall maximum. For the FmRpa_g6 simulation, this bump does not contain the overall maximum. For the FmR_g6 simulation, however, the increase caused by this bump is still slight when compared to concentrations that occur immediately after Calendar Year 2050 along the same 300:1 anisotropy simulation result (blue diamonds). There is a local concentration maximum in this time period, which most likely represents the

peak simulated concentration if the vadose zone domain were extended to the southeast. If the chosen anisotropy ratio were appreciably higher than 300:1, which would normally further reduce simulated aquifer concentrations, the impact of the lateral boundary preventing further spreading might become more noticeable. At an anisotropy ratio of 300:1, this effect looks to be minor.

The overall effect of anisotropy on simulated aquifer concentrations appears more important than the impact of the lateral boundary. Higher anisotropy ratios spread out contaminants further in the vadose zone, and thereby reduce simulated aquifer concentrations. This result is easily seen in the B and FmR simulations, which are well-behaved with uniformly monotonic increases in the simulated aquifer concentration as the anisotropy ratio decreases. For the FmRpa case, the results are not as well behaved. The 300:1 simulation results still have the lowest overall peak concentration. The 30:1 simulation results have the highest peak overall concentration, while the 3:1 and 1:1 results have approximately the same peak concentration. Different lithologic features are controlling the peak concentrations for the 30:1, 3:1, and 1:1 cases given the difference in location where the peak occurs over time compared to the 300:1 simulation result.

Overall, the impact of changing from an anisotropy ratio of 30:1 for the ABRA to 300:1 for the current Operable Unit 7-13/14 model is to reduce simulated aquifer concentrations for all simulations performed using the RI/FS model due to dilution from additional spreading of water and contaminants in the vadose zone before they enter the aquifer model. As a reminder, the basis for this change was improved calibration for CCl_4 transport. Even with this additional dilution, the model still overpredicts concentrations compared to the observed monitoring results in the aquifer, especially for nonsorbing contaminants (see Section 6.1).

6.4.8 No Sorption in Vadose Zone Interbeds

In the RI/BRA base case, 3.7% of the Pu-239 and Pu-240 inventory for Rocky Flats Plant waste streams was mobile and moved through the surficial sediment and the A-B interbed without sorption. Sorption of the mobile plutonium did occur in the base case in the deeper, nearly continuous B-C and C-D interbeds. This section presents an extreme bounding sensitivity case that completely eliminates sorption of plutonium in both the B-C and C-D interbeds. Advective spreading during transit of the vadose zone results in some dilution as the contaminant flux is more widely spread when it enters the aquifer model domain. Other than spreading in the vadose zone model, this sensitivity case is roughly equivalent to spreading the source term laterally and leaching it directly into the aquifer. In both the RI/BRA base case and this sensitivity case, the majority of plutonium (i.e., 96.3%) undergoes sorption in the surficial sediments and interbeds with the assigned distribution coefficient of 2,500 mL/g.

Figure 6-38 shows peak simulated aquifer concentrations anywhere along the southern INL Site boundary and at the extent of the southern model domain as a function of time for the base and no sorption in the vadose zone interbeds sensitivity case. As with other results, these concentrations are extracted from the second gridblock down from the top of the aquifer domain. Simulated concentrations from the base case are very low with INL Site boundary maximums of 7E-13 pCi/L for Pu-239 and 1E-13 pCi/L for Pu-240. With the extreme bounding case of no sorption in the vadose zone, the fraction of mobile fraction of plutonium from the source model migrates past the deeper B-C and C-D interbeds and into the aquifer, resulting in simulated concentrations that are approximately fifteen orders of magnitude higher than the base case concentrations at the INL Site boundary.

Comparing simulated values through the current time to monitoring results demonstrates the lack of credibility of these results. The maximum simulated concentration results anywhere in the aquifer through 2004 for the case without sorption in the interbeds were 3E+05 pCi/L for Pu-239 and 7E+05 pCi/L for Pu-240. The detections of plutonium in the aquifer (see Section 4 of the draft RI/BRA) show an overall maximum of 4.3 pCi/L in Well M4D in 1993. Although there are other detections, they are at a low level near the minimum detectable concentration and occur very sporadically. The no-sorption sensitivity case results dramatically overpredict even the maximum monitoring results by five to six orders of magnitude. Stated another way, if the sensitivity case were at all credible, there would be easily detectible plutonium in any aquifer well in the SDA vicinity. Since this is not the case, the sensitivity simulation results are not credible as there is no basis in reality for the results.

6.5 Feasibility Study Simulations

This section briefly describes simulations to be performed for the feasibility study, which are defined in Holdren and Broomfield (2004). Contaminant groupings for the feasibility study will remain the same, except that Group 6 COPCs will be further refined. The feasibility study report will contain simulation results and additional details regarding model modifications and implementation.

Feasibility study simulations will use the base-case model, but with changes to the source release, assigned water fluxes at land surface, and other changes to reflect possible remedial alternatives. All simulations are the same as the base-case simulation until Calendar Year 2010, at which time changes are implemented.

6.5.1 Modified Resource Conservation and Recovery Act Type C Surface Barrier

In this alternative, Pad A is left in place and incorporated into a Resource Conservation and Recovery Act Type C surface barrier to be installed over the SDA. The barrier is assumed to reduce the infiltration rate to 0.1 cm/year (0.04 in./year). The background infiltration rate of 1.0 cm/year (0.4 in./year) will remain the same outside the barrier. The barrier is assumed to preclude migration of gaseous-phase contamination to the atmosphere so that shallow VVET wells will be installed adjacent to the VOC source areas and integrated into the Operable Unit 7-08 VVET units. Routine extraction from deeper wells will cease in the year 2010. The shallow extraction system will operate 10 months per year until preliminary remediation goals for CCl_4 (INEEL 2005) are achieved. This simulation will also serve as the low-level waste composite analysis simulation (see Section 6.6).

6.5.2 Evapotranspiration Surface Barrier

This alternative will include installation of an evapotranspiration surface barrier over the SDA that reduces the infiltration rate to 0.1 cm/year (0.04 in./year). The background infiltration rate of 1.0 cm/year (0.4 in./year) will remain the same outside the barrier. The barrier will include a biotic barrier and an active gas collection layer. Waste will be retrieved from Pad A and transferred to the Low-Level Waste Pit without treatment or additional engineering in the pit. The VVET system will continue routine extraction from vadose zone wells 10 months per year until preliminary remediation goals for CCl_4 (INEEL 2005) are achieved.

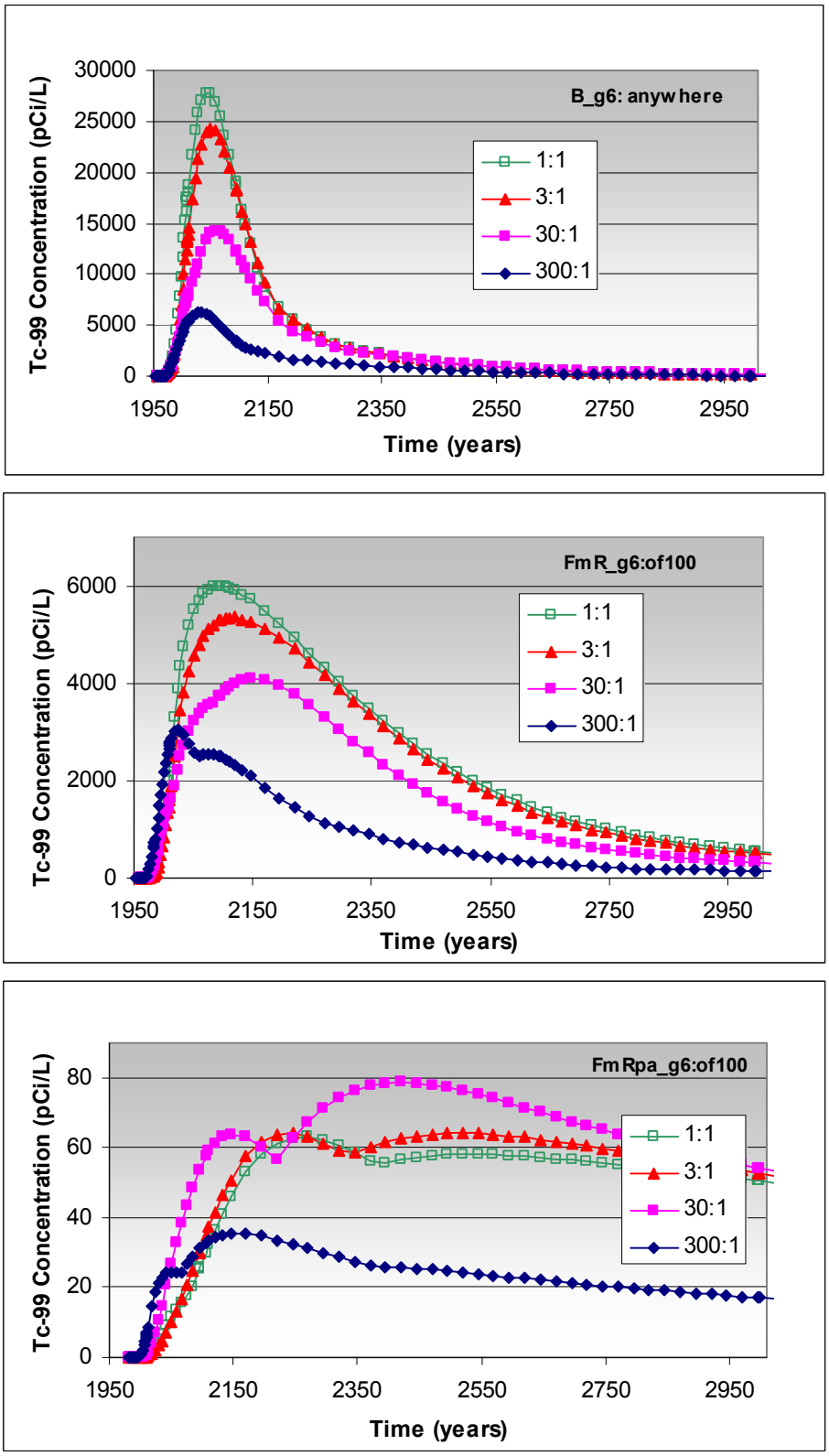

Figure 6-37. Time history of maximum simulated aquifer concentrations for a range of fractured basalt anisotropy ratios for B_g6, FmR_g6, and FmRpa_g6 simulations.

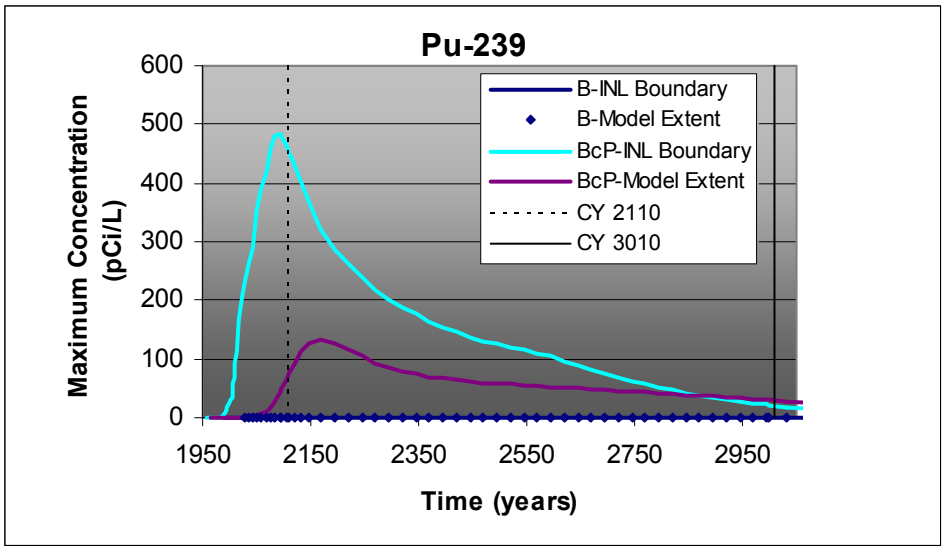

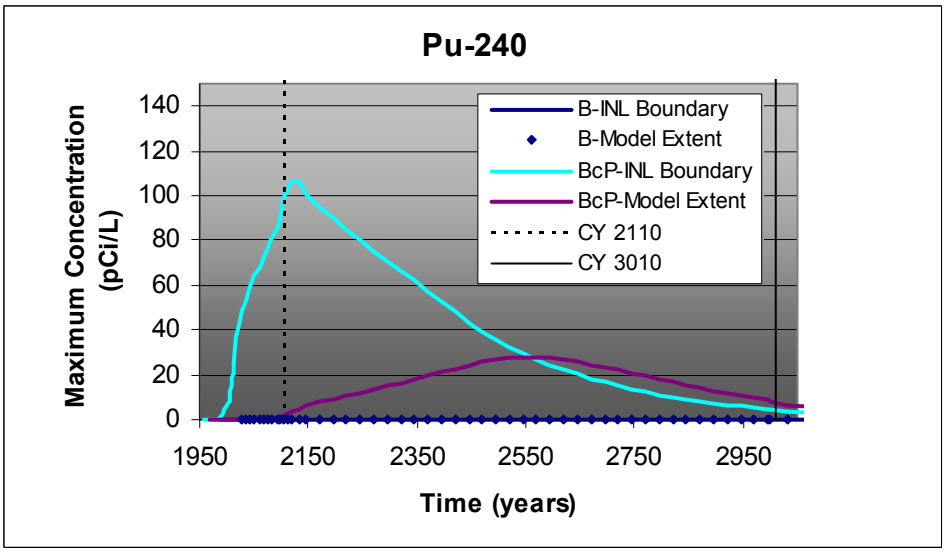

Figure 6-38. Comparison of the base (B) and the no sorption in the interbeds (BcP) maximum simulated concentration anywhere in the aquifer along the INL Site boundary and at the extreme southern extent of the model domain for plutonium-239 and plutonium-240.

6.5.3 In Situ Grouting

In this alternative, selected areas, based on contaminants of concern, will be grouted in situ. Waste from Pad A will be retrieved, treated ex situ, and returned to a pit in the SDA. The grouting only affects the release of contaminants. The waste continues to be simulated with the same hydrologic properties as surficial sediment. An evapotranspiration surface barrier that reduces the infiltration rate to 0.1 cm/year (0.04 in./year) will be installed over the SDA. The background infiltration rate of 1.0 cm/year (0.4 in./year) will remain the same outside the barrier. The barrier will include a biotic barrier and a passive gas collection layer. The VVET system will continue routine extraction from vadose zone wells 10 months per year until preliminary remediation goals for CCl_4 (INEEL 2005) are achieved.

6.5.4 Partial Retrieval, Treatment, and Disposal

This alternative will remove 1.6 ha (4 acres) of waste, targeting VOCs and transuranic waste. Waste from Pad A will be retrieved and sent to the Idaho Comprehensive Environmental Response, Compensation, and Liability Act Disposal Facility for treatment and disposal. An evapotranspiration surface barrier will be installed over the SDA that reduces the infiltration rate to 0.1 cm/year (0.04 in./year). The background infiltration rate of 1.0 cm/year (0.4 in./year) will remain the same outside the barrier. The barrier will include a biotic barrier and a passive gas collection layer. The VVET system will continue routine extraction from vadose zone wells 10 months per year until preliminary remediation goals for CCl_4 (INEEL 2005) are achieved. Results from this 1.6-ha (4-acre) partial retrieval, treatment, and disposal alternative can be scaled up or down to obtain approximations for retrievals of varying sizes as long as the same constituents are targeted.

6.5.5 Full Retrieval, Treatment, and Disposal

For this alternative, all buried waste will be removed. Waste from Pad A will also be retrieved and sent to the Idaho Comprehensive Environmental Response, Compensation, and Liability Act Disposal Facility for treatment, and then buried outside of the INL Site. An evapotranspiration surface barrier will be installed over the SDA that reduces the infiltration rate to 0.1 cm/year (0.04 in./year). The background infiltration rate of 1.0 cm/year (0.4 in./year) will remain the same outside the barrier. The barrier will include a biotic barrier and a passive gas collection layer. The VVET system will continue routine extraction from vadose zone wells 10 months per year until preliminary remediation goals for CCl_4 (INEEL 2005) are achieved.

6.5.6 Full Retrieval, Treatment, and Disposal with No Infiltration-reducing Cap

This is a feasibility study sensitivity case where all waste is removed and no infiltration reducing cap is placed over the SDA. This case mimics groundwater-pathway concentrations and the resulting risks that are attributable strictly to contaminants that have migrated into the vadose zone beyond the first basalt interface in the absence of an infiltration-reducing surface barrier.

6.5.7 Evapotranspiration Surface Barrier with 1.0-cm/year Infiltration

This is a feasibility study sensitivity case that is the same as the evapotranspiration surface barrier, but with a 1.0 cm/year (0.4 in./year) infiltration rate through the barrier (instead of 0.1 cm/year [0.04 in./year]), and an unchanged background infiltration rate of 1.0 cm/year (0.4 in./year). This simulation allows sensitivity to the infiltration rate through the barrier to be evaluated.

6.5.8 Modified Resource Conservation and Recovery Act Type C Surface Barrier with Low Background Infiltration

This is another feasibility study sensitivity case that is the same as the Modified Resource Conservation and Recovery Act Type C Surface Barrier simulation, except the background infiltration outside the SDA is assigned 0.1 cm/year (0.04 in./year) instead of 1.0 cm/year (0.4 in./year). This simulation allows sensitivity to the assigned background infiltration rate to be evaluated.

6.6 Radiological Low-Level Waste Performance Assessment Simulations

The radiological composite analysis and low-level waste performance assessment is being updated to maintain consistency with the fate and transport model used for the RI/FS. The composite analysis addresses the entire waste inventory buried in the SDA and uses radiological results from the Modified Resource Conservation and Recovery Act Type C Surface Barrier simulation defined in Section 6.5.1. A version of the Modified Resource Conservation and Recovery Act Type C Surface Barrier was also assumed for the performance assessment. For the purposes of the performance assessment and compliance with DOE O 435.1, the active low-level waste disposal facility has been defined to include Pits 17 through 20 and the soil vault rows. Additional simulations were required for the performance assessment to distinguish releases from the operating facility from contributions from the historical source terms. For all radionuclide simulations, except C-14, all source areas were nulled out, except for the soil vault rows, Pits 17 through 20, and the projected low-level waste disposal. These source areas are identified in Figure 4-21 as SVRs, P17-20, and LLW_proj. For the C-14 simulation, all source areas except Soil Vault Row 17, Soil Vault Row 20, and post-83 were nulled out. These source areas are identified in Figure 4-22. For the performance assessment simulations, only radiological COPCs were simulated.

Simulated aquifer concentrations were extracted using the same method described above and transferred to personnel conducting updates for the performance assessment and composite analysis. Simulation results were archived, along with those for the draft RI/BRA and the feasibility study.

7. SUMMARY

The groundwater-pathway flow and transport model previously used for the ABRA has been updated for use in the Operable Unit 7-13/14 RI/FS and radiological performance assessment and composite analysis. The updates consisted of the following:

1. Correcting slight errors in the ABRA

2. Using additional lithologic information from wells drilled subsequent to the ABRA modeling

3. Using additional hydrologic information from cores obtained subsequent to the ABRA modeling

4. Revising the spatially varying infiltration rate applied at the surface, including revising these same rates as they were used in the source-release modeling

5. Comparing updated model flow results to spatial trends observed with the deep tensiometer monitoring network

6. Removing the influence of additional water from the spreading areas above the C-D interbed in the vadose zone because it primarily served to dilute simulated aquifer concentrations for contaminants with long-half lives

7. Extending the aquifer domain southwestward

8. Recalibrating the CCl_4 dual-continua model, with the updated model having the larger CCl_4 inventory

9. Using the calibrated dual-continua model to simulate C-14 when it was allowed to partition into the gaseous phase and diffuse through the upper surface of the simulation domain

10. Including facilitated transport of Pu-239 and Pu-240 in the surficial sediment and A-B interbed

11. Making comparisons between simulated COPC concentrations and field-monitoring results in the surficial sediment, the vadose zone, and the aquifer. Comparisons were made for those analytes that have been identified as possibly being above background and exhibiting trends.

The RI/FS model mimics the observed large-scale trend of wetter conditions in the B-C interbed inside the SDA compared to outside. These field observations support the key conceptual model component that infiltration is higher inside the SDA than outside. For dissolved-phase transport, the results from the model are mixed. At some locations, the model underpredicts observed values, such as U-238 in the vadose zone. Some portions of this underprediction are due to gridblock averaging in the vadose zone model. In general, however, the model is conservative, because, at a larger scale, the simulated aquifer concentrations are either slightly underpredicted, in the case of chromium, or overpredicted, in the case of nitrate and Tc-99. The latter is overpredicted to the extent that the source release for Tc-99 will be revised and additional simulations performed for the feasibility study. The other contaminants that were simulated are predicted to be either not in the aquifer yet or to be present at concentrations below detectable levels. This disregards sporadic detections of plutonium isotopes and Am-241 as anomalies.

For transport of contaminants that partition between the aqueous and gaseous phases, the model generally mimics the observed spread and impact of the CCl_4 plume in the vadose zone and aquifer. The calibration to CCl_4 was successful. The impact of allowing C-14 to partition into the vapor phase was to reduce, by two orders of magnitude, the simulated groundwater-pathway concentrations. While there have been some C-14 detections in aquifer-monitoring wells, the model simulated concentrations still slightly overpredict observed values.

Considering that some portions of the modeling show representative behavior and others show conservative (e.g., overpredicting groundwater-pathway concentrations), the updated model developed to represent flow and transport in the groundwater pathway is appropriate to use in the RI/FS. This updated RI/FS model was used to simulate flow and transport of COPCs for the base case (i.e., no-action), sensitivity cases, and the feasibility study simulations. Results from the modified Resource Conservation and Recovery Act Type C surface barrier simulation also were used for comparison to the low-level waste comprehensive analysis. A variant of this simulation with only low-level waste streams provides results for the radiological low-level waste performance assessment. Some of the sensitivity cases were also simulated with just the low-level waste streams. In addition to the RI/BRA base-case and related sensitivity simulation results, the same parameterized flow and transport model was run with modifications to the infiltration rate and source release to reflect possible remedial alternatives for the feasibility study. These simulations are identified within this document.

All input files, TETRAD results files, and PV-Wave processing routines used to extract and portray the results are archived electronically. Appendix B describes this archive.

7.1 Limitations

The primary limitation of the RI/FS flow and transport model is the lack of definitive calibration targets for dissolved-phase transport of contaminants buried in the SDA down through the vadose zone. This lack of targets results from the complexity of flow and transport in the fractured basalt. On large scales with strong forcing functions, such as the Large-Scale Infiltration Test, the flow and transport has been shown to be primarily gravity-driven with little large-scale horizontal transport until an interbed was encountered. But with lower ambient infiltration conditions inside the SDA, heterogeneous waste disposal, and preferential flow in the fractured basalt, detecting large scale trends useful for model calibration has been difficult. Lower infiltration makes transport slower and, therefore, requires longer times to detect trends. Although the monitoring network in the vadose zone has been improved, preferential transport within fractured basalt makes it difficult to ensure that migrating contaminants have been or will be detected. While this lack of definitive large-scale transport for calibration is good from an overall environmental impact perspective, it does limit the ability to conclusively demonstrate that the transport represented from the model emulates the system.

Absent these calibration targets, the RI/FS model primarily still relies on comparisons between simulated and observed concentrations in the aquifer to make conclusions that the model is generally conservative. These aquifer comparisons have another limitation—uncertainty as to whether upgradient facilities, such as the Reactor Technology Complex or the Idaho Nuclear Technology and Engineering Center, contribute to contamination observed in the aquifer at the SDA. Absent this uncertainty, the model could be calibrated to mimic chromium, for example.

On a more positive note, the RI/FS model does include calibration and comparisons to measured interbed matric potentials from the deep tensiometer monitoring network and to CCl_4 transport in the vadose zone and aquifer, and can be seen to represent their general behavior. As a result, the model can be used to make predictive simulations for risk assessment with acknowledgment of uncertainty.

7.2 Uncertainty/Sensitivity

Uncertainty regarding flow and transport results is discussed qualitatively in this section, based on information obtained through performing sensitivity simulations in Section 6.4. Model uncertainty describes the degree to which a model represents the physical system being simulated. All models are simplifications of real physical systems. The issue is whether the model contains enough detail to adequately represent the physical system to the degree required, and whether the appropriate choice of inputs can be made to emulate that physical system. Quantifying model uncertainty is difficult. At best, uncertainty can be minimized by comparing results to known solutions and by calibrating the model to measured data.

Models used for this risk assessment were compared to measured data. Some components of the models had fewer available comparison data than others. The following list identifies those characteristics with the greatest effect on model uncertainty:

- Input from the source-release model—Contaminant inventories and release mechanisms are a primary source of uncertainty in the groundwater-pathway model results. Uncertainties in the flow and transport models have the potential to affect the groundwater-pathway concentrations, but not usually to the extent that the source-release modeling uncertainties do.

- Amount of water infiltrating through the waste, contacting the waste, and leaching contaminants from the waste—The current estimated infiltration rates inside the SDA, ranging from a background value of 1 cm/year (0.4 in./year) to as high as 10 cm/year (4 in./year), are reasonably conservative for the RI/FS model. These infiltration rates, applied as constants in perpetuity, should be conservative because over time natural processes of revegetation, sediment deposition, and compaction will likely reduce overall infiltration toward the lower background rate.

- Rate and direction of water and contaminant movement undergoing preferential flow through the fractured basalt portions of the vadose zone—Uncertainty is conservatively addressed through hydrologic parameterization that ensures rapid movement without any chemical interaction that would slow transport.

- Low-permeability region included in the aquifer flow and transport simulation—This low-permeability region limits dilution that may be occurring in the real system. The simulated aquifer concentrations in this region are dominated by water and contaminants entering from the vadose zone due to low horizontal velocities in the aquifer as water diverts around the low-permeability zone.

- Use of steady-state flow conditions in the vadose zone—Steady-state conditions, coupled with an assumption of linear equilibrium sorption, limits any potential influence from reactive transport that may be rate limited. While equilibrium sorption conditions are likely appropriate at depth in the vadose zone, where transient flow events get dampened, they may not be as appropriate in the near-field source area.

7.3 Areas for Improvement of the Remedial Investigation and Baseline Risk Assessment Model

Although the RI/FS model performs adequately for evaluating field-scale contaminant transport, because it provides conservative estimates of groundwater-pathway concentrations, there are still areas that could be improved. These are

- Determining whether upgradient facilities contribute to observed chromium would remove uncertainty regarding use of aquifer concentrations as calibration targets.

- Continued monitoring of the vadose zone and aquifer locations to obtain data to compare against model predictions to ensure the model remains reasonably conservative.

- Localized models, such as a two-dimensional, cross-sectional model, could better mimic chloride brine transport that results from infiltration through roadway ditches. This modeling would provide a cross check on appropriateness of the simplified treatment of flow through the fractured basalt in the RI/FS model.

- Limited quantitative evaluation of uncertainty could be accomplished using the approach developed for the low-level waste performance assessment, where a one-dimensional vadose zone model coupled with a three-dimensional aquifer model is calibrated to the results of the three-dimensional RI/FS model. The one-dimensional model is then run in a probabilistic fashion with inputs varied to assess a range of possible conditions.

8. REFERENCES

Anderson, Danny L. and Bruce H. Becker, 2006, *Source Release Modeling Report for OU 7-13/14*, ICP/EXT-05-01039, Idaho National Laboratory, Idaho Cleanup Project.

Anderson, S. R., D. J. Ackerman, M. J. Liszewski, and R. M. Freiburger, 1996, *Stratigraphic Data for Wells at and Near the Idaho National Engineering Laboratory, Idaho*, USGS Open-File Report 96 248, U.S. Department of Energy Idaho Operations Office DOE/ID-22127, U.S. Geological Survey.

Ansley, Shannon L., Catherine M. Helm-Clark, and Swen O. Magnuson, 2004, *Updated Stratigraphic Selections for Wells in the Vicinity of the Subsurface Disposal Area*, ICP/EXT-04-00207, Rev. 0, Idaho National Engineering and Environmental Laboratory, Idaho Completion Project.

Auer, L. H., N. D. Rosenberg, K. H. Birdsell, and E. M. Whitney, 1996, "The Effects of Barometric Pumping on Contaminant Transport," *Journal of Contaminant Hydrology*, Vol. 24, pp. 145–166.

Baca, R. G., S. O. Magnuson, H. D. Nguyen, and P. Martian, 1992, *A Modeling Study of Water Flow in the Vadose Zone Beneath the Radioactive Waste Management Complex*, EGG-GEO-10068, Rev. 0, Idaho National Engineering Laboratory.

Batcheller, Thomas A. and George D. Redden, 2004, *Colloidal Plutonium at the OU 7-13/14 Subsurface Disposal Area: Estimate of Inventory and Transport Properties*, ICP/EXT-04-00253, Idaho National Engineering and Environmental Laboratory, Idaho Completion Project.

Bear, J., 1972, "Dynamics of fluids in Porous Media," New York: American Elsevier Publishing Co.

Becker, B. H., J. D. Burgess, K. J. Holdren, D. K. Jorgensen, S. O. Magnuson, and A. J. Sondrup, 1998, *Interim Risk Assessment and Contaminant Screening for the Waste Area Group 7 Remedial Investigation*, DOE/ID-10569, Rev. 0, U.S. Department of Energy Idaho Operations Office.

Bishop, C. W., 1991, *Hydraulic Properties of Vesicular Basalt*, M.S. Thesis: University of Arizona, Tucson, Arizona.

Case, Marilyn J., Arthur S. Rood, James M. McCarthy, Swen O. Magnuson, Bruce H. Becker, and Thomas K. Honeycutt, 2000, *Technical Revision of the Radioactive Waste Management Complex Low-Level Waste Radiological Performance Assessment for Calendar Year 2000*, INEEL/EXT-00-01089, Idaho National Engineering and Environmental Laboratory.

Cecil, L. D., J. R. Pittman, T. M. Beasley, R. L. Michel, P. W. Kubik, P. Sharma, U. Fehn, and H. Gove, 1992, "Water Infiltration Rates in the Unsaturated Zone at the Idaho National Engineering Laboratory Estimated from Chlorine-36 and Tritium Profiles, and Neutron Logging," edited by Y. K. Kharaka and A. S. Meest, *Proceedings of the 7th International Symposium on Water-Rock Interaction*, *Park City, UT*, WRI-7, Rotterdam: Balkema.

Colwell, F. S., 1988, *Final Report: Microbial Examination of the RWMC Surface and Subsurface Soils and Biodegradation of Low Molecular Weight Hydrocarbons Using Microorganisms Indigenous to RWMC*, ST-BEG-03-88, Idaho National Engineering Laboratory.

DOE-ID, 2004, *Idaho National Engineering and Environmental Laboratory Operable Unit 10-08 Sitewide Groundwater Model Work Plan*, DOE/NE-ID-11188, Rev. 0, U.S. Department of Energy Idaho Operations Office.

DOE O 435.1, 2001, "Radioactive Waste Management," Change 1, U.S. Department of Energy.

EPA, 1999, *Understanding Variation in Partition Coefficient, K_d Values*, EPA 402-R-99-004A&B, U.S. Environmental Protection Agency.

Fabryka-Martin, J., A. Flint, and G. Gee, 1998, "Peer Review Team Report on Conceptual Models and Field Verification of Radionuclide Transport through the Vadose Zone at INEEL," Final Report, November 5, 1998, prepared for Idaho National Engineering and Environmental Laboratory.

Falta, R. W., I. Javandel, K. Pruess, and P. A. Witherspoon, 1989, "Density-Driven Flow of Gas in the Unsaturated Zone due to the Evaporation of Volatile Organic Compounds," *Water Resources Research*, Vol. 25, No. 10.

Fjeld, R. A., J. T. Coates, and A. W. Elzerman, 2000, *Final Report, Column Tests to Study the Transport of Plutonium and Other Radionuclides in Sedimentary Interbed at INEEL*, INEEL/EXT-01-00763, Rev. 0, Clemson University, Department of Environmental Engineering and Science, Clemson, South Carolina, for the Idaho National Engineering and Environmental Laboratory.

Freeze, R. A. and J. A. Cherry, 1979, *Groundwater*, Englewood Cliffs, New Jersey: Prentice-Hall.

GE, 1989, *Nuclides and Isotopes Fourteenth Edition Chart of the Nuclides*, General Electric Nuclear Energy.

Gelhar, L. W., 1986, "Water Resources Research," Vol. 22, No. 9, August 1986 Supplement, pp. 135S–145S.

Grossman, C. J., R. A. Fjeld, J. T. Coates, and A. W. Elzerman, 2001, *Task 7 Final Report: The Sorption of Selected Radionuclides in Sedimentary Interbed Soils from the Snake River Plain*, Administrative Record No. 24484, Prepared by the Department of Environmental Engineering and Sciences, Clemson University, Clemson, South Carolina, for the Idaho National Engineering and Environmental Laboratory.

Holdren, K. Jean and Barbara J. Broomfield, 2004, *Second Addendum to the Work Plan for the OU 7-13/14 Waste Area Group 7 Comprehensive Remedial Investigation/Feasibility Study*, DOE/ID-11039, U.S. Department of Energy Idaho Operations Office.

Holdren, K. Jean, Bruce H. Becker, Nancy L. Hampton, L. Don Koeppen, Swen O. Magnuson, T. J. Meyer, Gail L. Olson, and A. Jeffrey Sondrup, 2002, *Ancillary Basis for Risk Analysis of the Subsurface Disposal Area*, INEEL/EXT-02-01125, Rev. 0, Idaho National Engineering and Environmental Laboratory.

Housley, L. T., A. J. Sondrup, and M. D. Varvel, 2002, *A Compilation of Results from Shallow Soil-Gas Surveys of the Subsurface Disposal Area for Operable Unit 7-08*, INEEL/EXT-01-00026, EDF-ER-263, Rev. 1, Idaho National Engineering and Environmental Laboratory.

Hubbell, J. M., 1993, *Elevation of Surficial Sediment/Basalt Contact in the Subsurface Disposal Area, Idaho National Engineering Laboratory*, EGG-ER-10794, Idaho National Engineering Laboratory.

Hubbell, J. M., M. J. Nicholl, J. B. Sisson, and D. L. McElroy, 2004, "Application of a Darcian Approach to Estimate Liquid Flux in a Deep Vadose Zone," *Vadose Zone Journal*, Vol. 3, pp. 560-569.

Hull, Larry, Idaho National Engineering and Environmental Laboratory, to K. Jean Holdren, Idaho National Engineering and Environmental Laboratory, September 25, 2003, "Plutonium Kd Post Tally Jenkin's Comment."

Hull, Larry C. and Carolyn W. Bishop, 2003, *Fate of Magnesium Chloride Brine Applied to Suppress Dust from Unpaved Roads at the INEEL Subsurface Disposal Area*, INEEL/EXT-01-01173, Rev. 0, Idaho National Engineering and Environmental Laboratory.

INEEL, 2005, *Data Quality Objectives Summary Report for the Operable Unit 7-08 Post-Record of Decision Sampling*, INEEL/EXT-2000-00814, Rev. 2, Idaho National Engineering and Environmental Laboratory, Idaho Completion Project.

Jolley, Wendell, 2003, "Fiscal Year 2003 Pumping Test Results from Wells Located at the Radioactive Waste Management Complex," EDF-3777, Rev. 0, Idaho National Engineering and Environmental Laboratory.

Knobel, L. L., B. R. Orr, and L. D. Cecil, 1992, "Summary of Background Concentrations of Selected Radiochemical and Chemical Constituents in Groundwater from the Snake River Plain Aquifer, Idaho: Estimated from an Analysis of Previously Published Data," *Journal of the Idaho Academy of Science*, Vol. 28, No. 10.1, pp. 48.

Koeppen, L. Don, Gail L. Olson, Alva M. Parsons, Mitch A. Plummer, Paul D. Ritter, and A. Jeffrey Sondrup, 2005, *Fiscal Year 2004 OU 7-13/14 Environmental Monitoring Report for the Radioactive Waste Management Complex*, ICP/EXT-05-00795, Idaho National Laboratory, Idaho Cleanup Project.

Leecaster, Molly K., 2004, *Fiscal Year 2004 Geostatistical Modeling of Lithologic Characteristics in the Radioactive Waste Management Complex for OU 7-13/14*, ICP/EXT-04-00494, Idaho National Engineering and Environmental Laboratory, Idaho Completion Project.

Leecaster, Molly K., 2002, *Geostatistic Modeling of Subsurface Characteristics in the Radioactive Waste Management Complex Region, Operable Unit 7-13/14*, INEEL/EXT-02-00029, Rev. 0, Idaho National Engineering and Environmental Laboratory.

Leecaster, Molly K. and Laurence C. Hull, 2004, *Spatial Distribution of Neptunium and Uranium Partition Coefficient (K_d) for Interbed Sediments at a Radioactive Waste Subsurface Disposal Area*, ICP/EXT-03-00088, Idaho National Engineering and Environmental Laboratory, Idaho Completion Project.

Lerman, A., 1988, *Geochemical Processes: Water and Sediment Environments*, New York: John Wiley & Sons.

Lowe, Darren, Wayne Downs, Sheldon Smith, and W. Vincent Wilding, 2003, *Mass Release of Chlorinated Solvents through Oil, Adsorbent, and Polyethylene Bagging at the Radioactive Waste Management Complex*, ICP/EXT-03-00057, Rev. 0, Idaho National Engineering and Environmental Laboratory, Idaho Completion Project.

Magnuson, S. O., 1998, *Sensitivity of the SDA Flow and Transport Simulator to the Low Permeability Region in the Aquifer*, INEEL/INT-01066, Idaho National Engineering and Environmental Laboratory.

Magnuson, S. O., 1995, *Inverse Modeling for Field-Scale Hydrologic and Transport Parameters of Fractured Basalt*, INEL-95/0637, Idaho National Engineering Laboratory.

Magnuson, S. O. and D. L. McElroy, 1993, *Estimation of Infiltration from In Situ Moisture Contents and Representative Moisture Characteristic Curves for the 30', 110', and 240' Interbeds*, EG&G Engineering Design File #RWM-93-001.1, Idaho National Engineering Laboratory.

Magnuson, S. O. and A. J. Sondrup, 1998, *Development, Calibration, and Predictive Results of a Simulator for Subsurface Pathway Fate and Transport of Aqueous- and Gaseous-Phase Contaminants in the Subsurface Disposal Area at the Idaho National Engineering and Environmental Laboratory*, INEEL/EXT-97-00609, Rev. 0, Idaho National Engineering and Environmental Laboratory.

Martian, P., 2003, "Simulation of Carbon-14 Transport in a Mesoscale Experiment," MCP-3394, Rev. 0, Idaho National Engineering and Environmental Laboratory.

Martian, P., 1995, *UNSAT-H Infiltration Model Calibration at the Subsurface Disposal Area, Idaho National Engineering Laboratory*, INEL-95/0596, Idaho National Engineering Laboratory.

McCarthy, J. M., B. H. Becker, S. O. Magnuson, K. N. Keck, and T. K. Honeycutt, 2000, *Radioactive Waste Management Complex Low-Level Waste Radiological Composite Analysis*, INEEL/EXT-97-01113, Rev. 0, Idaho National Engineering and Environmental Laboratory.

McCarthy, J. M., R. C. Arnett, R. M. Neupauer, M. J. Rohe, and C. Smith, 1995, *Development of a Regional Groundwater Flow Model for the Area of the Idaho National Engineering Laboratory, Eastern Snake River Plain Aquifer*, INEL-95/0169, Rev. 1, Idaho National Engineering Laboratory.

McElroy, Deborah L. and Joel M. Hubbell, 2003, *Advanced Tensiometer Monitoring Results from the Deep Vadose Zone at the Radioactive Waste Management Complex*, INEEL/EXT-02-01276, Rev 0, Idaho National Engineering and Environmental Laboratory.

Mendoza, C. A. and E. O. Frind, 1990a, "Advective-Dispersive Transport of Dense Organic Vapors in the Unsaturated Zone, 1, Model Development," *Water Resources Research*, Vol. 26, No. 3, pp. xxx.

Mendoza, C. A. and E. O. Frind, 1990b, "Advective-Dispersive Transport of Dense Organic Vapors in the Unsaturated Zone, 2, Sensitivity Analysis," *Water Resources Research*, Vol. 26, No. 3, pp. xxx.

Miller, Eric C. and Mark D. Varvel, 2005, *Reconstructing the Past Disposal of 743-Series Waste in the Subsurface Disposal Area for Operable Unit 7-08, Organic Contamination in the Vadose Zone*, INEEL/EXT-01-00034, Rev. 1, Idaho National Laboratory, Idaho Completion Project.

Millington, R. J., 1959, "Gas Diffusion in Porous Media," *Science*, Vol. 130.

Mualem, Y., 1976, "A New Model for Predicting the Hydraulic Conductivity of Unsaturated Porous Media," *Water Resources Research*, Vol. 12, No. 3, pp. 513-522.

Nalla, Gopi, 2004, *Near-Field Simulation of Carbon-14 and Tritium Migration from Buried Beryllium Blocks in the Subsurface Disposal Area*, ICP/EXT-04-00321, Rev. 0, Idaho National Engineering and Environmental Laboratory, Idaho Completion Project.

Nimmo, J. R., K. S. Perkins, P. A. Rose, J. P. Rousseau, B. R. Orr, B. V. Twining, and S. R. Anderson, 2001, "2001 Kilometer-Scale Rapid Flow in a Fractured-Basalt Unsaturated Zone at the Idaho National Engineering and Environmental Laboratory," edited by B. H. Kueper, K. S. Novakowski, and D. A. Reynolds., *2001 Conference Proceedings*, *Toronto*, *March 26-28, 2001*.

Olson, G. L., 2004, *OU 7-13 and 7-14 Field Representative Glovebox Excavator Method Logbook – December 15, 2003 – February 24, 2004 (12/15/03 – 02/24/04) – Excavator Book*, ER-039-2004, Idaho National Engineering and Environmental Laboratory, Idaho Completion Project.

Parker, J. C., R. J. Lenhard, and T. Kuppusamy, 1987, "A Parametric Model for Constitutive Properties Governing Multiphase Flow in Porous Media," *Water Resource Research*, Vol. 23, No. 4, pp. 618-624.

Plummer, M. A., L. C. Hull, and D. T. Fox, 2004, "Transport of Carbon-14 in a Large Unsaturated Column," *Vadose Zone Journal*, Vol. 3, No. 1, pp. 109–121.

Roback, R. C., T. M. Johnson, T. L. McLing, M. T. Murrell, Shangde Luo, and Teh Lung Ku, 2001, "Uranium Isotopic Evidence for Groundwater Chemical Evolution and Flow Patterns in the Eastern Snake River Plain Aquifer," *Idaho-Geological Society of America Bulletin*, Vol. 113, No. 9, pp. 1133-1141.

Robertson, J. B., R. Schoen, and J. T. Barraclough, 1974, *The Influence of Liquid Waste Disposal on the Geochemistry of Water at the National Reactor Testing Station, Idaho, 1952-1970*, USGS Open-File Report IDO-22053, U.S. Geological Survey.

Rodriguez, R. R., A. L. Schafer, J. M. McCarthy, P. Martian, D. E. Burns, D. E. Raunig, N. A. Burch, and R. L. Van Horn, 1997, *Comprehensive RI/FS for the Idaho Chemical Processing Plant OU 3-13 at the INEEL--Part A, RI/BRA Report*, DOE/ID-10534, U.S. Department of Energy Idaho Operations Office.

Rood, A. S., 1999, *GWSCREEN: A Semi-Analytical Model for Assessment of the Groundwater Pathway from Surface or Buried Contamination, Theory and User's Manual Version 2.5*, INEEL/EXT-9800750, Idaho National Engineering and Environmental Laboratory.

Rousseau, Joseph P., Edward R. Landa, John R. Nimmo, L. DeWayne Cecil, LeRoy L. Knobel, Pierre D. Glynn, Edward M. Kwicklis, Gary P. Curtis, Kenneth G. Stollenwerk, Steven R. Anderson, Roy C. Bartholomay, Clifford R. Bossong, and Brennan R. Orr, 2005, *Review of the Transport of Selected Radionuclides in the Interim Risk Assessment for the Radioactive Waste Management Complex, Waste Area Group 7 Operable Unit 7-13/14, Idaho National Engineering and Environmental Laboratory, Idaho*, USGS Scientific Investigations Report 2005-5026, prepared in cooperation with the U.S. Department of Energy, DOE/ID-22192, U.S. Geological Survey.

Shook, G. Michael, J. Hope Forsmann, M. Elena Velasquez, and Swen O. Magnuson, 2003, "Improving Numerical Model Efficiency of an Existing, In-House Simulation Model," *Laboratory-Directed Research and Development, FY-2003 Annual Report*, INEEL/EXT-04-01772, Idaho National Engineering and Environmental Laboratory, pp. 197-199.

Smith, R. P., 2002, *Variability of the Aquifer Thickness Beneath the Idaho National Engineering and Environmental Laboratory (INEEL)*, INEEL/EXT-02-01022, Idaho National Engineering and Environmental Laboratory.

Sondrup, A. J., 1998, *Preliminary Modeling of VOC Transport for Operable Unit 7-08, Evaluation of Increased Carbon Tetrachloride Inventory*, INEEL/EXT-2000-00849, Rev. 0, Idaho National Engineering and Environmental Laboratory.

Sondrup, A. Jeffrey, Eric C. Miller, Edward H. Seabury, and Nick Josten, 2004, *Estimating Carbon Tetrachloride and Total Volatile Organic Compound Mass Remaining in Subsurface Disposal Area Pits*, ICP/EXT-04-00396, Idaho National Engineering and Environmental Laboratory, Idaho Completion Project.

van Genuchten, M. Th., 1980, "A Closed-form Equation for Predicting the Hydraulic Conductivity of Unsaturated Soils," *Soil Science Society of America Journal*, Vol. 44, pp. 892-898.

Vejvoda, Edward, 2005, *Summary of Rocky Flats Plant Waste Buried in the Subsurface Disposal Area*, ICP/EXT-04-00717, Idaho National Laboratory, Idaho Completion Project.

Vigil, M. J., 1988, *Estimate of Water in Pits During Flooding Events*, EDF-BWP-12, Idaho National Engineering Laboratory.

Vinsome, P. K. W. and G. M. Shook, 1993, "Multi-Purpose Simulation," *Journal of Petroleum Science and Engineering*, Vol. 9, pp. 29-38.

Visual Numerics, Inc., 2001, PV-WAVE User's Guide, unpublished work, 1990-2001.

Warren, J. E., and P. J. Root, 1963, "The Behavior of Naturally Fractured Reservoirs," *Transactions Society of Petroleum Engineers AIME*, Vol. 228, pp. 245-255.

Whitmire, D. L., 2001, *Summary Report: Simulation of Groundwater Flow near the Subsurface Disposal Area at the Idaho National Engineering and Environmental Laboratory,* INEEL/EXT-01-01643, Rev. 0, prepared by North Wind Environmental for Idaho National Engineering and Environmental Laboratory.

Wylie, A. H. and J. M. Hubbell, 1994, *Aquifer Testing of Wells M1S, M3S, M4D, M6S, M7S, and M10S at the Radioactive Waste Management Complex*, ER-WAG7-26, Rev. 1, Idaho National Engineering Laboratory.

Zitnik, James F., Aran T. Armstrong, Brian K. Corb, Mark H. Edens, Douglas B. Holsten, Patricia M. O'Flaherty, Janet Rodriguez, Tamara N. Thomas, Russell L. Treat, Wayne Schofield, and Kira L. Sykes, 2002, *Preliminary Evaluation of Remedial Alternatives for the Subsurface Disposal Area*, INEEL/EXT-02-01258, Rev. 0, prepared by CH2MHILL for the Idaho National Engineering and Environmental Laboratory.

Appendix A

Comparison of Simulation Results with TETRAD 12.7 and TETRAD 12.7ms

Appendix A

Comparison of Simulation Results with TETRAD 12.7 and TETRAD 12.7ms

This appendix provides a description of two test problems used to demonstrate comparability between TETRAD Version 12.7 and TETRAD Version 12.7ms. The former was the simulator used for the IRA (Becker et al. 1998) and ABRA (Holdren et al. 2002) models. The latter represents a revision of the Version 12.7 that was created to allow component-specific convergence criteria to be applied to decrease the amount of central processing unit time necessary for completing full-scale simulations for the Operable Unit 7-13/14 RI/FS (Shook et al. 2003). Computational gain results in the Version 12.7ms, because a looser convergence criterion can be applied to noncontaminant components. Shook et al. (2003) describes the agreement in results between the previous and revised versions as "in excellent agreement for each problem," based on a direct comparison of the two sets of results in terms of absolute and normalized agreement. No additional quantitative details are offered on the comparison of the results.

The purpose of this appendix is to graphically demonstrate this equivalence using two problems. One of the problems is the simplest example from the laboratory-directed research and development report. The other uses the U-238 simulation group from the ABRA. Overall, the two-simulation comparison in this appendix shows essentially the same results, demonstrating equivalence between the original Version 12.7 and the revised Version 12.7ms.

A-1. TEST PROBLEM 1: EX3DT

Test Problem 1 (i.e., ex3dt) was created to mimic, in a simplified fashion, the model previously applied with TETRAD 12.7 in the ABRA. The name given to the simulation is ex3dt, which is excerpted from "example 3-dimensional problem with transport." The ex3dt problem has a simplified grid and lithology that still contain surficial sediment, fractured basalt, and one sedimentary interbed with a centrally-located gap. Transient sources of water are applied at land surface and at depth on one side of the domain. This source undergoes decay to a daughter product.

A summary of physical and chemical processes included in the simulation is given, followed by a detailed problem description. Then simulation results comparing TETRAD 12.7 and 12.7ms are shown. Lastly, the complete TETRAD data deck for the ex3dt problem is included.

A-1.1 Listing of Processes Included in Simulation

- Advection
- Dispersion
- Diffusion
- Adsorption
- Radioactive decay
- Ingrowth.

A-1.2 Three-Dimensional Domain

- 165 m (541.3 ft) in x-horizontal direction, 19 gridblocks with variable grid spacing
- 165 m (541.3 ft) in y-horizontal direction, 19 gridblocks with variable grid spacing
- 61 m (200.1 ft) in the vertical direction, 24 gridblocks with variable grid spacing
- Vertical slice shown in Figure A-1.

A-1.3 Lithology

Two material property zones were simulated as indicated in Figure A-2. The gap in material Type 2 allows water and tracers to move vertically downward.

A-1.4 Hydrologic Properties

Material	1	2
Permeability, X-direction	3,500 mD	1 mD
Permeability, Y-direction	700 mD	1 mD
Porosity	0.48	0.15
van Genuchten alpha	2.0 m^{-1}	1.5 m^{-1}
van Genuchten beta (aka N)	1.8	1.2

A-1.5 General Transport Properties

- Two water-equivalent tracer constituents, a parent and a daughter product
- Half-life of parent (W2 in TETRAD nomenclature) is 34.657 days
- Half-life of daughter (W3) is 346.57 days
- Molecular diffusion is 1.0×10^{-5} cm^2/second (8.64×10^{-5} m^2/day)
- Tortuosity is uniform and assigned a value of 10
- Dispersion coefficients are 14.4 and 1.4 m for longitudinal and transverse, respectively.

A-1.6 Material-Specific Transport Properties

Material	1	2
Partition coefficient, tracer #1	0 mL/g	1,000 mL/g
Partition coefficient, tracer #2	0 mL/g	500 mL/g

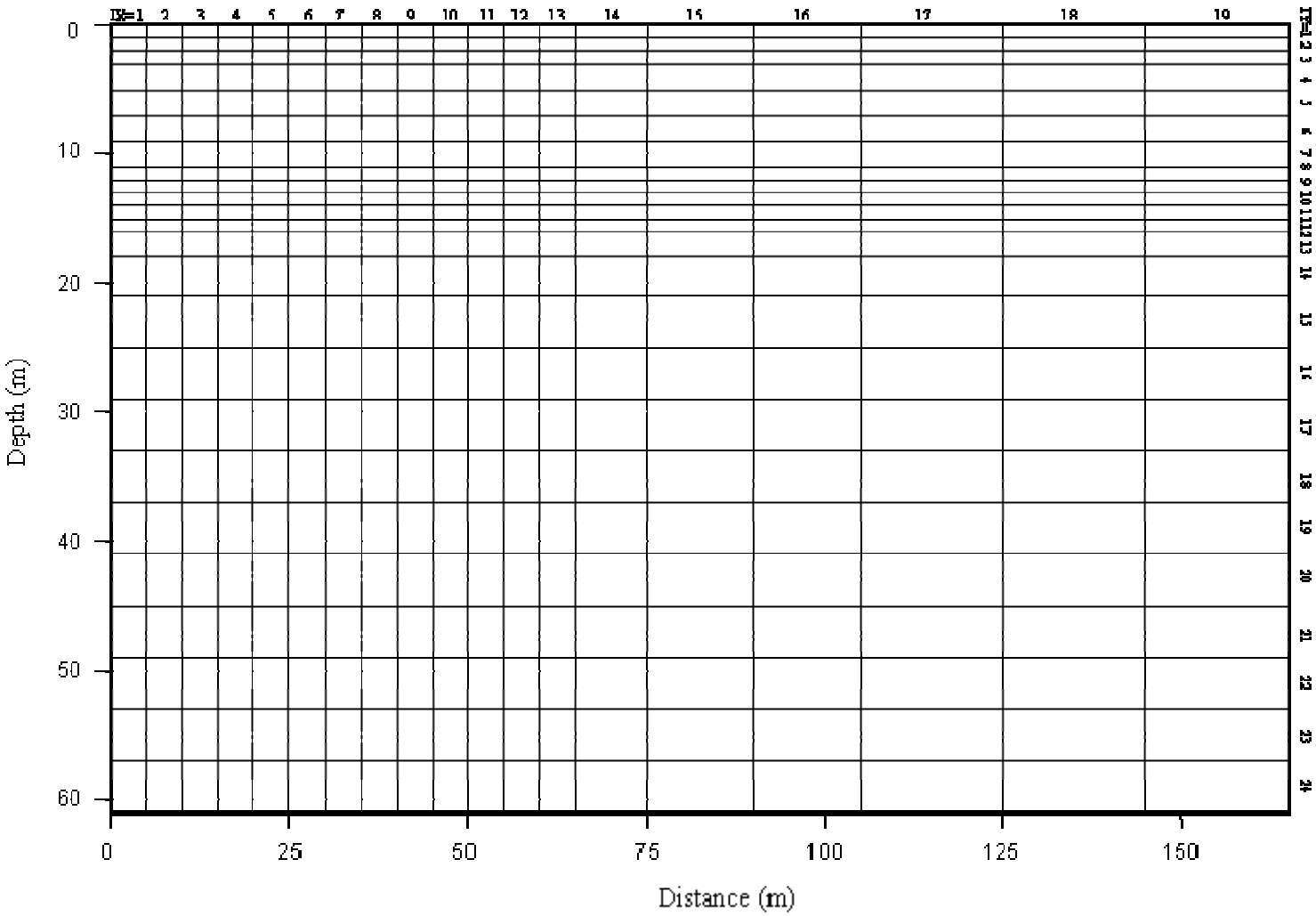

Figure A-1. Simulation domain.

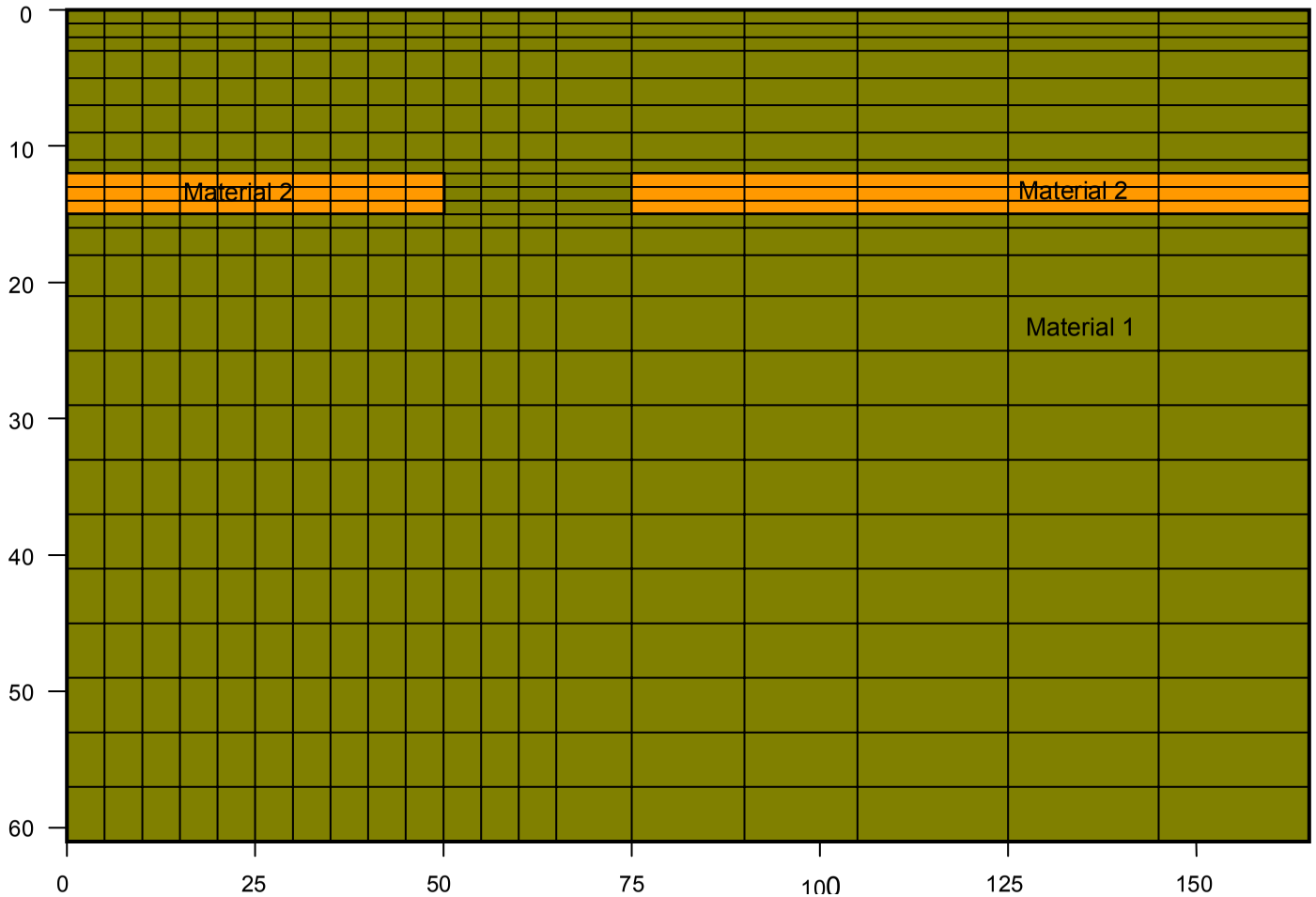

Figure A-2. Lithologic properties.

A-1.7 Boundary Conditions

Surface background infiltration rate is 1 cm/year (0.02738 kg/m^2/day).

A head differential of 2 m (6.6 ft) is applied from left to right across the lower 20 m (65.6 ft) (i.e., five gridblocks) of the simulation domain (see Figure A-3).

A-1.8 Transient Water Sources

A water flux is applied to emulate a surface flood at the rate of 100 cm/year (2.738 kg/m^2/day) for a 500-day duration from simulation time 1,000 to 1,500 days. This flood applies to the surface over the three gridblocks from 30 to 45 m (98.4 to 147.6 ft). The flooding flux supersedes the background infiltration rate for the time period it is applied.

An additional lateral influx of water is applied at the left edge of the simulation domain as indicated in Figure A-3. This influx consists of water applied at a rate of 1,000 cm/year over the 5-m (16.4-ft) surface of the indicated gridblock for 150 days beginning at simulation day 1,350. This equates to 2,055 m^3 of water being added at depth to the simulation domain over 150 days.

A-1.9 Tracer Loading

The parent tracer is loaded at a constant rate of 1.e-3 kg/m^2/day from simulation time 0 to 1,100 days.

A-1.10 Simulation Results

Simulation results are compared in time histories of the tracer mole fraction of the parent (W2), daughter mole fraction (W3), and water saturation (SW) in Figures A-4, A-5, and A-6, respectively. Tracer mole fractions can be seen to have the “excellent” agreement referred to in Shook et al. (2003). Water saturations also agree almost to the same extent, with the exception of comparison point four, where the TETRAD 12.7 result is slightly greater. This difference was not unexpected because a looser convergence criterion was used for the pure water component; and there was no difference in the transport of the tracers through this region.

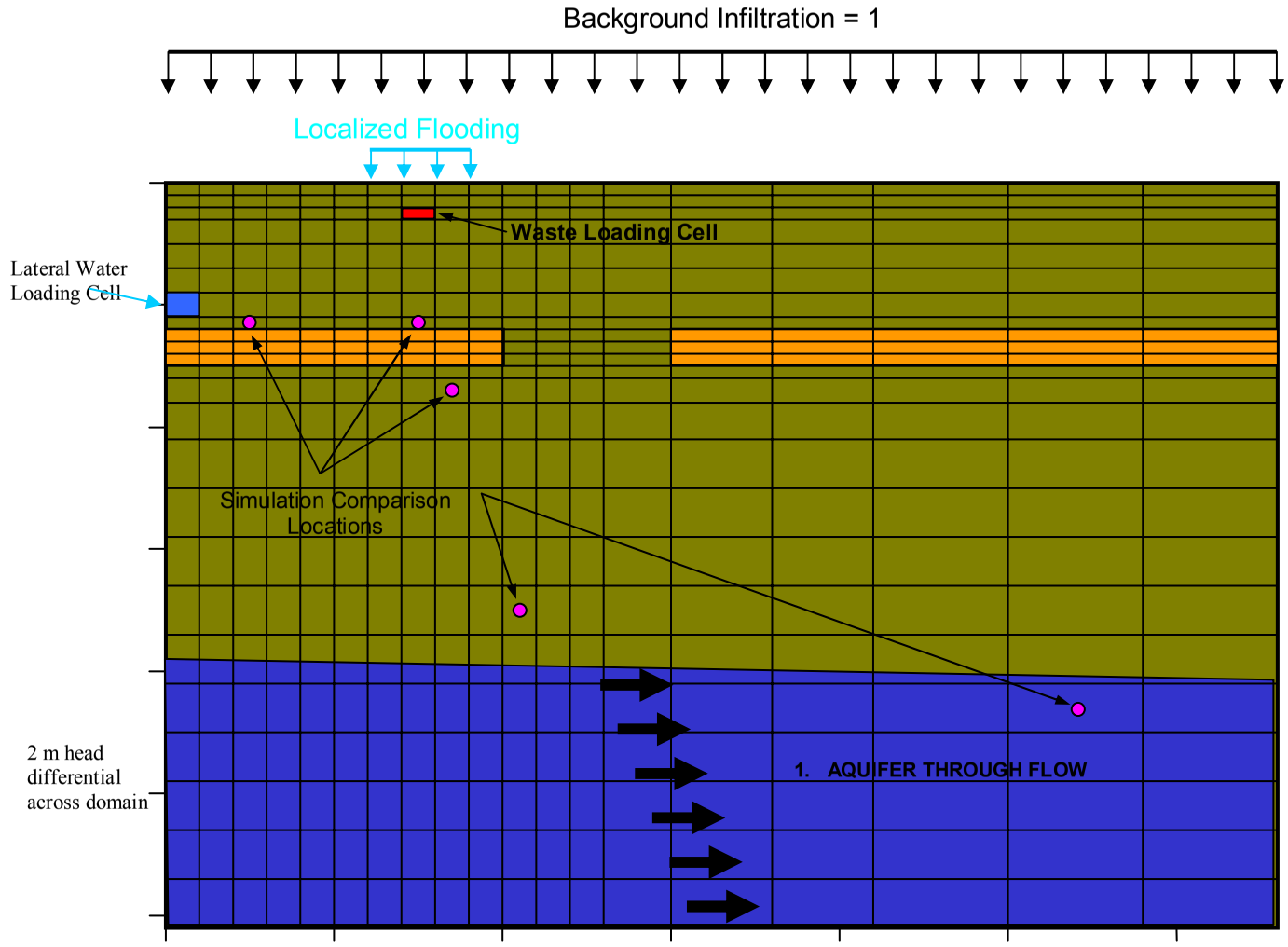

Figure A-3. Boundary conditions.

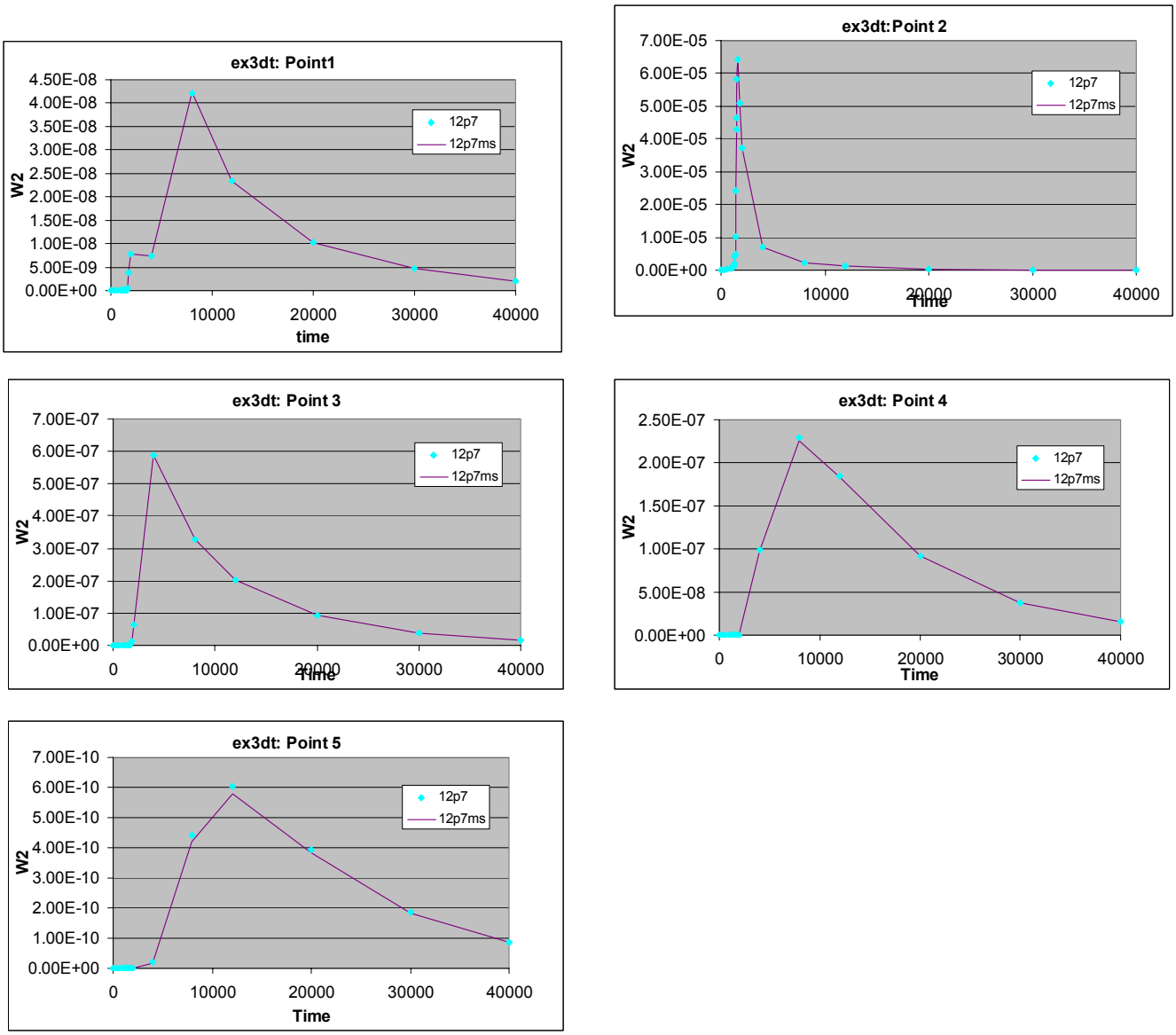

Figure A-4. Comparison of simulated mole fraction of parent (W2) at comparison points with TETRAD 12.7 and 12.7ms.

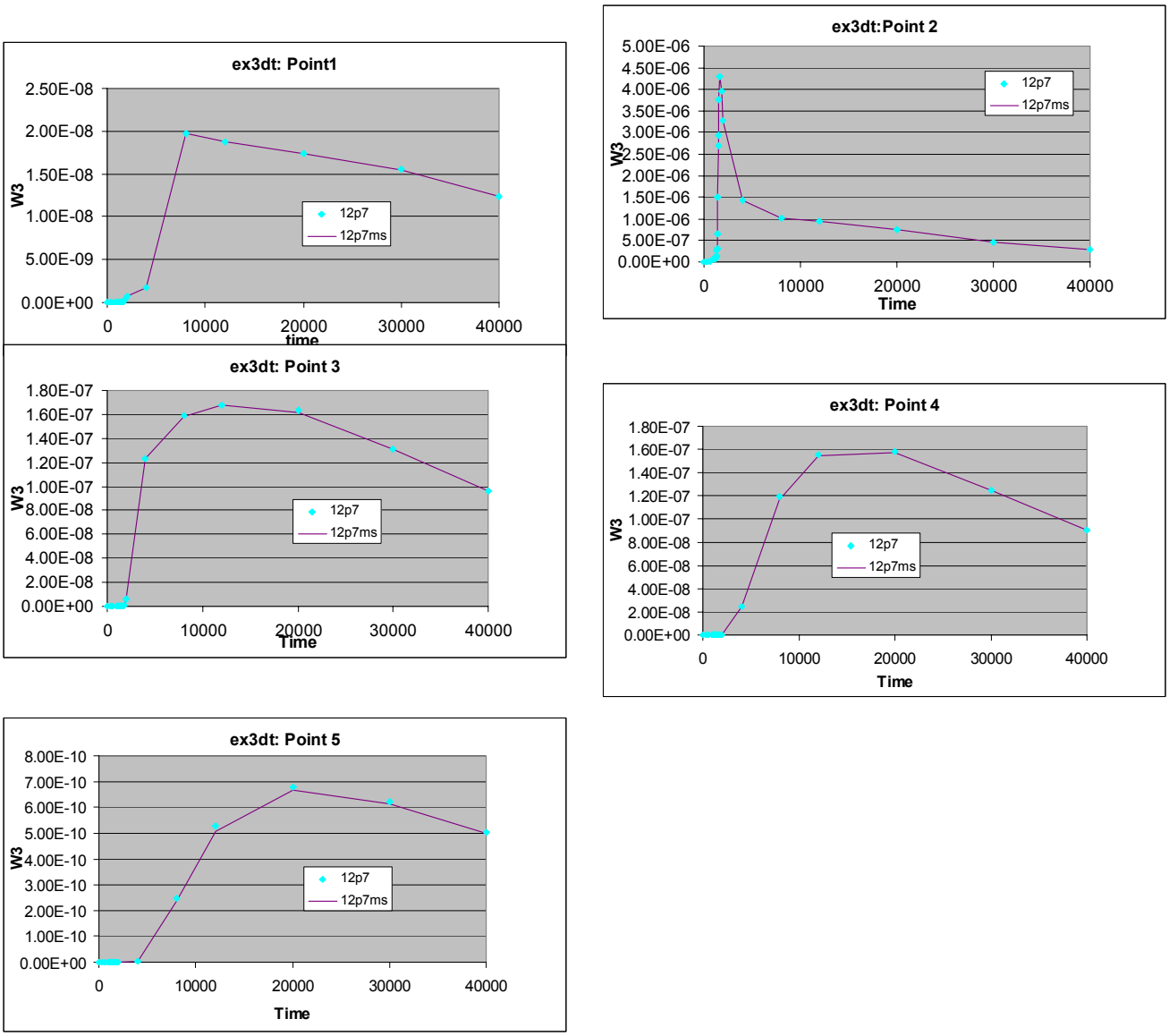

Figure A-5. Comparison of simulated mole fraction of daughter tracer (W3) at comparison points with TETRAD 12.7 and 12.7ms.

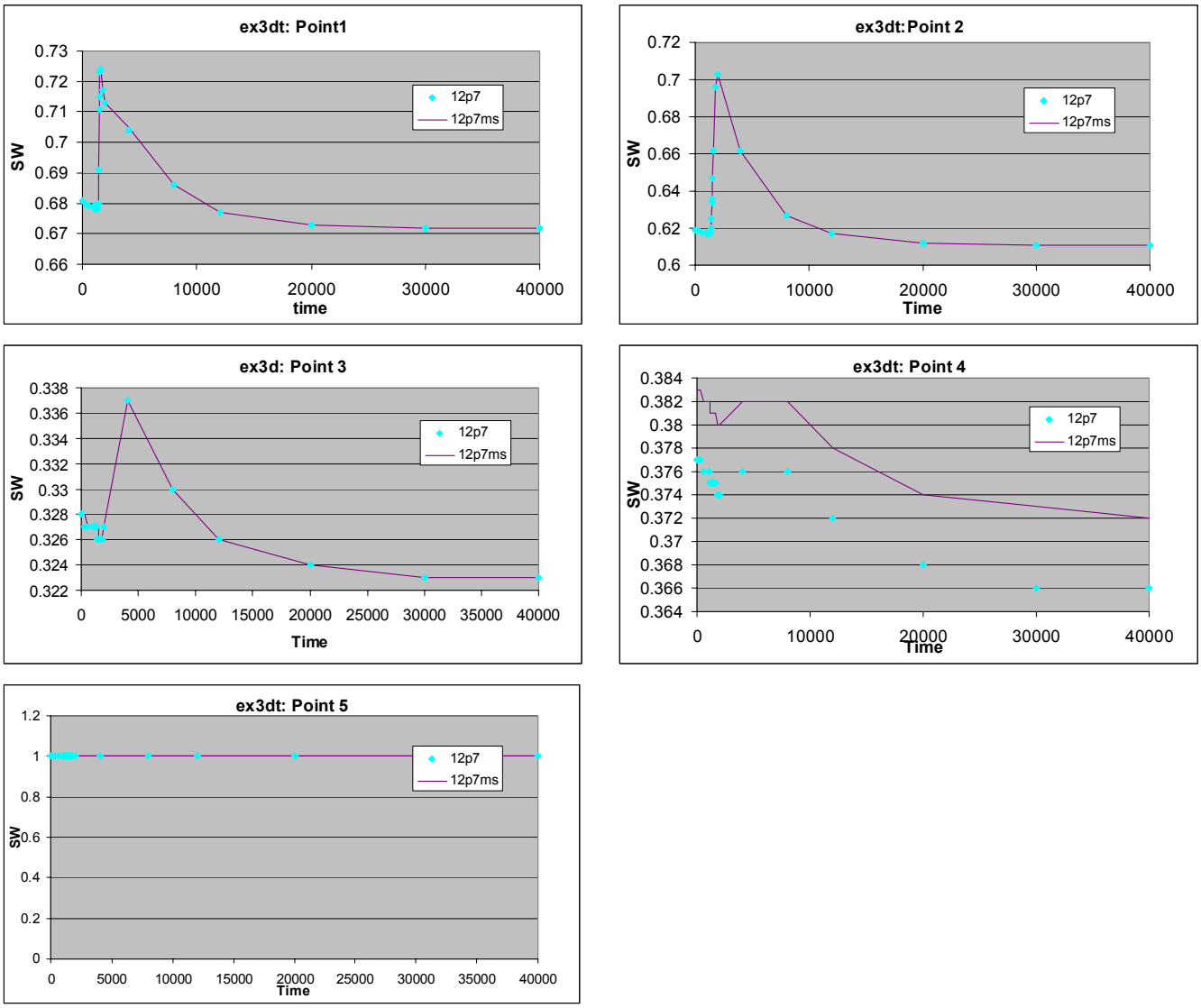

Figure A-6. Comparison of simulated water saturation (SW) at comparison points with TETRAD 12.7 and 12.7ms.

A-1.11 Simulation Deck

The input deck for problem ex3dt is given below. The same simulation deck was used with both the TETRAD 12.7 and 12.7ms data decks, with one exception—the 'SCALE' card was not used in the TETRAD 12.7 simulation because it represents loosening of the convergence criterion that can be achieved with the TETRAD 12.7ms simulator.

```
'COMMENT'  '3d variably saturated flow and transport simulation'
'TYPE'    2  5  3  0.  0.
'UNITS'   1  1  0  0
'DIMEN'  19 19 24  20
'PRINT'   0  1  0  2  0
'OUTFUN'  3  1  0  0  0  0  0  0  0  0
'OUTGEO'  0  0  0  0  0  0  0  0  2  0
```

```
'OUTPROP' 0  0  0  0  0  0  0  0  0  0
'OUTMISC' 0  0  0  0  0  0  0  0  0  0
'OUTREF'  3  1  0  0
'EXMBAL'  1
'NEWT'    ,7,1.e-7,,,,,,,,
'SCALE'   1.e+4   1.0  1.0  1.e+4  1.e+4
'TMSTEP'  ,4,,,,,0.6,,,,,,,
'ITER'   60  ,,,,,,,,,,,,,,,,
'DELX'   1
19  5. 5. 5. 5. 5. 5. 5. 5. 5. 5. 5. 5. 5. 10. 15. 15. 20. 20. 20.
'DELY'   1
19  19*5.
'DELZ'  1
24 1. 1. 1. 2. 2. 2. 2. 1. 1. 1. 1. 1. 2. 3. 4. 4. 4. 4. 3. 6. 3. 4. 4. 4.
'FTOPS'  0  0
'COMP'  1.E-7  101.325  0.  20.
'SHIFT'    1.e-5,,,,,,,,,,,,,,,
'PROPERTY'
'VANGEN'  99  1   2.0  1.8   0.0 0.15 0.0 0.1 1.0 0.0 1.0,,, material A
'VANGEN'  99  2   1.5  1.2   0.0 0.25 0.0 0.1 1.0 0.0 1.0,,, material B
'COMMENT' ' '
'DENCS'  1000. 1000. 1000.  1.22  1584.
1  1  1    2  1
18.02 18.02 18.02   29.  154.
'LIQDEN'
,,0.,101.325,15.,,,,,
,,0.,101.325,15.,,,,,
,,0.,101.325,15.,,,,,
300.,,,,,,
1584.,,,,,,
'CRITG'  1
,,,,,,,,
,,,,,,,,
,,,,,,,,
3771.8  132.8  .0032
5000.   550.  .0018
'LIQVIS'
,,,,,
,,,,,
,,,,,
.5  0.
1.  0.
'GASVIS'
.0181 0.  1.  0.  1.
.0181 0.  1.  0.  1.
.0181 0.  1.  0.  1.
.0181 0.  1.  0.  1.
.0181 0.  1.  0.  1.
'KVAL'  0.0 0.0 0.0   0.001  9.7e-5
1.186e7  -20.96  2.549e-3  3816.  46.13
1.186e7  -20.96  2.549e-3  3816.  46.13
1.186e7  -20.96  2.549e-3  3816.  46.13
8.621e8   0.  0.  3103.4  0.16
9.7   0.  0.  0.  0.
'TEMPMOD'     1   8664  1   15.
'DENRMOD'     1   8664  1   2700.
'WMOD'        1   8664  1   1.  0. 0.    0.  0.
```

```
'YMOD'        1   8664  1   0.  0. 0.    1.  0.
'XMOD'        1   8664  1   0.  0. 0.   .01  .1
'COMMENT'  ' assign porosities'
'PORZLAY'  1 0.48
'PORZLAY'  2 0.48
'PORZLAY'  3 0.48
'PORZLAY'  4 0.48
'PORZLAY'  5 0.48
'PORZLAY'  6 0.48
'PORZLAY'  7 0.48
'PORZLAY'  8 0.48
'PORZLAY'  9 0.15
'PORZLAY' 10 0.15
'PORZLAY' 11 0.15
'PORZLAY' 12 0.48
'PORZLAY' 13 0.48
'PORZLAY' 14 0.48
'PORZLAY' 15 0.48
'PORZLAY' 16 0.48
'PORZLAY' 17 0.48
'PORZLAY' 18 0.48
'PORZLAY' 19 0.48
'PORZLAY' 20 0.48
'PORZLAY' 21 0.48
'PORZLAY' 22 0.48
'PORZLAY' 23 0.48
'PORZLAY' 24 0.48
'COMMENT' 'put a gap in the low perm layer'
'PORMOD' 3051 3054  1  0.48
'PORMOD' 3412 3415  1  0.48
'PORMOD' 3775 3776  1  0.48
'PORMOD' 3070 3073  1  0.48
'PORMOD' 3431 3434  1  0.48
'PORMOD' 3792 3795  1  0.48
'PORMOD' 3089 3092  1  0.48
'PORMOD' 3450 3453  1  0.48
'PORMOD' 3811 3814  1  0.48
'COMMENT'  ' assign permeability'
'PERMZLAY'  1 2*3500.0  700.
'PERMZLAY'  2 2*3500.0  700.
'PERMZLAY'  3 2*3500.0  700.
'PERMZLAY'  4 2*3500.0  700.
'PERMZLAY'  5 2*3500.0  700.
'PERMZLAY'  6 2*3500.0  700.
'PERMZLAY'  7 2*3500.0  700.
'PERMZLAY'  8 2*3500.0  700.
'PERMZLAY'  9 3*1.0
'PERMZLAY' 10 3*1.0
'PERMZLAY' 11 3*1.0
'PERMZLAY' 12 2*3500.0  700.
'PERMZLAY' 13 2*3500.0  700.
'PERMZLAY' 14 2*3500.0  700.
'PERMZLAY' 15 2*3500.0  700.
'PERMZLAY' 16 2*3500.0  700.
'PERMZLAY' 17 2*3500.0  700.
'PERMZLAY' 18 2*3500.0  700.
'PERMZLAY' 19 2*3500.0  700.
```

```
'PERMZLAY' 20 2*3500.0  700.
'PERMZLAY' 21 2*3500.0  700.
'PERMZLAY' 22 2*3500.0  700.
'PERMZLAY' 23 2*3500.0  700.
'PERMZLAY' 24 2*3500.0  700.
'COMMENT' 'put a gap in the low perm layer'
'PERMMOD' 3051 3054  1  3*3500.0  700.
'PERMMOD' 3412 3415  1  3*3500.0  700.
'PERMMOD' 3775 3776  1  3*3500.0  700.
'PERMMOD' 3070 3073  1  3*3500.0  700.
'PERMMOD' 3431 3434  1  3*3500.0  700.
'PERMMOD' 3792 3795  1  3*3500.0  700.
'PERMMOD' 3089 3092  1  3*3500.0  700.
'PERMMOD' 3450 3453  1  3*3500.0  700.
'PERMMOD' 3811 3814  1  3*3500.0  700.
'COMMENT'  ' assign relative permeability tables'
'RKREG'      1 8664  1  1
'RKREG'   2889 3971  1  2      'low perm layer'
'COMMENT' 'put a gap in the low perm layer'
'RKREG'   3051 3054  1   1
'RKREG'   3412 3415  1   1
'RKREG'   3775 3776  1   1
'RKREG'   3070 3073  1   1
'RKREG'   3431 3434  1   1
'RKREG'   3792 3795  1   1
'RKREG'   3089 3092  1   1
'RKREG'   3450 3453  1   1
'RKREG'   3811 3814  1   1
'COMMENT'  ' sorption table with '
'ADSREG'     1 8664  1  1
'ADSREG'  2889 3971  1  2
'COMMENT' 'put a gap in the low perm layer'
'ADSREG'  3051 3054  1   1
'ADSREG'  3412 3415  1   1
'ADSREG'  3775 3776  1   1
'ADSREG'  3070 3073  1   1
'ADSREG'  3431 3434  1   1
'ADSREG'  3792 3795  1   1
'ADSREG'  3089 3092  1   1
'ADSREG'  3450 3453  1   1
'ADSREG'  3811 3814  1   1
'COMMENT'  'assign rad decay half-lives'
'SCRACK' 2  1  1.0  ,,,  decay  c2=>c3
      0.0    0.0   0.0  2.0e-2           0.0 0.0
'SCRACK' 3  1  1.0  ,,,  decay  c3=>c1
      0.0   2.0e-3 0.0  0.0              0.0 0.0
'MOLDIFF'  1.0
0.      8.64e-5 8.64e-5    0.   8.64e-5
0.      0.      0.         0.   0.864
0.      0.      0.         0.   0.
'TORMOD'      1  456        1      10.
'DISPER'  14.4  1.4  0.  0.  0.  0.
'ADSORP'   1   1   ,,,,,,,,,,,,Table 1 for Material 1
0.     0.    1.
0.     0.    1.
0.     0.    1.
0.     0.    1.
```

```
0.     0.    1.
'ADSORP'   1   2   ,,,,,,,,,,,,Table 2 for Material 2
0.     0.    1.
1000.  0.    1.
500.   0.    1.
0.     0.    1.
0.     0.    1.
'GVWRITE' -1  0
5 'W2' 'W3' 'SW' 'PW' 'PG'
'COMMENT' 'set initial conditions'
'PRES'       101.325   0.       0.012
'SATMOD'    1  6859   1   0.6  0.0       ,,,, entire vadose zone
'SATMOD' 2889  3971   1   0.001 0.0       ,,,, lowperm interbed
'SATMOD' 3051  3054   1   0.6  0.0       ,,,, interbed gap
'SATMOD' 3412  3415   1   0.6  0.0
'SATMOD' 3775  3776   1   0.6  0.0
'SATMOD' 3070  3073   1   0.6  0.0
'SATMOD' 3431  3434   1   0.6  0.0
'SATMOD' 3792  3795   1   0.6  0.0
'SATMOD' 3089  3092   1   0.6  0.0
'SATMOD' 3450  3453   1   0.6  0.0
'SATMOD' 3811  3814   1   0.6  0.0
'SATMOD' 6860  8664   1   0.0  0.0       ,,,, aquifer
'RECUR'
'TIMEYR'  0
'TIME'  -14000.  .001
'TIME'  -13998.  -1.
'AQUIFER'  'SSTATE'     1      361     1  3  2  ,,,,,,,,,,,,,,,,,,,,,,,,,
'COMMENT' 'aquifers right side boundary'
'AQUIFER'  'SSTATE'  6878     7220    19  1  1  ,,,,,,,,,,,,,,,,,,
'AQUIFER'  'SSTATE'  7239     7581    19  1  1  ,,,,,,,,,,,,,,,,,,
'AQUIFER'  'SSTATE'  7600     7942    19  1  1  ,,,,,,,,,,,,,,,,,,
'AQUIFER'  'SSTATE'  7961     8303    19  1  1  ,,,,,,,,,,,,,,,,,,
'AQUIFER'  'SSTATE'  8322     8664    19  1  1  ,,,,,,,,,,,,,,,,,,
'COMMENT' 'aquifers left  side boundary'
'AQUIFER'  'SSTATE'  6860     7202    19  1  1  ,,,,,,,,,,,,,,,,,,
'AQUIFER'  'SSTATE'  7221     7563    19  1  1  ,,,,,,,,,,,,,,,,,,
'AQUIFER'  'SSTATE'  7582     7924    19  1  1  ,,,,,,,,,,,,,,,,,,
'AQUIFER'  'SSTATE'  7943     8285    19  1  1  ,,,,,,,,,,,,,,,,,,
'AQUIFER'  'SSTATE'  8304     8646    19  1  1  ,,,,,,,,,,,,,,,,,,
'COMMENT'  'add del pres = 2 m of water on the left side'
'AQUADDP'            6860     7202    19  19.62
'AQUADDP'            7221     7563    19  19.62
'AQUADDP'            7582     7924    19  19.62
'AQUADDP'            7943     8285    19  19.62
'AQUADDP'            8304     8646    19  19.62
'MFLUX'      1  361  1  3     .02738  0.  0.  0.  0.
'TIME'  -12000.   -1.0
'TIME'  -10000.   -1.0
'TIME'  -7000.   -1.0
'TIME'  -5000.   -1.0
'TIME'  -3000.   -1.0
'TIME'  -1000.   -1.0
'TIME'  -500.    -1.0
'TIME'   0.      -1.0
'COMMENT' 'begin releasing tracer as component #2'
'MFLUX'   901 901   1  3      0.   1.e-3   0.  0.  0.
```

```
'TIME'   200.   -1.0
'TIME'   400.   -1.0
'TIME'   600.   -1.0
'TIME'   800.   -1.0
'TIME'   1000.   -1.0
'COMMENT' 'localized flood AT SURFACE'
'MFLUX'     159 161   1  3      2.738  0.  0.  0.  0.
'MFLUX'     178 180   1  3      2.738  0.  0.  0.  0.
'MFLUX'     197 199   1  3      2.738  0.  0.  0.  0.
'TIME'   1010.   -1.0
'TIME'   1030.   -1.0
'TIME'   1100.   -1.0
'COMMENT' 'end  releasing tracer as component #2'
'MFLUX'   901 901   1  3      0.   0.      0.  0.  0.
'TIME'   1150.   -1.0
'TIME'   1200.   -1.0
'TIME'   1250.   -1.0
'TIME'   1300.   -1.0
'TIME'   1350.   -1.0
'COMMENT' 'lateral influx of water at left boundary'
'MFLUX'  2319 2357  19  3      2.738  0.  0.  0.  0.
'TIME'   1360.   -1.0
'TIME'   1380.   -1.0
'TIME'   1400.   -1.0
'TIME'   1430.   -1.0
'TIME'   1460.   -1.0
'TIME'   1500.   -1.0
'COMMENT' 'return to ambient infiltration at top and no lateral influx'
'MFLUX'     159 161   1  3    .02738  0.  0.  0.  0.
'MFLUX'     178 180   1  3    .02738  0.  0.  0.  0.
'MFLUX'     197 199   1  3    .02738  0.  0.  0.  0.
'COMMENT' 'shut off lateral influx'
'MFLUX'  2319 2357  19  3     0.000   0.  0.  0.  0.
'TIME'   1510.   -1.0
'TIME'   1550.   -1.0
'TIME'   1600.   -1.0
'TIME'   1700.   -1.0
'TIME'   1800.   -1.0
'TIME'   2000.   -1.0
'TIME'   3000.   -1.0
'TIME'   4000.   -1.0
'TIME'   5000.   -1.0
'TIME'   6000.   -1.0
'TIME'   7000.   -1.0
'TIME'   8000.   -1.0
'TIME'   9000.   -1.0
'TIME'  10000.   -1.0
'TIME'  12000.   -1.0
'TIME'  14000.   -1.0
'TIME'  16000.   -1.0
'TIME'  18000.   -1.0
'TIME'  20000.   -1.0
'TIME'  22000.   -1.0
'TIME'  24000.   -1.0
'TIME'  26000.   -1.0
'TIME'  28000.   -1.0
'TIME'  30000.   -1.0
```

```
'TIME'  32000.   -1.0
'TIME'  34000.   -1.0
'TIME'  36000.   -1.0
'TIME'  38000.   -1.0
'TIME'  40000.   -1.0
```

A-2. TEST PROBLEM 2: B_GRP5

Test Problem 2 (i.e., b_grp5) compares TETRAD 12.7 and 12.7ms when applied to a full-scale SDA problem that was simulated in the ABRA. The TETRAD data deck for the U-238 simulation group (named b_grp5) from the ABRA was used. This data deck is too large to include in this appendix. A complete description of the simulation domain, parameterization, and source loading can be found in the ABRA. The b_grp5 simulation included U-238, U-234, Th-230, Ra-226, and Pb-210. The processes simulated included advection, dispersion, diffusion, adsorption, radioactive decay, and ingrowth. The simulations were performed with a relative convergence criterion of 1×10^{-7} for all components in the TETRAD 12.7 simulation. This same convergence criterion was applied to contaminants in the TETRAD 12.7ms simulation, but was relaxed four orders of magnitude for the pure water, air, and oleic components.

Comparisons in this section are provided as a time history of vertical flux values of components at individual gridblocks at the base of the simulation domain. These individual fluxes are the primary results of the vadose zone model for Operable Unit 7-13/14, because they are then used as input for the aquifer simulations. Figure A-7 shows where flux table comparisons were made with the numbers, indicating the specific flux tables where comparisons might be made.

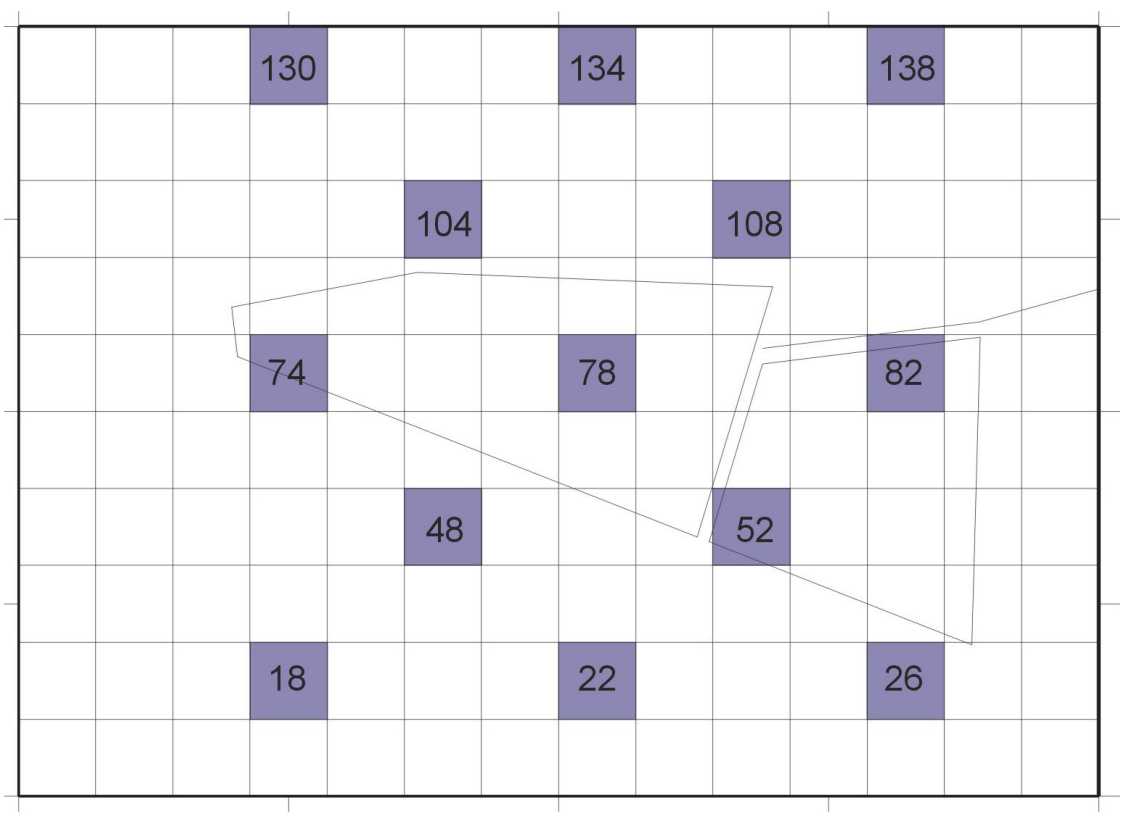

Figure A-7. Locations where fluxes from the Ancillary Basis for Risk Analysis vadose zone model were considered for comparison.

Simulation duration was just over 3,666,000 days or approximately 10,000 years. Figures A-8 through A-18 show time-history comparisons, with the time axis presented in simulation days.

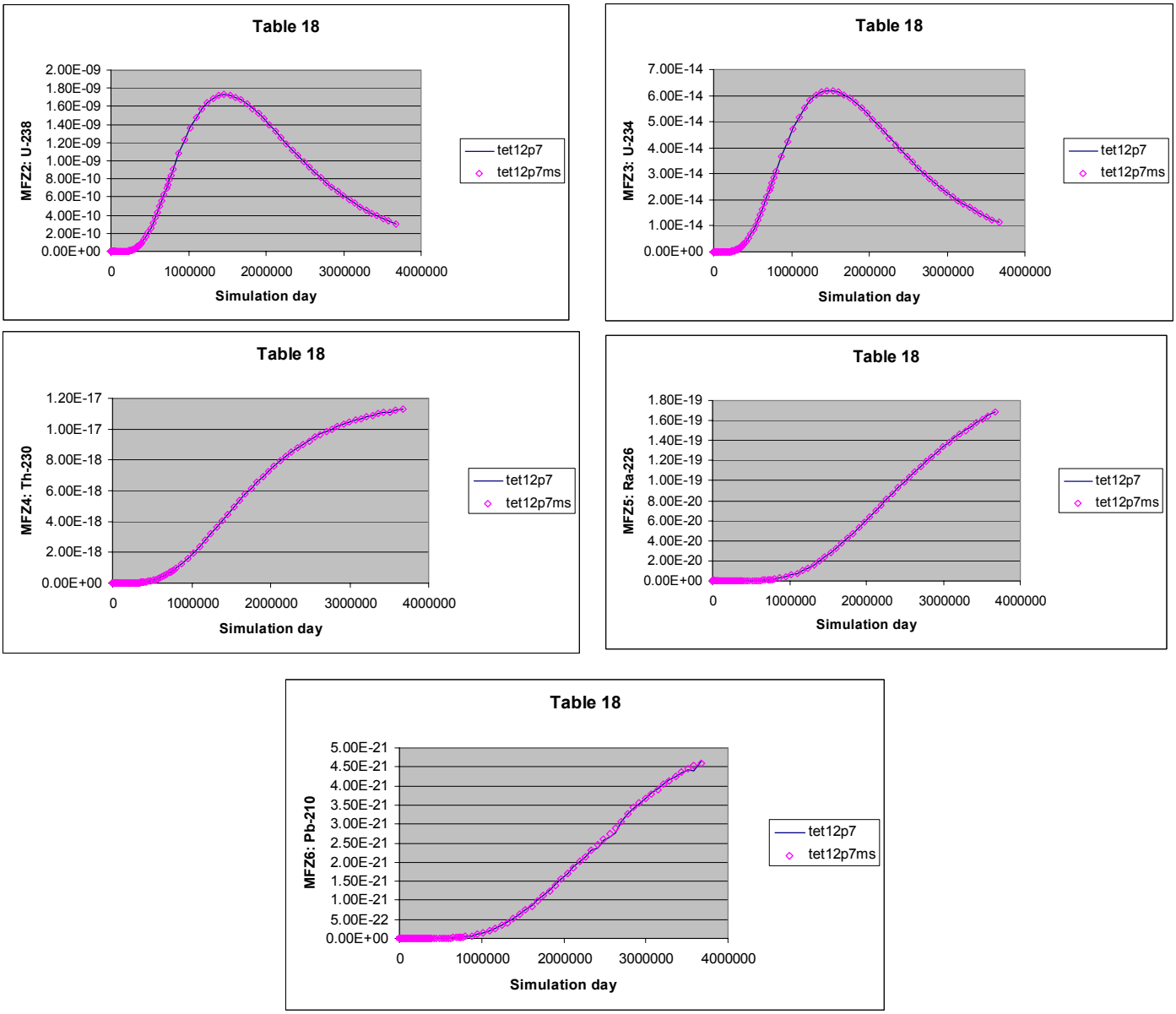

Figure A-8. Simulated flux of uranium-238, uranium-234, thorium-230, radium-228, and lead-210 at grid location 18 with TETRAD 12.7 and 12.7ms.

The first set of results in Figure A-8 shows absolute magnitude of flux for all five contaminants for both TETRAD 12.7 and 12.7ms. The results appear identical. Figure A-9 shows the percentage difference as a function of time, with the percentage calculated by normalized against the TETRAD 12.7 result. These percentage difference results are slightly more interesting and primarily show the effect of dividing by small numbers. All contaminants show a large initial spike in percent difference at very early times as the initial contaminant front advances to the bottom of the simulation domain, resulting in very low concentrations at early times in both simulations. These lead to division by small numbers in the percentage difference calculation that can result in a larger percentage difference due to precision limitations. Lead-210, being the last member of the decay chain, shows the widest degree of variability over the entire simulation period, likely due to the same reason of division by very small numbers as can be seen in the magnitude of the fluxes in Figure A-8.

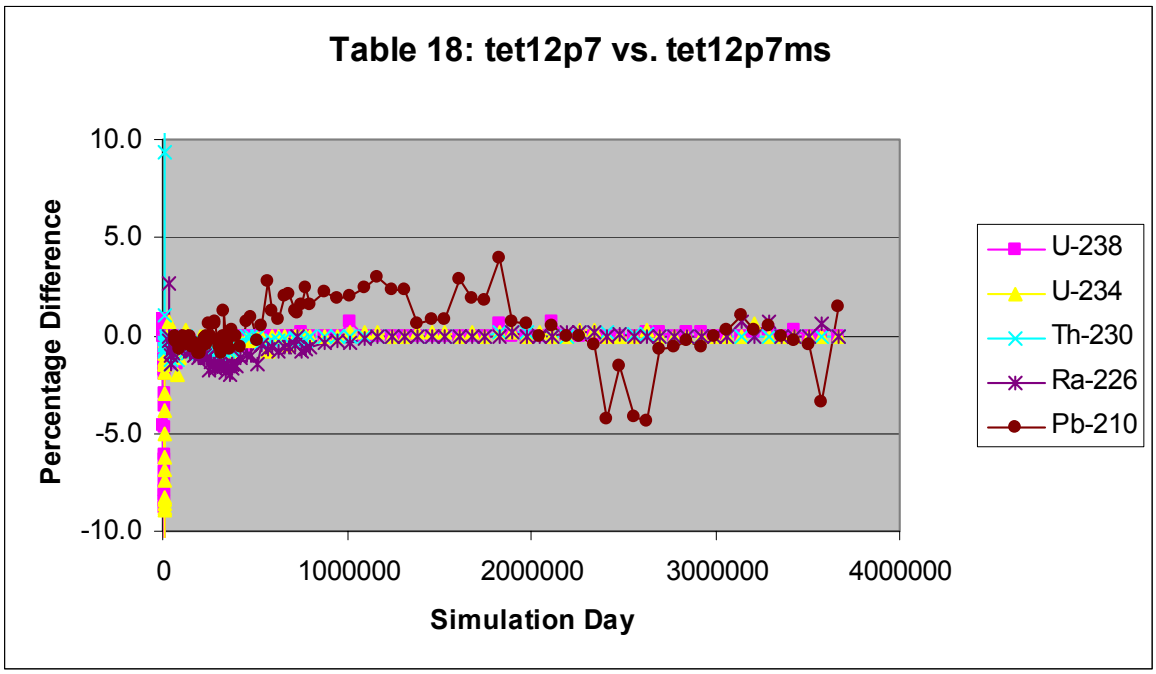

Figure A-9. Percentage difference between TETRAD 12.7 and 12.7ms fluxes as a function of time at grid location 18.

The only other grid location where the full sequence of fluxes from the vadose zone is shown is grid location 78, located directly beneath the SDA. These fluxes are shown in Figure A-10 with the percentage differences shown in Figure A-11. The percentage differences for grid location 78 are similar, but slightly different, from those for grid location 18 (shown previously). Grid 78 results lead to similar conclusions as those for grid 18. The magnitude of the fluxes over time show excellent agreement between TETRAD 12.7 and 12.7ms. The percentage differences also show very early deviation, likely due to precision limitations, with good agreement overall and the Pb-210 showing the most fluctuations over time.

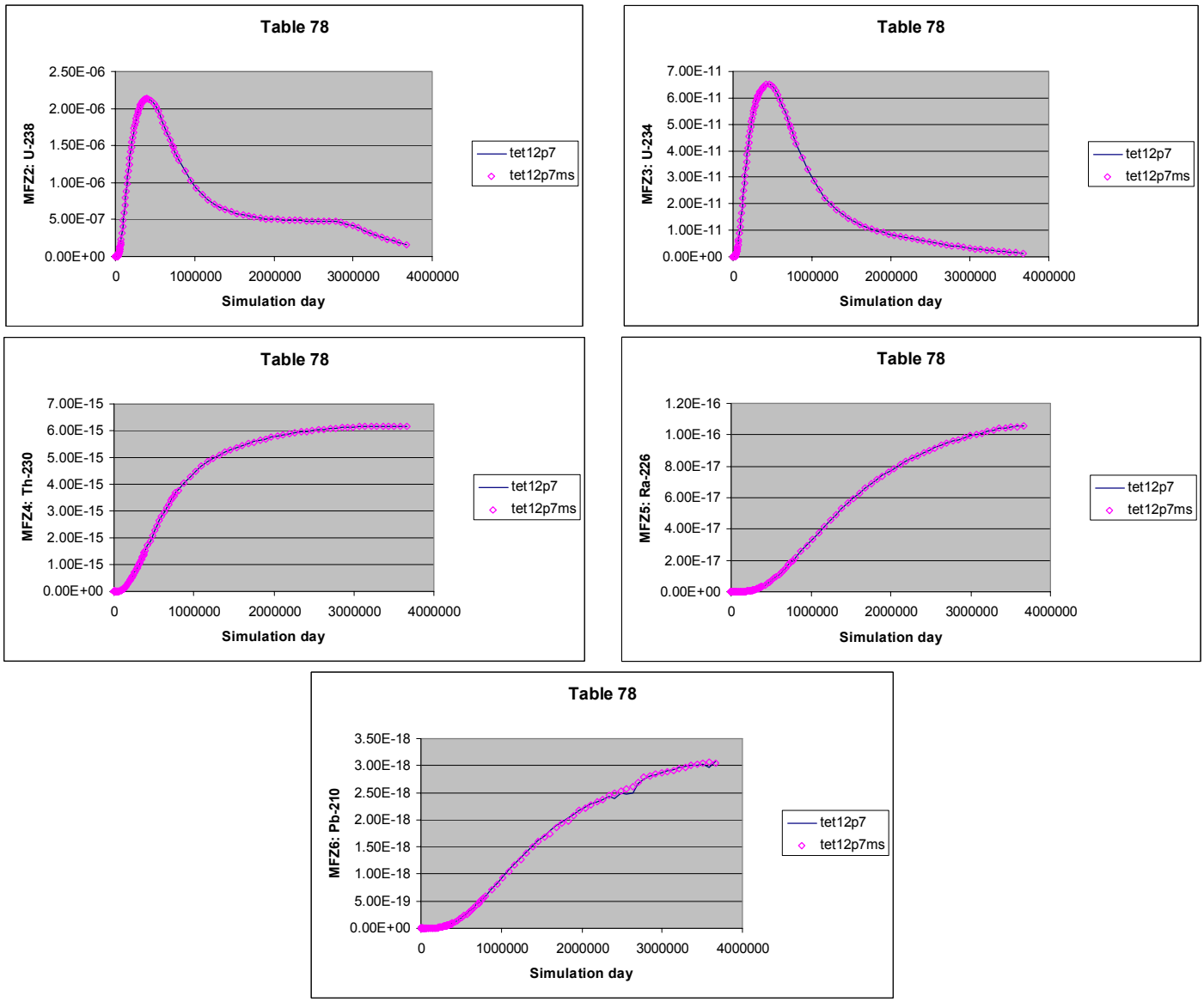

Figure A-10. Simulated flux of uranium-238, uranium-234, thorium-230, radium-228, and lead-210 at grid location 78 with TETRAD 12.7 and 12.7ms.

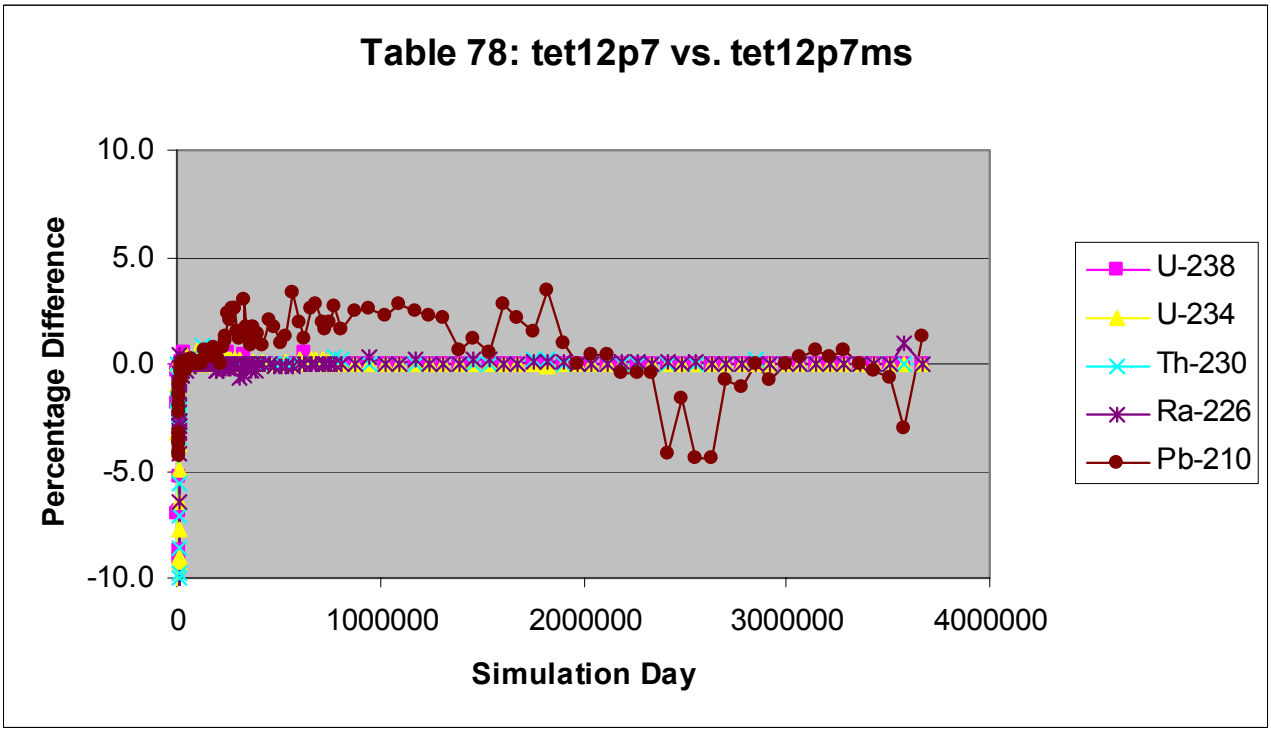

Figure A-11. Percentage difference between TETRAD 12.7 and 12.7ms fluxes as a function of time at grid location 78.

Percentage differences for most of the other indicated comparison locations from Figure A-8 are shown in Figures A-12 and A-13. Figures A-12 and A-13 also show the same result of excellent agreement between the TETRAD 12.7 and 12.7ms simulators.

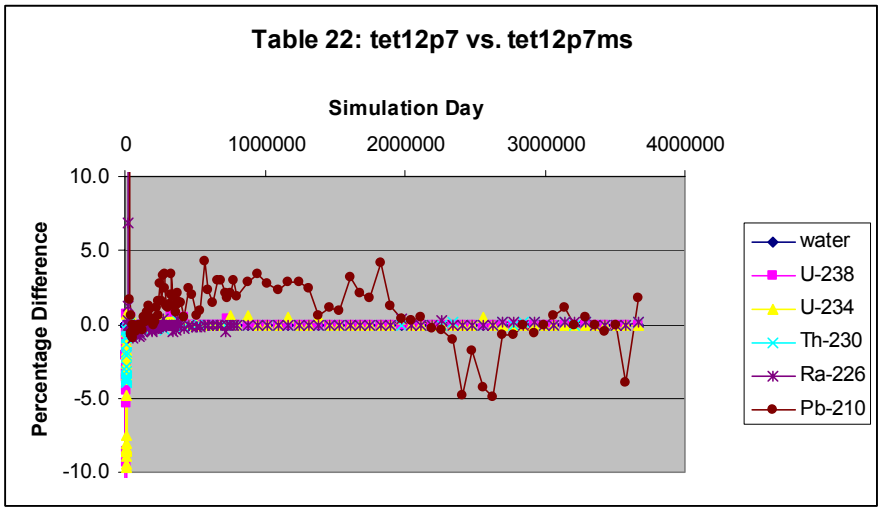

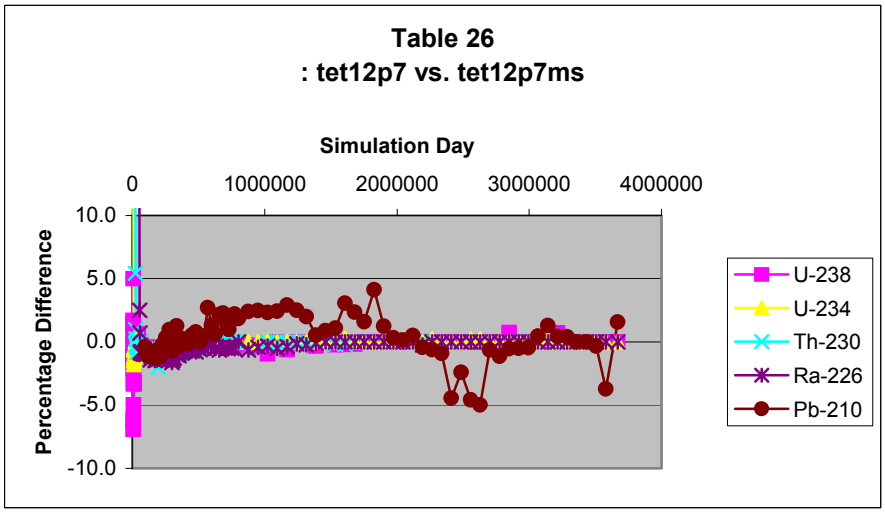

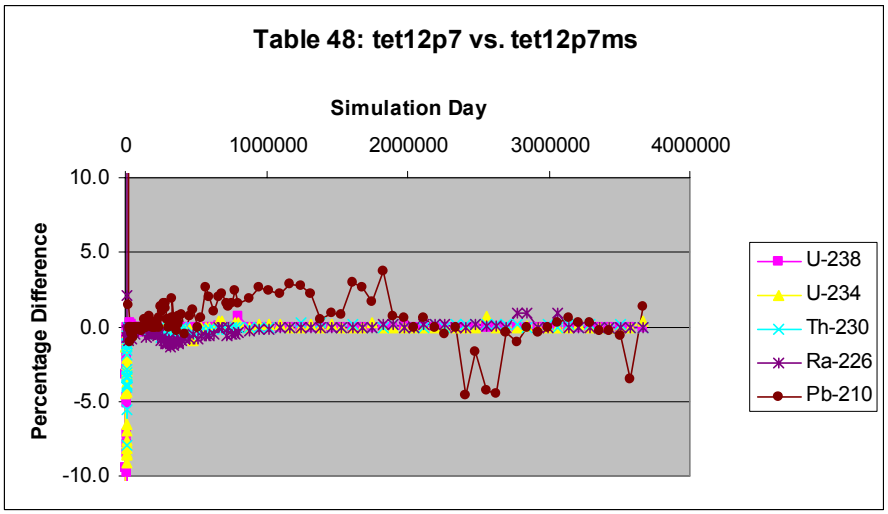

Figure A-12. Percentage difference between TETRAD 12.7 and 12.7ms fluxes as a function of time at grid locations 22, 26, and 48.

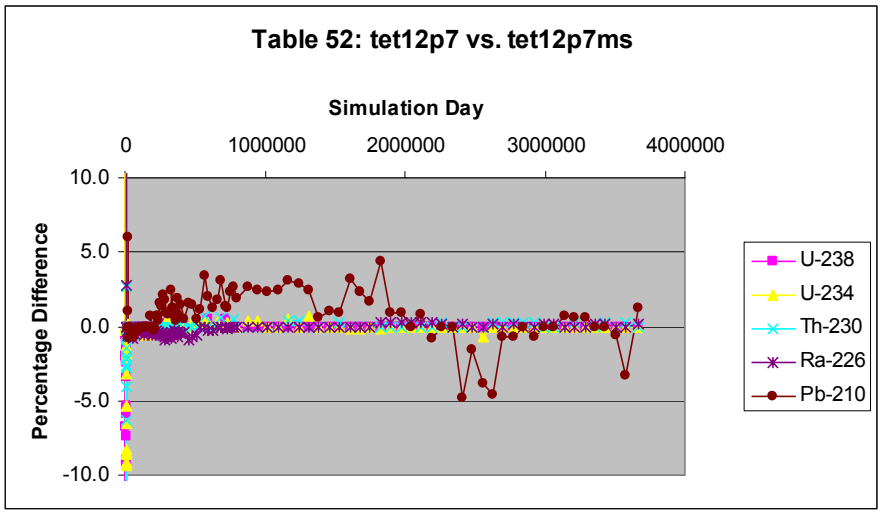

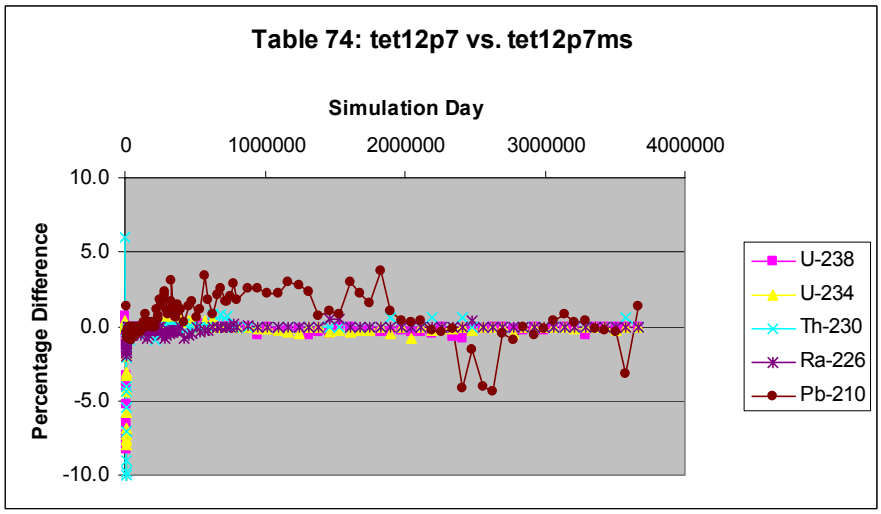

Figure A-13. Percentage difference between TETRAD 12.7 and 12.7ms fluxes as a function of time at grid locations 52 and 74.

A-3. SUMMARY

Overall, this set of simulations for both a simple and complex problem demonstrates equivalence between the TETRAD 12.7 and 12.7ms simulators.

Although it is not the focus of this appendix, the computational times for Problem Number 1 (i.e., ex3dt) were 66 central-processing-unit (CPU) minutes for TETRAD 12.7 and 44 CPU minutes for TETRAD 12.7ms, for a speedup factor of 1.5. The computational times for Problem Number 2 (i.e., b_grp5) were 40,752 CPU minutes for TETRAD 12.7 and 24,914 CPU minutes for TETRAD 12.7ms, for a speedup factor of 1.6.

A-4. REFERENCES

Becker, B. H., J. D. Burgess, K. J. Holdren, D. K. Jorgensen, S. O. Magnuson, and A. J. Sondrup, 1998, *Interim Risk Assessment and Contaminant Screening for the Waste Area Group 7 Remedial Investigation*, DOE/ID-10569, Rev. 0, U.S. Department of Energy Idaho Operations Office.

Holdren, K. Jean, Bruce H. Becker, Nancy L. Hampton, L. Don Koeppen, Swen O. Magnuson, T. J. Meyer, Gail L. Olson, and A. Jeffrey Sondrup, 2002, *Ancillary Basis for Risk Analysis of the Subsurface Disposal Area*, INEEL/EXT-02-01125, Rev. 0, Idaho National Engineering and Environmental Laboratory.

Shook, G. Michael, J. Hope Forsmann, M. Elena Velasquez, and Swen O. Magnuson, 2003, "Improving Numerical Model Efficiency of an Existing, In-House Simulation Model," *Laboratory-Directed Research and Development, FY-2003 Annual Report*, INEEL/EXT-04-01772, Idaho National Engineering and Environmental Laboratory, pp. 197-199.

Appendix B

Description of the Electronic Archive of Simulation Code, Input Files, Simulation Results, Software Management Agreement, and Listing of PV-Wave Processing Codes

Appendix B

Description of the Electronic Archive of Simulation Code, Input Files, Simulation Results, Software Management Agreement, and Listing of PV-Wave Processing Codes

This appendix contains the Software Management Agreement between Idaho Cleanup Project Operable Unit 7-13/14 and the INL Modeling and Measurement Group, a description of the Electronic Data Archive containing a frozen version of the TETRAD simulator, all simulation results for the Operable Unit 7-13/14 RI/BRA and feasibility study, and a listing and description of preprocessing routines used to generate the TETRAD data decks and to post-process the simulation results.

B-1. SOFTWARE MANAGEMENT AGREEMENT BETWEEN THE IDAHO CLEANUP PROJECT WASTE AREA GROUP 7 AND THE MODELING AND MEASUREMENT GROUP

B-1.1 Customer Requirements

The codes and analyses used to generate results that are used to make critical decisions for or by the customer will conform to the quality and documentation required by the customer.

A list of three software management requirements defined by the customer as critical and applicable to modeling activities being performed by the INL Modeling and Measurement Group in support of the Operable Unit 7-13/14 remedial investigation and feasibility study is given below. The work being performed falls under the INL Research and Development General Software Management Plan (PLN-1726 2004).

The following are three key requirements of the Operable Unit 7-13/14 remedial investigation and feasibility study:

1. Reproducibility of final results. Results presented as the final product to the Idaho Cleanup Project for acceptance by regulatory agencies must be reproducible.

2. Verifiability of final results. This will require that simulation results can be qualitatively verified by an expert in the field, using a similar simulation approach. To accomplish this, sufficient detail will be provided on the results generation processes, such that they could be independently verified. Sufficient detail includes an explanation of the predata analysis phase, simulation phase, post-processing phase, and an explanation of the results.

3. Review and approval of results. This requirement compliments the second requirement in that accuracy will be verified through a peer and customer review process.

B-1.2 Implementation of Requirements

The INL Modeling and Measurement Group will ensure that the following items are documented and placed in the project file at the time final results are released.

The first and second requirements from Section B-1.1 will be addressed through the following:

- Reference list of commercial software and version used in simulations
- Frozen version of noncommercial software and other routines used to generate results (e.g., electronic backup of Excel spreadsheets and PV-Wave routines)
- Frozen version of input and output results and files throughout data analysis and pre and post-processing stages
- Reference to the operating system and hardware specifications for reproducibility
- Documentation of the simulation and analysis process, including a flow chart or sequence of the data analysis steps that involved use of preprocessing steps, simulation phase, and post-processing phase. This will not include documentation of commercial software, but will include a description of internally written routines in the form of readme files or internal code comments.

The third requirement from Section B-1.1 will be met through the following:

- Internal (i.e., performing organization) peer review of results
  - Any customer-required external reviews
  - Performing organization management approval
  - Customer approval.

B-2. ELECTRONIC DATA ARCHIVE

The primary purpose of the electronic data archive is to document the TETRAD simulator used for Operable Unit 7-13/14 simulations, the simulation input files and results, and the pre and post-processing routines used to manipulate data for simulations. The archive resides on a file server called Schwartz and in a file partition called OU7_13_14.

B-2.1 TETRAD Simulator

The simulator used for all simulations was TETRAD 12.7ms (Shook et al 2003). Executable files for this version of TETRAD are stored in a subdirectory called ou7_13_14\1 Fate & Transport Modeling Archive\TETRAD simulator, frozen version. Since TETRAD is a proprietary code, the source files are not kept in this directory. The complete source files remain under control of the code custodian. The executables were used on an INL personal computer cluster named Squadron, administered by Mr. Alan Marley of the INL. The operating system on the Squadron personal computer cluster was Red Hat Linux release 7.3. The TETRAD source code was compiled on Squadron using the Linux f77 compiler.

Three TETRAD executables are found in the frozen version directory. The file tet12p7ms_off was the primary file used in RI/FS modeling and contains no limitations on output times. The file tet12p7ms_off_162 was used for C-14 simulations and otherwise would have had generated voluminous output every time pressures were imposed downhole during well drilling. Similarly tet12p7ms_off_261 was used for FmR_g11 simulations and had additional output times after Calendar Year 2110 for

evaluating when the VVET system could be shut off. Modifications to the TETRAD code to allow for limiting output to specific times are also included in this directory and are called "modifications for 162 specific output times" and "modifications for 261 specific output times."

B-2.2 Simulation Input Files and Results

The entire suite of TETRAD simulation results are archived on the Schwartz file server using a Windows Explorer file structure. This file structure is accessed using the Windows XP Professional operating system over the INL network and can be searched using the Windows Search utility. Simulations in the file structure are broken up into groups according to the purpose for which they were performed. Names of the directories identify the purpose. Four directories exist and are named "Simulations, BRA," "Simulations, FS," "Simulations, Initial Conditions," and "Simulations, PA-CA."

Development of a nomenclature to track simulations was necessary because of the extensive number and types of simulations performed for the RI/BRA and the feasibility study. Unique names were used in naming all input and output files from a simulation group; therefore, the results can be easily retrieved from project archival storage using keyword searches.

Table B-1 provides the nomenclature for the leading character string in the run names. The first letter is always a "B" for a RI/BRA-related simulation or an "F" for a feasibility study simulation. Letters in the remaining positions—two through four—were then used to identify attributes of a sensitivity case. The TETRAD simulator imposes an arbitrary limit of eight characters total for a unique run name. With the last four positions taken up with the group identifier, the unique leading string should only be four characters long to avoid extensive renaming of results, which was necessary in some cases. Table B-2 shows how these conventions were applied to define names for each of the simulation groups. Table B-2 gives the application that was being simulated and a detailed description of the simulation group. The "g*" indicates Groups 1 through 11 as appropriate for each name.

Each simulation group is further divided into up to 10 individual simulations for the groundwater pathway. Each simulation group did not always include all 10 simulations. In each individual simulation, there are two main divisions: one for the DUST source-release simulation and one for the TETRAD simulation. Only the TETRAD portion of this archive for each simulation will be further described in this appendix.

Each individual TETRAD simulation directory for the baseline risk assessment, the feasibility study, and the performance assessment and composite analysis usually is divided into three directories and sometimes four if surface fluxes were used in the risk assessment evaluation. The three standard directories that are always present are: 1) "BINS"—contains the binary TETRAD results for both the vadose zone simulation and the aquifer simulation, 2) "gwp maxc"—groundwater pathway maximum concentration results for anywhere in the aquifer, anywhere outside the SDA fence, and anywhere along the southern INL Site boundary, and 3) "input files"—the complete input files for the vadose zone simulation and for the aquifer simulation. The fourth directory that is sometimes present is called "surface fluxes" and contains post-processed results for the total flux of a contaminant released across the upper surface of the domain as a function of time. The results files from TETRAD were initially in ASCII files created by the grid view subroutine in TETRAD. These results contain requested output from the TETRAD simulator, consisting of values at every gridblock at each time. The ASCII files are post-processed into binary files, thus the name "BINS" for the subdirectory. The binary results files require less disk storage space and are at least an order of magnitude faster for reading into PV-Wave routines for subsequent post-processing. Only the binary results files are saved in the archive, not the original ASCII results files.

Table B-1. Run-naming nomenclature.

Run Descriptor	Run Attribute
Leading B	Baseline risk assessment
Leading F	Feasibility study
Leading a	Aquifer simulation
u	Upper-bound inventory
i	Infiltration
o	Outside the Subsurface Disposal Area
4	Pit 4
n	No
g	Grout
bc	B-C interbed
h	High
l	Low
k	Permeability
mR	Modified Resource Conservation and Recovery Act cap
et	Evapotranspiration cap
p	Partial
f	Full
R	Retrieval, treatment, and disposal
c	Cap
cP	Colloidal plutonium, in the No sorption in the B-C and C-D interbed sensitivity case
U	Uranium
Pa	Performance assessment (always preceded by FmR)

Table B-2. Simulation group names and descriptions.

Simulation Group Name	Application	Description
		BASELINE RISK ASSESSMENT
B_g*	Baseline risk assessment base case	Best-estimate inventories, average infiltration inside the Subsurface Disposal Area = 5.0 cm/year (2.0 in./year), and background infiltration outside the Subsurface Disposal Area = 1.0 cm/year (0.4 in./year)
		NO ACTION SENSITIVITY: Hold all values constant, as in the baseline risk assessment base case, except as noted.
Bu_g*	Upper-bound inventories	Upper-bound instead of best-estimate inventories
Bhi_g*	High infiltration in the Subsurface Disposal Area	Increased infiltration rate to 23 cm/year (9.1 in./year) assigned uniformly across the Subsurface Disposal Area
Bloi_g*	Low background infiltration	Reduce infiltration rate assigned outside the Subsurface Disposal Area boundary from 1.0 to 0.1 cm/year (0.4 to 0.04 in./year)
Bnbc_g*	No B-C interbed	Bounding case where B-C interbed gridblocks replaced with fractured basalt
B4ng_g*	No interim actions	Pit 4 inventory not reduced for the Accelerated Retrieval Project and beryllium blocks not grouted
Bnlk_g	No low-permeability zone in aquifer	Revise low-permeability region in the aquifer from 153 to 712,000 mD
BcP_g*	No sorption in the vadose zone interbeds	Bounding case where sorption of Pu-239 and Pu-240 does not occur in the B-C and C-D interbeds
		FEASIBILITY STUDY: All simulations apply best-estimate inventories (remaining or removed) and have an infiltration-reducing cover emplaced that reduces infiltration inside the Subsurface Disposal Area to 0.1 cm/year (0.04 in./year), unless noted otherwise.
FmR_g*	Modified Resource Conservation and Recovery Act Type C surface barrier	Pad A left in place and incorporated into cover
Fet_g*	Evapotranspiration surface barrier, 0.1 cm/year (0.04 in./year)	Pad A waste transferred to active Low-Level Waste Pit
FgU_g*	In situ grouting	In situ grouting selected areas; and Pad A waste retrieved, treated ex situ, and returned to a pit in the Subsurface Disposal Area
Fpr_g*	Partial retrieval, treatment, and disposal	Remove 1.6 ha (4 acres), targeting volatile organic compounds and transuranic waste; and Pad A retrieved and sent to the Idaho Comprehensive Environmental Response, Compensation, and Liability Act Disposal Facility
Ffr_g*	Full retrieval, treatment, and disposal	Remove all waste, including Pad A waste treated at the Idaho Comprehensive Environmental Response, Compensation, and Liability Act Disposal Facility, and buried outside of the Idaho National Laboratory Site

Table B-2. (continued).

Simulation Group Name	Application	Description
		FEASIBILITY STUDY SENSITIVITY
Feth_g*	Evapotranspiration surface barrier, 1.0 cm/year (0.4 in./year)	Same as evapotranspiration surface barrier, but with higher infiltration through cover of 1.0 cm/year (0.4 in./year)
Frnc_g	Full retrieval, treatment, and disposal with no cap	Same as full retrieval, treatment, and disposal, except no infiltration-reducing cover emplaced; infiltration remains as is in the remedial investigation and baseline risk assessment base case with spatial average of 5.0 cm/year (2.0 in./year)
		PERFORMANCE ASSESSMENT
FmRpa_g*	Performance assessment base case	Same as the Modified Resource Conservation and Recovery Act Type C Surface Barrier, but with only low-level waste sources active
FmRpaloi_g*	Performance assessment with low outside infiltration	Same as performance assessment base case, but with 0.1 cm/year (0.04 in./year) background infiltration outside the Subsurface Disposal Area

The "Simulations, Initial Conditions" directory contains initial condition simulation files for the vadose zone domain that were run for three different cases: (1) the base case with a background infiltration rate of 1.0 cm/year (0.4 in./year) applied uniformly over the entire upper surface of the model, (2) the lower background infiltration case, where the background infiltration was assigned as 0.1 cm/year (0.04 in./year), and (3) the no B-C interbed case, which had gridblocks that normally were assigned hydrologic and transport properties of the B-C interbed, but were assigned as fractured basalt instead and used a background infiltration rate of 1.0 cm/year (0.4 in./year) across the upper surface. Each of these initial condition directories contains files for simulations with two, three, four, five, and six water components. The different numbers of components were needed because the simulations groups had one, two, three, four, or five contaminants per group. Each initial condition subdirectory contains input files (".dat"), output file generated by TETRAD (".out") that reports various information during the simulation, TETRAD output files with GV names that contain user-requested results for each gridblock in the base and refined vadose zone simulation domains, and binary RESTART files. These binary RESTART files are used for restarting the dissolved-phase transport simulations from time zero, which corresponds to January 1, 1952. The use of the TETRAD restart capability alleviates the need to repetitively solve for the initial conditions and keeps the transport data decks smaller without all the grid and property assignments.

The dual-continua simulations do not have corresponding initial conditions simulation. Instead, they have the initial condition simulation incorporated into the transport deck.

Table B-3 lists subdirectories in the archive that contain TETRAD simulation results.

Table B-3. Simulation directories in electronic archive.

Baseline Risk Assessment Simulations	Feasibility Study Simulations	Performance Assessment and Composite Analysis Simulations
B_g#	FmR_g#	FmRpa_g#
Bu_g#	Fet_g#	FmRloi_g#
B4ng_g#	Feth_g#	FmRpaloi_g#
Bhi_g#	Fpr_g#	anisotropy simulations
Bloi_g#	Ffr_g#	FmRnlk_g#
Bnbc_g#	Frnc_g#	FmRnlkpa_g#
Bnlk_g#	FgU_g#	
BcP_g#		

B-2.3 Pre and Post-Processors

Routines used to pre and post-process data for Operable Unit 7-13/14 simulations were all written in the PV-Wave programming language. PV-Wave, Version 8.0, was used on a Dell Optiplex GX260 personal computer. The preprocessor routines are used in building portions of the TETRAD input decks. The post-processor routines work on results from TETRAD simulations. Both types of routines are archived in subdirectories under the \\Schwartz\ou7_13_14\1 Fate & Transport Modeling Archive\TETRAD Pre- & Post-processesors subdirectory. This subsection provides tables of the processing files and their specific function.

Table B-4 lists preprocessing routines that were used to generate portions of the TETRAD simulation input decks. Data files necessary to run the routines also are archived and are likewise described. Where common root names occur, the wildcard character "*" is used to abbreviate the names. The PV-Wave routines can be identified in the archive by their ".pro" extension. In general, output results from PV-Wave routines are named with an ".out" extension. These ".out" files were inserted into the TETRAD input files. The PV-Wave routines are generally presented in logical order of use with grid development and property assignments: first, routines to visualize grid, second, property results, and last, boundary condition assignments and source-term loading.

Table B-5 lists post-processing routines that were used to process results from TETRAD simulations. Data files necessary to run the routines are also archived and are likewise described. Where common root names occur, the wildcard character "*" is used to abbreviate the names.

The PV-Wave routines can be identified in the archive by their ".pro" extension. In general, output results from PV-Wave routines are named with an ".out" extension. These ".out" files were inserted into the TETRAD input files. The PV-Wave routines are separated within the archive by their general functional areas.

Table B-4. PV-Wave preprocessing routines.

PV-Wave Routine	Specific Function	Input Data Files	Location of Data Files
t2.pro	Generates base domain conformable vadose zone gridding, assigns lithology types to gridblocks, and populates a binary stratigraphy file with indicators for each gridblock	gridding.params_ref1 and lithology kriging results that are named S0*top, S0*bottom, AB*top, AB*bottom, BC*top, BC*bottom, CD*top, CD*bottom	gridding\FY04_grid\leecaster_results\no_overlaps
ref_2_from_1.pro	Generates first-level refined grid from base domain	gridding.params_ref2 and results from t2.pro stored in OUT subdirectory	gridding\FY04_grid\OUT
ref_3_from_2.pro	Generates second-level refined grid from first-level refined grid	gridding.params_ref3 and results from ref_2_from_1.pro stored in OUT subdirectory	gridding\FY04_grid\OUT
ftops.pro	Generates top elevations TETRAD FTOPS cards for base domain	grid_coordinates_ref1	gridding\FY04_grid\OUT
delmods.pro	Generates gridblock vertical thicknesses TETRAD DELMOD cards for base domain	grid_coordinates_ref1	gridding\FY04_grid\OUT
permssv.pro	Generates TETRAD PORMOD and PERMMOD cards for porosity and permeability for base and refined single-continua domains	Porosity*BC, Porosity*CD, Ksat*BC, Ksat*CD, grid_coordinates*, STRAT_FLAGS* (from t2.pro)	gridding\FY04_grid\leecaster_results\HydrData and gridding\FY04_grid\OUT
adsreg.pro	Generates TETRAD ADSREG cards for adsorption for base and refined single-continua domains	grid_coordinates*, STRAT_FLAGS*	gridding\FY04_grid\OUT
tormod.pro	Generates TETRAD TORMOD cards for tortuosity for base and refined single-continua domains	grid_coordinates*, STRAT_FLAGS*	gridding\FY04_grid\OUT
sda_BRA_flood_assigment.pro	Generates TETRAD MFREG cards for assigning floods for single-continua domain	grid_coordinates_ref3 and pltxy.params	gridding\FY04_grid\OUT

Table B-4. (continued).

PV-Wave Routine	Specific Function	Input Data Files	Location of Data Files
sda_BRA_infiltration_ assignment.pro	Generates TETRAD MFREG cards for assigning spatially varying infiltration for single-continua domain	pltxy.params	gridding\FY04_grid
sda_BRA_waste_ assigment.pro	Generates TETRAD MFREG cards for assigning spatial and vertical locations for applying all radiological contaminant mass, except tritium and C-14 from source-release model for single-continua domain	grid_coordinates3, STRAT_FLAGS3, and pltxy.params	gridding\FY04_grid\OUT
lith_out.pro	Interrogates either base or refined grids and output TETRAD gridblock indices; used for checking results of other routines	grid_coordinates*, STRAT_FLAGS*	gridding\FY04_grid\OUT
gen_lys_indices.pro	Uses lysimeter locations and depths to generate TETRAD gridblock indices for comparison between simulated and observed concentrations	"Carol Strong SDA Lysimeter Sampling Notebook.prn", pltxy.params, and grid_coordinates_ref*	gridding\FY04_grid\OUT
conpork.pro	Generates figures showing contours of kriged porosities and permeabilities and also measured data on which kriging was based	BCavgpork.txt, CDavgpork.txt, Porosity*BC, Porosity*CD, Ksat*BC, Ksat*CD, well_coords_list.dat	gridding\FY04_grid\leecaster_ results\HydrData, \gridding\FY04_grid\DATA
comp_kriged_w_data.pro	Generates figures showing contours of kriged porosities and permeabilities and also measured data on which kriging was based	sda_lith_data_for_well_plotting, well_coords_list, S0*top, S0*bottom, AB*top, AB*bottom, BC*top, BC*bottom, CD*top, CD*bottom	\gridding\FY04_grid\leecaster_ results\no_overlaps

Table B-4. (continued).

PV-Wave Routine	Specific Function	Input Data Files	Location of Data Files
perssmv_nbc.pro	Generates TETRAD PORMOD and PERMMOD cards for porosity and permeability for case of no B-C interbed for base and refined domains	Porosity*BC, Porosity*CD, Ksat*BC, Ksat*CD, grid_coordinates*, STRAT_FLAGS*	gridding\FY04_grid\leecaster_results\HydrData and gridding\FY04_grid\OUT
adsreg_nbc.pro	Generates TETRAD ADSREG cards for adsorption for case of no B-C interbed base and refined domains	grid_coordinates*, STRAT_FLAGS*	gridding\FY04_grid\OUT
tormod_nbc.pro	Generates TETRAD TORMOD cards for tortuosity for case of no B-C interbed base and refined domains	grid_coordinates*, STRAT_FLAGS*	gridding\FY04_grid\OUT
"14 × 10 × 80 grid values.xls"	Excel file to calculate gridblock numbers for assigning boundary conditions	NA	NA
permssv_frac.pro	Generates TETRAD PORMOD and PERMMOD cards for porosity and permeability for base and refined fracture portion of dual-continua domain	Porosity*BC, Porosity*CD, Ksat*BC, Ksat*CD, grid_coordinates*, STRAT_FLAGS*	gridding\FY04_grid\leecaster_results\HydrData and gridding\dual_FY04_grid\OUT
permssv_matrix.pro	Generates TETRAD PORMOD and PERMMOD cards for porosity and permeability for base and refined matrix portion of dual-continua domain	Porosity*BC, Porosity*CD, Ksat*BC, Ksat*CD, grid_coordinates*, STRAT_FLAGS*	gridding\FY04_grid\leecaster_results\HydrData and gridding\dual_FY04_grid\OUT
adsreg_frac.pro	Generates TETRAD ADSREG cards for adsorption for base and refined fracture portion of dual-continua domain	grid_coordinates*, STRAT_FLAGS*	gridding\dual_FY04_grid\OUT

Table B-4. (continued).

PV-Wave Routine	Specific Function	Input Data Files	Location of Data Files
adsreg_matrix.pro	Generates TETRAD ADSREG cards for adsorption for base and refined matrix portion of dual-continua domain	grid_coordinates*, STRAT_FLAGS*	gridding\dual_FY04_grid\OUT
tormod_frac.pro	Generates TETRAD TORMOD cards for tortuosity for base and refined fracture portion of dual-continua domain	grid_coordinates*, STRAT_FLAGS*	gridding\dual_FY04_grid\OUT
tormod_matrix.pro	Generates TETRAD TORMOD cards for tortuosity for base and refined matrix portion of dual-continua domain	grid_coordinates*, STRAT_FLAGS*	gridding\dual_FY04_grid\OUT
sda_dual_flood_assignment.pro	Generates TETRAD MFREG cards for assigning floods for dual-continua domains	grid_coordinates_ref3 and pltxy.params	gridding\dual_FY04_grid\OUT
sda_dual_infiltration_ assignment.pro	Generates TETRAD MFREG cards for assigning spatially varying infiltration for dual-continua domain	pltxy.params	gridding\dual_FY04_grid
sda_dual_waste_H3_C14_ assignment.pro	Generates TETRAD MFREG cards for assigning spatial and vertical locations for applying tritium and C-14 contaminant mass from source-release model for dual-continua domain	grid_coordinates3, STRAT_FLAGS3, and pltxy.params	gridding\dual_FY04_grid\OUT
sda_dual_waste_VOCS_ assignment.pro	Generates TETRAD MFREG cards for assigning spatial and vertical locations for applying volatile organic compound contaminant mass from source-release model for dual-continua domain	grid_coordinates3, STRAT_FLAGS3, and pltxy.params	gridding\dual_FY04_grid\OUT

Table B-4. (continued).

PV-Wave Routine	Specific Function	Input Data Files	Location of Data Files
almod_matrix.pro	Generates TETRAD ALMOD cards for sediment portions of matrix dual-continua domain	grid_coordinates*, STRAT_FLAGS*	gridding\dual_FY04_grid\OUT
gen_face_aquifers.pro	Generates TETRAD AQUIFER cards for side faces of dual-continua domain	None	NA
gen_face_diffbcs.pro	Generates TETRAD DIFFBC cards for side faces of dual-continua domain	None	NA
gen_tvbcs.pro	Generates TETRAD AQUADDP cards for time-varying surface atmospheric pressure boundary conditions in dual-continua domain	grid_coordinates*	gridding\dual_FY04_grid\OUT
permssv_frac_nbc.pro	Generates TETRAD PORMOD and PERMMOD cards for porosity and permeability for base and refined fracture portion of dual-continua domain for case of no B-C interbed	Porosity*BC, Porosity*CD, Ksat*BC, Ksat*CD, grid_coordinates*, STRAT_FLAGS*	gridding\FY04_grid\leecaster_results\HydrData and gridding\dual_FY04_grid\OUT
permssv_matrix_nbc.pro	Generates TETRAD PORMOD and PERMMOD cards for porosity and permeability for base and refined matrix portion of dual-continua domain for case of no B-C interbed	Porosity*BC, Porosity*CD, Ksat*BC, Ksat*CD, grid_coordinates*, STRAT_FLAGS*	gridding\FY04_grid\leecaster_results\HydrData and gridding\dual_FY04_grid\OUT
adsreg_frac_nbc.pro	Generates TETRAD ADSREG cards for adsorption for base and refined fracture portion of dual-continua domain for case of no B-C interbed	grid_coordinates*, STRAT_FLAGS*	gridding\dual_FY04_grid\OUT

Table B-4. (continued).

PV-Wave Routine	Specific Function	Input Data Files	Location of Data Files
adsreg_matrix_nbc.pro	Generates TETRAD ADSREG cards for adsorption for base and refined matrix portion of dual-continua domain for case of no B-C interbed	grid_coordinates*, STRAT_FLAGS*	gridding\dual_FY04_grid\OUT
tormod_frac_nbc.pro	Generates TETRAD TORMOD cards for tortuosity for base and refined fracture portion of dual-continua domain for case of no B-C interbed	grid_coordinates*, STRAT_FLAGS*	gridding\dual_FY04_grid\OUT
tormod_matrix.pro	Generates TETRAD TORMOD cards for tortuosity for base and refined matrix portion of dual-continua domain for case of no B-C interbed	grid_coordinates_*, STRAT_FLAGS*	gridding\dual_FY04_grid\OUT
gen_INJ_I_C_AQUADDP.pro	Generates TETRAD time-varying boundary conditions with downhole bottom pressures assigned for positive pressure well drilling	pltxy.params, air_drilled_wells_coords_list.dat, grid_coordinates_*	gridding\dual_FY04_grid\air_drilling, gridding\dual_FY04_grid\OUT
comb.pro	General program to create TETRAD MFLUXT cards for releasing contaminant mass from the source-release model into the vadose zone model; group.info contains scale factors for upscaling DUST source-release results for use in TETRAD	group.info and DUST source-release output files	src_loading\bra_input and all subdirectories of this directory
int_fluxes.pro	Integrate total mass out of the revised source-release files for checking against inventories input to source-release model	group.info and g*.inp_tet	src_loading\bra_input and source release directories

Table B-5. PV-Wave post-processing routines.

PV-Wave Routine	Specific Function	Input Data Files	Location of Data Files
gvo.pro, gvoall.pro	Converts TETRAD Gridview ASCII files into binary format. Gvoall.pro converts all grid view files in a subdirectory.	TETRAD ASCII Gridview files	Temporary storage directory
conaq.pro	Contours aquifer domain results.	group.info, binary results files	src_loading\bra_input
conct.pro	Extracts maximum concentration as a function of time from either anywhere in the aquifer model or outside the Subsurface Disposal Area fence. Used to hand off model concentrations for calculating equivalent risk.	group.info, binary results files	src_loading\bra_input
consmax.pro	Plan view contouring of vadose zone simulation results for saturation, capillary pressure, or vertical water flux by maximum within a lithologic zone, or by single slice through domain. Optimally superimposes monitoring results.	STRAT_FLAGS_*, pltxy.params	gridding\dual_fy04_grid\OUT, gridding\dual_fy04_grid
convers.pro	Cross section contouring for vadose zone contaminant concentrations. Field monitoring results are superimposed at lysimeter/perched water monitoring locations. Also, optionally overlays lithology by shading sediment gridblocks.	STRAT_FLAGS_*, group.info, binary results files, Koeppen monitoring results spreadsheet converted to ASCII text files, 'Carol Strong SDA Lysimeter Sampling Notebook.prn'	gridding\dual_fy04_grid\OUT, src_loading\bra_input, \monitoring data (under the pre and post-processors directory), gridding\FY04_grid\
cvst_lys.pro	Time history plotting of simulated contaminant concentration as a function of time at vadose zone monitoring locations. Overlays monitoring results from specific lysimeter and perched water monitoring locations.	group.info, binary results files, Koeppen monitoring results spreadsheet converted to ASCII text files, vzlocs.param	src_loading\bra_input, \monitoring data (under the pre and post-processors directory), postprocessing directorynnnn

Table B-5. (continued).

PV-Wave Routine	Specific Function	Input Data Files	Location of Data Files
plt_aq_conc.pro	Time history plotting of simulated contaminant concentration as a function of time at aquifer well locations. Overlays monitoring results from specific aquifer water monitoring locations.	group.info, binary results files Koeppen monitoring results spreadsheet converted to ASCII text files pltaq.params, all_well_coordinate_list, sda_well_list	src_loading\bra_input \monitoring data (under the pre and post-processors directory) processing\aq_well_locs\
plt_aq_pro.pro	Plots vertical profiles of simulated concentration in the aquifer for selected contaminants.	binary results files	—
times_ic.pro	Plots water saturation as a function of time during initialization period to allow determination of quasi steady-state conditions.	binary results files	—
vzflux.pro	Reads vadose zone model results and creates input files for loading time history of water and contaminant flux into corresponding gridblocks of the aquifer model. Also generates graphics file with time history flux for each gridblock.	binary results files	—
C14_inst_BRA.pro	Creates time history plot of C-14 contaminant flux through land surface, and creates an ASCII file of contaminant flux as a function of time for use in risk calculation.	binary results files	—
VOC_inst_BRA.pro	Creates time history plot of volatile organic compound contaminant flux through land surface, and creates an ASCII file of contaminant flux as a function of time for use in risk calculation.	binary results files	—
coniso.pro	Creates plan view contour plots of risk over time for a spatially-consistent receptor, using superposition to combine risks from an arbitrary number of contaminants.	*_input_files, table_conv_factors_BRA_FY05 tetrad_scale_facs_BRA_FY05	postprocessing\isopleth

B-3. REFERENCES

PLN-1726, 2004, "Research and Development General Software Management Plan," Rev. 0, Idaho National Engineering and Environmental Laboratory, Idaho Completion Project.

Shook, G. Michael, J. Hope Forsmann, M. Elena Velasquez, and Swen O. Magnuson, 2003, "Improving Numerical Model Efficiency of an Existing, In-House Simulation Model," *Laboratory-Directed Research and Development, FY-2003 Annual Report*, INEEL/EXT-04-01772, Idaho National Engineering and Environmental Laboratory, pp. 197-199.

Appendix C

Aquifer Model Domain Extension

Appendix C

Aquifer Model Domain Extension

This appendix contains a complete letter report from Mike Rohe to S. O. Magnuson and T. J. Meyers, March 9, 2004 which was titled "OU 7-13/14 ABRA Saturated Groundwater Model Update." This letter report documented the expansion of the Operable Unit 7-13/14 aquifer model domain.

C-1. INTRODUCTION

The original Operable Unit 7-13/14 ABRA saturated groundwater model (Holdren et al. 2002) was used to prepare cumulative risk contours resulting from simulation of eight groundwater contaminant groups. The downgradient end of the resulting cumulative risk contour line for 10^{-5} total risk exceeded the original saturated model domain. To capture the entire contour line within model boundaries, the domain was extended in the downgradient direction of groundwater flow. This letter report describes the effort required to expand the domain and reports the results of re-running the model. The model is fully saturated and based on the TETRAD numerical reservoir simulation code (Vinsome and Shook 1993). PV-Wave, an environmental analysis and visualization software (Visual Numerics 2001), was used to prepare model input and to process results.

C-2. DOMAIN EXTENSION

In the INL Site vicinity, groundwater in the Snake River Plain aquifer flows primarily south-southwest with some localized variation. Initially, the saturated model domain was extended only in the southern direction. The domain was expanded to 300% in this direction. After examining the results of contouring water levels in the extended domain, particularly in the southwestern portion of the domain, it was determined that the domain should also be extended in the west direction. The domain was increased to 200% in this direction, making the new domain three times the original north-south length and two times the original east-west length. The northeast corners of both the original and extended models are located in the same position since the domain extension only occurred to the south and west directions. The original and extended domains are shown in Figure C-1.

The original ABRA saturated model consisted of seven layers of grid cells sized 1,000 feet (304.8 m) per side with variable vertical thickness (Holdren et al. 2002). Each layer contained 34 columns and 27 rows of cells yielding 918 cells per layer and a total of 6,426 grid cells in the model. The original domain was a rectangle 6.4 mi (10.4 km) in the east-west direction and 5.1 mi (8.2 km) in the north-south direction covering an area of 33 mi^2 (85 km^2). The new domain retains the 1,000-ft (304.8 m) sided grid cells but now contains 68 columns and 81 rows per layer, seven layers, yielding 5,508 cells per layer for a total of 38,556 grid cells. The new domain is 12.9 mi (20.7 km) in the east-west direction and 15.3 mi (24.7 km) in the north-south direction covering an area of 198 mi^2 (512 km^2).

The refined grid area from the original model was maintained in the new model. This refinement matches the RWMC vadose zone model footprint onto the aquifer and is 7,000 ft (2134 m) by 5,000 ft (1,524 m) covering an area of 1.25 mi^2 (3.25 km^2). In the refined area, the grid cells are 500 ft (152.4 m) per side.

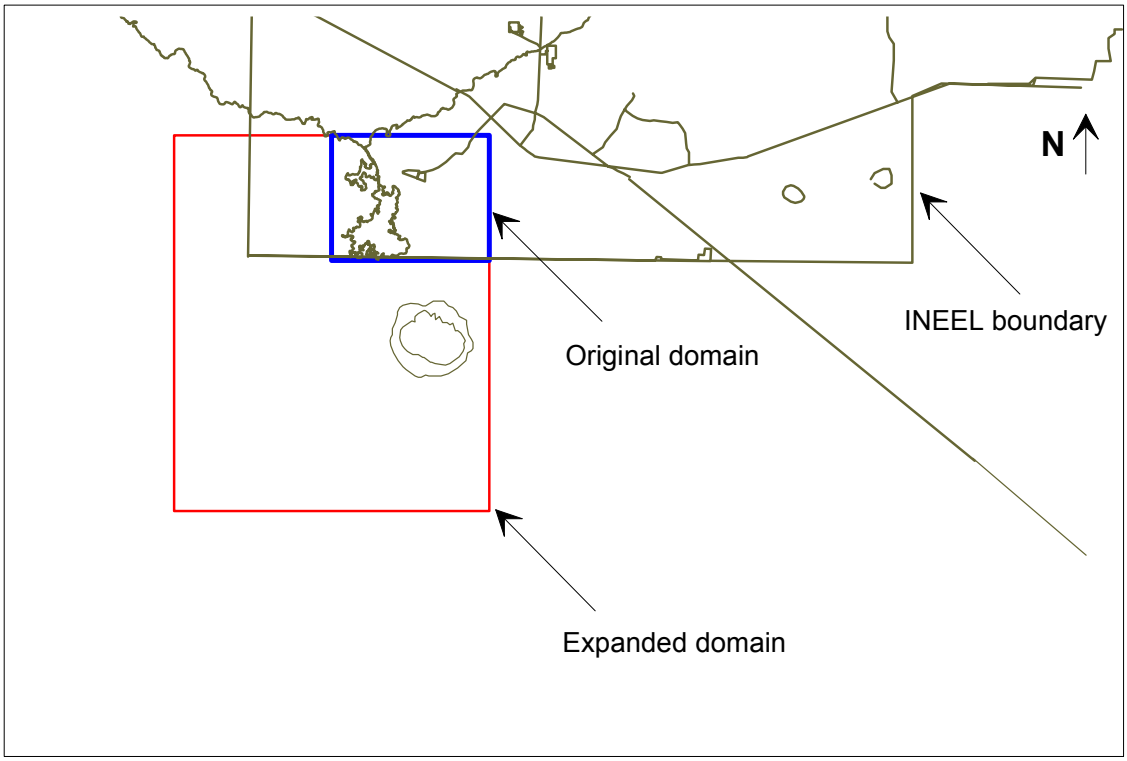

Figure C-1. Extended model domain compared to original Operable Unit 7-13/14 saturated groundwater model domain.

C-3. WATER-TABLE CONTOUR MAPS

Water-table maps were prepared using the Surfer mapping program (Golden Software 2000) to reveal groundwater flow characteristics and to supply fixed head values for boundary nodes in the new model domain. The original groundwater model used 77 aquifer wells in the vicinity of, or upgradient of, the RWMC to establish boundary heads. The new expanded domain model excludes 22 of these wells; these were mostly upgradient wells in close proximity or wells with missing data for fall 2003. These were replaced with 22 wells located mostly south of the RWMC in the extended domain.

The water-table contour map developed for the original ABRA saturated model covered 17 mi (27.4 km) by 13 mi (21.3 km) or 226 mi^2 (585 km^2) in area. The extended domain model required additional wells that cover a territory 52 mi (84.1 km) by 32 mi (51.8 km), for an area of 1,683 mi^2 (4,359 km^2). The expansion in model domain and mapped water-table area included a much larger change in hydraulic head than in the original model. The larger change in hydraulic head has an important effect on modeled water-table elevation and modeled velocities in the new model.

Groundwater elevation data were compiled for fall 2003 and range from September to November water levels. These data were assumed to represent a steady state condition. Borehole deviation correction factors were applied to water level data in those wells with available deviation logs. The resulting groundwater potentiometric contour map is shown in Figure C-2.

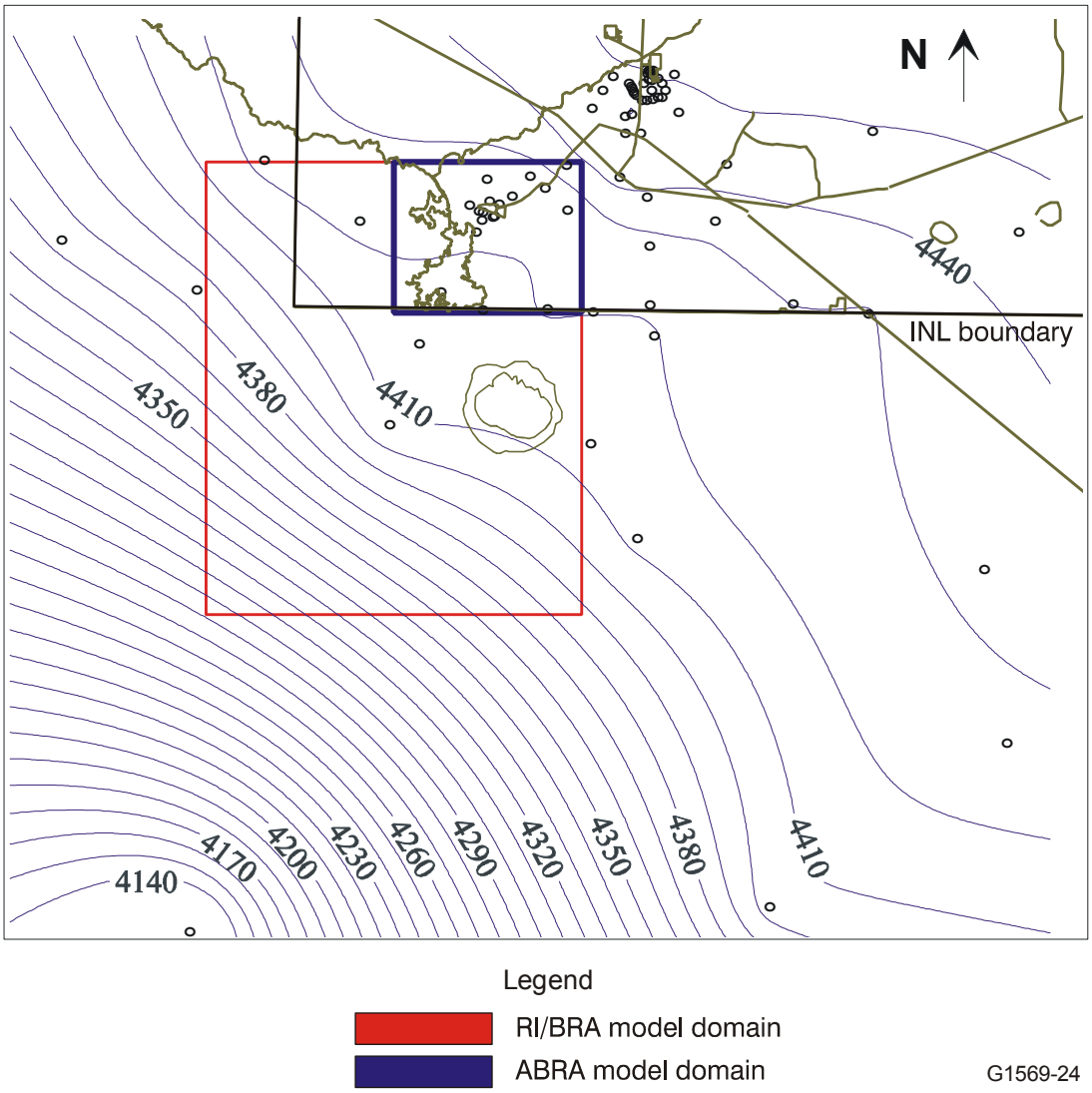

Figure C-2. Remedial investigation/baseline risk assessment-model domain with interpolated fall 2003 water-table contours (feet). Symbols indicate locations used for interpolation.

Additional water-table contour maps were prepared for fall (September through November) of 2001 and 2002. These were prepared using information from 94 and 95 aquifer wells, respectively. Figure C-3 compares the fall 2001 and 2002 maps with a contour map prepared for the extended domain using only the original model's 77 aquifer wells and water level data for fall 2000. The same extent is shown for all three maps and covers an area larger than either model domain. In the original model domain, the groundwater flow direction appears mostly southerly (Figure C-5 through C-37, Holdren et al. 2002). Yet, when expanded to the new domain, the fall 2000 water – map (Figure C-3a) agrees with the later maps (Figure C-3b and C-3c); the groundwater flow direction becomes more southwesterly due to a rapid decrease in water-table elevation.

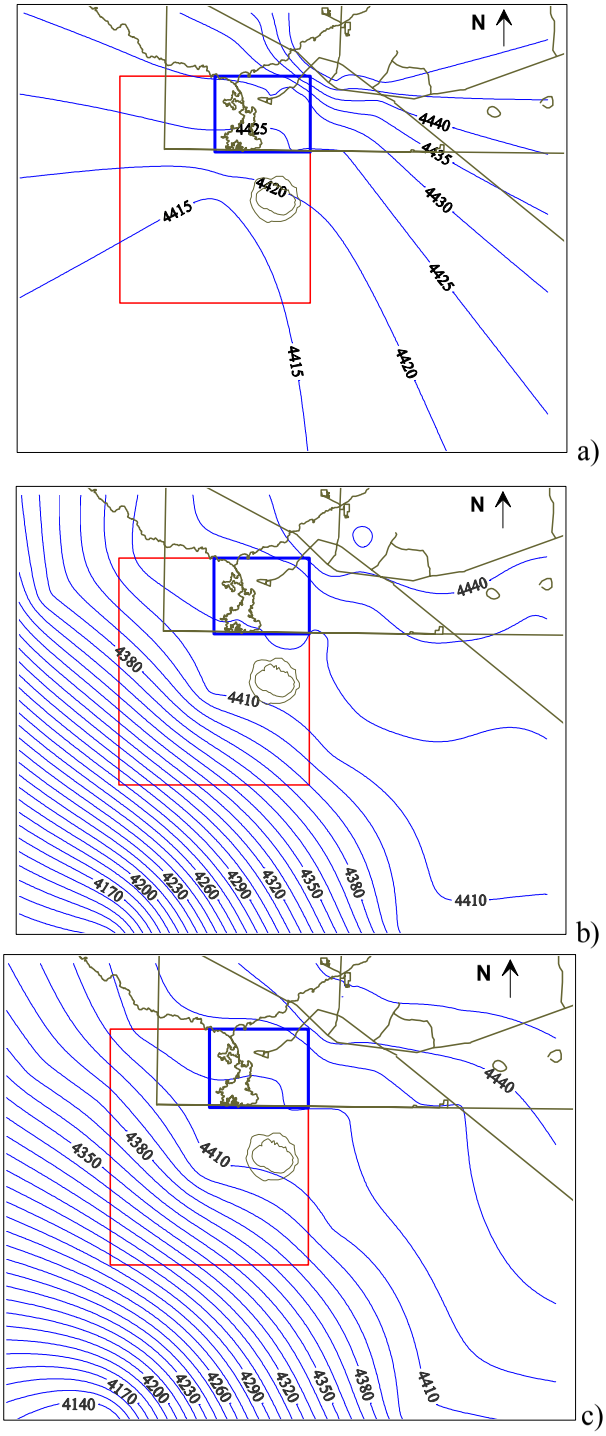

Figure C-3. Comparison of contour maps: (a) original 77 wells from fall 2000; (b) 94 wells in fall 2001; and (c) 95 wells in fall 2002 (original and extended model domains).

C-4. BOUNDARY CONDITIONS

Boundary conditions for the extended domain model were established as prescribed head conditions assuming steady-state conditions. Hydraulic head values were interpolated from the fall 2003 water-table contour map at each perimeter boundary node position using a PV-Wave program. The water–table map indicates a general southwest direction of flow. Figure C-4 shows the fall 2003 water-table map superimposed onto the new model domain. Also shown are the measured water level elevations at their respective locations.

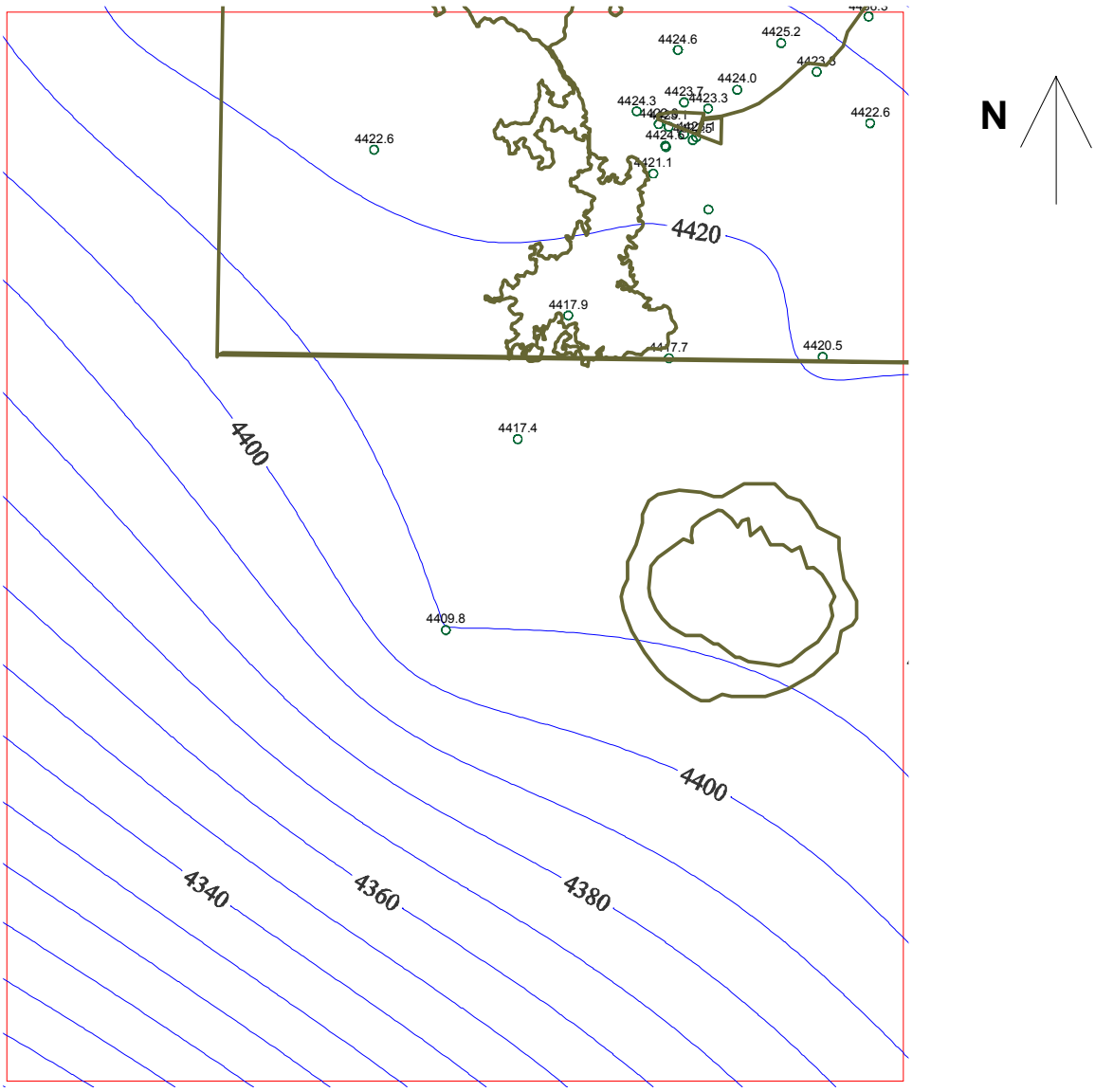

Figure C-4. Model domain with fall 2003 water-table contours.

The hydraulic head relief from the northeast corner to the southwest corner of the new domain is 157 ft (48 m) and extends over a distance of 20 mi (32.2 km). The resulting average hydraulic gradient is 7.8 ft/mi (0.0015 m/m). However, in the vicinity of the RWMC, the gradient is much lower and ranges

approximately 2 to 4 ft/mi (0.0004 to 0.0008). Only in the southwest portion of the domain does the large drop in hydraulic head in measured wells produce a gradient of approximately 13 ft/mi (0.002).

C-5. PERMEABILITY ZONES

The original ABRA saturated model contained three distinct permeability zones that were based in part on the 1994 Waste Area Group-10 regional aquifer modeling effort (McCarthy et al. 1995) as well as calibration required to match modeled heads to fall 2000 measured heads. The three zones had values of 153; 9,300; 712,000 mD (millidarcies) and are labeled as such in Figure C-5. The 153 mD zone was the lowest permeability zone and was located immediately downgradient of RWMC.

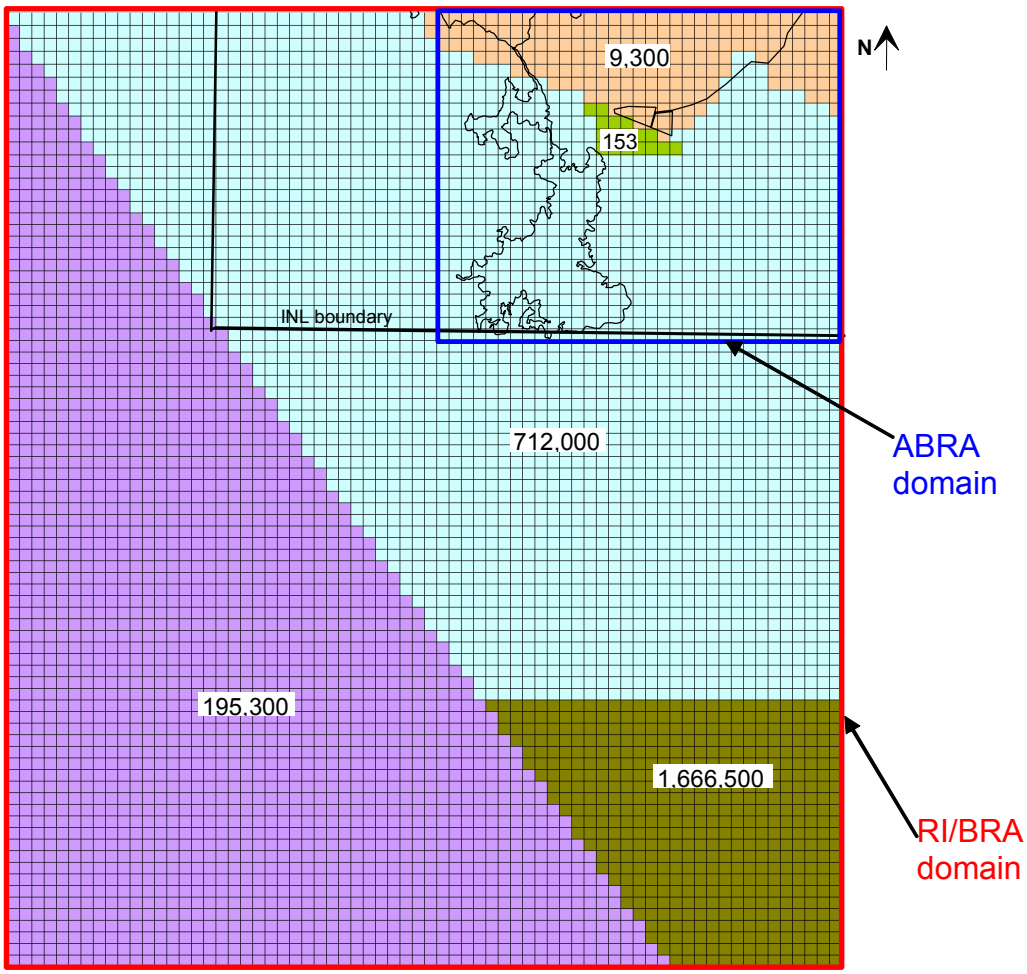

Figure C-5. Permeability zones in the extended remedial investigation/baseline risk assessment aquifer-model domain (values shown in mD).

Initially, the new model was run with only the three permeability zones from the original model. Permeability assigned to the extended domain was a uniform 712,000 mD. To be more consistent with Waste Area Group-10 groundwater modeling efforts, the extended domain was revised to incorporate portions of two additional permeability zones from the 1994 Waste Area Group-10 regional groundwater model. Zones 12 and 55, from Figure C-3 through C-16 of the report describing the 1994 Waste Area

Group-10 model (McCarthy et al. 1995), are downgradient of RWMC and are assigned constant permeability values of 195,300 and 1,666,350 mD, respectively (see Figure C-5).

C-6. MODELED VELOCITIES

The average linear velocity, also called superficial velocity, is a function of head gradient and permeability. The average linear velocity is the Darcian velocity divided by the porosity of the aquifer matrix. A uniform porosity of 0.062 was assumed for the entire domain. Figures C-6 through C-11 show the refined area and the original ABRA saturated model domain for three cases. These figures demonstrate the effect of boundary conditions and permeability on simulated average linear velocity. The figures show vectors representing the magnitude and direction of average linear velocity calculated at each grid cell. The magnitude of the average linear velocity is expressed in units of m/yr.

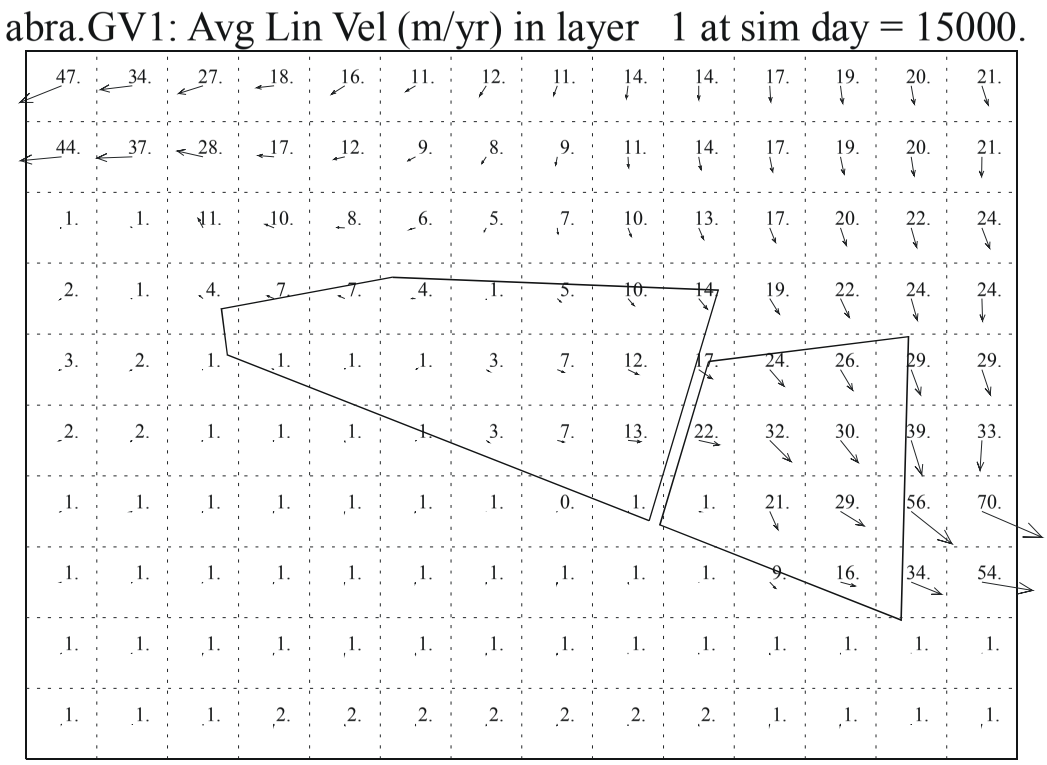

Figure C-6. Simulated aquifer velocities in the refined footprint beneath the Subsurface Disposal Area from the original Ancillary Basis for Risk Analysis model.

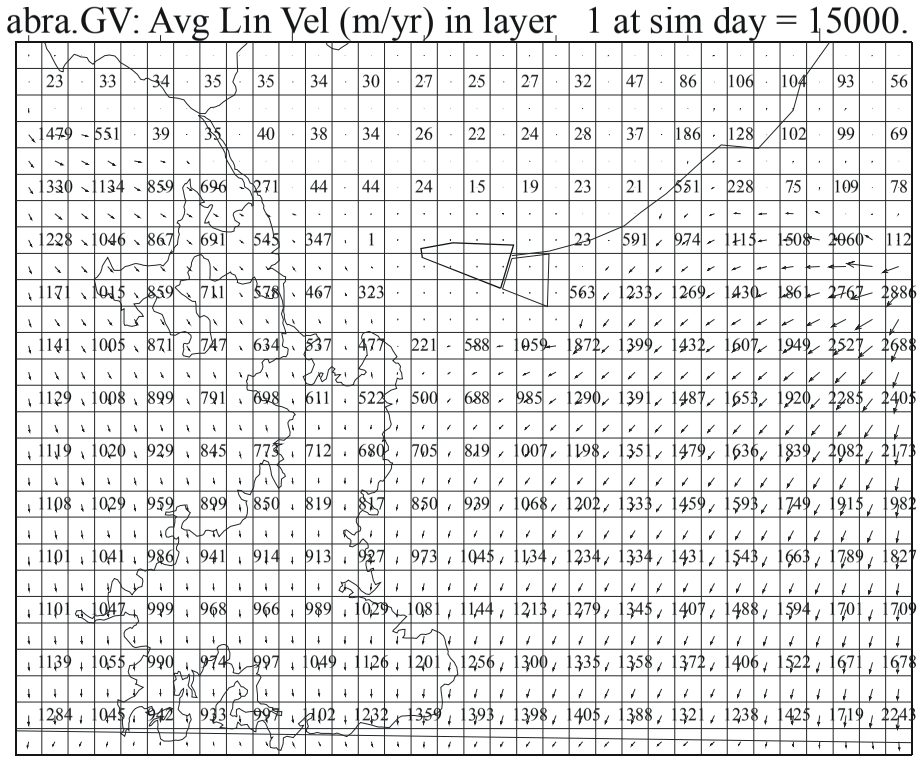

Figure C-7. Simulated aquifer velocities for the base domain from the original Ancillary Basis for Risk Analysis model.

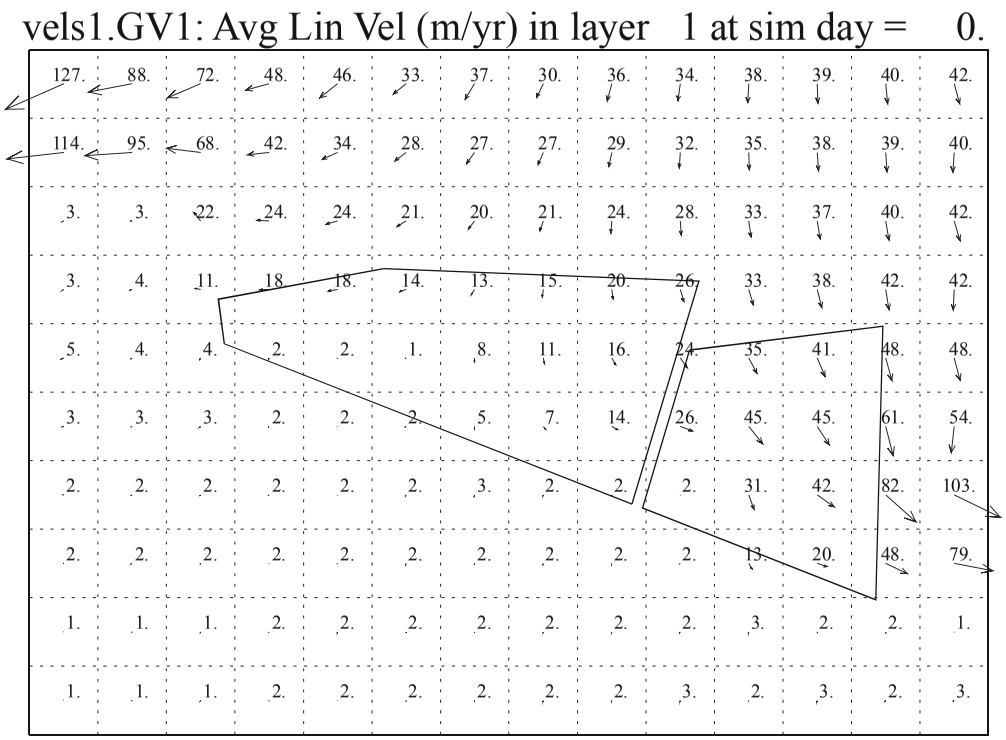

Figure C-8. Simulated aquifer velocities in the refined footprint beneath the Subsurface Disposal Area for uniformly assigned permeability of 712,000 mD in the extended domain.

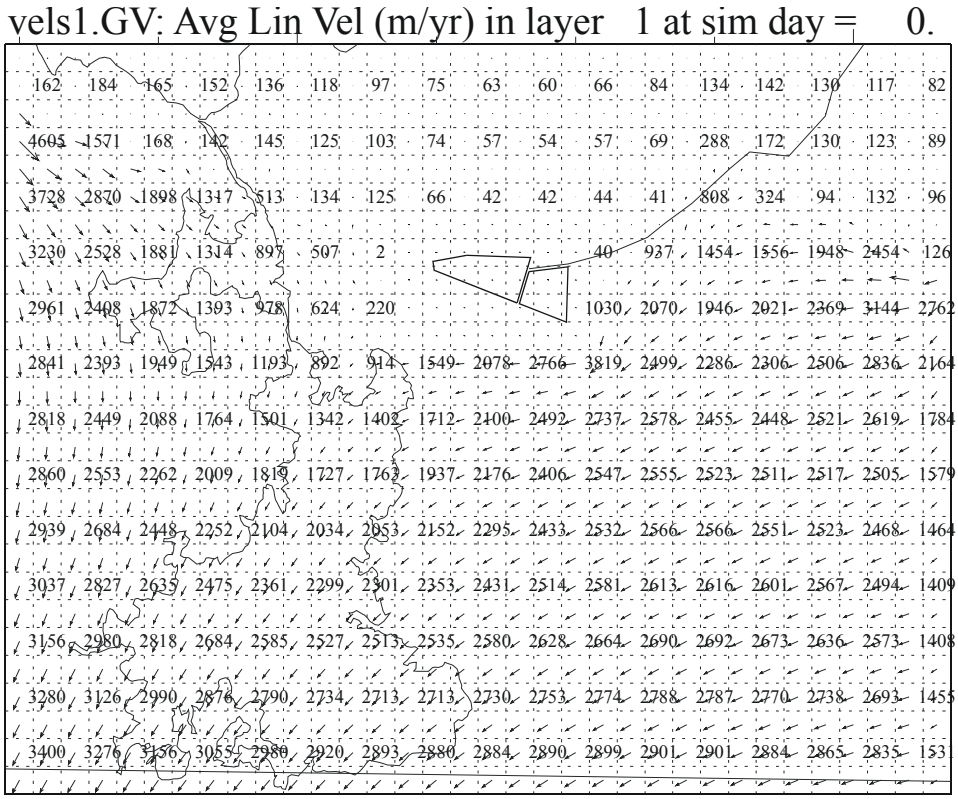

Figure C-9. Simulated aquifer velocities for the Ancillary Basis for Risk Analysis portion of the extended aquifer domain with uniformly assigned permeability of 712,000 mD in the extended domain.

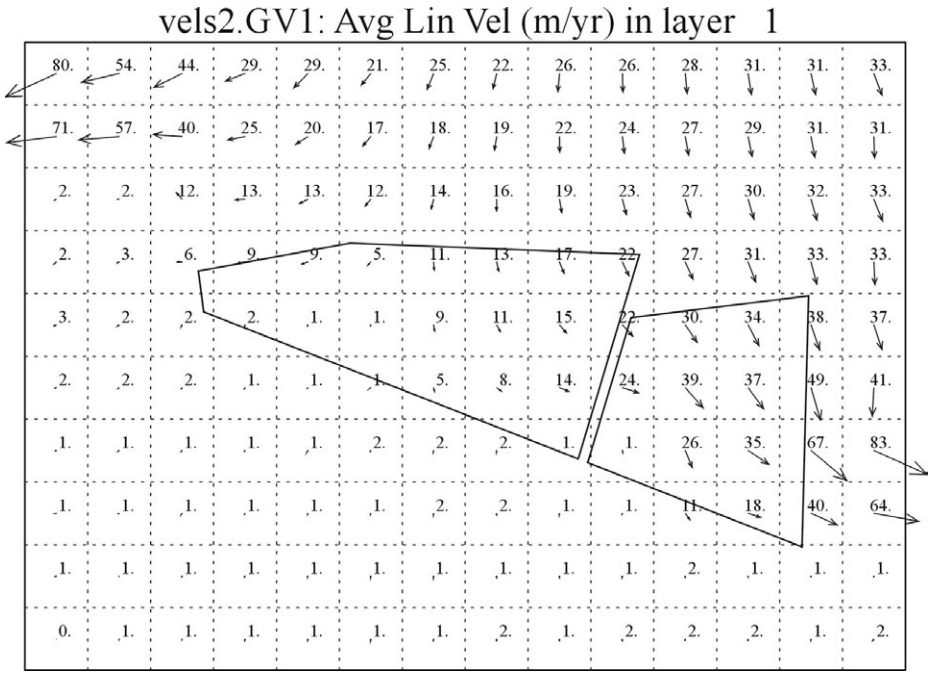

Figure C-10. Simulated aquifer velocities in the refined footprint beneath the Subsurface Disposal Area with permeabilities of 195,300 mD for Waste Area Group-10 Zone 12 and 1,666,350 mD for Waste Area Group-10 Zone 55 in the extended domain.

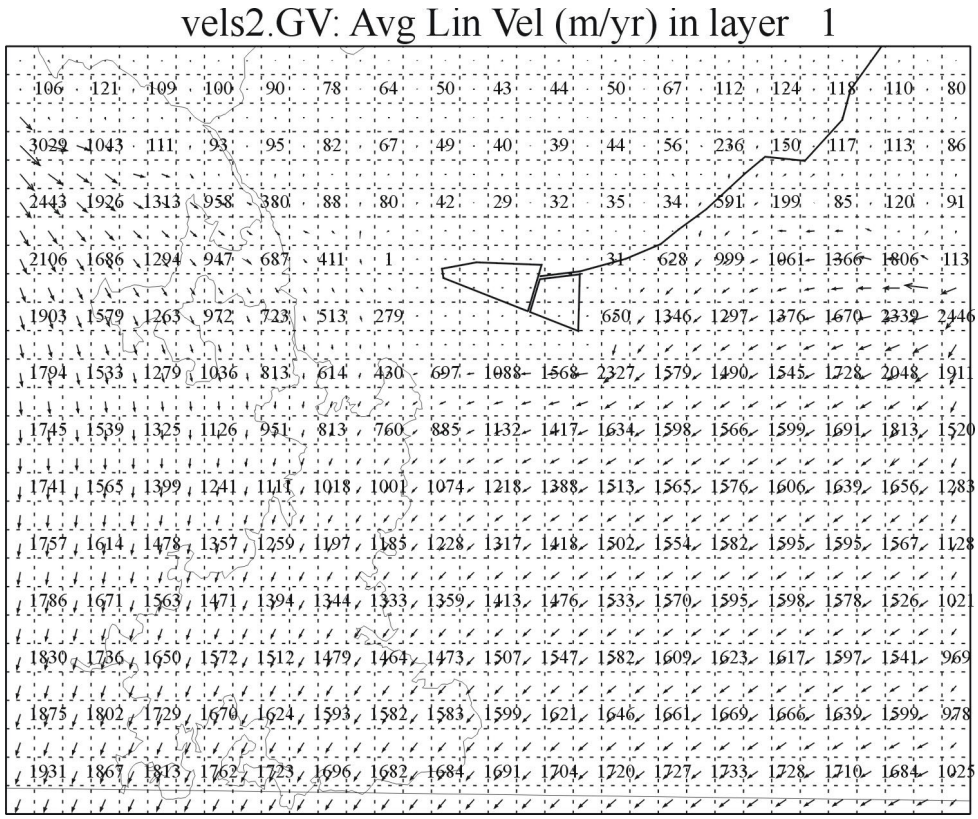

Figure C-11. Simulated aquifer velocities for the Ancillary Basis for Risk Analysis portion of the extended aquifer domain with permeabilities of 195,300 mD for Waste Area Group-10 Zone 12 and 1,666,350 mD for Waste Area Group-10 Zone 55 in the extended domain.

Figures C-6 and C-7 show average linear velocities calculated from the original ABRA model (original three permeability zones, original ABRA domain dimensions and boundary conditions). Figures C-8 and C-9 show the same refined area and original model domain but with the average linear velocities that result from expanding the domain to the new dimensions and using a uniform permeability of 712,000 mD for the entire expanded portion. Figures C-10 and C-11 show the effect on average linear velocity of incorporating the two Waste Area Group-10 permeability zones, Zones 12 and 55, with permeabilities of 195,300 and 1,666,350 mD, respectively.

The low permeability zone immediately downgradient of RWMC slows and refracts flow in the refined area. Resulting average linear velocities are approximately 1 to 2 m/yr in the refined area for all three cases (Figures C-6, C-8, and C-10). Figure C-6 shows velocities of less than 1 to 70 m/yr in the refined area of the original model. Figure C-7 shows the original modeled velocities range from 1 to 2,886 m/yr outside the refined area and is about 1,234 m/yr in the downgradient corner (southwest corner) of the original domain. The upper range of velocities, 2,886 m/yr (26 ft/d), is only slightly above the upper range of velocities (15 ft/d) predicted in earlier INL Site groundwater modeling (Robertson 1974).

Velocities increase in all locations as a result of expanding the domain with a relatively high uniform permeability of 712,000 mD and imposing a larger head drop across the domain (Figure C-8 and C-9). Figure C-8 shows a range of 1 to 127 m/yr in the refined area and Figure C-9 shows velocities more than doubling to 2 to 4,605 m/yr with about 3,400 m/yr in the downgradient corner of the original domain.

When the two additional Waste Area Group-10 permeability zones were incorporated into the extended domain, the velocities in Figures C-10 and C-11 are slowed somewhat relative to Figures C-8 and C-9 but are still higher than the original modeled velocities. This reduction results from a lower permeability of 193,500 mD that was assigned to the southwestern portion of the extended domain. Figure C-10 shows a range of 1 to 83 m/yr in the refined area and Figure C-11 shows a range of 1 to 3,029 m/yr outside the refined area with an average linear velocity of approximately 1,931 m/yr in the downgradient corner of the original model domain.

C-7. COMPARISON TO MEASURED WATER LEVELS

The simulated hydraulic heads from the extended domain model were examined for closeness of match to measured heads. Figure C-12 shows simulated contours and measured wells. A bilinear interpolation scheme was used in PV-Wave to determine simulated head at exact well locations since none of the actual wells are located exactly at a model grid centroid. Standard statistical summaries, such as mean error, mean absolute error, and root-mean squared error, are typically used to quantify simulation error (Anderson and Woosner 1992). These were calculated for the new model and are listed in Table C-1 for the set of 21 wells, common to both the original and extended models, that lies within the extended domain. Table C-1 also lists calculated residuals for these wells.

The original model was more closely calibrated to measured heads (root mean squared error = 1.57, mean average error = 1.08, and mean error = - 0.64; Holdren et al. 2002). The agreement of the new model is especially poor in locations furthest downgradient from RWMC (i.e., wells USGS-011 and USGS-125). This is the result of a large and non-uniform hydraulic gradient. The water-table elevation drops over 150-ft (46 m) across the extended domain. Though the original ABRA model was significantly better calibrated, it was only one-sixth the areal coverage with a total change in head of only 20 ft (6.1 m).

C-8. TRANSPORT SIMULATIONS

The extended model was used in TETRAD simulations with mass flux input from the ABRA vadose zone model (Holdren et al. 2002). Eight groups of contaminants were input to the model and a PV-Wave program was used to prepare resulting isopleths of equal cumulative risk for groundwater consumption. The resulting contour for 10^{-5} cumulative risk now barely crosses the INL Site southern boundary and is captured entirely within the extended domain. Figure C-13 shows the new cumulative risk isopleths resulting from this simulation. The most likely cause of the effective shorter extent of the 10^{-5} risk isopleth is greater dilution resulting from higher velocities in the extended domain.

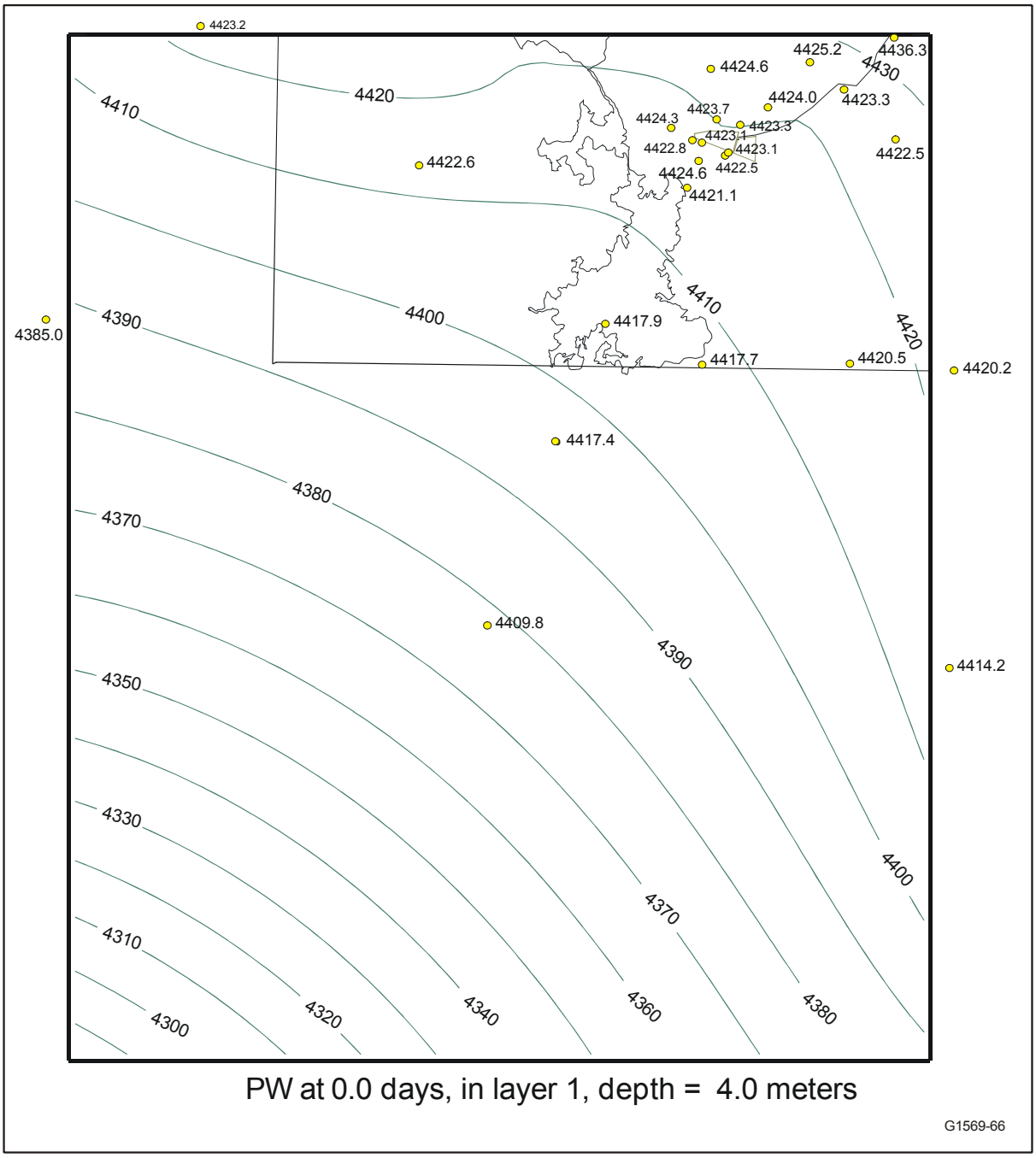

Figure C-12. Simulated water level contours and measured wells in extended domain.

Table C-1. Calculated residuals (simulated minus observed) and summary error statistics.

Well Name	Water-Table Elevation (ft, mean sea level) Observed	Simulated	Residual (ft)
A11A31	4421.91	4413.95	-7.96
RWMC M1SA	4422.81	4417.2	-5.61
RWMC M3S	4423.34	4419.93	-3.41
M4D	4425.04	4414.21	-10.83
RWMC M7S	4424.02	4420.95	-3.07
RWMC M11S	4425.24	4424.08	-1.16
RWMC M13S	4423.31	4420.97	-2.34
RWMC M14S	4424.56	4423.68	-0.88
USGS-009	4417.91	4405.12	-12.79
USGS-011	4409.81	4377.9	-31.91
USGS-086	4422.61	4412.78	-9.83
USGS-087	4423.73	4420.1	-3.63
USGS-088	4424.58	4414.36	-10.22
USGS-089	4424.28	4414.22	-10.06
USGS-105	4420.47	4416.12	-4.35
USGS-106	4422.55	4423.52	0.97
USGS-109	4417.74	4407.63	-10.11
USGS-117	4423.07	4417.89	-5.18
USGS-119	4422.48	4417.41	-5.07
USGS-120	4421.08	4412.19	-8.89
USGS-125	4417.36	4396.02	-21.34
Error statistics			
		Mean error	-8.0
		Mean absolute error	8.1
		Root-mean squared error	10.8

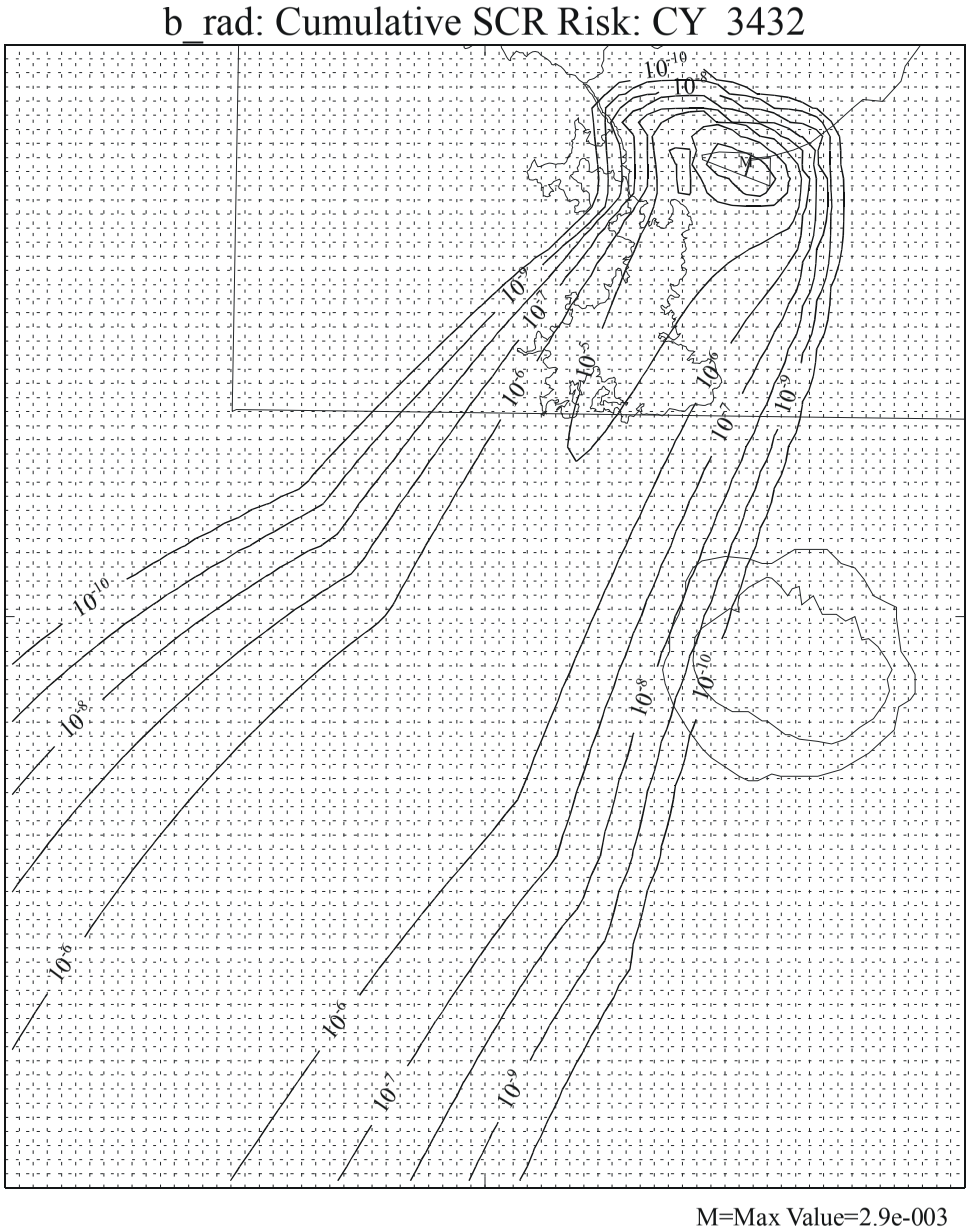

Figure C-13. Cumulative groundwater pathway risk contours from extended domain model.

C-9. CONCLUSION

The main objective of expanding the ABRA saturated model to fully encompass the 10^{-5} cumulative risk contour within the modeled domain was successfully accomplished. The model suffices for Operable Unit 7-13/14 risk modeling despite the water level error that resulted from significant changes in hydraulic head occurring over this new domain. These higher gradients increased the average linear velocity of groundwater throughout the saturated domain regardless of alternative permeability schemes. These higher velocities dilute cumulative risk thereby shrinking the overall risk contours relative to the original model results.

It should be noted that the extended domain prepared for this new model greatly exceeds Waste Area Group-7 boundaries. A model expanded to this degree may be more suited to Waste Area Group-10 modeling. Waste Area Group-10 includes miscellaneous and cumulative sitewide groundwater issues. The extended model and its subsequent water-table mapping and calibration issues represent work that may be best included in a new Waste Area Group-10 subregional-scale saturated groundwater model.

C-10. REFERENCES

Anderson, M. P. and W. W. Woessner, 1992, "Applied Groundwater Modeling, Simulation of Flow and Advective Transport," *Academic Press*, San Diego, 1992.

Golden Software, Inc., 2000, *Surfer Version 7.02 Surface Mapping System*, Golden, Colorado, 1993-2000.

Holdren, K. Jean, Bruce H. Becker, Nancy L. Hampton, L. Don Koeppen, Swen O. Magnuson, T. J. Meyer, Gail L. Olson, and A. Jeffrey Sondrup, 2002, *Ancillary Basis for Risk Analysis of the Subsurface Disposal Area*, INEEL/EXT-02-01125, Rev. 0, Idaho National Engineering and Environmental Laboratory.

McCarthy, J. M., R. C. Arnett, R. M. Neupauer, M. J. Rohe, and C. Smith, 1995, *Development of a Regional Groundwater Flow Model for the Area of the Idaho National Engineering Laboratory, Eastern Snake River Plain Aquifer*, INEL-95/0169, Rev. 1, Idaho National Engineering Laboratory.

Robertson, J. B., 1974, *Digital Modeling of Radionuclide and Chemical Waste Transport in the Snake River Plain Aquifer at the National Reactor Testing Station, Idaho,* U.S. Geological Survey, IDO-22054.

Vinsome, P. K. W. and G. M. Shook, 1993, "Multi-Purpose Simulation," *Journal of Petroleum Science and Engineering*, Vol. 9, pp. 29–38.

Visual Numerics, Inc., 2001, *PV-WAVE User's Guide*, unpublished work, 1990–2001.

Appendix D

Analysis of Aquifer Hydraulic Gradient in the Radioactive Waste Management Complex Vicinity

Appendix D

Analysis of Aquifer Hydraulic Gradient in the Radioactive Waste Management Complex Vicinity

This appendix contains analyses on groundwater flow directions in the RWMC vicinity that were conducted by Michael Rohe for Operable Unit 7-13/14 in September 2003. Comparisons are made to simulated aquifer velocities from the ABRA model (Holdren et al. 2002). The resulting gradient analysis is compared to the draft RI/FS model aquifer velocities in Section 4.4.3 of this report.

D-1. INTRODUCTION

The purpose of this appendix is to examine, in detail, the aquifer water-table configuration in the Waste Area Group 7 vicinity. Groundwater flows as a result of some type of gradient, typically, hydraulic gradient, which is the difference between potential energy at various points in the aquifer. Usually, water moves in the direction of the maximum gradient at a rate proportional to magnitude. Various methods exist to determine direction and magnitude of hydraulic gradient, based on the measured potentiometric or water-table surface. The slope and direction of slope of this table infers the direction of groundwater flow, assuming an unconfined aquifer and limited refraction of flow.

The hydraulic gradient direction can be determined by mapping contour lines of equipotential hydraulic head that are based on measured aquifer well water levels. A large area can be covered with contouring if sufficient well data are available. However, this method requires well measurements that are taken within the same time frame where results are representative of that time instant only. Gradient direction is determined from lines perpendicular to contours; and the magnitude is determined from the distance between these contours. However, this method has often produced confusing results in the vicinity of RWMC.

Figure D-1 shows some possible contour lines of equal hydraulic head, based on aquifer well water levels measured in October 2002. Figure D-2 shows similar contours lines for a refined area near the SDA. In both figures, the contour lines were drawn by hand to reflect best judgment with regards to field data. The hand-drawn contours in Figures D-1 and D-2 give some general idea of the direction and magnitude of the hydraulic gradient in the Waste Area Group 7 vicinity. However, the hand-drawn contours are specific to the October 2002 time frame and do not consider temporal gradient changes or changes occurring at different spatial scales.

D-2. METHODOLOGY

A different method of determining hydraulic gradient direction and magnitude involves the use of three points of hydraulic head data and is well-documented in literature (Freeze and Cherry 1979, Fetter 1981). These three points form a plane surface that is representative of the water-table surface in the vicinity of these three wells. From the strike and dip of this surface, groundwater hydraulic gradient can be determined. A series of such triangles can be used to find the range in directions for RWMC.

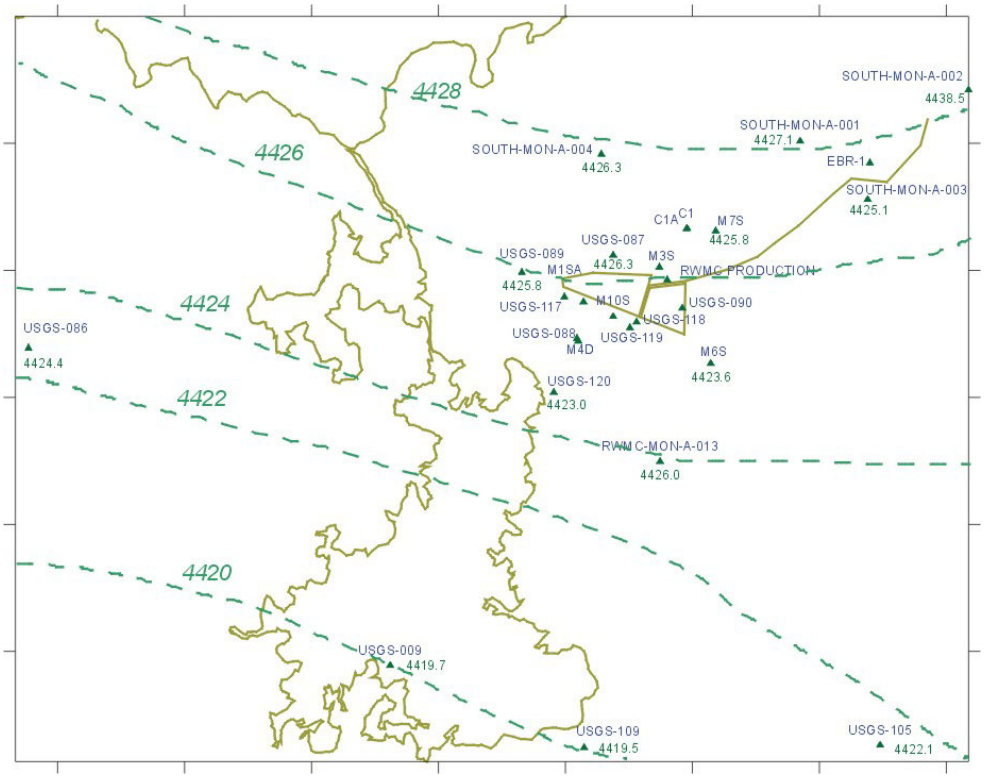

Figure D-1. Possible contour lines for October 2002 water level data.

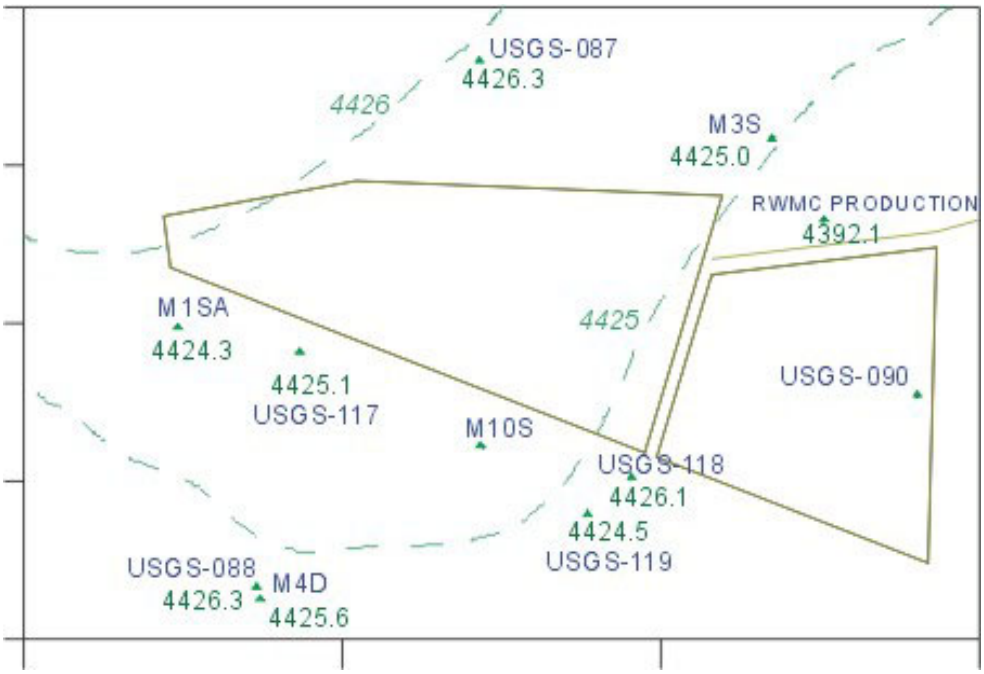

Figure D-2. Possible contour lines for water level data in the vicinity of the Subsurface Disposal Area based on October 2002 well measurements.

This method allows for examination of gradient at different well locations and over various size scales. More importantly, more time steps can be analyzed quickly and changes, if any, that can occur in gradient over time can be observed. Measurements must still be taken nearly simultaneously; however, long-term hydrograph records can be aligned between the three wells. Then, multiple calculations of gradient can be made.

Figure D-3 illustrates application of this method in the SDA area for Wells M3S, USGS-87, and USGS-117. Figure D-3 also includes directional frequency diagrams for the illustrated calculation and for the entire set of calculations using this combination of wells. The directional frequency histogram depicts calculated results of gradient direction. In these histograms, pie wedges are histogram bins with more frequent calculated directions extending pie wedges further from the center of the diagram. These histograms are similar to wind rose diagrams that are commonly used in atmospheric studies.

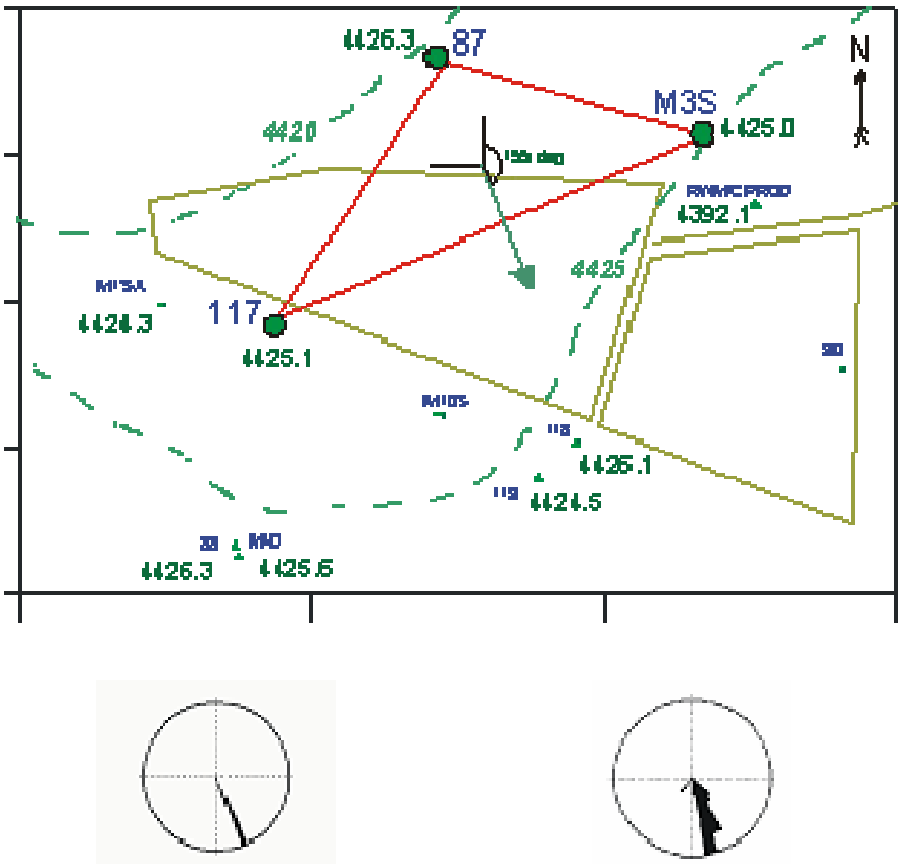

Figure D-3. Application of the three-point method (triangulation) for hydraulic gradient determination.

D-3. METHOD LIMITATIONS

Triangulation can be affected by errors in water-level measurements; these errors include errors in the manual measurement process, errors produced from well boreholes being deviated with respect to plumbness and straightness, errors in coordinate information for a given well, and errors associated with a time lapse between a given calculation's three water-level measurements.

The time-lapse error is often due to water levels changing over time in response to diurnal (daily) barometric pressure changes and synoptic weather effects (time scale of days and weeks). Several investigations at the INL Site have examined the response of aquifer wells to changing barometric pressure. Frederick and Johnson (1997) report typical diurnal barometric pressure changes of 3 cm (0.1 ft) (measured as water) and over 15.2 cm (0.5-ft) changes occurring at the synoptic time scale. They observed aquifer wells, such as USGS-059, in the Idaho Nuclear Technology and Engineering Center area respond to larger pressure changes with water level fluctuations of 9.1 cm (0.3 ft) or more. Hubbell et al. (2004) developed methods for minimizing barometric pressure changes on measured water levels. Their work in the RWMC area showed that 3-cm (0.1-ft) (as water) diurnal changes in barometric pressure have resulted in 6.1-cm (0.2-ft) water-level fluctuations in aquifer Well USGS-118.

The three-point solution for hydraulic gradient is especially sensitive to this barometric-induced error when applied to closely spaced wells. Figure D-4 illustrates the triangulation method at the SDA with "error bars" surrounding the individual well water elevations and are shown with respect to the hydraulic gradient field. These error bars extend 9.1 cm (0.3 ft) on either side of the elevation measurement and correspond to a possible error from barometric changes. The bars are only an approximation of the water-level error, but Figure D-4 shows that in a natural, low-hydraulic gradient of magnitude 5.0 ft/mi, the wells will need to be spaced sufficiently far apart so that these error bars do not overlap. Still, there exists at the INL Site the need to collect more accurate water level data that is unaffected by such barometric changes, which could be accomplished with methods such as those presented by Hubbell et al. (2004).

The corresponding hydrographs for these three wells are also provided in Figure D-4. For the most part, the water levels in Wells M3S and USGS-117 are approximately the same. Therefore, the line connecting these two wells forms a line of equipotential energy. The lines appear to separate and converge over time. Since these two wells are on the same equipotential line, the third well, Well 87, appears to strongly determine the direction and magnitude for these three wells. As a result, this combination may be less suitable than others due to this apparent bias.

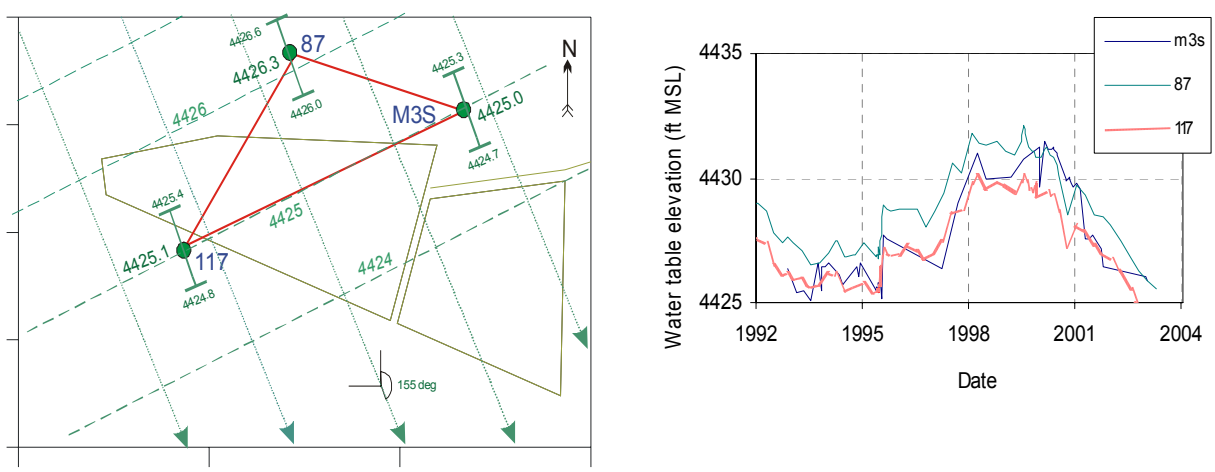

Figure D-4. Three-point solution and hydrographs for the M3S-87-117 combination.

D-4. SELECTING WELL COMBINATIONS

Many combinations are possible when selecting groups of three wells from a larger set of wells. The number of possible nonordered (i.e., listing each combination only once regardless of the order of wells in the combination) can be found from the following expression (from Devore and Peck 1990):

$$n!/(x!(n-x!) \qquad \text{(D-1)}$$

where:

n = number of wells in set

x = number to be combined.

The set of wells examined includes 25 aquifer wells (n = 25) with three wells required per each combination. Therefore, the possible combinations is

n	=	25
x	=	3
n!	=	1.55E+25
x!(n-x)!	=	6.74E+21
n!/(x!(n-x!)	=	2,300

Out of only 25 wells, over 2,000 three-well combinations are possible. Some criteria must be used in applying this method so that a manageable number of combinations can be identified that best reflects real gradient conditions. When combining these wells, it is important that certain factors be observed, which may indicate some wells should not be compared together. These factors include significant differences in completion depths and borehole diameters. In particular, the size and shape of the resulting triangle has a strong effect on whether the calculated gradients reflect reality or not. In this analysis, these factors were considered in developing a set of 40 different well combinations.

For each comparison, hydrograph records were aligned so that contemporaneous comparisons of water-table elevation data could be made. Borehole deviation correction factors were also applied. Prudent use of available groundwater elevation data also requires a high-level of confidence in well reference point elevations (i.e., land surface, measuring point, and brass cap monument).

D-5. RESULTS

Results of triangulation indicate that groundwater gradient in the vicinity of Waste Area Group 7 generally is south-southeast (approximately 159 degrees from north). Results for the entire set of 3,100 hydraulic-gradient calculations are shown in Table D-1. These results indicate that there is a great deal of variability in the hydraulic gradient (i.e., a standard deviation of 66 degrees for the entire set). The mean gradient magnitude (6.3 ft/mi) shows a similar high variance (10 ft/mi standard deviation). In general, water-level measurements were chosen to minimize the spread in measurement dates for each calculation of hydraulic gradient. Approximately 1 week (i.e., 8.6 days) is the average time between measurements for the entire set of calculations.

Table D-1. Summary of entire set of 3,100 three-point gradient calculations for the Radioactive Waste Management Complex covering 1972 through 2003.

Statistic	Direction (degrees)	Magnitude (ft/mi)	Number of days[a]
Minimum	0.2	0.1	0.0
Maximum	359	328	28
Mean	159	6.3	8.6
Standard Deviation	66	10.1	6.1

a. Number of days between each water-level measurement used in a particular gradient calculation.

Figure D-5 shows histograms for the results of all 3,100 calculations considered as a single set. The directional frequency histogram shows a large portion (i.e., approximately 31%) of the calculated gradients has an azimuth between 155 to 185 degrees (from north). The magnitude histogram shows over 50% are in the 3 to 7 ft/mi range. The histograms appear to be bimodal. A small portion (i.e., 11%) is in the range of 40 to 60 degrees and suggests some flow reversal occurs at RWMC.

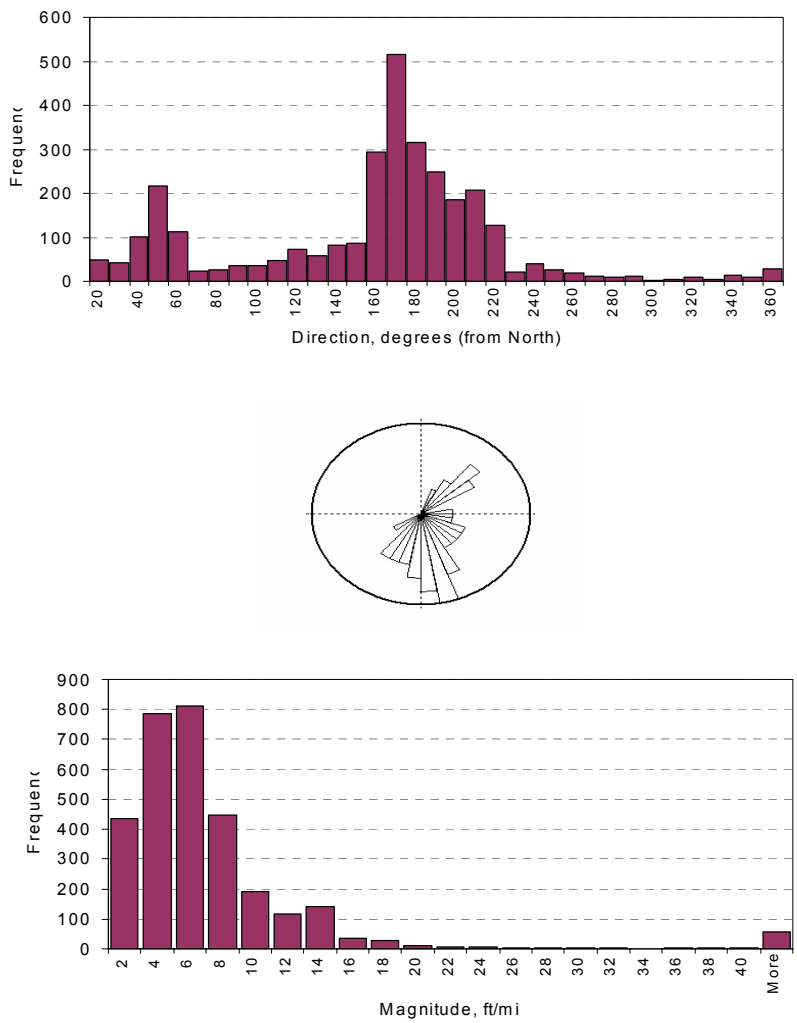

Figure D-5. Histograms for entire set of 3,100 gradient calculations.

Table D-2 lists results for the 40 three-well combinations. The table lists the individual wells in each combination, summary statistics for gradient direction and magnitude, the area covered by each combination of wells, the number of calculations performed for each combination, and the range in dates represented by these calculations. Also shown in Table D-2 is the range of screening depths represented by each three-well combination. This range was the difference between the least and greatest screened interval depth below the water table and was believed to be an indicator of how compatible a given set of wells is for comparing water-level measurements.

Figure D-6 shows mean gradient directions on a large scale. Each arrow is plotted at the centroid of the triangle formed by the three wells and represents the mean gradient direction. The arrow size is proportional to the area covered by the three-well combination. Larger area combinations produce results that appear consistent with the generally accepted south-southwestern gradient. For instance, combination "m12s-86-105" (i.e., Wells M12S, USGS-086, and USGS-105) covered 41.4 km^2 (16 mi^2) and produced gradient results of 199 ±1 degree mean direction and 3.5 ±0.1 ft/mi mean magnitude.
Smaller combinations, such as "m14s-m7s-89" (1.4 km^2 [0.55 mi^2]), produce highly variable results (168 ±50 degrees; 1.5 ±1.1 ft/mi) that are fairly inconsistent with the regional concept.

Figure D-7 shows the hydraulic gradient calculation results for a smaller region that matches the refined domain used in the ABRA (Holdren et al. 2002). As indicated in Tables D-1 and D-2, the directional frequency histograms for most of the three-well combinations show a great deal of variability. Very small combinations produce highly variable results (i.e., m1s-m4d-89), and are, perhaps, affected by barometric pressure or other sources of error that can cause the well hydrographs to cross each other frequently. These results may not be representative of the general movement of water in the RWMC vicinity.

Systematic errors, such as error in a land surface reference datum, may cause other small area combinations to produce unexpected results, even if those results have less variability. Otherwise, smaller triangulations that produce less variable results may reveal local-scale flow anomalies. In general, flow in the Eastern Snake River Plain aquifer is in a direction along the axis of the Snake River Plain (northeast to southwest). However, on local scales, such as at RWMC, flow may occur predominantly in directions parallel to vent corridors, fissures, and fracture orientations, which are, in general, perpendicular to the axis of the plain and parallel to the tectonic faulting of the Basin and Range geologic province. Larger triangulations generally yield gradients that point in the direction of regional flow, parallel to the axis of the plain, which follows a water-table shape that is similar to the regional topography, sloping from northeast to southwest.

Figure D-8 is the same as Figure D-7, except the results of the ABRA-simulated velocity are superimposed (arrows). These aquifer velocity simulations were prepared using a numerical groundwater model and reflect permeability distributions in the RWMC vicinity. The hydraulic head measurements, collected in the field from RWMC aquifer wells and used to triangulate gradient, show some agreement with these simulations. In particular, there is agreement between calculated gradient (based on field measurements) and simulated velocity in the significant southeastern flow that appears beneath the eastern portion of the SDA.

Table D-2. Summary of three-point gradient calculations (sorted by number of calculations).

Well 1	Well 2	Well 3	Number of Calculations	Area (mi^2)	Range in Penetration Depths (ft)	Gradient Direction		Magnitude		Date Range
						Mean (degrees from N)	Standard Deviation (degrees)	Mean (ft/mi)	Standard Deviation (ft/mi)	
A11A31	M11S	M14S	24	1.72	25	225	29	0.7	0.3	1999–2003
A11A31	M13S	USGS-89	10	2.12	15	172	19	1.7	0.4	1999–2003
A11A31	M7S	USGS-89	18	1.13	15	170	23	2.0	0.4	1999–2003
M10S	USGS-88	USGS-117	11	0.03	17	162	129	7.9	3.0	1992–2000
M10S	USGS-118	USGS-119	7	0.005	78	191	10	22.7	5.2	1994–2000
M11S	M12S	M13S	28	0.36	22	207	2	13.7	5.0	1999–2003
M12S	USGS-86	USGS-105	9	16.72	63	199	1	3.5	0.1	1999–2003
M12S	USGS-89	USGS-105	13	7.69	95	220	3	4.7	2.2	1999–2003
M13S	M14S	USGS-109	12	4.43	147	169	5	1.7	0.2	1999–2003
M13S	USGS-86	USGS-109	11	11.88	138	177	4	1.7	0.2	1999–2003
M14S	USGS-105	USGS-109	9	4.88	147	209	9	2.4	0.5	2000–2003
M1S	M3S	USGS-87	300	0.07	44	173	16	7.4	1.7	1992–2003
M1S	M4D	USGS-89	241	0.04	181	87	84	6.9	4.1	1992–2003
M1S	M6S	M7S	14	0.55	25	191	30	1.8	0.2	2001–2003
M1S	USGS-87	USGS-119	292	0.12	48	203	12	5	1	1992–2002
M3S	M10S	USGS-117	8	0.06	24	237	60	4.2	2.0	1992–2000
M3S	M11S	M14S	26	0.65	25	191	7	1.8	0.3	1999–2003
M3S	M4D	M6S	16	0.32	204	166	56	1.5	0.6	1992–2003
M3S	M6S	M7S	116	0.20	23	200	31	1.9	0.8	1992-2003
M3S	M6S	USGS-88	17	0.32	24	114	32	1.9	0.5	1992–2002
M3S	M7S	USGS-87	134	0.07	44	169	27	5.6	2.7	1992–2003
M3S	M7S	USGS-90	106	0.09	7	180	21	2.7	0.9	1993–1999

Table D-2. (continued).

Well 1	Well 2	Well 3	Number of Calculations	Area (mi^2)	Range in Penetration Depths (ft)	Gradient Direction		Magnitude		Date Range
						Mean (degrees from N)	Standard Deviation (degrees)	Mean (ft/mi)	Standard Deviation (ft/mi)	
M3S	USGS-87	USGS-117	296	0.07	44	159	12	5.4	1.2	1992–2003
M3S	USGS-117	USGS-118	20	0.09	46	240	55	2.9	1.3	1993–2003
M4D	M10S	USGS-117	9	0.03	178	250	152	9.6	10.0	1992–2000
M6S	M13S	M14S	6	1.43	15	166	2	1.3	0.1	2001–2001
M6S	M7S	M13S	10	0.56	23	154	2	2.0	0.2	2001–2002
M6S	M7S	USGS-89	4	0.71	23	157	4	1.9	0.2	2001–2002
M6S	USGS-87	USGS-120	18	0.55	63	184	17	2.9	0.4	1992–2003
M6S	USGS-90	USGS-119	23	0.10	73	187	68	1.4	0.8	1993–1999
M7S	M14S	USGS-89	12	0.55	17	168	50	1.5	1.1	1999–2003
USGS-87	USGS-88	USGS-89	190	0.19	37	122	95	12.8	21	1972–2003
USGS-87	USGS-88	USGS-90	167	0.21	41	114	39	10.4	19	1972–1999
USGS-87	USGS-89	USGS-90	163	0.17	41	110	53	7.1	4	1972–1999
USGS-87	USGS-89	USGS-117	221	0.10	37	193	29	5.5	21.8	1987–2003
USGS-87	USGS-90	USGS-118	7	0.10	66	146	22	3.5	0.2	1995–1999
USGS-88	USGS-89	USGS-90	172	0.24	5	103	57	15.6	28	1972–1999
USGS-88	USGS-89	USGS-117	203	0.07	18	44	23	14.3	31.9	1987–2003
USGS-89	USGS-90	USGS-120	70	0.49	43	167	26	2.4	1.5	1987–1999
USGS-117	USGS-119	USGS-120	132	0.14	32	171	21	2.7	0.8	1987–2003

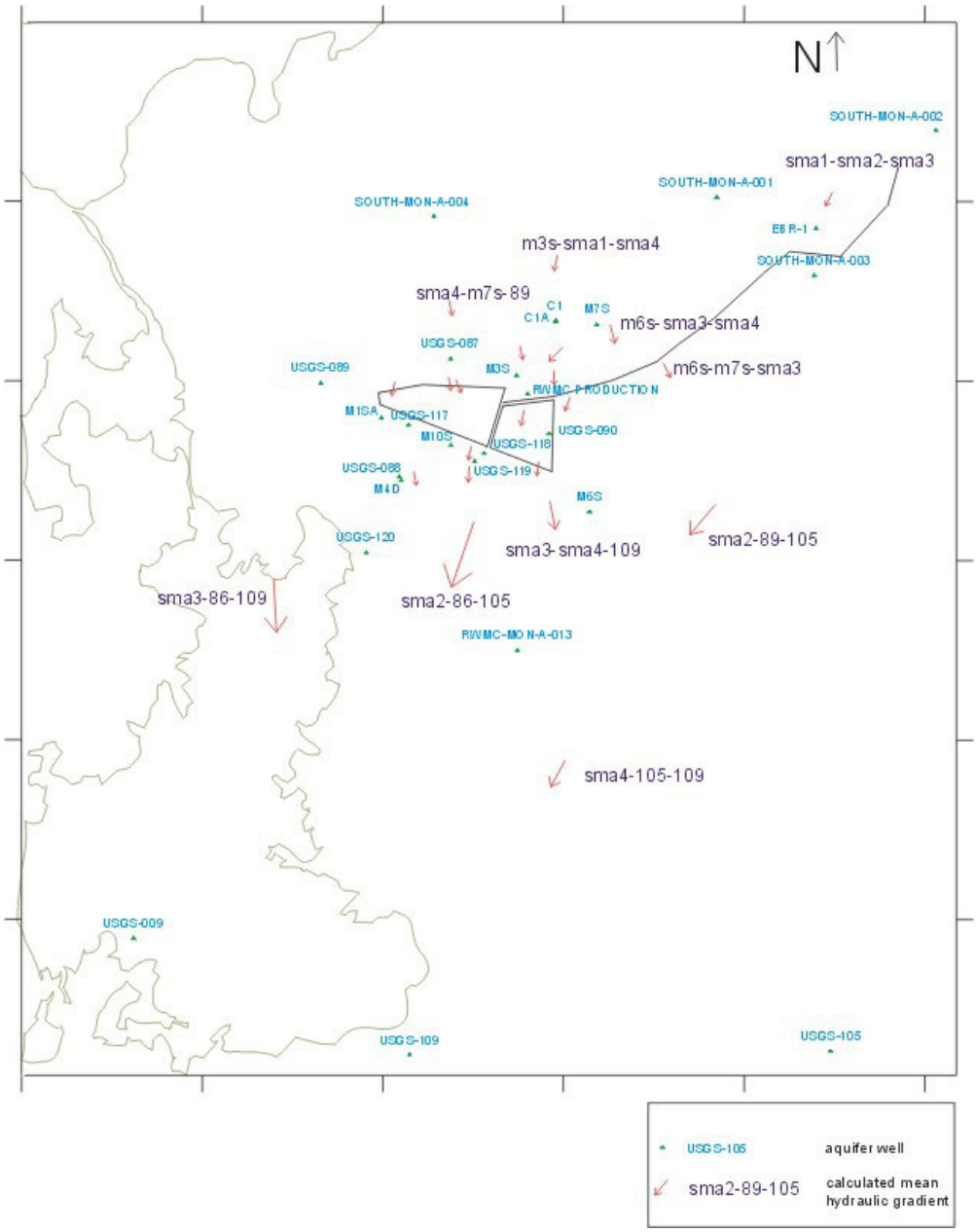

Figure D-6. Results of the mean hydraulic gradient direction for the Radioactive Waste Management Complex vicinity. Arrows are proportional to area represented by each three-well set.

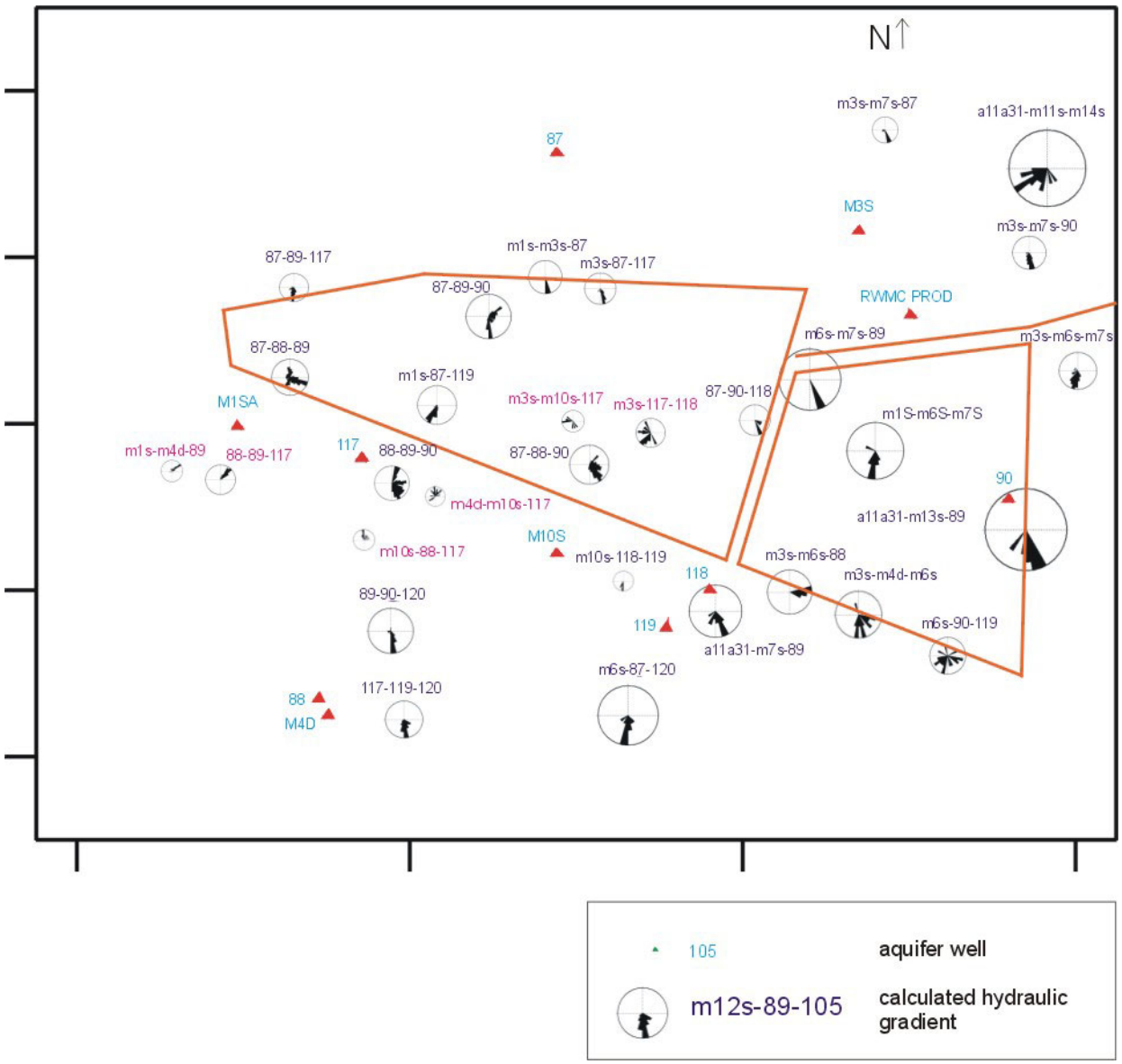

Figure D-7. Hydraulic-gradient directional frequency diagrams (i.e., rose diagrams). Rose diagrams are proportional in size to the area covered by the three-well combination (red font indicates very small combinations [i.e., < 0.10 mi^2]).

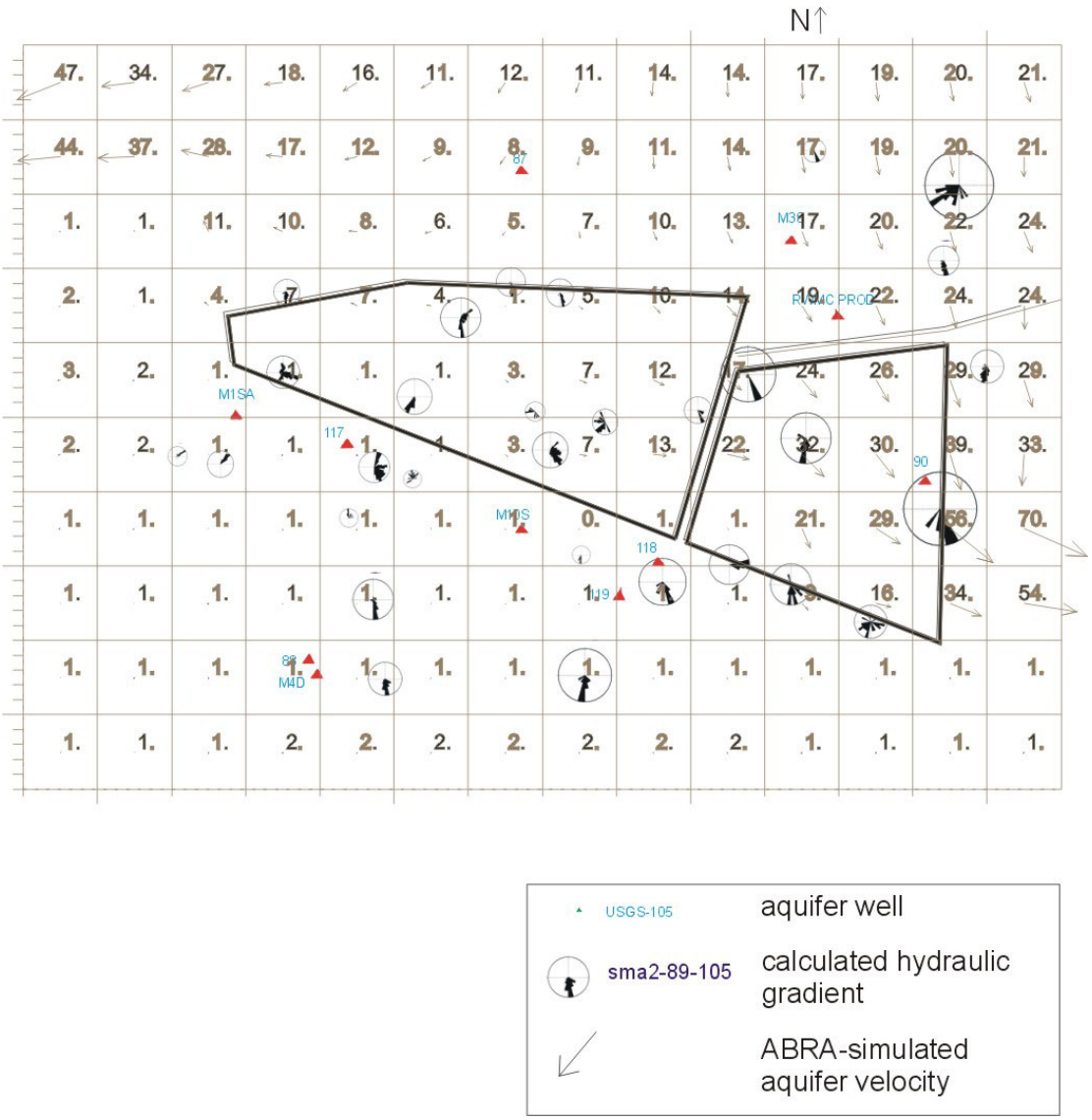

Figure D-8. Comparison of diagrams for the calculated, hydraulic-gradient directional frequency and the results of velocity simulations for the Ancillary Basis for Risk Analysis.

D-6. EFFECTS OF SEPARATION SCALE AND TEMPORAL CHANGES

It was discussed earlier that if the error associated with the measurement is greater than the difference in water-table elevation between two wells used to calculate hydraulic gradient, then the results of this calculation may be suspect. As mentioned, that can be the case for a three-well combination that covers a small area. Figure D-9 shows the effect that closely-spaced wells have on calculated gradients. These three wells cover an area less than 0.26 km^2 (0.10 mi^2) and, as a result, their hydrographs appear to cross one another. When the hydrographs change order (as to which one has the highest elevation), the calculated gradient dramatically changes direction but the relative magnitude may change only little. The resulting directional frequency diagram can be highly variable. This may be the result of barometric fluctuations or even pumping of the RWMC production well (note the well's water elevation in Figure D-2).

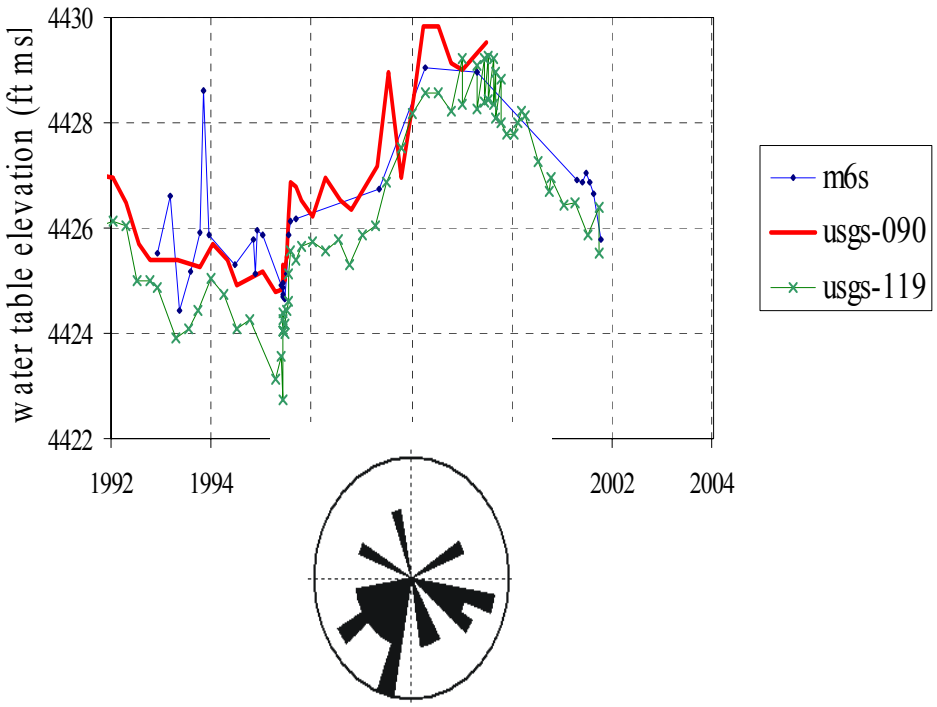

Figure D-9. Hydrograph and resulting rose diagram on the effect of closely-spaced wells on the calculated hydraulic gradient.

Localized recharge from surface waters in the vicinity of RWMC can also cause hydrographs to cross despite well separation distance. Several RWMC-area aquifer wells appear to be affected by flow in the Big Lost River. Some of these wells are located sufficiently far enough from each other such that their hydrograph separation exceeds typical barometric-induced fluctuations; however, their hydrographs have crossed each other in the past in response to stages of the Big Lost River. Figure D-10 depicts hydrographs for three wells used in a particular triangulation (i.e., Wells USGS-87, -88, -89). Also included in Figure D-10 is the river hydrograph for a station near Arco, Idaho. Although other gaging stations on this river are located closer to the INL Site, the Arco station has a much longer and complete record than closer stations; therefore, the Arco station is used in Figure D-10. Flow into the RWMC spreading areas (designed for Big Lost River diversion) appears to effect some groundwater flow reversal.

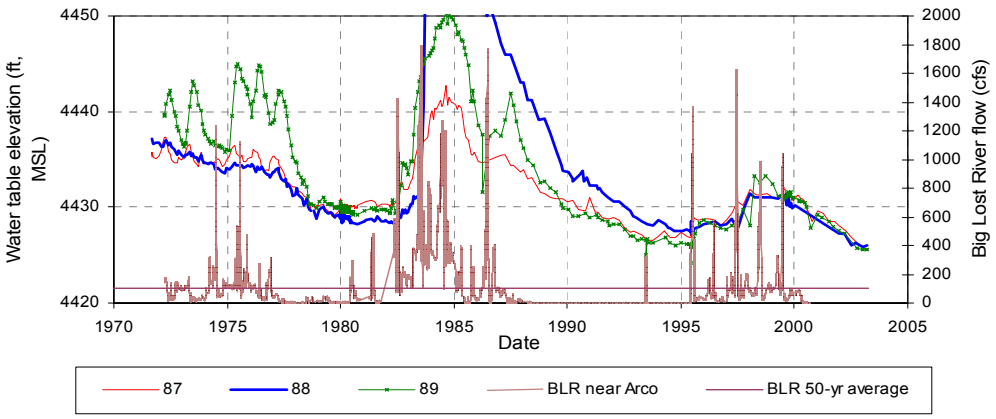

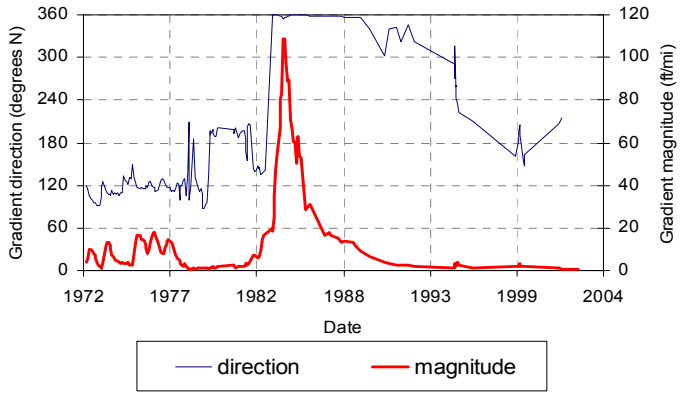

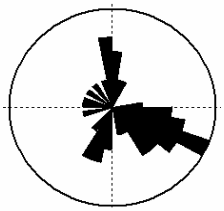

Figure D-10. Hydrographs for the 87-88-89 combination and Big Lost River near Arco, Idaho. The resulting gradient directional histogram is also shown.

The directional histogram shows three different major directions of gradient (approximately 120, 180, and 360 degrees from north), corresponding to different flows in the Big Lost River. Table D-3 summarizes flow conditions in the river and corresponding changes in hydraulic gradient as observed in Wells USGS-87, -88, and -89. Although Well USGS-88 may have a casing leak somewhere between land surface and the aquifer water table that results in spurious high-water levels in this well, other combinations show similar gradient reversals (see the -87-88-89 combination in Figure D-7). The RWMC spreading areas are located southwest of the SDA; groundwater mounding southwest of RWMC would cause gradient direction to point northeast.

Table D-3. Effects of the Big Lost River near Arco on hydraulic gradient (triad -87-88-89).

Period	Flow Type	Big Lost River Near Arco, Mean Discharge (cfs)	Mean Direction (degrees)	Mean Magnitude (ft/mi)
1971–1978	High	125	117	7
1979–1982	Low	29	186	5
1983–1988	High	306	356	48
1989–1995	Low	3	256	2

Finally, the hydraulic gradient in the RWMC area appears to change with time. Large changes in water availability, resulting from long-term (i.e., about 10-year) drought cycles, affect the water-table elevation. It appears that not all wells have the same response to these long-term cycles. As a result, the hydraulic gradient, as determined from aquifer well water-level measurements, appears to change in direction and magnitude over time. Figure D-11 shows directional changes of up to 90 degrees over the course of monitoring from 1993 to 2003 for the m3s-97–117 well combination.

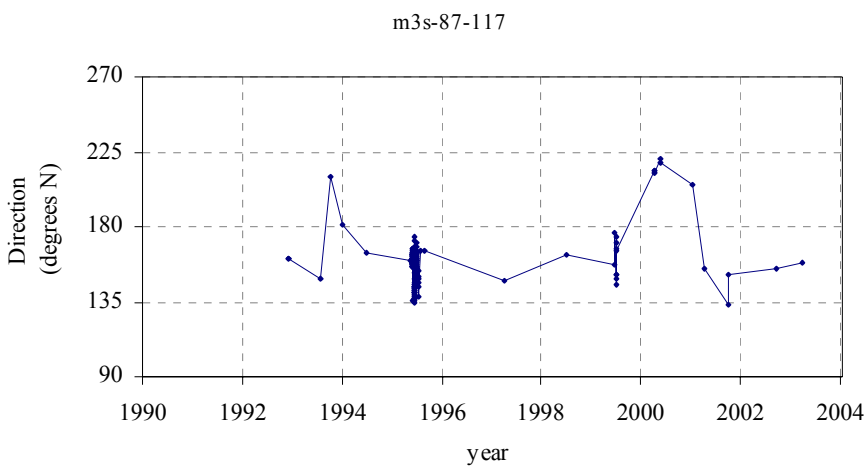

Figure D-11. Change in hydraulic gradient direction over time for one three-well combination (i.e., Wells RWMC-m3s, USGS-087, and USGS-117).

An outcome of this analysis is that there should be a certain minimum area required for using water-table elevation data to determine hydraulic gradient direction and magnitude. At RWMC, like other facilities at the INL Site, there appears to be highly variable local hydraulic gradients that are inconsistent with the regional gradient.

The water table beneath RWMC, and elsewhere at the INL Site, is not a flat, uniform surface. The water table has undulations, ridges, and bumps caused by local heterogeneity. Quite possibly the water is moving in a direction counter to regional gradient over small distances. Figures D-12 and D-13 show the effects of scale on calculated hydraulic gradient. These figures suggest that variance is minimal after an area of about 5.2 km^2 (2 mi^2) is exceeded.

D-7. CONCLUSIONS

Although there are practical limitations to application of the triangulation method for calculating hydraulic gradient (i.e., well separation scales of 5.2 km^2 [2 mi^2] or more, error-free water level data, and accurate land surface reference data), this method can be used to examine gradients at different spatial and temporal scales. The hydraulic gradient in the RWMC vicinity appears to be mostly 160 to 190 degrees (from north) at about 3 to 7 ft/mi magnitude. Variance is quite high in this area (up to 150 degrees and 32 ft/mi for direction and magnitude, respectively). These may be associated with data error, spatial scaling, or recharge from the Big Lost River. Localized heterogeneities in the aquifer matrix may affect gradients at smaller spatial scales. However, when examined at different time scales, flow in the Big Lost River (and to the RWMC spreading areas) appears to contribute to gradient reversals.

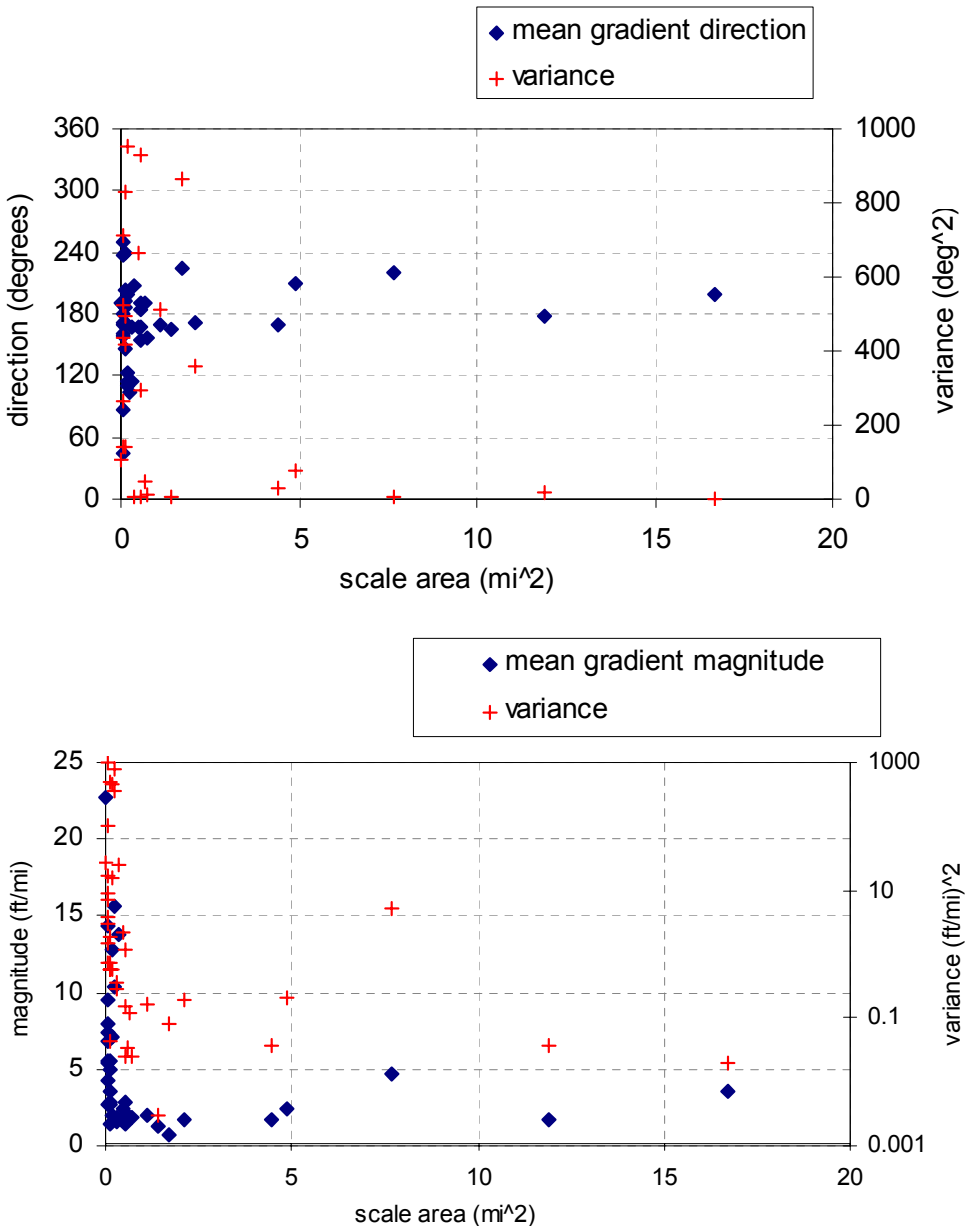

Figure D-12. Effect of scale size on the calculated hydraulic gradient direction and magnitude. (Note the use of logarithmic scale for magnitude variance.)

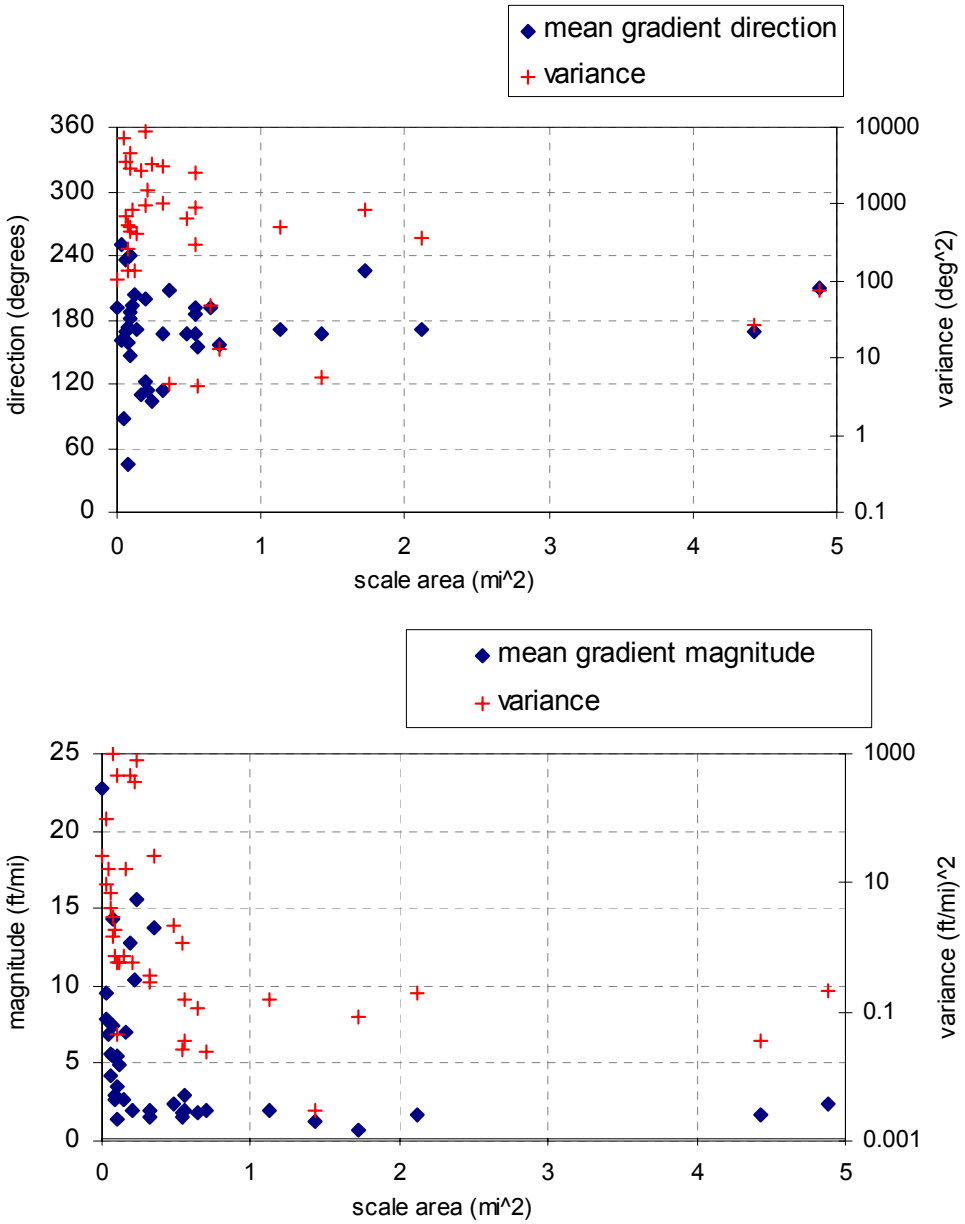

Figure D-13. Detailed view of the effect of scale size on the calculated hydraulic gradient direction and magnitude. (Note the use of logarithmic scale for variance.)

D-8. REFERENCES

Devore, J. L. and R. Peck, 1990, *Introductory Statistics*, West Publishing Co., St. Paul.

Fetter, C. W., Jr., 1981, "Determination of the Direction of Groundwater Flow," *Ground Water Monitoring Review*, Fall 1981.

Frederick, D. B. and G. S. Johnson, 1997, Depth and Temporal Variations in Water Quality of the Snake River Plain Aquifer in Well USGS-59 near the Idaho Chemical Processing Plant at the Idaho National Engineering and Environmental Laboratory, Research Technical Note 97-1, Idaho Water Resources Research Institute, Moscow, Idaho.

Freeze, R. A. and J. A. Cherry, 1979, *Groundwater*, Englewood Cliffs, New Jersey: Prentice-Hall.

Holdren, K. Jean, Bruce H. Becker, Nancy L. Hampton, L. Don Koeppen, Swen O. Magnuson, T.J. Meyer, Gail L. Olson, and A. Jeffrey Sondrup, 2002, *Ancillary Basis for Risk Analysis of the Subsurface Disposal Area*, INEEL/EXT-02-01125, Rev. 0, Idaho National Engineering and Environmental Laboratory.

Hubbell, J. M., M. J. Nicholl, J. B. Sisson, and D. L. McElroy, 2004, "Application of a Darcian Approach to Estimate Liquid Flux in a Deep Vadose Zone," *Vadose Zone Journal*, Vol. 3, pp. 560–569.

Appendix E

Comparison of Additional Interbed Hydrologic Properties to Estimated Values

Appendix E

Comparison of Additional Interbed Hydrologic Properties to Estimated Values

This appendix presents a comparison of measured interbed hydrologic properties to those estimated in the Leecaster (2002) kriging, which is implemented in the RI/FS model. Additional data are presented first and are followed by comparison data. This material comes from a draft report prepared by Larry Hull, Cheryl Whitaker, and Joel Hubbell with contributions from Molly Leecaster and Larry Blackwood. The material in this appendix provides substantiation for properties assigned in the RI/FS model.

E-1. ADDITIONAL RESULTS FOR HYDROLOGIC ANALYSES OF INTERBED SAMPLES

Hydrologic analysis results found in this section are documented in Schaffer (2004). Interbed core samples were recovered during well-drilling activities in Fiscal Year 2003 by the Operable Unit 7-08 Project. Figure E-1 shows well locations where additional core samples were taken for hydrologic property analyses.

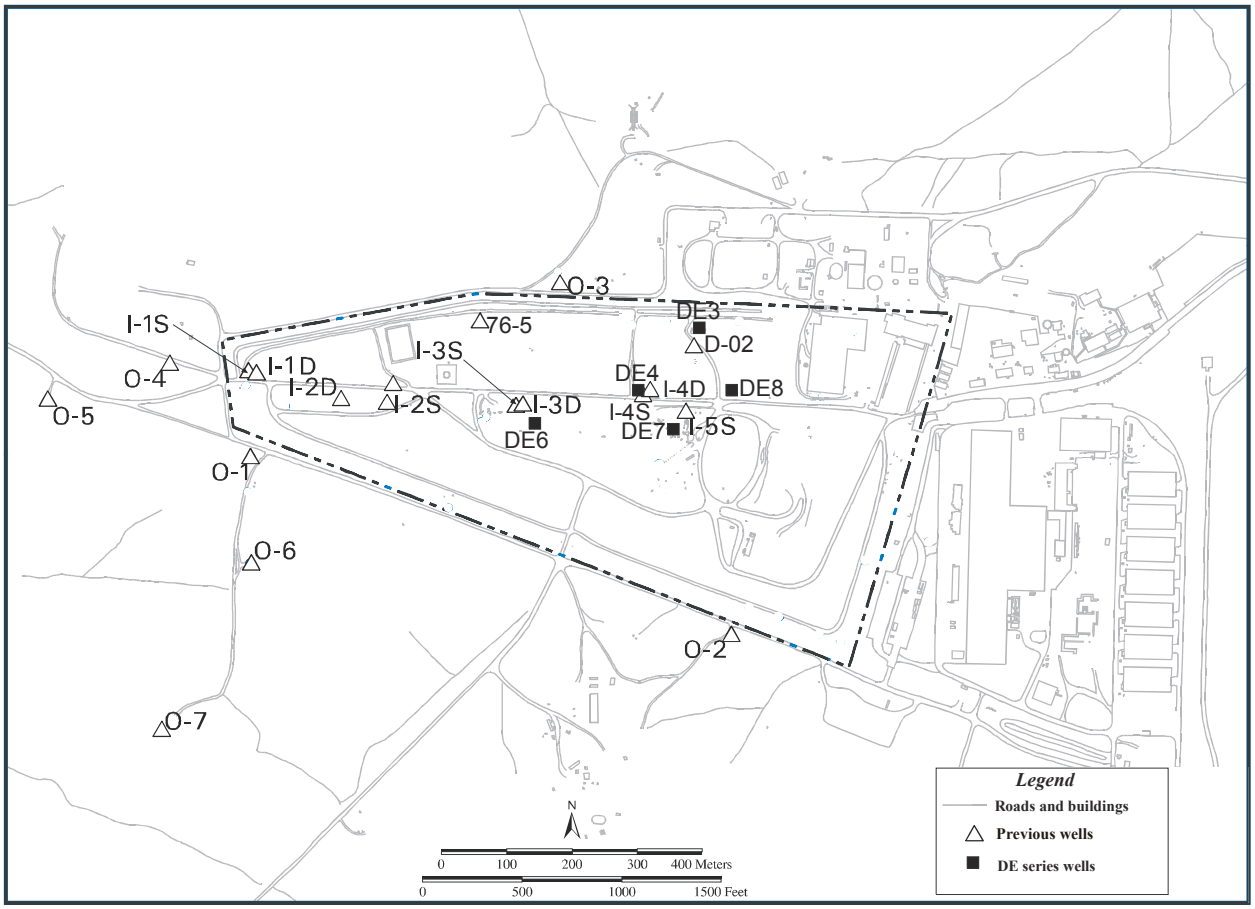

Figure E-1. Current and previous well locations for interbed core hydrologic properties analysis.

Samples for analysis of hydrologic properties were taken from the uppermost section of the core interval, nearest the basalt layer above the interbed and from a distinct coarse-to-fine (e.g., sand to silt or clay) sediment interface, when available. Samples for analysis of hydrologic properties required an intact sample approximately 15 cm (5.9 in.) long.

Samples were analyzed for saturated hydraulic conductivity, porosity, moisture characteristics (i.e., seven-point moisture release curve), grain size, initial volumetric water content, and dry bulk density (Table E-1). Results (Table E-2) were compared with previous analyses of hydrologic properties done on core and interbed material at RWMC to assess the degree of continuity within the interbeds. The data were also compared to hydrologic parameters used in the TETRAD model for Operable Unit 7-13/14 to determine whether the model is conservative or not with respect to these properties.

Table E-1. Sampling of core hydrologic properties and analysis approach for the Subsurface Disposal Area.

Objective	Data Use	Measurement	Method	Detection Level
Obtain samples from stored interbed cores for analyses of hydrologic properties.	Determine spatial variation of interbed layers underlying the Subsurface Disposal Area. Support Waste Area Group 7 modeling. Provide additional characterization to update and test correlation ranges present in Leecaster (2002) in support of the Ancillary Basis for Risk Analysis (Holdren et al. 2002).	1. Saturated hydraulic conductivity	1. ASTM D2434–68 and *Methods of Soil Analysis* (Chapter 28, Klute 1986)	1. $\pm 1 \times 10^{-7}$ cm/s
		2. Porosity	2. *Methods of Soil Analysis* (Chapter 18, Klute 1986)	2. ± 0.01
		3. Moisture characteristic (seven points)	3. ASTM D2325-68 and *Methods of Soil Analysis* (Chapter 26, Klute 1986)	3. ± 0.01%
		4. Particle size analysis (standard sieves [wet] #4-200/hydrometer analysis)	4. ASTM D422-63	4. ± 1 μm
		5. Initial volumetric water content	5. ASTM D2216-98/D4643-00 (ASTM 2000b)	5. Not applicable
		6. Dry bulk density	6. ASTM D2937-00e1 and *Methods of Soil Analysis* (Chapter 13, Klute 1986)	6. Not applicable
		7. Calculated unsaturated hydraulic conductivity	7. Not applicable	7. Not applicable

ASTM = American Society for Testing and Materials (now known as ASTM International)

Table E-2. Hydrologic properties of interbed sediment.

Well Name	Well Alias	Sample Depth (ft bls)	Bulk Density (g/cm^3)	Moisture Content (%)	Total Porosity (%)	Saturated Hydraulic Conductivity (cm/s)
RWMC-1810	DE-3	243.3	1.67	17.3	29.8	1.30E-03
RWMC-1813	DE-4	233.1	1.59	25.7	34.6	2.62E-04
RWMC-1813	DE-4	239.3	1.64	22.9	31.1	7.27E-05
RWMC-1816	DE-6	240.2	1.67	19.4	30.7	5.13E-04
RWMC-1819	DE-7	242.5	1.61	20.9	32.1	7.99E-04
RWMC-1819	DE-7	247.5	1.64	18.8	31.7	1.32E-03
RWMC-1819	DE-7	249	1.79	18.1	23.2	4.54E-04
RWMC-1822	DE-8	233.4	1.60	4.4	35.2	8.33E-02
RWMC-1822	DE-8	240.7	1.50	17.9	37.2	3.04E-03
RWMC-1822	DE-8	242	1.82	12.6	21.6	1.29E-05

E-2. CURRENT RADIOACTIVE WASTE MANAGEMENT COMPLEX RESULTS FOR ANALYSES OF INTERBED HYDROLOGIC PROPERTIES AND PREVIOUS HYDROLOGIC PROPERTIES

Results of current hydrologic properties were compared with previous work by Leecaster (2002). The analytical approach is given below.

Porosity and hydraulic conductivity were measured in ten samples from five new locations in 2004. Permeability was calculated by multiplying hydraulic conductivity by 9.66E + 07. The measurements were taken from C-D interbed soil and were located close to previous sample sites (see Figure E-1). New porosity and permeability results were compared with predicted values derived by universal kriging and inverse distance weighting, respectively. Discussion of these methods and rationale for use are presented and described by Leecaster (2002). Table E-3 lists the new wells, the closest well from Leecaster (2002), measured values for porosity and permeability, predicted values, prediction intervals, and the values at the nearest well.

Table E-3. Comparison of new C-D interbed core porosity and permeability to model predictions and near-well values.

New Interbed Core	RWMC-1810 (DE-3)	RWMC-1813 (DE-4)	RWMC-1816 (DE-6)	RWMC-1819 (DE-7)	RWMC-1822 (DE-8)
Closest well (distance ft)	D02 (202.2)	I4-D (57.2)	I3-D (174.8)	8801D (37.5)	D02 (454.5)
Observed porosity (%)	29.8	34.6 31.1	30.7	32.1 31.7 23.2	35.2 37.2 21.6
Predicted porosity	45.20	30.98	42.10	47.07	48.43
Prediction interval porosity	(37.4-53.0)	(26.6-35.3)	(35.1-49.1)	(43.6-50.6)	(38.4-58.5)
Closest observed porosity	43.02	29.88	44.2	48.86	43.02

Table E-3. (continued).

New Interbed Core	RWMC-1810 (DE-3)	RWMC-1813 (DE-4)	RWMC-1816 (DE-6)	RWMC-1819 (DE-7)	RWMC-1822 (DE-8)
Observed permeability (mD)	737.36	271.22 75.26	39.89	827.12 1,366.46 469.98	86,231.88 3,147.00 13.35
Predicted permeability	476.18	290.74	504.63	230.34	498.98
Prediction interval permeability	(169.3-783.0)	(0-616.1)	(145.9-863.3)	(0-524.0)	(161.6-836.4)
Closest observed permeability	321.27	3.00	339.23	10.80	321.27

All porosity values, except those from Well RWMC-1813 (DE-4), were lower than porosities measured nearby and were less than the lower-bound of the prediction intervals.

Four of ten permeability values were within the predictions intervals. For those outside, two were below the lower limit and four were greater than the upper limit. Eight of the ten permeability values were greater than permeability values measured nearby. Small sample size makes analysis of results more uncertain, but, given that condition, the data do not suggest significant bias in the model.

In general, predictions were not very close to new data values. For both permeability and porosity, sample size was small and small-scale variability was large compared with the overall variance, making spatial modeling difficult and highly uncertain. The porosity variogram was modeled with a 0 nugget, indicating that the small-scale variance is negligible. This may be a shortcoming of the model. Setting the nugget to 33% of the total variance (sill) did not improve the correspondence between the new porosity results and the prediction intervals. Therefore, although a zero nugget may be a shortcoming of the model, increasing the nugget alone does not improve correspondence between the new values and the predictions.

An easting trend was originally fit to the porosity data, owing to a couple of large values on the east and small values on the west. However, the effect of this seems to be small because predictions at the new 2004 locations vary little if the trend is removed.

Spatial modeling with so few sample locations and large small-scale variability is difficult. However, it is an improvement from predicting an overall mean or median for the whole area. Although the new data do not match the model very well, the new results are closer to the model predictions than to the overall median (68 mD). Therefore, we conclude that modeling spatial distribution of permeability is an improvement from predicting an overall mean or median for the whole area.

E-3. REFERENCES

ASTM D422-63, 2002, “Standard Test Method for Particle-Size Analysis of Soils,” ASTM International.

ASTM D2325-68, 2000, “Standard Test Method for Capillary-Moisture Relationships for Coarse- and Medium-Textured Soils by Porous-Plate Apparatus,” ASTM International.

ASTM D2937-00e1, 2000, “Standard Test Method for Density of Soil in Place by the Drive-Cylinder Method,” ASTM International.

ASTM D2434-68, 2000, "Standard Test Method for Permeability of Granular Soils (Constant Head)," ASTM International.

ASTM D4643-00, 2000, "Standard Test Method for Determination of Water (Moisture) Content of Soil by the Microwave Oven Method," ASTM International.

Holdren, K. J, H. B. Becker, N. L. Hampton, L. D. Koeppen, S. O. Magnuson, T. J. Meyer, G. L. Olson, and A. J. Sondrup, 2002, *Ancillary Basis for Risk Analysis of the Subsurface Disposal Area*, INEEL/EXT-02-01125, Rev. 0, Idaho National Engineering and Environmental Laboratory.

Klute, A., 1986, "Methods of Soil Analysis Part 1 Physical and Mineralogical Methods," 2nd Edition, eds. G. S. Campbell, R. D. Jackson, M. M. Mortland, D. R. Nielsen, and A. Klute, Madison: American Society of Agronomy, Inc., Soil Science Society of America, Inc.

Leecaster, M. K., 2002, *Geostatistic Modeling of Subsurface Characteristics in the Radioactive Waste Management Complex Region, Operable Unit 7-13/14*, INEEL/EXT-02-00029, Rev. 0, Idaho National Engineering and Environmental Laboratory.

Schaffer, J. M., INL, to Katie Hain, DOE, September 24, 2004, "Contract No. DE-AC07-99ID13727—Transmittal of Limitations and Validations Report for Interbed Core Sampling Conducted in November 2003 for Waste Area Group 7," CCN 52247.

Appendix F

Reanalysis of B-C Interbed Porosity Spatial Variability

Appendix F

Reanalysis of B-C Interbed Porosity Spatial Variability

This appendix contains the reanalysis of the B-C interbed porosities for the variogram and kriging results. Leecaster (2002) used minimum instead of average porosities from each location where core samples were evaluated for the B-C interbed.

The values (i.e., mean porosity) used in the analysis are given in Table F-1 and are seen in Figure F-1. There was no evidence of a spatial trend based on a regression of locations (all p-values were greater than 0.15). The incorrect data did show a trend. Because the data were not significantly different from normal (Shapiro-Wilk p-value = 0.57), the raw data were used to determine the variogram and krige predictions. Because of the small number of sample locations, anisotropy was assumed without verification and an omni-directional variogram was used. The variogram cloud (Figure F-2) suggests spatial correlation at short lags; however, the empirical variogram (Figure F-3) with at least five pairs of points used for each value plotted does not suggest spatial correlation at short lags. Based on previous work and the variogram cloud, a spherical model with range = 1,000 ft, sill = 38, and nugget = 0 (Figure F-3) was used in ordinary kriging. The resulting kriging predictions on the four grids (Table F-2) are presented in Figures F-4 through F-7. Grids 1, 2, and 3 correspond to the base and refined grids for the RI/FS model shown in Figure 4-2 of this document.

Table F-1. Mean porosity for the B-C interbed.

Well	Mean Porosity
I1-S	25.6
I2-S	29.4
I3-S	26.4
I4-S	47.5
O-1	32.5
O-2	28.4
O-3	33.8
O-5	29.9
O-6	39.8
O-7	34.9
O-9	35.5
BG-91	35.5
BG-94	36.5
BG-95	32.7
BG-96	43.2
D15	37.9
UZ98-2	46.1

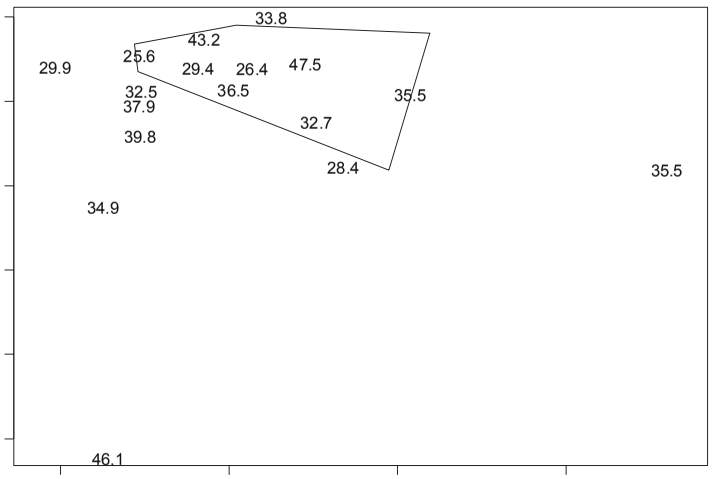

Figure F-1. Mean porosity value for the B-C interbed. Sampling locations shown relative to the Subsurface Disposal Area.

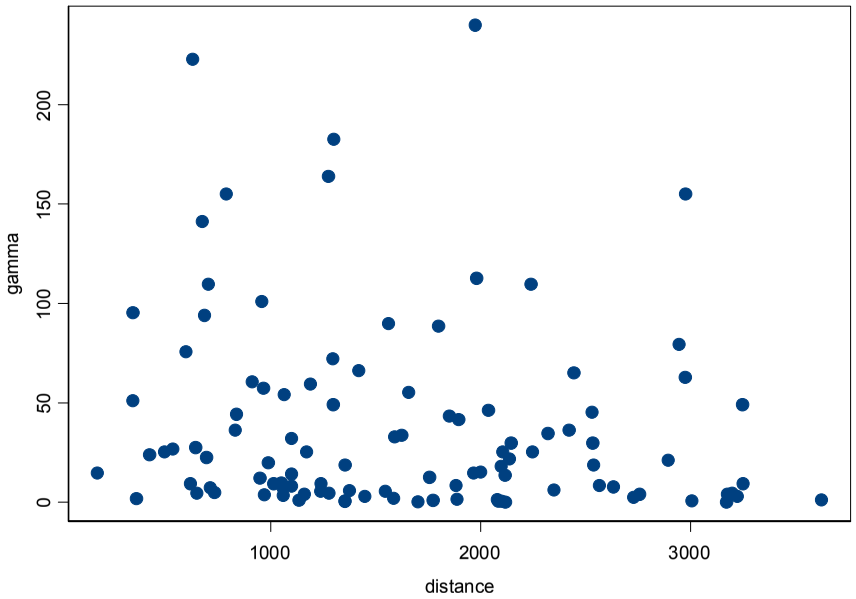

Figure F-2. Variogram cloud for mean porosity from the B-C interbed.

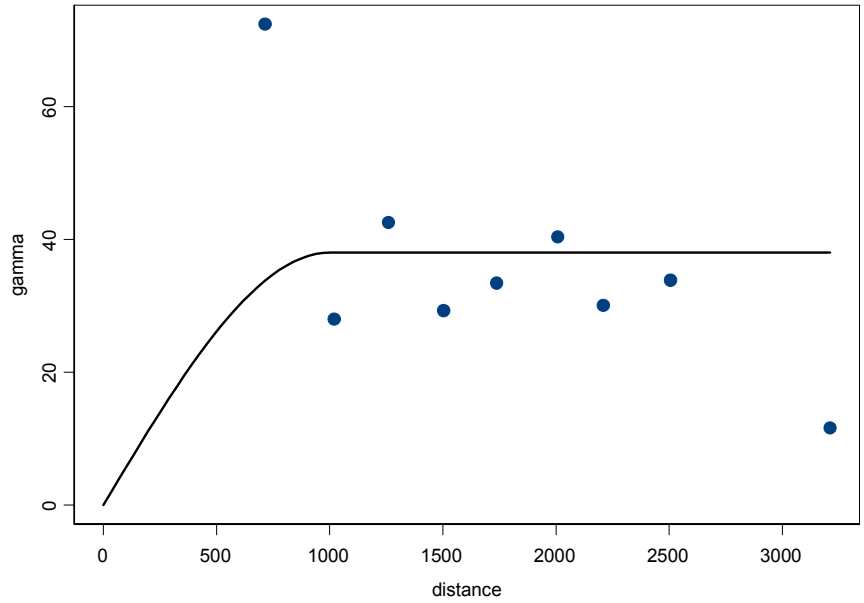

Figure F-3. Empirical variogram for mean porosity from the B-C interbed with spherical model (range = 1,000 ft, sill = 38, and nugget = 0).

Table F-2. Prediction grids.

	East-West		North-South	
Grid	Interval (ft)	Number	Interval (ft)	Number
0	1,000	17	1,000	13
1	500	14	500	10
2	250	18	250	12
3	125	28	125	14

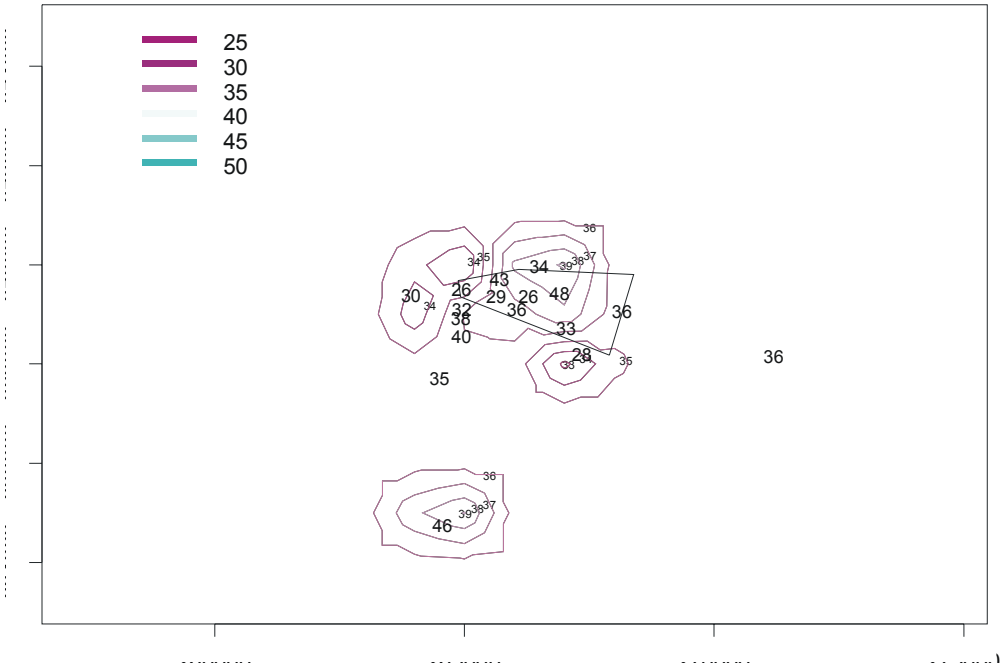

Figure F-4. Ordinary kriging predictions for mean porosity from the B-C interbed for grid 0.

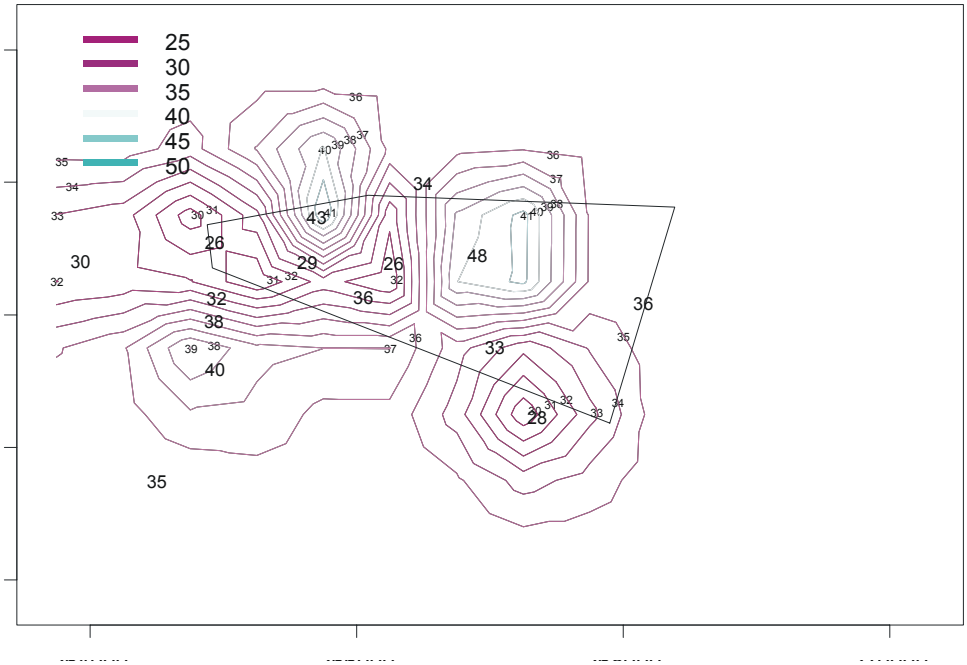

Figure F-5. Ordinary kriging predictions for mean porosity from the B-C interbed for grid 1.

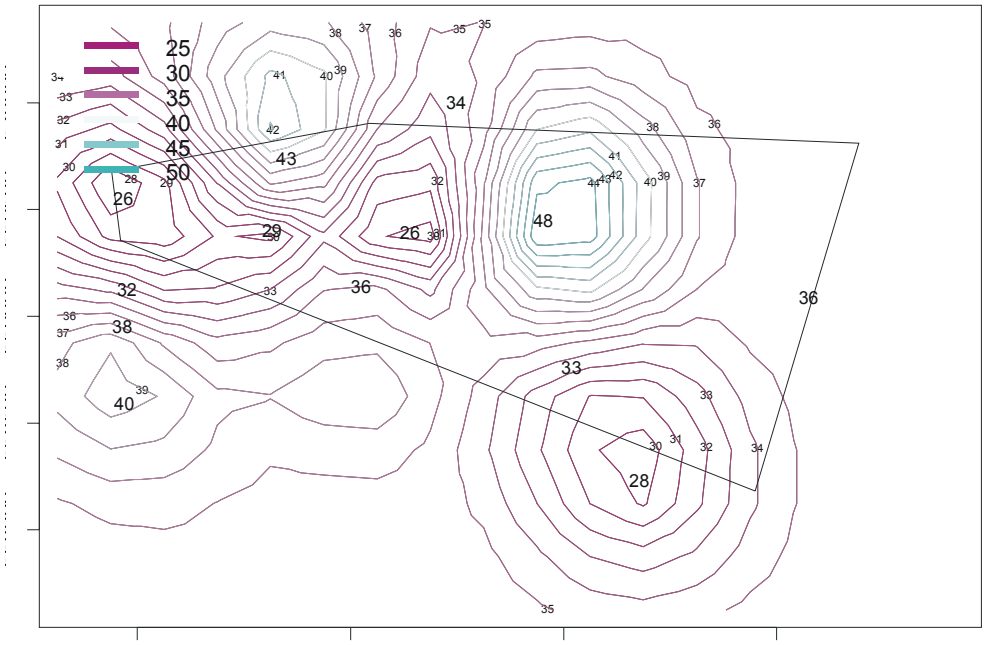

Figure F-6. Ordinary kriging predictions for mean porosity from the B-C interbed for grid 2.

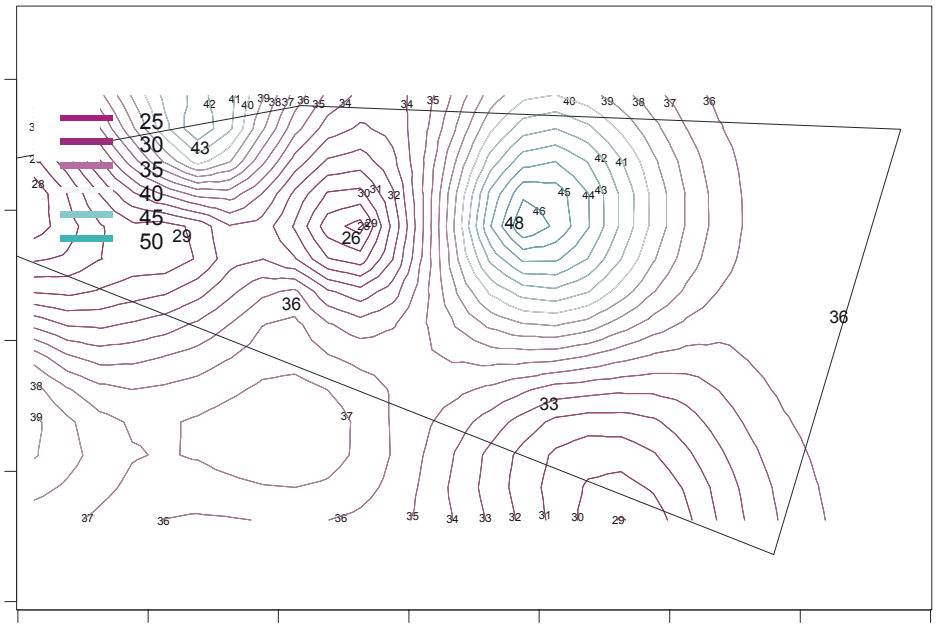

Figure F-7. Ordinary kriging predictions for mean porosity from the B-C interbed for grid 3.

REFERENCES

Leecaster, Molly K., 2002, *Geostatistic Modeling of Subsurface Characteristics in the Radioactive Waste Management Complex Region, Operable Unit 7-13/14*, INEEL/EXT-02-00029, Rev. 0, Idaho National Engineering and Environmental Laboratory.

Appendix G

Complete Carbon Tetrachloride Vapor-Phase Model Calibration Results

Appendix G

Complete Carbon Tetrachloride Vapor-Phase Model Calibration Results

This appendix contains the complete set of final CCl_4 vapor-phase model calibration results. Figure G-1 contains time-history comparisons of model results to observed data at each vapor port. Figure G-2 contains comparisons of time-averaged vertical profiles at each vapor monitoring well.

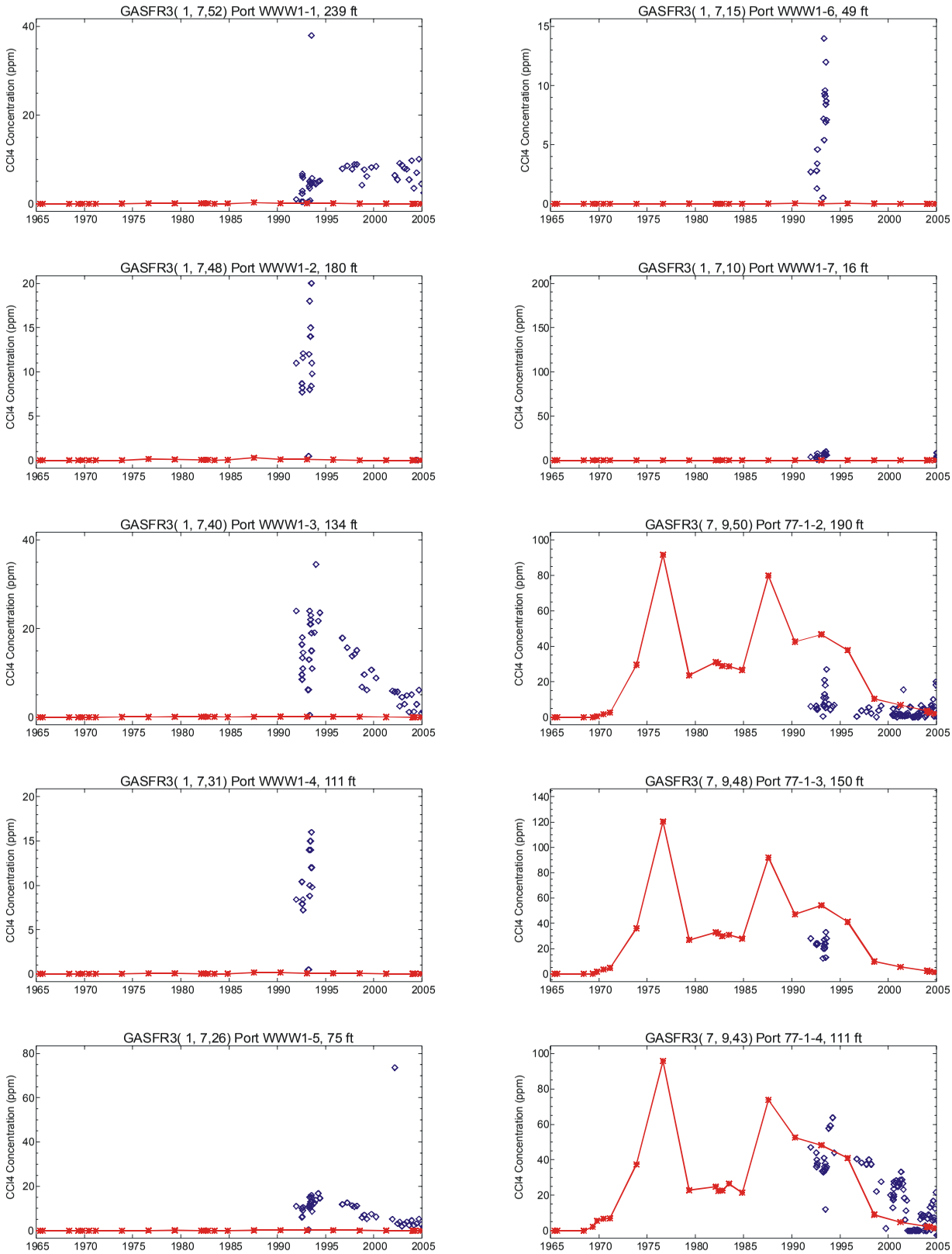

Figure G-1. Comparison of simulated (stars) and measured (diamonds) time histories of carbon tetrachloride vapor concentrations through the year 2005 for each vapor monitoring port. The port name and depth in feet below land surface are indicated above each graph.

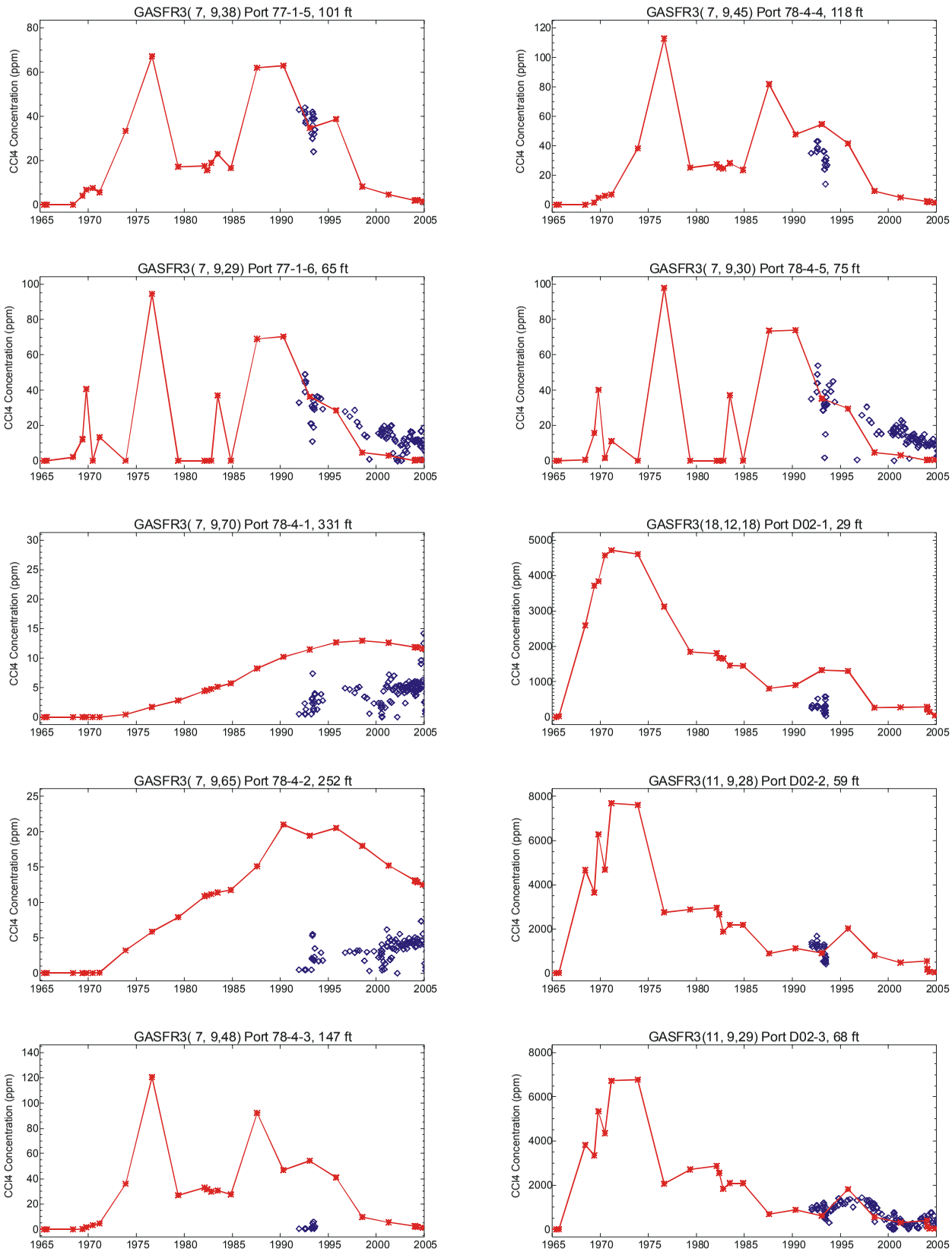

Figure G-1. (continued).

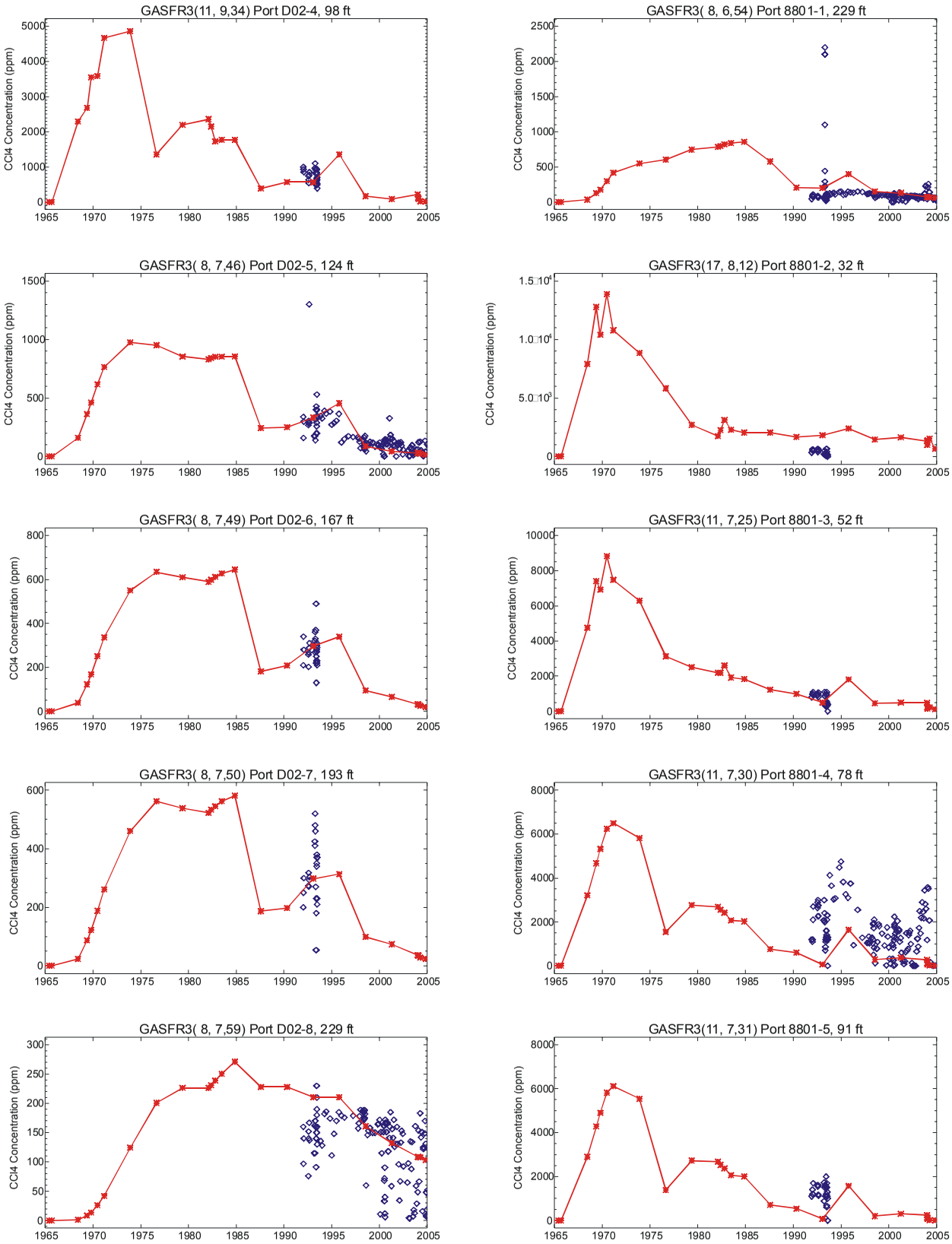

Figure G-1. (continued).

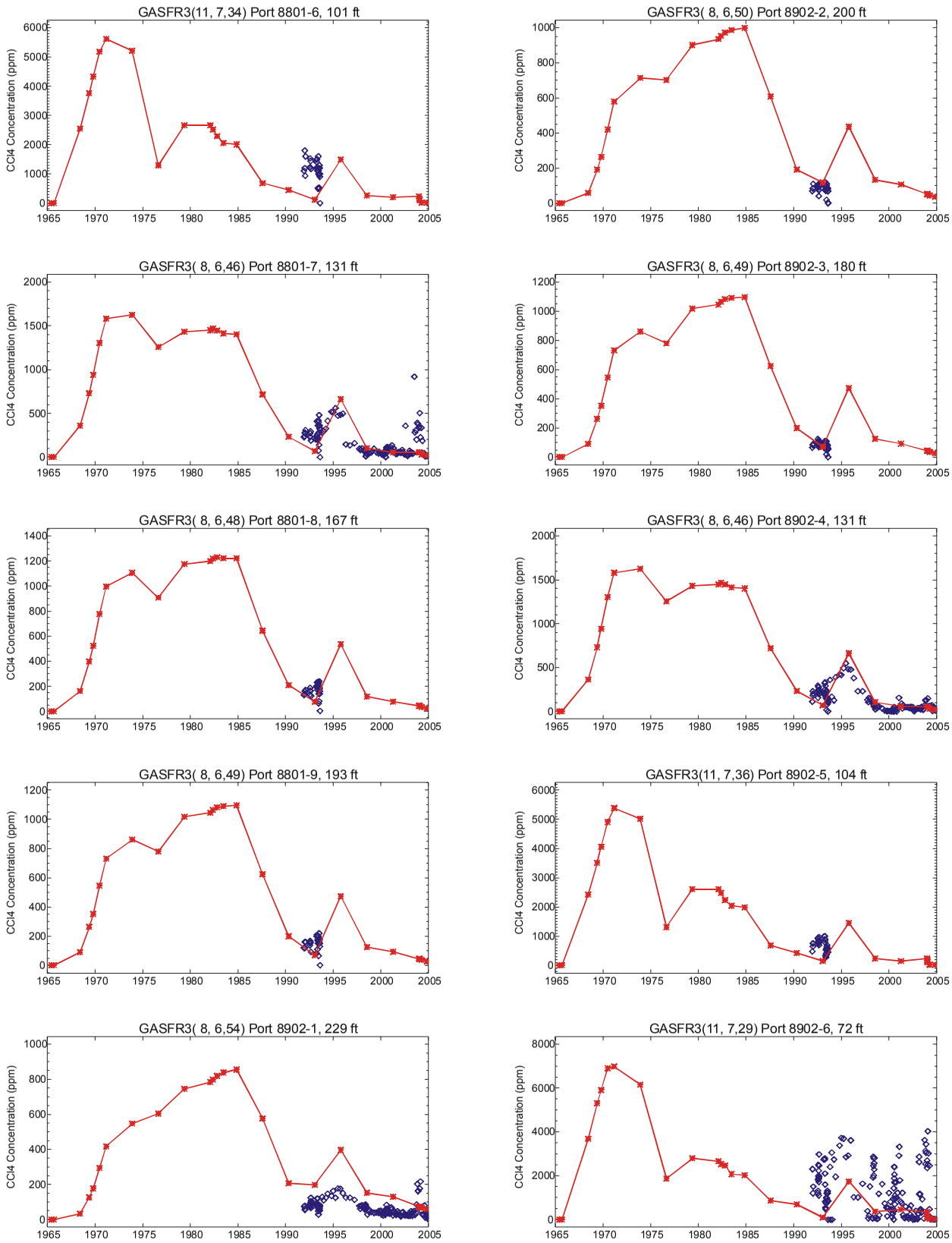

Figure G-1. (continued).

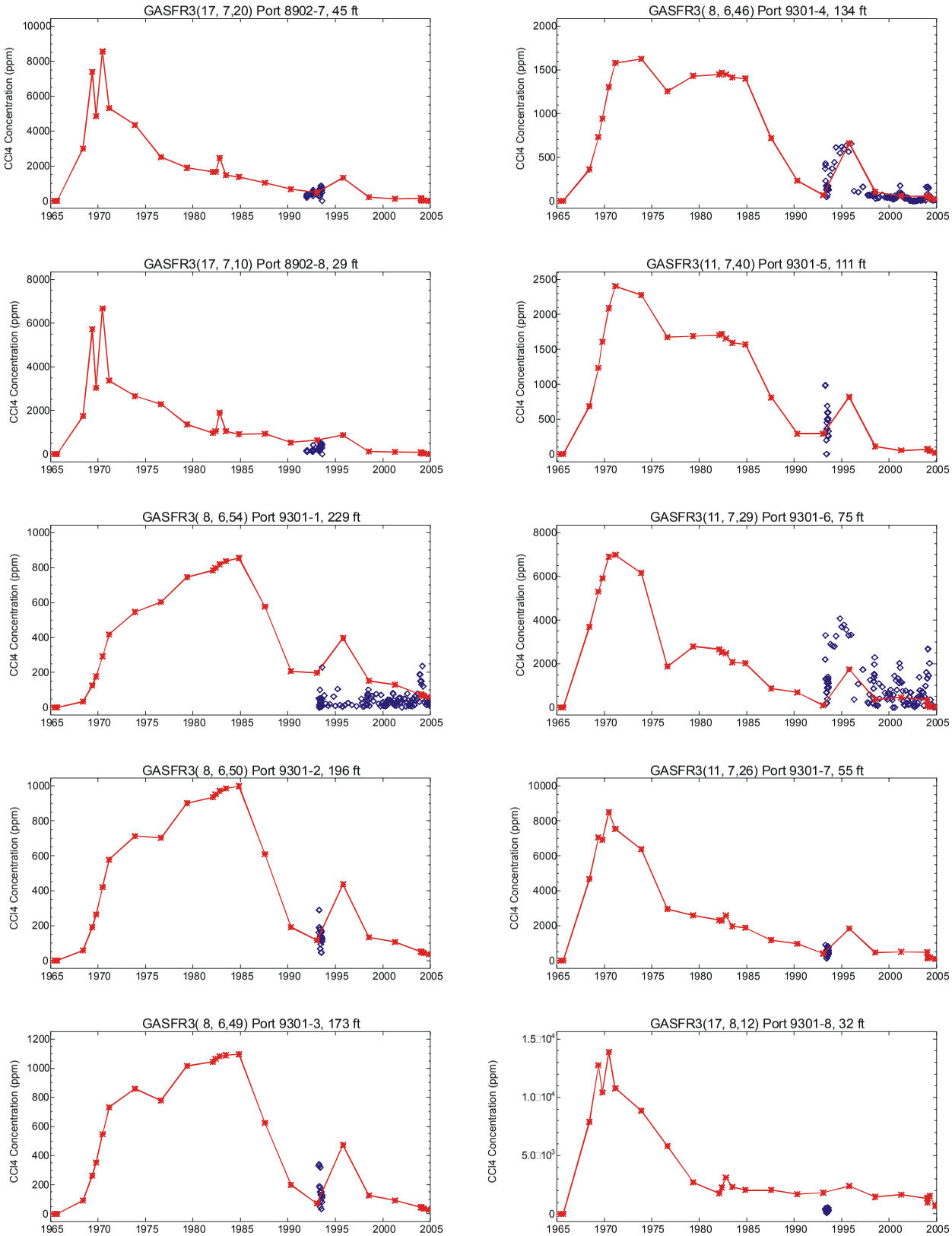

Figure G-1. (continued).

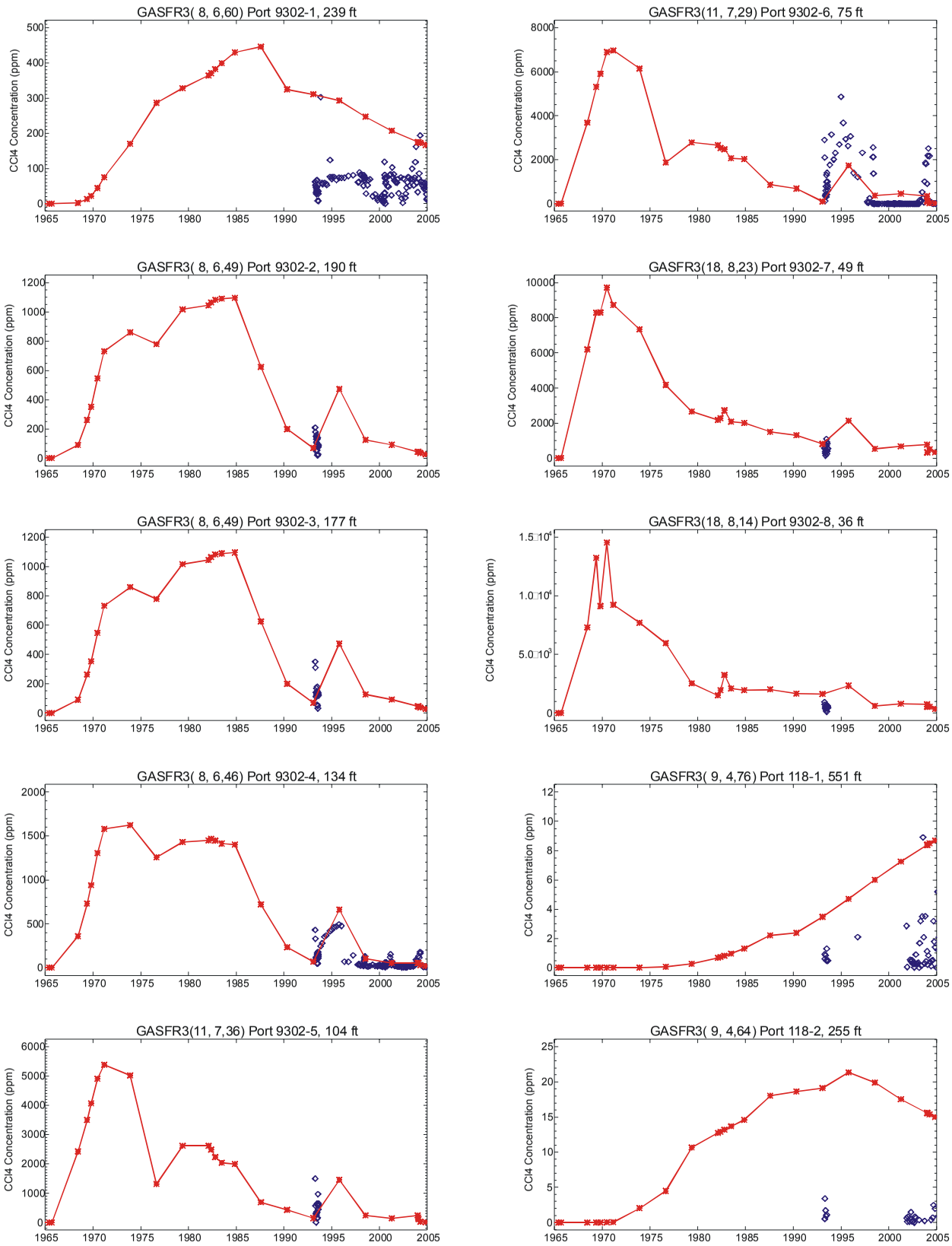

Figure G-1. (continued).

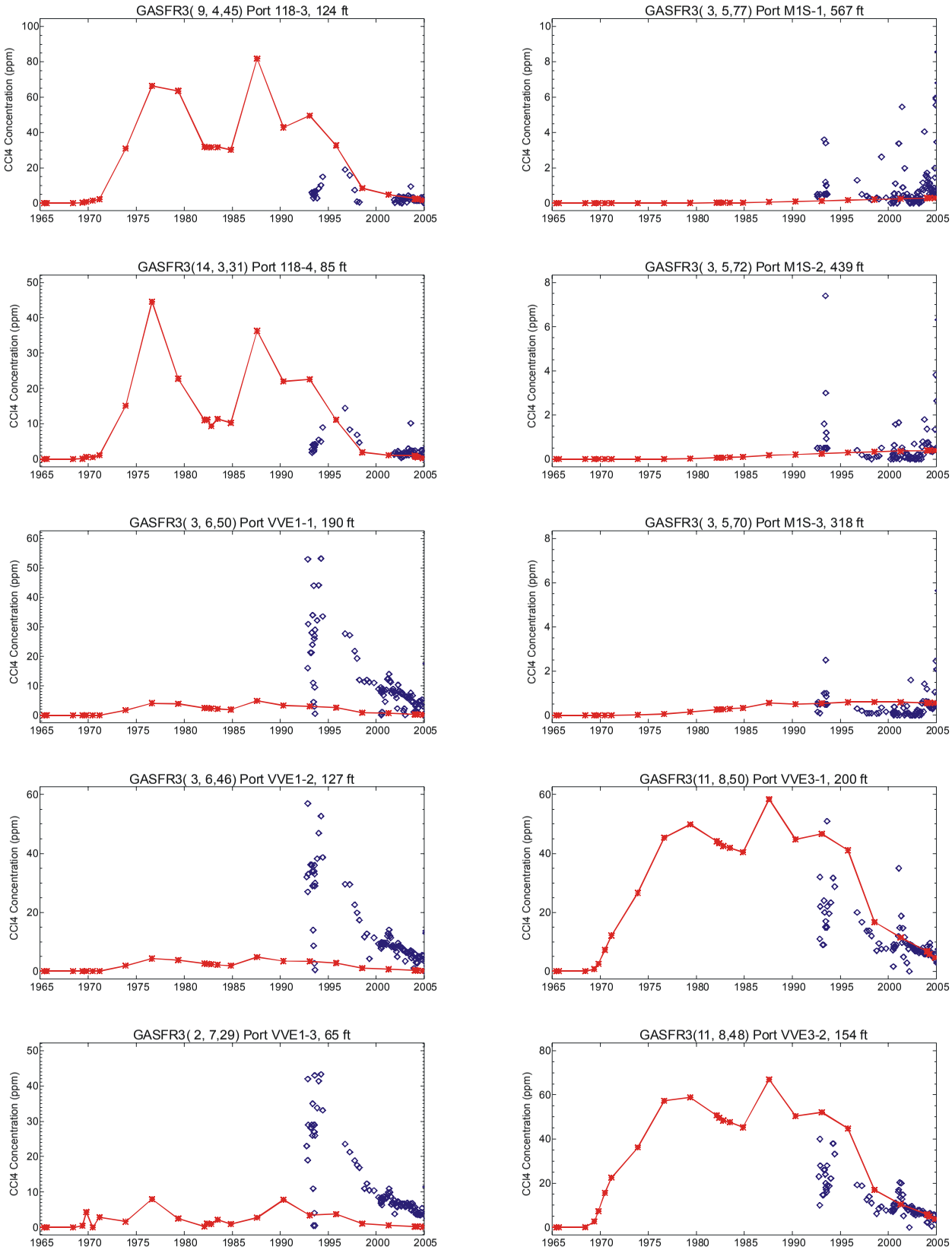

Figure G-1. (continued).

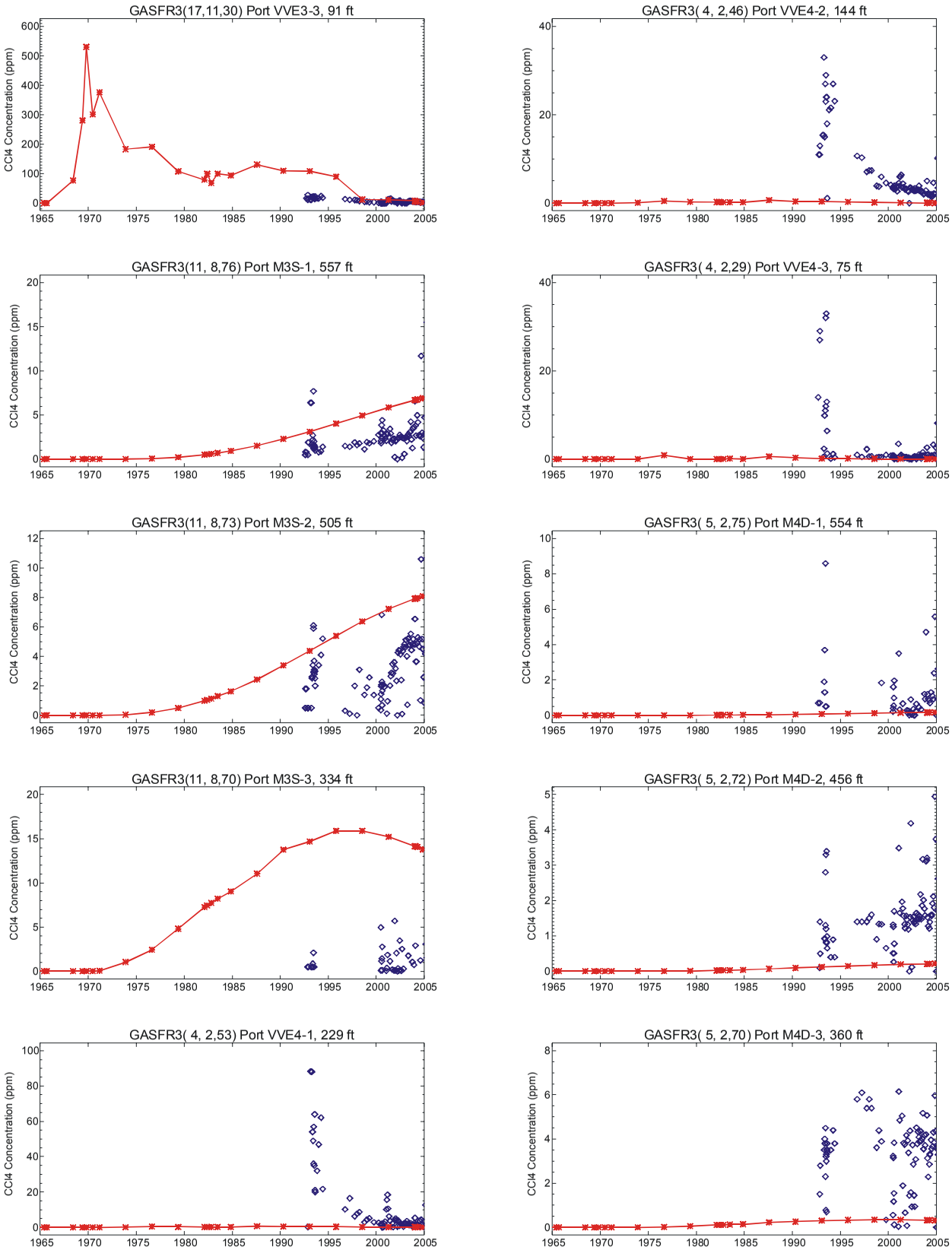

Figure G-1. (continued).

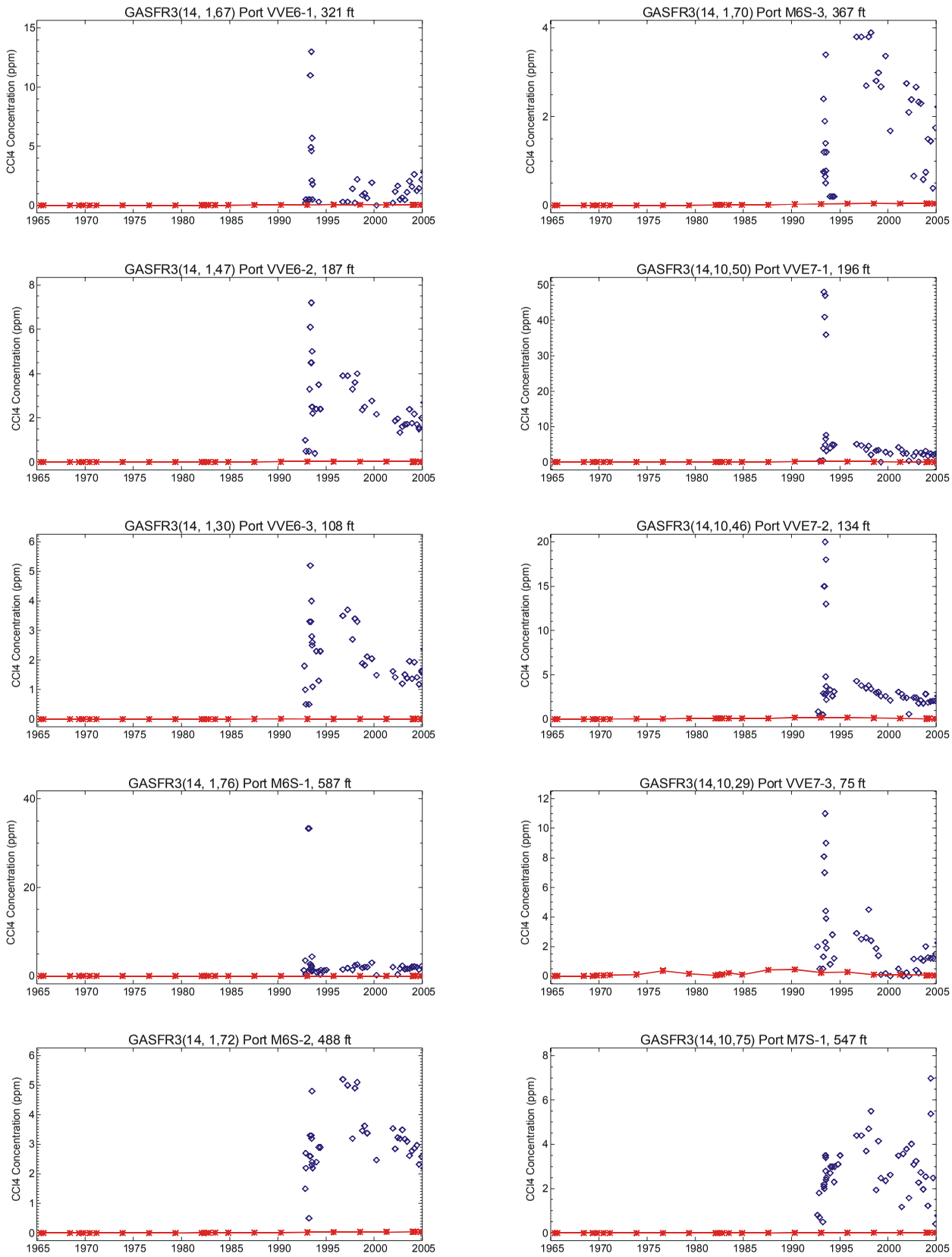

Figure G-1. (continued).

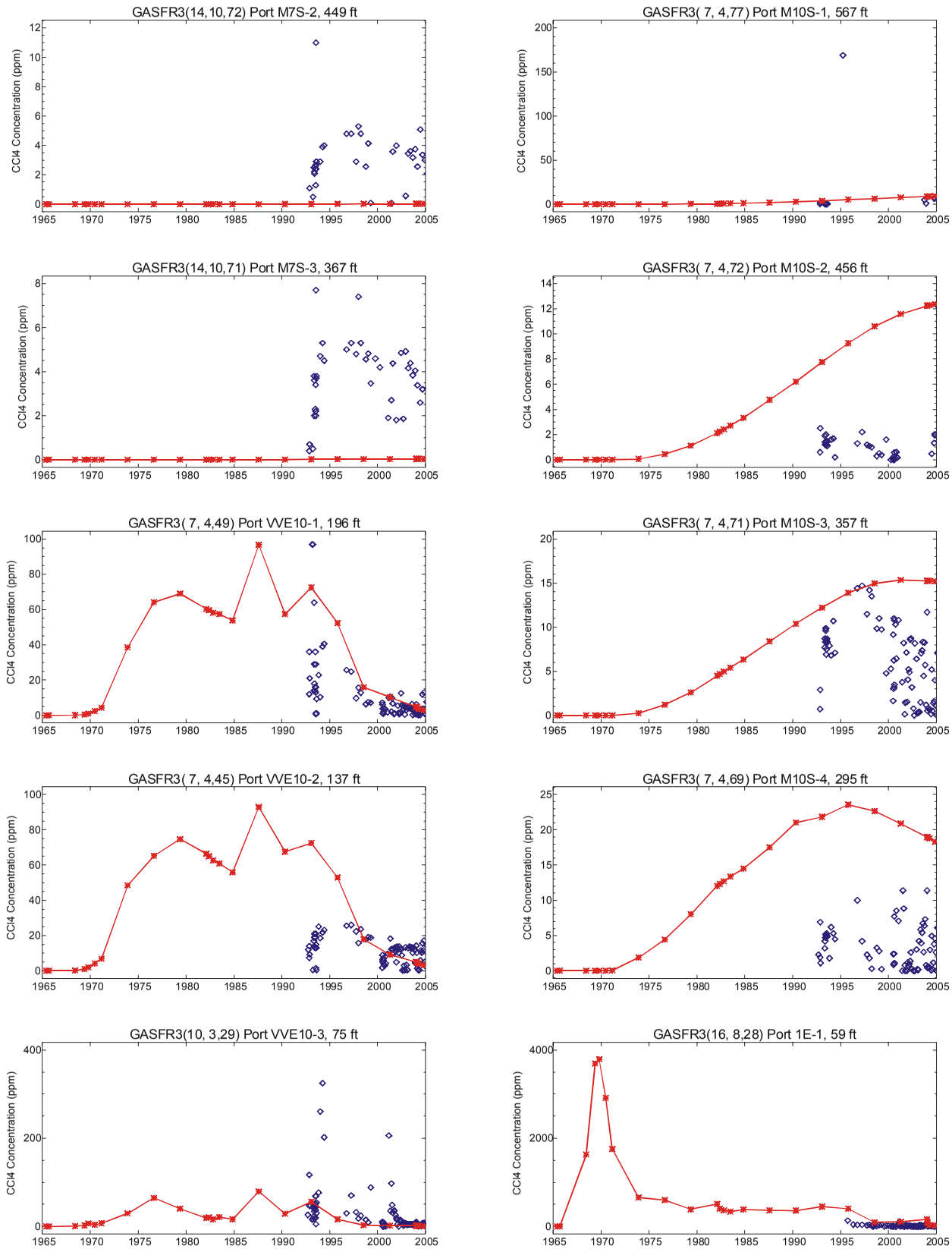

Figure G-1. (continued).

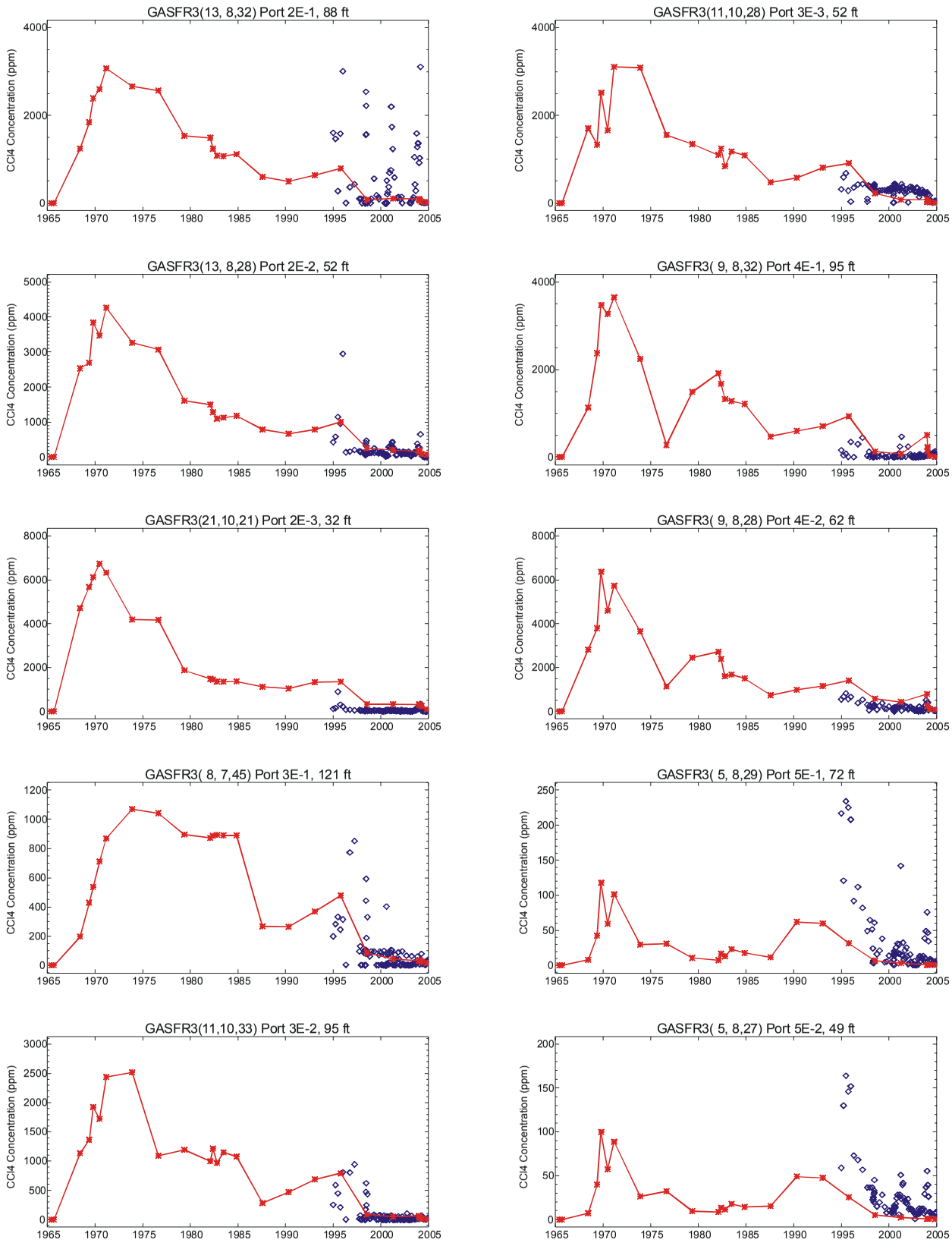

Figure G-1. (continued).

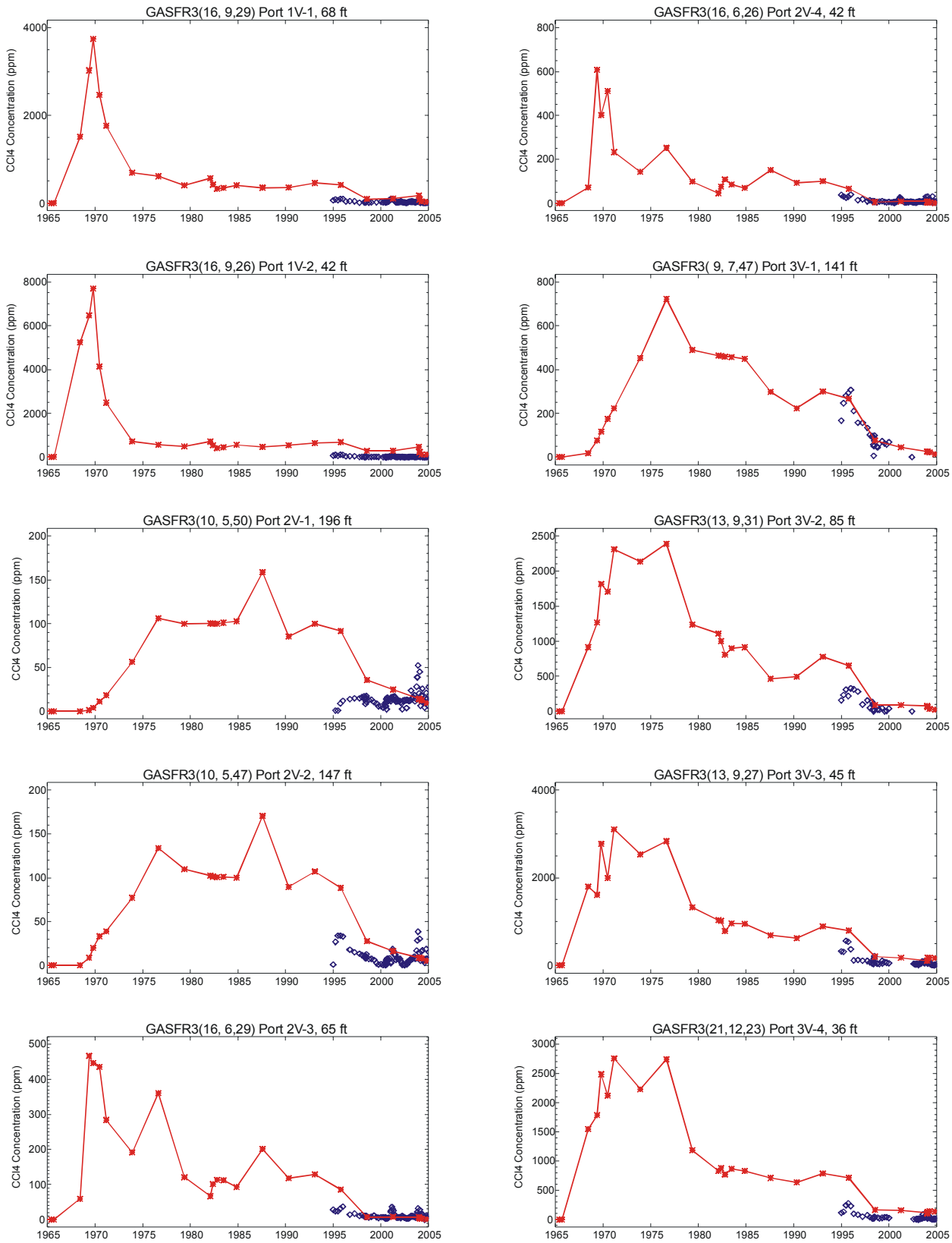

Figure G-1. (continued)

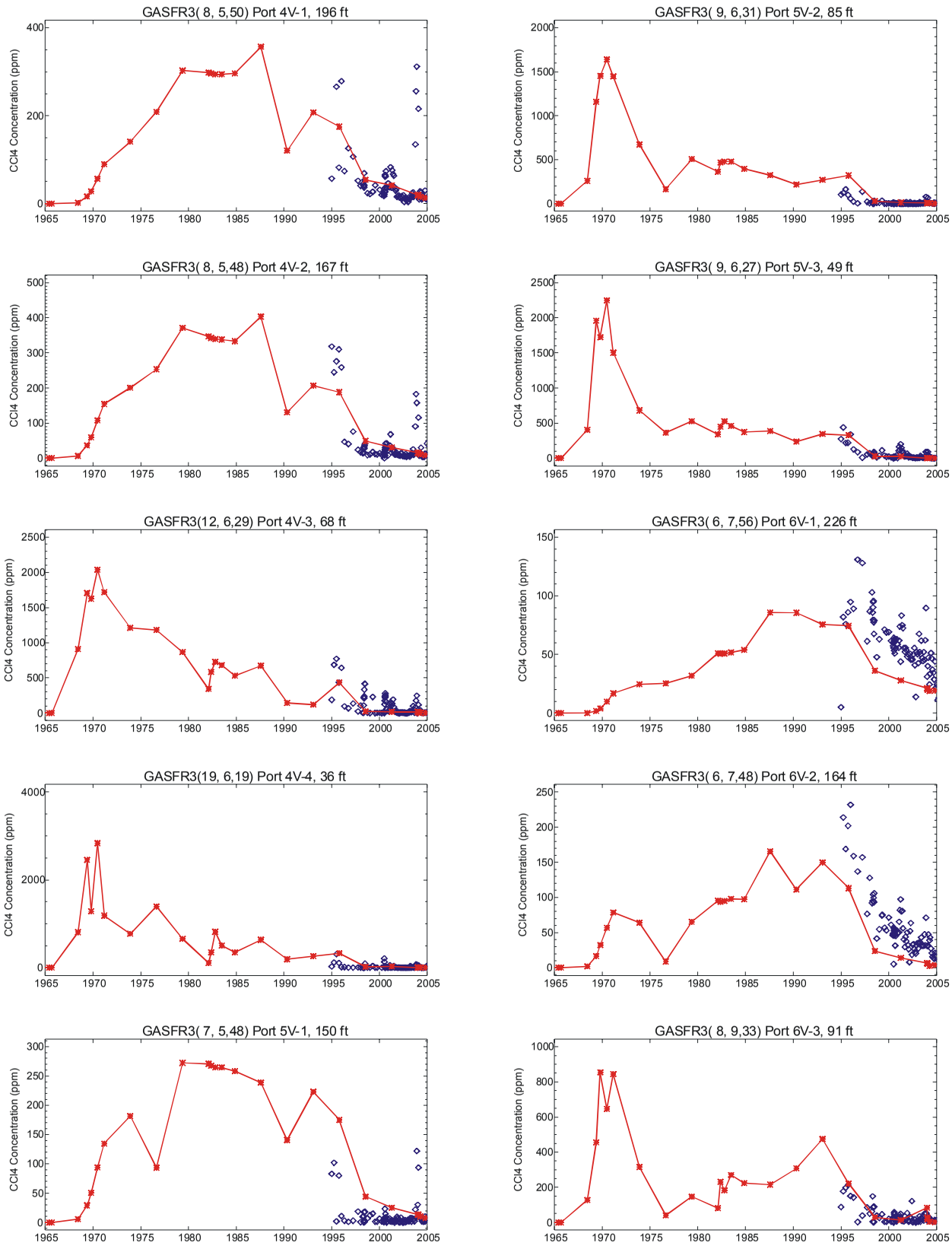

Figure G-1. (continued)

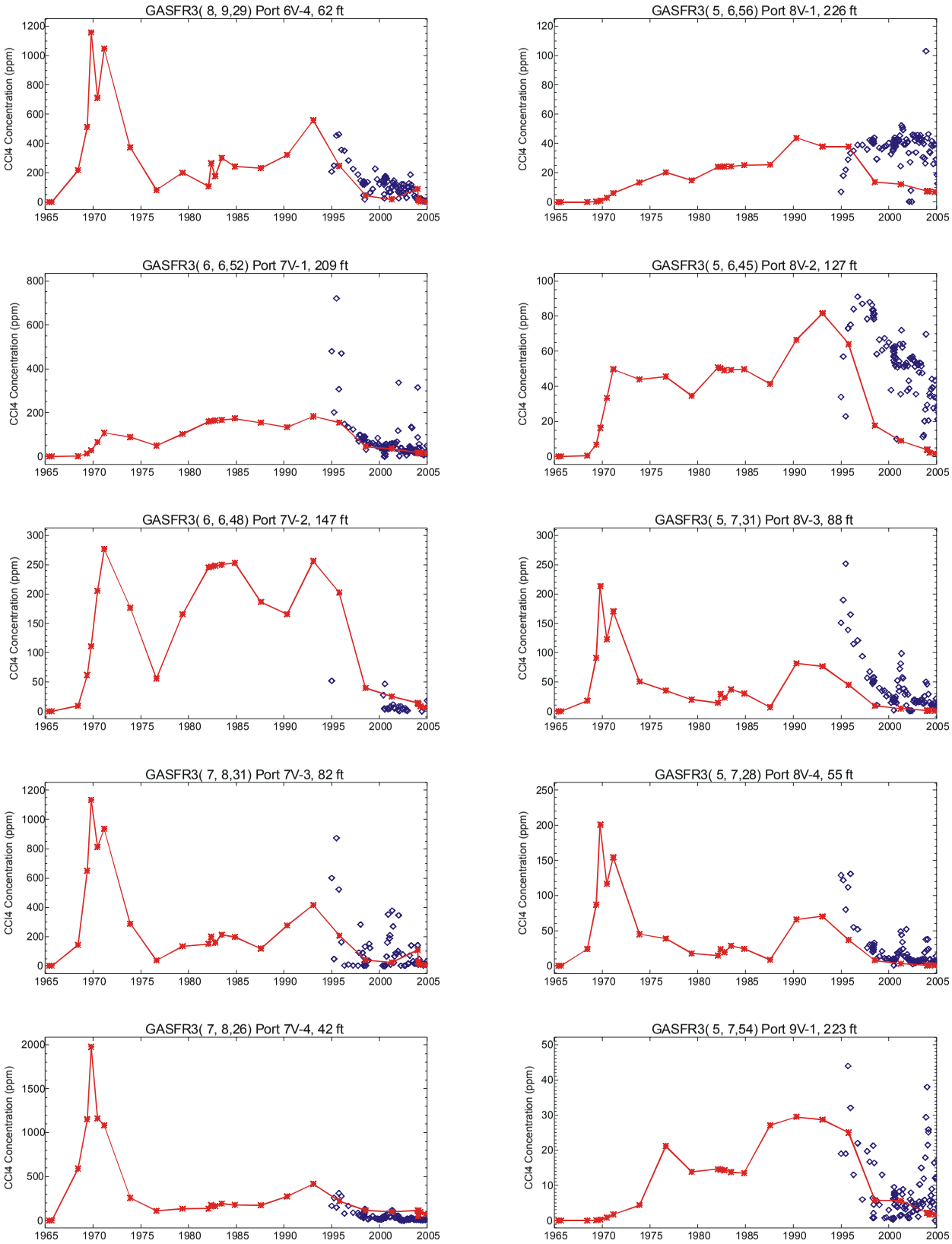

Figure G-1. (continued).

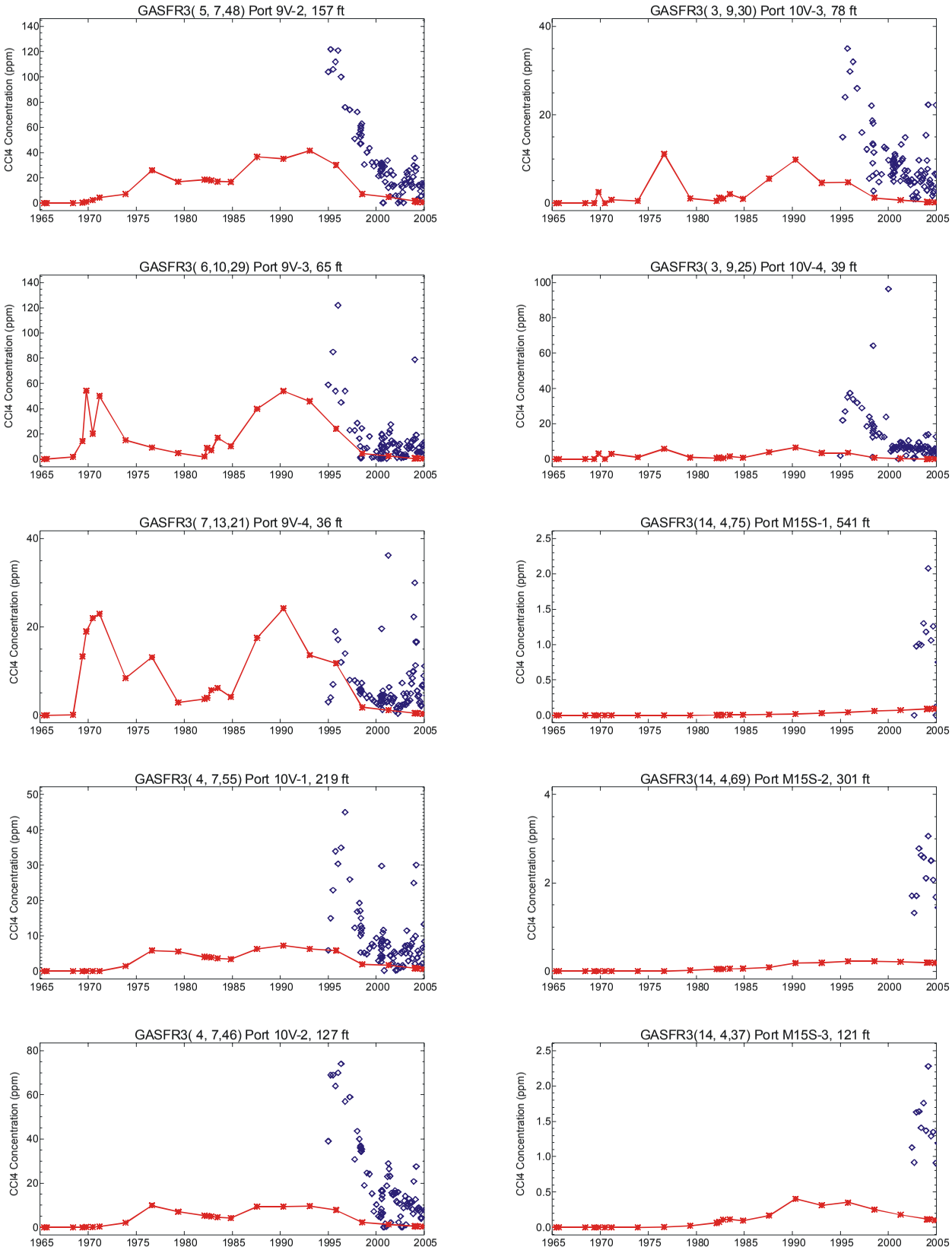

Figure G-1. (continued).

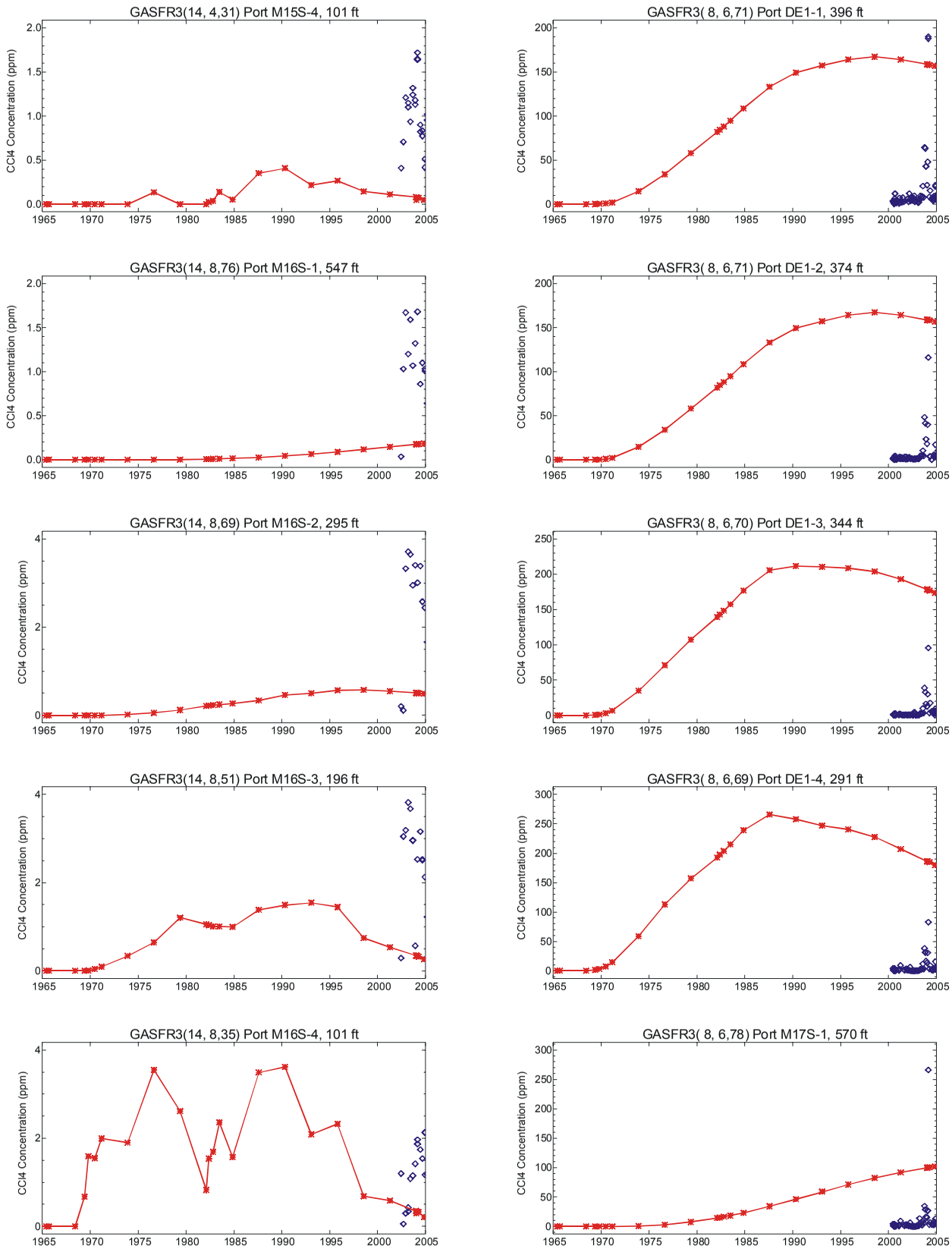

Figure G-1. (continued).

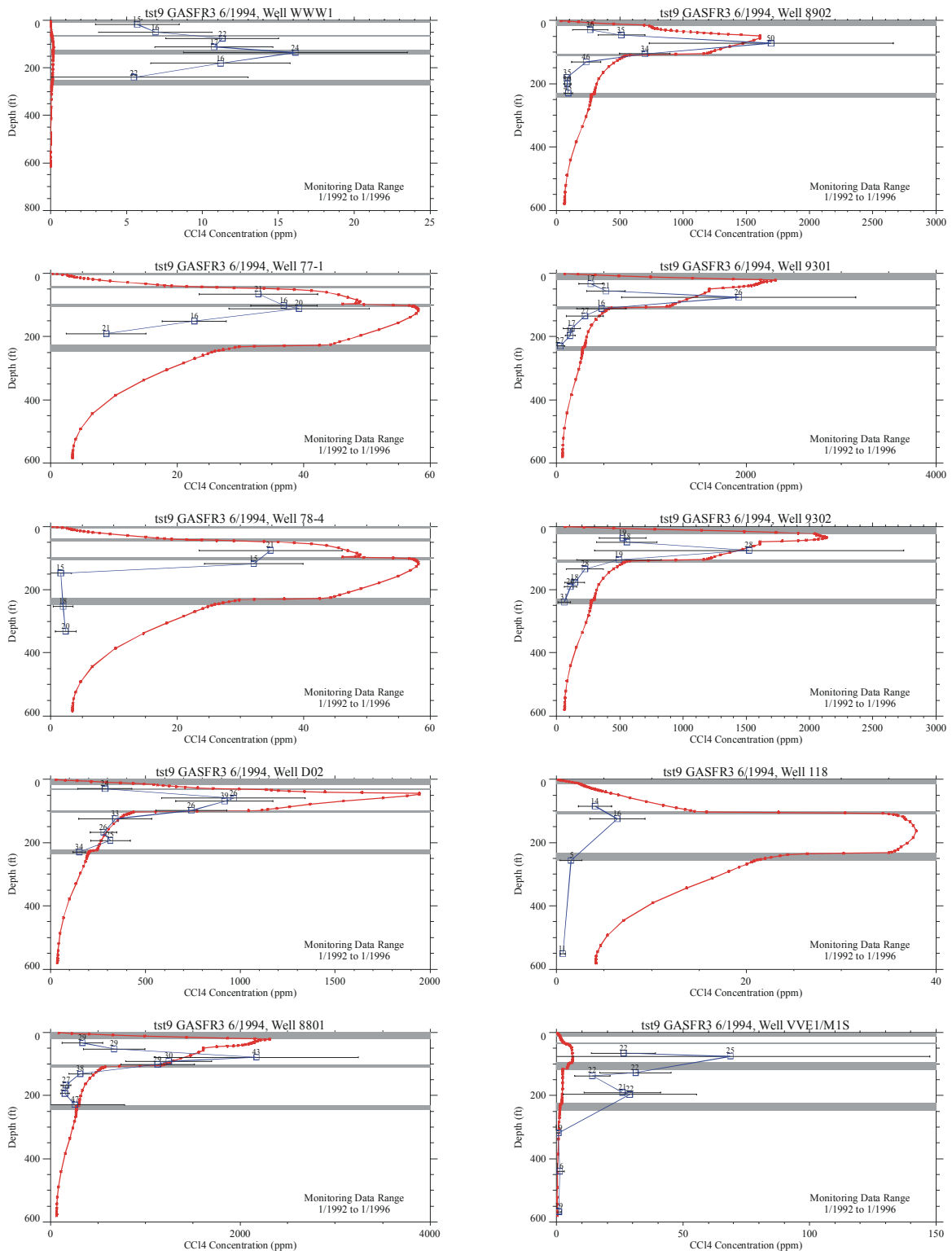

Figure G-2. Comparison of simulated and measured vertical profiles of carbon tetrachloride vapor concentrations at each vapor monitoring well. The well name is indicated above each graph. The simulated data is from June 1994. The measured data was averaged over a 4-year period (i.e., 1992 to 1996). The number above each measured data point is the number of data points used to calculate the average.

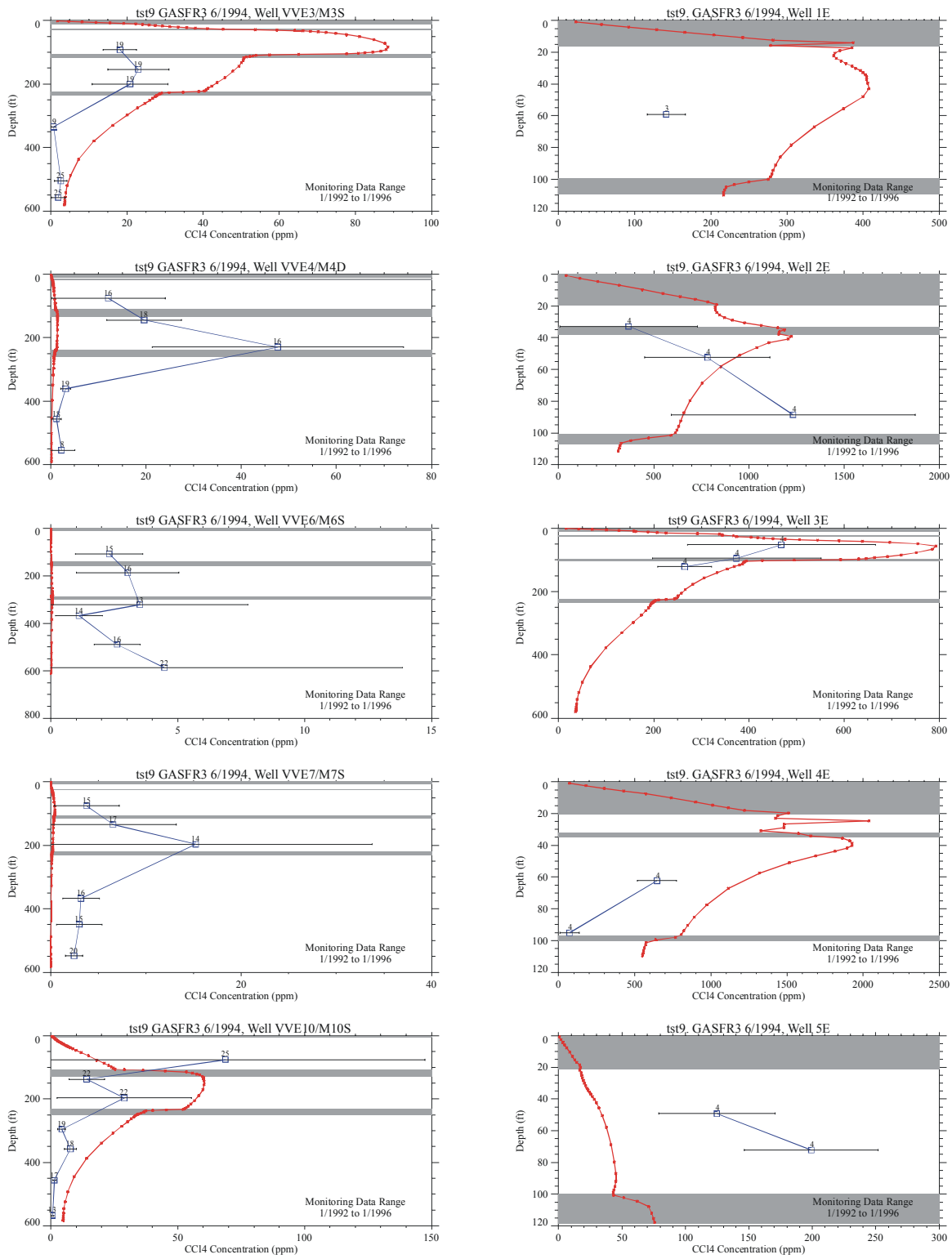

Figure G-2. (continued).

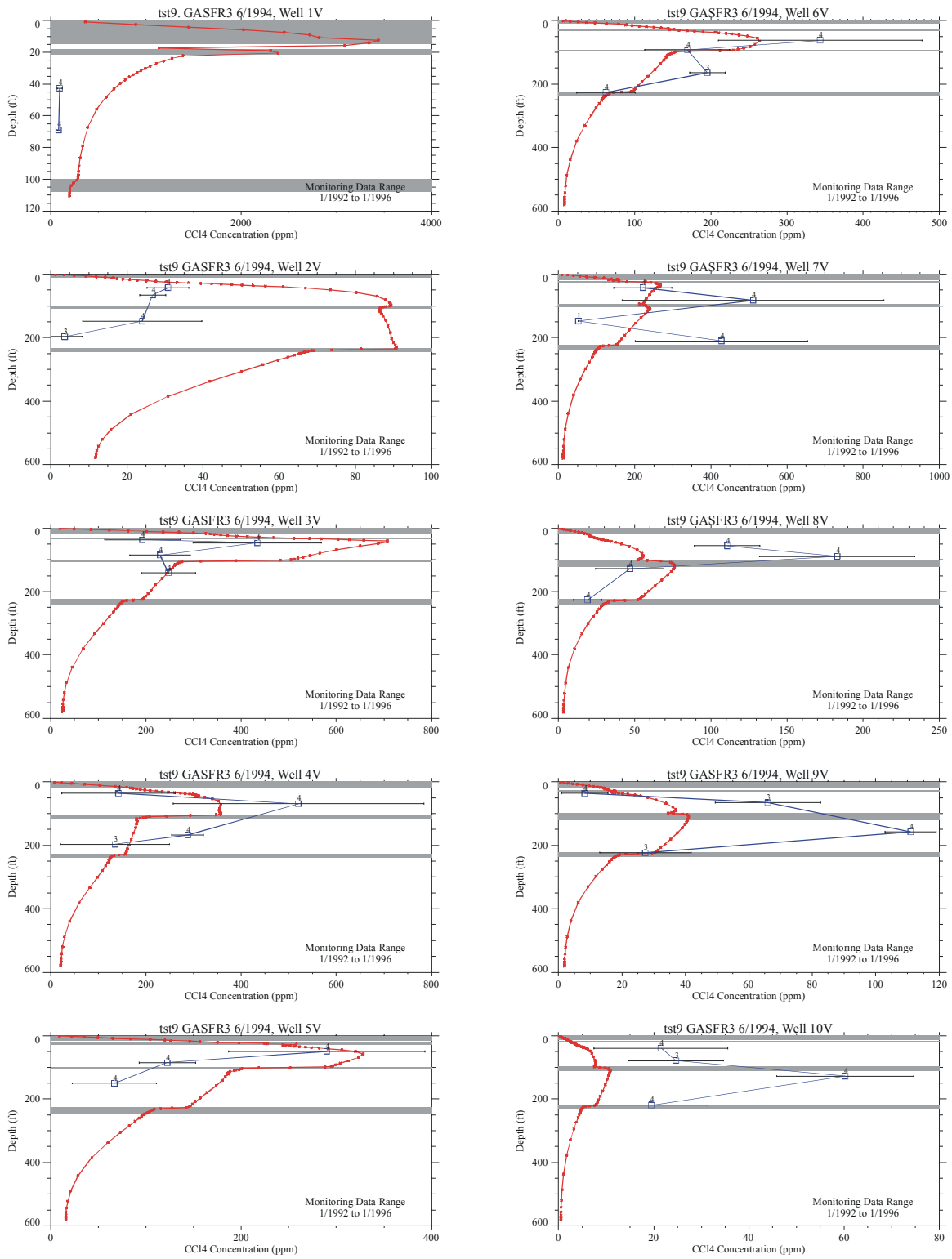

Figure G-2. (continued).

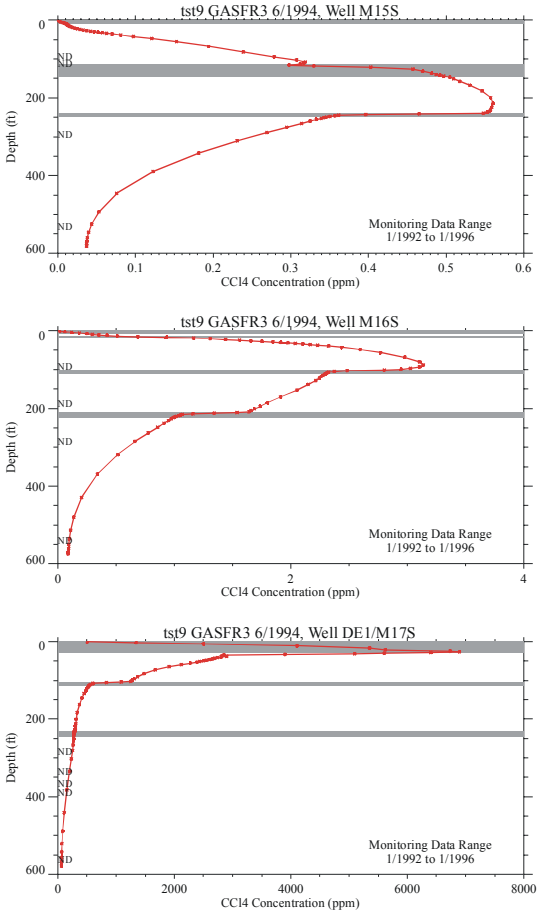

Figure G-2. (continued).

Appendix H

Operable Unit 7-13/14 Numerical Dispersion Evaluation

Appendix H

Operable Unit 7-13/14 Numerical Dispersion Evaluation

Numerical dispersion arises from the discrete finite difference approximation to continuous derivatives necessary as part of solving the governing equations for conservation of mass and momentum. The finite difference approximations use Taylor series expansions, which have multiple terms. Generally, for simplicity of coding, only the first derivative term in the expansion is used for differencing and the higher order derivative terms are neglected. Solutions obtained with this approach are only first order accurate. Finite difference approximations are used for both temporal and spatial derivatives.

Control of numerical dispersion can be accomplished by limiting the size of time steps and by increasing spatial discretization. Also, there are numerical techniques to improve representation of the derivatives. The TETRAD simulator has options available to reduce spatial numerical dispersion through use of higher order approximations of spatial derivatives. Numerical dispersion, due to time differencing, can be reduced by imposing smaller time steps, which is accomplished by specifying a lower convergence criterion.

Numerical dispersion was investigated empirically by invoking TETRAD options to control spatial dispersion, and by reducing convergence criterion to reduce the time step to control temporal dispersion. These simulations were performed for both the aquifer and the vadose zone domain. The aquifer domain results are presented first and have more detail because they could be run quickly, most simulations completing within 24 hours. The vadose zone simulation was performed using information gained from the aquifer simulations to define one simulation.

H-1. AQUIFER DOMAIN NUMERICAL DISPERSION IMPACTS

Aquifer test simulations were performed using U-238 (B_g5), C-14 (B_g8), and nitrate (B_g10) to see if results from the draft RI/BRA base-case simulation were substantially impacted by numerical dispersion. Substantial would mean that results were affected such that groundwater pathway risks for that contaminant would increase past the 1.E-05 break point for deciding that the contaminant was a contaminant of concern. These contaminants were chosen to represent a range of contaminants from long-lived to nondecaying and from sorbing to nonsorbing. The aquifer simulations all used contaminant flux from the corresponding draft RI/BRA base-case vadose zone simulation without modification. The effect of dispersion in the vadose zone simulations is discussed below.

For each simulation, two methods were used to reduce numerical dispersion. The TETRAD option to use higher order differencing was used to reduce spatial dispersion. This is indicated by successively higher values of a TETRAD input parameter called “DISC”. The convergence criterion was used to reduce temporal numerical dispersion. For each simulation, impact was determined by extracting the maximum concentration as a function of time, both anywhere outside the SDA fence in the refined aquifer simulation domain and along the INL Site boundary in the base aquifer domain. Therefore, four figures are presented for each of the three contaminants in Figures H-1 through H-12.

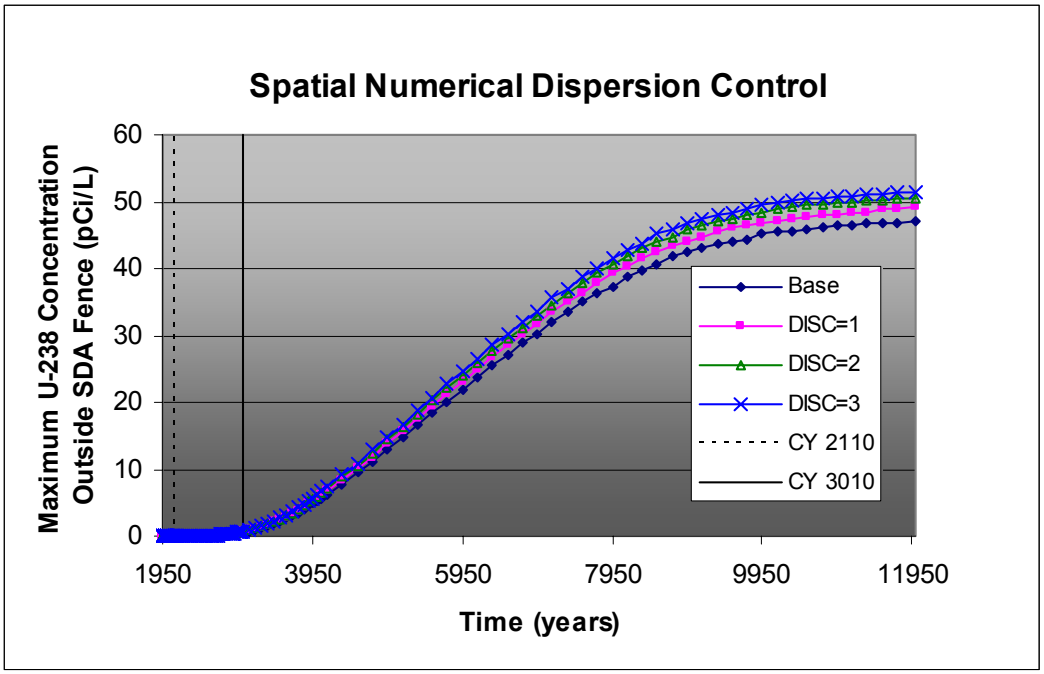

Figure H-1. Maximum simulated uranium-238 concentration outside the Subsurface Disposal Area fence with increased control of spatial numerical dispersion.

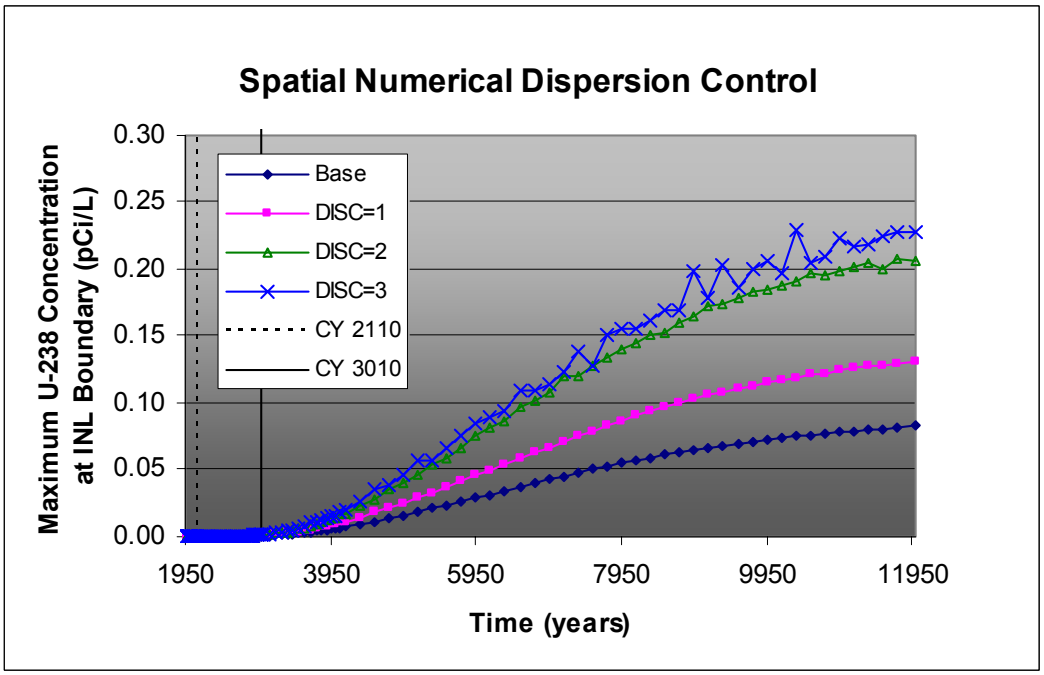

Figure H-2. Maximum simulated uranium-238 concentration along the Idaho National Laboratory Site boundary with increased control of spatial numerical dispersion.

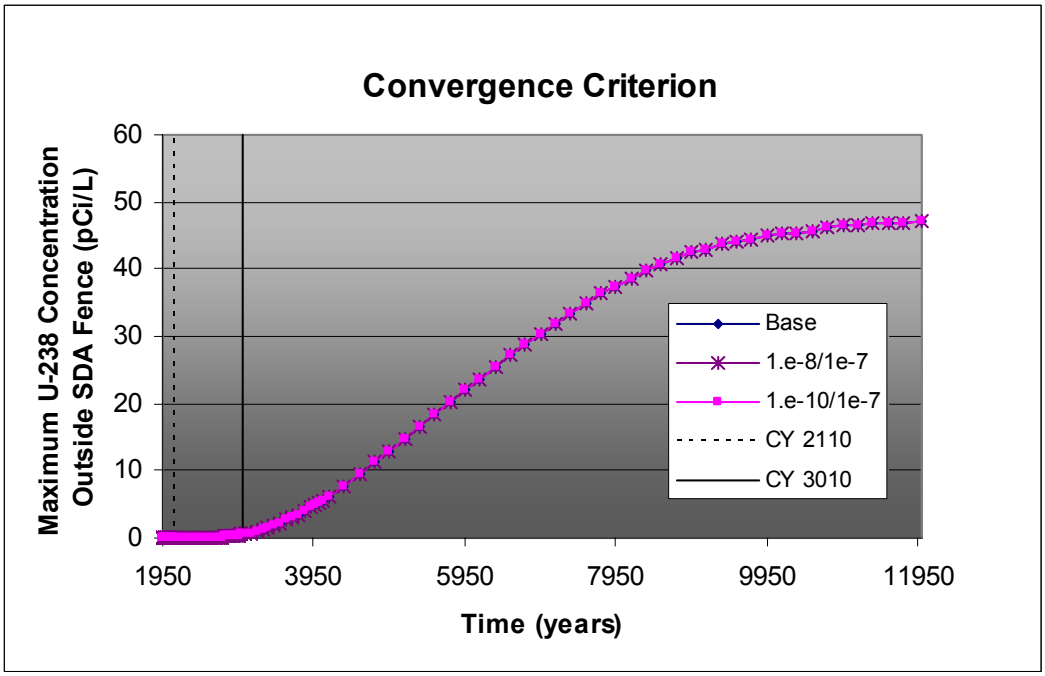

Figure H-3. Maximum simulated uranium-238 concentration outside the Subsurface Disposal Area fence with increased control of temporal numerical dispersion through smaller convergence criterion.

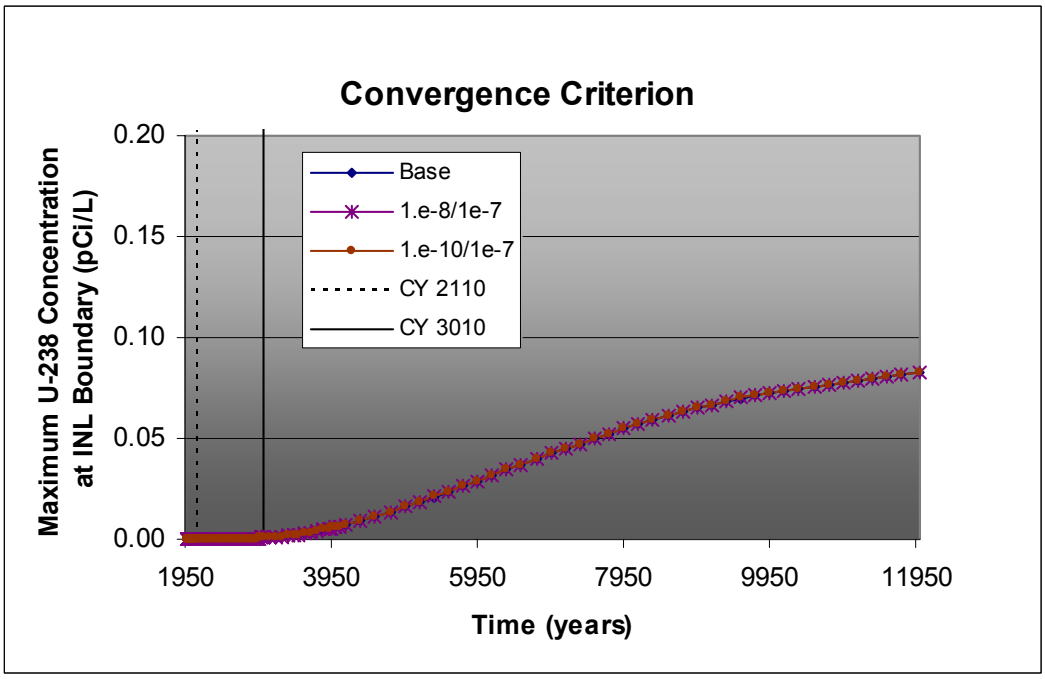

Figure H-4. Maximum simulated uranium-238 concentration along the Idaho National Laboratory Site boundary with increased control of temporal numerical dispersion through smaller convergence criterion.

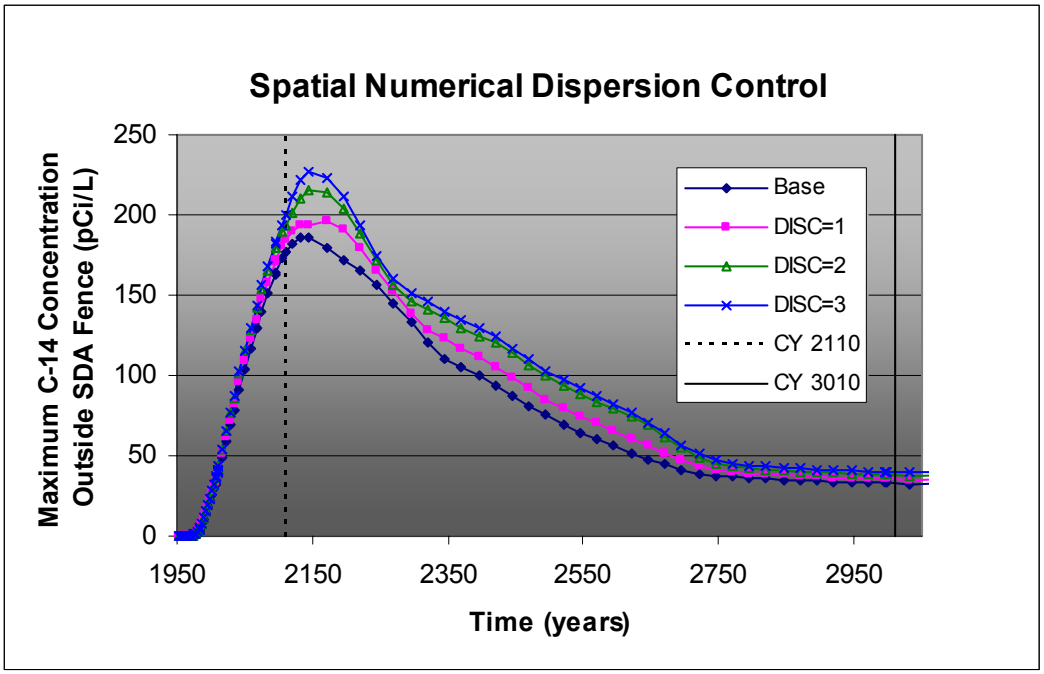

Figure H-5. Maximum simulated carbon-14 concentration outside the Subsurface Disposal Area fence with increased control of spatial numerical dispersion.

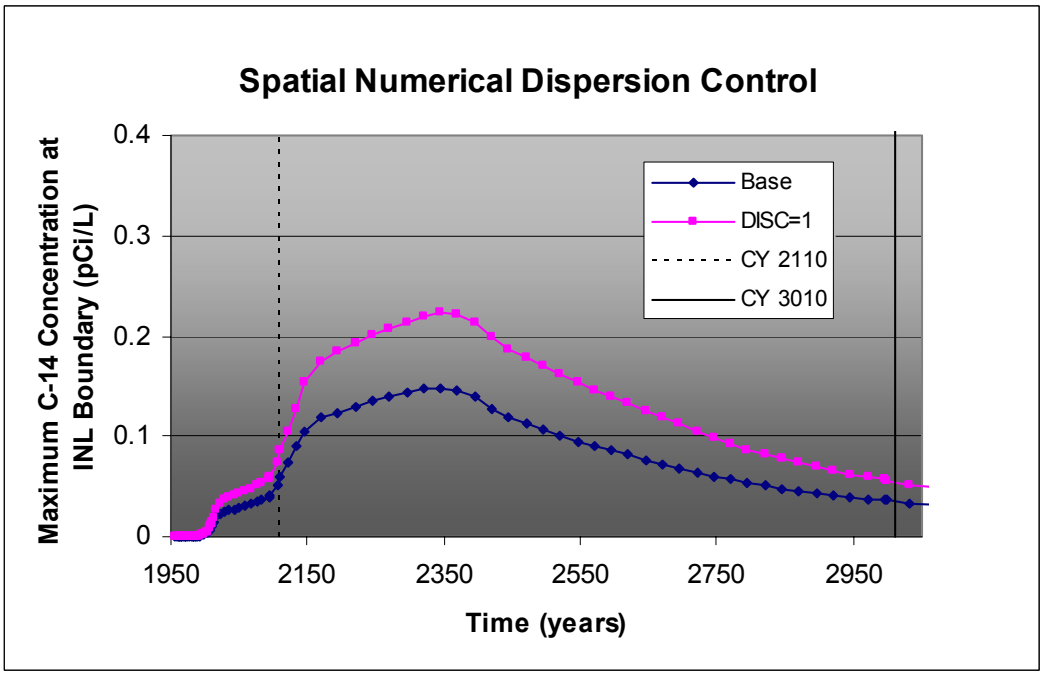

Figure H-6. Maximum simulated carbon-14 concentration along the Idaho National Laboratory Site boundary with increased control of spatial numerical dispersion.

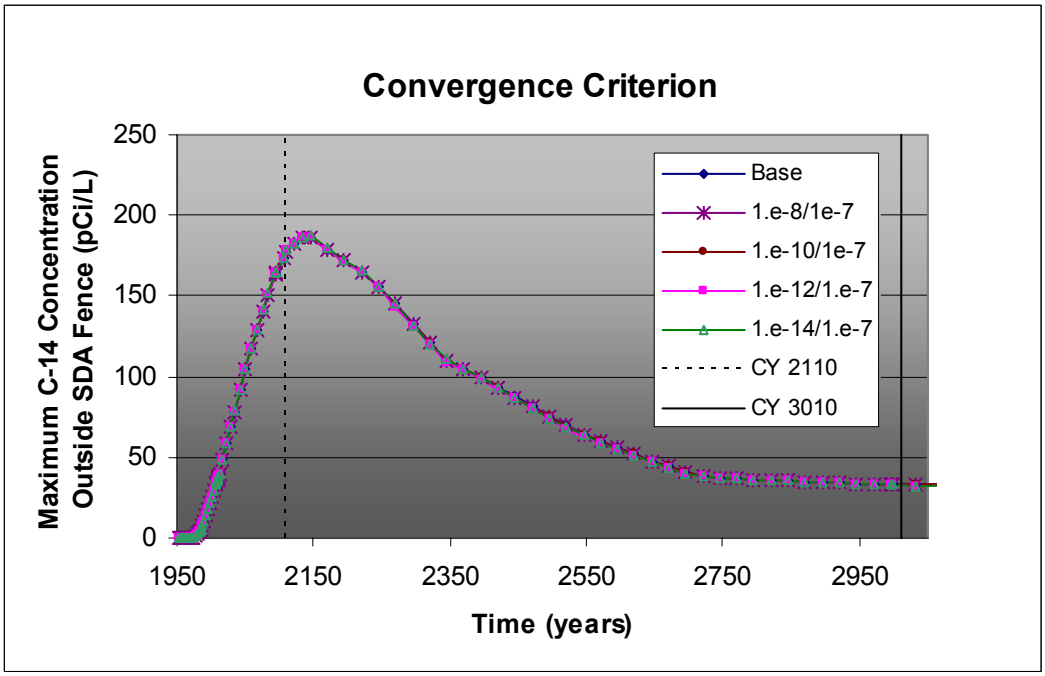

Figure H-7. Maximum simulated carbon-14 concentration outside the Subsurface Disposal Area fence with increased control of temporal numerical dispersion through smaller convergence criterion.

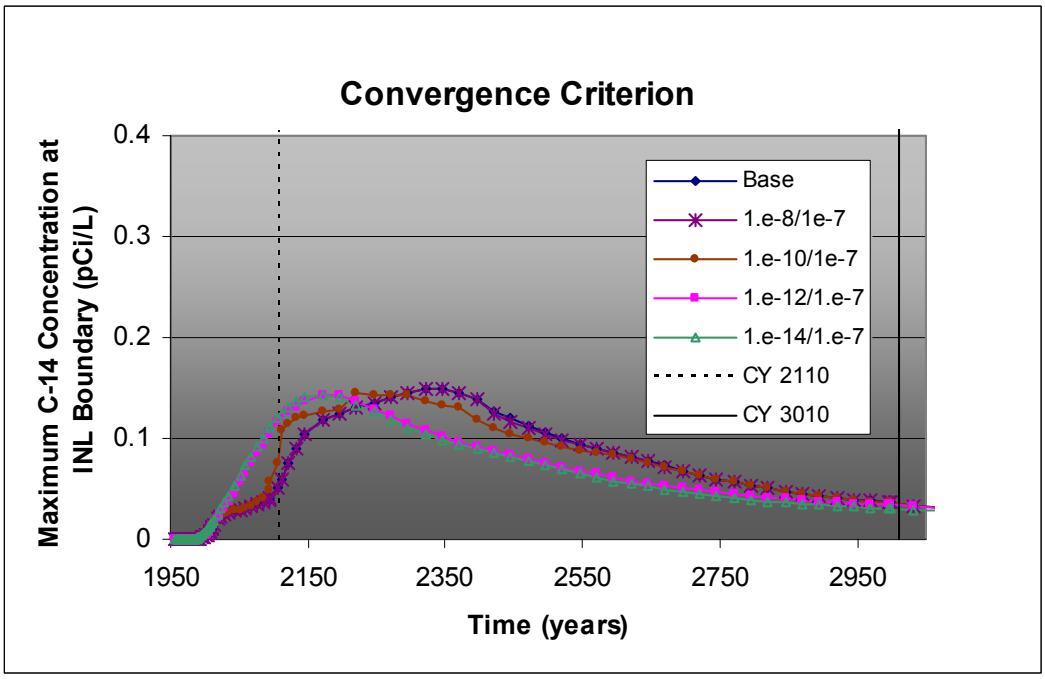

Figure H-8. Maximum simulated carbon-14 concentration along the Idaho National Laboratory Site boundary with increased control of temporal numerical dispersion through smaller convergence criterion.

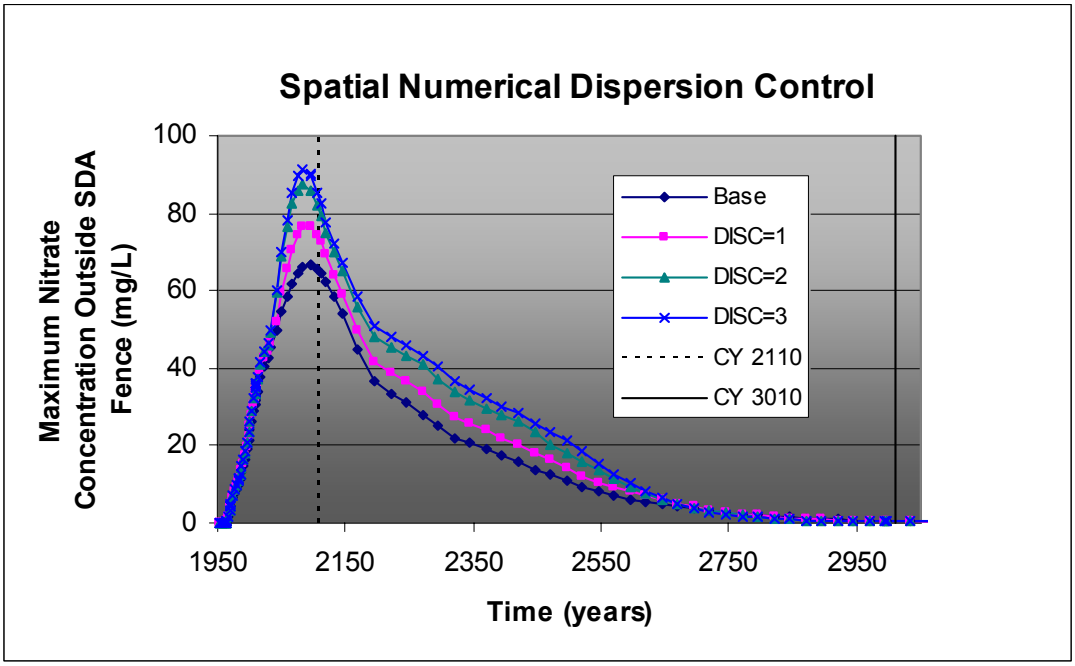

Figure H-9. Maximum simulated nitrate concentration outside the Subsurface Disposal Area fence with increased control of spatial numerical dispersion.

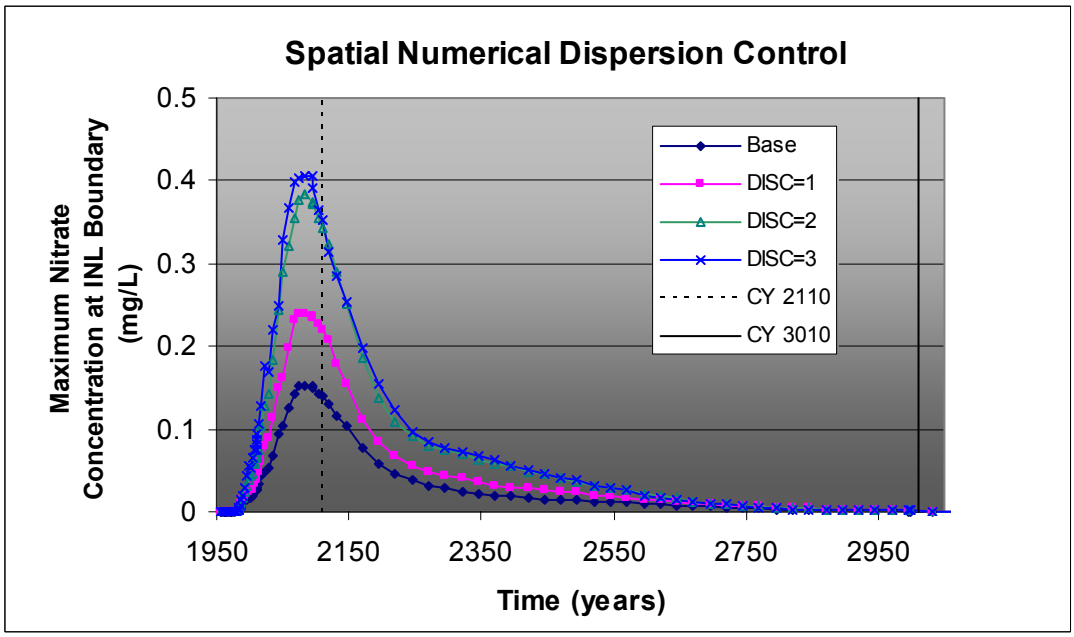

Figure H-10. Maximum simulated nitrate concentration along the Idaho National Laboratory Site boundary with increased control of spatial numerical dispersion.

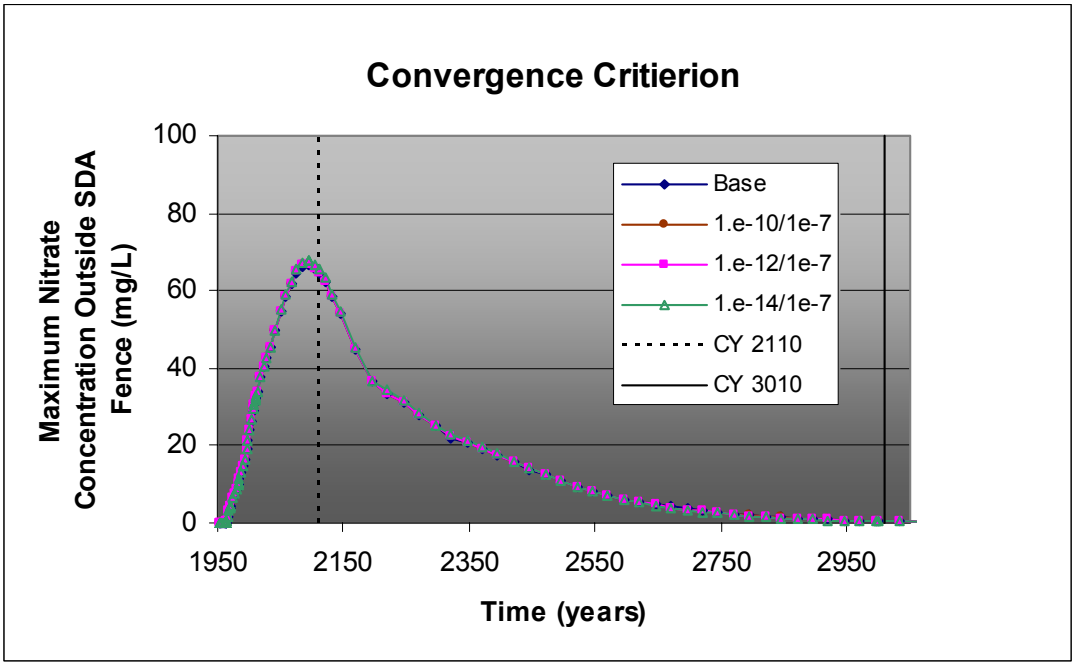

Figure H-11. Maximum simulated nitrate concentration outside the Subsurface Disposal Area fence with increased control of temporal numerical dispersion through smaller convergence criterion.

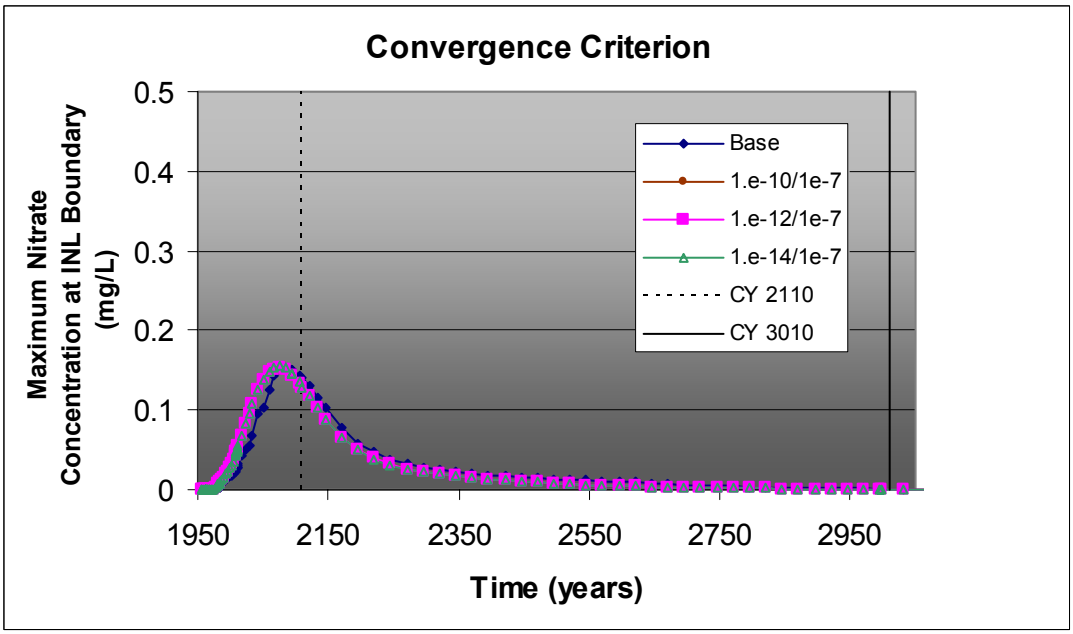

Figure H-12. Maximum simulated nitrate concentration along the Idaho National Laboratory Site boundary with increased control of temporal numerical dispersion through smaller convergence criterion.

Some observations can be made from comparing aquifer simulation results with varying levels of control on numerical dispersion. Overall, the impacts from numerical dispersion are generally small. These impacts will be evaluated quantitatively through use of scale factors. In general, impacts from spatial numerical dispersion are larger and more visible in the figures than those from temporal numerical dispersion. The impact is more apparent at the INL Site boundary than for outside the SDA fence. It is important to note that these time-history plots are for the maximum simulated concentration over time and that the location of this maximum can and does move over time. Therefore, although it appears that the total amount of mass in the system is different, the total is the same. In the C-14 simulation results, for example, the simulated maximum at any point in time with additional dispersion control is always greater than the maximum at the same point in time for the base simulation without dispersion control. As greater dispersion control is used, sometimes simulation results become unstable. This can be seen in the U-238 results at the INL Site boundary where, with the DISC parameter values of 2 and 3, the results become more variable. For the C-14 results at the INL Site boundary, the results for the DISC values of 2 and 3 are not shown because they became so unstable.

The impact from reducing convergence criterion and, therefore time step, can only be seen further away at the INL Site boundary. This was expected since the maximum concentrations extracted from the simulation results outside the SDA fence are close to the source of mass loading into the aquifer simulation, limiting the amount of numerical dispersion that could occur. Impact of the temporal numerical dispersion at the INL Site boundary location is primarily to the timing of the peak, but not to the magnitude of the peak simulated concentration.

To quantitatively assess potential impact to simulated concentrations and risks, peak values from the simulated time histories are used to create factors that can be applied to the draft RI/BRA groundwater pathway risk results to estimate the impact of numerical dispersion. These peak values were taken from simulations with improved spatial dispersion control since they yielded the largest change. Table H-1 shows peak concentrations from all simulated times and factors that would result at the two potential receptor locations, namely anywhere outside the SDA fence and along the INL Site boundary.

Table H-1. Peak concentration (pCi/L or mg/L) at receptor locations.

		U-238	C-14	Nitrate
Maximum outside Subsurface Disposal Area fence	Base	47.1	190	66.7
	With dispersion control	51.5	227	91.4
	Factor	**1.09**	**1.19**	**1.37**
Maximum along Idaho National Laboratory Site boundary	Base	0.082	0.148	0.153
	With dispersion control	0.227	0.223	0.406
	Factor	**2.75**	**1.51**	**2.65**

The maximum impact of numerical dispersion is a factor of 1.37 for outside the SDA fence and 2.75 for the INL Site boundary. To estimate impact to simulated risk, these maximum-derived factors are applied in Table H-2 to peak groundwater pathway risks for both potential receptor locations.

Table H-2. Peak 1,000-year groundwater pathway receptor risks and hazard indices for draft remedial investigation and baseline risk assessment base case and with maximum increase due to increased numerical dispersion control.

	Outside the SDA Fence Base-Case Risk	Maximum-Derived Dispersion Factor of 1.37	Along the INL Site Boundary Base-Case Risk	Maximum-Derived Dispersion Factor of 2.75
Am-241	1.E-13	2.E-13	1.E-16	4.E-16
Np-237	9.E-08	1.E-07	6.E-11	2.E-10
U-233	4.E-06	6.E-06	2.E-09	7.E-09
Th-229	3.E-07	4.E-07	1.E-10	3.E-10
Am-243	3.E-15	4.E-15	5.E-18	1.E-17
Pu-239	1.E-15	2.E-15	2.E-18	6.E-18
U-235	2.E-07	2.E-07	2.E-10	5.E-10
Pa-231	3.E-07	4.E-07	3.E-10	7.E-10
Ac-227	5.E-07	7.E-07	4.E-10	1.E-09
Pu-240	4.E-16	5.E-16	3.E-19	9.E-19
U-236	9.E-07	1.E-06	5.E-10	1.E-09
Th-232	6.E-15	8.E-15	3.E-18	8.E-18
Ra-228	4.E-14	6.E-14	2.E-17	5.E-17
Pu-238	2.E-24	2.E-24	2.E-27	6.E-27
U-234	9.E-08	1.E-07	7.E-11	2.E-10
Th-230	8.E-11	1.E-10	5.E-14	1.E-13
Ra-226	1.E-11	2.E-11	6.E-15	2.E-14
Pb-210	3.E-11	5.E-11	2.E-14	4.E-14
U-238	1.E-06	1.E-06	1.E-09	1.E-09
U-234	5.E-07	7.E-07	5.E-10	1.E-09
Th-230	5.E-10	7.E-10	3.E-13	9.E-13
Ra-226	9.E-11	1.E-10	5.E-14	1.E-13
Pb-210	2.E-10	3.E-10	1.E-13	3.E-13
Tc-99	2.E-04	3.E-04	3.E-07	9.E-07
I-129	5.E-05	7.E-05	9.E-08	3.E-07
Cl-36	1.E-06	2.E-06	2.E-09	6.E-09
C-14	1.E-05	1.E-05	8.E-09	2.E-08
Carbon tetrachloride	5.E-04	6.E-04	9.E-07	3.E-06
Methylene chloride	5.E-06	7.E-06	1.E-08	3.E-08
Nitrate	1.E+00	1.E+00	2.E-03	6.E-03
Carbon tetrachloride	1.E+01	2.E+01	2.E-02	7.E-02
Methylene chloride	3.E-02	4.E-02	5.E-05	1.E-04
Tetrachloroethylene	2.E-01	2.E-01	4.E-04	1.E-03

As can be seen from Table H-2, there are no instances of a contaminant having a peak risk in the base case that switches from below 1.E-5 to above 1.E-5. This means it is highly likely that if extensive dispersion control had been invoked all along for the aquifer simulations, there would be no difference in identification of contaminants of concern.

The impact to simulation processing time of the various dispersion control efforts was surprising. The tighter convergence controls had the expected impact of up to one order of magnitude or more increase in simulation time from the base case, which ranged from 7 hours of processing time for the C-14 simulation to 24 hours for the U-238 simulation. The impacts of invoking the higher order solution to control spatial dispersion, however, had essentially no impact on simulation time, except for the U-238 simulation, which took more than an order of magnitude longer for solutions with the TETRAD DISC parameter set to 2 or 3. In hindsight, using some improvement in dispersion control in space that would have resulted in less numerical dispersion would not have had an impact. However, since there was not a well-defined plume in the aquifer that could be definitively tied to dissolved-phase transport from the SDA, there was nothing to explicitly calibrate against and the actual dispersion is not a concern at the present time.

H-2. VADOSE ZONE DOMAIN NUMERICAL DISPERSION IMPACTS

The impact of numerical dispersion in the vadose zone simulation domain was harder to assess because of the longer simulation processing times needed to run the vadose zone model. Rather than run each of the equivalent cases that were done for the aquifer model, one simulation was run with a three-order magnitude reduction in the convergence criterion (from 1.E-7 to 1.E-10) and using the TETRAD dispersion control parameter DISC set to 3. This simulation was only performed for nitrate, since it had the highest impact in the aquifer simulation for the receptor anywhere outside the SDA fence. The vadose zone flux from this simulation was input into an aquifer simulation without any dispersion control, so the impact of controlling numerical dispersion only in the vadose zone could be seen. Figure H-13 shows the comparison of the maximum simulated concentration for a receptor anywhere outside the SDA fence for the base simulation and a simulation with dispersion control. Figure H-14 likewise shows impacts on the maximum simulated concentration along the INL Site boundary.

Figures H-13 and H-14 show that the net effect on maximum simulated aquifer concentrations from reducing numerical dispersion in the vadose zone is very slight. The magnitude for the receptor location anywhere outside the SDA fence is essentially unchanged and timing is accelerated just slightly. At the INL Site boundary receptor location, the magnitude increases very slightly.

Given the very slight impacts of numerical dispersion in the vadose zone, an additional multiplicative factor to apply to the groundwater pathway risks from the draft RI/BRA was not estimated. Overall, from a perspective of both the vadose zone and aquifer simulation domains, the impact of numerical dispersion on the groundwater pathway results was minor.

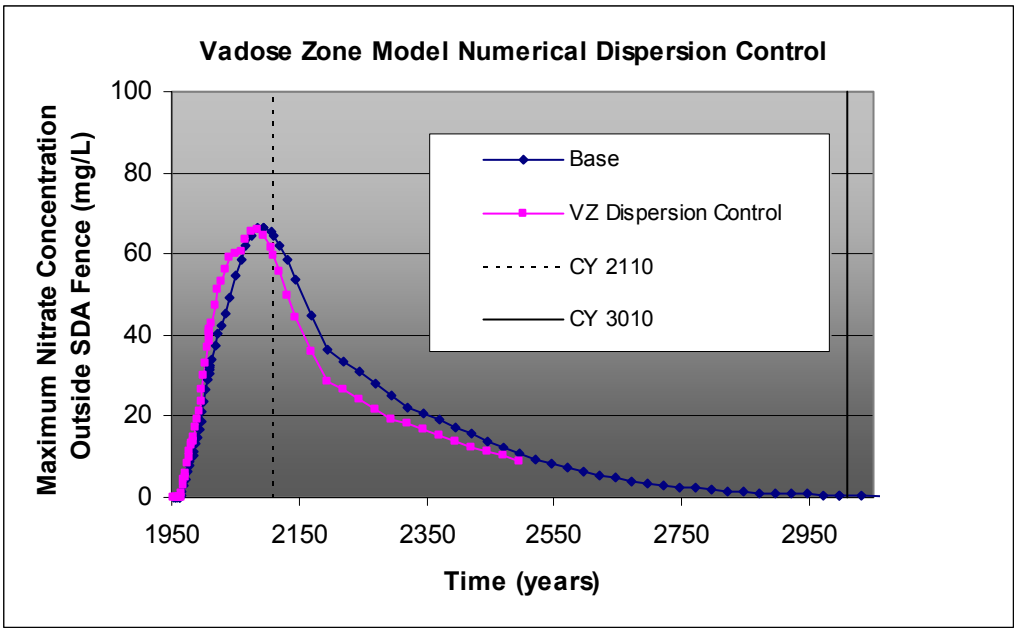

Figure H-13. Maximum simulated nitrate concentration outside the Subsurface Disposal Area fence with increased control of both spatial and temporal numerical dispersion in the vadose zone simulation.

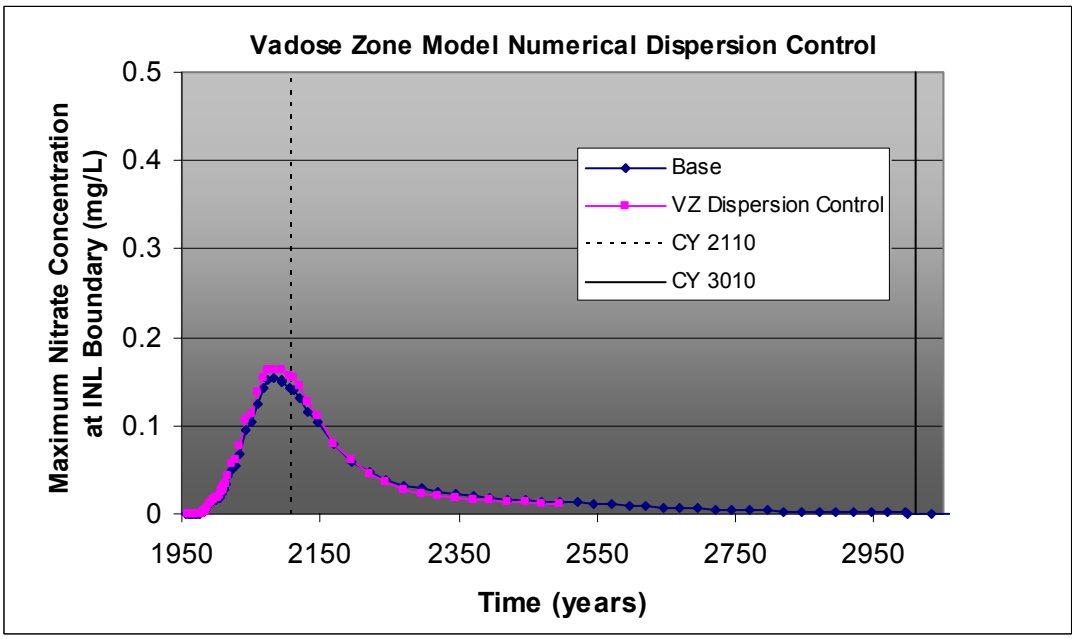

Figure H-14. Maximum simulated nitrate concentration along the Idaho National Laboratory Site boundary with increased control of temporal numerical dispersion through smaller convergence criterion.